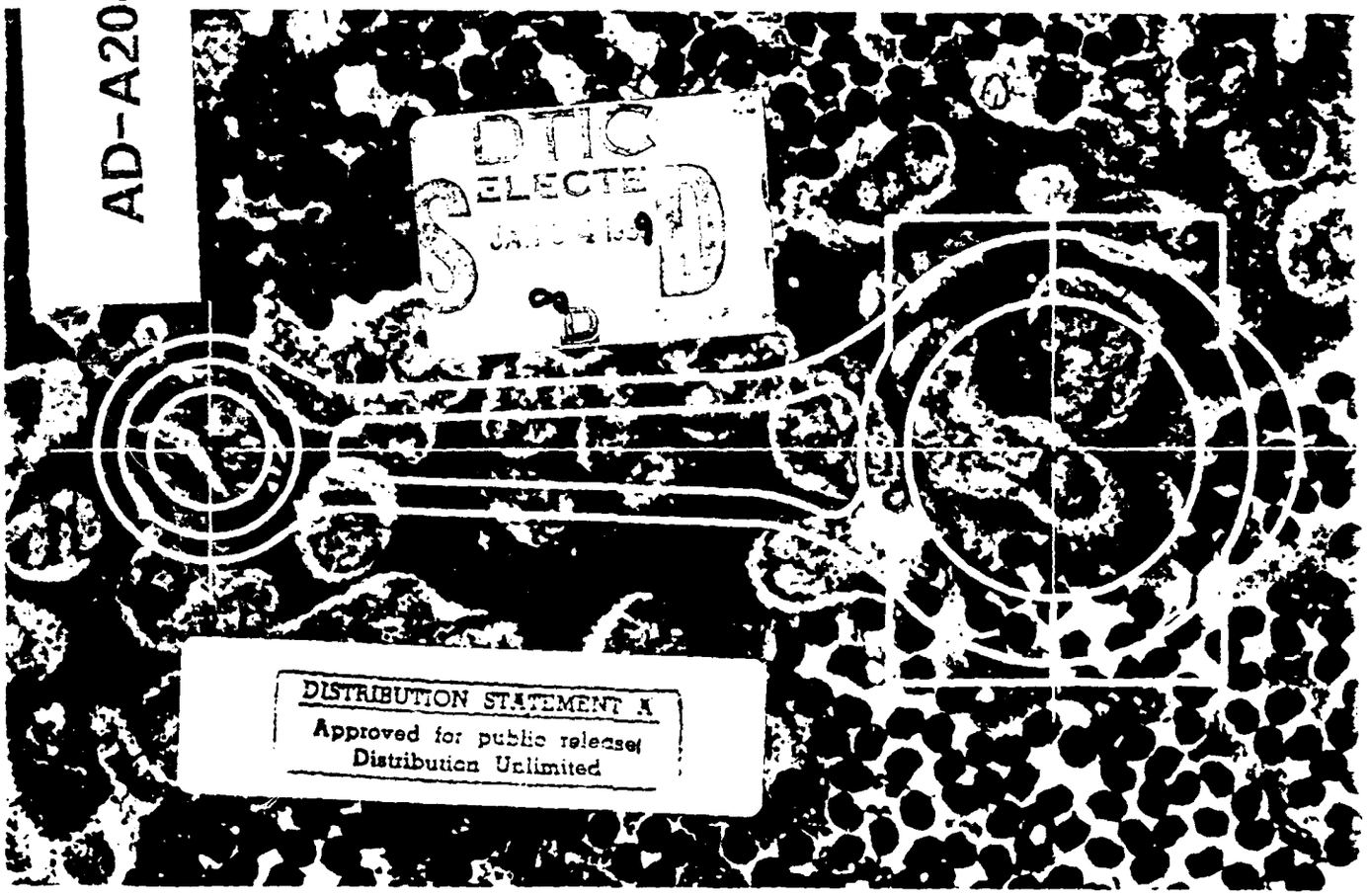
DTIC FILE COPY

25297.2-MS-CF
(1)

CAST REINFORCED METAL COMPOSITES

AD-A204 642

Edited by S. G. Fishman, A. K. Dhingra



CONFERENCE PROCEEDINGS

ASM INTERNATIONAL™

UNCLASSIFIED

SECURITY CLASSIFICATION OF THIS PAGE (When Data Entered)

REPORT DOCUMENTATION PAGE		READ INSTRUCTIONS BEFORE COMPLETING FORM
1. REPORT NUMBER ARO 25297.1-MS-CF	2. GOVT ACCESSION NO. N/A	3. RECIPIENT'S CATALOG NUMBER N/A
4. TITLE (and Subtitle) 1988 World Materials Congress Proceedings 24-30 Sep 88, Chicago Eight Volumes		5. TYPE OF REPORT & PERIOD COVERED Final 1 Oct 87 - 31 Mar 89 6. PERFORMING ORG. REPORT NUMBER N/A
7. AUTHOR(s) S. G. Fishman and A. K. Dhingra, editors		8. CONTRACT OR GRANT NUMBER(s) DAAL03-87-G-0128
9. PERFORMING ORGANIZATION NAME AND ADDRESS ASM International Detroit, MI 48202		10. PROGRAM ELEMENT, PROJECT, TASK AREA & WORK UNIT NUMBERS N/A
11. CONTROLLING OFFICE NAME AND ADDRESS U. S. Army Research Office P. O. Box 12211 Research Triangle Park, NC 27709		12. REPORT DATE 1988 13. NUMBER OF PAGES
14. MONITORING AGENCY NAME & ADDRESS(if different from Controlling Office)		15. SECURITY CLASS. (of this report) Unclassified 15a. DECLASSIFICATION/DOWNGRADING SCHEDULE

16. DISTRIBUTION STATEMENT (of this Report)

Submitted for announcement only.

17. DISTRIBUTION STATEMENT (of the abstract entered in Block 20, if different from Report)

18. SUPPLEMENTARY NOTES

The view, opinions, and/or findings contained in this report are those of the author(s) and should not be construed as an official Department of the Army position, policy, or decision, unless so designated by other documentation.

19. KEY WORDS (Continue on reverse side if necessary and identify by block number)

Composites, Sheet Steels, Electronic Materials, Wear Resistance, Precipitation Phenomena, High Integrity Castings, Inclusions, HSLA Steels

20. ABSTRACT (Continue on reverse side if necessary and identify by block number)

The proceedings of the 1988 World Materials Congress were published by ASM and consits of the following volumes:

1. Microalloyed HSLA Sttels Conference Proceedings
2. Inclusions and Their Influence on Material Behavior
3. High Integrity Castings
4. Precipitation Phenomena: Deformation and Aging
5. Wear Resistance of Metals and Alloys

(over)

DD FORM 1 JAN 73 1473 EDITION OF 1 NOV 65 IS OBSOLETE

UNCLASSIFIED

SECURITY CLASSIFICATION OF THIS PAGE (When Data Entered)

88 12 28 025

ABSTRACT CONTINUED:

6. Electronic Materials and Processing
7. Corrosion-Resistant Automotive Sheet Steels
8. Cast Reinforced Metal Composites

CAST REINFORCED METAL COMPOSITES

Proceedings of the

International Symposium on Advances in Cast Reinforced Metal Composites

Held in conjunction with the
1988 World Materials Congress
Chicago, Illinois, USA
24-30 September 1988

Edited by
S. G. Fishman and A. K. Dhingra

Sponsored by
ASM/TMS Metal Matrix Composites Committee

Published by

ASM INTERNATIONAL

The Publication of this Conference Proceedings of the 1988 World Materials Congress has been made possible by the generous contributions of the U.S. Bureau of Mines, The U.S. Army Research Office, Cytemp Specialty Steel, ELETROMETAL S.A., and Dofasco Inc.

Copyright © 1988
by
ASM INTERNATIONAL™
All Rights Reserved

No part of this book may be reproduced, stored in a retrieval system, or transmitted, in any form or by any means, electronic, mechanical photocopying, recording, or otherwise, without the prior written permission of the publisher. No warranties, express or implied, are given in connection with the accuracy or completeness of this publication and no responsibility can be taken for any claims that may arise.

Nothing contained in this book is to be construed as a grant of any right or manufacture, sale, or use in connection with any method, process, apparatus, product, or composition, whether or not covered by letters patent or registered trademark, nor as a defense against liability for the infringement of letters patent or registered trademark.

Library of Congress Catalog Card Number: 88-071717
ISBN: 0-87170-339-4
SAN: 204-7586

Printed in the United States of America

ORGANIZING COMMITTEE

Program Organizers

Dr. Steven Fishman
Office of Naval Research
Co-Chairman

Dr. Ashok Dhingra
DuPont Company
Co-Chairman

Dr. James Cornie
Massachusetts Institute of Technology

Dr. Irwin Greenfield
University of Delaware

Prof. Henry Rack
Clemson University

Prof. Pradeep Rohatgi
University of Wisconsin-Milwaukee

Dr. Ram Bhagat
The Pennsylvania State University

Dr. Anil Sachder
General Motors Research Laboratories

Dr. Mehmat Gungor
Westinghouse R&D Center

Dr. William Harrigan
DWA Composites Specialties, Inc.

Dr. Susan Schuon
General Motors Research Laboratories

Dr. Salim Dermarkar
Cegedur Pechiney

Dr. David Lloyd
Alcan International Ltd.

Sold by:
ASM International
9639 Kinsman Road
Metals Park, OH 44073
Price:

Accesion For
NTIS CRA&I
DTIC TAB
Unannounced
Justification
By 85.00 per call
Distribution /
Availability Codes
Dist | Avail and/or Special
A-1 21

DTIC COPY INSPECTED 6

PREFACE

This volume contains the text of papers presented at the "International Symposium on Advances in Cast Reinforced Metal Composites," held in Chicago, Illinois, September 26-30, 1988, as part of the ASM INTERNATIONAL "World Materials Congress."

Fiber reinforced metals offer the potential to be the next generation of advanced composite materials offering many advantages over fiber reinforced plastics including higher temperature capability, superior environmental stability, better transverse, shear, and fatigue properties. Metals reinforced with particles, whiskers, short or continuous fibers of stiff, strong ceramics have been investigated for the past two decades. Although many matrices, including lead, zinc, copper, steel, nickel, and silver have been considered, the greatest effort by far has been with the lighter alloys, aluminum and magnesium. One of the major problems limiting the development of metal matrix composites has been the lack of a practical method for fabrication of composites. A variety of fabrication methods have been investigated to prepare aluminum and magnesium composites. These include hot pressing of blended powders, both above and below the liquidus temperature, diffusion bonding of thin metal foils containing wrapped fibers, or fibers precoated with matrix alloy, liquid infiltration of fiber preforms or fiber tows which are subsequently pressed into simple sheets, plasma spraying, superplastic forming, electroplating, electroforming, mechanical alloying, extrusion, etc. The mechanical behavior of most of these composites are very attractive, in terms of enhanced stiffness, strength, abrasion resistance, creep resistance, high temperature properties, and lower density. In spite of this, however, the industrial development of these materials has remained limited. The two major reasons for the lack of industrial application of this promising class of materials has been their cost and the complexity of fabrication using many of the processes mentioned above.

In the 1960's and 1970's considerable R&D resources were expended both by the DOD/NASA and the industry to develop Boron-Aluminum composite system using diffusion bonding technology. However, high cost of boron fibers combined with relatively high cost of composite fabrication limited applications to aerospace in space shuttle tubes. A major milestone in fiber reinforced metal matrix composite technology was reached in 1982 when Toyota Motor Corporation demonstrated the commerical production and use of the first metal matrix composite piston insert for automotive application in the diesel engine car. This metal matrix piston insert made of alumina-silica fiber reinforced aluminum composite by casting technology created large interest in "Cast Reinforced Metal Composites" for potential automotive engine applications, such as pistons, connecting rods, wrist pins, valves, valve seats, brake calibers, engine blocks, cranks, etc. In the past few years, a number of potentially low cost processing methods based on casting technologies have been demonstrated which also have the capability of forming complex-shaped parts. Several composites casting technologies based on liquid metal processing, involving infiltration of continuous or staple fiber preforms, casting of slurries of ceramic particles in molten matrices, or inclusion of ceramic particles in streams of liquid metal by various rapid solidification techniques are being investigated. In the future, development of low cost stiff inorganic fibers combined with commerically proven metal casting technologies (such as squeeze casting, die casting, centrifugal casting, continuous casting, slush casting) for practical composite fabrication of near net shape metal composite components will open up new market opportunities for the metal industry.

The underlying philosophy of this symposium was to bring together the technical communities from academic and industrial laboratories who are involved in fundamental studies, processing methodologies, and applications analyses of metal composites, specifically for the purpose of discussing cast composites. Initially eight sessions were planned, but because of the overwhelming response, it was necessary to increase the number of sessions to ten. The symposium was truly international in nature, in that participants from twelve different countries presented papers.

In this book, the ten sessions of the symposium are redistributed into five sections and an overview, describing the historical interest in metal composites. Section I is concerned with "Fundamentals of Cast Composites," and includes wetting theory, kinetics of infiltration, metal/ceramic interfacial considerations, and processing models.

Section II is entitled "Squeeze Casting of Metal Composites," and concentrates on processing methodology of casting under pressure.

Section III, "Microstructure/Property Relationships of Cast Composites," includes tensile, creep, and other mechanical properties of cast composites. This section also includes comparison of properties of cast and powder composites, the effect of manufacturing parameters, and the relation between specific microstructural variations and mechanical behavior.

Section IV, "Mechanical/Thermal Behavior of Cast Composites," includes the effect of fiber orientation, matrix alloying, secondary treatments, such as heat treatment, thermal cycling, etc., on mechanical behavior. This section also includes papers on residual stresses. Deformation processing and ultrasonic measurements.

The last section, Section V entitled "Tribology, Damping, Corrosion and Erosion of Cast Composites," covers the nonmechanical properties of cast metal composites.

This symposium volume is prepared from camera-ready manuscripts. In order to meet the time constraint imposed by ASM INTERNATIONAL, so that the book would be available at the time of the conference, it was not possible to prepare a more aesthetically pleasing endeavor. It was felt, however, that it was more important to make this state-of-the-art information available to the many attendees at the time of the World Congress. This is the sole compendium concerned specifically with cast metal composites to date. We thank the individual authors for completing their papers within the extremely stringent time necessitated by the publishing deadline.

The symposium chairmen were S. G. Fishman, Office of Naval Research; A. K. Dhingra, DuPont Company, Composites Division; M. Gungor, Westinghouse Electric Corporation; M. Suery, Institute Nationale Polytechnique de Grenoble; S. Dermarkar, Cegedur Pechiney; A. Sachder, General Motors Research Laboratores; D. Lloyd, Alcan International; S. Schuon, General Motors; I. Greenfield, University of Delaware; W. Harrigan, DWA Composites Specialties Inc.; R. Bhagat, University of Pennsylvania; J. Quenisset, Laboratoire de Chimie du Solide du CNRS; J. Dinwoodie, Imperial Chemical Industries; H. Rack, Clemson University; J. Cornie, Massachusetts Institute of Technology; H. Fukunaga, Hiroshima University; P. Rohatgi, University of Wisconsin; and M. Ruch, HYDRO ALUMINUM Metallurgical R&D Center.

Steven G. Fishman
Office of Naval Research
Arlington, Virginia

Ashok K. Dhingra
DuPont Company
Wilmington, Delaware

September 1988

TABLE OF CONTENTS

INTRODUCTION

Metal Matrix Composites — An Overview 1
A. Kelly, University of Surrey, Guildford, Surrey, UK

FUNDAMENTALS OF CAST COMPOSITES

Kinetics of Fiber Preform Infiltration 7
A. Mortensen, V. J. Michaud, Massachusetts Institute of Technology, Cambridge, MA, USA; L. Masur, American Superconductor Corp., Cambridge, MA, USA; J. A. Cornie, M. C. Flemings, Massachusetts Institute of Technology, Cambridge, MA, USA

Modelling of Particle Segregation During Centrifugal Casting of Al-Matrix Composites 15
L. Lajoye, M. Suéry, Institut National Polytechnique de Grenoble, Saint Martin D'Heres, France

Wettability of SiC Particulates with Zn and Zn-Al Alloys 21
T. R. Fletcher, J. A. Cornie, K. C. Russell Massachusetts Institute of Technology, Cambridge, MA, USA

The Wetting Kinetics of Aluminum and Its Alloys on Single-Crystal SiC 27
V. Laurent, D. Chatain, Domaine Universitaire, Saint Martin D'Heres, France; X. Dumant, Cegedur Pechiney, Centre de Recherches de Voreppe, Voreppe, France; N. Eustathopoulos, Domaine Universitaire, Saint Martin D'Heres, France

Bonding of SiC and Aluminum 33
S. Li, University of Maryland, College Park, MD, USA; P. Jena, Virginia Commonwealth University, Richmond, VA, USA; R. J. Arsenault, University of Maryland, College Park, MD, USA

Solidification Processing of an Aluminum/Alumina Composite 39
M. N. Gungor, Westinghouse R&D Center, Pittsburgh, PA, USA; J. A. Cornie, M. C. Flemings, Massachusetts Institute of Technology, Cambridge, MA, USA

Solidification Processing of Particulate Ceramic-Aluminum Alloy Composites 47
T. Z. Kattamis, University of Connecticut, Storrs, CT, USA; J. A. Cornie, Massachusetts Institute of Technology, Cambridge, MA, USA

Anisotropy of Friction and Wear of Fiber Reinforced Epoxy-Resins 53
M. Cyffka, E. Hornbogen, Institut für Werkstoffe Ruhr-Universität Bochum, Bochum, FRG

Transfer of Particles and Fibres from Gas to Liquid During Solidification Processing of Composites 61
P. K. Rohatgi, R. Asthana, University of Wisconsin-Milwaukee, Milwaukee, WI, USA

Chemical Analysis and Bonding at the Fiber-Matrix Interface in Model Aluminum Matrix Composites 67
Y. Le Petitcorps, T. Stephenson, F. Girot, R. Naslain, Laboratoire de Chimie du Solide CNRS, Université de Bordeaux I, Talence, France

Studies of Interfaces in Light Metal Matrix Composites by Transmission Electron Microscopy 71
J. Taftø, K. Kristiansen, Norsk Hydro, Porsgrunn, Norway; H. Westengen, A. Nygard, Hydro Magnesium, Porsgrunn, Norway; J. B. Borradaile, Hydro Aluminum, Håvik, Norway; D. O. Karlsen, University of Oslo, Oslo, Norway

Porosity in Foundry Composites Prepared by Vortex Method 77
S. Ray, University of Roorkee, Roorkee, India

Wetting of Solids by Liquid Metals in Relation to Squeeze Casting of MMC's 81
F. Delannay, Université Catholique de Louvain, Louvain-La-Neuve, Belgium; L. Froyen, A. Deruyttere, Katholieke Universiteit Leuven, Leuven, Belgium

Mixing Quality Modeling in the Manufacture of Cast Metal Matrix Particulate Composites 85
P. K. Rohatgi, R. Asthana, M. A. Khan, University of Wisconsin-Milwaukee, Milwaukee, WI, USA; P. Ostermier, AVCO Textron Inc., New Haven, CT, USA

SQUEEZE CASTING OF METAL COMPOSITES

A Literature Survey on Fabrication Methods of Cast Reinforced Metal Composites 93
Zhang Zhu, Chongqing University, Chongqing, Sichuan, P.R.China

Squeeze Casting Processes for Fiber Reinforced Metals and Their Mechanical Properties 101
H. Fukunaga, Hiroshima University, Saijo, Higashi-Hiroshima, Japan

Mechanical Properties of Aluminum Alloys Reinforced with Continuous Fibers and Dispersoids 109
S. Yamada, S. Towata, H. Ikuno, Toyota Central R&D Labs., Inc., Nagakute, Aichi, Japan

Manufacturing of Composites by Squeeze Casting 115
S. K. Verma, J. L. Dorcic, IIT Research Institute, Chicago, IL, USA

High Performance Metal-Matrix Components Manufactured by Squeeze-Casting 127
J. Charbonnier, S. Dermarkar, M. Santarini, Pechiney, Voreppe Research Center, Voreppe, France; J. Fages, M. Sabatie, Aérospatiale, Chatillon s/s Bagneux, France

Effect of Squeeze Casting Conditions on Infiltration of Ceramic Preforms 133
J. M. Quenisset, R. Fedou, F. Girot, Y. Le Petitcorps, Laboratoire de Chimie du Solide CNRS, Université de Bordeaux I, Talence, France

Solidification Under Pressure: Aluminum and Zinc Alloys Containing Discontinuous SiC Fibre 139
A. A. Das, A. J. Clegg, Loughborough University of Technology, UK; B. Zantout, Government of Syria, Damascus, Syria; M. M. Yakoub, University of Damascus, Damasus, Syria

Squeeze Casting and Property Evaluation of Alumina Fibre Reinforced Aluminium-Silicon Alloy Matrix Composite 149
S. Ahmed, V. Gopinathan, P. Ramakrishnan, Indian Institute of Technology, Bombay, India

Microstructures and Properties of Zinc-Alloy Matrix Composite Materials 155
J. A. Cornie, Massachusetts Institute of Technology, Cambridge, MA, USA; R. Guerriero, L. Meregalli, I. Tangerini, Nuova SAMIM Centro Richerche Venizia, Venizia, Italy

Partial Remelting and Forming of Al-Si/SiC Composites in Their Mushy Zone 167
M. A. Bayoumi, M. Suéry, Institut National Polytechnique de Grenoble, Saint Martin D'Heres, France

Liquid Pressure Forming of Engineered Metal Matrix Composites 173
N. Mykura, Yeovil, Somerset, England

High Pressure Squeeze Casting of Unidirectional Graphite Fiber Reinforced Aluminum Matrix Composites 179
R. J. Sample, R. B. Bhagat, M. F. Amateau, The Pennsylvania State University, State College, PA, USA

Squeeze Cast Metal Matrix Composites: Evaluation of Their Strength, Damping Capacity and Corrosion Resistance 185
R. Bhagat, M. F. Amateau, J. C. Conway, Jr., J. M. Paulick, J. M. Chisholm, J. M. Parnell, D. G. Siedensticker, The Pennsylvania State University, State College, PA, USA

System Optimization for Squeeze Cast Composites 195
C. R. Cook, D. I. Yun, W. H. Hunt, Jr., Alcoa Laboratories, Alcoa Center, PA, USA

MICROSTRUCTURE/PROPERTY RELATIONSHIPS OF CAST COMPOSITES

Mechanical Properties of SiC Whisker Reinforced Aluminum Alloys Fabricated by Pressure Casting Method 205
T. Kobayashi, M. Yosino, H. Iwanari, M. Niinomi, Toyohahsi University of Technology, Toyohahsi, Japan; K. Yamamoto, Tokyo Yogyo Co., Ltd., Tajimi, Japan

Tensile and Creep Microstructures of Cast 2014 Al/20 v% SiCp Composite 211
M. N. Gungor, P. K. Liaw, M. G. Burke, Westinghouse Research and Development Center, Pittsburgh, PA, USA

Enhancement in the Properties of a Squeeze-Cast Aluminium Magnesium Alloy Containing Delta-Alumina Fibre 217
A. A. Das, A. J. Clegg, Loughborough University of Technology, Loughborough, Leicestershire, UK; B. Zantout, Government of Syria, Damascus, Syria

Effect of Manufacturing Variables on the Structure and Properties of Squeeze Cast C/Al MMC's 225
A. P. Diwanji, I. W. Hall, University of Delaware, Newark, DE, USA

The Strengthening of PM vs. Melted SiC/Al Composites 231
R. J. Arsenault, S. B. Wu, University of Maryland, College Park, MD, USA

Dendritic Segregation in Particle-Reinforced Cast Aluminum Composites 237
J. W. McCoy, F. E. Wawner, University of Virginia, Charlottesville, VA, USA

Modification and Refinement of Silicon in Cast Al-Si-Graphite Particle Composites 243
S. Das, S. B. Prasad, T. K. Dan, C.S.I.R., Bhopal, India; P. K. Rohatgi, University of Wisconsin-Milwaukee, Milwaukee, WI, USA

Influence of Solidification Conditions on Segregation of Aluminum-Silicon Carbide Particle Composites 249
P. K. Rohatgi, F. M. Yarandi, Y. Liu, University of Wisconsin-Milwaukee, Milwaukee, WI, USA

Structure and Properties of Liquid Metal Processed SiC Reinforced Aluminum 257
M. Skibo, Dural Aluminum Composites Corporation, San Diego, CA, USA; P. L. Morris, D. J. Lloyd, Alcan International Ltd., Kingston, Ontario, Canada

Properties of Shape Cast Al-SiC Metal Matrix Composites 263
D. J. Lloyd, B. Chamberlain, Alcan International Ltd., Kingston, Ontario, Canada

MECHANICAL/THERMAL BEHAVIOR OF CAST COMPOSITES

Effect of Matrix Strengthening and Fiber Orientation on the Mechanical Behavior of Cast Boron-Magnesium Composites 271
A. K. Dhingra, DuPont Company, Wilmington, DE, USA;
L. B. Gulbransen, Washington University, St. Louis, MO, USA

Mechanical Properties and Microstructure of C/Mg Composites Subjected to Thermal Exposure and Thermal Cycling 281
S. J. Swindlehurst. I. W. Hall, University of Delaware, Newark, DE, USA

Mechanical Behavior of High-Conductivity In-Situ Ultrafine Microcomposites 289
R. W. Hayes, J. L. Yuen, N. E. Paton, G. Schnittgrund, Rockwell International/Rocketdyne Division, Canoga Park, CA, USA

Study of Acoustic Emission Due to the Multiple Fibre Fracture in A Single SiC (CVD) Filament-Aluminum Matrix Model Composite 297
T. Boniface, P. Fleischmann, R. Fougeres, P. F. Gobin, D. Rouby, Groupe d' Etude de Metallurgie Physique et de Physique des Matériaux, France; F. Lonca-Hugat, M. Boivin, Laboratoire de Mecanique des Solides, France

Thermal Cycling of Alumina (FP)/Magnesium Alloy Composite 301
C. S. Lee. Michigan State University, East Lansing, MI, USA; K. K. Chawla, New Mexico Institute of Mining and Technology, Socorro, NM, USA;
J. M. Rigsbee, University of Illinois, Urbana, IL, USA;
M. Pfeifer, Northwestern University, Evanston, IL, USA

The Effect of Fibre/Matrix Interfaces on the Age-Hardening Characteristics of δ-Alumina Fibre Reinforced AA6061 309
C. M. Friend, I. Horsfall, S. D. Luxton, R. J. Young, Royal Military College of Science (Cranfield), Swindon Wilts, England

Residual Stresses in Continuous Graphite Fiber Al Metal Matrix Composites 317
Hun Sub Park, Gui Sheng Zong, H. L. Marcus, The University of Texas at Austin, Austin, TX, USA

Deformation Mechanism Mapping of SiC/Al Metal Matrix Composite Materials 321
F. R. Tuler, J. T. Beals, C. Demetry, D. Zhao, Worcester Polytechnic Institute, Worcester, MA, USA; D. J. Lloyd, Alcan International Ltd., Kingston, Ontario, Canada

Effect of Rapid Solidification on Microstructure and Properties of Cast SiC_p/Al Metal Matrix Composites 327
W. R. Loué, W. H. Kool, Delft University of Technology, Delft, The Netherlands

Effect of Magnesium Concentration on the Shear Strength of Unidirectional Alpha-Alumina/Aluminum Composites 335
W. D. Johnston, I. G. Greenfield, University of Delaware, Newark, DE, USA

Ultrasonic Techniques in Evaluation of Metal Matrix Particulate Composites 341
P. K. Rohatgi, University of Wisconsin-Milwaukee, Milwaukee, WI, USA;
S. Raman, Indian Institute of Technology, Madras, India; B. S. Majumdar, Battelle Memorial Institute, Columbus, OH, USA; A. Banerjee, Institute für Metallforschung, West Berlin, FRG

TRIBOLOGY, DAMPING, CORROSION AND EROSION OF CAST COMPOSITES

Friction, Wear and Interfacial Temperatures in Metal-Graphite Composites 347
D. Kuhlmann-Wilsdorf, D. D. Makel, University of Virginia, Charlottesville, VA, USA; N. A. Sondergaard, D. W. Maribo, David Taylor Naval Ship Research and Development Center, Annapolis, MD, USA

Influence of Reinforcement on the Tribological Behaviour of an Aluminum Alloy 361
A. P. Monteiro Baptista, A. Barbedo de Magalhães, R. Neto, J. Duarte, Universidade do Porto, Porto, Portugal

Tribological Behavior of Al Alloy-Graphite and Al Alloy-Microcrystalline Carbon Particle Composites 367
P. K. Rohatgi, N. B. Dahotre, Y. Liu, M. Yin, T. L. Barr, University of Wisconsin-Milwaukee, Milwaukee, WI, USA

Damping Capacity of Aluminum Alloy Matrix Composites 375
P. K. Rohatgi, R. Asthana, A. Kumar, University of Wisconsin-Milwaukee, Milwaukee, WI, USA; D. Nath, Banaras Hindu University, Varansi, India; S. Schroeffer, Control Data Corporation, Minneapolis, MN, USA

Corrosion of Metal Matrix Composites 383
T. Otani, Komatsu Ltd., Japan; B. McEnaney, V. D. Scott, University of Bath, Bath, UK

***Micromechanism* of High Speed Abrasive Waterjet Cutting of Cast Metal Matrix Composites** 391
P. K. Rohatgi, N. B. Dahotre, S. C. Gopinathan, D. Alberts, K. F. Neusen, University of Wisconsin-Milwaukee, Milwaukee, WI, USA

Logarithmic Decrement Measurements on Mechanically Alloyed Aluminum and SiC Particulate Reinforced Aluminum Matrix Composites 399
R. B. Bhagat, M. F. Amateau, E. C. Smith, The Pennsylvania State University, State College, PA, USA

Damping Behavior of Squeeze Cast Planar Random Carbon Fiber Reinforced 6061 Al Matrix Composites 407
R. B. Bhagat, M. F. Amateau, E. C. Smith, The Pennsylvania State University, State College, PA, USA

METAL MATRIX COMPOSITES - AN OVERVIEW

A. Kelly
University of Surrey
Guildford, Surrey GU2 5XH, UK

Abstract

Metal matrix composites have been little used. The promise of them is considered under three heads. Metal matrices at low temperatures, high temperature metallic matrices and laminar structures.

TABLE I LISTS IN MATRIX FORM composite materials which have been seriously experimented upon or are in use.

The table is schematic in form and the choice of columns and matrix are explained in the caption. The well commercialised composite materials among the examples listed are outlined in boxes. The vast majority of boxes occur with polymer matrices and/or with polymer or glass fibres. Composites containing metal fibres occur but only one example of a metal matrix. There is a good deal of promise and excitement however.

Table I

MATRIX \ FIBRE	Metal	Ceramic	Cement	Glass	Elastomer	Polymer
Metal	W (Cu, Al, Ni (nimonic)); Steel (W); W (Cu); WC, B, SiC (Co); Al, Ti			SiO_2 SiO- (Al, Cu)		Kevlar -on- Al; ARMOUR?
Ceramic	Mo (Al_2O_3)	SiC (Cordierite); SiC; C		Glass resin + ARMOUR; Al_2O_3 or B_4C		Aramid Glass; Aramid Al_2O_3; BODY ARMOUR; Roof Tiles; Optical Fibre
Cement	Steel (Portland)	Asbestos (Cement); C (cem); Al_2O_3 (cem)		Glass (High Al cem); Cemfil (Portland)		Nylon (MDF); Polyprop (cem); Kevlar (cem)
Glass	Chicken netting; Window glass	SiC (LAS); C (Borosil)		LAMINATED GLASS		LAMINATED GLASS?
Elastomer	Steel (isoprene); TIRE BELTING	C (Isoprene); Asbestos GASKETS, Neoprene, NBR		E Glass (Isoprene); TIRE		Nylon, Polyes. Aramid; isoprene; BELTING TIRE
Polymer	Steel (Phenolic); BRAKES; Cu; Peek; Cu ELEC. PVC INS.	C (Epoxy); C (Peek); Asbestos (Phenolic); FRICTION PRODUCTS		GRP; E glass PCBs; Epoxy; Glass (Phenolic); FRICTION PRODUCTS	Isoprene Butadiene; Epoxy Styrene; TOUGHENED PLASTICS	Aramid (Polyes. Phenol.); Aramid (Epoxy); Phenolic; Phenolic; FRICTION PRODUCTS; BODY ARMOUR; Polyester or Nylon GEO-TEXTILES; PVC film

TABLE: COMPOSITE MATERIALS SERIOUSLY EXPERIMENTED UPON OR IN USE

The table is arranged so that the columns refer to the fibre within the composite and the rows to the matrix. Thus $\frac{W}{Cu}$ means a tungsten fibre in a copper matrix. The "fibre" is not always strictly fibrous in form eg it could be a plate.

Hybrids are not considered. Well commercialised materials are outlined in boxes. Cements and Elastomers are almost exclusively used as matrices but this may change. Some gaps arise due to fabrication difficulties, eg an elastomer or polymer could well improve a ceramic as far as impact resistance is concerned, but this does not occur because ceramics are fabricated at high temperature.

METAL MATRICES AT LOW TEMPERATURE

Metal-matrix composites have recently been reviewed by Chou et al (1) and by Feest (2). So far as reinforced fibrous composites for aerospace are concerned, the interest in a metallic matrix centres on the use of lower density metals and the avoidance of the disadvantages of a matrix based on a thermosetting resin. Epoxy and similar resins possess low thermal conductivity, and a high thermal expansion coefficient. They show dimensional instability, hygrothermal degradation, material loss in high vacua and are susceptible to radiation damage and embrittlement at low temperatures. The lighter metals do not possess these disadvantages.

Many metal matrix systems involving reinforcing fibres have been explored including Be, B, C, silicon carbide and alumina (of various types) fibres in Al as well as B, SiC, Be and W in Ti, and B in Mg. Reinforcement of the light metals Al or Mg is occurring in many cases in order to reduce wear or reduce creep, for example ICI Saffil in Al alloys. Squeeze casting is often the method of introduction employed. The density of Al reinforced with 50-60 vol. % of continuous Al_2O_3 fibres is only some 40% of that of steel but the tensile strength and stiffness in the fibre direction can be the same (Table 2). The fatigue strength in the fibre direction is similar to the value for steel and so such a composite has been produced to make connecting rods in the Toyota experimental FX-1 engine.

When wear, stiffness (as distinct from very high strength), controlled thermal expansion and/or moderate increases in temperature of service are the aim, it is often not necessary to use fibres. Fibres are usually expensive to make compared with other forms of inherently strong solids. By methods based on powder metallurgy very (comparatively) cheap forms of B_4C, SiC and other strong solids can be introduced into aluminium, magnesium and copper matrices. Volume fractions as high as 40% can be obtained and the materials can be forged slowly and welded. Some properties obtained at room temperature taken from the commercial literature are given in Table 2.

Elastic moduli as high as 208 GPa can be obtained with particles of SiC in aluminium. The mechanical properties of these systems will bear a familial relation to those of the "hard metals", cf WC in Co (see for example, Almond (3)). A lot will be learned by application to particulate-reinforced Al alloys of the principles of obtaining toughness, strength and reproducible properties in the hard metals.

Some potential mmcs with putative applications are listed in Table 3.

HIGH TEMPERATURE METAL MATRICES

Figure 1 shows the 1000 rupture strengths of various materials at elevated temperatures. Composites, particularly directionally solidified fibrous composites, figure prominently. The Nitac and Cotac (not shown) series of alloys are characterized by a very regular distribution of apparently unfaulted fibres. Precipitation and solution strengthening is optimized so as to take full advantage of the fibre strengthening due to 13% for Nitac 13, of (Ta + V) C fibres (Rabinovitch et al (4)). The γ-$\gamma'Cr_3C_2$ aligned *eutectic* is included, because although the high-temperature strength is inferior to that of the Nitac and Cotac series, it overcomes two of the major barriers to the commercial exploitation of *in situ* composites, namely extremely stringent processing conditions and relatively (to current superalloys) poor oxidation and corrosion resistance (McLean et al (5)). If directionally solidified fibre eutectics are to become commercially acceptable it will, according to Meetham (6), be necessary to develop alloys processable under less stringent conditions (as γ-$\gamma'Cr_3C_2$ succeeds) and to accommodate the anisotropy of properties.

TABLE 2. PROPERTIES OF PARTICLE- AND FIBRE-REINFORCED METALS

	E / GPa	σ / MPa	ρ / Mg m^{-3}	$E/g\rho$ / 10^4 cm	$\sigma/g\rho$ / 10^4 cm	strain to failure (%)
24 vol. % B_4C in Mg	86	418	1.92 (calc.)	4.4	2.2	0.78
30 vol. % SiC in Al	120	434	2.87	4.2	1.5	3.0
60 % (aligned) Al_2O_3 in Al						
longitudinal	262	690	3.45	7.8	2.0	0.3
transverse	152	185	3.45	4.4	0.53	0.6

E, Young's modulus; σ, yield strength; ρ, density

Table 3

Matrix	Fibre	Potential Applications
Aluminium	Graphite	Satellite, missile and helicopter structures
Magnesium		Space and satellite structures
Lead		Storage battery plates
Copper		Electrical contacts and bearings
Aluminium	Boron	Compressor blades and structural supports
Magnesium		Antenna structures
Titanium		Jet engine fan blades
Aluminium	Borsic	Jet engine fan blades
Titanium		High-temperature structures and fan blades
Aluminium	Alumina	Superconductor restraints in fusion power reactors
Lead		Storage battery plates
Magnesium		Helicopter transmission structures
Aluminium	Silicon carbide	High-temperature structures
Titanium		High-temperature structures
Superalloy		High-temperature engine components
Superalloy	Molybdenum	High-temperature engine components
Superalloy	Tungsten	High-temperature engine components

Figure 1 demonstrates that ceramic materials offer the most promise for extension of service temperature. Graphite at very high temperatures is used as a composite (in reducing atmosphere) as carbon reinforced with carbon fibres. It will be interesting to see whether monolithic ceramics provide adequate properties other than rupture strength; particularly toughness. The ceramic may be carried by a metal in a metal matrix composite or have toughness provided by the incorporation of fibres.

Although nickel base alloys are the most developed for high temperature use, there is much promise in the use of ceramic reinforcement to extend the properties of metals used at lower temperatures then nickel alloys, for example, those based on Ti. A very comprehensive account of continuous silicon carbide fibre reinforced titanium has been given by McElman and Mittrick (13).

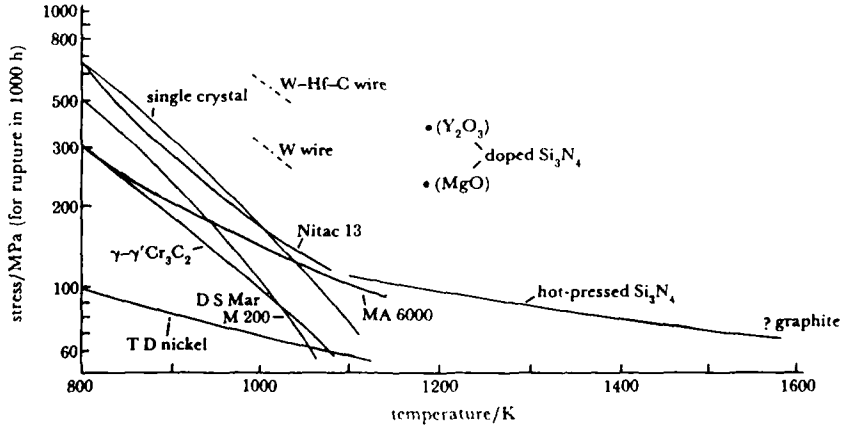


FIGURE 1 1000 h rupture strength of various materials

4. LAMINAR STRUCTURES

There is a rapidly increasing interest in layered microstructures due to (a) the production of epitaxial layers of different composition in the microelectronics industry, leading to quantum-well devices and (b) because vacuum evaporation is one efficient means of evading ingot metallurgy and the restrictions of alloy composition enforced by the conventional phase diagram. Coevaporation of the main alloy constituents is thermally efficient, (Bickerdike (7)) and the method of collection leads directly to a laminated microstructure in a nominally macroscopically homogeneous alloy (for example (6-9 %) Cr-0.6-1.5% Fe-Al (percentages by mass) or else a laminated structure is specifically sought by evaporating layers of different composition for example Al-Ti-Al-Fe. Such layered deposits are not made too slowly for example 18 kg h^{-1} is attained when working on the 0-100 Kg scale.

The high strength of evaporated alloys is derived from the microstructure of the deposits and its further development by working into wrought products. Al-Fe layered microstructures may be heavily rolled and retain the layered microstructure. Within the individual layers there can be a significant contribution to the yield strength from solid solution and dispersion strengthening as well as from dislocation substructure and small grain size: the grain size must be no larger than the layer thickness in one direction and often the grains are equiaxed in three dimensions. With modern techniques uniform layers as thin as one atom diameter may be deposited.

A new type of strengthening - not previously recognised by metallurgists and materials scientists (eg Brown (8)) arises when the thickness of the layers of, say, two pure metals is reduced below 100 nm or so. This was predicted by Koehler (9) and satisfactorily confirmed by Lehoczky (10).

Suppose a specimen is prepared consisting of alternate layers of pure metals (or other materials) A and B. If the elastic constants differ, dislocations will require a large external stress to drive them from the material of lower elastic constant (say A) into that of higher (B). If the layers are thin enough it may not be possible for a Frank-Read source to operate in either layer and then single dislocations will be the mode of plastic deformation. Lehoczky, following Koehler, finds that the tensile stress in the A layers necessary for penetration of the interface is

$$\sigma_z^A = \sigma_{im} + \sigma_i^A \qquad (1)$$

where $\sigma_m = RG_A/8\pi$ and $R = (G_B-G_A)/(G_B+G_A)$ and σ_i^A is the friction stress in A.

The condition that a Frank-Read source operates in A is

$$\sigma_z^A = 2\alpha G_A b_A / (\tfrac{1}{2} t_A) \qquad (2)$$

In both equations σ_z^A represents the tensile stress in material A due to an applied stress σ_z on the composite, G is the shear modulus (taken to be C_{44}), b the Burger's vector and t the thickness. Setting $\sigma_i^A = 0$, we predict that Koehler strengthening will occur when the right hand side of equation (1) is less than the right hand side of (2) so

$$t \leq \left[32\pi\alpha/R\right] b_A \qquad (3)$$

For an Fe-Al layer structure taking $\alpha = 1$, this predicts that Koehler strengthening will occur when the layer thickness of the aluminium is less than ca. 47 nm. Actually, Bickerdike et al (7) find a large increase in microhardness of Al-Fe deposits at thicknesses less than about 70 nm.

Accurate tensile tests on foils of Al interspersed with either Cu or Ag have been performed by Lehoczky. In Cu-Al foils containing layers of equal thickness the tensile yield stress increases inversely as the first power of the layer thickness down to a value of 70 nm and thereafter remains constant at the remarkably high value, for pure metals, of 650 MPa. The ultimate tensile strength (UTS) of such foils is close to 700 MPa; the tensile fracture stress follows a $t^{-\frac{1}{2}}$ relationship at thicknesses greater than 70 nm. For Al-Ag foils where the difference in elastic moduli is much less than in Al-Cu (R much smaller) the critical thickness for observation of Koehler strengthening is 230 nm and the strength attained is much less.

The Al-Fe system is very interesting because high hardnesses (and presumably high strengths) are obtained with very small Fe layers, for example, 25 nm of Al and 2% by mass)(0.7 vol%) of Fe which corresponds to 1.7 nm layers. Clearly very high values of strength:mass ratio are possible, for example, a layered structure containing 7.3% (by mass) of iron (2.6 vol %) has a tensile strength (closely equal to the yield strength) of 804 MPa and a specific gravity of 2.82 giving a value of σ/ρ 285 MPa: 28.5 x 10^5cm which is high for an Al alloy.

Such high-strength foils show a stress-strain curve in tension rather like that of fibrous composites even though both phases may be pure metals, particularly when the layer thickness becomes very small, for example 20 nm.

The possibilities are intriguing if one considers other possible combinations of layers, for example Al-Ti, Al-Mg, both of which have been successfully made by evaporation. If means other than evaporation

are considered, perhaps in concert with it, layer structures of Al-C, Al-SiC, Al-B or Al-AlN (or the same non-metal with Mg) become a possibility. The non-metal would appreciably increase the stiffness, the Koehler effect would strengthen the aluminium, and the resistance to crack propagation in the brittle non metal would be increased by the same effect as occurs in laminates where both phases may be considered brittle.

By direct measurement Lehoczky found an apparent increase in the Young modulus of his Al-Cu foils at thicknesses of the layers of less than about 50 nm. Though the measurements indicate an increased stiffness, whether or not there is a genuine increase in Young's modulus in foils containing thin layers is a very intriguing question at the present time. It has usually been assumed that Young's modulus of a pure pore-free solid cannot be greatly changed except by feeding in energy, for example, in piezoelectric materials. Hilliard and his co-workers at Northwestern University have reported a number of times (see, for example, Baral et al (11)) observing very large increases in the measured stiffness of foils containing layers less than 3 nm thick. The foils are single crystals and of course account must be taken of the crystalline anisotropy. A very large increase in the Young modulus in the plane of the foil is found in Ag-Pd, Cu-Ni, Au-Ni and Cu-Pd but *not* in Cu-Au (Henein & Hilliard (12)) when there is marked compositional modulation normal to the plane of the foil with a wavelength of 2.0-3.0 nm. The effect disappears at longer wavelengths and at very short ones and is according to these authors very large, for example, by a factor of 2-3. Theoreticians have sought explanations for a genuine increase in the Young modulus in terms of Fermi-surface-Brillouin-zone interactions.

Were the effect found to be real it would be of extreme interest for structural materials, particularly for Al-base layer structures such as Al-Fe mentioned above, because the possibility arises of varying and controlling both strength and stiffness by varying layer thickness.

REFERENCES

1. Chou, T. W., A. Kelly, and A. Okura, Composites 16, 187 (1985)
2. Feest, E. A., Metals and Materials 4, 273 (1988)
3. Almond, E. A. Deformation characteristics and mechanical properties of hardmetals. In "Science of Hard Materials" (ed. R. K. Viswanadhan, D. J. Rowcliffe & J. Gurland), p 517 New York; Plenum Publishing Corporation (1983)
4. Rabinovitch, M., J. F. Stohr, T. Khan & H. Bibring, Directionally solidified composites for application at high temperature. In "Fabrication of Composites" (ed. A. Kelly & S. T. Mileiko) Amsterdam: North Holland (1983)
5. McLean, M., P. N. Quested, P. J. Henderson & K. Menzies, Development of the = Cr_3C_2 in situ composites. In "In Situ Composites IV" (ed. F. D Lemkey, H. E. Cline & M. McLean). New York: North Holland (1982)
6. Meetham, G. W., Metall. Mater. Technologist 14, 387 (1982)
7. Bickerdike, R. L., D. Clark, J. N. Easterbrook, G. Hughes, W. N. Mair, P. G. Partridge, H. C. Ranson, Int. J. Rapid Solidification 1, 305 (1985)
8. Brown, L. M. In Proc. 5th International Conference on Metals and Alloys (ed.P. Haasen, V. Gerold & G. Kosterz) Vol. 3, p 1551. Oxford: Pergamon Press (1979)
9. Koehler, J. S. Phys. Rev. B2, 547 (1970)
10. Lehoczky, S. L., J. Appl. Phys. 49, 5479 (1978);(see also Phys. Rev. Lett. 41, (1978)
11. Baral, D., J. B. Ketterson and J. E. Hilliard, J. Appl. Phys. 57, 1076 (1985)
12. Henein, G. E. and J. E. Hilliard, J. Appl. Phys. 54, 728 (1983)
13. McElman, J. A. and M. A. Mittrick in "Advancing with Composites", Int. Conf. on Composite Materials, Milan, Centro Materiali Compositi, Naples, pp 177-299 (1988)

KINETICS OF FIBER PREFORM INFILTRATION

Andreas Mortensen, Veronique J. Michaud, James A. Cornie, Merton C. Flemings
Massachusetts Institute of Technology
Cambridge, Massachusetts, USA

Larry Masur
American Superconductor Corp.
Cambridge, Massachusetts, USA

ABSTRACT

The various fluid flow and heat transfer mechanisms governing the infiltration of fibrous preforms by a liquid metal are presented in a description of the process and its governing laws based on recent experimental and theoretical work at M.I.T. The influence of adjustable parameters of the process such as preform or metal temperature, applied pressure as well as external cooling from the mold is discussed. Conclusions are drawn from this work for optimization of the infiltration process for metal matrix composites, with particular focus on infiltration of fibers initially at a temperature below that at which solid metal forms.

THE LIQUID METAL INFILTRATION process for fabricating fiber reinforced metals consists of the injection and subsequent solidification of liquid metal into the interstitial spaces within a collection of ceramic fibers. This process is at present well established, and an increasing number of fibrous composite materials are being produced on both a commercial scale and in laboratories via one or another form of infiltration: squeeze casting, pressure casting, die casting, gravity casting, etc [1]. Fundamental principles governing the kinetics of infiltration and the microstructural evolution of the composite are therefore of considerable practical interest. Recent progress on the physics of the process is presented in what follows [1 - 4]. The present paper will address the topic in somewhat condensed form, to propose a more synthetic view of the process and in particular to outline practical consequences of recent work on the subject.

DESCRIPTION OF THE PROCESS AND GOVERNING EQUATIONS.

Consider the infiltration of a composite such as the simplified selectively reinforced part described in Figure 1. Molten metal is poured at temperature T_m into a cavity of initial temperature T_c which contains a preform of the fibers, preheated to a temperature T_f. The metal infiltrates the preform under a positive pressure differential ΔP_μ between that in the metal at the entrance of the preform P_o and the pressure at the infiltration front. This latter pressure is equal to the pressure in the gaseous atmosphere in the non-infiltrated portion of the preform, P_a, diminished by the pressure drop at the infiltration front ΔP_γ:

$$\Delta P_\mu + \Delta P_\gamma = P_o - P_a.$$

Several equations have been proposed for calculating the capillary pressure drop at the infiltration front ΔP_γ. The authors have recently proposed an expression for this pressure drop [5], on the basis of a simple analysis of the energy required for reversible infiltration of a porous body:

$$\Delta P_\gamma = (\sigma_{FL} - \sigma_{FA}) S_f \qquad (1)$$

$$= - \sigma_{LA} \cos(\theta)\ S_f \quad \text{(provided } \theta \text{ exists)}$$

where σ_{FL} is the fiber/liquid metal interfacial energy, σ_{FA} is the fiber surface energy, σ_{LA} is the surface tension of the metal, θ is the contact angle of the metal on the reinforcement and S_f is the specific surface area (i.e. the fiber surface area per unit volume of metal matrix) of the region of the preform that is being infiltrated at time t. In the limiting case of $\theta = 0$, this expression is identical to that derived by Carman in 1941 for capillary rise in sands using a force balance at the infiltration front [6]. For the case of a fibrous preform consisting of fibers of uniform radius r_f, S_f is given by:

$$S_f = \frac{2 V_f}{r_f (1 - V_f)} \qquad (2)$$

Fluid flow within the preform will be governed by Darcy's law, provided the relevant Reynold's number

$$R_e = \frac{2 r_f \rho_m v_o}{\mu V_f} \qquad (3)$$

is less than about one [7]. This will generally be the case in the

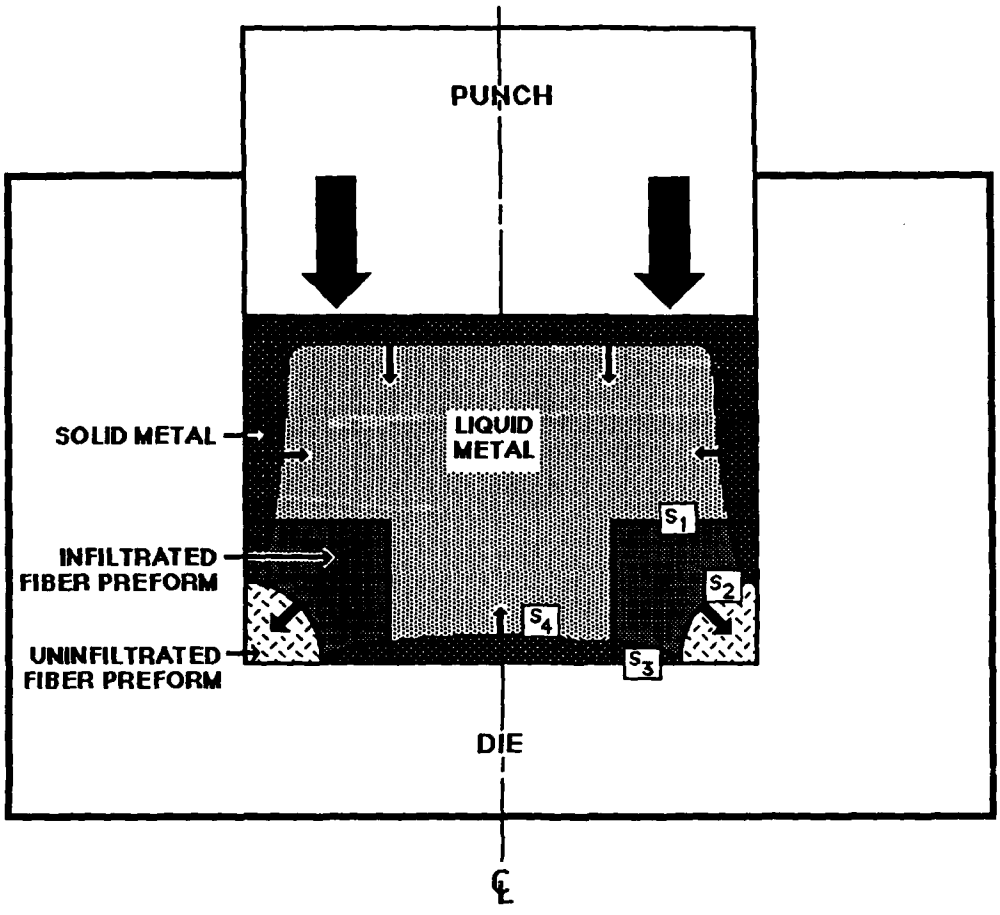


Figure 1 - Generalized three-dimensional problem of infiltration of a fibrous preform. In this case, the part is a simplified version of a selectively reinforced piston manufactured by squeeze casting. S1 denotes the preform entrance, S2 the infiltration front, S3 the mold-casting interface and S4 the solidification front. Both S3 and S4 are moving boundaries.

infiltration of metal marix composites due to the fine scale of the reinforcement. Flow of the fluid can then be analysed on the scale of an elementary volume element dV that is small on the scale of the casting, but comprises at least several fibers so that fluid velocity and pressure can be averaged over this volume element. Fluid flow is then measured by the "superficial" velocity or "seepage" velocity v_o, a vector of direction given by the average flow direction of the liquid and of magnitude equal to the volume of liquid flowing per unit time through a unit surface cut into the porous medium perpendicular to the average flow direction. Darcy's law then correlates the pressure gradient in the liquid and the superficial velocity:

$$\mathbf{v_o} = -\frac{\mathbf{K}}{\mu}[\mathrm{grad}(P) - \rho_m \mathbf{g}] \qquad (4)$$

where

$\mathbf{v_o}$ = superficial velocity of liquid metal

μ = viscosity of liquid metal

$\mathbf{K}$ = (symmetric) permeability tensor of the preform.

P = pressure in the metal

ρ_m = density of the metal

$\mathbf{g}$ = gravity field vector.

If we assume that both the liquid matrix and the preform are incompressible, the continuity equation is:

$$\mathrm{div}\,(\mathbf{v_o}) = 0 \qquad (5)$$

The pressure drop ΔP_μ is then the integral of the pressure gradient from the preform entrance to the infiltration front, and increases with increasing flow velocity of the metal, increasing viscosity of the metal and decreasing permeability of the preform. The energy required for the infiltration process is then the sum of two terms, corresponding respectively to the volume of metal displaced multiplied by the sum of the two terms $(\Delta P_\mu + \Delta P_\gamma)$ of the total driving pressure gradient. The

former term measures an irreversible energy expenditure due to viscous losses in the flowing metal while the second term measures the minimum energetic requirement of the process (positive or negative according to wettability of the preform), due to capillarity.

Heat and solute transport can also be analyzed on the scale of the same volume element dV if heat transfer is rapid enough within that element to equalize temperature and if diffusion is rapid enough to homogenize the liquid composition within dV. One can then characterize the element with a single temperature T and a single liquid solute composition, given by the concentration C_{iL} in solute i of the liquid. The heat transfer equation is then:

$$\rho_c c_c \frac{\partial T}{\partial t} + \rho_m c_m v_o \cdot \text{grad}(T) = \text{div}\,(k_c\, \text{grad} T) + (1-V_f)\,\rho_m L \frac{\partial g_s}{\partial t} \qquad (6)$$

where:

$\rho_c c_c$ = volumetric heat capacity of composite, = $\rho_f c_f V_f + \rho_m c_m (1-V_f)$,

$\rho_f c_f$ = volumetric heat capacity of fibers,

$\rho_m c_m$ = volumetric heat capacity of metal,

V_f = volume fraction fibers in the composite,

k_c = thermal conductivity tensor in the composite,

T = temperature,

g_s = fraction solid,

L = latent heat of solidification of the metal.

Solute conservation dictates:

$$\frac{\partial((1-V_f)\overline{C_i})}{\partial t} = -\,\text{div}(C_{iL} v_o) \qquad (7)$$

where

C_{iL} = concentration of solute i in liquid metal phase

$\overline{C_i}$ = average concentration of solute i in total metal phase for each solute element, if density differences between liquid and solid metal phases are neglected. Depending on the solidification mechanism, an additional relationship correlates the average concentration with the liquid metal composition and fraction solid metal g_s:

$$\overline{C_i} = f(C_{jL}, g_s) \qquad (8)$$

while the composition of the liquid and the temperature in dV are linked by the phase diagram if equilibrium is assumed at the solid/liquid metal interface:

$$C_{iL} = g(T) \qquad (9).$$

In the case of a binary alloy, there will be eight unknowns: v_{ox}, v_{oy}, v_{oz}, P, T, C_L, g_s, and C at each point of the preform and one parameter, time. Equations (4) to (9) yield eight relations between these unknowns. The problem is therefore defined by specification of the boundary conditions, and of a relation giving the value of the permeability(ies) at each point of the infiltrated preform as a function of the nature of the fibers including their volume fraction, and the volume fraction solid metal present g_s. Calculation of K can be based on the Blake-Kozeny approximation or on appropriate relationships derived for the particular preform in question [1,3,8]. Of particular interest is the role played by the fraction solid metal g_s present in the composite during infiltration, because the permeability will depend largely upon the solidification morphology of that solid metal phase.

There is at least one moving boundary in this problem, the infiltration front S_2 in Figure 1. There will in general be a second moving boundary, delineating the region of fully solid metal, S_4 in Figure 1, which is formed by concomitant solidification of the whole casting due to external cooling at the mold wall. The anisotropic and inhomogeneous nature of many fiber preforms may further complicate the problem. The permeability of preforms consisting of parallel fibers is greater by a factor of about two along the fiber axis compared to along an axis transverse to the fibers [8]. Flow of the metal will therefore be much more rapid parallel to the fibers. Furthermore, the distribution of the fibers is never regular, and there will be regions of high volume fraction fiber, and therefore opposing higher resistance to penetration by the liquid metal, due to increased capillary forces in these regions (equations (1) and (2)) and due to a much lower permeability in these regions. The infiltration front will then be very irregular, as metal will first penetrate the preform along wider channels, and later complete infiltration of the preform into regions of higher local V_f either by transverse flow from the larger channels or longitudinally as in Fukunaga and Goda's experiments [9].

The presence in this problem of moving boundaries, the anisotropy of the permeability tensor and the presence of *inhomogeneous packing in most fiber preforms complicate* immensely its solution for the most general case. The approach in research has therefore been to utilize model systems which facilitate analysis and data acquisition. This approach allows to (i) determine fundamental physical phenomena underlying the problem, in particular validation or definition of equations presented above, and (ii) suggest possible approximations facilitating treatment in cases of practical interest. Recent results along these lines from research at MIT is presented in the following section. A complete presentation of experimental procedures and results and of their theoretical analysis will be given elsewhere [1-4].

UNIDIRECTIONAL PLANE FRONT INFILTRATION.

a - EXPERIMENTAL PROCEDURE. The matrix metal, aluminum or an aluminum-base alloy, is unidirectionally infiltrated into preforms of Saffil™ alumina fibers with a pressure caster, using pressurized gas to force molten metal into an evacuated die. Figure 2 is a sketch of the device. It consists of two main components: the pressure vessel, containing the melt furnace and crucible, and the cap, attached to which are the control valves and the die. There are also feedthroughs for thermocouples, power leads, and a pressure transducer. The die is attached to the center of the cap and can be evacuated.

To operate the device the cap is placed on the pressure vessel, immersing the bottom of the die in the molten metal. The vessel is then pressurized with nitrogen, forcing the metal up through the die and into the fibers. Gas feed-through lines feature a large diameter, allowing full pressurization in less than 1.2 seconds. The metal and the fibers do not come in

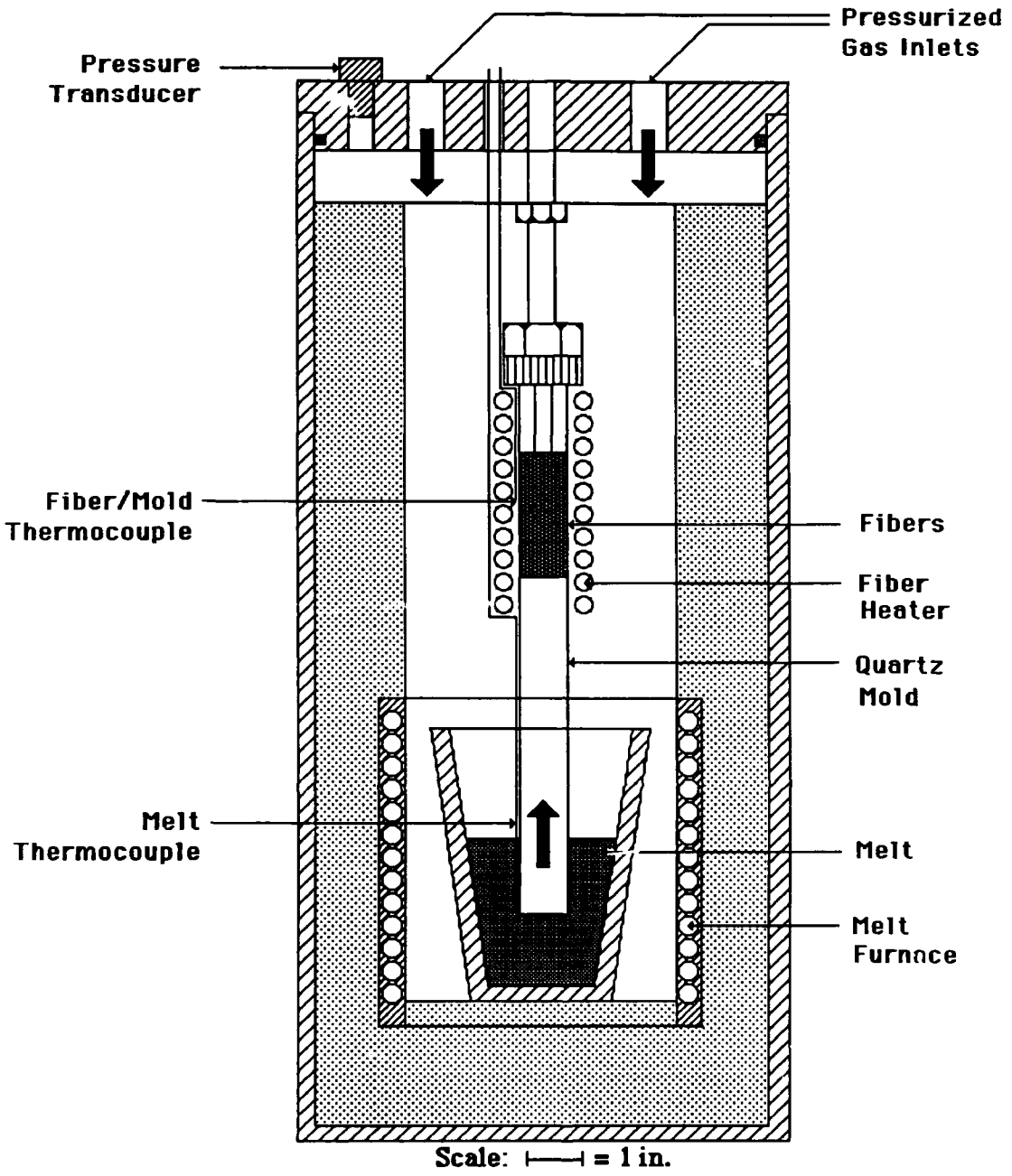


Figure 2 - Schematic drawing of pressure casting apparatus for unidirectional infiltration of fiber preforms by molten aluminum.

contact until infiltration begins, which enables accurate and independent control of the fiber and metal temperatures. In addition, because of the design of the device, the die need only sustain the compressive stresses imposed by the pressurized gas: heavy-walled metal dies common to other pressure casters are replaced with a quartz tube.

A technique was developed to measure the position of the molten metal front as it moves through the fiber preform during infiltration. This is achieved by inserting a SiC filament between the preform and the quartz tube mold. A potential is applied between the filament and the metal crucible, with the molten metal acting as a switch to close the circuit. A chart recorder then measures the potential drop across the SiC filament over time. As the metal infiltrates the preform, the potential measured across the filament decreases due to the decrease in effective electrical length of the SiC filament.

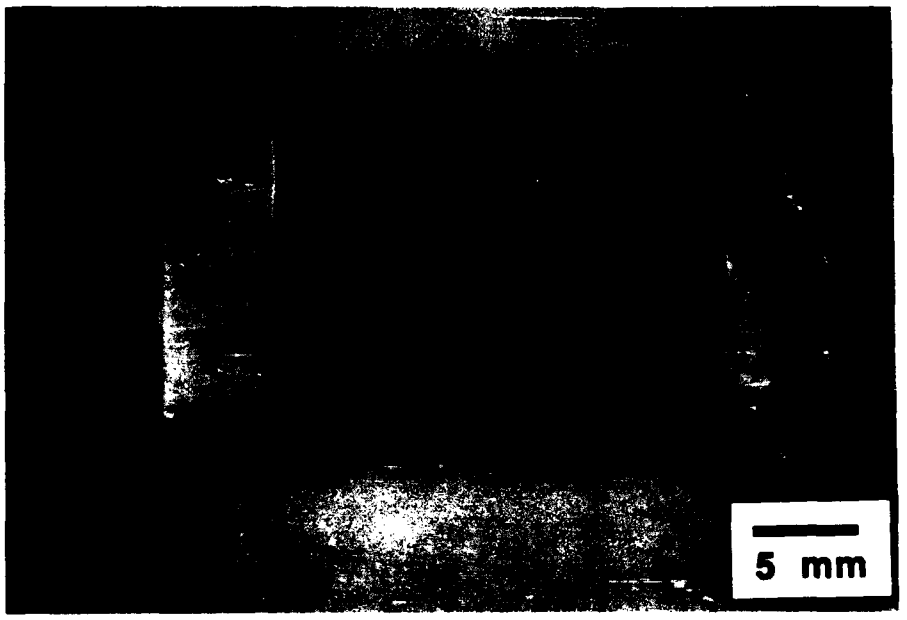


Figure 3 - Sample of unidirectionally infiltrated Saffil™ alumina reinforced aluminum produced in apparatus schematically described in Fig. 2. Infiltration was from left to right. Note the relatively plane infiltration front.

Monitoring the potential drop during infiltration then allows a calculation of the position of the metal front and its velocity over time.

The experimental procedure yields a dynamic measure of infiltration kinetics during infiltration under constant applied pressure, and produces a sample of composite (Figure 3), which can be investigated using conventional metallography and chemical analysis. The relatively planar and well defined infiltration front observed with these preforms and the unidirectionality of the infiltration path simplify considerably analysis of the infiltration process, and the equations given above can be tested against experimental data.

b - CASE OF A PURE METAL. In the case of a pure metal, liquid and solid metal can only coexist at the melting point of the metal T_M if equilibrium is assumed at the solid/liquid interface. Therefore, the problem is much simplified, since there can be no heat transport where solid metal is present, and therefore g_S cannot vary continuously in the composite. Furthermore, with a pure metal, the composition is no longer an issue, and equations 7 to 9 are irrelevant.

If the initial fiber temperature is above the metal melting point, no solid metal will form, save for solidification due to cooling at the mold walls. The problem is then one of uncoupled fluid flow in that the infiltration kinetics can be derived first independently, to yield, for unidirectional infiltration, the position of the metal front as a function of time:

$$L^2 = \int_0^t \frac{2 K \Delta P_{\mu(t)}}{\mu (1-V_f)} dt \qquad (10)$$

$$= \frac{2 K \Delta P_{\mu}}{\mu (1-V_f)} t \text{ if the applied pressure is constant}$$

If the initial fiber temperature is below the melting point of the metal, some solid metal will form at the infiltration front to heat the fibers up to the metal melting point by release of latent heat. In the case of a pure metal, this solid metal must solidify as a sheath surrounding the fibers since solidification is limited by heat transfer to the cold fibers. This assumption is substantiated by measured infiltration kinetics, predicted as above, but with a changed value of permeability in the region close to the infiltration front, which can be predicted by increasing the effective fiber diameter and volume fraction to account for a volume fraction solid g_s in the metal phase. g_s is given by a thermal equilibration at the infiltration front:

$$g_s = \frac{\rho_f c_f V_f (T_M - T_f)}{\rho_f L (1-V_f)} \qquad (11)$$

Formation of this solid metal phase will substantially influence the kinetics of infiltration when the fibers are initially below the melting point of the metal. Low T_f will be deleterious from the point of view of infiltration kinetics, but

may result in vastly improved composite properties due to reduced chemical reactions between the fibers and the metal [10]. Experiments with high purity aluminum have demonstrated the validity of these assumptions, and the physics of infiltration by a pure metal are presently fairly well understood [2,3,9].

c - CASE OF AN ALLOY. In the case of an alloy, the problem is more complex with cold fibers than in the case of a pure metal because: (i) solid and liquid metal can coexist over a range of temperatures, making heat transfer posible within the region of partly solid metal, (ii) the morphology of the solidifying metal is no longer that of a sheath surrounding the fibers because solidification is now controlled by solute diffusion and (iii) mass transfer must also be accounted for.

Even with a slightly impure matrix, the infiltration kinetics can be noticeably reduced when the fibers are initially at a temperature below the metling point of the metal [2,11]. This effect is interpreted as arising due to a different morphology of solid formed in contact with cold fibers.

Experiments have been reported elsewhere wherein it was shown that macrosegregation results in the composite after infiltration with Al-4.5wt%Cu of a preform initially at a temperature below the liquidus of the metal [12]. A theoretical analysis of the problem, to be presented in a forthcoming publication [4], allows to predict the concentration profile in the composite. The problem is solved for unidirectional infiltration with constant applied pressure P_o, based on the equations given above, and the resulting concentration profile is given in Figure 4. It is seen that variations in concentration and in fraction solid are predicted in the composite during infiltration, which agree qualitatively with data reported in reference [12].

d - EFFECT OF EXTERNAL COOLING. As mentioned above, the effect of concomittant solidification is to complicate significantly the problem. For example, macrosegregation observed in a composite with an alloyed matrix will be a result of the dual contributions of solidification due to the fibers, treated analytically as reported above, and of solidification from the mold walls interacting with fluid flow in the preform during infiltration, Figure 5. Both will redistribute solute in the composite, and the macrosegregation profiles reported earlier are a result of both processes.

It was shown following the experimental procedure described above that solidification due to external cooling also influences fluid flow in the case of a pure metal [2]. With a constant applied pressure, the total infiltrated length of composite is solely determined by external cooling. Also, feeding of solidification shrinkage will depend on external cooling from the mold walls. The importance of mold temperature and external cooling must not, therefore, be underestimated in interpreting occurences of incomplete infiltration of a preform (other causes may exist, however, such as incomplete venting of gases initially in the preform).

CONCLUSIONS

From a practical point of view, the following can be concluded from results presented above and from previous work on the infiltration of metal matrix composites:

1 - The infiltration of a fibrous preform is a moving boundary problem, the solution of which is therefore generally not trivial. The basic equations governing the process and given above have been substantiated by experimental work on unidirectional infiltration of Saffil™ alumina preforms by aluminum and aluminum alloys. These equations must,

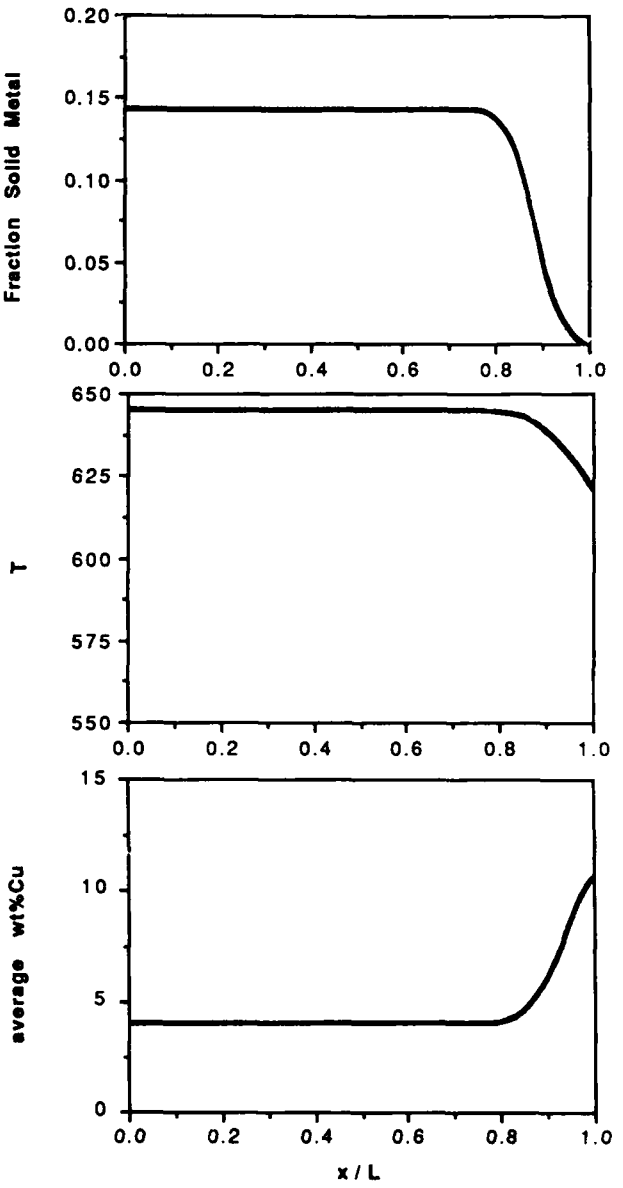


Figure 4 - Calculated fraction solid metal, temperature and average metal composition for Al-4.5 wt%Cu infiltrating a preform of 24 Vol.% Saffil™ fibers initially at 550°C with no metal superheat. No external cooling, $L/\sqrt{t}$ = 0.018 m/$\sqrt{s}$, where L is the total infiltrated length, x is distance along the infiltrated composite with x=0 at the preform entrance and t is time.

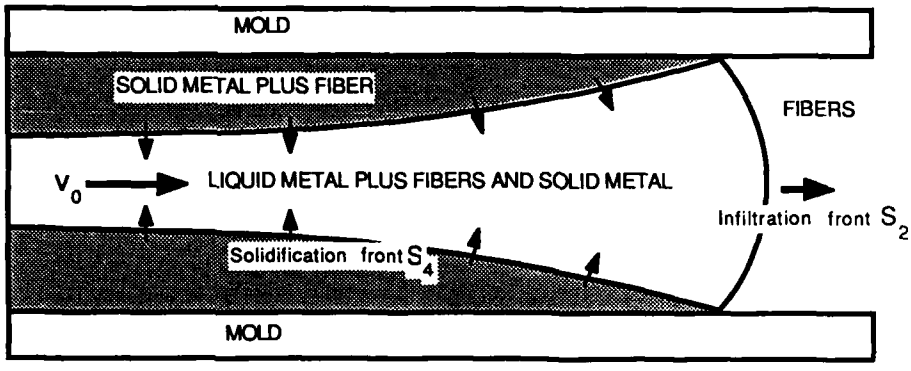


Figure 5: Schematic drawing of solidification due to external heat losses during unidirectional infiltration.

however, be modified to take into account additional effects such as preform compressibility, heat released by chemical reactions between fibers and metal, etc.

2 - Infiltration of fibers initially at a temperature below the liquidus or the melting point of the metal is possible and results in the formation of solid metal between the fibers at the infiltration front. Infiltration kinetics are then determined to a large extent by the amount and morphology of this solid metal.

3 - The grain size of the matrix and the extent of fiber/matrix interfacial reaction can therefore be largely influenced by controlling the initial preform temperature. A low initial fiber preform temperature will result in a fine-grained matrix and reduced interfacial reactions between fibers and metal. Additionally, in the case of an alloy matrix, macrosegregation will then be observed within the composite.

4 - External cooling from the mold wall results in solidification of the matrix during infiltration. In the case of unidirectional infiltration under constant applied pressure, flow of the metal ceases due to choking by fully solid metal formed by solidification from the mold walls at the preform entrance.

ACKNOWLEDGEMENTS.

Support of IST/SDIO through ONR contract N000-14-84-K-0495, of the General Motors Corporation and of the Aluminum Company of America (ALCOA) in the form of one (A.M.) of the authors' chair at MIT is gratefully acknowledged.

REFERENCES

1. A.Mortensen, L.J. Masur, J.A. Cornie and M.C. Flemings, "Infiltration of Fiber Preforms by a Pure Metal Part I: Theory", unpublished work, MIT, 1988.

2. L.J. Masur, A. Mortensen, J.A. Cornie and M.C. Flemings, "Infiltration of Fiber Preforms by a Pure Metal Part II: Experiment", unpublished work, MIT, 1988.

3. L.J. Masur, "Infiltration of Fibrous Preforms by a Pure Metal", Ph.D. Thesis, Department of Materials Science and Engineering, MIT, February 1988.

4. A. Mortensen, V. Michaud, J.A. Cornie and M.C. Flemings, "Infiltration of Fiber Preforms by Al-4.5wt%Cu Part I: Theory", unpublished work, MIT, 1988.

5. A.Mortensen and J.A.Cornie, *Metallurgical Trans.* **18A** (1987), pp.1160-1163.

6. P.C Carman, *Soil Science* **52** (1941) pp.1-14.

7. S. Ergun: *Chem. Eng. Prog.* **48** (1952) pp.89-94.

8. G.W.Jackson and D.F.James: *Can. J.of Chem. Eng.* **64** (1986) pp.364-374.

9. H. Fukunaga and K. Goda: *Bull. of Japan. Soc. of Mech. Eng.* **27** (1984) pp.1245-1250.

10. H. Fukunaga and K. Goda: *J. of Japan Inst. of Metals* **49** (1985) pp.78-83.

11. L.J. Masur, A. Mortensen, J.A. Cornie and M.C. Flemings, Proceedings of the Sixth International Conference on Composite Materials ICCM 6, F.L.Matthews, N.C.R.Buskell, J.M.Hodgkinson and J.Morton Eds., London, Elsevier, 1987, pp.2.320-2.329.

12. Experimental work by L.J.Masur, cited by J.A.Cornie, A.Mortensen and M.C.Flemings, Proceedings of the Sixth International Conference on Composite Materials ICCM 6, F.L.Matthews, N.C.R.Buskell, J.M.Hodgkinson and J.Morton Eds., London, Elsevier, 1987, pp.2.297-2.319.

MODELLING OF PARTICLE SEGREGATION DURING CENTRIFUGAL CASTING OF Al-MATRIX COMPOSITES

L. Lajoye,* M. Suéry
Institut National Polytechnique de Grenoble
E.N.S. de Physique de Grenoble
Génie Physique et Mécanique des Matériaux
B.P. 46 - 38402 - Saint Martin D'Heres, Cedex, France

*Present Address:
Les Bronzes d'Industrie
57360 - Amneville, France

Abstract

During centrifugal casting of Al-melts containing suspended ceramic particles, segregation of the particles occurs either to the outer or to the inner part of the casting depending on their relative density compared to that of the melt. A model is presented to predict particle distribution in the casting after solidification. It considers the propagation of the solid-liquid interface and the movement of the particles due to centrifugal acceleratin which takes place either in the opposite or in the same direction as the solidification front. Using likely assumptions for the interaction between the particles and the solid-liquid interface, the model predicts that segregation is strongly influenced by the density difference between the particles and the melt, the size of the particles, the heat transfer coefficient between the metal and the mould and the pouring rate and to a lesser extent by the other parameters. These theoretical predictions are in good agreement with experimental observations in the case of Al-Si alloys containing suspended SiC particles introduced into the melt by the compocasting technique.

CENTRIFUGAL CASTING involves pouring a liquid metal into a rapidly rotating mould, which may be mounted either horizontally or vertically, and continuing the rotation until solidification is complete. The principal advantages of the technique are good mould filling combined with good microstructural control which usually give excellent mechanical properties. Centrifugal casting is thus used for many types of alloys producing a wide variety of diameters and thicknesses. This technique was experimented very recently with aluminum melts containing suspended particles such as ZrO_2 (1), SiC (2), Gr (3) and Mica (4) leading to segregation either to the outer or the inner part of the casting depending on their relative density compared to that of the melt. These studies were essentially concerned with the feasability of the process and the characterization of the product, except that with SiC (2) in which some modelling of the particle segregation was already considered.

The aim of this work is to develop such a model taking into account the propagation of the solid-liquid interface and the movement of the particles due to centrifugal acceleration. Prediction of the model taking into account the various parameters involved in the process, will be compared with experimental observations obtained in Al-Si alloys containing suspended SiC particles.

MODELLING OF PARTICLE SEGREGATION DURING CENTRIFUGAL CASTING

Particle segregation occurs during centrifugal casting owing to their density difference with the melt. However two phenomena are involved in the process : the solidification of the alloy which normally takes place from the periphery to the inside of the casting and the movement of the particles in the melt which can occur either in the opposite or in the same direction as the solidification front depending on their relative density. This movement can thus be altered by the solid-liquid interface leading to non homogeneous distribution of the particles after solidification. Prediction of particle segregation involves considering the result of such an interaction as a function of the various parameters of the process. Before doing this, the solidification of the casting on one hand and the movement of particles in a centrifuged liquid on the other will be considered separately.

MODELLING OF SOLIDIFICATION - Let us consider the solidification of a hollow cylindrical part of external radius Re and inner radius Ri into the steel mould of a vertical centrifugal

casting machine. The mould is initially preheated at a temperature T_m which is smaller than the pouring temperature of the liquid metal T_c.
In order to solve the heat flow problem inside the tube material the basic assumptions are :

- no heat loss from the inside bore
- instantaneous filling of the mould with liquid at $T = T_c$
- purely one dimensional heat flow, perpendicular to the mould wall, the effect of the bottom and the cover of the mould being neglected
- heat transfer from the casting to the mould characterized by a heat transfer coefficient h which decreases as solidification proceeds.

Using cylindrical coordinates, the heat flow equations is :

$$\frac{\partial H}{\partial t} = \frac{K}{\rho}\left(\frac{\partial^2 T}{\partial r^2} + \frac{1}{r}\frac{\partial T}{\partial r}\right) \qquad (1)$$

with ρ : density
K : thermal conductivity
H : enthalpy

It was solved in the casting and in the mould with heat flux conditions at the interfaces using the finite difference method (5). N_1 points were considered in the casting and N_2 in the mould which thus lead to $N_1 + N_2$ equations at each time step.

In order to take into account the contraction of the casting during solidification which introduces an air gap between the casting and the mould, h was assumed to vary as :

$$h = h_o \left(\frac{h_F}{h_o}\right)^{\frac{e}{e_o}} \qquad (2)$$

where e is the solidified thickness of the casting at time t and e_o the thickness after solidification. h_o and h_F are initial and final values of h. Details of the calculation together with the parameters used are given in (6).

MOVEMENT OF A SOLID PARTICLE IN A LIQUID - Under a constant acceleration, the velocity of a spherical particle of radius R_p is deduced from the Stokes law and given by :

$$V_p = \frac{2 R_p^2 (\rho_p - \rho_L)\,\gamma}{9\,\eta} \qquad (3)$$

where γ is the acceleration, ρ_p and ρ_L are the densities of the particle and the liquid respectively and η is the viscosity of the liquid.

During vertical centrifugal casting, a particle which is suspended in the liquid is submitted to a vertical acceleration due to gravity g and to a centrifugal acceleration $\gamma = w^2 x$, where w is the angular rotation velocity of the mould and x the distance of the particle to the rotation axis. Generally γ, is much greater than g which allows the vertical displacement of the particle to be ignored.

The movement of the particle is described by:

$$\frac{4}{3}\pi R_p^3 w^2 x (\rho_p - \rho_L) - 6\pi\eta R_p \frac{dx}{dt} = \frac{4}{3}\pi R_p^3 \rho_p \frac{d^2x}{dt^2} \qquad (4)$$

which gives the position of the particle at any time t :

$$x = x_o \exp\left(\frac{2w^2 (\rho_p - \rho_L) R_p^2}{9\,\eta} \cdot t\right) \qquad (5)$$

where x_o is the position of the particle at time $t = 0$.

This equation is valid only for Reynolds number associated with the particle smaller than 2 (7) which is the case of small ceramic particles moving in liquid aluminum.

CENTRIFUGAL CASTING OF THE COMPOSITE MATERIAL - Several phenomena have to be considered when a liquid containing suspended particles is solidified in a mould rotating at high velocity :

- the interaction between the solidification front and the moving particles
- the variation of the viscosity of the liquid before complete solidification
- the possible interaction between particles in the liquid
- the pouring rate which influences the initial position of the particles in the mould before their movement in the liquid.

Assumptions are the following :
- The motion of the particles is stopped by the liquidus front : the particles do not move in the mushy zone of the casting and they are not rejected by the solidification front. The first assumption is reasonable owing to the rapid increase of the viscosity of a melt with the increase of the fraction of the solid phase. It is to be noted also that the viscosity of the liquid varies with temperature which will affect the segregation velocity of the particles by mean of Eq. (4) or (5). Consequently, the pouring temperature of the alloy can have an effect on this velocity. It will be assumed as negligible in the model.

The second assumption seems also to be reasonable in most cases since it was shown recently that rejection of SiC particles by a moving Al solid-liquid interface only occurs if the velocity of the front is less than 0.1 mm/s

for stationary particles (8). During centrifugal casting the solidification rate is usually of the order of several mm/s and particles denser than the liquid will still increase the relative velocity front/particles. Entrappment can thus be possible only for particles which are much lighter than the liquid which is not common for the particles usually used as reinforcement in Al-alloys.

- Eq. (5) is valid only for the motion of an isolated particle in a liquid. For large particle volume fractions, interaction between particles occurs thus reducing their velocity. It is assumed that the reduction of the velocity can be described by an increase of the apparent viscosity of the liquid according to (9) :

$$\eta_{app} = \eta_L \left(1 + \frac{5}{2} V_p + 7{,}6\ V_p^2\right) \qquad (6)$$

where η_L is the viscosity of the liquid and V_p the volume fraction of particles.

It is assumed furthermore that segregation of the particles can only occur up to a maximum volume fraction taken equal to 52% for granular particles (10).

- The pouring rate of the alloy in the mould is constant and the concentration of the particles in the liquid before pouring is homogeneous.
- Solidification of the alloy starts at some given time Δt after the liquid enters the mould. This delay is due partly to the setting up of the alloy and the extraction of the superheat. Δt is considered as a parameter.

RESULTS AND DISCUSSION

THEORETICAL PREDICTION - Numerical resolution of the solidification and particle segregation problems allows the determination of :

- the variation of the temperature with time at any given point of the part and the mould
- the variation with time of the rate of the liquidus front
- the segregation profile of the reinforcing elements in the centrifuged part.

Only the last result will be presented here by considering the various parameters which can influence it. These parameters can be classified into two categories :

- those which have an effect on the solidification rate :
  - . the pouring temperature
  - . the heat transfer coefficient at the mould-metal interface i.e. the nature of the coating used to protect the mould against adhesion of the liquid metal
  - . the mould temperature.
- those which influence the displacement velocity of the particles :
  - . the density difference between the elements and the melt
  - . the size of the elements
  - . the centrifugal acceleration
  - . the pouring time.

In addition to these parameters, the influence of Δt will also be considered in the calculation.

Fig. 1 to 8 shows the influence of all the previously mentioned parameters on the segregation profile of the particles from the

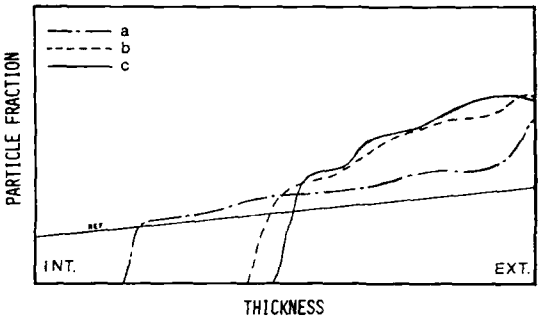


Fig.1 - Influence of pouring temperature T_c on particle segregation :
a) T_c = 630°C ; b) T_c = 700°C ; c) T_c = 800°C

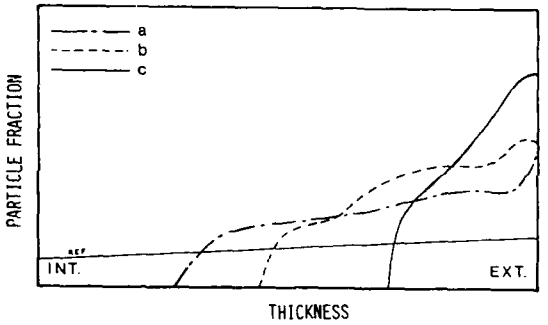


Fig.2 - Influence of mould coating on particle segregation :
a) graphite coating :
h_o = 2 cal.cm^{-2}.°C.s $h_F = h_o/10$
b) BN coating :
h_o = 0.5 cal.cm^{-2}.°C.s $h_F = h_o/5$
c) fiberfrax coating :
h_o = 0.1 cal.cm^{-2}.°C.s $h_F = h_o/10$

internal (INT) to the external (EXT) region of the part. The straight line "REF" corresponds to the initial particle fraction introduced in the alloy ; it increases from the inside bore to the periphery since it represents a particle fraction per unit length and not per unit volume. For each figure three values of the studied parameter are chosen, the other parameters being held constant:

pouring temperature T_c : 700°C
mould temperature T_m : 150°C
pouring time : 3 s
centrifugal acceleration at the periphery:
γ = 100 g
= 981 m.s^{-2}

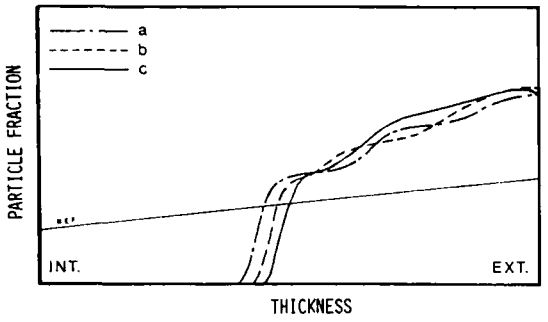


Fig.3 - Influence of mould temperature T_m on particle segregation :
a) t_m = 50°C ; b) t_m = 200°C ; c) t_m = 400°C

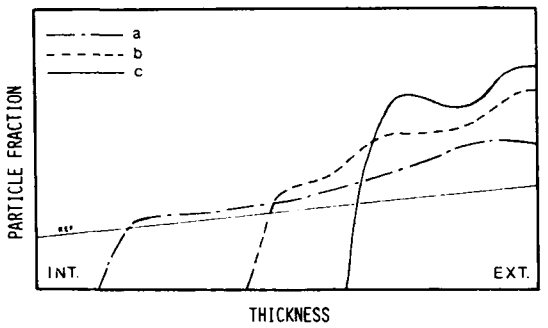


Fig.4 - Influence of density difference $\rho_p - \rho_L$ between the particles and the liquid on particle segregation :
a) $\rho_p - \rho_L = 0.1$ g.cm^{-3}
b) $\rho_p - \rho_L = 0.5$ g.cm^{-3}
c) $\rho_p - \rho_L = 3$ g. cm^{-3}

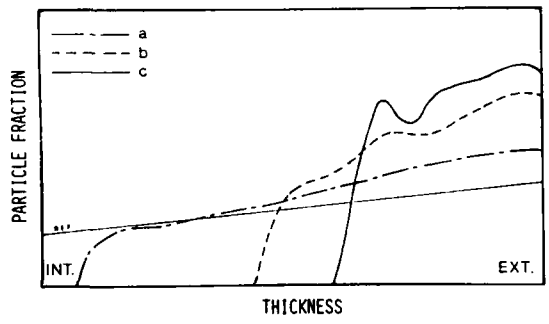


Fig.5 - Influence of particle radius R_p on particle segregation :
a) R_p = 5 µm ; b) R_p = 15 µm ; c) R_p = 30 µm

$\rho_p - \rho_L = 0.5$ g. cm^{-3}
$R_p = 15$ µm
$\Delta t = 0.2$ s.
$h_o = 0.5$ cal. cm^{-2}.°C. s.
$h_F = 0.1$ cal. cm^{-2}.°C. s.

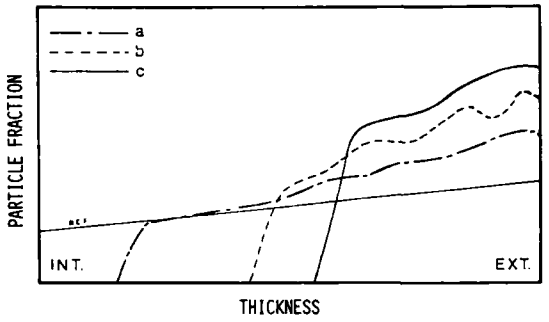


Fig.6 - Influence of centrifugal acceleration at the periphery γ on particle segregation :
a) γ = 20 g ; b) γ = 100 g ; c) γ = 300 g

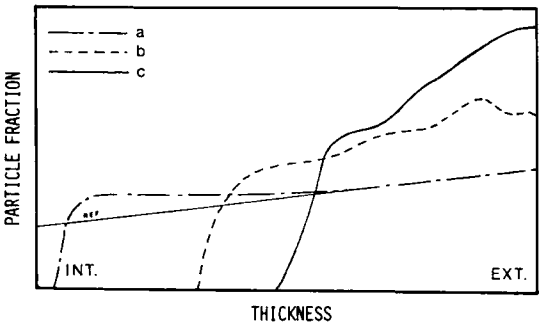


Fig.7 - Influence of pouring time t_c on particle segregation :
a) t_c = 6 s ; b) t_c = 3 s ; c) t_c = 1 s.

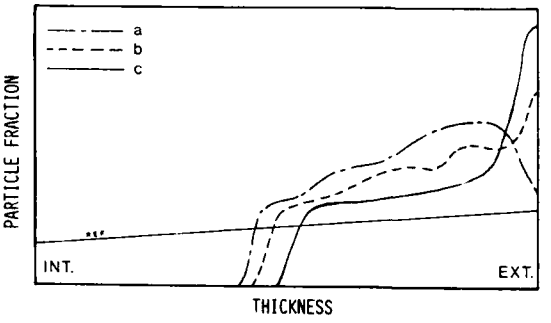


Fig.8 - Influence of solidification delay Δt on particle segregation :
a) Δt = 0 ; b) Δt = 0.3 s ; c) Δt = 1 s.

Moreover the liquidus and solidus temperatures were taken equal to 610°C and 580°C and the viscosity of the alloy to 2.5 x 10^{-3} Pa.s. This case corresponds approximately to SiC particles in Al alloys.
The curves of fig. 1 to 8 show several common characteristics :

- segregation of the particles towards the periphery leads to a region completely free of

particles whose thickness depends on the process and material parameters.

- the reinforced zone is sharply defined with an abrupt transition from the reinforced to the particle-free zone.
- some accumulation of particles is observed at the periphery of the casting ; this accumulation is essentially due to the solidification delay Δt (as shown in figure 8). Indeed, this delay allows segregation of the particles to occur to a large extent before solidification starts whereas no delay ($\Delta t = 0$) should lead to a particle fraction at the periphery very close to the initial one.

These theoretical results allow classification of the parameters which are dominant for the segregation of the particles during centrifugal casting. However the classification must take into account the fact that, for several of them, the range of variation is limited either by the material or by the process. Segregation is thus primarily influenced for a given composite by the heat transfer coefficient between the metal and the mould, the pouring rate, the size of the particles and the centrifugal acceleration and to a lesser extent by the pouring temperature and the mould temperature.

COMPARISON OF THE PREDICTION WITH EXPERIMENTAL RESULTS

Experiments were performed with Al-Si alloys containing SiC particles of various sizes introduced in the melt by mechanical stirring in the mushy zone. After the completion of addition of the particles, the mixture was reheated up to the fully liquid state and poured into the rotating cylindrical steel mould of a vertical centrifugal casting machine. The mould was 120 mm inside dia. and 80 mm height giving rise to casting of 25 to 30mm thickness (fig.9).

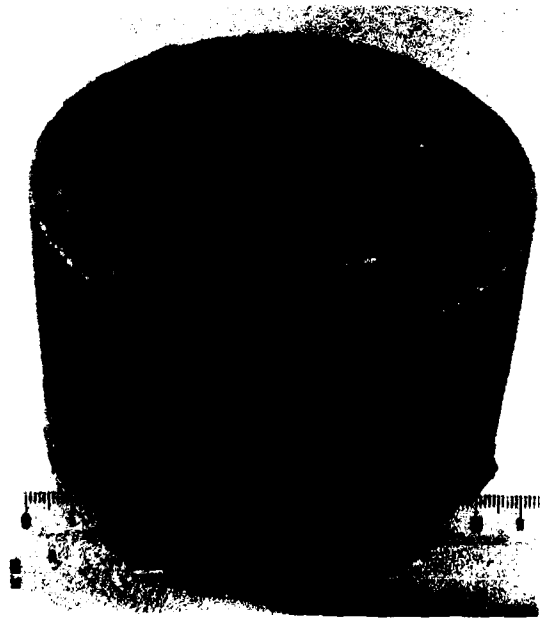


Fig.9 - Part obtained by centrifugal casting.

After solidification, the casting was taken out of the mould, sectioned and polished for the study of the distribution of the SiC particles. Figure 10 shows such a distribution for particles with different diameters 7, 29 and 45 μm. Segregation has occurred and it obvious that the extent of the particle-free zone increases with increasing particle size in agreement with theoretical prediction. Figure 11 shows the comparison between theory and experiment in the form of the variation of the particle fraction with the position in the thickness of the casting. Good agreement is observed taking into consideration the difficulty of the experimental determination of particle volume fraction by image analysis which is very sensitive to metallographic preparation of the specimen surfaces. Another

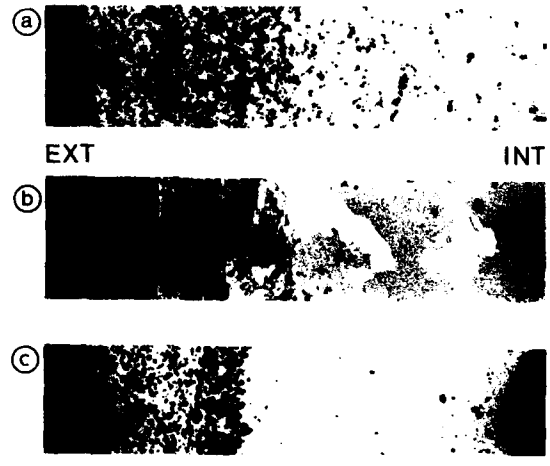


Fig.10 - Macrophotographs of a radial section of AS7G03/SiC centrifugal castings containing particles of various diameters :
a) 7 μm ; b) 29 μm ; c) 45 μm.

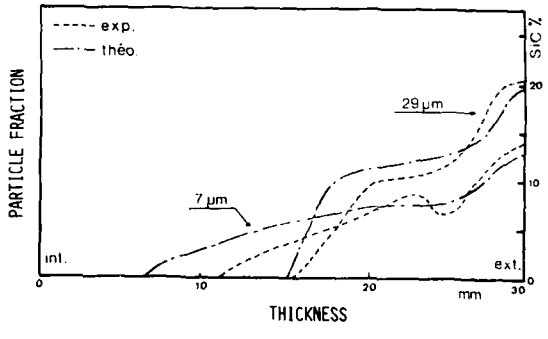


Fig.11 - Comparison of particle segregation profiles determined experimentally and theoretically for particle diameters of 7 and 29 μm.

comparison is shown in figure 12 for the influence of the pouring time. Other experimental results can be found in the work by Lajoye (6).

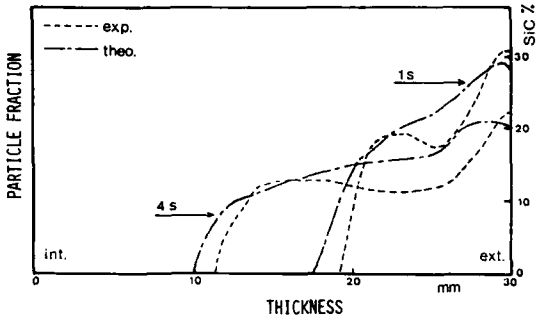


Fig.12 - Comparison of particle segregation profiles determined experimentally and theoretically for pouring times of 1 s (600 $cm^3.s^{-1}$) and 4 s (150 $cm^3.s^{-1}$).

CONCLUSION

Modelling of particle segregation during centrifugal casting of liquid metal containing suspended particles was performed taking into account the rate of displacement of the solidification front and the motion of the particles in the centrifuged liquid. Using likely assumptions for the interaction between particles and the solidification front, the model predicts that the heat transfer coefficient between the metal and the mould, the pouring rate, the particle size and the centrifugal acceleration are the most important parameters that control the distribution of the particles after solidification. The predictions are in good agreement with experimental observations obtained with Al-Si alloys containing suspended SiC particles, which allow the experimental conditions to be optimized for fabricating a casting with the appropriate reinforced zone.

Acknowledgement

The authors gratefully acknowledge the "Ministère de l'Education Nationale" and "les Bronzes d'Industrie" for their participation on the financial support of this work.

REFERENCES

1. Banerji, A., P.K. Rohatgi and W. Reif, Proc.of E.MRS Conference "Advanced Materials Research and Developments for Transport - Composites", Strasbourg, Nov. 85. Ed. P. Lamicq, W.J.G. Bunk and T.G. Wurm, Les Editions de Physique, France, (1985)

2. Lajoye, L. and M. Suéry. "Solidification Processing 87", 473-476, Sheffield, 21-24 Sept. 1987.

3. Krishnan, B.P., H.R. Shetty and P.K. Rohatgi. AFS Transactions 66, 73-80 (1976).

4. Nath, D. and P.K. Rohatgi, Composites, April 1981, 124-28.

5. Vasseur S., Thesis, Institut National Polytechnique de Lorraine (1982).

6. Lajoye L., Thesis, Institut National Polytechnique de Grenoble (1988).

7. Szekely, J. "Fluid Flow Phenomena in Metals Processing" p. 256, Academic Press, New York (1979).

8. Dhindaw, B., A. Kacar and D.M. Stefanescu. Proc. of ASM Europe, Sept. 1987.

9. Schowalter, W.R., "Mechanics of Non-Newtonian Fluids" p. 288, Pergamon Press (1978).

10. Sasikumar, R. and B.C. Pai, "Solidification Processing 87", 481-483, Sheffield 21-24 sept. 1987.

WETTABILITY OF SiC PARTICULATES WITH Zn AND Zn-Al ALLOYS

T. R. Fletcher, J. A. Cornie
Department of Materials Science & Engineering
Massachusetts Institute of Technology
Cambridge, Massachusetts, USA

K. C. Russell
Department of Materials Science & Engineering
Department of Nuclear Engineering
Massachusetts Institute of Technology
Cambridge, Massachusetts, USA

ABSTRACT

The wettability of 8.37 μm SiC particulates with liquid Zn, Zn-4.5Al, Zn-11Al, Zn-27Al, and ZA12 has been studied using pressure infiltration. Threshold pressures for infiltration of compacts of SiC particulates with these metals have been determined experimentally. Works of immersion have been calculated from threshold pressures to obtain a more fundamental measure of wettability.

REINFORCEMENT OF ZN AND ZN-AL ALLOYS WITH SIC PARTICULATES is expected to improve their strength to weight ratio and dimensional stability while utilizing their advantages of relatively low cost and low processing temperature. Possible applications include transmission gears and other automotive parts. Fabrication of particulate metal matrix composites by casting is potentially one of the most attractive processing routes, but its success depends upon good wettability between the liquid metal and the ceramic particulate. In this paper, wettability has been measured by pressure infiltration of liquid metal through a uniformly packed powder specimen, as was done by S.-Y. Oh et al. for Al-alloy matrix composites with SiC and B_4C dispersoids(1).

BACKGROUND

WETTABILITY-Wettability can be simply defined as the ability of a liquid to wet a solid surface. When wetting is complete, the liquid forms an even continuous film over the solid surface.The extent of wetting depends upon the surface energies important in the particular physical setup. For example, the equilibrium configuration of a drop of liquid resting upon a flat solid surface is determined by the balance between liquid-vapor interfacial energy γ_{lv}, solid-vapor interfacial energy γ_{sv} and solid-liquid interfacial energy γ_{sl} ,as shown in Figure 1. This balance determines a contact angle between the liquid and solid, which is commonly used as a measure of wettability.

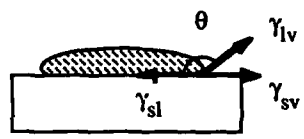


Figure 1: Schematic diagram of a liquid drop on a solid showing the balance of surface energies and the formation of a contact angle.

However, wettability can also be measured by the work necessary to immerse a solid in a liquid(2). This method is more appropriate to measurements being made on particulate material. As pictured in Figure 2, the work of immersion is the work done on the system in exchanging a solid gas interface for a solid liquid interface or

$$W_i = \gamma_{sl} - \gamma_{sv} \qquad (1)$$

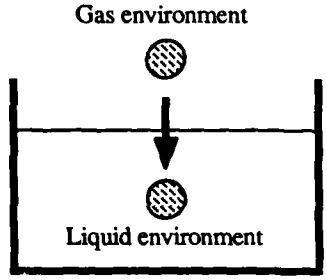


Figure 2: Illustration of immersional wetting for a solid particle. The work of immersion is $\gamma_{sl} - \gamma_{sv}$.

When the infiltration distance of a liquid metal into a particulate ceramic compact is measured as a function of applied pressure at constant time it is found that some non-zero pressure must be applied before infiltration will occur (1). A threshold pressure for infiltration of fibrous ceramic preforms has also been observed(3,4). The work of immersion is related to the threshold pressure through the following equation(1,5):

$$W_i = \frac{P_{th} w}{(1-w)\rho S'} \quad (2)$$

where w is the void fraction of the compact, ρ the density of the particulate and S' the surface area per unit mass of particulate.The derivation assumes that infiltration takes place reversibly and can be described in simple thermodynamic terms.

FLUID FLOW-The usual way to describe flow through a porous medium is with Darcy's law. For unidirectional flow Darcy's law can be written as:

$$v_0 = \frac{K}{\mu}\frac{dP}{dx} \quad (3)$$

where v_0 is the superficial velocity of the fluid (the velocity of the fluid as measured by the volumetric flow rate per unit cross sectional area where the cross section is taken perpendicular to the average direction of flow), K is the permeability of the medium, μ is the viscosity of the liquid metal, and dP/dx is the pressure drop at the infiltration front. Gravity effects have been neglected in this formulation. The equation which relates the superficial velocity v_0 to the actual velocity dL/dt in the porous medium by means of the void fraction of the medium w is:

$$v_0 = w\frac{dL}{dt} \quad (4)$$

Under conditions of constant permeability and constant pressure, Eq. (3) and Eq. (4) can be combined and integrated to obtain the following relationship between infiltration length L, time t, and pressure drop due to viscous drag ΔP_μ:

$$\frac{L}{\sqrt{t}} = \sqrt{\frac{2\Delta P_\mu K}{\mu w}} \quad (5)$$

When a threshold pressure is necessary for infiltration and caused by capillary effects, ΔP_μ is equal to the total pressure drop ΔP_T minus the the capillary pressure drop ΔP_γ (3,4). In this work, ΔP_T is measured experimentally as P_{app}. Therefore, if P_{th} is taken as ΔP_γ, Eq. (5) can be rewritten as:

$$L = \frac{2K}{\mu w}\sqrt{(P_{app}-P_{th})}\sqrt{t} \quad (6)$$

The parabolic infiltration predicted above has been observed for dynamically monitored infiltration of Saffil alumina fiber preforms with molten aluminum (3,4). However, static measurements of the infiltration of 10 mm SiC particulates with Al alloys show a linear relationship between L and $(P_{app}-P_{th})$ for a given holding time at pressure(1). The linear behavior may be due in part to the dependence of threshold pressure on hold time observed for some alloys (6). A more thorough investigation of this unusual infiltration behavior is planned.

EXPERIMENTAL METHODS

MATERIALS-The SiC particulates used had a mean diameter by volume percent of 8.37 μm and a surface area of 870 m^2/kg as measured by BET. The Zn used was of 99.99% purity; the Al used to prepare the alloys was of 99.999% purity. The alloys tested were Zn-4.5 Al, Zn-11Al, Zn-27 Al, and commercial alloy ZA12. ZA12 composition limits are: 10.5 to 11.5 Al, 0.5 to 1.0 Cu, 0.01 to 0.02 Mg, 0.005 max Pb, 0.075 max Fe, 0.05 max others (total), with the remainder Zn. The Zn-Al phase diagram is shown in Figure 3.

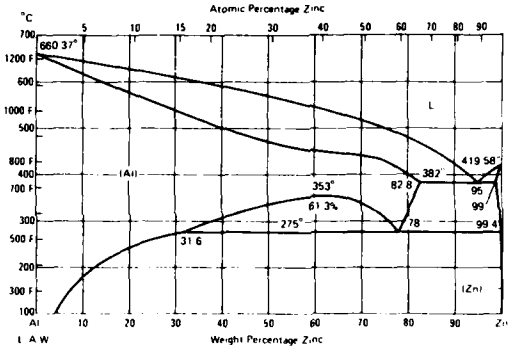


Figure 3: Al-Zn phase diagram (7).

COMPACT PREPARATION-Compacts of approximately uniform density were prepared as described in reference 1. In these experiments, the average compact void fraction,w, was 47% with a standard deviation 1.3%. This w value is similar to that obtained in previous work (1)

PRESSURE INFILTRATION-The device used to perform the pressure infiltration experiments is shown schematically in Figure 4. Each specimen was immersed in the liquid metal and allowed to preheat for about 5 minutes before the chamber was pressurized with N_2 gas. An Ar atmosphere was maintained in the compact during infiltration. After 5 minutes, the chamber was vented , the specimen was removed from the melt and allowed to air cool, and the infiltration length was measured.

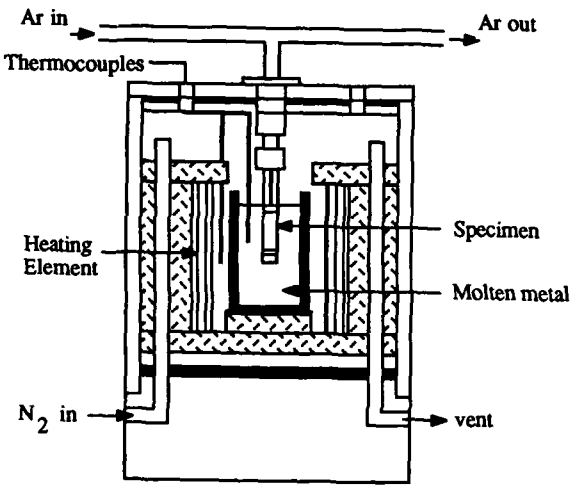


Figure 4: Sketch of the pressure chamber used for pressure infiltration.

INFILTRATION RESULTS

A typical plot of infiltration distance versus applied pressure is given in Figure 5. As shown in the figure, the fluid flow behavior is neither perfectly linear nor parabolic. This is partially due to the limitations on infiltration imposed by compact length; with a longer compact it might be possible to observe more of the drop-off in infiltration length at higher pressures characteristic of parabolic infiltration. Some scatter also exists in the data, along with a few points with abnormally low infiltration distances which may be caused by a different mechanism. If the infiltration behavior of Zn alloys is similar to that of Al alloys, infiltration distances may also be influenced by a variation in threshold pressure with holding time. A better measurement of fluid flow behavior would be obtained by measuring infiltration distance as a function of time during the infiltration; development of this kind of dynamic measurement technique for ceramic compacts is in progress.

THRESHOLD PRESSURE AND WORK OF IMMERSION RESULTS

The threshold pressure for infiltration is taken as the intercept of a penetration distance versus pressure curve fitted to the data. Both linear and parabolic fits to non-zero infiltration distances were used in order to determine the difference in predicted threshold pressure. The results are given in Table 1.

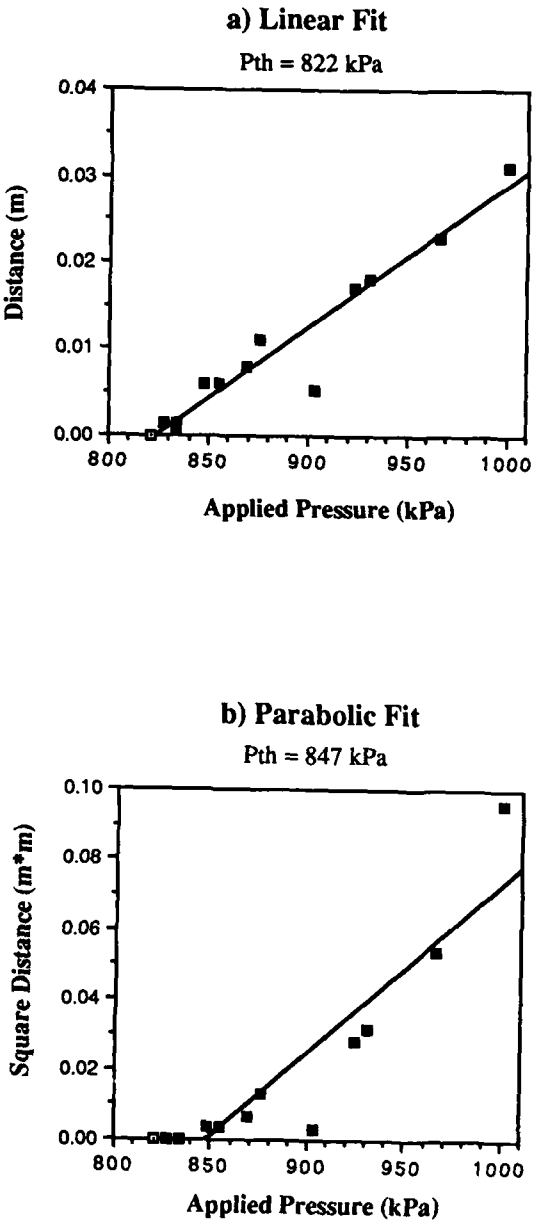


Figure 5: Plots of infiltration distance versus applied pressure for Zn at 645 +/- 5 C.

Table 1: Threshold Pressures for Zn-Al Alloys

METAL	TEMPERATURE	Pth (LINEAR FIT)	Pth(PARABOLIC FIT)
ZN	545 ^{0}C	841 kPa	872 kPa
	645 ^{0}C	822 kPa	847 kPa
ZN-4.5AL	545 ^{0}C	835 kPa	869 kPa
ZN-11AL	545 ^{0}C	1200 kPa	1200 kPa
	645 ^{0}C	819 kPa	852 kPa
ZA12	645 ^{0}C	830 kPa	857 kPa
ZN-27AL	545 ^{0}C	1210 kPa	1210 kPa
	645 ^{0}C	845 kPa	871 kPa

The difference in absolute values of threshold pressure obtained by linear and parabolic fits for any alloy is less than five percent. In addition, the differences in threshold pressure between alloys are about the same for the two fits. For simplicity, the threshold pressures are taken to be those obtained with a linear fit. These are shown in Figure 6. The uncertainty in intercept associated with curve fitting is such that the differences in threshold pressure among the alloys are probably not significant except for the case of Zn-11Al and Zn-27Al at 545 ^{0}C . These two alloys show a much higher threshold pressure, about 1200 kPa as compared to about 830 kPa. Using 47% as the average compact void fraction and 3217 kg/m^3 as the density of SiC, threshold pressure data has been converted into work of immersion data and displayed in Figure 7. These work of immersion values, about 0.380 J/m^2 for Zn-11Al and Zn-27Al at 545 ^{0}C and 0.263 J/m^2 for the rest of the alloys, are the same order of magnitude of those obtained for Al alloys (6).

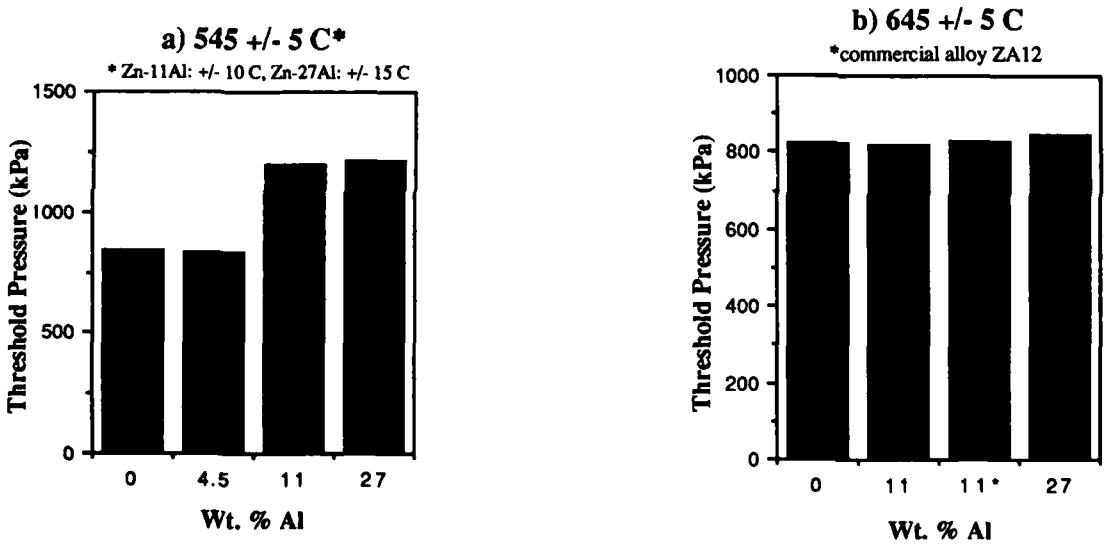


Figure 6: Threshold pressures for Zn-Al Alloys.

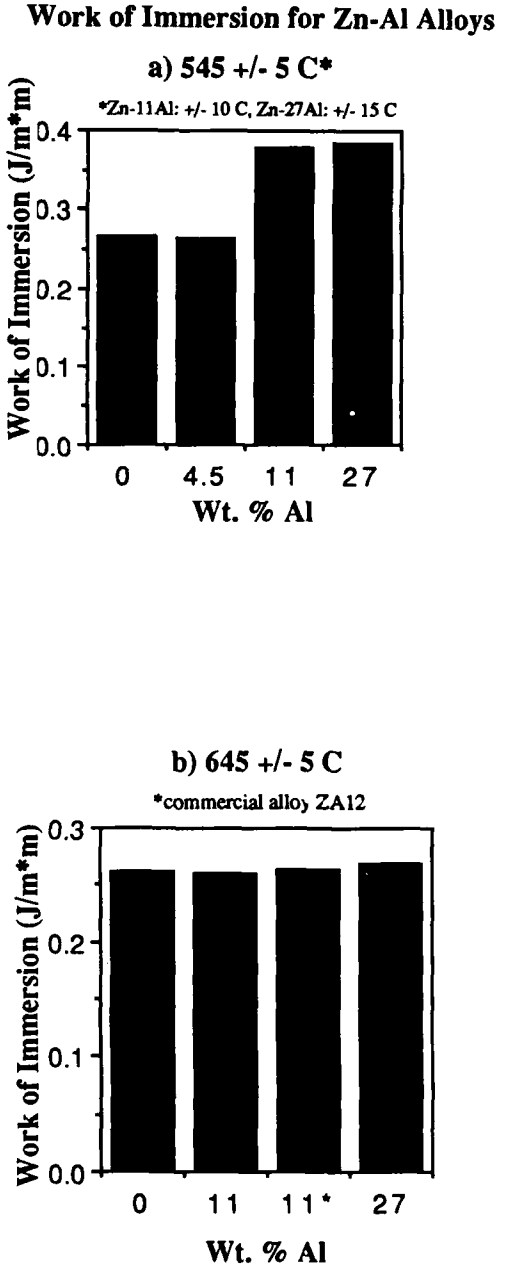


Figure 7: Work of immersion for Zn-Al Alloys.

SUMMARY

1. Threshold pressures for Zn at 545 ^{0}C and 645 ^{0}C, Zn-4.5Al at 545 ^{0}C, Zn-11Al at 645 ^{0}C, ZA12 at 645 ^{0}C, and Zn-27Al at 645 ^{0}C are all about 830 kPa. This converts to a work of immersion of 0.263 J/m^2.

2. Threshold pressures for Zn-11Al and Zn-27Al at 545 ^{0}C are about 1200 kPa. This converts to a work of immersion of 0.380 J/m^2.

ACKNOWLEDGEMENTS

International Lead and Zinc Research Organization

SDIO/IST /ONR

REFERENCES

1. S.-Y. Oh, J.A. Cornie and K.C. Russell, Met. Trans. A in press.

2. H. J. Osterhof and F. R. Bartell, J. Phys. Chem. 34, (1930), 1399-1411.

3. L. J. Masur, PhD Thesis, Department of Materials Science and Engineering, MIT, February 1988.

4. T. Wong, B.S. Thesis, Department of Mechanical Engineering, MIT, January, 1988

5. A. Mortensen and J.A. Cornie, Met. Trans, 18A (1987), 1160-1163.

6. S.Y. Oh, J.A. Cornie and K.C. Russell, Met. Trans. A in press.

7. "ASM Metals Reference Book", 2nd ed, American Society of Metals, Metals Park, Ohio (1983), p. 481.

THE WETTING KINETICS OF ALUMINIUM AND ITS ALLOYS ON SINGLE-CRYSTAL SiC

V. Laurent, D. Chatain, N. Eustathopoulos
LTPCM, UA 29 CNRS, ENSEEG, Domaine Universitaire
BP 75, 38402 Saint Martin D'Heres, Cédex, France

X. Dumant
Cegedur Pechiney, Centre de Recherches de
Voreppe, BP 27, 38340 Voreppe, France

ABSTRACT

The time dependence of contact angle in the Al/single-cristal SiC system was investigated in the 973 to 1173 K temperature range by the sessile drop method in a vacuum of 2×10^{-5} Pa.

After deoxidation of Al, the contact angle θ, equal to 125°, decreased gradually to a value of about 60°, the rate of change of θ being strongly temperature-dependent. This wetting process is controlled by SiC dissolution in the liquid metal. Additions of silicon to aluminium inhibited the formation of Al_4C_3 at the interface but did not affect either the general wetting behaviour or the contact angle values. No noteworthy improvement in wettability in the Al/SiC system was obtained by alloying Cu, Sn and Ti with Al. The presence of a silica film on the SiC surface appeared to have a beneficial but limited effect on the wetting of SiC by aluminium.

THE STUDY OF THE WETTABILITY OF ALUMINIUM/CERAMIC SYSTEMS by the classical sessile drop method gives rise to a number of difficulties related to the appearance of an oxide layer surrounding the Al drop (|1|,|7|). The presence of this oxide film leads to experimental curves as described in Fig.1(a).
High and nearly constant contact angles are measured up to a temperature between 1173 K and 1273 K depending on the experimental conditions (vacuum, oxygen partial pressure), where a sharp decrease in the contact angle occurs. At this point, the oxide layer evaporates, resulting in the development of a real Al/ceramic interface and consequently allowing the study of intrinsic wetting in these systems. However the wetting of ceramics by Al in the low temperature range is not well-known.

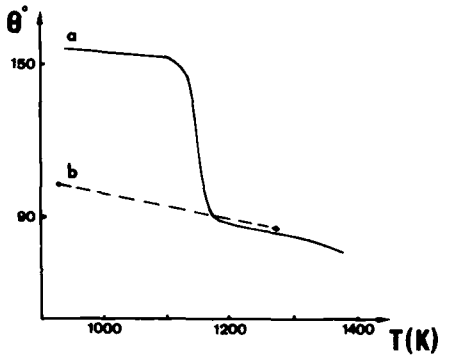


Fig.1 : Variation of contact angle with temperature for the Al/Al_2O_3 system.
(a) Typical shape of experimental wetting curve obtained in this system under vacuum ($P = 10^{-2} - 10^{-4}$ Pa),
(b) according to |1| ($P = 2\text{-}5 \times 10^{-5}$ Pa).

As the most interesting temperature range for composite elaboration is below 1173 K, this work is predominantly aimed at studying the kinetics of wetting in the Al/SiC system below this temperature. The experimental conditions are selected to eliminate the influence of the oxide layer on wetting.

The (Al-C-Si) ternary phase diagram was established experimentally by J.C. Viala et al |2|. No two-phase field exists with SiC and pure liquid Al in equilibrium. From the melting point of aluminium, SiC reacts with Al to form aluminium carbide, Al_4C_3, and an Al-Si alloy :

$$SiC(s) + Al(l) \rightleftarrows Al_4C_3(s) + (Si)_l \qquad (1)$$

But the reaction can be avoided by prior alloying of silicon to Al at a content corresponding to the three-phase (Al-Si) liquid-Al_4C_3-SiC equilibrium. This particular value of silicon content increases with temperature as indicated on Fig.2.

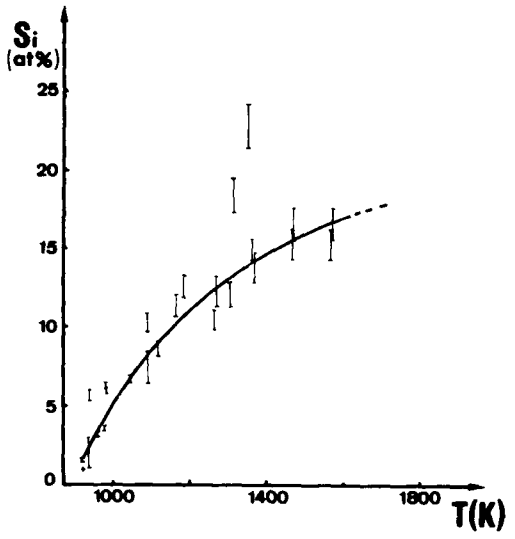


Fig.2 : Variation of silicon content of the (Al-Si) alloy in equilibrium with SiC and Al_4C_3 as a function of temperature |2|.

EXPERIMENTAL SET-UP

The ultra-high vacuum apparatus employed for the sessile drop experiments (total pressure less than $5x10^{-5}$ Pa throughout the experiment) is described in detail in |3|. A molybdenum heater surrounded by molybdenum radiation shields is located in a water-cooled stainless-steel chamber, which has two windows enabling the sessile drop on the substrate to be illuminated and projected on a screen. Contact angles are measured directly from the image of the drop section with an accuracy of ± 1°. An oxygen electrochemical gauge measured a low and temperature-independent oxygen partial pressure of about 10^{-15}Pa inside the molybdenum screens.

The SiC single crystal material consists of a black variety of the hexagonal structure type. The major surfaces used in the experiments are {0001} orientations of the hexagonal structure. A SIMS analysis of the surface of SiC single crystals shows that the major metallic impurities are Al and Cu in the ppm range. Samples are polished to a 0.1 µm diamond finish. The polishing action produces a smooth surface with a 0.015 to 0.035 µm roughness range and also eliminates the oxide film developed by oxidation of SiC in air at room temperature. The purity of the aluminium employed was 99.9999 %. Sample weight was approximately 10 mg. The Al specimen is freshly cut on all of its faces a few minutes before introducing it into the furnace since a very short exposure to air limits the thickness of the oxide coating to less than 30 Å |4|.

After evacuating the system to $3x10^{-5}$Pa, the wetting experiments were carried out. They consisted in following the constant temperature time-dependent variation in advancing contact angle until a steady-state is observed.

RESULTS AND DISCUSSION

During recent investigations of the wetting of aluminium oxide by liquid aluminium |1|, the experimental conditions (high vacuum, low oxygen partial pressure and fresh metallic surfaces) were shown to inhibit the influence of the oxide layer on the wettability from the melting point. This inhibiting effect has been ascribed to a mechanism of oxide film reduction by liquid aluminium producing the gaseous suboxide Al_2O. The authors observed a sharp decrease in the contact angle from a high value greater than 150° to a value of about 110° within the first ten minutes of holding at the melting point. After the decrease, the change in the contact angle with time is negligible as can be seen on Fig.3.

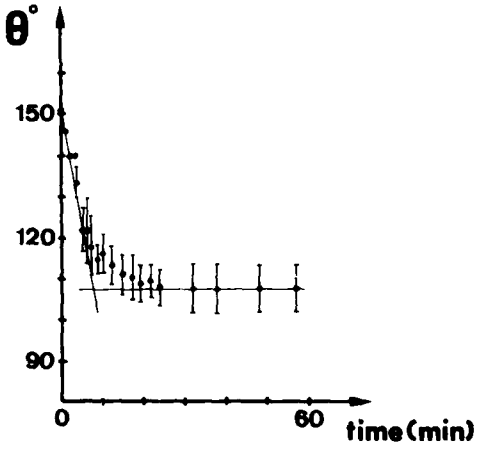


Fig.3 : Time dependence of contact angle obtained with the Al/Al_2O_3 system at 933 K ($P = 2\text{-}5\ 10^{-5}$Pa)

The variation of the final steady contact angle with temperature showed a linear decrease in the entire temperature range investigated. This variation is presented in Fig.1 by the broken line (b).

The kinetics of wetting in the Al/SiC system is more complex than that previously described with the Al/Al_2O_3 system. The time dependence of the contact angle at fixed temperature observed with this system is illustrated by the diagram in Fig.4. Three

kinetic areas may exist. The first area, where the contact angle decreases in about ten minutes from the "θ_o" instantaneous angle value (equal to 150 ± 5°) to the "θ_1" value, is similar to the steep variation observed with the Al/Al_2O_3 system, at the beginning of the experiment (Fig.3). This denotes the deoxidation of the Al drop and results in the θ_1 value which is of great interest for any applications involving brief contact between liquid Al and SiC, in which case, a real Al/SiC interface is set up (mechanical breakdown of the oxide layer or reduction of the layer under high vacuum). The average value of the θ_1 angle is slightly temperature-dependent : it is equal to 125 ± 10° at 973 K and 110 ± 10° at 1073 K.
In the third area, the contact angle remains virtually constant, equal to the "θ_f" value regarded as the steady state contact angle. It is evaluated at 60 ± 5° in the 973 to 1073 K temperature range and 55 ± 5° at the higher temperatures investigated.

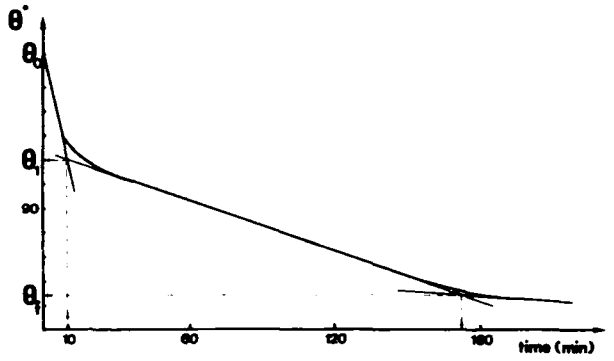


Fig.4 : General shape of kinetic wetting curve obtained with the Al/SiC system at fixed temperature. The definition of particular contact angle values is clearly indicated.

The time-dependent wetting curve differs from that obtained with the Al/Al_2O_3 system only by the middle-kinetic area which must result from the reaction (1) at the Al/SiC interface until equilibrium or a steady state is established. This statement is supported by the fact that the slope $d\theta/dt$ increases sharply with increase in temperature. This is illustrated by the example of a kinetic curve shown in Fig.5. The value of the slope is multiplied by 5 when the temperature is raised from 1050 to 1150 K.
Ultimately, when the temperature is raised directly to a high level ($T \geq 1123$ K), the deoxidation kinetics and the greatly accelerated middle kinetics follow each other continuously and the θ_1 angle can no longer be evaluated. Such an experimental curve obtained by a straight increase in the temperature to 1143 K is shown in Fig.6.

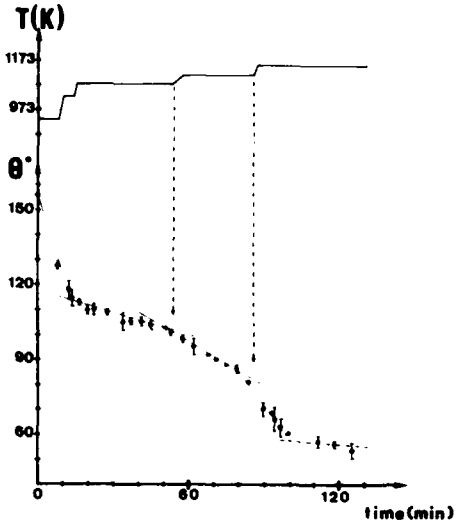


Fig.5 : Time-dependent wetting curve showing the effect of temperature on middle kinetics.

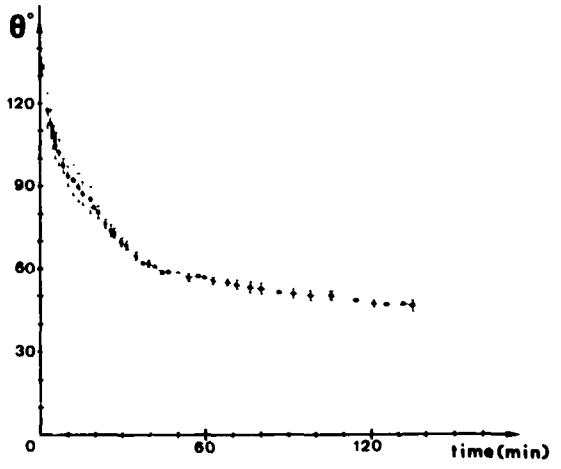


Fig.6 Variation of contact angle with time at 1143 K.

In this case, 20 minutes are needed to reach the steady state instead of more than 3 hours at 1073 K.
The reaction between SiC and Al initiating the middle kinetics has been studied in detail by J.C. Viala et al [5]. They observed that the reaction proceeds in two steps. In a first stage, the silicon carbide dissolves in the liquid metal :

$$SiC\ (s) \rightleftharpoons (Si)_l + (C)_l \qquad (2)$$

Secondly, the Al_4C_3 compound precipitates growing in random islands on the SiC surface. The scanning electron micrograph in Fig.7 shows an interface zone at the bottom of the solidified aluminium drop on its SiC substrate after heat treatment up to 1173 K. This zone was revealed after an ultramicrotomy cut of the Al drop which pulled out a part of the interface. The extended heat treatment results in a thick layer of Al_4C_3 aggregates.

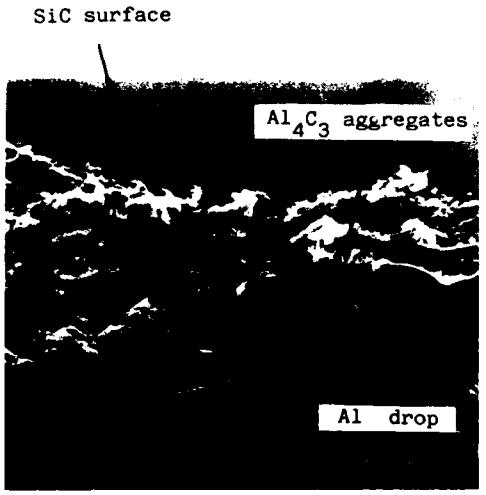


Fig.7 : Scanning electron micrograph showing Al_4C_3 aggregates at the bottom of the Al drop (heat treatment up to 1173 K)(x1000).

To appreciate the relation between the wetting behaviour in the Al/SiC system and the Al_4C_3 formation, wetting experiments were performed with Al-Si alloys in which the silicon was added in such an amount to eliminate the reaction in the investigated temperature range. The time-dependence of wetting angle obtained with an Al-18 at% Si alloy held at 1073 K is shown in Fig.8.

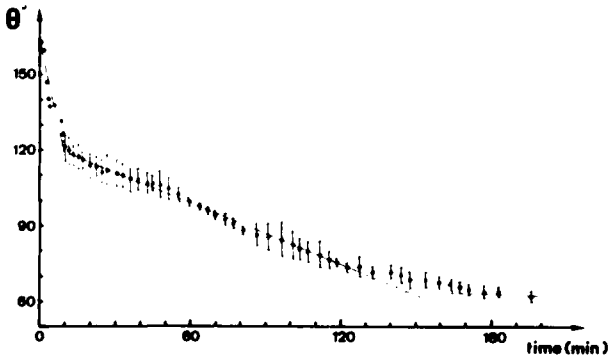


Fig.8 : Variation of contact angle with time obtained with the Al-18 at% Si/SiC system at 1073 K.

The kinetics of wetting exhibits the same three areas of θ variation with time : the deoxidation area, the middle kinetics area and, finally, a near-zero slope area. Moreover, the wettability of SiC is not significantly affected by the addition of silicon : both θ_1 and steady-state θf values are similar to those obtained with pure Al. The formation of Al_4C_3 was effectively avoided by the addition of silicon in a 18 at% content : the scanning electron micrograph in Fig.9 shows no reaction product in the interface zone revealed by means of drop solidification shrinkage.

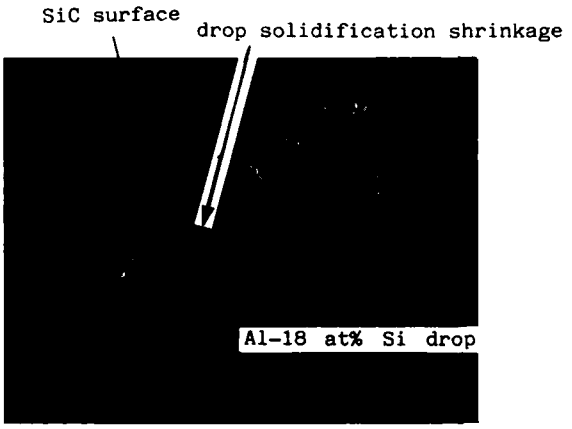


Fig.9 : Scanning electron micrograph showing the bottom of an Al-18 at% Si drop on its sustrate after heating to 1043 K (x420) .

From these results, it appears that the continuous but sluggish wetting behaviour of the Al/SiC system is not rate-determined by the Al_4C_3 formation but is controlled by the dissociation process of silicon carbide to Si and C. The dissociation of SiC continues until the liquid metal is saturated with carbon at a very low content. The non-zero value of the slope dθ/dt at the end of the wetting curve is likely to be a bulk effect and indicates that a steady-state, rather than a real equilibrium, is reached.

Very often, the production of Al/SiC composites involves a double $Al/SiO_2/SiC$ interface, since the silicon carbide reinforcement employed is oxidized naturally or on purpose. The study of oxidized SiC surface wetting by aluminium by the classical sessile drop method gives rise to a major difficulty : the kinetics of oxidation of the Al surface in contact with silica conflicts with the kinetics of Al deoxidation as described previously, extending the study of the wetting behaviour to higher temperatures or longer holding times |3|. Obviously, such conflict does not happen during the production of composites by squeeze-casting

or semi-solid casting as, in both processes, the oxide film on the Al surface if it exists, will be mechanically disrupted.

Wetting experiments were performed using the wetting tensiometric method, which enables effective and direct contact between the aluminium and silica surfaces, after prior deoxidation of the metal by high-temperature treatment under vacuum |1|. The contact angles formed by the meniscus on the vertical solid when the solid is dipped into the melt, were measured at two temperatures : 1003 K and 1173 K. Their values, of around 100° at both temperatures, are found to be similar but somewhat lower than those obtained in the Al/SiC system after Al deoxidation. It can be concluded that the SiC oxidation has a beneficial but limited influence on the wetting of SiC by aluminium.

The effect of the addition of Cu (5 at%), Sn (4 to 11 at%) and Ti(0,22 at%) was studied by the sessile drop method. Copper is a classical alloying element of Al, titanium a strong carbide former and tin is known to produce a significant decrease in the surface tension of Al |6|. The general wetting behaviour and θ_1 contact angle values with any element addition are found to be similar to those obtained with pure aluminium. Additions of the alloying element affect only the value of the steady-state contact angle θ_f. In the 1073 to 1123 K temperature range investigated, the θ_f value rises from 60 ± 3° to 70 ± 2° with Cu alloying and is lowered to 47 ± 2° by Sn addition. This latter effect can be easily explained by the inherent effect of Sn on the liquid-vapour tension of Al.

CONCLUSIONS

The wetting kinetics of aluminium and its alloys on SiC single crystals was investigated in the 973-1173 K temperature range under experimental conditions (high vacuum, low oxygen partial pressure, fresh metallic surfaces) allowing an effective metal-substrate interface to develop as early as at the melting point of Al.

The time-dependence of contact angle exhibits three distinct areas. First a rapid deoxidation of Al results in a steep decrease in the contact angle from 150° to 125° at 973 K and to 110° at 1073 K. Then a gradual change in contact angles is observed after which the steady state develops. The steady contact angle varies slightly with temperature between 60° and 55°. The middle kinetics which is considerably accelerated with increase in temperature is due to the dissolution of SiC in the liquid metal.

Silicon is alloyed to Al in such amounts as to prevent Al_4C_3 formation at the interface. Neither the general wetting behaviour nor the contact angle values differ appreciably from those obtained with the pure Al/SiC system.

The additions of other elements - Cu, Sn and Ti - to aluminium do not induce a noteworthy improvement in the wetting of SiC. The oxidation treatment of the SiC surface is found to have a beneficial but limited effect on the wettability in the Al/SiC system.

ACKNOWLEDGEMENT

This work was done under a contract with Pechiney Voreppe who the authors thank for the assistance given. They are also grateful for useful discussions held with J.C. Viala.

References

1 V. Laurent, D. Chatain, C. Chatillon and N. Eustathopoulos, in press, Acta Metall.
2 J.C. Viala, P. Fortier, C. Bernard and J. Bouix, "Developments in the Science and Technology of Composite Materials", A.E.C.M., Bordeaux, 1985.
3 V. Laurent, D. Chatain and N. Eustathopoulos, J. Mater. Sci. 22, 244-250 (1987).
4 A. Bianconi, Phys. Rev. B19, 2837 (1979).
5 Dr. F. Bosselet and Dr. J.C. Viala, Laboratoire de Physicochimie Minérale 1, Université Claude Bernard - Lyon 1, 43 boulevard du 11 novembre 1918, 69622 Villeurbanne Cédex, France, private communication.
6 L. Goumiri, J.C. Joud, P. Desré and J.M. Hicter, Surf. Sci. 83, 471 (1979).
7 J.J. Brennan and J.A. Pask, J. Am. Ceram. Soc. 51, 569 (1968).

BONDING OF SiC AND ALUMINUM+

S. Li, R. J. Arsenault
Engineering Materials Group
University of Maryland
College Park, Maryland 20742-2111 USA

P. Jena*
Physics Department
Virginia Commonwealth University
Richmond, Virginia 23284-2000 USA

ABSTRACT

The total energies of a number of clusters modelled to represent the Al/SiC interface have been calculated as a function of distance separating the two surfaces of SiC and Al. The adhesive energy of the interface is calculated by minimizing the total energies corresponding to various crystallographic orientations of the SiC and Al surfaces. The results are used to provide semiquantitative understanding of the bonding mechanism and the effect of reconstruction at the Al/SiC interface.

ARSENAULT AND CO-WORKERS have shown[1,2] that the mechanism by which strengthening occurs is due to the difference between the coefficient of thermal expansion of SiC and Al. This results in a high dislocation density that is generated primarily at the interface. If a weak bond exists between the metal and the matrix, the metal pulls away and expands freely. Consequently, no dislocations are generated at the interface. Thus, a good bond at the interface is necessary for the production of high dislocation density.

Although several experimental investigations[3,4] based on macromechanics have reported the Al/SiC bond to be good, no basic understanding of the mechanism of this bonding exists. The reasons for this are twofold: First, the nature and composition of the interface are not fully known. For example, there are three hypotheses[5-7] concerning the interface between SiC and Al matrix. (1) There is a SiO_2 layer at the interface. (2) There is an Al_4C_3 film at the interface. (3) There is nothing at the interface, i.e., the interface is formed simply by two surfaces of SiC and Al. Secondly, even if one ignores this uncertainty in the composites at the interface, the problem is too complicated for a theoretical study at the atomic level due to reduced symmetry and large number of atoms per unit cell. Thirdly, any attempt to use interatomic potentials across the interface are doomed to failure for many reasons.

To illustrate this problem further, let us enumerate all the possibilities one needs to explore for a fundamental understanding of the bonding at the interface. (1) The interface can be formed by surfaces of different crystallographic orientations of SiC and Al. (2) SiC has two different structures, α and β. The whiskers are in the β-phase whereas the particulates have the α-structure. Furthermore, there are six different polymorphic structures for α-SiC. (3) The interface can be formed between C and Al layers or Si and Al layers. (4) The atoms at the interfaces formed by all orientations of SiC and Al surfaces do not constitute a commensurate structure (i.e., there is a lattice missmatch at the interface). This is illustrated in Figs. 1, 2, and 3 where we show the unreconstructed (i.e., no atomic distortions have been allowed) surfaces of Al(111) [110] ∥ α-SiC($000\bar{1}$) [$2\bar{1}\,\bar{1}0$], Al(100) [100] ∥ α-SiC($000\bar{1}$) [$2\bar{1}\,\bar{1}0$] and Al (100) [100] ∥ β-SiC ($2\bar{1}\,\bar{1}$) [111] respectively. We have chosen the (0001) surface of α-SiC and ($2\bar{1}\,\bar{1}$) surface of β-SiC since they represent, respectively, the largest area of the reinforcement. Similarly, Al(111) and (100) surfaces represent low index planes. In. Fig. 1, note that there are different regions at the interface where atoms are situated differently. For example, in the region A, the atoms are nearly on the on-top posi-

* Physics Department, Virginia Commonwealth University, Richmond, VA 23284-2000.

+ This research was partially supported by the Office of Naval Research under Grant N00014-85-K-0007 and the Computer Science Center of the University of Maryland.

tion, whereas in region C, the atoms are near the bridge position. The regions B, D, and E represent different patterns, somewhat intermediate between on-top and bridge positions. The unit cell, therefore, contains a rather large number of atoms, thus making any ab initio studies of bond energies virtually impossible. Figures 2 and 3 pose similar problems. (5) One would expect the atoms at the interface to reconstruct, i.e., move into lower energy positions. No experimental or theoretical studies are available that could shed light on the atomic configurations at the interface.

Given all the problems outlined above, it is not surprising that there are not microscopic theoretical studies of SiC/Al interface to date. One technique that is ideally suited for studying electronic structure and bonding at interfaces is the slab method based upon fully linearized augmented plane waves (FLAPW)[8]. Here one can calculate accurately the total energies of the interface as a function of interlayer separation. Unfortunately, in the present problem, the large number of atoms per unit cell would make this technique intractable.

Systems with complicated geometries are often modelled by molecular clusters. Here, one represents an otherwise infinite solid by a small cluster of atoms whose coordinates are determined from the structure of the extended system. One hopes that the results are not very sensitive to the size of the cluster and/or to the boundary conditions imposed at the cluster surface. Using pseudopotentials, one can treat about 30 atoms in a cluster self-consistently[9]. These calculations are computer intensive and impractical for the present study due to the complexity of the SiC/Al interface alluded to in the above.

Semi-empirical studies[10,11], therefore, provide an alternative route. We use the intermediate-neglect of differential-overlap (INDO) method to study adhesion at SiC/Al interfaces. Although semi-empirical and semi-quantitative, our study represents the first attempt at understanding the bonding at SiC/Al interface from an atomic viewpoint. By minimizing the total energy of the cluster, we determine the equilibrium separation between adjacent layers at the interface and its adhesion energy. Calculations are repeated for different crystallographic orientations as well as for varying atomic composition at the interface. The details of the calculation method are described elsewhere[12].

RESULTS AND DISCUSSIONS

In the present cluster model, the energy necessary to create the interface is defined by[13],

$$\Delta E = (E_{Al} + E_{SiC}) - E \qquad (1)$$

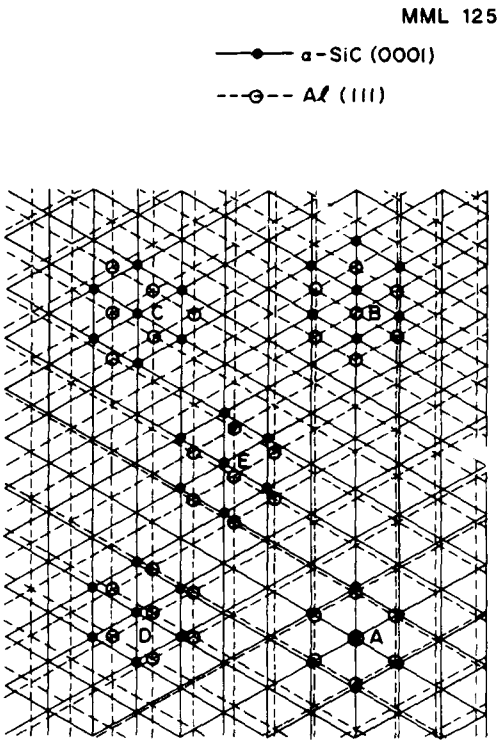


Fig. 1. Unreconstructed Al (111) [110] ∥ α-SiC (0001) [2$\bar{1}$ $\bar{1}$0].

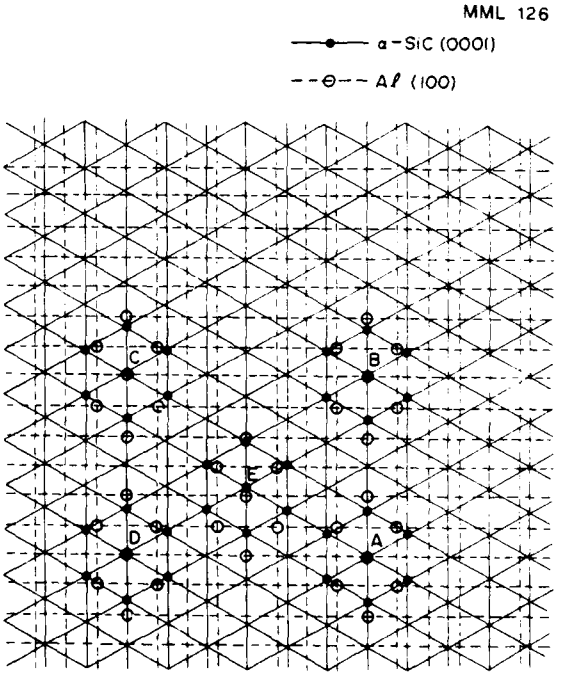


Fig. 2. Unreconstructed Al (100) [100] ∥ α-SiC (0001) [2$\bar{1}$ $\bar{1}$0].

Here E_{Al} and E_{SiC} are the total energies of the Al and SiC clusters, respectively. E is the total energy of the Al/SiC composite. This is calculated by varying the distance between cleavaged surfaces of Al and SiC and E corresponds to the minimum in this energy. The cleavaged basal plane of SiC could contain either Si or C atoms. The results of ΔE/atom and $\nu = \Delta E/(A_{SiC} + A_{Al})$ are presented in Table I for the clusters shown in Fig. 1.

A reconstruction of the interface can take place by two different methods. The first method involves the introduction of dislocations at the interface. The misfit between the two lattices is

$$\delta = (a_{SiC} - a_{Al})/a_{Al} = 0.073 , \qquad (2)$$

where $a_{SiC} = 3.07$ Å, and $a_{Al} = 2.86$ Å. This misfit can be accommodated by two sets of parallel dislocations, the sets of parallel dislocations are perpendicular to each other. The spacing between the dislocations is given by[14]

$$D = \frac{b'}{\delta} = 40.0 \text{ Å} , \qquad b' = (a_{SiC} + a_{Al})/2 . \qquad (3)$$

In the ideal condition, the lattice misfit can be completely accommodated without a long-range strain fields, but the extra energy due to the structural distortions, i.e., the core

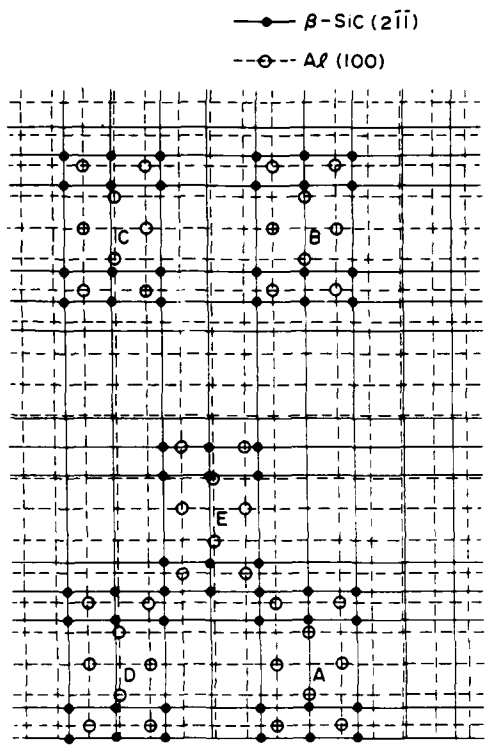


Fig. 3. Unreconstructed Al (100) [100] ∥ β-SiC (2$\bar{1}$ $\bar{1}$) [111].

Table I. Calculated Results for Different Regions Shown in Fig. 1.

First Layer of SiC	Region	E (Hartree)	E_{Al} (Hartree)	E_{SiC} (Hartree)	ΔE (eV)	ΔE/atom (eV/atom)	ν_2 (eV/Å^2)
	near on top (A)	-118.7039	-26.9485	-91.6031	-2.88	0.20	0.063
	near bridge (C)	-118.6012	-26.7335	-91.6031	-7.20	0.51	0.157
C	B	-118.7434	-26.9485	-91.6031	-5.22	0.37	0.114
	D	-118.6052	-26.9485	-91.6031	-1.46	0.10	0.032
	E	-118.6273	-26.9485	-91.6031	-2.06	0.14	0.045
	near on top (A)	-117.3018	-26.9485	-90.2001	-4.16	0.29	0.091
	near bridge (C)	-117.2636	-26.7335	-90.2001	-8.98	0.64	0.196
Si	B	-117.3808	-26.9485	-90.2001	-6.32	0.45	0.138
	D	-117.2257	-26.9485	-90.2001	-2.10	0.15	0.046
	E	-117.2713	-26.9485	-90.2001	-3.34	0.23	0.073

energy of the dislocations caused by the interface dislocations, must be considered. The core energy is estimated as $E_c = \mu b^2/10$ per atomic spacing[15], where μ is the shear modulus of Al (29 GPa) and b is the Burgers vector of Al (2.86 Å). For Al, the E_c = 0.38 eV per atom spacing. Now, if we consider a square with an area (A) of 40 × 40 $Å^2$, it contains a dislocation length (L) which is equal to 2 × 40 Å. Therefore, the core energy increased in this area can be calculated as follows

$$E_c' = \frac{E_c L}{2A} \qquad (4)$$

If the above defined values of E_c, L, and A are employed, then E_c' = 0.07 eV/$Å^2$. Recall that the average value of the adhesive energy of the Al atoms (reconstructed Al structure) in both the bridge and on top position with either the C or Si as the first layer is 0.162 eV/$Å^2$. Now, the core energy presence has to be subtracted if the Al reconstruction is to occur as the result of the introduction of dislocations at the interface. Therefore, the adhesive energy would be (0.162 eV/$Å^2$ - 0.007 eV/$Å^2$) 0.155 eV/$Å^2$. This adhesive energy is much larger than the surface energy of pure Al, which is 0.055 eV/$Å^2$.

The second possible method is that the misfit is accommodated entirely by long range strains. To estimate the strain energy (per unit area[16]), the following formula can be used.

$$E_e = \frac{1}{2} B \left(\frac{\delta V}{V}\right)^2 h \qquad (5)$$

where δV is the change in volume due to the strained Al lattice, h is the Al film thickness, and B is the bulk modulus. Using B = 57.5 GPa, $\delta V/V = 3 \times 0.073$, h = 20 Å, we obtain E_e = 0.170 eV/$Å^2$, and we wold have the adhesive energy as 0.162 - 0.170 = - 0.008 eV/$Å^2$ which means a bond would not occur.

Therefore, the likely arrangement is two sets of parallel dislocations which are perpendicular to each other to allow the arrangement of the atoms in the bridge and on top position. If this is the case, the adhesive energy of the SiC/Al interface would be 2 - 3 times greater than the surface energy of Al. There are no reported values of surface energy of SiC, however Mullins[17] has argued that the work, E(∞) required to separate two adjacent atomic planes of area A can be estimated as the surface-free energy, or the elastic work required to move them through a distance x. The adhesive energy per unit area is

$$\nu = \frac{E(\infty)}{2A} = \frac{Y}{2} \int_0^{a_c} \left(\frac{x}{a_o}\right) dx \quad \alpha \quad Y \qquad (6)$$

where Y is the Young's modulus, a_c is the distance at which separation takes place, and a_o is the atomic radius. The surface energy is approximately proportional to the elastic modulus. Since the elastic modulus of SiC and Al are 483 and 69 GPa, respectively, this means that the surface energy of SiC will be 7 times larger than Al. According to our results, the adhesive energy of reconstructed Al with SiC is 2 - 3 times greater than Al. This seems reasonable for the SiC/Al composites, and it is in agreement with the experimental result[4] which found that the bond strength between SiC/Al was greater than that of Al/Al.

CONCLUSIONS

From the above discussed results, some conclusions can be drawn:

1. The bond strength between SiC and Al could possibly be 2 to 3 times stronger than the bond between Al and Al.
2. At the interface, if the Al atoms are unreconstructed, the adhesive energy between Al (111) and α-SiC (0001) is nearly the same as the surface energy of the pure Al. If the Al atoms are reconstructed, and the two sets of dislocations are perfectly introduced, the adhesive energy is 2 ~ 3 times larger than pure Al.

REFERENCES

1. R. J. Arsenault and N. Shi, Mat. Sci. & Eng., 81, 175 (1986).
2. M. Vogelsang, R. J. Arsenault, and R. M. Fisher, Metall. Trans. A, 17, 379 (1986).
3. A. P. Divecha, S. G. Fishman, and S. D. Karmarkar, J. Met., 33, 12 (1981).
4. Y. Flom and R. J. Arsenault, Mat. Sci. & Eng., 77, 191 (1986).
5. R. J. Arsenault and C. S. Pande, Scripta Met., 18, 1131 (1984).
6. L. Porte, J. Appl. Phys., 6, 635 (1986).
7. S. R. Nutt, "Interfaces in Metal-Matrix Composites", A. K. Dhingro and S. G. Fishman, eds., p. 157, The Metallurgical Society, Inc., PA (1986).
8. O. K. Andersen, O. Jepsen, and M. Sob, "Electronic Band Structure and Its Applications", ed. M. Yussouff, p. 1, Springer-Verlag (1987); M. Weinert and A. J. Freeman, J. Mag. Magn. Materials, 38, 23 (1983).
9. D. E. Ellis, Handbook on the Physics and Chemistry of the Actinides, eds. A. J. Freeman and G. H. Lander, p. 1, Elsevier Publishers, B. V. (1985); M. R. Press, S. N. Khanna, and P. Jena, Phys. Rev. B, 36, 5446 (1987).
10. J. A. Poole and D. L. Beveridge, "Approximate Molecular Orbital Theory", McGraw Hill, (1970).
11. J. Ferrante and J. R. Smith, Phys. Rev. B, 19, 3911 (1979).
12. S. Li, R. J. Arsenault, and P. Jena, to

be published.
13. I. P. Batra, Phys. Rev. B, 29, 7108 (1984).
14. D. A. Porter and K. E. Easterling, "Phase transportation in metals and alloys", Van Nostrand Reinhold (UK) Co. Ltd. (1984).
15. R. E. Smallman, "Modern Physical Metallurgy", Butterworth & Co. (Publishers) Ltd. (1985).
16. N. H. Fletcher and K. W. Lodge, "Epitaxial Growth", ed., J. W. Mathews, Academic, New York, (1975) parts A and B.
17. W. W. Mullins, "Metal Surface", p. 23, ASM, Metals Park, Ohio, Joint ASM-AIME Seminar, (1963).

SOLIDIFICATION PROCESSING OF AN ALUMINUM/ALUMINA COMPOSITE

M. N. Gungor
Westinghouse R&D Center
Pittsburgh, Pennsylvania 15235 USA

J. A. Cornie, M. C. Flemings
Massachusetts Institute of Technology
Cambridge, Massachusetts 02139 USA

ABSTRACT- Al-4.5w%Cu/FP-Al_2O_3 unidirectional fibrous composites with volume fractions up to 0.55 were fabricated by pressure infiltration. Following infiltration and subsequent solidification the metal matrices were re-melted and re-solidified to study the mechanisms of the solidification. Since the fibers determined the available space for dendritic growth, the final microstructure of the composite alloy was significantly influenced by solidification conditions. The coarsening kinetics of the secondary dendrite arms and solid-state diffusion were rapid. Consequently, microsegregation in the composite alloy was reduced significantly compared to that in the unreinforced alloy.

INTRODUCTION- Fiber reinforced metal matrix composites (MMC's) are promising materials for future industrial applications where lightweight structures, and engineerable mechanical and physical properties might be required. Successful development of these applications could depend on successful development of composite processing techniques. Although various processing techniques have been available for fibrous metal matrix composite systems, casting and solidification processes have been drawing much attention recently since they offer near-net shape processing capability, selective reinforcement, controllable microstructures, and perhaps most importantly lower cost compared to that of composite materials produced by other composite processing techniques. A number of researchers have studied various aspects of cast composites including pressure infiltration of of fiber bundles by molten metal, squeeze casting, interfacial reactions, and structure and properties which have been reviewed recently (1-6).

The object of this paper is to present the results of a study on the solidification processing of Al-4.5w%Cu in the presence of continuous Al_2O_3 fibers. In this study, a pressure infiltration approach was taken to produce the metal matrix composite specimens which were subsequently re-melted and re-solidified at various rates to study solidification process. A particular goal was to examine coarsening kinetics and microsegregation behavior of the matrix alloy as a function of solidification time.

EXPERIMENTAL WORK- The metal matrix material used had an average 4.6 wt% Cu concentration. The fibers, polycrystaline α-alumina, 20 microns in average diameter (a.k.a. "Fiber FP"), were provided by the E.I. Du Pont Company, Delaware. A small billet of the alloy was pressure infiltrated into a continuous fiber preform. The experimental procedure regarding the infiltration of the fiber preform has been reported previously (7,8). Following pressure infiltration and solidification, the cast specimens were cut into smaller lengths. These smaller specimens subsequently were placed in a graphite container and were heated in an electric resistance furnace above the liquidus temperature of the matrix alloy, and solidified with the controlled cooling rates.

The metallographic samples were prepared in transverse and longitudinal directions with respect to fibers. The samples were mounted and diamond polished. Following the polishing, samples were etched with an etchant (consisted of 2 g NaOH / 4 g $KMnO_4$/1000ml distilled water) for 15-30 seconds at room temperature. This etchant reveals the microsegregation patterns between the Al-rich dendrite core (α phase) and Cu-rich interdendritic region (α+θ eutectic). Detailed information on the metallographic preperation of the samples has been reported elsewhere (3,7,8). Samples were examined using an optical microscope. The average secondary dendrite arm spacing was determined using optical microscopy and the analytical methods described in detail in references 9-11. Similarly the details of the experimental method that was employed in using a Cameca Camebax scanning electron microprobe to determine microsegregation have been reported in references 8 and 12.

RESULTS AND DISCUSSION- Figure 1 shows four transverse microstructures typical of those obtained in this work. The microstructures are for solidification times varying from 1.3 to 750 seconds. Note that some coring, indicative of a dendritic growth is seen in the two samples at the shorter solidification times, but is not obvious in the microstructures at the longer solidification times. Also, the amount of eutectic clearly decreases with increasing solidification time. Longitudinal sections of the same samples are shown in Figure 2. Here the dendritic structure is

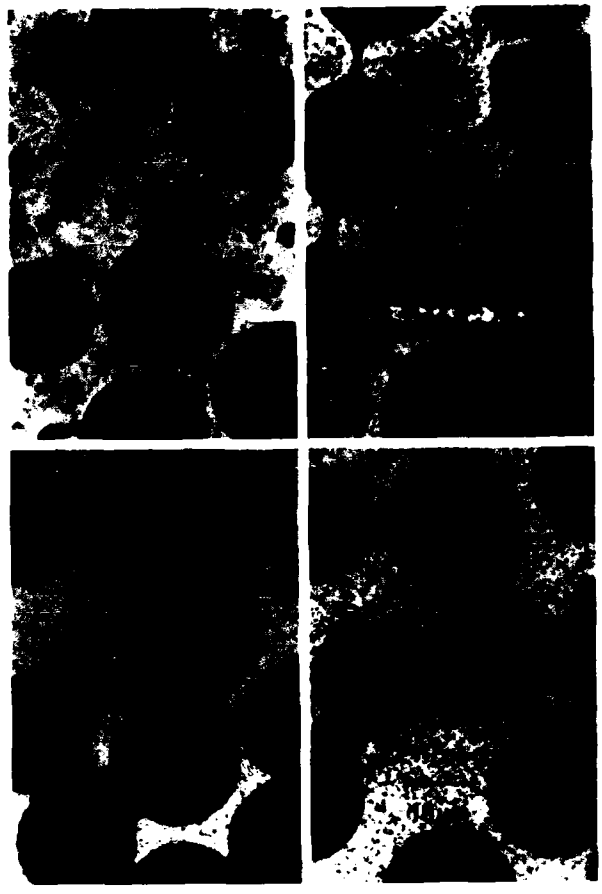


Figure 1. Transverse microstructures of Al-4.5w%Cu/ 55v%FP-Alumina composite solidified in (A)-1.3 s, (B)-18 s, (C)-192 s and (D)-750 s. Note distribution and morphology of the second phase, θ. (A) and (B) display non-equilibrium eutectic (α+θ), (C) shows divorced eutectic (θ) and (D) contains no second phase.

even more revealed, again especially in the two samples at the shorter solidification times. Some residual dendritic structures (coring and eutectic) are evident but much less obvious in the two longer solidification time samples.

A general observation of this work is that when the dendrite arm spacing that would be present in the absence of fibers is of the order of, or smaller than, the fiber spacing, the familiar dendritic pattern with extensive coring is observed metallographically. Figures 2-a and 2-b are examples, in which dendritic growth is readily apparent in composite samples that solidified in 1.3 and 18 seconds. On the other hand, for the samples shown in Figures 2-c and 2-d for longer

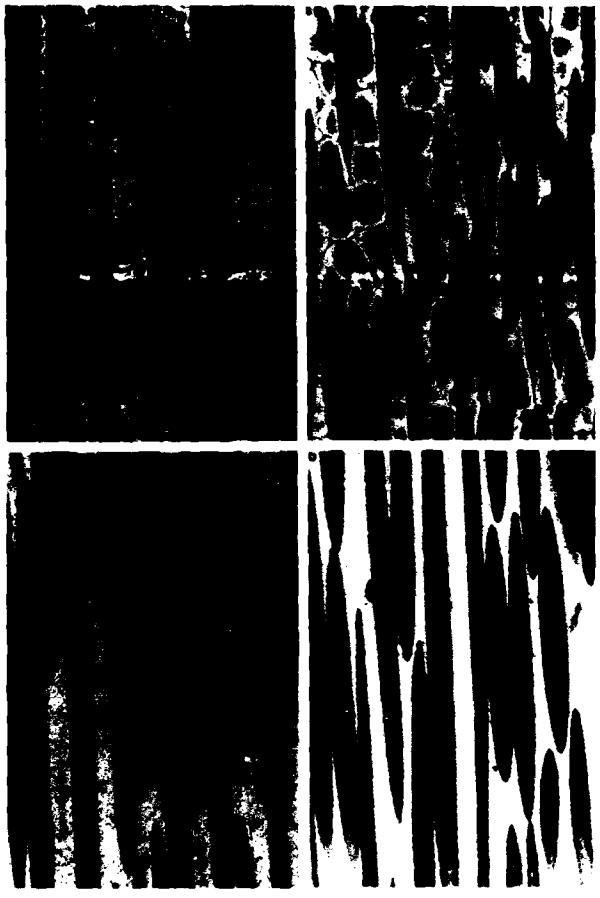


Figure 2. Longitudinal microstructures of Al-4.5w%Cu/ 55v%FP-Alumina composite solidified in (A)-1.3 s, (B)-18 s, (C)-192 s and (D)-750 s. Note dendritic morphology, coring of the primary matrix phase, segregation of interdendritic eutectic, and size of the secondary dendrite arms which are smaller or comparable to fiber spacing in (A) and (B) but larger in (C) and (D).

solidification times of 192 and 750 seconds, respectively, the presence of the fibers have had a substantial effect on the dendritic structure. In this case, the "usual" coarsening behavior, and microsegregation patterns observed in the unreinforced alloy (12) have been changed in the reinforced alloy. Based on these microstructural observations, idealized solidification processes for the unreinforced and reinforced Al-4.5wt%Cu alloys as illustrated in Figure 3 may be proposed for relatively longer solidification times and lower thermal gradients.

The measured average secondary dendrite arm spacings of the reinforced alloy are plotted in

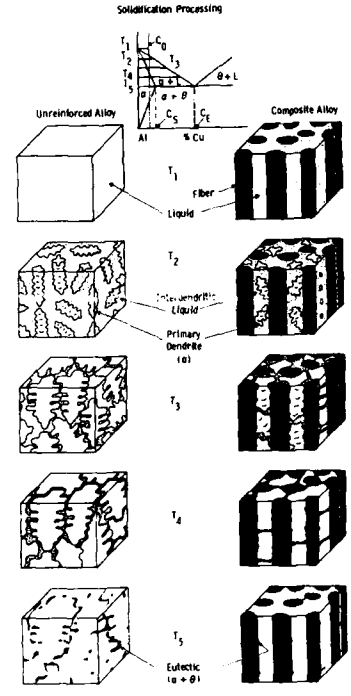


Figure 3. Illustrations of equiaxed solidification of Al-4.5wt% Cu in the absence (left) and presence of the fibers (right) under slow cooling and low thermal gradients. Corresponding temperatures T1(above liquidus) through T5 (eutectic) are shown in the schematic Al-Cu phase diagram at the top.

Figure 4. in the same plot, the average secondary dendrite arm spacing in the unreinforced alloy is also plotted using the relationship developed previously (9):

$$\lambda = 7.5\ t_f^{0.39} \qquad (1)$$

where λ is secondary dendrite arm spacing in microns and t_f is solidification time in seconds. The data for the reinforced alloy was fitted to a linear relationship also shown in Figure 4. This relationship was found to be:

$$\lambda = 9.7\ t_f^{0.51} \qquad (2)$$

Note that the exponent in Eqn. [2] is higher than that in Eqn. [1] which suggests more rapid dendrite arm coarsening kinetics in the composite alloy. [Alternatively, $t_f \sim \lambda^{1/3}$ in the unreinforced alloy, and $t_f \sim \lambda^{1/2}$ in the composite alloy.]

Based on the experimental observation on the

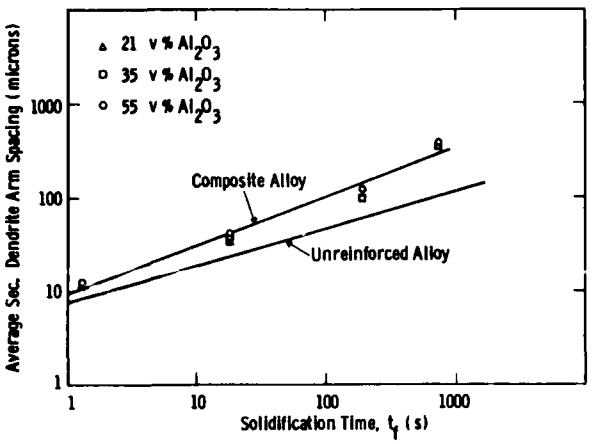


Figure 4. Average secondary dendrite arm spacing vs. solidification time relationship of the Al-4.5wt%Cu /FP-Alumina composites. The curve for unreinforced Al-4.5wt%Cu is plotted using Eqn. [1] for comparison.

microstructures, we propose three coarsening mechanisms that may occur during the solidification process of the composite alloy.

A. Coarsening by Ripening: A simple physical model for ripening of secondary dendrite arms in the presence of the fibers is illustrated in Figure 5 which contains two dendrite elements (A and B) confined by two "plates" of fibers. The geometry of each dendrite is a cylinder with a hemispherical cap. The radii of dendrites are "a" and "r", where, because dendrite A is larger than dendrite B a>r. The distance between the centers of A and B is "λ" and and the lengths of the dendrites measured from the center of the element to the tip of the hemispherical caps are l_2 and l_1 for the dendrites A and B respectively. We assume temperature and λ are constant, and that, initially, $l_2=l_1=l_0$. Since r<a, the liquid solute concentration in equilibrium with "r" is less than that in equilibrium with "a". This provides a driving force for ripening to occur as follows. The smaller dendrite tend to melt and the larger element tend to grow by the transport of solvent from B to A, and the transport of solute from A to B via diffusion in the liquid. Thus, B is assumed to melt uniformly along its lengtn until it disappears. It is also assumed that the dendrite A grow only along its length and thus its radius does not change. In this model, the diffusion distance is not a constant and is approximated as the distance between two tips. i.e., the diffusion distance is $\lambda-(l_1+l_2)$.

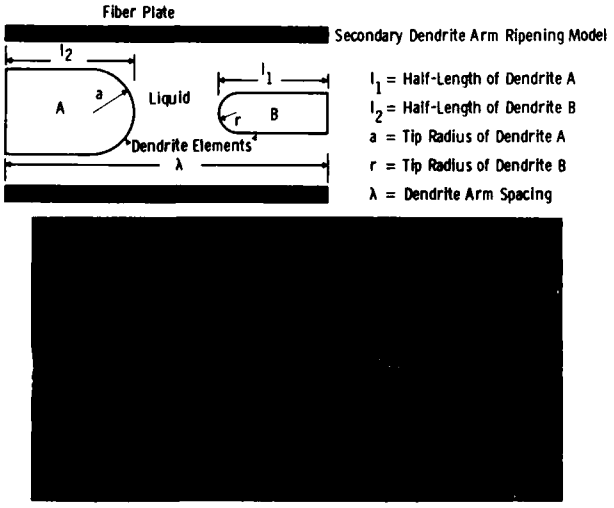


Figure 5. A secondary dendrite arm ripening model. Two cylindrical dendrite elements A and B with hemispherical gaps are constrained by two fiber plates (above). Surface energy difference at the two tip radii would result in remelting of B. Microstructural evidence of the proposed model is shown (below).

Assuming a constant concentration gradient between A and B and unidirectional diffusion of solute flux, J toward B can be written as:

$$J = -D_L(C_L^r - C_L^a)/\rho[\lambda-(l_1+l_2)] \quad (3)$$

where D_L is the diffusion coefficient, ρ is the liquid density, and C_L^r and C_L^a are liquid compositions in equilibrium with the dendrite tip "r" and the dendrite tip "a" respectively. Assuming the partition ratio, k is constant, mass balance at the solid-liquid interface of the dendrite B can be written as:

$$J = -[C_L^r(1-k)/\rho]\, dl_1/dt \quad (4)$$

where t is time. Combining Eqns. [3] and [4] with consideration of no total volume change of dendrites A and B, and integrating $l_1=l_0$ and $l_1 = 0$ yields a "critical time" t_c expression for disappearance of the dendrite B:

$$t_c = -(\alpha/\beta)\, l_0 + (\delta/2\alpha)\, l_0^2 \quad (5)$$

where α , β and δ are constants that are given in Appendix A. From geometrical considerations,

$l_0 = \lambda f_s/2$ where f_s is fraction solid. Thus, Eqn. [5] becomes:

$$t_c = -(\beta f_s/2\alpha)\, l + (\delta f_s/8\alpha)\, \lambda^2 \qquad (6)$$

Eqn. [6] indicated that $\lambda \sim t^{1/2}$ which is different than the conventional coarsening models (11,13,14) that predict $\lambda \sim t^{1/3}$. A calculation based on the values given in Appendix A yielded a critical time of 1.5 seconds. Microstructural evidence for the proposed ripening model is shown in Figure 5 which shows a small dendrite arm (remelting) and a large dendrite arm (growing).

A second simple physical model for ripening is also proposed which is illustrated in Figure 6. The interstices in the composite where the matrix lie are not isolated. In fact, they are interconnected and are varied in size. We assume interstices as cylinders fitted between the neighboring fibers. These interstices are then connected with channels

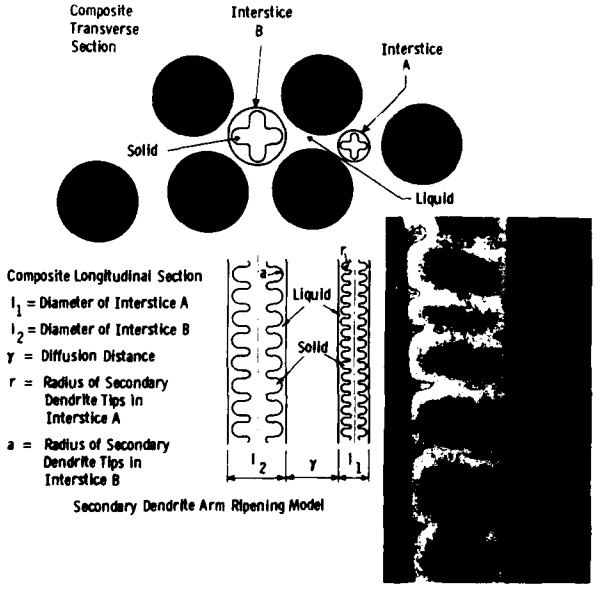


Figure 6. A model for ripening of the secondary dendrite arms growing in a small interstice A and a large interstice B. Due to the surface energy diference, dendrite tips in A would enriched in solute resulting remelting in A. Microstructural evidence of the model is shown (right). [Microstructure also shows evidence of coalescence in the large interstice as arrowed.]

between the fibers. Figure 6 shows one dendrite growing in the smaller interstice, A, and another dendrite growing in the larger interstice, B. The diameters of two interstices are l_1 and l_2, respectively ($l_1 < l_2$). the distance between two interstices is γ. The secondary dendrite arm tip radii are "r" and "a", respectively ($r < a$).

A physical model based on the explanation given above may then be outlined as follows:

* In the very earliest stages of solidification before any dendrite arm has a radius approaching half of its interstice, we expect that the fibers do not influence the dendritic growth and for ripening to occur by the $t^{1/3}$ law.
* When the size of the secondary dendrite arms begins to approach the size of the smaller interstice, A, the growth would slow down and stop. At the same time, the dendrites in the larger interstice, B, can grow further and enlarge their radii. At this point there will be a strong driving force for the transport of solvent from A to B, and the transport of solute from B to A. At this stage ripening could occur according to the $t^{1/2}$ law, because now the different interstices can no longer ripen independently.
* Coalescence proceeds prefentially in the larger interstices when volume fraction solid exceeds a critical value.
* Ripening of the type proposed above occurs to the very end of solidification so that the last liquid (residual eutectic) will always been in the smallest interstices as observed experimentally.

B. Coarsening by Coalescence: Microstructural evidence suggests that coalescence is very effective and rapid in the composite alloy during solidification as shown in Figure 6. In the micrographs presented in this figure, what was once liquid (brighter color) between two adjacent secondary arms has been removed by coalescence. As in ripening the solid-liquid surface energy is the driving force for coalescence.

Rapid kinetics of coalescence in the composite alloy can be explained by the shorter diffusion distance between the secondary dendrite tips and roots due to the restricted solidification volumes imposed by the presence of the fibers. This concept was modelled by Mortensen (15,16) who developed an expression that predicts a critical time for removal of the liquid between two secondary

dendrite arms and is given by:

$$t_c = -m_L C_0/G R \{[(G R l_i^2 \lambda/4D_L\Gamma) + 1/(1-f_{si})]^{1-k} - 1\} \quad (7)$$

where C_0 is the average alloy composition, G R is the cooling rate, l_i is the initial secondary dendrite arm length, λ is the secondary dendrite arm spacing, Γ is the Gibbs-Thompson constant and the other symbols are as indicated before. Typical critical times computed using eqn. [7] are about 180 and 1090 seconds for the composite alloy and unreinforced alloy solidified in 750 seconds, respectively. i.e., in the composite alloy complete coalescence will be achieved whereas in the unreinforced alloy it will not be achieved. The values used in this calculation are given in Appendix A.

C. Solid State Diffusion Driven Coarsening:
A third proposed mechanism for coarsening is driven by solid-state diffusion at the solid/liquid interface. As illustrated in Figure 7, this mechanisms involves sintering two growth fronts which are restricted by two fibers. The curvatures of these two fronts must be equal so that usual growth process which rely on solute rejection would stop or be sluggish. i.e. the solid-liquid interfaces would reach an equilibrium state. The liquid remaining between the two radii then can only be removed by solid-state back diffusion from the solid-liquid interface. i.e. the solute from the liquid diffusing into the solid at the solid-liquid interfaces will result in further growth of these interfaces toward each other. When the two fronts touch, surface energy-driven coalescence would rapidly operate to remove or reduce the remaining liquid. Microstructural evidence to support this process is shown in the same figure which contains the solid-liquid interfaces that are in equilibrium and coalescence stages.

Typical microsegregation data obtained from the microprobe analysis are presented in minimum composition vs. solidification time plot shown in Figure 8. These data clearly show that amount of microsegregation in the composite alloy was reduced compared to that in the unreinforced alloy. We conclude that the responsible mechanisms by

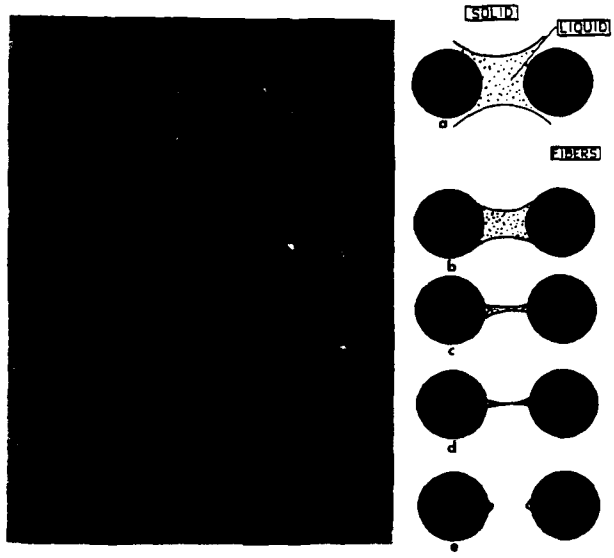


Figure 7. A model for solid-state diffusion driven coarsening which involves two growth fronts pinned by two fibers (a). When the radii of the two fronts become equal, growth is sluggish (b), and would only proceed further with diffusion (c). Remaining liquid would be removed by coalescence (d and e).

which microsegregation are reduced in the composite alloy are a combination of increased solid-state diffusion (due to a shorter diffusion distance which is controlled by the fiber spacing) and rapid coarsening kinetics.

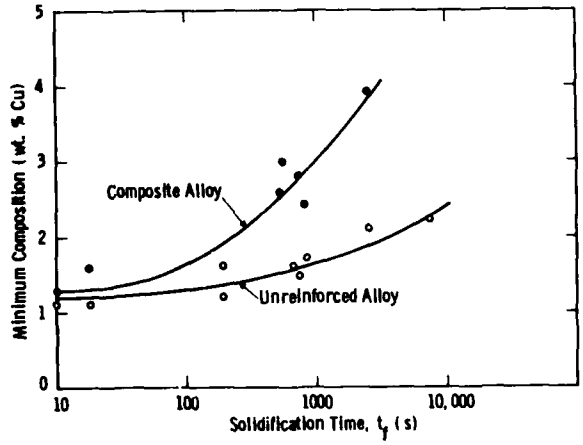


Figure 8. Minimum composition vs. solidification time relationships in Al-4.5wt%Cu and Al-4.5wt%Cu /FP-Alumina showing significant increase of minimum composition in composite matrix compared to the unreinforced matrix as the solidification time increases.

In summary, mechanisms of the coarsening for the secondary dendrite arms of the Al-4.5wt%Cu alloy

in the presence of the continuous alumina fibers were studied. The coarsening models were proposed and supported by the metallographic evidence. The coarsening kinetics in the presence of the fibers are rapid. As a results, dendritic morphology and microsegregation behavior of the matrix are altered compared to the unreinforced alloy. Practical aspects of these results could be utilized in controlling matrix and interface microstructures of the fiber reinforced composites, which are particularly important for transverse properties.

APPENDIX A-

The constants in Eqns. [5] and [6]:

$$\alpha = [2\,\Gamma\,D_L T / m_L(1-k)\,(\,C_L - (2\,\Gamma/\,m_L)\,(1/r))\,]\,[(1/r)-(1/a)]$$

$$\beta = \lambda - l_o\,[1+(r^2/a^2)]$$

$$\delta = 1 - (r^2/a^2)$$

Data used in calculation of t_c for ripening in Eqn. [6]: $\Gamma = 910^{-8}$ Km, $D_L = 510^{-9}$ m^2/s, T=908 K, C_L= 7.7 wt%Cu, f_s= 0.5, r=5 10^{-6} m, a=10^{-5} m, λ=2 10^{-4} m, l_0= 510^{-5} m.

Data used in calculation of t_c for coalescence in Eqn. [7]: l_i= 10^{-5}m for composite alloy, l_i= 5 10^{-5} m for unreinforced alloy, λ = 8 10^{-5} m, f_s = 0.6, Γ =9 10^{-8} Km, D_L= 5 10^{-9} m^2/s, m_L = -3.33 K/wt%Cu, k = 0.17, G R = 0.13 K/s (corresponds a 750 second solidification time), C_o = 4.6 wt%Cu.

ACKNOWLEDGEMENT- This work sponsored by the U.S. Army under contract DAAK-10-85-R-0085.

REFERENCES:

1. A. Mortensen, J. A. Cornie, and M. C. Flemings, Feb. 1988, pp.12-19.
2. J. A. Cornie et al., Bull. Amer. Cer. Soc., 65, 1986, pp. 293-304.
3. A. Mortensen, M. N. Gungor, J. A. Cornie and M. C. Flemings, J. Metals, March 1986, pp. 30-35.
4. J. A. Cornie, A. Mortensen and M. C. Flemings, Proc. 6th Int. Conf. and 2nd Eur. Conf. on Comp. Materials, Eds; F. L. Mathews, N. C. R. Buskell, J. M. Hodgkinson and J. Morton, Elsevier Publ., London, 2, pp. 2.297-2.319.
5. T. W. Clyne and J. F. Mason, Met. Trans. A., 18A, August 1987 pp. 1519-30.
6. P. K. Rohatki, R. Asthana and S. Das, Int. Metals Rew., 31, 1986, pp. 115-139.
7. A. Mortensen, M. N. Gungor, J. A. Cornie and M. C. Flemings, Proc. of ICCM V, Eds., Harrigan, W. C., Strife, J. and Dhingra, A. K., 1985, pp. 809-23.
8. M. N. Gungor, Sc.D. Thesis, Dept. of Materials Sci. and Eng., Massachusetts Institute of Technology, 1986.
9. B. P. Bardes and M. C. Flemings, Trans. AFS, 74, 1966, pp. 406-12.
10. M. C. Flemings, Solidification Processing, McGraw-Hill, New York, 1974, pp. 146-54.
11. K. P. Young and D. H. Kirkwood, Met. Trans., 6A, 1975, pp. 197-205.
12. M. N. Gungor, J. A. Cornie and M. C. Flemings, Interfaces in MMC's, Proc. of TMS Annual Meeting, Eds., Dhingra, A. K. and Fishman, S. G., 1986, pp.121-35.
13. T. Z. Kattamis, J. C. Coughlin, Trans. AIME, 239, 1967, p. 1504.
14. M. Kahlweit, Scripta Metallurgia, 2, 1968, p. 251.
15. A. Mortensen, Ph. D. Thesis, Dep. of Mat. Sci. and Eng., Massachusetts Institute of Technology, 1986.
16. A. Mortensen, J. A. Cornie and M. C. Flemings, Met. Trans. A, 19A, March 1988, pp. 709-721.

SOLIDIFICATION PROCESSING OF PARTICULATE CERAMIC-ALUMINUM ALLOY COMPOSITES

T. Z. Kattamis
University of Connecticut
Storrs, Connecticut 06268 USA

J. A. Cornie
Massachusettes Institute of Technology
Cambridge, Massachusetts 02139 USA

Abstract

Particulate SiC-aluminum alloy matrix composites were processed by vigorously mixing the carbide in a semi-solid alloy slurry. The rheology of Al-4.5wt%Cu-1.5wt%Mg alloy slurry in absence or presence of a carbide dispersion was investigated with a high temperature Couette viscometer, as a function of fraction solid, shear rate and cooling rate. In absence of SiC and for a given cooling rate the apparent viscosity increased with increasing volume fraction primary aluminum-rich phase and decreasing shear rate. At constant shear rate, it also increased with increasing cooling rate. The primary phase particle size decreased with increasing initial shear rate, cooling rate and copper concentration in the alloy. Above the liquidus temperature the incorporation of SiC in the melt led to a linear increase of apparent viscosity with added volume fraction carbide.

IT HAS BEEN ESTABLISHED that particulate ceramic-aluminum alloy matrix composites may be processed by vigorously mixing the carbide or oxide particulates in a semi-solid alloy slurry[1,2] and casting it in molds. A typical microstructure of an aluminum-base composite, such as SiC-reinforced 2024 alloy would then consist of larger particles of aluminum-rich α-phase which coarsened substantially during isothermal mixing and are surrounded by a fine dendritic α-phase which solidified from the remaining liquid during subsequent fast cooling. The interdendritic spaces are occupied by an α/Al_2Cu eutectic. Idiomorphic particles of $Al_6(Mn,Fe)$ and occasionally particles of Mg_2Si which result from reaction of magnesium with SiO_2 that is always present on the carbide particulates, as well as SiC particulates appear dispersed within the dendritic structure. It is highly desirable that the distribution of SiC in the matrix be uniform. This could be achieved in the first place by:
(1) Refining and uniformly distributing the coarse α-phase particles within the specimen and; (2) preventing or limiting carbide particle pushing by the advancing dendritic interface during solidification. It could also be achieved by completely remelting and resolidifying the system. In fact, it has previously been demonstrated that once the SiC particulates have been incorporated in the system they are not rejected during subsequent remelting and they do not sediment, despite the density difference between carbide (3.17 g/cm^3) and melt (2.73 g/cm^3), provided vigorous mixing is maintained.

During isothermal holding of a dendritic alloy above the nonequilibrium solidus, hence in presence of a certain amount of liquid the remaining unmelted solid gradually coarsens by remelting at higher curvature sites, diffusion through the liquid and freezing at lower curvature sites. Thus, the dendritic structure gradually breaks-up into fragments which spheroidize rapidly and coarsen. Assuming a purely diffusion-controlled process, the coarsening rate for a binary system was found to be proportional to the surface tension, solute diffusivity through the melt and temperature, and inversely proportional to the square of the radius of curvature[3,4] and solute concentration. In presence of forced convection the coarsening rate becomes inversely proportional to the product of the radius of curvature times the solute diffusion boundary layer thickness. Hence, enhanced convection leads to substantially faster coarsening.

The purpose of the present work was to: (1) Study the viscous flow behavior of a semi-solid slurry of Al-4.5wt%Cu-1.5wt%Mg alloy without or with a dispersion of SiC particulates. This ternary system was selected because its phase diagram is fairly well known and its composition is close to that of 2024 alloy and; (2) establish the dependence of primary α-particle size on process variables

EXPERIMENTAL PROCEDURE

A ductile cast iron Couette viscometer lined with graphite was used for determining shear stress and shear rate, hence the apparent viscosity of the solid plus liquid mixture, as a function of fraction solid, cooling rate and shear rate, following the procedure previously reported[5,6]. The alloy was contained in the 5 mm annular gap between an outer cylinder (cup) which is rotated and an inner cylinder (bob) which is stationary. Torsional forces on the bob were measured with a torque dynamometer. Slippage was prevented by machining vertical grooves along the graphite faces of the bob and the cup which sat inside a large steel container that could be rotated by a variable speed motor at velocities between 10 and 80 rps, or shear rates between about 71 and 570 s^{-1}. The viscometer was placed inside a resistance furnace whose temperature was accurately controlled, using chromel-alumel thermocouples. Rapid cooling of about 0.33 K/s was achieved by spraying water on the surface of the cup. The maximum shear stress and shear rate at the surface of the bob can be calculated, respectively, from : $\tau = (T/2\pi h)(1/\beta^2R^2)$ and $\dot{\gamma} = 2\Omega/(1-\beta^2)$, where T is torque, h is height of ther bob, R is the radius of the cup and $\beta = R_o/R$, where R_o is the radius of the bob. Hence, the apparent viscosity $\eta_a = \tau/\dot{\gamma} = T(1-\beta^2)/4\pi h\beta^2R^2\Omega$, where Ω is angular velocity.

RESULTS AND DISCUSSION

Metallic slurries exhibit a thixotropic behavior. Thus, upon application of shear the shear stress decreases with time due to structural breakdown of the solid until a steady state value is reached. An equilibrium is then established between the rate of breakdown of aggregated larger particles and the rate of structural redevelopment through particle coalescence. The time required to attain equilibrium is inversely proportional to the shear rate. For thixotropic systems the variation of shear stress versus shear rate increasing from zero to a maximum value and gradually decreasing again to zero, exhibits a hysteresis loop whose area indicates the extent of thixotropy. Figure 1 illustrates the increase in apparent viscosity of the alloy slurry with fraction solid at various shear rates. The superheated melt was cooled at 0.03 K/s to various temperatures corresponding to various fractions solid, while being sheared at various rates. The specimens were held at those temperatures for various lengths of time prior to water-cooling. During the isothermal hold: (1) The volume fraction solid slightly increases, because of back-diffusion of copper and magnesium in the solid which is also in the process of coarsening; (2) the apparent viscosity gradually decreases. The maximum value of viscosity indicated by the top of the bars at the points in Figure 1 corresponds to the viscosity of the slurry at the beginning of the isothermal holding period and the minimum value to that at the end of the holding period. For a given volume fraction solid this decrease in apparent viscosity with time at constant shear rate or with shear rate for a given isothermal holding time may be attributed to the dependence of the structural breakdown of the solid on time and shear rate. Results are replottred in Figure 2 which shows that for a given fraction solid and at constant initial shear rate the apparent viscosity decreases with decreasing cooling rate, because then a longer time is available for breaking down the aggregated solid particles.

The decrease in average particle size with increasing shear rate at cooling rates of 0.008 and 0.33 K/s and at a volume fraction solid of about 0.4 is illustrated in Figure 3. In these runs the specimens were continuously cooled at constant rate from the superheated melt state to a temperature corresponding to a volume fraction solid of about 0.4 and immediately quenched without isothermal holding in order to avoid further coarsening. This decrease is lower at higher cooling rates, because then the time during which shearing operates and breaks-up the solid aggregates is much shorter. The same figure shows that for a given initial shear rate the particles are finer at higher cooling rate, because then the initial dendritic structure is finer and so are the resulting dendritic fragments, hence the particles. The effect of composition on average particle size for specimens continuously cooled at 0.008 K/s to a temperature at which the volume fraction solid is 0.4 is illustrated in Figure 4 versus initial shear rate. It is clear that for a given initial shear rate an increase in copper content at constant magnesium content yields a finer primary aluminum-rich phase particle size. This decrease in particle size may be attributed to slower coarsening kinetics with increasing solute concentration in the liquid.

Apparent viscosity measurements in the liquid alloy are reported in Figure 5 versus temperature for melts without silicon carbide particulates, as well as for melts containing carbide at volume fractions of about 0.10 and 0.20. The latter specimens were processed by mixing the carbide particulates in a semi-solid alloy slurry and subsequently completely remelting the alloy. The measurements were taken at different temperatures while the mixture was being sheared. The viscosity in all three cases increases very slightly with decreasing temperature. However, it increases very rapidly with further cooling below the nucleation temperature of the solid. At a given temperature the viscosity also increases with increasing volume fraction dispersed SiC (20um). In this figure the bars associated with the points indicate an erratic variation in measured values, not a systematic change in viscosity with time of shearing, as in Figures 1 and 2. The measured viscosities of the melt exempt of carbide particulates are in fairly good agreement with results by Girot[7]. The effect of SiC particulate additions on apparent viscosity is illustrated in Figure 6 for three different temperatures: 750, 700 and 650°C. The dependence is linear but the slope decreases with increasing temperature. The three lines corresponding to the above temperatures may be represented, respectively, by: $\eta_r = \eta_a/\eta_o = 1+2.14V_f$, $\eta_r = 1+2.75V_f$ and $\eta_r = 1+3.18V_f$, where η_r is relative viscosity, η_o is melt viscosity in absence of carbide and V_f is volume fraction added carbide. These results correspond fairly closely to the first two terms of the experimental expression of

Thomas[8] : $\eta_r = 1 + 2.5V_f + 10.05V_f^2 + A\exp BV_f$, where A and B are constants. The last term in this expression becomes predominant only at $V_f > 0.25$[8]. The slope of the straight lines in Figure 6 may be expressed as a function of temperature, T , by: $(1-1.12\times10^{-3}T)/(0.7-1.64\times10^{-3}T+1.09\times10^{-6}T^2)$. This behavior was observed also by Girot[7] and could be explained by assuming that for a given shear rate at a higher temperature, hence at a lower viscosity the carbide particles are aggregated in clusters, whereas at a lower temperature or a higher viscosity they are dispersed individually[7].

CONCLUSIONS

1) At constant cooling rate the apparent viscosity of Al-4.5wt%Cu-1.5wt%Mg alloy semi-solid slurry undergoing vigorous shear increases with increasing volume fraction primary aluminum-rich phase and decreasing shear rate. At constant shear rate, it increases with increasing cooling rate.
2) The particle size of primary aluminum-rich phase in a semi-solid aluminum alloy under shear decreases with increasing shear rate, cooling rate and copper content in the alloy.
3) After addition of SiC to the alloy its apparent viscosity under shear above the liquidus temperature increases linearly with volume fraction dispersed carbide.

Acknowledgment

The authors are grateful to IST-SDIO-ONR for support under contract No. N0014-85-K-0645 and to Dr. Steven G. Fishman, Program Manager, for his continued interest in this work.

REFERENCES

1. Mehrabian, R., Riek, R. and M. C. Flemings, Met. Trans.,5, 1899-1905, 1974
2. Levi, C. G., Abbaschian, G. S. and R. Mehrabian, Met. Trans. A, 9A, 697-711, 1978
3. Skolianos, S. and T. Z. Kattamis, Proceedings of the "Solidification Processing 87" Conference, Sheffield, U.K., 207-210, Sept. 21-24, 1987
4. Wilson, P. W., Kattamis, T. Z. and Y. Shiohara, accepted for publication, J. Mater. Sci.
5. Spencer, D. B., Mehrabian, R. and M. C. Flemings, Met. Trans., 3, 1925-1932, 1972
6. Joly, P. A. and R. Mehrabian, J. of Mater. Sci., 11, 1393-1418, 1976
7. Girot, F., Doctoral Thesis, Université de Bordeaux I, January 1987
8. Thomas, D. G., J. Colloid. Sci., 20, 267, 1965.

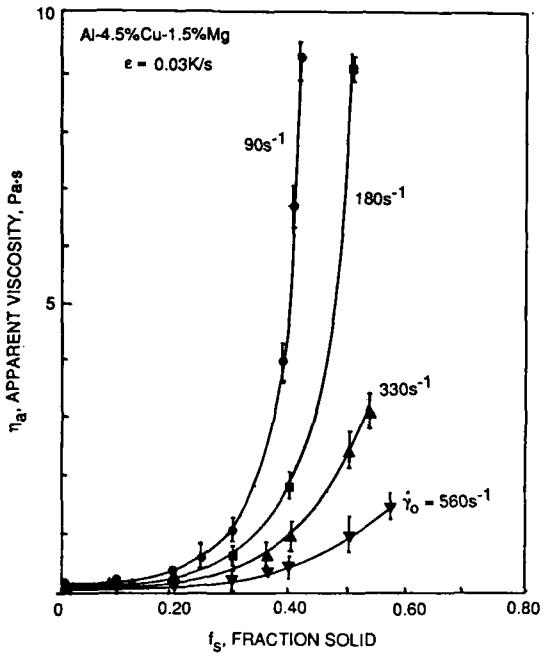


Fig. 1: Apparent viscosity versus fraction primary aluminum-rich phase and shear rate. Al-4.5%Cu-1.5%Mg specimens cooled at 0.03 K/s.

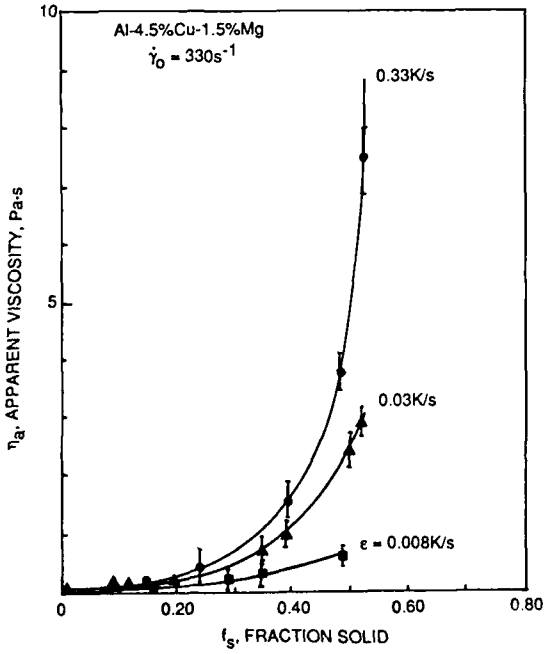


Fig. 2: Apparent viscosity versus fraction primary aluminum-rich phase and cooling rate. Al-4.5%Cu-1.5%Mg specimens sheared at 330 s^{-1}.

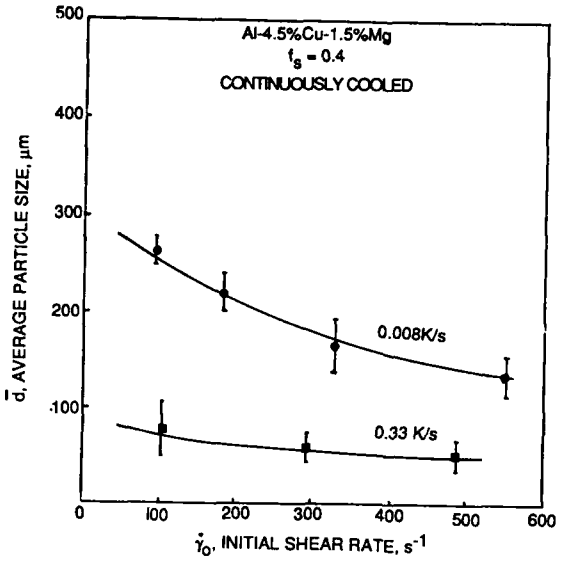


Fig. 3: Average particle size of primary aluminum-rich phase versus initial shear rate. Al-4.5%Cu-1.5%Mg specimens continuously cooled at two different rates to 627 °C (fraction solid = 0.4).

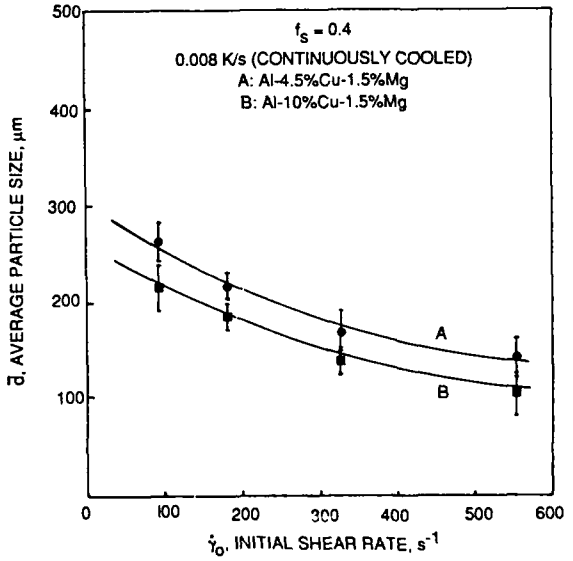


Fig. 4: Average particle size of primary aluminum-rich phase versus initial shear rate. Al-4.5%Cu-1.5 %Mg and Al-10%Cu-1.5%Mg specimens continuously cooled at 0.008 K/s to 627 °C (fraction solid = 0.40).

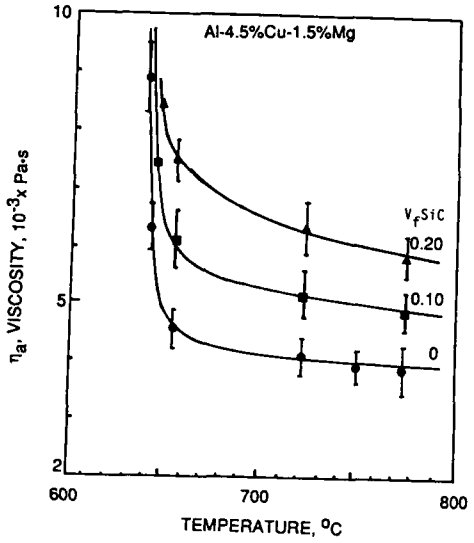


Fig. 5: Apparent viscosity versus temperature and volume fraction added SiC. Al-4.5%Cu-1.5%Mg alloy.

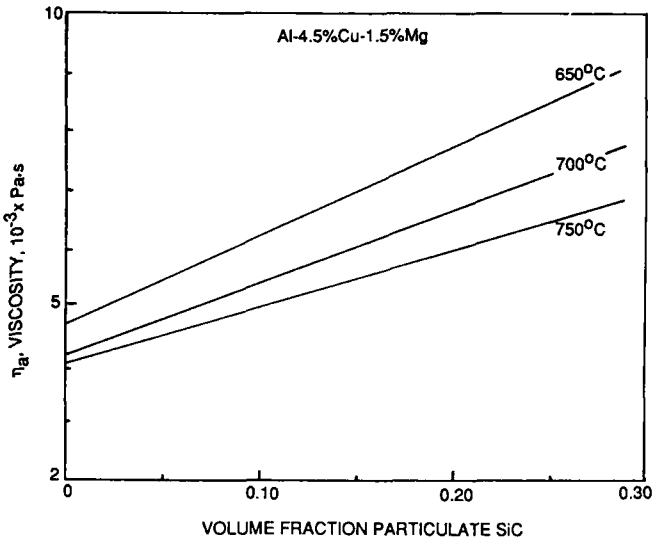


Fig. 6: Apparent viscosity versus volume fraction added particulate SiC and temperature. Al-4.5%Cu-1.5%Mg alloy.

ANISOTROPY OF FRICTION AND WEAR OF FIBER REINFORCED EPOXY-RESINS

M. Cyffka, E. Hornbogen
Institut für Werkstoffe
Ruhr-Universität Bochum, Bochum, FRG

Abstract

Principle considerations are presented to characterize the tribological properties of composite materials with ductile anisotropic microstructure. Carbon fibres in a matrix have been used as model materials to measure angular relations of friction and abrasive wear. Wear resistance showed a much more pronounced anisotropy than friction. The results were interpreted by micromechanisms observed by SEM. The conclusion is that a tensorial description is not feasible because qualitative change in wear mechanisms are found at angular ranges intermediate between the 3 principle directions. These results represent well the situation in many metal matrix composites.

Introduction

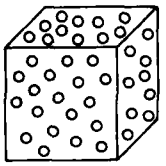
There exists a multitude of tribological requirements for engineering materials, for example coefficient of friction $\mu \rightarrow$ min, wear rate $w \rightarrow$ min for bearings, $\mu \rightarrow$ max, w = min for brakes, but μ = min and w = max for good maschineability. Such combinations can be achieved by composites, the components of which supply different tribological functions in suitable microstructures [1]. The properties of these composites can be improved still further if an anisotropic microstructure leads to directionability of properties [2]. The tribological loading conditions should be oriented in a favorable way to the structure of the material. For this purpose it is necessary, to characterize the directionality of tribological properties in a similar way [3] as it is known for a long time for the mechanical properties of crystal structures as well as for composite materials. One, two or three principle directions x_1, x_2, x_3 have to be defined for the volumetric wear rate. From this 3 componentes of a wear tensor follow:

$$\begin{aligned} \Delta a_1 &= w_{11}x_1 + w_{12}x_2 + w_{13}x_3 \\ \Delta a_2 &= w_{21}x_1 + w_{22}x_2 + w_{23}x_3 \\ \Delta a_3 &= w_{31}x_1 + w_{32}x_2 + w_{33}x_3 \end{aligned} \qquad (1a)$$

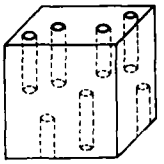
$$w_{ij} = \frac{da_i}{dx_j} \qquad (1b)$$

Twice this number is required if different signs of the direction of sliding leads to unlike wear mechanisms. The components w_{11}, w_{22}, w_{33} come into play only for erosion by particles of an angle of incidence larger than zero. The residual six components are reduced down to one for an isotropic material (Fig. 1a). a_1, a_2, a_3 are the dimensions of the material, da_i/da_j the removal of matter per sliding path (Fig. 1b).
There exist only few systematic investigations of the directionability of μ and w of composite

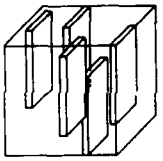
materials [4]. The question should be raised whether a tensorial description of the properties is justified for arbitrary angle α, β (Fig. 2) between structure and sliding direction. It is the purpose of the present investigation to obtain such data for uniaxally reinforced epoxy resins (CFRE). From this the principle understanding should be improved, and rules for an optimum use of composite materials in tribological systems should be obtained.



$w_{12}=w_{13}=w_{21}=w_{23}=w_{31}=w_{32}$



$w_{12}=w_{21}\neq w_{13}=w_{23}\neq w_{31}=w_{32}$



$w_{12}\neq w_{13}\neq w_{21}\neq w_{23}\neq w_{31}\neq w_{32}$

Fig. 1: a) Different numbers of principle wear rates da_i/da_j;

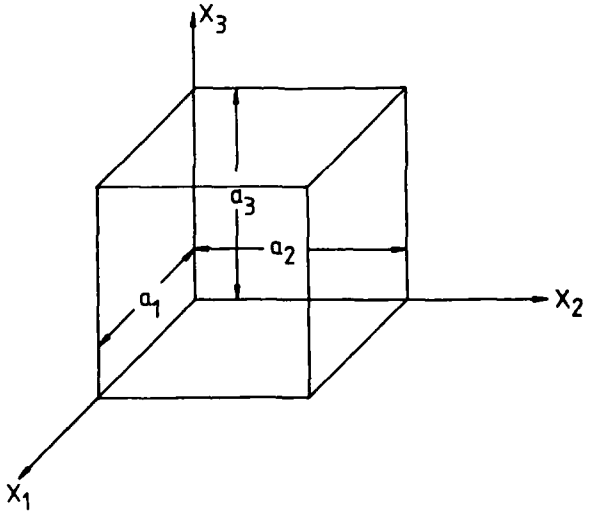


Fig. 1: b) coordinate system used for the description of sliding directions x_j and materials dimensions a_i.

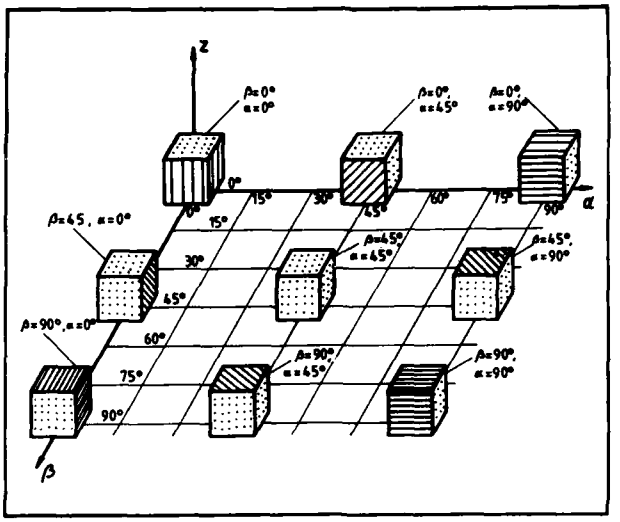


Fig. 2: Coordinate system for the characterization of fiber orientation. The α/β-plane represents the sliding plane, the α-axis the direction of loading.
+ α: down-stroke ; - α: up-stroke

Materials and Experimental Results

A CFRE was investigated with 40% fibers of 7 μm diameter. Fig. 3 shows the surface of such a material in two sections. Unlubricated abrasive wear was measured against SiC, Al_2O_3 and flint. With a hardness (DPH) of 2500, 1800, 900 respectively. Three grain sizes were available for Al_2O_3 with surface roughness of 7, 70 and 100 μm. The compressive load was constant at σ = 0.33 MPa. A sliding velocity of V = 200 mm/min was used in an experimental set-up which is shown in figure 4.

The following relation is valid for the volumetric wear rate w.

$$w = \frac{\Delta m}{\Delta s \cdot \rho \cdot A} \qquad (2)$$

The ratio $\Delta m/\Delta s$ corresponds to the removed mass per sliding path, ρ and A are density and nominal area of the specimen.

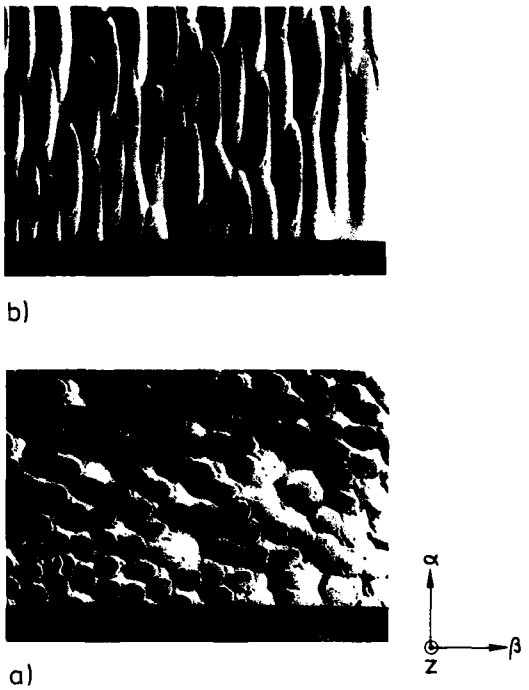


Fig. 3: Different morphology of the cut surface of the carbon fibers as a function of fiber orientation.
a) (α = 0°/β = 0°)
b) (α = 75°/β = 0°)

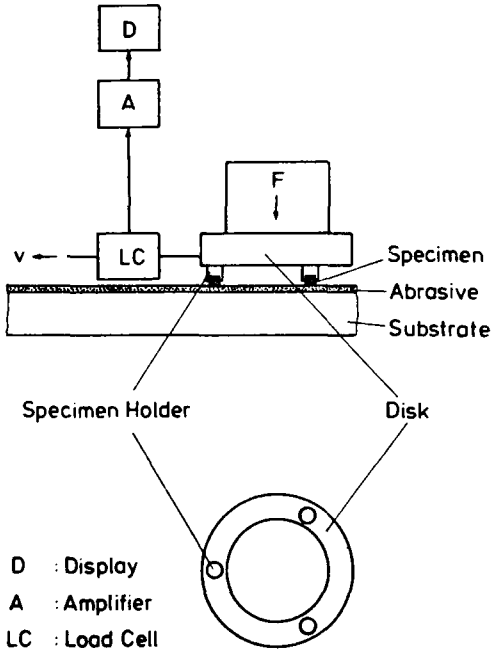
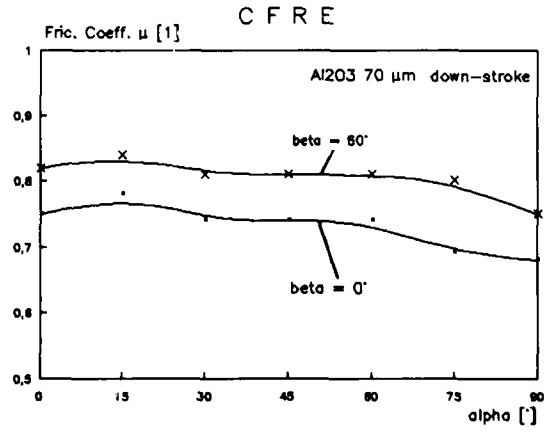


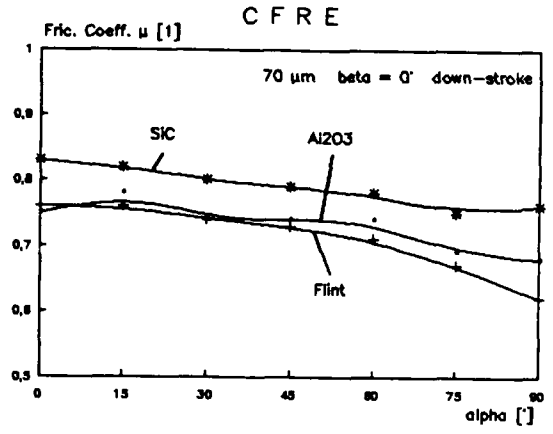
Fig. 4: Pin-plate set-up for the measurement of the coefficient of friction μ and the wear rate w.

Essential results on the effect of orientation (α,β) as well as of size and hardness of the abrasive have been summarized in Fig. 5a-d. A pronounced decrease of μ with angle β is quite evident, the same is true for decreasing hardness and roughness of the abrasive. Not surprising is the effect of the sign of the sliding direction $\pm x_j$ (down-/up-stroke). It is important for the analysis that the same areal fractions of carbon and resin of fibers exist for certain orientations while the forces acting on the interfaces must be different (Fig. 6). Surprising is the angular dependence of w, which shows the inverse course as that of μ (Fig. 7a). For decreasing angles the wear rates are lowered. This course can also be observed for decreasing hardness of the abrasive (Fig. 7b), and a decreasing roughness of Al_2O_3 (Fig. 7c). In the range of α > 45°, β = 0°, the effect of the sign of sliding direction increases. Different from up-stroke loading, there exists a local maximum at α = 75° for down-stroke direction. This extreme value can be observed at any hardness and roughness (Fig. 7b,c).

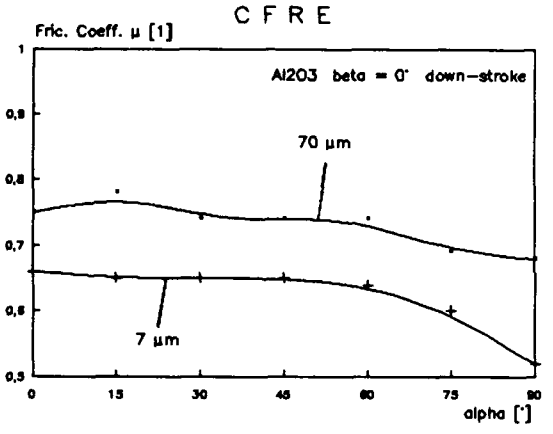
Fig. 5: Coefficients of friction of CFRE, effects of:



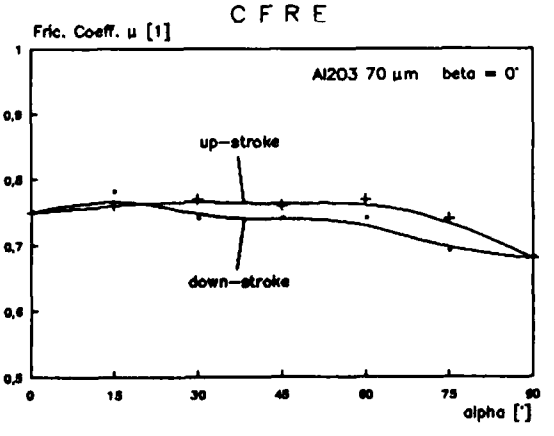
a) fiber orientation



b) hardness of the abrasive



c) grain size of the abrasive



d) sign of the sliding direction

Discussion

The coefficient of friction μ is reduced by 20%, if the fiber axis is oriented parallel to the direction of sliding (Fig. 5a,c). Besides the different components of force acting at the interfaces the anisotropy of the surface energy can contribute to this effect. For fibers which are cut perpendicularily a higher surface energy and therefore adhesive force are expected as compared to parallel fibers [5]. The relation between the abrasive coefficient of friction and the angles of orientation (α,β) is explained in fig. 6. In spite of equal areal fraction in the surface (α = 30°, β = 0° and α = 0°, β = 30°) the latter orientation shows a higher μ-value. The reason is that at a higher normal force F_N is required to act at phase boundary fiber/matrix (see Fig. 2).

It must be noted that the angular dependence of friction and wear is different. In the range α > 45° and β = 0° (comp. fig. 2) high wear rates are found for down-stroke loading (Fig. 7d). Observations and the models derived from it are shown in fig. 8. For the α = 75°/β = 0° orientation the fibers fail easily by brittle fracture as a consequence of the higher fiber length l_B (Fig. 8a). After removal of the hard fibers the soft epoxy matrix can be easily removed by abrasion and the next set of fibers can be cracked easily. This model is confirmed by the effect of a change in sign of the direction of sliding (Fig. 7d). For an up-stroke motion this effect and a maximum wear rate is absent (Fig. 8b). It is, however, found for all other abrasives (Fig. 7b).

The effect of grain size on the wear rate is much more pronounced that on the coefficient of friction. This indicates that the effect of adhesion is less on wear than on friction.

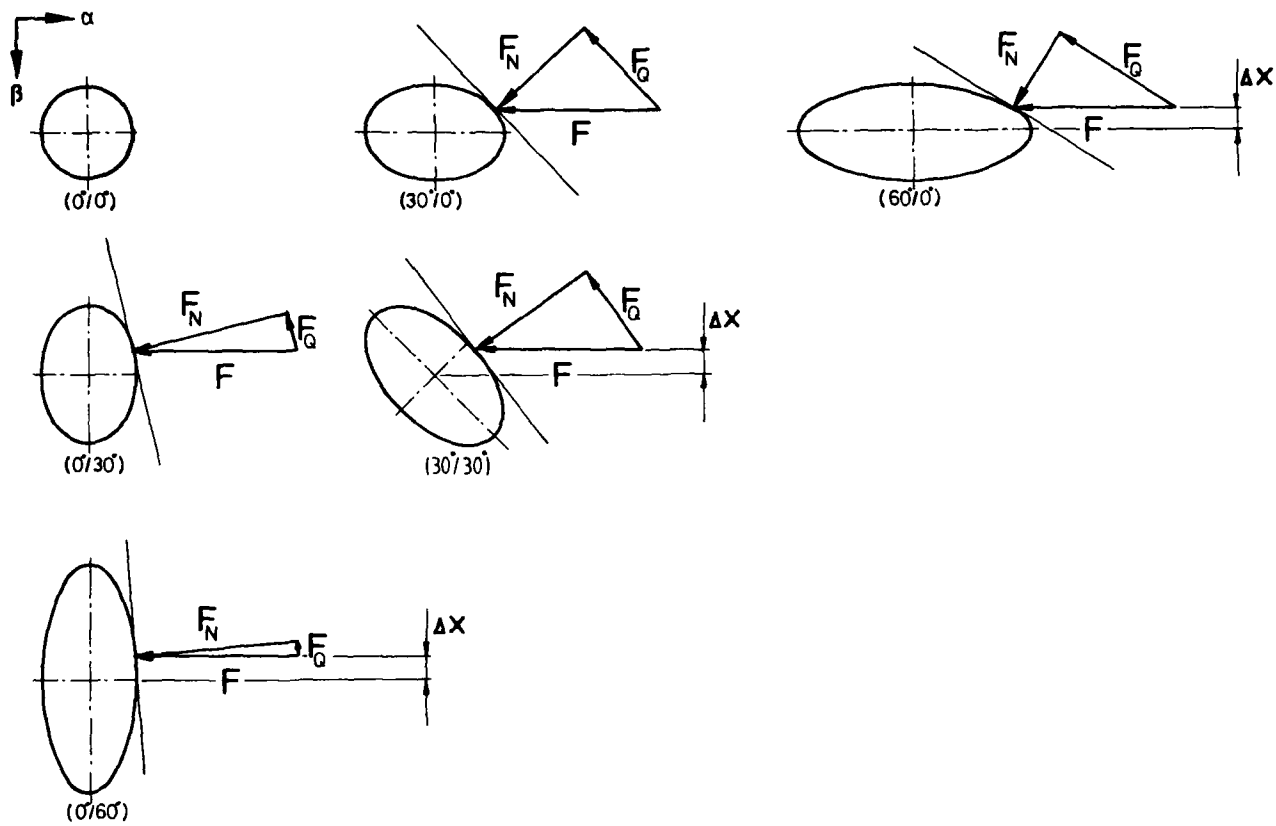
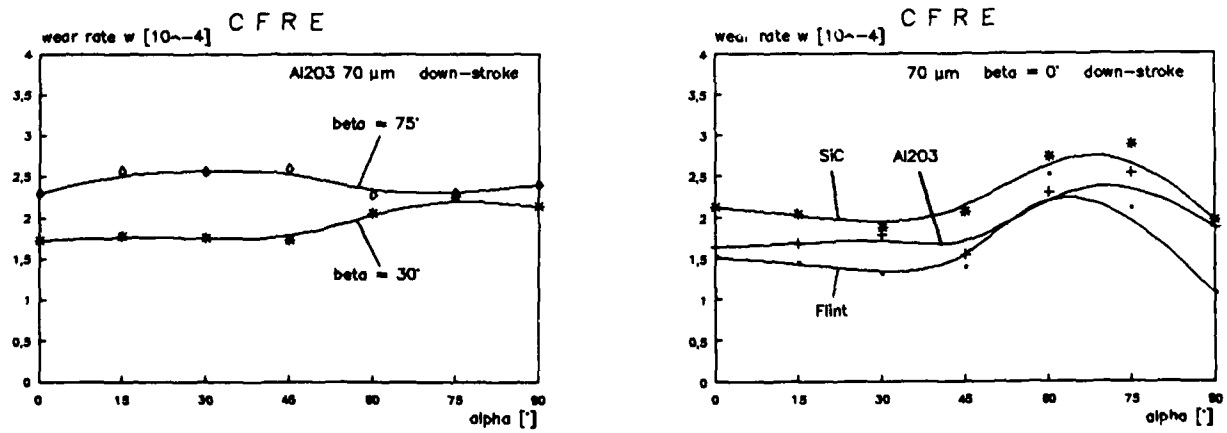


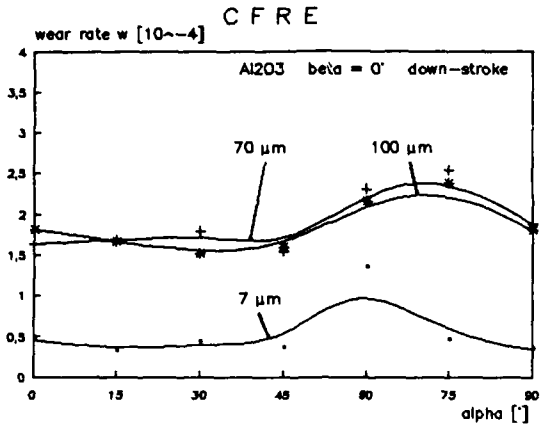
Fig. 6: Components of forces acting at the interface of an individual carbon fiber with different orientations. In spite of constant fiber cross section the forces can be different: $F_N(0°/30°) > F_N(30°/0°)$.

Fig. 7: Wear rates of CFRE, effect of:

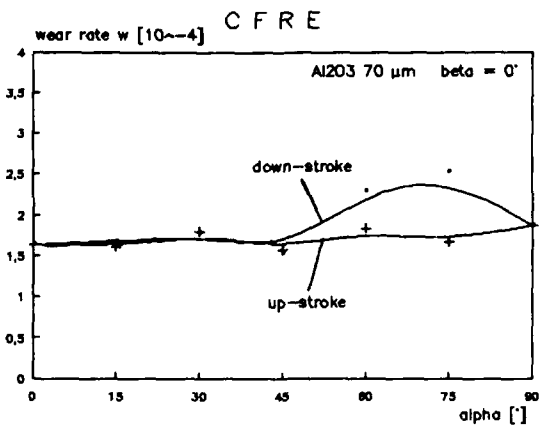


a) fiber orientation

b) hardness of abrasive

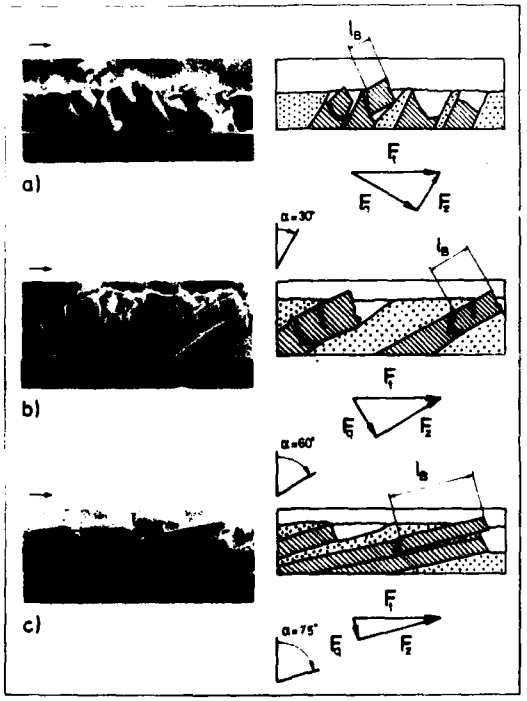


c) grain size of abrasive

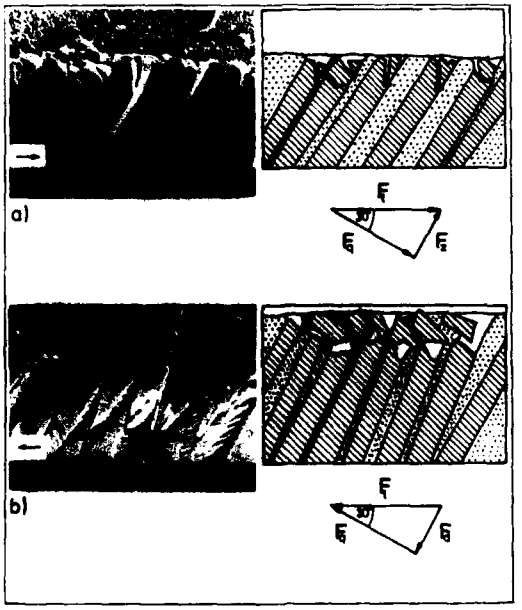


d) sign of sliding direction

Fig. 8: Cross sections of worn CFRE specimens. The arrows indicate the direction of sliding.



a) with increasing angle α the exposed fiber length l_B increases.
a) α = 30°, b) α = 60°, c) α = 75°



b) Different wear mechanisms as a function of sign of the direction of sliding.
a) down-stroke, b) up-stroke

Conclusions

The following rules can be established for certain combinations of friction μ and wear w for the utilization of microstructural anisotropy and down-stroke conditions.

	α	β	
$\mu \rightarrow$ min:	90°	90°	
$\mu \rightarrow$ max:	0°	0°	(3)
w $\rightarrow$ min:	0°	0°	
w $\rightarrow$ max:	75°	0°	

Our present understanding of the micromechanisms indicates, that simple angular relations do not exist for abrasive wear. There are qualitative changes in the intermediate range. An example is the wear maximum at α = 75°, β = 0°. The final conclusion is that a straight forward tensorial description of wear of fiber composites is not yet possible.

References

[1] Friction and Wear of Polymer Composites, K. Friedrich, ed., Elsevier, Amsterdam 1986.

[2] E. Hornbogen, Friction and Wear of Materials with Heterogeneous Microstructures, in: [1], S. 61-88.

[3] M. Cyffka, E. Hornbogen, Description of Anisotropic Wear Rates of Polymer-Base Composites, J. Mater. Sci. Lett. 5 (1986) 424-426

[4] D. Hull, An Introduction to Composite Materials, Cambridge University Press, London (1981).

[5] D.C. Prevorsek, R. K. Sharma, Fiber-Fiber Coefficient of Friction: Effect of Modulus and tan δ, J. Appl. Polymer Sci. 23 (1979) 173-184

TRANSFER OF PARTICLES AND FIBRES FROM GAS TO LIQUID DURING SOLIDIFICATION PROCESSING OF COMPOSITES

P. K. Rohatgi, R. Asthana
Materials Department
University of Wisconsin-Milwaukee
Milwaukee, Wisconsin, USA

ABSTRACT

Transfer of particles, platelets or fibers from gas phase to liquid phase and then from liquid phase to solid phase are the two major steps in fabrication of metal matrix composites through solidification processing. In this paper earlier theories of energetics of transfer of spherical and flake shaped particles from gas phase to liquid phase have been extended to spheroidal and needle shaped particles and fibers. The effects of fiber diameter, fiber volume and wetting behavior have been computed for selected composite systems, and compared with limited experiments on dispersion of particles or fibers in melts. Suggestions have been made to extend the theories of transfer of particles and fibers from gas to liquid phase to transfer from liquid phase to solid phase during solidification to develop a unified theory of solidification processing of composite materials.

INTRODUCTION

SEVERAL EXPERIMENTAL TECHNIQUES have been developed over the last two decades to synthesize cast metal-matrix composite materials by mechanically mixing fibers or particles in a fully or partially molten alloy, followed by solidification of the resulting slurry (1). In these solidification techniques of synthesizing composite materials the transfer of particles, platelets and fibers from the gas phase (or vacuum) to a melt is a major step during processing. The ceramic dispersoids generally used are not accepted by metallic melts unless special techniques are employed to transfer these ceramics to a molten metal. Earlier theories (2,3) for the energetics of transfer of spherical and flake shaped solid particles from gas to a melt have shown that poor immersional wetting presents a major obstacle to achieving high particle recoveries in solidified castings. These theories predict magnitudes of energy input required for particle introduction into melts which have been confirmed experimentally. In this paper the earlier theories of spherical and flake shaped particle transfer have been extended to ellipsoidal particles, and fibers. The theory presented here is in good qualitative agreement with recent experiments on cast metal ceramic composites.

The transfer of a particle to a melt is said to be complete when the particle enters the liquid by replacing the entire gas-solid interface by an equal solid-liquid interface. During intermediate steps when the particle is partially submerged and in contact with two fluids (liquid and gas), the condition of equilibrium is expressed by

$$\gamma_{GS} = \gamma_{LS} + \gamma_{LG} \cos\theta \qquad (1)$$

where θ is the contact angle and γ's are the specific interfacial energies of subscripted interfaces. Neumann et al. (4) have made a thermodynamic analysis for particle transfer to a melt across a flat gas-liquid interface assuming negligible effect of buoyancy forces. This paper considers surface energy as well as buoyancy and potential energies to establish a thermodynamic criterion predicting conditions for spontaneous transfer of particles to a melt.

THEORY OF PARTICLE TRANSFER FROM GAS TO MELT

A generalized theoretical analysis is made for the energetics of transfer from gas to melt of an ellipsoidal particle generated by revolving the ellipse

$$\frac{x^2}{a^2} + \frac{y^2}{b^2} = 1$$

about y axis and shown in Fig. 1. The following assumptions are made:

1. The process of transfer is an equilibrium process i.e., the equilibrium surface ther-

modynamics (e.g., Young-Dupre equation) is applicable at phase junctions at all stages during submersion.
2. The specific interfacial energy is isotropic.
3. The gas-melt interface is flat and devoid of any oxide film.
4. Neighboring particles do not interact with each other.
5. The effects of thermal gradients, melt convection and chemical reactions at the melt-particle interface are negligible during the time for complete submersion.

The total energy change on transferring the particle of Fig. 1 in a melt is considered to be the sum of the changes in surface, buoyancy and potential energies, i.e.,

$$\Delta E_t = \Delta E_S + \Delta E_B + \Delta E_P \qquad (2)$$

ΔE_S: SURFACE ENERGY - The net change in the surface energy of the particle in a partially submerged state is

$$\Delta E_S = \Delta E_{SL}(\omega) + \Delta E_{LG}(\omega) + \Delta E_{SG}(\omega) \qquad (3)$$

where each term on right-hand side of equation (3) refers to interfacial energies of subscripted interfaces expressed as functions of semi-apical angle ω (Fig. 1). Since the area $\Delta A_{SL} = \Delta A_{GS}$, Eqs. (1) and (3) can be combined and rewritten as:

$$\Delta E_S(\omega) = \gamma_{LG}(\Delta A_{LG} - \Delta A_{SL} \cos\theta) \qquad (4)$$

Calculations for ΔA_{LG} and ΔA_{SL} based on the particle geometry shown in Fig. 1 give surface energy term as:

$$\Delta E_S(\omega) = \pi \gamma_{LG} b^2[- (\frac{a}{b})^2 \sin^2\omega + (1 - \frac{a^2}{b^2}) (\frac{\cos^4\omega - 1}{2}) + 2\cos\theta \{\frac{a^2}{b^2}(\cos\omega - 1) + (\frac{a^2}{b^2} - 1)(\frac{1-\cos^3\omega}{3})\}] \qquad (5)$$

ΔE_B: BUOYANCY ENERGY - The change in the buoyancy energy or the work done by the force of buoyancy on the particle during its immersion in the melt through an angle ω is

$$\Delta E_B = - \int_0^{\omega} V(\omega)\, \rho_m\, g\, d\bar{Y}_\omega \qquad (6)$$

where $V(\omega)$ is the volume of liquid displaced, ρ_m is the density of the melt and $\bar{Y}_\omega$ is the distance along Y-axis the C G of the particle is displaced during its immersion through an angle ω. The buoyancy energy term for the ellipsoid of revolution shown in Fig. 1 is found to be

$$\Delta E_B(\omega) = - \frac{\rho_m g \pi a^2 b^2}{48} [108 \ln\{\frac{2}{3} + \frac{\cos\omega}{3}\sqrt{R}\} + 39 - 40\sqrt{R}\cos\omega + R^4 \cos^4\omega] \qquad (7)$$

where

$$R = [\frac{a^2}{b^2} - (\frac{a^2}{b^2} - 1)\cos^2\omega]$$

ΔE_P: POTENTIAL ENERGY - Considering the liquid surface to be the potential energy datum, the potential energy term for the solid particle of density ρ_p shown in Fig. 1 is readily obtained as:

$$\Delta E_p(\omega) = - \frac{4}{3} \pi a^2 b^2 \rho_p g [1 - \sqrt{R}\cos\omega] \qquad (8)$$

Therefore, the total free energy change in transferring the ellipsoidal particle of Fig. 1 from gas phase to liquid phase at constant temperature and pressure is the sum of energy contributions in Eqs. (5), (7) and (8).

Special Cases - Two special cases namely sphere and fiber are treated below:

(i) Sphere (a = b). The energy terms of Eqs. (5), (7) and (8) reduce to:

$$\Delta E_S(\omega) = \pi a^2 \gamma_{LG}[- \sin^2\omega + 2\cos\theta(\cos\omega - 1)] \qquad (9)$$

$$\Delta E_B(\omega) = - \frac{\rho_m g \pi a^4}{48} [108 \ln(\frac{2 + \cos\omega}{3}) + 39 - 40\cos\omega + \cos^4\omega] \qquad (10)$$

$$\Delta E_p(\omega) = - \frac{4}{3} \pi a^4 \rho_p g(1 - \cos\omega) \qquad (11)$$

(ii) Fiber ($\frac{a}{b} << 1$):

$$\Delta E_S(\omega) = \pi b^2 \gamma_{LG}[\frac{(\cos^4\omega - 1)}{2} - \frac{2}{3}\cos\theta(1 - \cos^3\omega)] \qquad (12)$$

$$\Delta E_B(\omega) = - \frac{\rho_m g \pi a^2 b^2}{48} [108 \ln(\frac{2 + \cos^2\omega}{3}) + 39 - 40\cos^2\omega + \cos^8\omega] \qquad (13)$$

$$\Delta E_p = - \frac{4}{3} \pi a^2 b^2 \rho_p g \sin^2\omega \qquad (14)$$

ENERGY REQUIREMENTS FOR COMPLETE SUBMERSION

The total energy for complete submersion of a solid particle is obtained by integrating the surface, buoyancy and potential energy changes between $\omega = 0$ to $\omega = \pi$, i.e.,

$$\Delta E_T = \int_0^{\pi} [\Delta E_S(\omega) + \Delta E_B(\omega) + \Delta E_p(\omega)]\, d\omega \quad (15)$$

However, the change in E_T as a function of degree of immersion (ω going from 0 to π) determines the energy changes during the transfer from gas phase to liquid phase. This energy path has been the determining criterion as to whether the transfer is spontaneous or not.

DISCUSSION

ELLIPSOID - The theoretical calculations for total change in energy ($\Delta E_S + \Delta E_B + \Delta E_p$) during transfer of ellipsoidal graphite particles of various sizes in molten Al are shown in Figs. 2 and 3 as a function of the angle of immersion ω for two different wetting conditions. The energy changes occurring during immersion from $\omega = 0$ to $\omega = \pi$ of Ni coated graphite particles (contact angle $\simeq 60°$) are negative, indicating spontaneous acceptance of particles by the melt owing to improved immersional wetting. After a large initial decrease in the energy at low ω further immersion is accompanied by progressively smaller energy decreases until the last stages of immersion ($\omega \rightarrow \pi$) are reached when small external energy input is required to completely submerge the particle. On the other hand, ΔE_T sharply increases when uncoated graphite particles (contact angle $\simeq 157°$) are introduced into molten Al at its melting point, indicating that external energy must be supplied to overcome the thermodynamic free energy barrier for complete immersion. With increasing particle sizes the energy barrier for complete submersion becomes progressively more pronounced. However the total energy change ΔE_T is practically equal to the surface energy change during transfer since $\Delta E_S >> \Delta E_B$ and ΔE_p.

SPHERE - Figure 4 shows the computed surface energy ΔE_S vs semi-apical angle ω plots for submersion of a spherical graphite particle into various liquids under different wetting conditions. Contact angles $\theta > 90°$ (uncoated graphite spheres) invariably lead to a steep rise in the surface energy barrier with increasing ω; the increase in ΔE_S being larger, greater the values of melt surface tension and wetting angle θ. For contact angles $\theta < 90°$ (Ni-coated graphite) a large initial decrease in the surface energy is followed by a modest increase in the energy during the later stages of immersion as shown in Fig. 4. The surface energy change for transfer of both uncoated ($\theta \simeq 60°$) and Ni coated ($\theta \simeq 0°$) graphite spheres in molten Ni ($\gamma_{LG} = 1900$ erg cm^{-2}) is negative, indicating spontaneous transfer of particles to the melt. The large value of surface tension of liquid metals compared to water ($\gamma_{LG} = 72$ erg cm^{-2}) is responsible for the greater difficulty in transferring graphite to liquid metals than to water.

Figure 5 shows the variation of ΔE_S with ω for introduction of graphite spheres of various sizes into molten Al under two different wetting conditions. Since ΔE_S varies with the square of particle size whereas the buoyancy and potential energies vary with the fourth power of sphere radius, the former tends to override the latter energy contributions at the small particle sizes generally used in synthesizing cast metal-matrix particulate composites. Therefore, from a practical viewpoint it is sufficient to consider the surface energy contribution alone when the thermodynamic feasibility of particle transfer to a melt is to be assessed. Figure 5 confirms the previous wettability criterion according to which acute wetting angles favor spontaneous particle transfer and obtuse wetting angles favor spontaneous rejection of particles from the melt. This criterion for spontaneous dispersion or rejection of particles is in qualitative agreement with particle injection experiments as shown in Table 1. This agreement with spherical particles gives enough confidence in this approach to extend it to ellipsoidal particles and fibers.

FIBERS - For the case of a fiber ($a/b << 1$) the energetics for particle transfer depend upon the surface tension, wetting angles and the fiber axial ratio. Figures 6 and 7 depict the theoretical variation of surface energy and buoyancy energy changes with ω for graphite fibers of various sizes when they are introduced into molten Al. Similar to the cases of previous particle geometries, energetics favor spontaneous fiber entry into melts when wetting angle $\theta < 90°$. When the wetting angle is greater than 90°, spontaneous entry of fibers will not be energetically favored. Recent experiments by Satyanaryana et al. (5) on dispersion of carbon fibers in a 7010 alloy matrix melt confirm that surface modification of carbon fibers was necessary to improve the wettability ($\theta < 90°$), dispersibility and fiber recovery in the castings. Figure 8 shows a typical microstructure of C fiber/7010 alloy composite synthesized by mixing surface modified carbon fibers into the matrix alloy (5). Similar results have been reported on other systems (6) where surface modification and external agitation of the melt was found necessary to introduce fibers in a melt.

Since the wetting angle is also influenced by the test temperature and contact times, optimum combination of processing conditions can give rise to good interfacial wetting and bonding. Higher temperature and times can cause rapid degradation of reinforcement surface as well as severe oxidation of the melt. The influence of a continuous adherent oxide film on the surface of the melt can be easily incorporated in the above theoretical framework by considering two stages of transfer--namely transfer across a gas-oxide film interface and

transfer across an oxide-melt interface. The entire set of equations with appropriate values for wetting characteristics and densities of phases under consideration is still valid. It is also instructive to note that the eventual engulfment or rejection of dispersed particles, platelets or chopped fibers by solidifying interfaces during the solidification stage can be treated analogously by considering the energetics of transfer across a melt-solid interface. By employing the equation-of-state approach suggested by Omenyi and Neumann (7), the appropriate interfacial energies and wetting angles for the melt-particle-solid system can be calculated. These values can then be used in the energetics analysis presented here to determine the energetics of particle engulfment by solidifying interfaces, and will be discussed in a future paper.

CONCLUSIONS

The thermodynamic analysis presented here for particle transfer across a gas-liquid interface allows computations to be made of the absolute magnitudes of major energy contributions occurring during immersion of particles of various shapes and sizes as a function of wetting characteristics and the densities of the phases. A criterion whereby the thermodynamic feasibility of the process of particle transfer can be characterized has been established and confirmed qualitatively with the results of gas injection experiments reported elsewhere. The poor immersional wetting between ceramics and metallic melts, and the relatively large interfacial areas of fine ceramic particles necessitate improvements in wetting and use of mechanical agitation. Recent experiments on synthesis of cast metal ceramic composites by introducing particles, platelets and fibers into a melt provide further qualitative confirmation of the analysis presented here.

ACKNOWLEDGMENTS

The authors are grateful to Dr. R.N. Yadav of R.R.L. Bhopal (India) for help in early computations.

REFERENCES

1. Rohatgi, P.K., "Cast Metal-Matrix Composites," Metals Handbook: Casting, vol. 15, 9th Ed., A.S.M. (in press) (1988).
2. Prabhakar, K.V. and P.K. Rohatgi, in Proc. Symposium on Quality Control of Engineering Alloys and the Role of Metals Science, Delft, Netherlands, 215 (1977).
3. Rohatgi, P.K., "Interfacial Phenomena in Cast Metal Ceramic-Particle Composites," Interfaces in Metal Matrix Composites, Eds. A.K. Dhirgra and S.G. Fishman, TMS/AIME, Mar (1985).
4. Neumann, A.W., C.J. Van Oss and J. Szekely Kolloid-Z4Z Polymere 251, 415 (1973).
5. Satyanaryana, K.G., B.C. Pai, M.R. Krishnadev and C.G. Krishnadas Nair, Proc. of 32nd International SAMPE Symposium, April 6-9, 880 (1987).
6. Rohatgi, P.K., R. Asthana and S. Das, Int. Metals Revs. 31(3), 115 (1986).
7. Omenyi, S. N. and A. W. Neumann, J. Appl. Phys. 47, 3956 (1976).

TABLE 1. Behavior of Particles During Gas Injection into Melts (2).
(↓: Particle enters the melt; ↑: Particle rejected from the melt)

	Melt	γ_{LG} (erg/cm^2)	ρ_m (g/cc)	Particle	Size (μm)	ρ_p (g/cc)	Wetting Angle (degree)	Particle Behavior
1	Zn	820	7.14	Gr	80	2.0	157	↑
2	Zn	820	7.14	Ni-coated Gr	80	4.0	60	↓
3	Fe	1850	7.00	Gr	80	2.0	130	↑
4	Fe	1850	7.00	Ni-coated Gr	80	4.0	60	↓
5	Ni	1900	8.90	Gr	80	2.0	67	↓
6	Ni	1900	8.90	Ni-coated Gr	80	4.0	0	↓
7	Cu	1300	8.92	Gr	80	2.0	140	↑
8	Mg	563	1.76	Gr	80	2.0	60	↓
9	Mg	563	1.76	Ni-coated Gr	80	4.0	40	↓
10	Al	900	2.71	Gr	80	2.0	160	↑
11	Al	900	2.71	Gr	250	2.0	160	↑
12	Al	900	2.71	Ni-coated Gr	250	4.0	70	↓
13	Al	900	2.71	Al_2O_3	80	3.9	130	↑
14	Al-1 Cu	850	2.79	Gr	80	2.0	60	↓
15	Al-1 Ni	865	2.80	Gr	80	2.0	60	↓

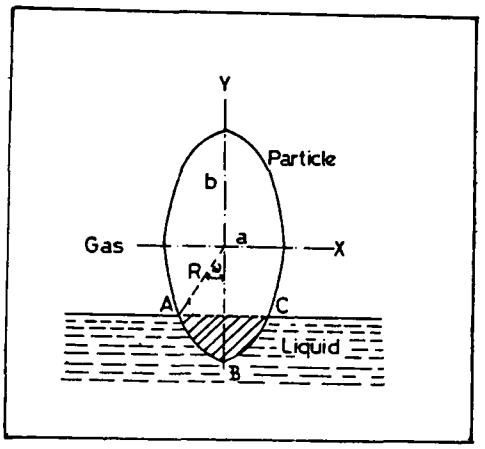


Fig. 1. Schematic of a partially submerged ellipsoid shaped particle.

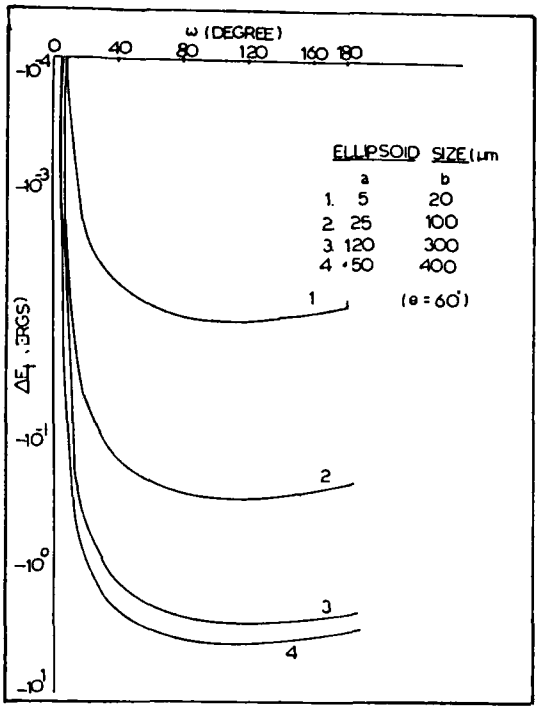


Fig. 2. ΔE_T vs ω plots for ellipsoidal graphite particles in molten Al (θ = 60°).

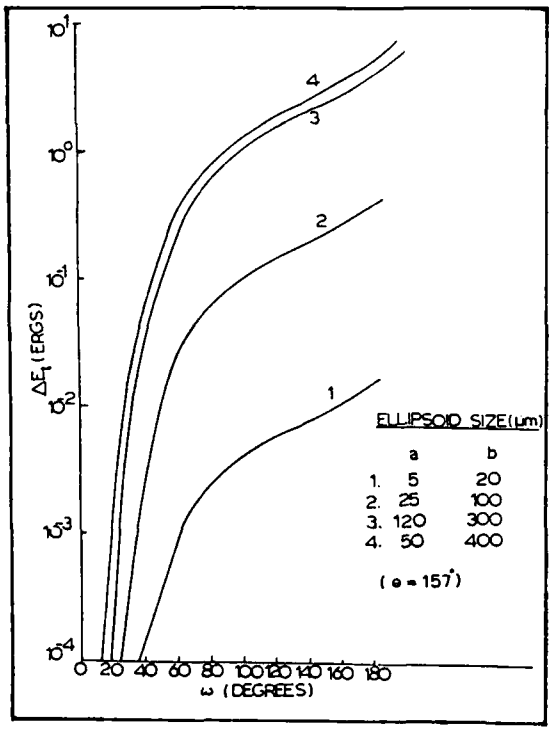


Fig. 3. ΔE_T vs ω plots for ellipsoidal graphite particle in molten Al (θ = 157°).

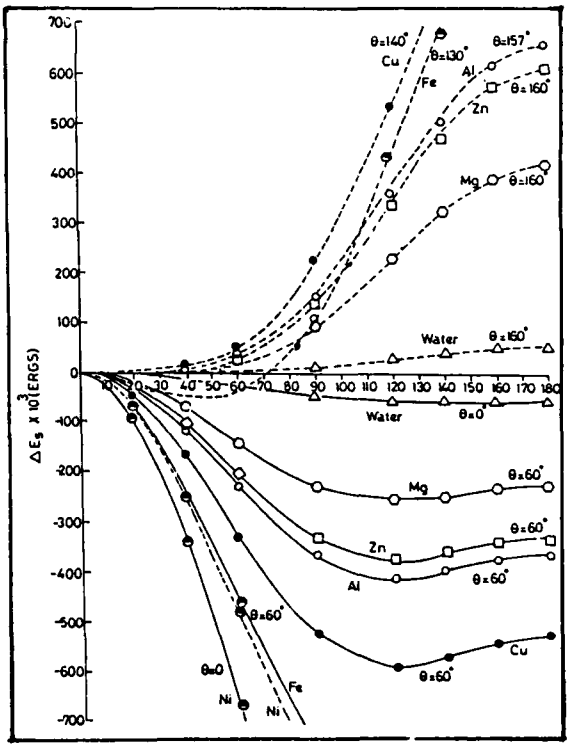


Fig. 4. ΔE_S vs ω plots for 80 μm graphite sphere in various liquids.

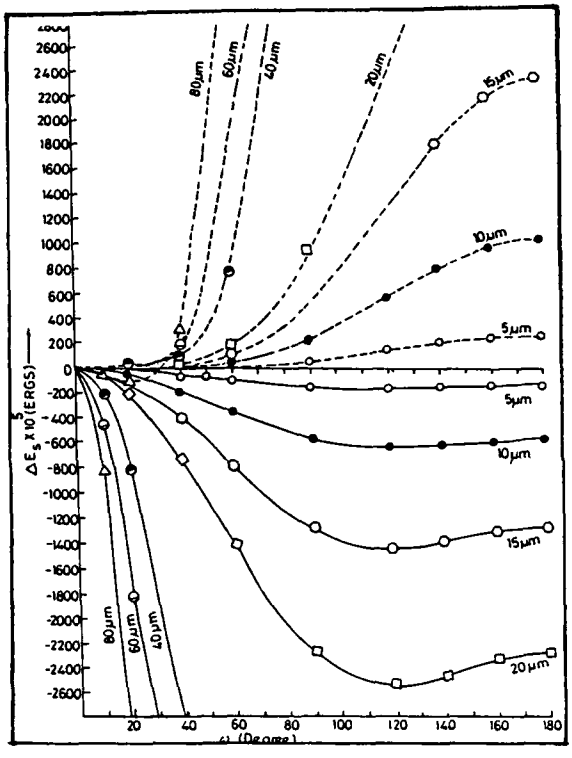


Fig. 5. ΔE_S vs ω plots for graphite spheres of various sizes in Al melt (θ = 157°, θ = 60°).

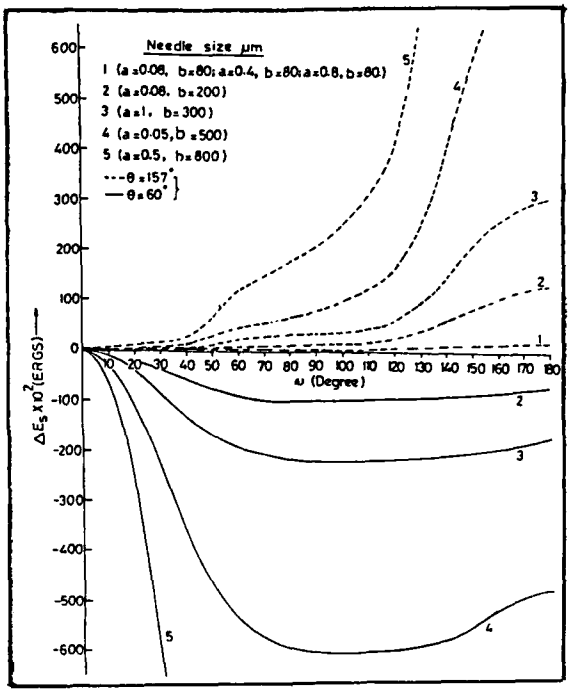


Fig. 6. ΔE_S vs ω plots for graphite fibers in molten Al for θ = 157° and 60°.

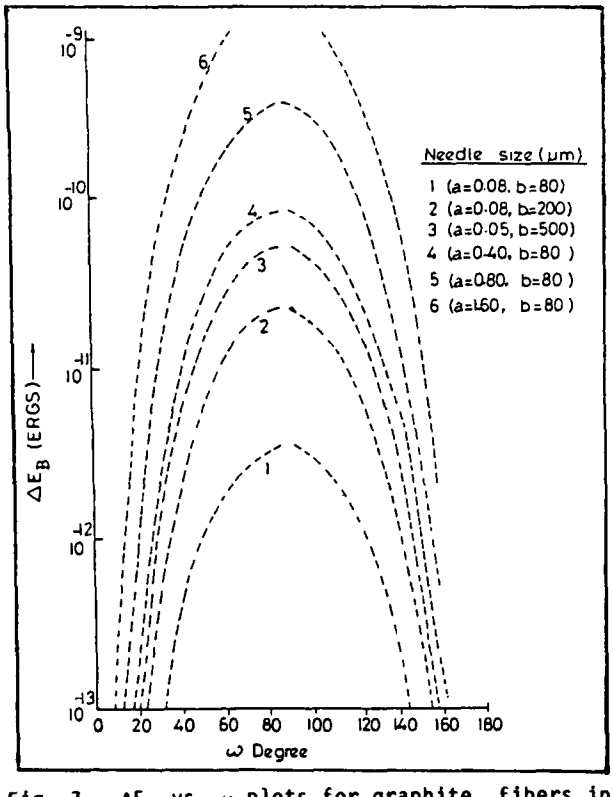


Fig. 7. ΔE_B vs ω plots for graphite fibers in Al melt.



Fig. 8. Cast 7010 alloy containing surface modified carbon fibers (courtesy of K. G. Satyanaryana et al.).

CHEMICAL ANALYSIS AND BONDING AT THE FIBER-MATRIX INTERFACE IN MODEL ALUMINUM MATRIX COMPOSITES

Y. Le Petitcorps, T. Stephenson, F. Girot, R. Naslain
Laboratoire de Chimie du Solide CNRS
Université de Bordeaux I,
351 Cours de la Libération - 33405 Talence, France

ABSTRACT

Adhesion mechanisms at fiber-matrix interfaces in aluminum matrix composites were analysed using model micro-composites. The interfacial shear strength was calculated from the fiber critical lengths measurements. The study showed the role played by (1) the allowing elements in the matrix, (2) the quantity of silica associated with the reinforcement, (3) the annealing treatment (T_6) on the adhesion between the fiber and matrix. Such a test indicates the parameters which are susceptible to modify the mechanical behavior of the composite.

THE FINAL PROPERTIES OF ALUMINUM MATRIX COMPOSITES are linked to the nature of the bonding at the fiber-matrix (FM) interfaces. The mechanisms which take place at the interfaces between short fibers (or whiskers) and an aluminum alloy matrix have largely been studied on a physico-chemical basis [1,2,3]. These studies have shown the role played by the matrix alloying elements on the composition of the so-called interphase [4,5]. Estimating the adhesion of the reinforcement to the matrix is often made from microscopic observations of the rupture surfaces However it is rarely measured.

A simple method to determine the interfacial FM adhesion has been developed for polymeric matrix composites and very recently applied to metal matrix composites (MMC) [6,7]. Model materials whose reinforcement is a silicon carbide CVD filament of large diameter (Ø ≃ 100 µm), have been prepared according to conditions close to those used in squeeze-casting for the infiltration of preforms. The interfacial shear strength τ_i has been derived from fiber critical length data as a function of the processing parameters.

FRASER FRAGMENTATION TEST

The principle of the Fraser test consists in breaking a filament in matrix under tension loading and relating the fragment lengths to the interfacial shear strength τ_i (Fig.1) [8].



Fig.1: Fragmentation sequence of a silicon carbide filament after tensile testing within a metal matrix

In order to induce failure of the fiber into fragments of length equal to $L_c/2$ (where L_c is the critical length), the matrix must undergo plastic deformation. This condition is generally verified when $\varepsilon^{Rc} \simeq \varepsilon^{Rm} > 3 . \varepsilon^{Rf}$ (where ε^{Rc}, ε^{Rm} and ε^{Rf} are respectively the rupture strains of the composite, matrix and fiber) [9].

The interfacial shear strength is then expressed by the following relation:

$$\tau_i = [\sigma^{Rf} . d/2] [L^{1/m}/L_c^{(m+1)/m}]$$

σ^{Rf} : fiber rupture strength for the gauge length L
d : fiber diameter
m : Weibull modulus of the fiber in the presence of the matrix
L_c : fiber critical length

EXPERIMENTAL

Model composites were obtained by casting an aluminum alloy (Al-7Si-0.6Mg) in a mold containing a silicon carbide filament held slightly in tension with the following experimental conditions: - temperature of the liquid metal: 750°C, - fiber temperature: 500°C, - casting duration: 15s, - air cooled.

The most promising materials for large scale applications are obtained by infiltrating a preform of short fibers (alumina - silica, silicon carbide) with an aluminum alloy matrix. These preforms usually contain silica (in the fiber and / or binder), the role of which is: (i) to assure the structural integrity of the preform and (ii) to induce a chemical reaction between the reinforcement and the alloying elements of the matrix (ex Mg). To reproduce similar conditions in model composites, silica was deposited on filaments by (1) oxidation of the fiber between 900 and 1000°C in air, and (2) cathodic pulverization (PVD) of a silica target on the fibers surface. The resulting silica film thickness falls within the range 100 - 2000 Å. The composites were annealed to improve the mechanical performance of the matrix alloy: a T_6 treatment (4h at 540°C, water quench, 8h at 170°C) was applied to all the model composites in order to show its influence on the adhesion at the FM interface.

The *single* filament composites were tested in tension at ambient temperature. An acoustic sensor was used to relate the strain of the material to the acoustic emission which was produced at different stages of tension loading. The acoustic emission parameters were chosen in order to avoid the recording of the signal corresponding to the plastic deformation of the matrix. At a strain close to the rupture strain of the prestressed fiber ($\varepsilon^{Rf} \simeq 1.2\%$), a sudden increase in acoustic emission appears which seems to correspond to the beginning of breakage of the fiber. The signal then increases rapidly with strain and stabilizes at a strain of the order of 3%. This strain is thought to be the limit for which the fiber fragments attain a length equal to $L_c/2$. The specimens were chemically etched by hot caustic soda to dissolve the matrix and to collect the fiber fragments by filtering. The fiber lengths were measured by optical microscopy.

RESULTS AND DISCUSSION

Effects of Magnesium and T6 Annealing Treatment

The absence of magnesium in the matrix leads to large critical fiber lengths (L_c > 2000 µm) no matter whether silica is present or not and whatever the nature of the annealing treatment. During casting, the FM interface results from the interaction between an aluminum front covered by an alumina skin and a silica film on the fiber. After cooling, resulting Al_2O_3-SiO_2 adhesion is found to be weak ($\tau_i \simeq 50$ MPa).

When pure aluminum is replaced by an alloy, the critical lengths decrease (2000 < L_c (µm) < 700). The effect of the alloying elements is (i) to lower the F/M contact angle, (ii) to decrease the liquidus temperature and, as a result, (iii) to increase the interaction time between the alloy and the fiber, in the liquid state. Magnesium may break the alumina skin (by diffusion) and chemically react with the fiber to form thermodynamically favorable phases such as the spinel Mg_2SiO_4 or Al_2O_4Mg, oxides (MgO), or intermetallics (Mg_2Si).

The above conclusions on the magnesium effect can be illustrated by interface analyses performed on real alumina-aluminum alloy composites (i.e. prepared from Saffil fibers) (Fig. 2). The intermetallic compound Mg_2Si was observed by T.E.M. as large precipitates at the F/M interface for high Mg concentrations in the original alloy (1.1 wt%) Ion sputtering and Auger analysis of the interface revealed an interphase whose thickness was of the order of 3000 Å. The chemical shift of Mg peak in Auger electron spectra indicates that magnesium has been oxidized in contact with the fiber. Examinations of rupture surfaces reveal intrafiber failure for that concentration of magnesium.



Fig.2: Transmission electron micrographs of the fiber/matrix reaction zone in Al_2O_3-SiO_2/Al-7Si-1.1Mg composite (dark field)(x 300000)

For a lower Mg content in the alloy (0.3%), the interphase was thinner (<1000 Å). Fractographic analysis indicated a fiber-matrix debonding. The T_6 treatment lowered the critical length and favored chemical reactions at the fiber-matrix interface [10]. X-ray spectrometry analysis showed that the Mg concentration around the fiber increased with the T_6 treatment. As a result of this reaction, the interfacial adhesion strength increased. However, this reaction could be an extension of fiber degradation when the magnesium content

in the alloy is very high.

Influence of the thickness of the silica film

The inherent silica layer on a silicon carbide fiber in the as-received state is thin (< 100 Å). The liquid alloy reacts first with this thin silica film during casting and then attacks the silicon carbide substrate. Under such conditions, the FM interface is particulary strong (Fig.3) and fragments of SiC are observed to adhere to the matrix upon examination of rupture surfaces.

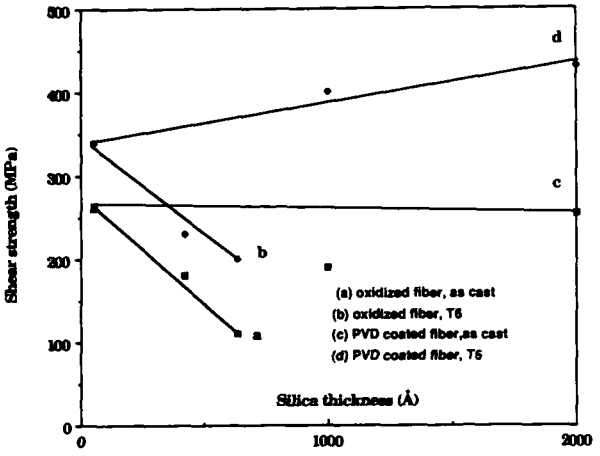


Fig.3: Evolution of the interfacial shear strength τ_i as a function of the thickness of silica, the annealing treatment and the deposition method for a single SiC-fiber / Al-7Si-0.6 Mg)

When the thickness of silica increases, the evolution of the interfacial shear strength τ_i is different depending on the SiO_2-deposition method

When silica was obtained by oxidation, the stress τ_i was found to be inversely proportional to the silica thickness whatever the annealing treatment (Fig.3). During the composite casting, the alloy did not completely react with the silica layer ($e_{SiO_2} \simeq 400 - 600$ Å) and the fractographic analyses indicated that the debonding occured at the SiC/SiO_2 interface (Fig.4). This decohesion is caused by thermo-mechanical stresses at the interface due to differences in the coefficients of thermal expansion (CTE) of the constituents ($\alpha_{SiC} > \alpha SiO_2$). The radial stresses which develop during cooling at the oxide-coated fiber are more intense as the silica thickness increases. The model composites containing fibers coated with silica by P.V.D. had a high interfacial shear strength (Fig.3). Silica was deposited at low temperature ($\theta < 300°C$) so that the thermo-mechanical stresses between SiC and SiO_2 were weak even for large SiO_2-thicknesses values. Contrary to the previous case, the silica layer thickness had little effect on the interfacial adhesion (Fig.3).



Fig.4: S.E.M. fractography of a model composite SiC / Al-7Si-0.6 Mg (T_6 treated) for $e_{SiO_2} = 600$ Å (x 2000)

CONCLUSIONS

Although the interfacial shear strength τ_i may have been overestimated ($\tau_i \simeq (\sigma^E/2)$) by uncertainties in the values of σ^{Rf} and m, this test has pointed out the role of (i) the allowing elements of the matrix (magnesium) and (ii) the annealing treatments on the interfacial FM adhesion. This study has shown that a thick layer of silica is unnecessary to improve the FM adhesion. However, it is beneficial to have a minimum thickness of silica to protect the fiber during casting. These trends observed for the τ_i values are compatible with S.E.M. fractography observations and chemical analyses performed on similar materials manufactured by foundry technics. The measurements of critical lengths of the fiber seem to be a useful approach to predict the mechanical behavior of new MMC.

ACKNOWLEDGEMENTS

The authors thank Peugeot SA for its financial support.

REFERENCES

1 G.R. Cappleman, J.F. Watts, T.W. Clyne, Journal of Materials Science 20 (1985) pp.2159-2168.

2 A.A. Das and S. Chatterjee, The Metallurgist and Materials Technologist (1981) pp.137-142.

3 D. Webster, The metallurgical Society of AIME, Vol.13A (1978) pp. 1511-1519.

4 C.G. LEVI, G.J. Abbaschian and R. Mehrabian Metallurgical Transaction A, volume 9A (1978) pp. 697-711

5 A. Kohyama, N. Igata, Y. Imai, H. Teranishi and T. Ishikawa, ICCM 5 (1985) pp. 609-621.

6 W.D. Bascom, R.M. Jensen and L.W. Corder ICCM 6 (1987) Vol. 5, pp.424-438.

7 Yoshihiro Sawada, Abio Shindo and Yoichiro Nakanishi, ICCM 6 (1987) vol.5, pp. 448-457.

8 W.A. Fraser, F.H. Anker and A.T. Dibenedetto, 30th. Tech. Conf. 1975, Reinf. Plast/comp. Instit, The SPI, Inc., Section 22-A.

9 S.Ochiai and K. Osamura, Zeitschrift für Metallkunde 77-4 (1986) pp. 255-259.

10 J.E. Hack, R.A. Page and C.R. Leverant, Metallurgical Transactions A, vol 15A (1984) pp. 1389-1405.

11 D.L. Baty, J.P. Price and B.G. Coleman, Metal Matrix Composites 87, Proceedings, Pennsylvania (1987).

STUDIES OF INTERFACES IN LIGHT METAL MATRIX COMPOSITES BY TRANSMISSION ELECTRON MICROSCOPY

J. Taftø, K. Kristiansen
Research Centre, Norsk Hydro
3901 Porsgrunn, Norway

H. Westengen, A Nygard
Hydro Magnesium
3901 Porsgrunn, Norway

J. B. Borradaile
Hydro Aluminium, Karmøy Fabrikker
4265 Håvik, Norway

D. O. Karlsen
Department of Physics
University of Oslo, Blindern Oslo 3, Norway

Metal matrix composites (MMC) were fabricated using two techniques, in one of these by stirring Al_2O_3 and olivine particles into Al-alloy melts. Consistent with other works we observe that the particles are more easily dispersed when the Al-melt contains Mg. We observe that a fraction of the Mg atoms forms oxide particles near the metal/ceramic interface. In the other technique Mg alloy -Al_2O_3 composites were fabricated by infiltrating Al_2O_3 powder with Mg alloy using a technique involving selfgenerated vacuum, while attempts to apply this technique to the Al-melts were unsuccessful, suggesting that the oxide layer on the Al-melt acts as a diffusion barrier. We find evidence of a connection between the Mg-melts's ability to generate vacuum by reaction with air and the improved wettability of particles by Al-alloys with increasing Mg-content. Another significant observation is the replacement of cations at the outer layer of the ceramic particles by more electropositive cations from the melt.

A POTENTIAL LOW COST technique to manufacture metal matrix composites (MMC) is to stir ceramic particles into the metal melt (see e.g. 1). Several factors influence the final product, one very important being the metal melt's ability to wet the ceramic particles (2,3,4). The term wetting is here used in a wide sense, including chemical reactions as well. For a given metal the wettability depends on many parameters: 1) Type of particles, their shape, size, surface roughness and surface chemistry of the outer atomic layers. 2)Alloying elements in the melt. 3) Gas environment of the particles when injected into the melt. 4) Stirring, temperature and holding time in the melt

We have studied MMC fabricated by stirring caramic particles, in particular Al_2O_3- and olivine particles into Al-melts and Al-Mg alloys with different amounts of Mg. We will present some of our observations, in particular those obtained by the use of transmission electron microscope (TEM) techniques. The experimental results will be discussed with special emphasis on chemical reactions at the metal/-ceramic interface and at the interface between trapped air bubbles and the matrix. Attention will also be focussed on the improved wettability when the Al-melt contains Mg. Experiments using selfgenerated vacuum (5) will also be presented and discussed, and these experiments which clearly demonstrates some macroscopic effects closely related to wetting, will be presented first.

EXPERIMENTS AND OBSERVATIONS

INFILTRATION OF MG (AZ91) INTO AL_2O_3 POWDER USING SELFGENERATED VACUUM

- An interesting method to fabricate MMC is to take advantage of a technique involving a self-generated vacuum which works well for Mg (6). A tube of stainless steel, sealed on the top end, is put into the Mg melt. A reaction takes place between the Mg and the O_2 and N_2 in the air, resulting in the formation of vacuum and the tube is filled with liquid Mg. We have performed experiments where we filled a stainless steel tube with platelet shaped α-Al_2O_3 particles of typical dimensions 10 μm and a packing density of 25%. The tube was put into a (Mg-9%Al-1%Zn)-melt heated to 700 °C. From experiments using different holding times, we find that the liquid Mg alloy fills the region near the wall of the tube first, and then gradually infiltrates the Al_2O_3 powder further away from the wall, until eventually Mg fills up most of the available space in the tube of diameter 3.5 cm. Fig. 1 shows scanning electron microscope (SEM) images from a run cooled down after a relatively short holding time. Fig. 1a is from a region near the steel wall.

The higher magnification image of fig. 1b is from a region futher away from the steel wall where the infiltration is at its initial stage. Here we observe condensed drops on the Al_2O_3 particles. These are also seen using TEM, (fig. 2a). Electron energy loss spectroscopy (EELS) of the K edges showed that the drops contained a large amount of Al besides Mg, but no detectable amount of the light elements C, N and O, except for a thin layer of oxide on the surface of the drops due to exposure to air after the infiltration. Fig. 3 shows the EELS plasmon spectrum of one of the drops compared with the plasmon spectrum of pure Al. The features of the plasmon spectrum is typical of a metallic phase, and the plasmon energy, E_p = 12.6 eV, suggests a composition roughly halfway between Mg and Al. E_p for Mg and Al are 10.5 eV and 15.0 eV, respectively. Electron diffraction indicates that the phase is $Al_{12}Mg_{17}$. In electron diffraction we also observe MgO, and the MgO is at the surface of the Al_2O_3 particles as is evident from the dark field TEM image in fig. 2b. X-ray diffraction confirmed the presence of $Al_{12}Mg_{17}$ and MgO.

AL_2O_3 PARTICLES STIRRED INTO AL ALLOYED WITH MG - α-Al_2O_3 particles of typical diameter 20 μm were injected from air into Al-alloys containing 0, 2, 4 and 8 w.t.% Mg, respectively, while stirring the melt which was heated to 725 °C. With increasing Mg content the Al_2O_3 particles became more easily dispersed as may be evident from the SEM images of fig. 4a and 4b. Using electron diffraction and EELS we identify MgO ang $MgAl_2O_4$ particles near the Al/Al_2O_3 interface and in pores in the matrix. We find that the Mg containing oxides are more abundant at higher Mg-content.

OLIVINE PARTICLES STIRRED INTO AL ALLOYED WITH MG - Typically 50 μm size olivine particles of composition $(Mg_{0.9}Fe_{0.1})_2SiO_4$ were stirred into Al-alloy melts. We observe a trend similar to the one for Al-alloys with Al_2O_3-particles. Mg in the Al-alloy aided dispersion. Fig. 5 shows a SEM image for a run containing 5% Mg in the Al-melt. We notice that the olivine particles are nicely dispersed. Using TEM on ionthinned samples we observe a several thousand Å thick reaction zone between the matrix and the olivine fig. 6 and EELS and electron diffraction show that the reaction product is microcrystalline MgO. The opening between the thick MgO layer and the matrix seen in fig. 6 is quite typical, whereas we observe intimate contact between the microcrystalline MgO and the olivine particles.

DISCUSSIONS

When powder of clustered small ceramic particles are injected into the metal melt from air, some air will be injected as well. A rough estimate of the volume ratio between air and particle is (1-p)/p, where p is the packing density of the particles. For the particles used here with p<0.5 we thus introduce a larger volume of air (at atmospheric pressure) than of Al_2O_3. The instantaneously poor wettability of ceramic particles by liquid metals results in the ceramic particles being attached to the air bubble after injection. Thus despite the higher density of Al_2O_3 than of liquid Al, the injected particles tend to emerge to the surface when the wettability is poor. One way to solve this problem is by introducting an agent that improves the wettability so that the air, but not the particles, emerge to the surface. Another possibility is to eliminate the air through chemical reactions by converting the O_2 and the N_2 in the air bubbles to solid oxides and nitrides, which is, indeed, what happens using the selfgenerated vacuum technique for a Mg-melt.

In the following we argue that the ability to eliminate air bubbles (generate vacuum) by reaction between the air and the metal melt also is responsible for the improved dispersion of Al_2O_3, olivine and other ceramic particles (7,8) in Al-alloy melts with increasing Mg content. Energeticly it would be favorable with complete reaction between pure liquid Al and air too, because the formation of Al_2O_3 and AlN are exothermic reactions. However, in this case the initially formed thin oxide layer on the air bubble acts as a diffusion barrier preventing futher reaction. A temperature above 950 °C is necessary for the penetration of liquid Al through the oxide layer (see e.g. 2). An interesting evidence is found in a work by Abranow & al (9). They observed that Al can be saturated with hydrogen by bubbling moist argon through an Al-melt, but not by bubbling moist air.

It is not known which concentration of Mg in an Al-Mg alloy is required to selfgenerate vacuum, but for low Mg concentrations the Mg-atoms have to diffuse over long distances in the melt and the generation of vacuum takes a long time. The situation is much more favorable when small air bubbles of the order 1 mm in diameter are trapped in the melt. Then, with a Mg-concentration above 1%, diffusion over less than 0.1 mm is sufficient to convert the air into Mg oxides and Mg nitrides. The observation of MgO and $MgAl_2O_4$ in the matrix when Al_2O_3 particles are stirred into Al-Mg melts, in many cases close to the Al_2O_3 particles is in favor of this explanation why the Al_2O_3 and olivine particles are more easily dispersed at higher Mg-concentration in the Al-alloy melt. Note the analogy to

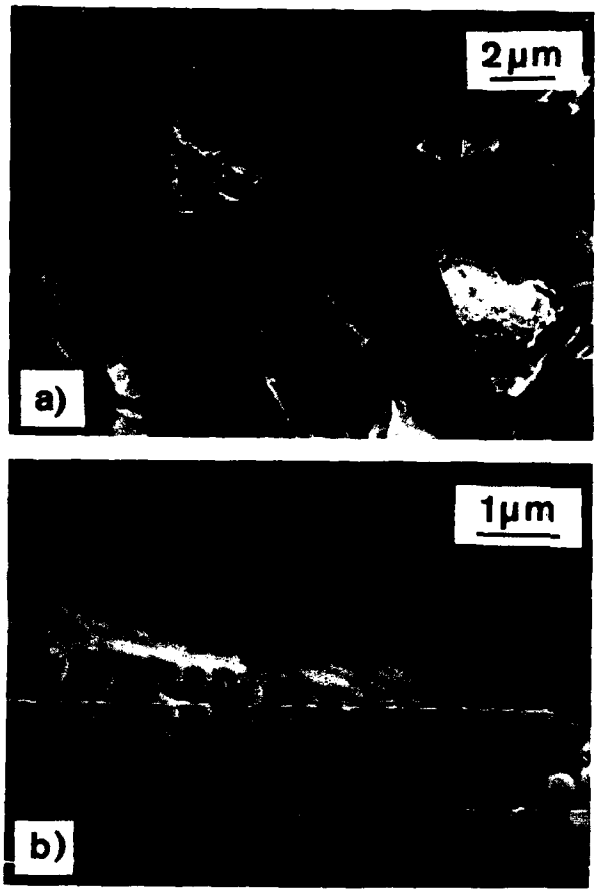


Fig. 1. Scanning electron microscope images at different stages of infiltration of Al_2O_3 powder with Mg (AZ91) using the selfgenerating vacuum technique. a) Infiltration nearly completed. b) Initial stage of infiltration showing condensed $Al_{12}Mg_{17}$ drops on the Al_2O_3 particles.

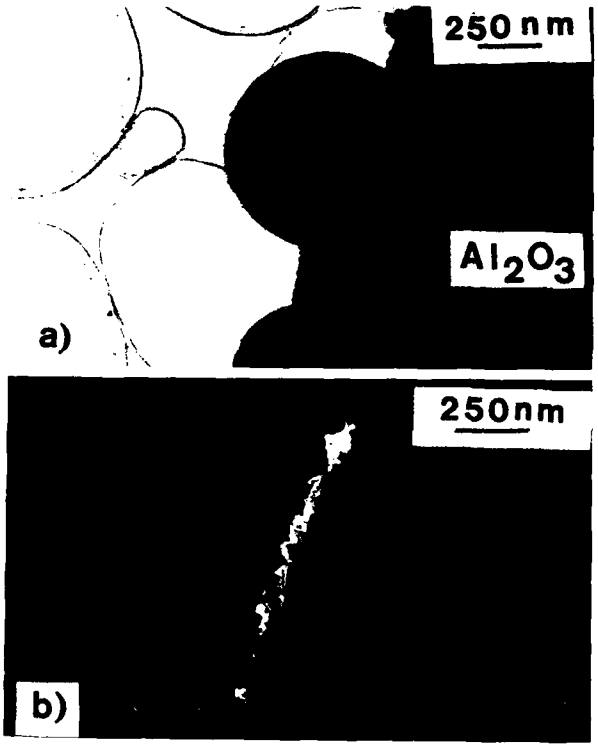


Fig. 2. TEM images corresponding to fig. 1 b. a) $Al_{12}Mg_{17}$ drops on the Al_2O_3 particle. b) Darkfield image showing the microcrystalline MgO particles on the Al_2O_3 particles. Only the fraction of MgO crystallites with Bragg reflections inside the objective aperture lightens up.

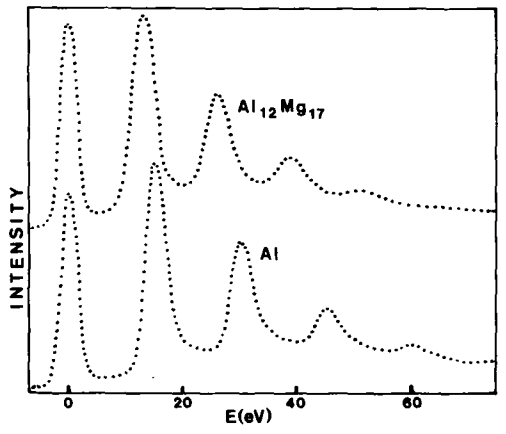


Fig. 3. Comparision of the EELS plasmon spectrum from relatively thick areas of a $Mg_{12}Al_{17}$ drop (upper) and Al (lower). From left we see the zero loss peak, 1. plasmon loss, 2. plasmon loss etc.

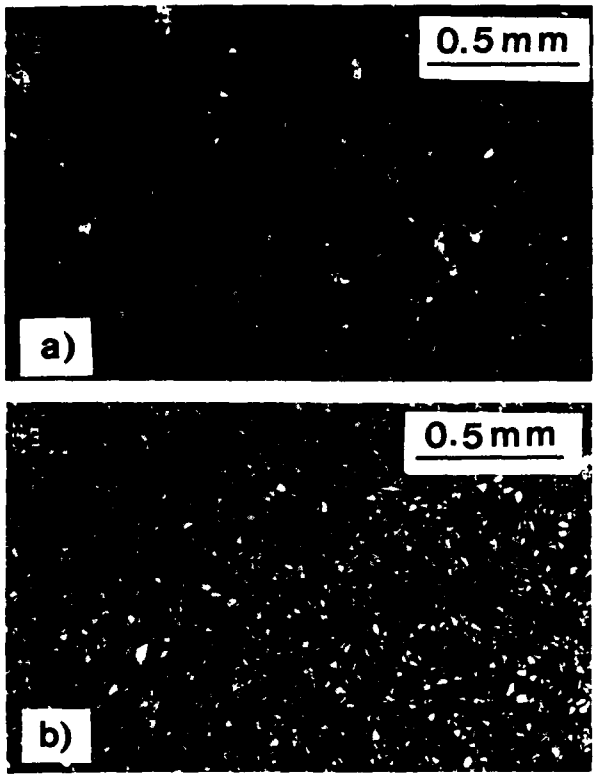


Fig. 4. Scanning electron microscope images of Al_2O_3 particles in Al alloys. a) 2 wt % Mg in Al b) 4 wt % Mg in Al.

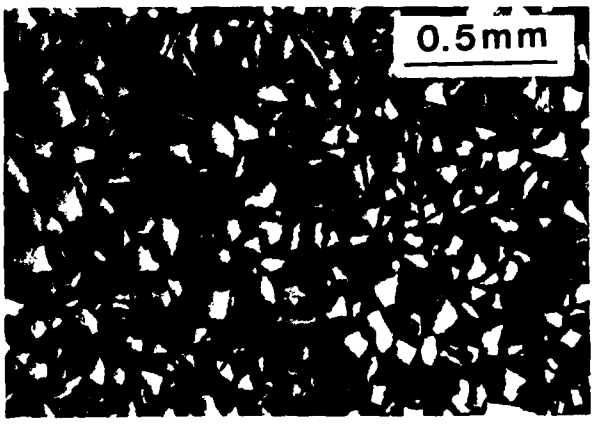


Fig. 5. Scanning electron microscope image of olivine particles in Al-5 % Mg.

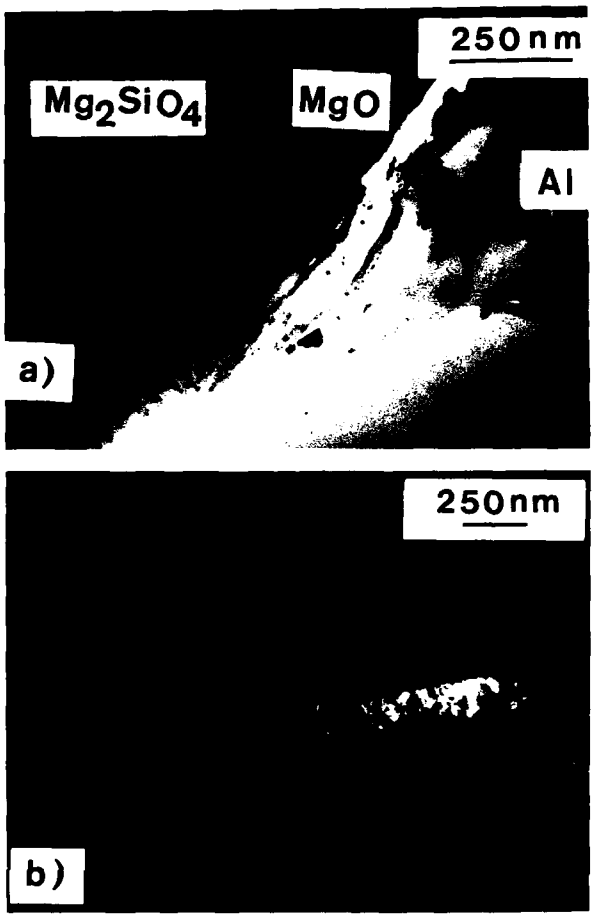


Fig. 6. Bright field (a) and dark field (b) image of the crystalline MgO layer between the olivine ($(Mg_{0.9}Fe_{0.1})_2SiO_4$) and the Al-5 % Mg.

corrosion of Al-Mg alloys. On pure Al a preventive oxide film of 20-50 Å is formed while with increasing Mg concentration the film grows to greater thickness. Thus far we have not observed any nitrides in the Al-Mg melt, and more work is needed in order to account for the majority element of air.

Other interesting observations are the exchange of cations at the surface of the ceramic particles by replacing them by more electropositive cations. With olivine in Al-Mg alloys we observe that a quite thick layer on the olivine particle is transformed into MgO (fig. 6). This can be explained by the reaction:

$$Mg_2SiO_4 + 2\ Mg \rightarrow 4\ MgO + Si$$

Here two Mg atoms from the metal matrix have replaced one Si atom. The Si atoms diffuse into the matrix.

A similar reaction is observed by the use of the selfgenerating vacuum technique where we at the initial stage of infiltration (fig. 1b) and fig. 2b)) observe MgO on the surface of Al_2O_3 particles:

$$Al_2O_3 + 3\ Mg \rightarrow 3\ MgO + 2\ Al$$

The presence of $Al_{12}Mg_{17}$ rather than nearly pure Mg in the drops on the Al_2O_3 surface is consistent with this reaction. It appears that the interchange of Al and Mg in the oxide takes place while Mg is in the vapor phase, because the surface of Al_2O_3 is quite evenly covered with MgO. Similar reactions have been proposed for other systems (1,10).

SUMMARY

We have observed that large volumes of vacuum can be generated by reaction between a Mg melt and air, but not by using an Al melt. This demonstrates some important macroscopic aspects of dynamic wetting involving chemical reactions, and suggests that the metal atoms ability to penetrate through the initially formed oxide or nitride layer is crucial in order to eliminate air and thereby obtain intimate contact between ceramics and metal melts. The situation is similar when injected ceramic particles are trapped on small air bubbles in the melt, but then even a small concentration of more electropositive metal atoms capable of penetrating through the oxide/nitride layer on the air bubble is sufficient in order to eliminate the air bubble because of the smaller dimensions involved. Thus there is no need for diffusion over long distances. This is supported by the observation that ceramic particles are more easily dispersed in Al melts containing a few percent Mg than in pure Al melts.

To conclude, many other factors influence the quality of a MMC. Chemical reactions and bonding at the interface between the metal and the ceramic are very important. In this work we observe that cations from the melt tend to replace more electronegative cations in the ceramic particles, and it is observed that the reaction zone may become very thick (several 100 nm) when the difference in electronegativity is large.

ACKNOWLEDGEMENT

We are grateful to J. Gjønnes, P. Kofstad and Chr.J. Simensen for valuable discussions.

REFERENCES

1. Rohatgi, P.K., B.C.Pai and S.C.Panda, J.Mater. Sci 14, 2277-2286 (1979)
2. Delanny F., L.Froyen and A.Deruyttere, J.Mater. Sci 22, 1-16 (1987)
3. Mortensen, A., J.A.Cornie and M.C.Flemings, J. of Metals 40, 12-19 (1988)
4. Mortensen, A. and J.A.Cornie, Met.Trans 18A, 1160-1163 (1987)
5. Reding J.N. and M.R.Bothwell, U.S.Patent 3. 364, 976
6. Lawrence G.D. Amer. Foundrymen's Soc., Trans. 45, 283-286 (1972)
7. Quigley, B.F., G.J.Abbaschian, R.Wunderlin and R.Mehrabian, Met. Trans 13 A, 93-100. (1982)
8. Nutt. S.R. and R.W.Carpenter, Mater. Sci and Engin. 75 169-177 (1985)
9. Abramov, A.A., Ya, A.Podval'nyi and V.B.Zelov. Russian J. of Phys. Chem. 54, 1630-1633 (1980)
10. Kannikeswaran K and R.Y.Lin, J. of Metals 39, 17-19 (1987)

POROSITY IN FOUNDRY COMPOSITES PREPARED BY VORTEX METHOD

S. Ray
Department of Metallurgical Engineering
University of Roorkee, Roorkee (U.P) 247667 INDIA

ABSTRACT

Foundry composites have been fabricated by stirring the melt with particles and pouring the resulting slurry in a mould. The application of stirring gives rise to formation of vortex sucking in both externally added particles, if any, and air bubbles together and separately. The porosity in the composites is proportional to its particle content. In addition, the process variables like the stirring speed, position and the diameter of the stirrer affects the porosity content similarly to that observed for particle content. The mechanical properties like ultimate teneile strength of the composite reduces lineaIy with porosity and the porosities play an important role in the fracture process.

A NUMBER of particulate composites have been made either by adding particles externally (1,2) or by mainipulating solidification as in rheocasting (3), to result in spherical primary particles embedded in a matrix. Most of the fabrication methods have employed stirring to create a vortex. The negative pressure differential existing at the vortex helps to suck externally added particles into the liquid metal. However, the vortex also sucks in air bubbles in the particle-melt slurry resulting in large porosities in cast composites (4)
Broadly, there are two types of foundry methods for making composites with externally added particles, depending on the temperature at which the particles are introduced in the melt. In liquid metallurgy process (1) the particles are added above the liquidus temperature of the Molten alloy whereas in compocasting the particles are introduced into a semi-solid slurry at a temperature between the solidus and the liquidus temperature of the alloy. In both these processes vortex is used and the composites have high porosIty.(4)

The strength of particulate composites reduces drastically with volume percent porosity as compared to that in matrix alloy without particles (5). Thus, the interrelation of process variables in vortex method, the resulting porosity and the associated strength is of central importance and the present article examines these aspects in foundry composites.

EXPERIMENTAL PROCEDURE

In the processes for making foundry composites there are three process parameters related to stirring - stirring speed, position and the diameter of the stirrer. Generally, the diameter and the position of the stirrer are expressed as dimensionless ratio with respect to the diameter at the top of the liquid and the height of the liquid inthe crucible respectively. The schematic diagram of the experimental set up used in our laboratory for both rheo-and compo-casting is shown in Fig. 1.

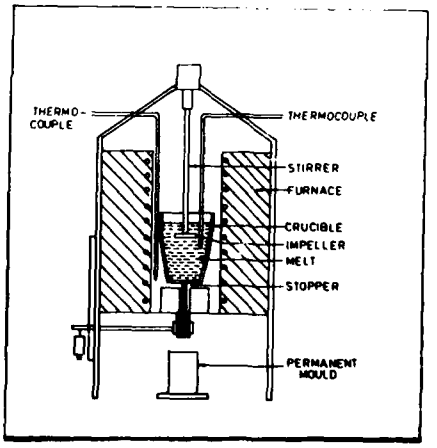


Fig. 1: Schematic Diagram of Experimental set-up.

A graphite crucible having an arrangement for

bottom pouring is heated inside a resistance heating Muffle furnace. About 500 gms of Aluminium of commercial purity is melted in the crucible heated to 1005 K. The melt is allowed to cool and the alloying additions are performed at desired temperature. When the temperature of the melt is above 20 to 30 K above the pouring temperature preheated stirrer is introduced in the melt. Agitation of the melt is started at the desired speed and the particles, if required, are added to the vortex. The stirring is continued to prepare a homogeneous slurry. At the pouring temperature the slurry is cast into a permanent steel mould of size 25 mm x 30 mm x 300 mm, by removing the graphite stopper from the bottom of the crucible. Stirring is continued till the end of pouring and the cast ignot is cooled by spraying water immediately.

RESULTS AND DISCUSSION

POROSITY MEASUREMENTS - The cast composite contains matrix, particles and porosities. The relative amounts of each of these constituents are to be determined for a quantitative correlation of properties with relative amounts of constituents. Quantitative metallography is often not accurate for determining relative amounts of particles or porosities by point counting because the particles are sometimes, embedded deep inside the pores. So, density measurement is combined with the results of quantitative metallography to obtain thevolume fraction of particles and porosities.

The density of the Matrix or the particles are generally taken from literature or determined by X-ray diffraction. The density of the cast composite is determined by weight loss Method. If there are no voids in the composite, its density, ρ_{th}, can be written as,

$$\rho_{th} = V_p \rho_p + (1 - V_p) \rho_M \ldots\ldots\ldots (1)$$

Where V_p and ρ_p are volume fraction and the density of the particles and ρ_M is the density of the Matrix. The measured density of cast composites with porosity ρ_{mes}, can be written as

$$\rho_{mes} = (1 - V_T)\rho_M + V_p \rho_p \ldots\ldots (2)$$

Where, V_T is the volume fraction of porosity and particles together as determined by point counting and it can be expressed as,

$$V_T = V_p + V_o \qquad \ldots\ldots\ldots\ldots (3)$$

combining Eqs. (1), (2) and (3) one can write that the volume fraction of porosities, V_o, is given by,

$$V_o = \frac{\rho_{th} - \rho_{mes}}{\rho_M} \qquad \ldots\ldots\ldots (4)$$

POROSITY IN CAST COMPOSITES - The variation of porosity withthe pouring temperature in rheocast Al -10 wt.% copper alloy is shown in Fig.2. As the viscosity of the semi-solid

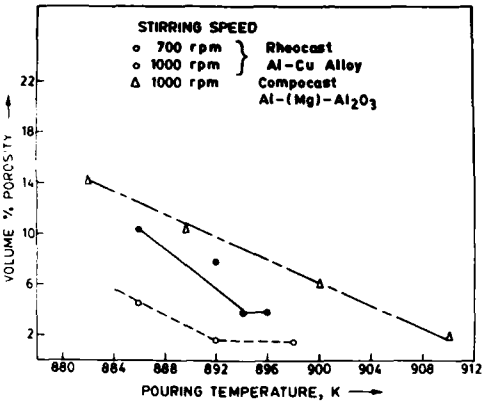


Fig. 2: Variation of porosity with pouring temperature in rheocast and compcast composites.

alloy increases due to larger volume fraction of primary particles at lower pouring temperature the porosity increases. The upward movement of the air bubble due to buoyancy becomes slow as the liquid is more viscous. Also, the bubbles get attached to the particles in the slurry and the force of buoyancy is counteracted. A similar trend in variation of porosity with pouring temperature is observed in compocast Al-Al_2O_3 composites as shown in Fig. 2. Here, the extent of porosity is higher in Al-Al_2O_3 composites due to the additional contribution of externally added Alumina particles. The difference in alloying addition in rheo-cast and compocast composites may have also made some difference. It is further observed in Fig. 2 that a higher stirring speed in rheocast Al-Cu alloy has enhanced the level of porosity. It may be attributed to a higher suction at thevortex at higher speed till an optimum speed is reached as it has been observed in the case of compocast alloys also (4).

The helpful role of particles in retaining air bubbles is further revealed in Fig.3 where a master curve for variation in porosity with the extent of externally added particles has been plotted for compocast Al(Mg) - Al_2O_3 composites fabricated under different levels of process variables. A clear trend of an increase in porosity with particle content is discernible. The scatter may be attributed to difference in the extent, shape and size of primary particles, and tothe role of process variables.

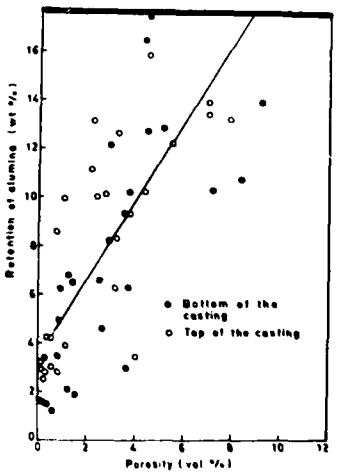


Fig.3: Variation of Porosity with particle content in compo-cast composites.

The earlier investigations of Ghosh and Ray (6) have confirmed that the variation of porosity content with the process variables follows closely the trend observed for the externally added particle content. The increase in stirring speed, height of the impeller from the bottom and the diameter of the impeller is accompanied by an increase in porosity upto an optimum level for each of these process variables. The extent of particle incorporation also increases upto this level but beyond it both the porosity and particle content reduces rather drastically. Further, it has been observed that porosity gives rise to increasing non-uniformity in distribution as characterised by standard deviation in the distribution of inter particle distance. It may be due to a cluster of particles attaching to an air bubble in the slurry.
Fig.4 shows the distribution of porosity at the top and the bottom of the ingot compocast under different combinations of process variables. It is interesting to observe that the

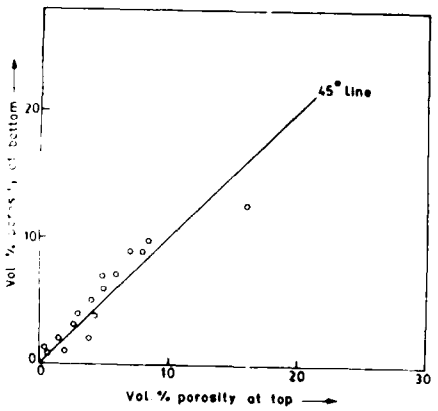


Fig.4: Porosity content at the top and bottom of compo-cast ingots.

extent of porosity at the bottom of the ingot is often more than that at the top. This again gives credence to the hypothesis of particles attaching to bubbles to make it possible for the bubble to settle at the bottom.
A cold model investigation on mixing of non-wettable plastic beads in water has revealed that effective particle incorporation occurs when the vortex develops to the extent of exposing a part of the stirrer blades.It has also been observed that when the radius of the forced vortex region at the centre exceeds the radius of the continuous region of a four blade stirrer vortex forms below the stirrer causing enhanced suction of particles and air bubbles. These inferences of cold model experiment (7) appears to provide explanation for the variation of particle and porosity content with the process variables. At present investigations are goingon to attempt incorporation of externally added particles by turbulent mixing with baffles which will break the vortex and its suction effect.
MECHACHANICAL PROPERTIES - If one assumes that the stress distribution around each pore is independent of the presence of other surrounding pores it can be shown (8) that the strength of the composite will reduce linearly with porosity. The ultimate tensile strength, σ_p, of a composite containing a volume fraction of porosity, p, can be expressed as,

$$\frac{\sigma_p}{\sigma_0} = 1 - \alpha p \qquad \ldots(5)$$

where α represents the magnitude of weakening of the composite with each percent of porosity and is a function of rate of change of stress around a pore and the distance at which the stress becomes uniform. Thus, α is characteristic of shape, size and distribution of pores, and the material. σ_o is the strength of the composite in absence of pores. The linear model of ultimate tensile strength as given by eqn. (5), breaks down beyond a critical porosity content, $p_c = 100/n^2$, where n is the ratio of pore radius to the radius at which the stress becomes uniform around the pore. In metals and alloys p_c is quite small but in composites it is quite large as it has been observed in both rheocast and compocast alloys (5). The ultimate tensile strength in rheocast Al-10 wt% cu alloy is observed to vary with porosity as given below (9).

$$\sigma_p = \sigma_o - 4.71 \times \text{vol.\% porosity} \ldots(6)$$

similarly, the ultimate tensile strength in compocast Al(Mg) - Al_2O_3 composites obeys the following relation.

$$\sigma_p = \sigma_0 - (1 \text{ to } 3.5) \times \text{vol.\% porosity} \ldots(7)$$

The co-efficient of vol.% porosity increases from 1 to 3.5 when the particle content changes from 1 to 14 volume percent.
Porosity plays a significant role in the fracture process. Ghosh and Ray (10) have

observed that engineering fracture strain of a composite with a given Alumina content, increase s linearly with the inverse in porosity. However, this correlation is lost when the porosity content is below a critical limit and it has been observed that the void nucleating strain is very low for Al(Mg)-Al_2O_3 composite due to debonding at particle - matrix interface. In case of composites with higher porosity the fracture takes place by growth and coalescence of these pores.

ACKNOWLEDGEMENT

The author is grateful to his students for their collaboration on investigations relating to different aspects of particulate composites. The discussions and encouragement of Prof. P.K. Rohatgi are thankfully acknowledged.

REFERENCES

Ray,S. and P.K. Rohatgi, Indian Patent 124305A, 1972.

Badia, F.A and P.K. Rohatgi, Trans.AM. Foundrymen's Soc. 79, 402 (1969)

Mehrabian, R. and M.C. Flemings, "New trends in Materials Processing", p.98,ASM, Metals Park (1976)

Ghosh, P.K., S.Ray and P.K. Rohatgi,Trans. Jpn. Inst. Met. 25, 440-444 (1984)

Ghosh, P.K., P.R. Prasad and S.Ray, Z. Mettalkd. 75, 934-937 (1984)

Ghosh, P.K. and S. Ray, Communicated to Trans, AM. Foundrymen's Soc. (1987)

Ghosh, P.K. and S. Ray, Communicated Trans. Jpn. Inst. Met (1987)

Ghosh, P.K. and S.Ray, Ind. J. Tech. 26, 83-94 (1988)

Prasad, P.R., S. Ray, J.L. Gaindhar and M.L. Kapoor, Scripta. Met. 19, 1019-22 (1985)

Ghosh, P.K. and S. Ray, J. of Mat. Sci. 21, 1667-74 (1986)

WETTING OF SOLIDS BY LIQUID METALS IN RELATION TO SQUEEZE CASTING OF MMC's

Francis Delannay
Université Catholique de Louvain
Louvain-La-Neuve, Belgium

Ludo Froyen, Andre Deruyttere
Katholieke Universiteit Leuven
Leuven, Belgium

ABSTRACT

This contribution aims at recalling the fundamentals of wetting of solids by liquid metals. The present state of understanding of the phenomena processing wetting of oxides and carbides is reviewed. One emphazises the problem of characterizing non-equilibrium wetting conditions. The bearings of this body of science on the practice of squeeze casting are critically assessed, by consideration of the various other important parameters which influence the infiltration process and the properties of the final product.

THE WETTABILITY OF A SOLID

The wettability of a solid by a liquid is indicated by the "contact angle" which is related to the three surface tensions γ_{sg}, γ_{sl} and γ_{lg} of solid-gas, solid-liquid and liquid-gas interfaces by the Young-equation.

$$\gamma_{lg}\cos\theta = \gamma_{sg} - \gamma_{sl} \qquad (1)$$

The condition for wetting is :

$$\cos\theta > 0 \text{ or } \gamma_{sg} > \gamma_{sl}$$

During infiltration of a fiber preform by a liquid metal in squeeze casting, the minimum pressure difference at the liquid metal front may be expressed as

$$P \doteq -\frac{(\gamma_{sg} - \gamma_{sl})}{r} \qquad (2)$$

where r is a characteristic size of the pores being infiltrated, which depends on the size, shape and volume fraction of the reinforcing fibers [1,2]. In the non-wetting case, relation (2) expresses the minimum pressure to be applied to the liquid in order to force infiltration.

It is often helpful to think of the interface tension γ_{sl} with reference to the tensions γ_{sg} and γ_{lg} by defining the "work of adhesion" W_a according to the Dupré relation :

$$W_a = \gamma_{sg} + \gamma_{lg} - \gamma_{sl} = \gamma_{lg}(1+\cos\theta) \qquad (3)$$

W_a may thus be determined directly by measuring θ and γ_{lv} in the "sessile drop" experiment. The condition for wetting under vacuum then writes :

$$W_a > \gamma_{lg}$$

This means that the energy of the bonds created across the interface must exceed the surface tension of the liquid. This condition is much more severe for liquid metals (for which γ_{lg} is of the order of $1 Jm^{-2}$) than for ordinary liquids (for which γ_{lg} amounts to a few $10^{-2} Jm^{-2}$).

By combining (2) and (3), one writes

$$P \doteq -\frac{W_a - \gamma_{lg}}{r} \qquad (4)$$

which shows that if γ_{lg} is constant, the minimal pressure for infiltration varies like $-W_a$. Hence, it makes sense to try to understand the fundamental contributions governing the magnitude of the work of adhesion.

WETTING OF OXIDES AND CARBIDES

Like in the study of adsorption of molecules on a surface, it is convenient to distinguish physical and chemical contributions to W_a.

Physical interactions are always active. One considers generally that thet arise mainly from the "dispersion" interaction resulting

from the attraction between instantaneous dipoles across the interface. The London formula allows to evaluate this contribution to Wa as

$$W_{a\,disp} = n\,\frac{3}{2}\,\frac{\alpha_1\,\alpha_2}{R^6}\,\left(\frac{I_1\,I_2}{I_1\,I_2}\right) \qquad (5)$$

where n is the number of pairs if atoms involved per unit surface area of the interface, I_1 and I_2 are the first ionization potentials of the atoms in the pairs, α_1 and α_2 are their polarizabilities and R is the distance between them. In the case of liquid metal-solid interfaces, the values of $W_{a\,disp}$ calculated in this way never exceed $0{,}6\,Jm^{-2}$ [3,4]. Hence, wetting of a solid by a liquid metal implies at least some contribution from chemical interactions.

In contrast to physical interactions, chemical interactions involve a change transfer across the interface (mass tranfer can also proceed under non-equilibrium conditions). It is widely believed that chemical interaction will contribute to Wa only if the standard free energy change associated with a possible reaction between atoms or molecules belonging to the interface is negative. In the case of a metal/oxide (me/MeOx) interface for example, one must consider not only the interactions of the metal atoms with oxygen decribed by

$$me + \frac{y}{2}\,O_2 \longrightarrow meO_y \qquad \Delta G^\circ_{me}$$

$$MeOx \longrightarrow Me + \frac{x}{2}\,O_2 \qquad \Delta G^\circ_{Me}$$

but also the dissolutions of the atoms and molecules in the solid and liquid described by

$$Me \longrightarrow [Me]_{me} \qquad \Delta G^\circ_1$$

$$MeO_y \longrightarrow y\,[O]_{me} + me \qquad \Delta G^\circ_2$$

$$meO_y \longrightarrow [meO_y]_{MeO_x} \qquad \Delta G^\circ_3$$

where the brackets indicate a dissolution in the indexed phase [5,6]. Most theories of wettting and adhesion are based on the interpretation of changes of Wa among series of samples in terms of changes of the standard free energy of such reactions. Let us consider the cases of wetting on oxides and carbides.

The wetting of oxides by liquid metals has been most extensively investigated. The first model aiming at explaining the wetting behaviour at metal-oxide interfaces was proposed by McDonald and Eberhart in 1965 [3]. They shown that, for a series of liquid metals for which ΔG°_{me} is negative, the work of adhesion on alumina varies linearly as a function of ΔG°_{me}. They write

$$W_a = a - b\,\Delta G^\circ_{me} \qquad (6)$$

where a is the contribution of physical interactions calculated according to (5) and b is a constant.

Although accounting for the general observation that on a given oxide Wa roughly increases with increasing $-\Delta G^\circ_{me}$, this model gives no clue to the variation of Wa of the same liquid metal onto different oxides, nor for the drastic increase of Wa with increasing concentration of oxygen in the melt. These effects are accounted for in the model proposed by Naidich in 1981 [4], who attributes a mayor role to oxygen in solution in the liquid metal. This oxygen would create me^{2+}-O^{2-} clusters which would strongly adsorb at the metal-oxide interface due to the electrostatic attraction between me^{2+} and the oxygen anions at the oxide interface. In this case, the chemical contribution to Wa would increase with

$$-\Delta G_R = -\,(\Delta G^\circ_{me} + \Delta G^\circ_{Me})$$

Numerous experiments have indicated however that a significant role was also played by the solubility of the Me metal in the melt. In 1986, Rivollet et al proposed a new model taking into account the chemical interactions between the me metal of the liquid and the Me metal of the oxide [7,8]. These interaction my be evaluated from the enthalphy of mixing of Me in me. The model applied only for non-reactive liquid metal/oxide systems ($\Delta G_R = \Delta G^\circ_{me} + \Delta G^\circ_{Me} > 0$) i.e. when the interactions me-O are not dominant. These authors show that, in such cases, the work of adhesion of different metals or alumina varies as

$$W_a = -\,\frac{C}{N^{1/3}\,V^{2/3}_{me}}\,[\Delta H^\infty_{O(me)} + \frac{2}{3}\,H^\infty_{Al(me)}] \qquad (7)$$

where C is a constant, N is the Avogadro number, V_{me} is the molar volume of the liquid metal and ΔH^∞_{O} (me) and $\Delta H^\infty_{Al(me)}$ are the enthalpies of mixing at infinite dilution of oxygen and aluminium in the liquid metal.

The wetting of carbon and carbides by liquid metals can be rationalized in a similar way by considering three chemical contributions : the affinity of the me metal for carbon, the stability of the MeC_x carbide and the enthalpy of mixing of Me in the me melt. The mayor contribution to this subject remains the work of Naidich and co-

workers [4]. A summary may be found in reference [1].

WETTING AND SQUEEZE CASTING

The present state of our understanding of wetting phenomena which has been summarized here, mainly deals with equilibrium wetting conditions studied by "sessile drop" experiments. The question now arises of the actual bearings of this science upon the processes of fabrication of MMC's by squeeze casting. Several points need to be successively considered in the context.

1. Unless operating under ultra high vacuum (which is impossible in the practice), the surface of most liquid metals is covered with an oxide skin which partially prevents direct interaction of the liquid with the surface of the reinforcement. It is now widely recognized that wetting by aluminium alloys is often governed more by the stability of this oxide skin than by the actual work of adhesion of the metal itself. One still lacks a precise understanding of the role of alloying elements on the stability of this skin.

2. Non-equilibrium wetting conditions always prevail during infiltration. There is little doubt that , in most squeeze casting experiments, solidification is completed long before thermodynamic equilibrium is reached at the interface. The value of the role of adhesion determining the minimum infiltration pressure is thus expected to differ fairly widely from the value of W_a measured in a sessile drop experiment (as pointed out by Aksay et al [9], the dynamic value of γ_{sl} can even become negative). In recent years, several attempts have been made to design experiments allowing quantitative measurements of ΔP, cos θ and W_a under dynamic conditions similar to those which prevail during squeeze casting. The first study based on such an approach has been published by the group of Cornie et al [10,11]. Figure 1 shows a similar experimental setup which was built independently in our group in 1985. In this case, the threshold pressure for infiltration is measured by recording the change of the resistivity of a carbon fiber inserted along the wall of the alumina crucible containing the powder preform to be infiltrated [12]. These experiments are in progress and they should allow a more comprehensive assessment of the differences between dynamic and static wetting conditions.

3. One should bear in mind that the viscosity of the liquid metals also plays a mayor role during infiltration. This effect is especially important when some proportion of a solid preform whose temperature is lower than the melting point of the liquid [13]. As a matter of fact, the very high pressure used in many squeeze casting processes is primarily justified by the necessity to complete infiltration before a too extensive solidification of the metal has occured. Little literature is available on the effect of alloying elements on the viscosity of the liquid during infiltration.

4. Cheap squeeze casting methods for large scale production of MMC's will have to be carried out under atmospheric pressure. An important parameter in this case is the proper venting of the gazes leaving the preform. It can be demonstrated that gas entrapment can be avoided only when the liquid wets the solid. As a particular example, figure 2 presents a SEM micrograph of cavities left along contacts between fibers in a Al/SiC (Nicalon) composite prepared by squeeze casting in air under 20MPa pressure [14]. The fiber preform had been heated above the temperature of the liquid metal in order to avoid solidification during infiltration. The width of the metal front along the cavities amounts to about 1 μm. Still, one calculates easily that, even in the most defavorable case (θ=180°) 20MPa pressure should allow the infiltration of pores down to a size of less than 0.1 μm. Hence, the size of the remaining cavities in such a MMC is governed by the entrapment of gases during infiltration and not by the wetting of metal/fiber interface.

5. Many recent works have enlighted the role of the bond strength at metal/reinforcement interface on the mechanical properties of MMC's. This bond strength depends very drastically on the thermal history of the composite, on the alloying elements present in the matrix and on the nature of the fiber surface, which can be modified by coatings (the present emphasis on the design of cheap production methods suitable for higher volume applications of MMC's has however caused a decrease of the interest of fiber coating). Recipes designed to improve wetting during infiltration often induce a too high bond strength at the interface which can in turn confer a poor toughness to the casting.

CONCLUSION

The microstructure and properties of cast MMC's are influenced by a large number of parameters of the squeeze casting process. Wetting during infiltration plays a mayor

role but its importance should not be overestimated. Although our understanding of the phenomena governing equilibrium wetting has kept improving in recent years, one still lacks a sufficient knowledge of the non-equilibrium wetting conditions prevailing during infiltration.

REFERENCES

1. F. Delannay, L. Froyen and A. Deruyttere, J. Mater. Sci. 22, 1-16 (1987).
2. A. Mortensen and J.A. Cornie, Metall. Trans. A. 18A, 1160-1163 (1987).
3. J.E. McDonald and J.G. Eberhart, Trans. Metall. Soc. AIME 233, 512 (1965).
4. J.V. Naidich, Prog. Surf. Membr. Sci. 14, 353 (1981).
5. J.T. Klomp, J. Physique (in press).
6. J.T. Klomp in "Ceramic Microstructures. Role of Interfaces" (in press).
7. I. Rivallet, D. Chatain and D. Eustathopoulos, J. Chim. Phys. 83, 561 (1986).
8. D. Chatain L. Condurier and N. Eustathopoulos, Revue Phys. Appl. 23 (1988) (in press).
9. I.A. Aksay, C.E. Hoge and J.A. Pask, J. Phys. Chem. 78, 1178 (1974).
10. J.A. Cornie, A. Mortensen and M.C. Flemings, Proceedings of the Sixth International Conf. on Composite Materials, ICCM VI, (F.L. Matthews, N.C.R. Buskell, J.M. Hodginson and J. Morton, eds), Elsevier, London 1987, pp. 2.297-2.319.
11. S.Y. Oh, K.C. Russell and J.A. Cornie, Metall. Trans. (in press).
12. F. Delannay, L. Froyen and A. Deruyttere, internal report MTM, Leuven, 1985 (unpublished).

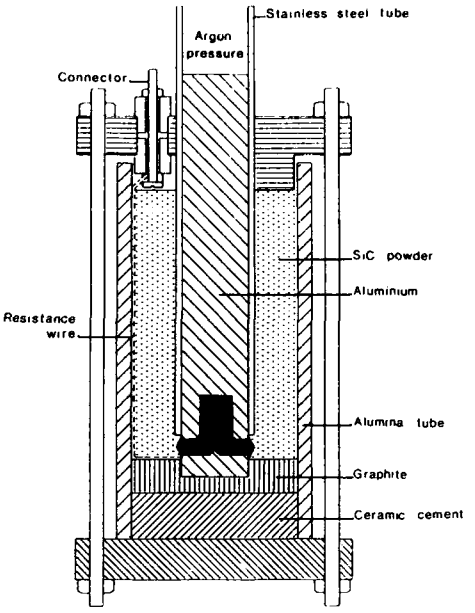


Fig. 1 : Schematic experimental set-up for quantitative characterization of the pressure assisted infiltration process.

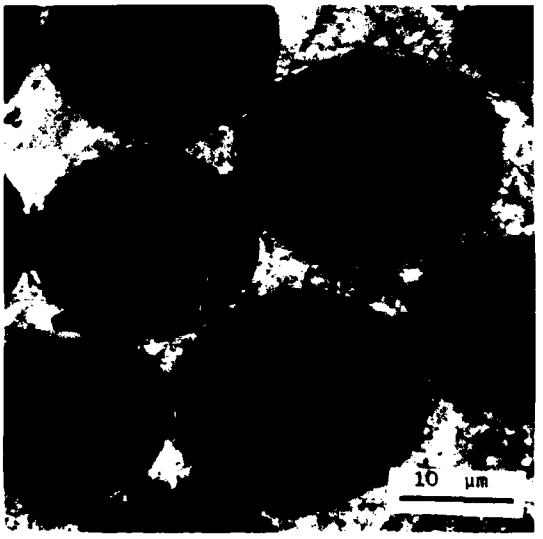


Fig. 2 : SEM micrograph of Al-SiC composite prepared by squeeze casting showing cavities along fiber contacts.

MIXING QUALITY MODELING IN THE MANUFACTURE OF CAST METAL MATRIX PARTICULATE COMPOSITES

P. K. Rohatgi, R. Asthana, M. A. Khan
Materials Department
University of Wisconsin-Milwaukee
Milwaukee, Wisconsin 53201 USA

P. Ostermier
AVCO Textron Inc.
New Haven, Connecticut, USA

ABSTRACT

An experimental investigation with a water model was conducted to determine the quality of mixing which can be obtained when a mechanical impeller is used to disperse ceramic particles in fluids to make composites. Ceramic particles including silicon carbide and graphite were impeller mixed in water being used as a transparent medium. The experimental variables were impeller blade angle, impeller speed and type of particles. Mixing quality was determined by taking samples from the impeller mixed system at measured locations. The studies indicate that it is difficult to obtain an absolutely uniform distribution of silicon carbide particles in fluids by mixing. Considerable local variation in silicon carbide percentage was observed in water and these are likely to be found in molten aluminum systems. These heterogeneities would influence the final distribution of particulates in cast metal matrix composites.

INTRODUCTION

ONE OF THE RECURRING PROBLEMS in synthesizing cast metal-matrix particulate composites by liquid metallurgy techniques (where particles are stirred in the melt prior to casting) is how to adjust the various processing variables in order to obtain a uniform or required distribution of particles throughout the casting volume. Another related problem is how to maintain the same distribution in successive castings made from a large batch of metal containing dispersed particles. While a few surface-property related applications (e.g., bearings of Al-graphite) require segregation of dispersed particles at selected surfaces, most applications require a homogeneous distribution of particles throughout the casting volume. Although an ideally homogeneous distribution of particles may be difficult to achieve, the less-than-perfect distribution that is obtained via casting techniques is adequate for several applications.

As the basic liquid metallurgy process of making composites consists of several steps, like transfer of particles into the melt, formation of a stable suspension and subsequent solidification, the final distribution in the casting depends on the influence that each intermediate step exerts on modifying the particle arrangement. The principal factors affecting uniformity of particle distribution in a casting are:

(1) Aggregation and skeleton formation during entry of particle in the melt due to improper wetting in a quiescent melt.

(2) Settling or flocculation of individual particles and particle aggregates in the melt before and during solidification owing to density differences.

(3) Localized pushing of particles by solidifying interfaces causing microinhomogeneity in particle distribution.

The distribution profiles of particles in cast matrices can be influenced by all of the above factors which are intrinsic to the process. Furthermore, the presence of particle aggregates in the initial powder prior to mixing and turbulence generated due to gravity transfer of suspensions to a die can also influence the initial distribution, affecting final configuration of particles in the cast structure.

Formation of floccules or aggregates of SiC in cast Al alloys is frequently observed. In real polydisperse systems of particles having a wide size distribution, the tendency for flocculation is compounded due to autocatalytic effects: the initial particle size disparity catalyzes further size disparity as a result of flocculation. Polydispersity and non-sphericity of SiC further enhance the tendency for flocculation in the presence of shear gradients in the melt (1). However, very little quantitative

information is available on flocculation behavior in the presence of shear gradient in a melt (1).

As the in-situ observation of particle and fluid dynamical behavior during processing of molten metal-ceramic particle composites is not always feasible, and as the initial processing conditions can not always be optimized retrospectively from a knowledge of the final particle distribution in a casting, qualitative transparent models of the real system satisfying certain geometrical and dynamical similarity constraints can be constructed in order to study the mixing quality in the liquid state as a function of the processing variables. Previous work (2) has demonstrated that movement of graphite particles in Al alloy melts can be simulated by using graphite particles dispersed in impeller mixed water. Figure 1 shows typical dispersion curves recorded by an optical method relating transmitted light intensity as a function of stirring/holding time. A unit referred to as absorbance was used to define the change in particle concentration from the transmitted light vs. time plots:

$$\log I_o - \log I_i = K \sum_{i=1}^{n} K_i \cdot N_i \cdot D_i^2$$

where I_o and I_i are the incident and transmitted light intensities; K is the optical coefficient of cell and particle form; K_i is the coefficient of absorbance of particle of diameter D_i and number concentration N_i. The area base data of the above equation can be converted to volumetric base data from

$$\text{Vol. Base Data} \equiv (\log I_o - \log I_i) \cdot D_i$$

The present study examines the degree of heterogeneity that exists during impeller mixing of particle-fluid slurries. Water-silicon carbide was used as a transparent model under the simulated conditions shown in Table 1. This heterogeneity can either be compounded or reduced during subsequent stages of the processing of composites. The transparent modeling work reported here was qualitatively validated with selected experiments on the dispersion of silicon carbide particles in Al alloys. Such studies combined with simulation of solidification of transparent suspensions are likely to yield information on optimum stirring conditions, power requirements, crucible and impellers geometry, and pouring mechanisms to obtain uniform distribution.

EXPERIMENT

Figure 2 shows schematic of a cylindrical plexiglass container filled with water. This was stirred using a rotating impeller and powders of silicon carbide (average size: 10 μm) were added from the top. The procedure consisted of a series of runs at varied rpm and impeller blade angles. The power was supplied to the mixture via a one quarter inch variable speed drill motor chucked with the rotating shaft of the impeller. The motor speed was regulated with a VARIAC controller, and the flow and dispersion observations were recorded. Samples were taken from the mix during stirring using a thin pipette of diameter less than 3% of that of the mixing vessel itself. This size of sampling tube permitted the withdrawal of small samples with very little disturbance to the local mix. The samples withdrawn from the agitated mix were weighed on an analytical balance and evaluated for percent silicon carbide present. With the aid of a stroboscope, the voltages supplied by the VARIAC were converted into the shaft rpm of the impeller. The type of impeller used was a three blade turbine with a constant blade angle and width along its blade length and an adjustable blade pitch.

The following parameters were used in the determination of the degree of mixing. The arithmetic mean was used to determine the best estimate of the mean of the population from which the samples are drawn. The frequency distribution (Fig. 3) gives an idea of the degree of mixing.

RESULTS AND DISCUSSION

The flow in mechanically stirred vessels is 3-dimensional and, under the conditions shown in Table 1, highly turbulent (3). The speed or impeller rpm in all cases coupled with blade angle became the controlling variable in achieving a good mix. As the rpm was increased, however, the size and depth of vortex increased. With 25 vol% SiC powders, the average vortex depths at mixing speeds investigated were from 0.5 inch to 1 inch. The detrimental effects of vortexing arise when the vortex becomes too deep and turbulent, and the possibility of suction of air or gases increases.

A few particles, other than silicon carbide, were also stirred in water and their mixing was studied.

The density of the introduced particles appeared to affect the dispersion time. As the density of the particle increased, the time to dispersion increased, indicating that lift force was required and, hence, longer times were needed to lift the particles in suspension. A marked increase in rpm is also required with an increase in particle density to achieve complete dispersion. Of the ten samples taken, the mean was found to be 25.16874 vol% SiC as compared to a batch mean (weighed before mixing) of 24.5 vol% SiC; this difference is due to some loss of silicon carbide during mixing. The standard deviation was calculated to be 2.26667, indicating that there is measurable heterogeneity in the suspension.

From the data of Fig. 3, it is seen that the volume percent silicon carbide increases toward the bottom of the vessel until just near the blades where the shear rate becomes high and

TABLE 1

Comparison Between Al-SiC and Water-SiC Systems

Property	Al-SiC System	Water-SiC System
Surface Tension	~ 900 dynes/cm	~ 72 dynes/cm
Liquid Density	~ 2.8 g cc^{-1}	~ 1.0 g cc^{-1}
Contact Angle	157° (at 900°C)	$\theta < 90°$
Liquid Viscosity	~ 0.014 Poise	~ 0.0089 Poise
Particle Density	3.2 g cc^{-1}	3.2 g cc^{-1}
Temperature	700°C	30°C
Liquid Surface	Oxide Film Present	No Oxide Film
Effective Viscosity (25 vol% SiC)	0.0319 Poise	0.0203 Poise
$(\frac{\text{Tank Diameter}}{\text{Impeller Diameter}})$	---	1.107
Reynolds Number	4.52×10^4	1.62×10^4
Froude Number	4.01	1.88

the volume percent SiC drops off. This indicates that the change in blade angle could effectively reduce the lift of the particles from the bottom of the vessel, thereby resulting in a mix which is lighter on top and heavy in the middle.

Returning to the case of favorable geometry and random sampling, the separate radial and vertical variations were plotted to determine the variation of the mix with respect to the distance from the impeller, and swirl or centrifugal effect (Figs. 4 and 5). It can be seen from these figures that from top to the bottom of the mix there is a variation from the batch mean. Near the blades, there is a 2% lower silicon carbide content than the mean value. An interesting observation from Fig. 4 is the swirl effect of the particles caused by centripetal acceleration in the rotation of the impeller. It is conceivable that silicon carbide particles which are more dense than water would be flung radially outward by the rotation of the impeller yielding a region along the container periphery of increased volume percent SiC. This is indeed the case, particularly in low viscosity mixes where baffling is essential to direct flow streams vertically and prevents particle segregation that results from uncontrolled swirl. However, as the effect of viscous drag in the slurry increases, as in this case, a viscosity level is reached where the drag becomes sufficient to provide its own baffling effect and create a spiralling stream pattern which returns to the impeller after a partial rotational circuit in the tank. This pattern is inherent in the flow contours. The results obtained show a lack of swirl effect. The average sample volume fraction varied from -1.0% to +2.0% of the batch mean.

In Fig. 6, which shows radial and axial distribution of silicon carbide particles in water, when the rpm was 392, there is depletion of particles near the wall compared to other radial locations. The reason obviously is low velocity due to high shear rate.

Figure 6 also shows axial distribution of silicon carbide particles. The concentration of particles below the impeller is about 2% below the batch mean. This is presumably due to the existence of very high axial velocities in the region between the blade and the side walls of the tank. This region imparts very high velocities to the heavier particles and hence mostly suspends them above the impeller. Therefore, as a result of particle crowding above the impeller, there is a 2% depletion of silicon carbide below the impeller. It is also seen from this figure that the maximum concentration of particles occurred about 2.5 inches below the fluid surface. This probably happens due to collisions among particles traveling toward the surface and those returning from the surface.

Experiments such as the one reported here can be used to relate the impeller and crucible geometries, degree of agitation, and power requirements through various dimensionless groups. Thus, empirical correlations can be established between impeller Reynold's number

$$N_{Re} = \left(\frac{ND^2\rho}{\mu}\right)$$

and the dimensionless power number

$$N_P = \left(\frac{P}{N^3D^5\rho}\right)$$

where N = revolutions per sec, ρ = fluid density, μ = fluid viscosity, P = power input and D = impeller diameter. These correlations can be worked out for different geometries and dimensions of impeller, the tank to impeller diameters ratio (T/D), and the size and number of baffles. These correlations can then be used in the preliminary selection of process parameters for best solid-liquid mixing in the actual molten metal-ceramic particle systems.

A comparison between the real and the model systems shown in Table 1 indicates some correspondence between the various fluid properties and dimensionless dynamical groups like Reynolds and Froude numbers. The magnitude of N_{Re} ($\sim 10^4$) in the two systems are reasonably matched and indicate approach to turbulent flow conditions.

The computed effective viscosities of monodisperse suspensions of silicon carbide in Al and water are also fairly close as shown in Table 1. The computations of the effective viscosity of suspensions were made by using the modified Einstein equation

$$\mu_{eff} = \mu_o\,[1 + 2.5\phi + 10.52\phi^2]$$

where μ_o is the fluid viscosity and ϕ is the volume fraction of particles.

There are, however, important basic differences between Al/SiC system and its transparent aqueous analogue even in the absence of stirring. For example, the thermal (Brownian) flocculation effects and natural convection could be significantly higher in an Al/SiC system than in the water/SiC model systems. An approximate estimate of collision frequency based on the mean free time for collisions between dispersed particles (1) in 12 vol% SiC/Al suspension at 660°C shows it to be 2.27 hrs^{-1}, 8.2 s^{-1}, and 8.2 x 10^{-3} s^{-1} for SiC particles of average size 20 μm, 1 μm and 0.10 μm respectively. The corresponding collision frequencies in quiescent water at room temperature for the above system are 7 hrs^{-1}, 25 s^{-1}, and 0.03 s^{-1} respectively. These computations of collision frequencies in the two systems show that decrease in particle size and higher melt temperature can considerably increase the collision frequency and subsequent flocculation kinetics. The relative roles of thermal motion, stokes sedimentation and flocculation in Al/Al_2O_3, Al/SiC and Cu/SiC (4) generally confirm the dominance of thermal effects only at very fine (0.1 - 0.2 μm) particle sizes. Since the room temperature water model used in this study used relatively coarser (~ 10 μm) SiC particles, Brownian effects are expected to be negligible.

Another difference between the real and the model systems in the absence of agitation is related to the relative rates of damping of thermal gradients and fluid currents in the presence of silicon carbide. Figure 7 shows a plot of normalized Prandtl numbers (Pr_{eff}/Pr_o) as a function of vol% SiC in Al melt. The computations were made by calculating the effective specific heat of Al/SiC suspensions using the weight average rule of mixture (5). The effective thermal conductivity was calculated from (5)

$$\left(\frac{\lambda_{eff}}{\lambda_o}\right) = \frac{2\lambda_o + \lambda_d - 2\phi(\lambda_o - \lambda_d)}{2\lambda_o + \lambda_d + \phi(\lambda_o - \lambda_d)}$$

where λ_o and ϕ_d are the thermal conductivities of Al alloy without particles and of the dispersed particles themselves.

The increasing Prandtl number ratio with volume fraction ϕ indicates that temperature gradients in the suspension are damped more slowly compared to the fluid flow as the volume percent silicon carbide in the mixture is increased. At higher values of ϕ this trend could eventually reflect a change in the Nusselt number ratio and therefore in the mode (conductive or convective) of heat transfer from the suspension to say, mold walls during solidification. However, these changes are not expected to be significant at low volume percent particles as shown for Al/graphite system (6). These projections of fluid flow and heat flow behavior are, however, quite simplistic as they neglect local disturbances in the position of suspended particles due to natural convection and stokes settling, and, with suitable modifications for shape difference, at best represent the situation for fibre/molten metal composite systems where the initial configuration of reinforcing fibers is not modulated by fluid currents or stokes settling.

CONCLUSIONS

This study on mixing of silicon carbide particles in fluids indicates that even with a cold fluid, like water at room temperature, considerable heterogeneity exists in the concentration of dispersed particles. When 25 vol% SiC (average size: 10 μm) is stirred into water using an impeller, variations in local concentrations of silicon carbide of the order of five percent remain in fluid. A comparison of stirred water--SiC and Al-SiC systems--suggests that considerable variations in local concentration

of silicon carbide could be present in the stirred melts of Al-SiC systems which could be further increased during subsequent solidification processing.

REFERENCES

1. G. D. Parfitt, Dispersion of Powders in Liquids, John Wiley & Sons, New York (1973).
2. Asthana, R., Modeling vortex technique of dispersing particles in melts using an aqueous medium, Technical Report No. MO-1(85)-15, R.R.L. (Bhopal) India, 1985.
3. J. Y. Oldshue, Fluid Mixing Technology, McGraw Hill (1983).
4. Deruyttere, A., L. Froyen, S. De Bondt, Adv. Space Res., 6(5), 101-110 (1986).
5. Perry and Chilton, Chemical Engineering Handbook, McGraw Hill, Kogakush.
6. Asthana, R., S. Das, T. K. Dan, P. K. Rohatgi, J. Materials Sc. Lett., 6, 1039-42 (1986).

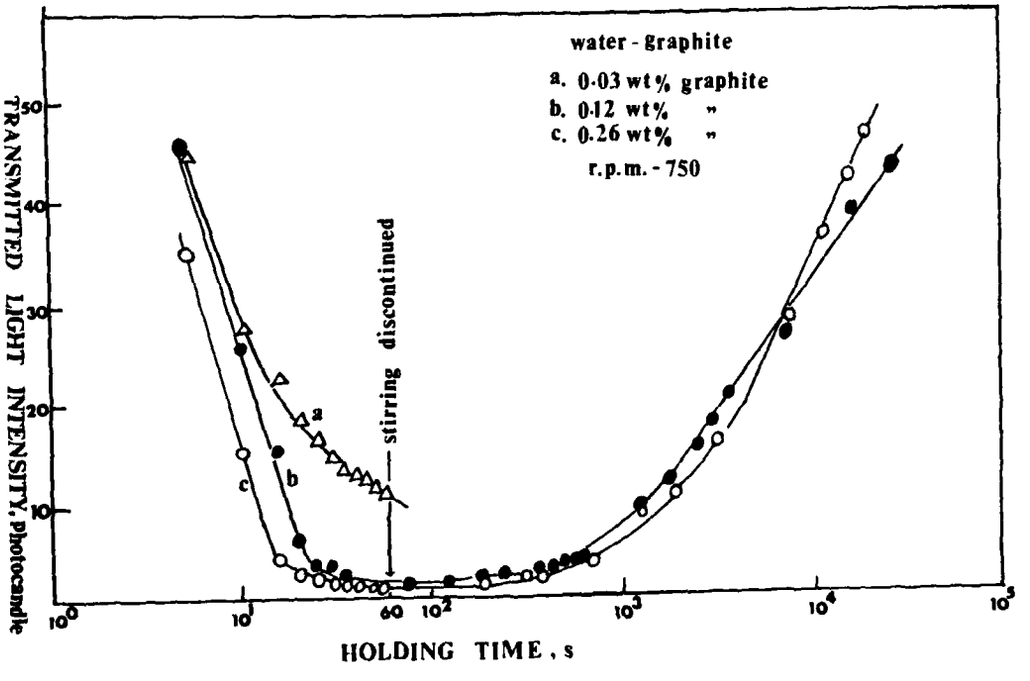


Fig. 1. Typical dispersion curves for impeller mixed graphite water systems.

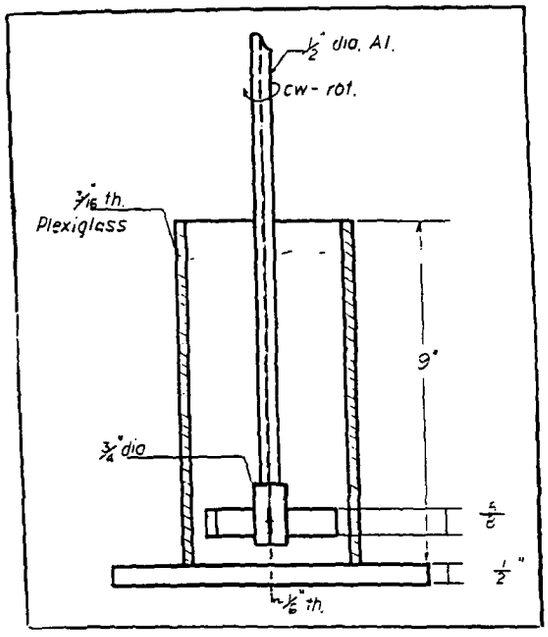


Fig. 2. Schematic of the experimental setup.

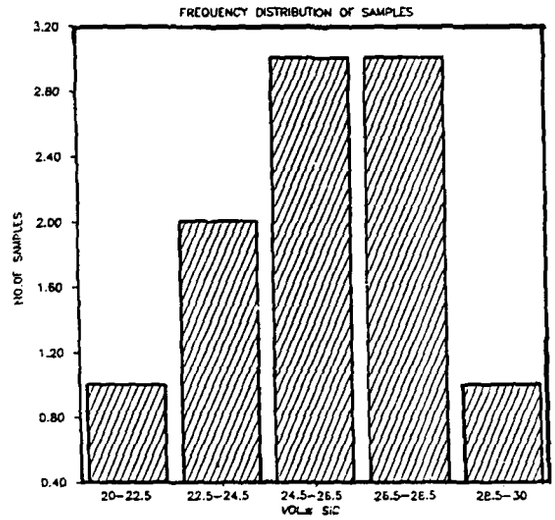


Fig. 3. Frequency histogram of vol% silicon carbide vs. number of samples.

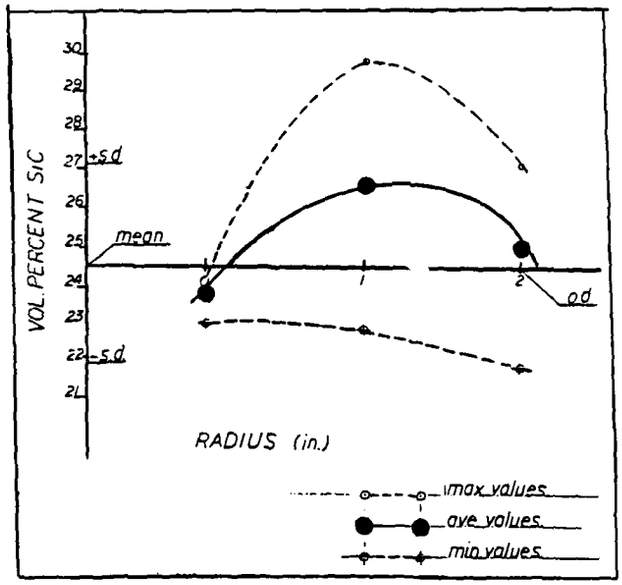


Fig. 4. Radial concentration profile of silicon carbide in impeller mixed water-SiC system (rpm = 280).

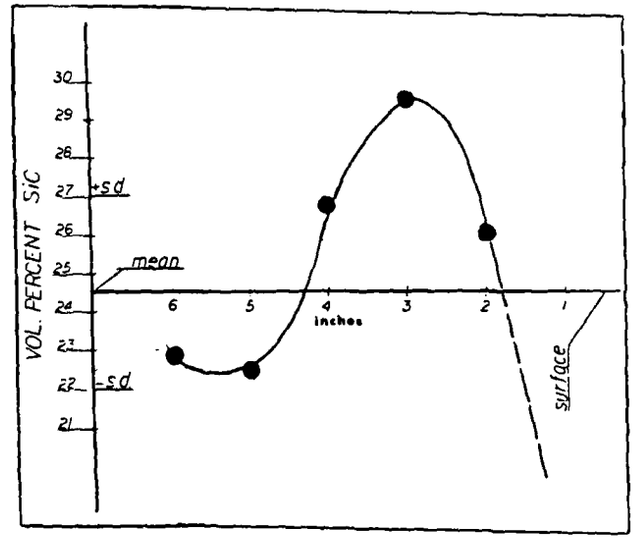


Fig. 5. Axial concentration profile of silicon carbide in impeller mixed water-SiC system (rpm = 280).

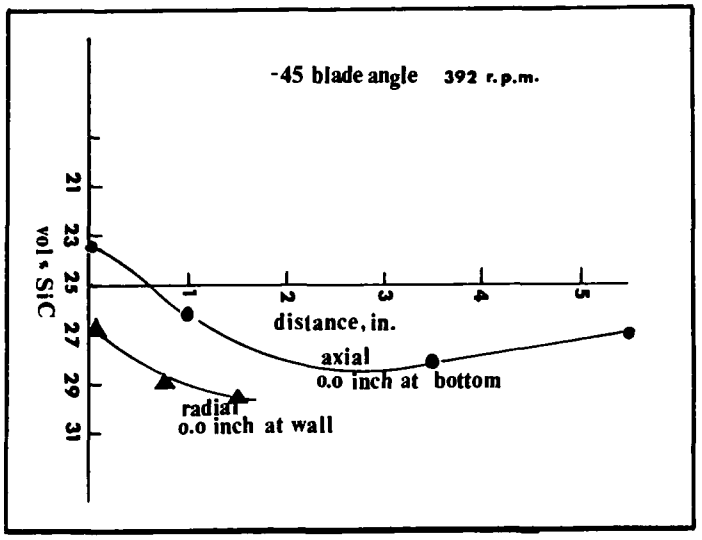


Fig. 6. Axial and radial concentration profiles for impeller mixed water-SiC system (rpm = 392).

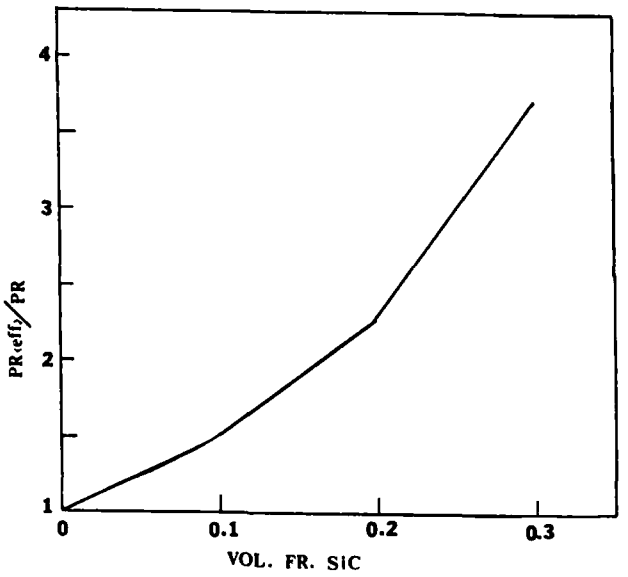


Fig. 7. Prandtl number ratio of composite melt to the base alloy melt as a function of volume percent silicon carbide.

A LITERATURE SURVEY ON FABRICATION METHODS OF CAST REINFORCED METAL COMPOSITES

Zhang Zhu
Chongqing University
Chongqing, Sichuan
P.R.China

*Corresponding address in June 1988-Feb. 1989:
Department of Materials
Imperial College of Science and Technology
London SW7 2BP UK

Abstract

Casting methods for metal matrix composite fabrication have the advantages of simplicity , flexibility, cheapness and ease of production of components with complex shapes. In this paper the casting fabrication methods to produce metal matrix composites have been systematically reviewed. Some applications and features of these methods have been mentioned. It is pointed out that squeeze casting and compocasting are promising methods. Different casting methods can be used according to different requirements.

METAL MATRIX COMPOSITES (MMCs) are now attracting enormous interest, because of their superiority in strength, stiffness, wear resistance, elevated temperature strength or other properties. Techniques for MMC fabrication available are, for example: the powder metallurgy technique [1] diffusion bonding of thin sheet interleaved with ceramic fibres [2,3], extrusion and drawing methods [4,5]. However, these techniques are very cumbersome and expensive. Therefore, the foundry method fo. MMC fabrication has been developed. The advantages of the casting fabrication method are (a) simplicity, speediness, and cheapness, (b) production of composite parts of complex shapes or near-net-shape, (c) ease of fabrication of selectively reinforced components, (d) suitability for various kinds of metal matrices and reinforcements. A selectively reinforced Toyota piston, made by the casting method, is in mass production . " Present production is said to be in excess of 28,000 units per month. The Japanese are now said to be offering these pistons on the open market at a price significantly below that of conventionally made pistons", was reported in 1985[6].

Many metals have been considered as possible matrices in cast MMCs: aluminium, magnesium, copper, zinc, lead, iron, nickel and nickel-based superalloys etc. [7,8,9]. Various kinds of continuous and discontinuous fibres, whiskers, particles and wires are used as reinforcements which may be made either from boron, or graphite, alumina, silicon carbide steel, tungsten, titanium and molybdenum, etc. in MMCs. The principal factors in the casting method are wetting, bonding, distribution and damage characteristics of reinforcements in the matrix.

Because MMCs are required to have not only strength, but also specific functions such as hardness, lightness, wear-resistance, damping ability and permeability, depending on where they are used, generally speaking, the production method of these functional materials is unique and specific, due to the unique and specific properties of the material. There is an extensive but widely dispersed literature dealing with the various fabrication methods for MMCs. In this paper it is intended systematically to review the cast fabrication methods to produce MMCs and to try to outline the applications of these methods.

SQUEEZE CASTING

One of the most important casting methods is squeeze casting on which a lot of research [10-13] has been done, because this process has been used commercially for the production of automotive, aerospace and other engineering applications.

Squeeze casting is based on pressurised solidification. The squeeze casting process is shown basically in Fig.1[14]. In this process, preform used to selectively reinforce a casting, containing the required composition of fibres at a chosen volume fraction, with the desired shape, is first preheated to a proper temperature. The heated preform is put into the die cavity just prior to the addition of the molten alloy. A measured quantity of modified and filtered metal is poured into a preheated die cavity located on the bed of a hydraulic press. The press is

moved to close off the die cavity and pressurise the liquid metal. Pressure is maintained until solidification is complete. Then the press is opened and the component ejected.

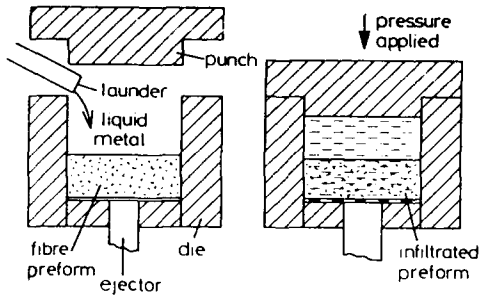


Fig.1 Squeeze casting of composites[14]

The key of the process is that solidification is finished under high pressure, which is several orders of magnitude greater than the melt pressure developed in conventional foundry practice [15]. Pressures applied to the system are up to 100 MPa, these are necessary to overcome capillary effects and frictional forces experienced by the liquid flowing through the interfibre channels. Once pressure is applied, the melt front passes quickly through the preform at a velocity of about 30mm per second. During the squeeze casting the pressure can amount to a few thousand atmospheres, with a consequent increase in the freezing temperature, ΔT. For Al-based alloys the freezing temperature may increase by 10-25C, depending on pressure, during squeeze casting [16]. In fact this is equal to reducing the superheat temperature of the melt or to undercooling of the melt, resulting in rapid solidification of the melt. Furthermore, the high rate of heat removal achieved in squeeze casting is also helpful to the rate of solidification. This is because the applied pressure tends to force the solidifying metal against the die and eliminate the air gaps between the casting surface and the die wall. The combination of undercooling with high heat transfer rates ensures a fine-grained equiaxed structure [17]. The high pressures employed during solidification result in the formation of a porosity-free, high-integrity near net shape casting with smooth surfaces and excellent microstructure. Strength and fatigue life of this casting are much longer than those of a conventional gravity casting. The high pressure employed promotes wetting of most ceramic fibres. Selective reinforcement is realised by placing preforms of ceramic fibres in appropriate locations within casting die. A major limitation is the size of parts that may be cast because of the high pressure requirements.

COMPOCASTING METHOD

Compocasting is a promising method for preparing MMCs reinforced by discontinuous fibres, whiskers or particles. M.C.Flemings[18] has pointed out that when metal alloys are vigorously agitated during solidification, the solid which forms has a special non- dendritic structure. Partially solidified metals with this structure behave as highly fluid slurries at solid fractions as high as 60%. The process of taking a highly fluid, semi-solid, nondendritic slurry and casting it directly is termed rheocasting.

Mechrabian et al.[19] used the term compocasting to describe an application of the rheocasting. In the compocasting process particulate or fibrous materials are incorporated into the partially solid alloy and the resultant composite may be cast. An outstanding advantage of compocasting is the ability to incorporate material which is not wetted by the alloy. The non-wetting material can be dispersed by the stirring action and is mechanically trapped by the solid particles of alloy. Settling, flotation, or agglomeration are also prevented by the presence of the solid alloy particles.

Several schematics of compocasting equipment have been reported [20-23], as, for example, the compocasting equipment shown in Fig.2[22]. A hollow rotor is incorporated in the design of the equipment to facilitate the addition of the particulate materials (graphite powder in this case). The required quantity of graphite particles is stored in the hollow rotor so that their temperature equilibrates with that of the alloy slurry. This ensures that addition of graphite particles to the alloy slurry does not result in a reduction in temperature or a consequent reduction in viscosity. The rotor prevents surface agitation of the melt and consequent air entrapment. it also permits graphite particles to be introduced below the surface of the melt at the shearing zone.

The compocasting procedure is as follows: The melt is poured into the preheated compocasting unit and stirring is initiated at the rotor speed required to provide the desired shear rate. Then, the temperature is gradually lowered until the alloy is 30-50% solid. At this temperature the non-metallic particulates are added by turning the injector down. The power input is controlled such that the total per cent of solids, non-metals and solid spheroids of the alloy, does not exceed about 50%. Stirring is continued until interface interactions between the particulates and the matrix promote wetting. After mixing the composite slurry is bottom poured into a preheated crucible for die casting or squeeze casting.

Using this method aluminium alloys containing up to 8wt.% uncoated graphite particles[22], 2-30wt.% Al_2O_3 and SiC particles[21], up to 15vol.% SiC fibre [20] or SiC whisker [23], and

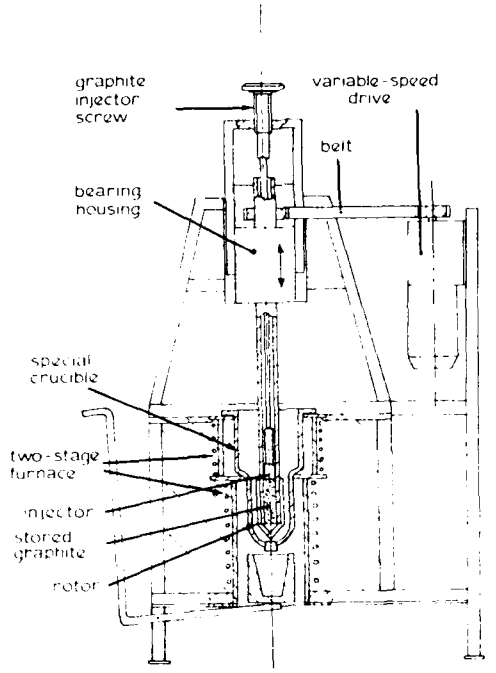


Fig.2 Schematic diagram of compocasting equipment[22]

up to 23 vol.% Al_2O_3 fibre[24] have been prepared successfully with a macroscopically homogeneous distribution of the particles or fibres.

ATOMISING AND GAS INJECTION METHODS

Several methods for dispersing solid particles in molten alloys using gas atomising technique have been developed[25-28] . One of the atomising equipments is shown in Fig.3[25], which consists of a melting furnace, a gas atomising nozzle, a particle supplier and a mould. When the stopper is raised, the melt in the crucible flows down from the bottom of the crucible. The melt stream is changed into fine droplets by the gas blown-off from the nozzle. Since the pressure in the space enveloped with the jet stream and the nozzle is reduced by the jet, particles falling from the upside of the nozzle are sucked in the corn-shaped space, engulfed in the jet and mingled with the molten droplets. Then, the atomised melt is rapidly solidified in a mould to keep a good distribution of dispersed particles. Reference[25] shows that particles larger than 30 μm in dia. are successfully dispersed and the distribution of dispersed particles is improved by adding 2% Ca in Al alloys and 0.5% Ti in Cu alloys.

Using a similar atomizing method, iron particles are sprayed into the Al melt stream, the fine mingled molten droplets are not sprayed into a mould, but are deposited on a moving substrate. A deposited strip of a two-phase metallic material is produced, with a negative shape of the surface of the substrate[26].

Alcan International, Banbury, U.K., has produced a variety of product forms of SiC particle/Al alloy MMCs based on this method [28].

M.Hasegawa et al. have developed a spray-dispersion method for producing dispersion strengthened steel [27,29,30,31] . Using a plasma-spray powder feeder, nonmetallic powder was sprayed into the steel stream during pouring into an ingot with argon gas pressurised below 1 MPa. TiO_2, Al_2O_3, ZrO_2, CeO_2, WO_3, ThO_2, WC, TiC and CeS

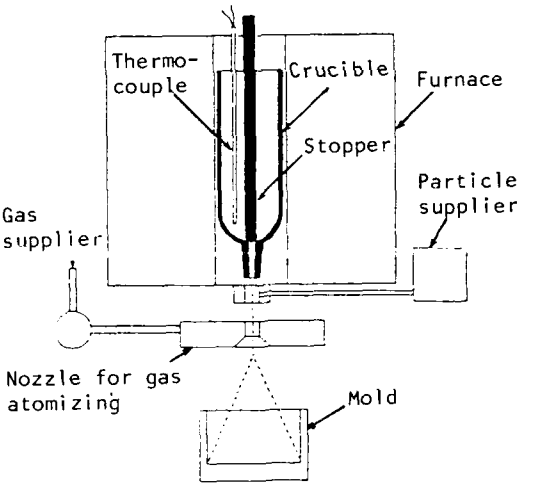


Fig.3 Schematic of atomizing apparatus[25]

powders were selected as spraying particles. The controlling element such as V, Ti, Cr, Ni, Co, Mo, Nb, and so forth, which improve the surface tension of molten steel and the interfacial tension at the particle-molten steel interface, were added to the steel, so that the sprayed powder was further reduced in size in steel. The average size of fine dispersed particles in steel was about 800Å. The volume fraction of the sprayed particles in steel was about 0.65-2.5% (vol.). Different kinds of steels and nickel -based alloys were tested. The properties of steel were improved with proper dispersed particles.

The gas stream injection method for dispersing particles in Al alloy casting was introduced by Badia[32], a small hand gun was built to inject Ni-coated graphite powder into Al alloy heats by means of a N_2(g) stream baths. After injection the melts were stirred and cast into permanent moulds.

PRESSURE CASTING

Several pressure casting methods have been used for preparing MMCs. The pressure used is much lower than that in squeeze casting. Fig.4 is a device developed for the unidirectional pressure infiltration into a fibrous preform under controlled processing conditions[33]. The operating principle of the device is to use pressurised gas to force molten metal into an evacuated die. The device consists of two main components: the pressure vessel, containing the melt furnace and crucible,and the cap, attached to which are the control valves and the die. The die is attached to the centre of the cap and can be evacuated. The vessel is pressurised with nitrogen about 3 MPa pressure forcing the metal up through the die and into the fibres, forming composite. Al-Cu alloys containing 18vol.% and 24vol.% Al_2O_3 fibre have been fabricated with this device.

Another pressure casting technique is relatively simple[34] : pre-heating the particle aggregate in a special mould and then adding 3MPa pressure to the molten metal poured on the

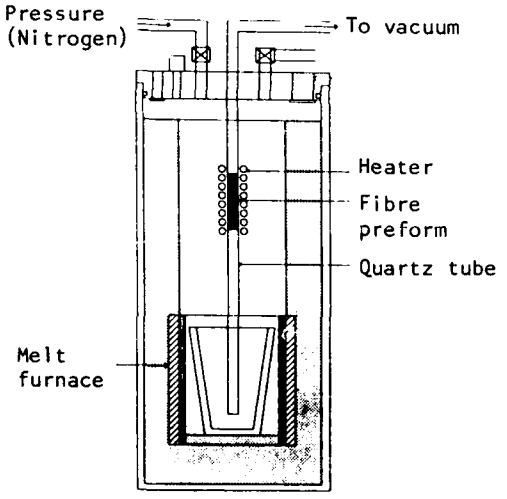


Fig.4 Schematic of hydrostatic pressure infiltration device[33]

particle aggregate so as to encourage penetration, which results in a metal-particle composite.

Pressure casting can be used to increase the fibre concentration in the composites and for simultaneous two-dimensional alignment of the fibres following compocasting[24] . After compocasting the composite produced contains discontinuous fibres which are randomly oriented in three dimensions. The composite is superheated to approximately 50K above the alloy liquidus. A continuous porous ceramic filter is inserted inside the female die half. The superheated composite is poured on the filter, and the top is pressed down on it. About 50% to 70% excess of liquid metal is thus squeezed out into the fine holes of the porous filter. Finally, the composite is cut away from the ceramic filter. The compression of the composite in this way has two purposes: it concentrates the fibres above the filter, and aligns them into a random two-dimensional mat. This process also can be used for producing high-volume fraction and dual-layered composites of particle/metal mingled melt after compocasting [21].

VACUUM CASTING

Making MMCs under vacuum, better wettability between nonmetallic reinforcements and metal melts can be achieved with less oxidisation occurring.

E.I.du Pont de Nemours & Co., Inc. Wilmington, U.S.A. have developed a fabrication technique based on vacuum casting to incorporate continuous fibres into metal matrices[35]. The major operations include: first, preparation of a handleable flexible fibre tape using about 5% fugitive binder such as polyethyl acrylate and, then, the tape is changed into a preform with the fibre orientation and volume loading desired in the final product. After this preform being put in a casting mould, the fugitive binder is burned off and the mould vacuum infiltrated with molten metal. A variety of α-Al_2O_3 fibre/Al and α-Al_2O_3 fibre/Mg composite components containing volume loading 30-60% fibre have been prepared in this manner.

Another method using vacuum techniques for cast-in-place hardfacing of castings has been developed[36], in which metal poured into a sand mould is drawn by vacuum into a layer of abrasion-resistant powder (or grain) placed on a wall of the mould cavity. The infiltrated powder provides a metallurgically-bonded, abrasion-resistant coating on the casting. In this way castings with an abrasion-resistant surface on a tough matrix can be produced. AISI1020 and 4340 steels, austenitic manganese steels, and both gray and ductile cast irons have been successfully coated with CrC, WC, and WC-10%Co.

DIRECT INFILTRATION METHOD

Direct infiltration is a most widely used and simple method for continuously infiltrating fibre tows by passing them through a bath of molten metal[37,38,39]. The fibre volume fraction may be controlled by adjusting the drawing rate. Composites produced in this manner may contain pores.

PELLET METHOD

Graphite can be introduced to the melt in the form of a pellet compact consisting of coated

graphite powder and base alloy powder to produce cast Al-graphite particle composite[40]. The pellets are made by pressing mixtures of nickel-or copper-coated graphite particles and aluminium powders together. For the most efficient recovery of graphite particles in the castings, the pellets should be made from a mixture of 67 wt% of 80μm copper- or nickel-coated powder and 33wt% of 400μm size aluminium powder. When aluminium alloys were melted at a temperature 750—850 C, the pellets were plunged into alloy melts using refractory-coated mild-steel cups which were withdrawn after a few sec. The melts were then stirred manually and cast into permanent moulds.

The pellet method has the advantage of greater reproducibility and flexibility. However, one of the potential disadvantages of the pellet technique is that the pellet contains a layer of oxide on the aluminium powder which gets dispersed in the melt.

VORTEX METHOD

The vortex method employing an impeller mixer is a technique for producing particle/metal composites[41,42,43]. The impeller mixer stirs the melt to create a vortex into which particles can be placed and incorporated in the melt. The same impeller mixer, at reduced speeds, is an effective means of controlling particle dispersion after introduction. The graphite particle coated by nickel or copper has been tried successfully in Al alloys[41,44]. Later investigations showed that it is possible to disperse less than 3wt% of uncoated but pre-heat-treated (heated to 400 C in air for 1 h) graphite in Al alloy melts by the vortex method[45]. A variety of graphitic/Al castings have been produced both by permanent mould and die casting, including bearings and pistons using the vortex method.

CENTRIFUGAL METHOD

Centrifuging during solidification of an axisymmetric part can be used effectively to segregate heavy or light non-metallic additions to the outside and inside extremities of the part prior to solidification.

Using the centrifugal method, a casting with particle reinforced outer layer has been produced[46] . Al-11% Si alloy, graphite particle and Al_2O_3 particle were put in a crucible which was also used as a mould. After the aluminium alloy melt, the crucible was located in a centrifugal casting device. The melt solidified under the centrifugal force Finally, the particles were segregated into the outer layer of the casting forming a particle /Al composite layer.

APPLICATION OF ULTRASONIC VIBRATIONS

The application of ultrasonic vibrations and addition of surface-active elements to the melt is an aid to the dispersion and retention of uncoated graphite particles[47] , because the graphite particle surfaces are cleaned by the ultrasonic vibrations in the bath, freeing them of adsorbed gases and impurity films. When molten matrix material infiltrates the reinforcing material under gravity, supersonic vibration can be used to get rid of voids in the cast material. B/Mg composites 6.35 mm in diameter and 102 mm in length have been fabricated[48] . Specimens fabricated by this method show an interaction zone and pores at the interface between fibre and matrix.

METHODS OF PRODUCING METALLIC FOAMS[49,50]

Metallic foams with high porosity ranging from 40-98% (Vol.) are gas/metal matrix composites. These light weight materials possess unusual properties, such as impact energy absorption capacity, air and water permeability, and low thermal conductivity etc.. The application of metallic foams is growing.

Foamed metals can be prepared by adding a blowing agent, such as TiH_2 or ZrH_2 to a molten metal and heating the mixture to decompose the blowing agent to form gas. The gas expands causing the molten metal to foam. After solidification metallic foams are obtained.

The foamed metals with an interconnected cellular structure can be made by casting metal around granules introduced into the casting mould. These granules, such as sodium chloride, can be soluble, which is later leached out to leave a porous metal[51] ; conversely, granules can also be incorporated into metal by vigorously stirring[52] .

An interesting investment casting method has been reported for producing metallic foam in Japan[53] . In this procedure a fluid refractory material is poured in voids of a spongy foamed plastic and hardened. Then, the integral plastic-refractory material is heated so as to vaporize the plastic component and a mould having spongy lattice pores is produced. Molten metal is poured into this mould and solidified. The refractory is then removed and a metallic foam having the same sponge form as the original spongy plastic is obtained.

DIRECTIONAL SOLIDIFICATION METHOD

There has been a great interest in unidirectionally solidified eutectic composites[54,55]. Most investigations have been focused on nickel or cobalt based alloys, Al_3Ni-Al and Al-$CuAl_2$[56] .

There is an example for producing aircraft engine turbine blades by NiTiC superalloy reinforced with tantalum monocarbide whiskers by this method[57]. In a directional solidification furnace, a mold of a turbine blade shape was fixed to a water cooled copper chill which was lowered

from the furnace at a controlled rate. Melt of NiTaC casting charge was poured into the mold. In an appropriate atmosphere the casting was unidirectionally solidified at 0.64 cm/h, turning it into the eutectic superalloy reinforced with tantalum monocarbide whiskers.

Takao Yakou et al[58] have discovered that when the solidification rate was controlled to 2.2×10^{-5} m/s by directional solidification method, Al-6wt% Ni eutectic alloy became an Al_3Ni continuous fibre/Al composite. The diameter of the fibres was 0.7μm. There was a space of 2μm between each two fibres. The fibres grew in parallel direction. The Al matrix was a single crystal with <011> solidification direction. When the eutectic alloy was solidified with furnace cooling, it became an Al_3Ni particle/Al composite.

Other methods for fabricating unidirectionally solidified eutectic alloys are shown in references[59,60].

Different casting methods for metal matrix composite fabrication have different characteristics and thus can be used for different requirements. Therefore, it is important to work further on the casting methods.

REFERENCES

1. Watanabe, T., "Powder Metallurgy", Gijutsushoin, (1976), 47.
2. Smith, P.R. and FRoes, F.H., J. of Metals, Mar. 1984,vol.36, 19-26.
3. Shota, I. and Watanabe, O., J. Mater. Sci. 14 (1979) 699-704.
4. Gigerenzer, H., Pepper, R.T. and Lachman, W.L., ICCM-II Proc. Op Cit 175-188.
5. Froes, F.H. and Pickens, J.R., J. of Metals, Jan. 1984, vol.36 14-28.
6. Aronson, B., Machine Design, Aug. 1985, 68-73.
7. Kreider, K.C., (ed.), "Metallic Matrix Composites" (Academic Press, New York, 1974).
8. Viala, J.C. and Bouix, J., Mater. Chem. Phys. 11(1984) 101.
9. Mehan, R.L. and Bolon, R.B., J. Mater. Sci. 14 (1979) 2471.
10. Abe, Y., Horikiri, S., Fujimura, K. and Ichiki, E., ICCM-IV Proc. (ed. T. Hayashi et al.), 1982, 1427-1484.
11. Tanaka, J., Ichikawa, H., Hayase, T., Okamura, K. and Malsuzawa, T., ibid, 1982, 1407-1413.
12. Clyne, T.W. and Bader, M.G., ICCM-V, Proc.(ed. W.C. Harrigan, Jr et al.) 1985, 755-771.
13. Clegg, A.J., in 'Aluminium technology 86', (ed. T. Sheppard), Paper 89, Synopsis, P731, 1986, London.
14. Harris, S.J., Mater. Sci. and Tech., Mar. 1988, vol.4, 231-239.
15. Rajagopal S., J. Applied Metal Working of ASMI., No.4 (1981) 3-14.
16. Zantout, B., Das, A.A. and Franklin, J.R., The Metallurgy of Light Alloys Spring Residential Conf.(The Inst. of Metallurgists, Mar. 1983) No.20
17. Das, A.A. and Chatterjee, S., The Metallurgist and Material Technologist (Mar. 1981), 137-142.
18. Flemings, M.C., Rheocasting, Proceedings of a Workshop held at the Army materials and Mechanics Research Center, MC/C-78-35.
19. Mehrabian, R., Riek, R.G. and Flemings, M.C., Met. Trans., 1974, 5, (8), 1899-1905.
20. Milliere, C. and Suery, M., Mater. Sci. and Tech., Jan. 1988 vol.4, 41-51.
21. Hosking, F.M., Folgarportillo, F., Wunderlin, R. and Mehrabian, R., J. Mater. Sci., 17(1982) 477-498.
22. Gibson, P.R., Clegg, A. J. and Das, A.A., Mater. Sci. and Tech., July 1985, vol.1, 559-567.
23. Girot, F.A., Albingre, L., Quenisset, J. M. and Naslain, R., J. of Metals, Nov. 1987, 18-26.
24. Quigley, B.F., Abbaschian, G.J., Wunderlin, R. and Mehrabian, R., Met. Trans., 13A(1982) 93-100.
25. Toru Namai, Yoshiaki Osawa and Masao Kikuchi, IMONO (J. Japan Foundrymen's Soc.) 56(1984), 10.
26. Richard, A., U.K. Patent 2115014A (1983).
27. Hasegawa, M. and Takeshita, K., Met. Trans., 9B(1978) 383-388.
28. White, J., Hughes, I.R., Willis, T.C. and Jordan, R.M., in '4th international Al-Li conference' (ed. G.Champier et al.), 347-353, 1987, Paris.
29. Hasegawa, M. and Takeshita, K., Tetsu-to-Hagane, 1976, 62, 201-209.
30. Hasegawa, M. and Takeshita, K., tetsu-to-Hagane, 1977, 63, 294-302.
31. Hasegawa, M. and Takeshita, K., Bull. Jap. Inst. Met., 1976, 15, 462-466.
32. Badia, F.A., Trans. AFS, 77(1969), 402-406.
33. Cornie, J.A., Mortensen, A. and Flemings, M.C., Proc. of ICCM-VI (ed. F. L. Mathews, et al.), 1987, 2.297-2.319.
34. Nagata, S., Kitahara, A., Akiyama, S. and Ueno, H., Trans. AFS, 93(1985) 49-54.
35. Dhingra, A.K., Phil. Trans. R. Soc. Lond. A294, (1980), 559-564.
36. Davis, K.G. and Magny, J.G., Trans. AFS. 89 (1981) 385-402.
37. Harrigan, W.C. and Flowers, R.H., "Failure Modes in Composites IV" (ed. Cornie et al.) AIME, 1977, 319.
38. Pepper, R.T. and Penty, R.A., J. Composite Mater., 8, 29(1974).
39. Kendall, E.G., "Composite Materials vol.4, Metallic Matrix Composites" (ed. K.G. Kreinder), Academic, 1974.
40. Pai, B.C. and Rohatgi, P.K., J. Mater. Sci. 13(1978) 329-335.
41. Badia, F.A., MacDonld, D.F. and Pearson, J.R., Trans. AFS, 79(1971) 265-268.
42. Patton, A.M., J. Inst. Met., 1972, 100, 197-201.
43. Badia, F.A., Trans. AFS, 79(1971) 347-351.
44. Surappa, M.K. and Rohatgi, P.K., Met. Tech., Oct.(1978) 358-361.
45. Krishnan, B.P., Surappa, M.K. and Rohatgi, P.K., J. Mater. Sci., 16(1981) 1209-1216.

46. Sngishita, IMONO (J. Jap. Foundrymen's Soc.), 57(1985), 2.
47. Gorbunov, V.G., Parshin, V.D. and Panin, V.V., Russ, Cast. Prod., Aug.(1974) 348-349.
48. Paultnoi, K.I., Salibecov, S.E., Svetlov, I.L. and Chubarov, V.M., 'Structure and Properties of Composite Materials'(1979).
49. Davies, G.J. and Shu Zhen, J. Mater. Sci., 18(1983) 1899-1911.
50. Gardner, A.R., Prod. Eng. 38(1967) 141.
51. Kuchek, H.A., US Patent 3236706(1966).
52. Kreigh, J.R. and Gibson, J.K., US Patent 3055763(1962).
53. Jpn. Ind. Tech. Bull, 8(1980) 19.
54. Lekkev, F.D., Cline, H.E. and Mclean, M., "In Situ composite IV" (North Holland, 1982)
55. Thompson, E. R., Ann. Rev. Mater. Sci., 12 (1982) 213.
56. Chadwick, G.A., Met. Sci, 1975, 9, 300-304.
57. Gigliotti, M.F.X. and Greskovich, C., Met. Trans. 11A (1980) 319-322.
58. Takao Yakou and Tadashi Hasegawa, J. Japan Inst. Met., vol.50, 10(1986),900-907.
59. Erickson, J.S., Owczarski, W.A. and Curran, P.M., Metal Prog. 99(1971), 58.
60. Cetel, A.D., Gell, M. and Glatz, J.W., Proc. Conf. on In-Situ composites 3(1979), 292-302.

SQUEEZE CASTING PROCESSES FOR FIBER REINFORCED METALS AND THEIR MECHANICAL PROPERTIES

Hideharu Fukunaga
Department of Mechanical Engineering
Hiroshima University
Saijo, Higashi-Hiroshima, 724 Japan

Abstract

This article presents a fundamental and practical manufacturing process and the controlling parameters for fabricating fiber reinforced metals (FRM) by squeeze casting. In this process, a final infiltration pressure of several hundered atmospheres is required to eliminate porosity in FRM castings. Extremely high pressures beyond that required to eliminate porosity yields no further improvement in the tensile strength of SiC fiber (Nicalon) reinforced aluminum composites. The use of evacuated SiC whisker preforms prior to squeeze casting resultes in improved strength reliability.

FIBER REINFORCED METALS fabricated by squeeze casting present a new class of materials that offers another selection and new solutions to the machine designer for synthesizing a high performance machine such as the internal combustion engines, industrial robots, turbo-machinery, variable speed rotary compressors and so on. Nowadays, Japan produces a large quantity of and various kinds of ceramic fibers and whiskers. Since manufacturing process and quality controls are rapidly being established, there can be seen increasing numbers of experimental castings of FRM for high performance machine component at may companies.

Fiber reinforced metals at the present state of the art, however, do not appear to be competitive with conventional materials for civil use because of fiber cost. The cost of the function performed by a given component must also be considered throughout a given system from beginning to end. Such value analysis is quite complicated and it is necessary to consider the manhours required to fabricate the final product it replaces, and to consider service life of the system and many other factors.

Fiber reinforced metal has already offered excellent performance in several applications limited to industrial use. Developers of fiber reinforced metals are now vigorously persuing numerous applications where weight saving, high strength at moderate temperatures, wear resistance, thermal stability, and durability in vacuum and atomic oxygen environments are of primarily importance. Examples are: bolts in special duty applications (1), direct injection diesel piston (2-11), connecting rods (12-14), fan-blades (15), impeller of jet engine (16), gun tube (17), missile guidance system (18), helicopter transmission housing (19), centrifugal rotating drum (19), space station truss (20), spinning machine parts (21), power semiconductor devices (22), and so on.

Most of the above applications are fabricated by the squeeze casting method because of its high productivity and excellent net-shape formability. With this process, very few of the above applications can achieve the projected strength based on the rule of mixture. The composites have still less reliability of strength compared to the ingot metals. Hence, the many problems remain to be solved for the squeeze casting process. In this article, fundamental guide lines and recommendations are offered for the fabrication of sound composites by squeeze casting.

SQUEEZE CASTING

The fabrication process of FRM by squeeze casting is illustrated in Figures 1, 2, and 3. Shown in these frgures are direct and indirect squeeze casting machine designs with vertical type and horizontal types of machines respectively. In both processes, the ceramic fiber preform is pre-heated to several hundred degrees centigrade (T_f) below the melting temperature of matrix metal and then set into a metal die, which is pre-heated to 250 to 350C. The molten Al or Mg alloy at a temperature T_a above its melting temperature is squeeze ! into the fiber preform by a hydraulic press to form the mixture of fibers and molten metal. The mixture is forced to solidify in a short time due to rapid heat transfer resulting from good contact between die and molten metal under a pressure of several hundred atmospheres.

The direct process as shown in Figure 1 has no runner and a good yield of molten metal to a part, but is difficult to obtain the exact part configuration. On the otherhand, in the indirect process as shcwn in Figures 2 and 3, net shapes can be obtained but excess metal remains in the runner. However, the indirect processis is capable of producing two or more casting in one shot. Therefore, the indirect process is preferable.

The squeeze casting process is characterized by high productivity and ease of fabrication. In addition, the method can also be used to infiltrate fibers that are difficult to wet with molten matrix metals. The problem of fiber degradation can be limited to some extent by selecting the process conditions (23).

In each process, there are many parameters to be controlled, i.e. molten metal temperature just before contact to

the fiber preform, preform temperature, die temperature and its temperature gradient, applied pressure, and plunger speed. Figure 4 illustrates a typical time chart for controlling parameters. This figure shows slow plunger speed, short-time infiltration, the gradual movement of plunger to compensate the shrinkage of melt, high final squeeze pressure, and rapid cooling of FRM castings.

FABRICATION METHOD OF THE PREFORM

The fiber is fabbricated into preform to give a final machine part composed of given volume fraction, fiber orientation and the shape of the reinforced region. Figure 5 shows a schematic of two methods of preform fabrication, including press forming in the lower figure and suction forming in the upper figure. In both cases, short fibers are mixed homogeneously with water accompanied by a small addition of binder. The chopped fibers are piled up around the filter in a suction forming operation to form a preform. During press forming, the slurry is poured into the mold and dewatering is conducted while the final preform is shaped. The point is to give homogeneous distribution of fiber and enough strength of preform to avoid disorder of fiber or crushing the preform during the infiltration process. In general, when the fiber preform is less than 10% of the volume fraction of fiber, it is difficult to infiltrate the molten metal without excessive deformation of the preform. The critical volume fraction of fiber with or without deformation depends not on the so-called squeeze pressure, but primarily on the infiltration speed.

Y. Fujita et al. have recently developed a new technique in their report (24). In order to fabricate sound composites, they eliminated aggregate clusters of whiskers and outgassed the slurry after agitation. They improved the fracture strength of SiCw/6061 by 26% with the above treatment.

Another unique technique has been developed to minimize the direct contact between continuous fibers by S. Towata et al. (25, 26), in which whiskers or particulates are distributed among continuous fibers. In their report, it was revealed that additional reinforcement were extremely efficient in improvement of the strength of composites fabricated by squeeze casting.

PRESSURE NECESSARY FOR INFILTRATION INTO FIBER PREFORM

The pressure difference necessary for infiltrating the molten metal into a fiber preform can be evaluated by Hagen-Poisiulle's equation for uniform cross section of flow channels, or by Darcy's law for non-uniform cross section of flow gaps, as present in equation (1) or (2) respectively.

$$\partial p/\partial x = -32\mu \cdot u /32\, de^2 \qquad (1)$$

$$\partial p/\partial x = -\mu \cdot u/K \qquad (2)$$

where

- μ : coefficient of viscosity,
- u : mean velocity of fluid,
- de : Hydraulic equivalent diameter of non-circular pipe

and

- u : velocity equivalent to flow rate in the fiber preform without fibers,
- K : filtration coefficient.

The equations tell us that the faster the infiltration velocity, the higher the required pressure. According to the simple calculation and the experiment, the required pressure difference is unexpectedly low; less than 5 atmospheres in conventional squeeze casting conditions. In addition to the work required to overcome capillarity cannot be neglected in regard to pressure to infiltrate the molten metal. This pressure is estimated as $4\gamma_i/d_f$ (27, 28), where γ_i is the interface energy between fiber and molten metal, d_f is the diameter of the fiber. In this estimation the contact angle is assumed to be 180° which is slightly large. The pressure necessary for overcomming capillary resistance is 4.5 atmospheres for the combination of continuous silicon carbide fiber (Nicalon) and aluminum when V_f=38%, γ_i=1450 erg/cm^2, and d_f=13μm. The pressure is a considerably large value when compared to pressures calculated from equation 1 above. However, the total sum of the infiltration pressures is very small compared to the final squeeze casting pressure. Attention should be paid that the pressure necessary for infiltration does not exceed the strength of fiber preforms.

CONTROLLING PROCESS PARAMETERS

There are several fundamental factors of squeeze casting process. The appropriate program for fabrication of sound FRMs has much to do with fabrication conditions. After some trial-and-error, it was found that the quality of FRM depends mainly on the temperatures of the molten metal and fiber, infiltration speed and final squeeze pressure, as well as die design. In the following section, the effect of the parameters on the strength of composites is briefly reviewed. Above all, the effect of pressure is stressed and discussed in detail. Here the quality of FRM was evaluated by tensile testing and metsallography.

1) Molten metal temperature and fiber temperature- The FRM fabrication experiments were carried out at various molten metal and fiber preform temperatures to determine the optimum temperature range which leads to the maximum tensile strength. In the case of the combination of SiC_{pcs} fiber and commercially pure aluminum, the specific temperature range is shown in Figure 6 by the shadowed area. The reasons for the permissable temperature range for processing arise from lines 1 to 3 respectively.

1)The temperature of molten metal must be higher than its melting point as far as the liquid method is adopted (line 1).

2) If the T_f and T_a are too high, the high strength composites are not obtained due to the degradation fo the fiber. SiC_{pcs} fiber is relatively non reactive with molten aluminum. According to an experiment on SiC_{pcs}/Al system with V_f=38%, the enthalpy Q needed to make FRM per unit volume is less than 355 cal/cm^3 (line 2). Although this limit may be a straight line and the Q value may change depending upon the system, the establishment and observance of the limit is essential.

On the other hand, if the T_a or T_f is too low, molten metal cannot flow around the fiber. Hence, there will be non-infiltrated areas. Therefore, T_a and T_f must be higher than some minimal value. (line 3 and 3'). These temperatures are to ensure the narrowest path for the molten metal to flow between fibers even though solidified layer is formed. The tendency discussed above seems to be true for fabricating composites using fibers that are reactive with molten metals. On the other hand, since the SiC whiskers have very little reactivity with aluminum alloy up to 850C the processing temperatures do not strongly effect the composite strength.

The data of Figure 7 (24), shows that the tensile strength is relatively insensitive to processing temperature over the range investigated.

2) Infiltration speed- The infiltration velocity of molten metal front is given by equation (3).

$$u = A \cdot v / S(1-Vf) \qquad (3)$$

where A : diameter of plunger
v : plunger speed
S : apparent area of metal front plane in preform
V_f : volume fraction of fiber

It is notied here that the infiltration velocity u relates to the infiltrating pressure p by equation (1) or (2). Therefore, both parameters cannot be controlled at the same time; either speed or pressure is the objective of control. In may cases, the melt flow going between fibers is of laminar flow, which has Reynolds number lower than 100. Therefore, the hydraulic interaction between molten metal and fiber is small. An experiment shows no effect of composite tensile strength on infiltrating speed ranging 1 to 5 cm/s on the tensile strength of the composite, in Figure 8, where 38% SiC_{pcs} fiber reinforced aluminum is fabricated by squeeze casting with plunger speed being the only variable.

Another experiment demonstrated the severe deformation of the preform with 10% volume fraction of short fibers, when the infiltration speed of molten aluminum increased beyond 20 cm/s. There exists a critical infiltration beyond which the preform is deformed or crushed. this velosity, of course, depends upon the compressive strength of the preform.

3) Final squeeze pressure- In the squeeze casting process, the high pressure is applied to molten metal to compensate for solidification shrinkage and to provide for a high heat transfer coeficient at the interface between molten metal and metal die. An elementary experiment was performed to determine the pressure required to eliminate voids in castings. In the fabrication of SiC_{pcs}/pure aluminum composites, the results obtained are shown in Figure 9. The tensile strength was almost constant beyond a pressure of 24.5 MPa. Defects such as pin holes, however, were found on the fracture surface when the pressuer was less than 24.5 MPa. Therefore, pressures as great as 49 MPa are needed to fabricate sound composites. High pressure may improve the tensile strength of composites by achieving good interfacial bonding between matrix and fiber. This concept, when put into practice, resulted in the data of Figures 10 and 11, which show the variation of tensile strength with final pressure and the microstructures of composites respectively. No detectable improvement was observed even if the pressure applied was 2000 atmospheres and no visible change in microstructure, compared to conventional squeeze casting pressure, was observed. One possible reason is that the fiber employed originally had a smooth surface and was considerably easier to wet with the aluminum matrix. In another investigation, however, it has been reported that pressure plays a significant role in improving the interfacial bonding between graphitic particles and aluminum matrix (29). So, it may be said that pressure can improve the bonding of interface for fibers difficult to wet, and of rough surface. Figure 12 also shows the effect of final squeeze pressure on the tensile strength of SiC_w/6061 composite fabricated by a direct squeeze casting. According to the results, sound and high tensile composites are attained by applying low final pressures compared to the indirect squeeze casting process. This is because of efficient pressure propagation due to no runner. Moreover, the result means that effective pressure of 100 to 300 atmospheres is sufficient to eliminate voids and the composites can be safely heat-treated without blistering.

4) Vacuum squeeze casting- The fiber preform includes a considerable volume of air. The air must be displaced with molten metal without turbulence during the squeeze casting process. It is doubtful that perfect displacement is attained in conventional squeeze casting. An attempt was introduced to determine the strength and its variability for SiC_w/6061 alloy composites fabricated by vacuum squeeze casting (30) in which the air in the whisker preform was exhausted before infiltration. The result, as shown in Figure 13, revealed an increase in bending strength of about 6% and a reduction of the scatter. The reason for this improvement in properties is that the inherent cavities formed during the infiltrating process was decreased in the size and the number by exhausting air prior to infiltration. It is supported by minute SEM analysis of fracture surfaces. Therefore, Vacuum squeeze casting is recommended for the production of complex shaped MMC castings with high reliability.

SUMMARY

In this article, the author discussed the effects of squeeze casting parameters such as process temperatures, infiltration speed, and pressure on the soundness of FRMs. Squeeze casting has become a powerful method to fabricate FRMs machine part because of the high productivity and excellent formability. The fundamental guide lines for the precess have been almost established. However, FRM is still not acknowledged as a material which can be designed for order because there are may difficulties involved in making the fibers oriented a in desired direction with a desired volume fraction. Further development is in progress to make continuous fiber preforms. In order to put FRM into practical use not only in aeroplanes but also in machine parts for general purposes, lowering the cost of fibers is certainly necessary, but more important is the understanding of the reason the high variability in composite strength. Such an understanding will require further research into the squeeze casting process.

REFERENCES

(1) T.Nisimura, A.Arai, M.Morita, H.Kashiwaya, K.Kiryu, and T.Miyamoto, ECCM-1, Developments in the Science and Technology of Composited Materials, Seq. 1985, Bordeaux, France, pp 628-633.

(2) J.Dinwoodie, Automotive Applications for MMCs Based on Short Staple Alumina Fibers, SAE Tech.Pap.Ser., No. SAE-870437 (1987), pp 1-11.

(3) R.R.Bowles, D.L. Mancini, and M.W.Toaz, Metal Matrix Composites Aid Piston Manufacture, Manf.Eng., Vol 98, No. 5 (1987), pp 61-62.

(4) F.K.Chi, R.D.Austen, R.D.Maier, and T.W.Krucek, Short Ceramic Fiber Reinforced Aluminum Alloy, SAE Tech.Pap.Ser., No. SAE-870440 (1987), pp 1-7.

(5) M.W. Toaz, R.R. Bowles, and D.L. Mancini, "Squeeze Casting Composite Components for Diesel Engines," Ind Heat, Vol. 54, No. 3 (1987), pp 17-19.

(6) Y. Suganuma and A. Tanaka, "Reliability in Application of Fiber Reinforced Metal, - Reliability assurance activity in development of FRM piston ring grove" (in Japanese), Journal of the J.S.M.E., Vol. 90, No. 827 (1987), pp 1289-1295.
(7) U.S.Patent No. 4, 4587, 177 (May 6, 1986), Aluminum Metal Matrix Composite Diesel Piston, Light Metal Age, Vol. 44, No. 11-12 (1986), pp 29-32.
(8) M.A.H.Howes, "Ceramic-reinforced MMC Fabricated by Squeeze Casting," J.Met., Vol. 38, No. 3; J.Metal-Matrix Composites in reciprocating Engines," Ceram. Eng. Proc. Vol 5, No. 718 (1984), p 643.
(9) M.A.H.Howes, "Ceramic-reinforced Metal Matrix Composite Fabricated by Squeeze Casting," Adv. Compos., pp 223-230.
(10) K. Marsden, "Commercial Potentials for Composites," Journal of Metals, Vol. 37, No. 6 (1985), pp 59-62.
(11) M.W. Toaz, "Near Net Shape Composite Castings with Tailored Engineering Properties," Adv. Compos., (1985), pp 231-237.
(12) K.Arita, T.Okuyama, and T. Hosomura, "Advanced Composite Materials and Its Application" (in Japanese), Science of Machine, Vol. 39, No. 3 (1987), pp 346-352.
(13) K. Ohori, H. Watanabe, and Y. Takeuchi, "Silicon Carbide Whisker Reinforced Aluminum Composites: Fabrication and Properties, Alum. Technol. 86, (1986), pp 732-735.
(14) F. Folgar, W.H. Krueger, and J.G. Goree, "Fiber FP/Metal-Matrix Composites in Reciprocating Engines," Ceram. Eng. Proc. Vol. 5, No. 7/8 (1984), p 643.
(15) S.Masaki, "Composites for Aircraft Engines" (in Japanese), J. Jpn. Gas Turbine Soc., Vol. 14, No. 55 (1986), pp 14-23.
(16) T. Nakamura and Y. Nishiyama, "Development of FRM Composite Impeller" (in Japanese), J. Iron and Steel Inst., Vol. 73, No. 5 (1987), p662.
(17) N.E. Doweling and R.B. Brown, "Fatigue and Fracture of Al/SiC Metal Matrix Composite Material for Gun Tube Application," PB Rep., No. Bp-86-242252 (1986), pp 1-36.
(18) "Technologies, Metal Matrix Composites: Super Stars of Tomorrow?" Mod. Met., Vol. 43, No. 7 (1987), pp 160-161.
(19) F. Kanatani, S. Matsui, T. Atsuta, and Y. Yamada, "Manufacturing of Fiber-Reinforced Metal (FRM) and its application to Structural Members" (in Japanese), K.H.I. Technical Review, No. 90 (1985), pp 1-11.
(20) D.E. Bowles and D.R. Tenney, "Composite Tubes for the Space Station Truss Structure," SAMPE Tech. Cont. Adv. Master. Process Eng., Vol. 18 (1986), pp 414-428.
(21) F. Gomi and N. Miyamoto, "Application of SiC Whisker Reinforced Aluminum Alloy to Spinning Machine Parts," Proc. 109th Annual Meeting of Japan Foundry Association, May 1985, p 72.
(22) K. Kuniya, H. Arakawa, T. Sakaue, H. Minorikawa, K. Akeyama, and T. Sakamoto, "Application of Copper-Carbon Fiber Composites to Power Semiconductor Devices," J. Jpn. Inst. Metals (in Japanese), Vol. 50, No. 6 (1986), pp 583-589.
(23) H. Fukunaga and K. Goda, "Formation and Role of the Solidified Layer on a Fiber During the Fabrication of Fiber Reinforced Metal by the Liquid Process," J. Jpn. Inst. Metals, Vol. 49, No. 1 (1985), pp 78-83.
(24) Y. Fijita and H. Fukumoto, "Influence of Fabrication on Conditions on Mechanical Properties of SiC Whisker Reinforced Aluminum Alloy Composites," 2nd SAMPE, Japan (1987).
(25) S.Towata and S. Yamada, "Mechanical Properties of Aluminum Alloys Reinforced with Continuous Silicon-Carbide Fibers and Whisker or Particulates," Trans. Jpn. Inst. Metals, Vol. 27, No. 9 (1986), pp 709-716.
(26) S. Towata, H. Ikuno, and S. Yamada, "Mechanical Properties of Silicon Carbide fiber Reinforced Aluminum Alloys with Whisker or Particulates" (in Japanese), J. Jpn. Inst. Metals, Vol. 51, No. 3 (1987), pp 248-255.
(27) K.F. Sahm, Verbundewerkst. Tag., a (1974), pp 269-286.
(28) A. Mortensen and J.A.Cornie, "On the Infiltration of Metal Matrix Composites," Metal. Trans. A, Vol. 18, No. 6 (1987), pp 1160-1163.
(29) B.K. Prasad, T.K. Dan, and P.K. Rohatgi, "Pressure-Induced Improvement in Interfacial Bonding Between Graphite and the Aluminum Matrix in Graphitic-Aluminum Particle Composites," J. Mater. Sci. Lett., 6 (1987), pp1076-1078.
(30) H. Fukunaga, K. Goda, Y, Kurita, and Y. Fugita, "Strength and Reliability of Silicon Carbide Whisker Reinforced Aluminum Composites by Squeeze Casting Including a Vacuum System," ICCM-6, Vol. 2 (1987). pp 2362-2371.

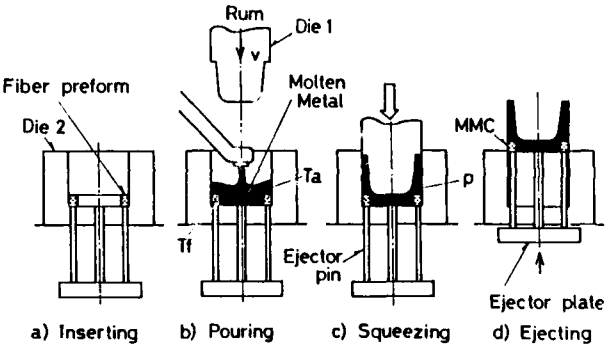


Fig.1 Direct squeeze casting operations, in which the molten metal is poured on the preform directly.

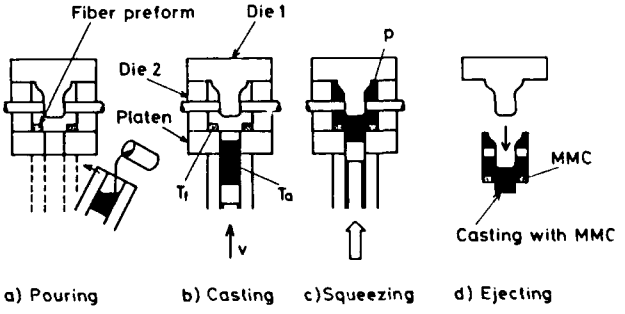


Fig.2 Indirect squeeze casting operations with a vertical type of machine.

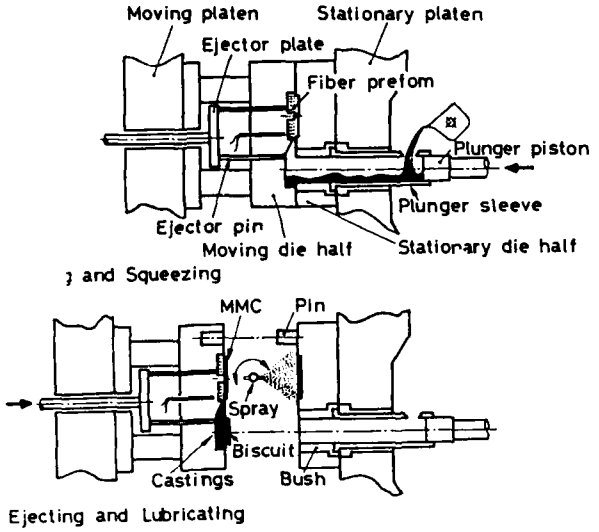


Fig.3 Indirect squeeze casting operations with a horizontal type of machine.

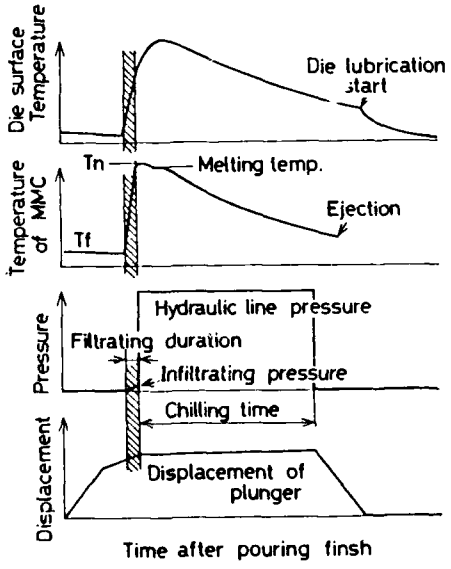


Fig.4 Typical time chart of squeeze casting process.

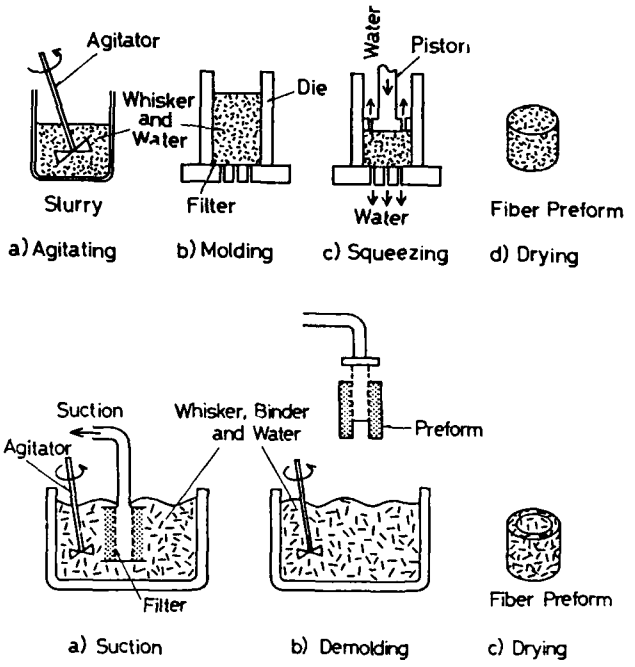


Fig.5 Fabrication processes of short-fiber preform, showing suction forming in the upper and press forming in the lower.

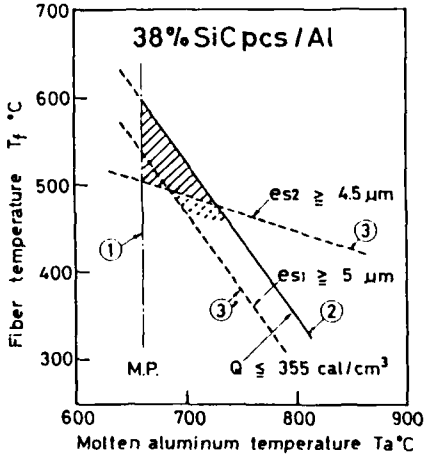


Fig.6 Optimum process temperatures (shadowed area) determined by indirect squeeze casting and tensile testing (SiC_{PCS}/Al, p=49 MPa), where Q and the enthorpy introduced the composite per unit volume and e means the gap between-fibers to allow a molten metal flow.

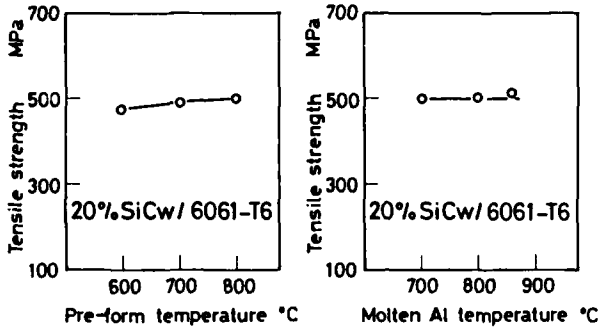


Fig.7 Effect of process temperatures on the tensile strength of 20% silicon cabide whisker reinforced 6061 aluminum alloy-T6, fabricated by a direct squeeze casting.

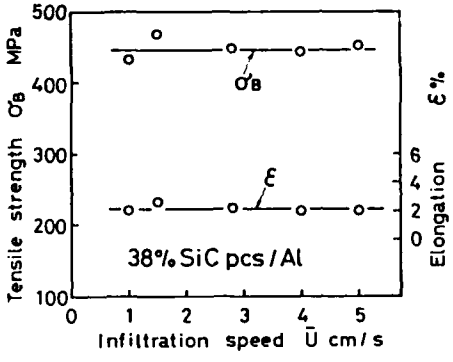


Fig.8 Effect of infiltration speed on tesile strength of SiC_{PCS}/Al composites fabricated under the same conditions as Fig.6.

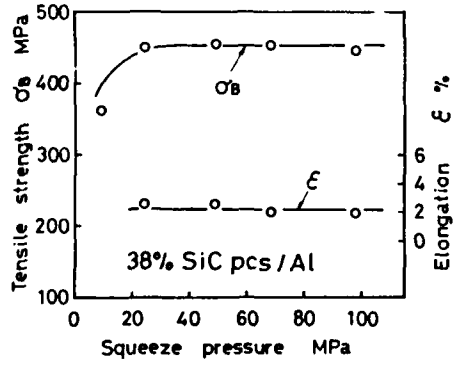


Fig.9 Effect of final squeeze on tensile strength of SiC_{PCS}/Al composite fabricated by indirect squeeze casting.

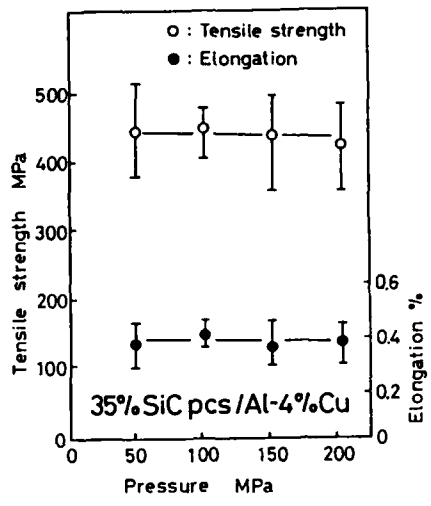


Fig.10 Effect of extreme high squeeze pressure up to 20,000 atomspheres on tensile strength of SiC_{PCS}/Al-4%Cu composites.

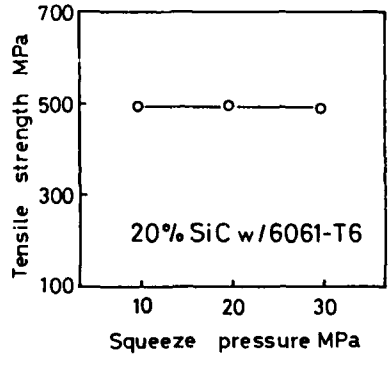


Fig.12 Effect of final squeeze pressure on tensile strength of SiC whisker/ 6061 alloy fabricated by direct squeeze casting.

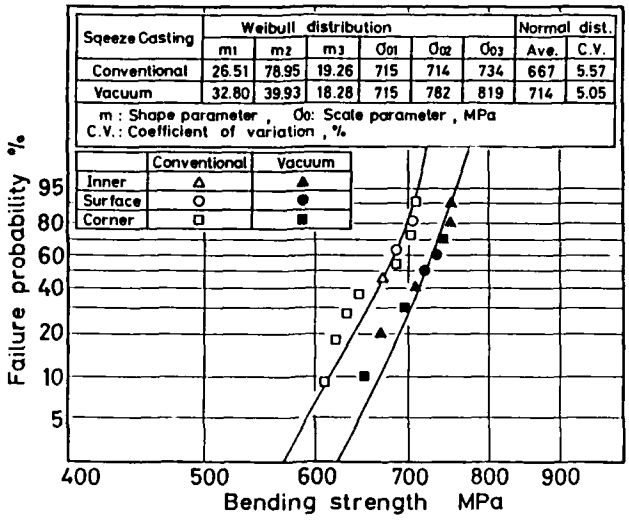


Fig.13 Comparison of strength distribution of 4mm thickness composites between conventional and vacuum squeeze casting, showing defect type, Weibull parameters and normal distribution parameters.

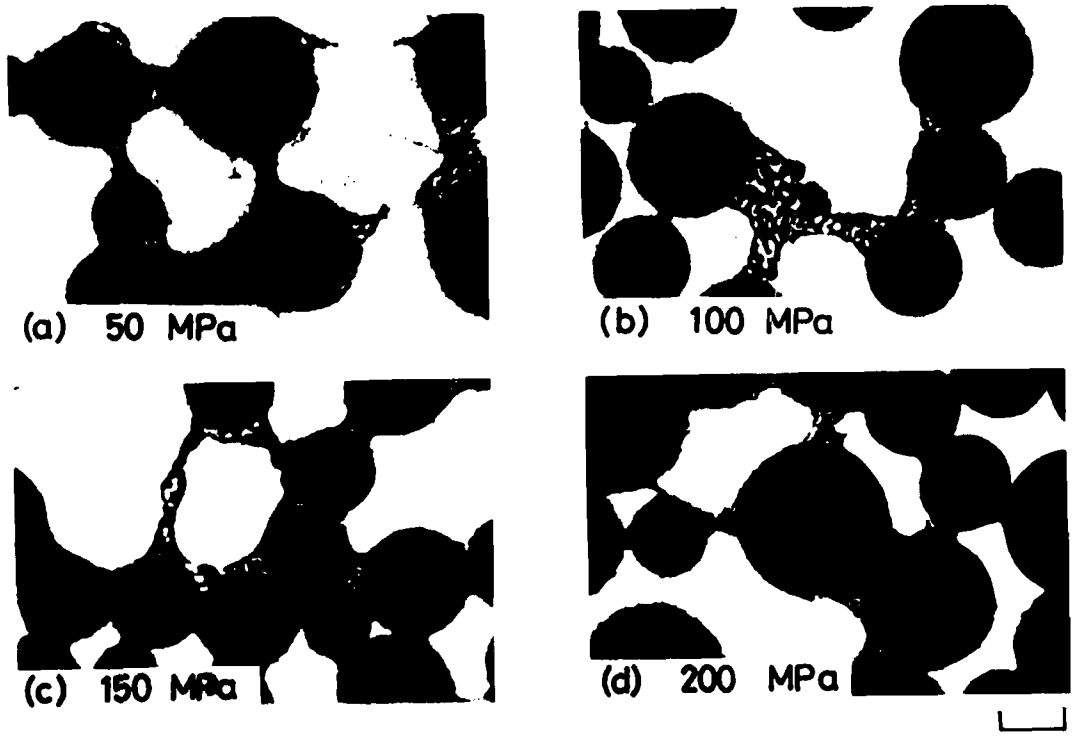


Fig.11 Microstructures of SiC_{pcs}/Al-4%Cu composites fabricated by squeeze casting under high pressures, showing no visible change of structure.

MECHANICAL PROPERTIES OF ALUMINUM ALLOYS REINFORCED WITH CONTINUOUS FIBERS AND DISPERSOIDS

Sen-ichi Yamada, Sin-ichi Towata, Hajime Ikuno
Toyota Central R&D Labs., Inc.
Nagakute, Aichi, 480-11, Japan

ABSTRACT

A hybrid technique, which can break through the problems during MMCs fabrication by squeeze casting, is developed. The addition of dispersoids improved the strength of multifilament type fiber-reinforced composites in the longitudinal and transverse directions. Several hybrid effects on the composite strength are investigated.

INTRODUCTION

Metal matrix composites are expected as aerospace and automotive materials, because of their light weight, high modulus and high strength. An important aspect of squeeze casting is its fabricability to near net shape of composites. There are three important factors for obtaining high strength composites in this process. At first, the fiber/matrix compatibility is an important factor. Many studies have been reported on the reaction between fibers and matrix[1,2]. The reinforcement-matrix interface behavior is the most outstanding problem for getting good transverse strengthened composites. However, higher strength composites are not expected, if the fibers are subjected to a chemical damage by the alloying elements in the matrix alloy. However, the performance of MMCs is influenced by not only the fiber-matrix reaction but also the morphology of precipitates in the matrix. The crack propagation in composites is considerably affected if the diameter of reinforcing fibers are comparable to that of the precipitates[3].

The toughness of matrix has a major influence on crack propagation of MMCs. The strength of pure aluminum matrix composites is the highest. Brittle fracture is caused by coherence between fibers and precipitates, even if there is no interaction zone on the fiber surface.

Improper fiber distribution, particularly fiber to fiber contact can cause a decrease of the composite strength, since it induces initiation of cracks.

In the present study, the effects of these three factors on the fracture behavior of the composites were investigated.

EXPERIMETAL PROCEDURE

Si-Ti-C-O fibers produced from organometallic polymer (11μm dia.) were incorporated in pure aluminum, Al-4%Cu, Al-3%Si and Al-5%Mg alloy matrices by squeeze casting. Whiskers or particulates were beforehand mixed with fiber yarns. The fiber cut to 150 mm length were immersed in ethyl alcohol and longitudinally inserted into a steel pipe with several windows on its side walls. Preheating of the fibers and removing of the sizing resin were carried out in nitrogen gas atmosphere within an electric furnace at 1030 K (about 60 K above the liquidus temperature of the matrix alloys). The pouring temperature of the molten aluminum alloy was also about 1030 K. The casting pressure and time were 90 MPa and 60 s, respectivity. The speed of the punch operation was 5 mm/s.

MICROSTRUCTURE OF COMPOSITES

The transverse cross section of the composites are shown in Fig. 1. It can be seen that neither voids nor interaction layers among the fibers and matrices were shown in the cross sections. The distribution of fibers was fairly uniform in all the composites. In the conventional fiber composites, many contacts between fibers were observed in sharp contract with hybrid composites. In the particulate hybrid, almost all of the particulates were distributed around the fibers. But in the whisker hybrid, whiskers were distributed in the space between the fibers with random orientation and were locally coalesced.

LONGITUDINAL AND TRANSVERSE STRENGTH

The longitudinal flexural strength of the composite are shown in Fig. 2 (a). The flexural strength of pure aluminum MMCs particulate hybrids was about 1.5 GPa, which was about three times as large as than that of conventional composites, although they have lower fiber volume. The strength of the Al-4%Cu matrix particulate hybrids was about 1.0 GPa and the whisker hybrid was about 0.75 GPa.

The transverse flexural strengths of the composite are shown in Fig. 2 (b). The strengths of Al-4%Cu matrix whisker hybrids was the highest 0.35 GPa, which was about two times as large as that of conventional composite of Al-4%Cu matrix.

TOUGHNESS OF MATRIX

Solidification mechanism is important factor for practical application of MMCs. The flexural strengths of the composites was shown in Fig. 2. The strengths of particulate or whisker hybrid MMCs were comparable with the ROM strength value in spite of the use of Al-Cu alloy matrix. They were 0.3 or 0.4 GPa strength for the transverse direction to the fibers. In the particulate hybrid, small dimple pattern were observed in the matrix region and the fibers surface. It was indicated that strong fiber-matrix bonds were achieved.

As mensioned before[4], the Al-Cu alloy matrix composite indicated a lower longitudinal strength, although there were no reaction zone in the interface. Because the eutectic $CuAl_2$ was found in the narrow spaces joining two fibers region. However, there is no joining precipitates between the fibers in the hybrid composite.

In Al-Cu matrix composite, the solidification will start in the center part of the inter-fiber spaces and it will progress towards the fiber surfaces. As a consequence, the copper concentration increases near the fiber surface[5]. Fig. 3 shows that the eutectic phase tends to solidify adjacent to the fiber surfaces. Copper rich zones around the Tyranno fibers which indicate the $CuAl_2$ is noticeable around the fiber surface or bridging the fibers. In the hybrid composite, the copper rich zones coexist with dispersoids. As shown in this figure, the primary aluminum solidification occur between fibers followed by the progress of solidification, towards the fiber. Then, most of the eutectic phases are separated by the addition of dispersoids.

COMPATIBILITY

Table 1 shows the longitudinal flexural strength by the three point flexural tests. The strength of convensional composites was 0.5 GPa for pure aluminum matrix, 0.45 GPa for Al-4%Cu matrix, 0.35 GPa for Al-3%Si matrix, and 0.15 GPa for Al-5%Mg matrix composite. However, hybrid composite provided higher strengths. There was no fibers pulled out observed in aluminum alloy matrix composite.

The tensile strength was measured by use of fibers extracted from the composites. The monofilament fibers for the test were prepared by dissolving the matrix with a warm 10%NaOH solution and ultrasonic cleaning of the extracted fibers. the strength of fibers extracted from pure aluminum and Al-4%Cu matrix composite decreased a little from the original strength, while that of the extracted fibers from Al-5%Mg matrix composite decreased remarkably. In the Al-3%Si matrix composite, the degradation of fiber strength was larger in conventional composite than in hybrid composite.

In Table 1, σ_F is the flexural strength and σ_{ROM} is the strength calculated from simple rule of mixture by using the extracted fiber strength. As shown in this table, the σ_F/σ_{ROM} ratios were substantially lower than the ROM values in conventional composite.

These results suggest that the fracture of the composites is influenced by the characteristic of the matrices.

THERMAL CYCLE FATIGUE

A wide gap of the thermal expansion coefficient between fiber and matrix cause the thermal fatigue, for example, splitting at the fiber/matrix interface. Therefore, the thermal fatigue resistance is important factor in the high temperature use of MMCs. Fig. 4 shows the residual expansion of the transverse direction after thermal cycle (room temperature to 573 K). In the conventional composite, the residual expansion increased during the thermal cycling. However, the hybrid composite did not show the dimensional change after 1000 cycles. The degradation of strength is also substantially small in the hybrid composite. It was revealed in this result that the hybrid composites is stronger against the thermal cycle fatigue.

SUMMARY

New types of fiber-reinforced aluminum alloys, in which whiskers and/or fine particulates are distributed among the continuous fibers, were developed by a squeeze casting process. By the addition of whiskers and/or particulates, both the longitudinal and the transverse strengths were substantially improved. The effects of addition of whiskers and/or particualtes are; the first is separation of continuous fibers, which leads to the inhibition of the direct fiber-to-fiber contact. The direct contact of fibers causes the inperfection of infiltration of molten metal and the stress concentration of fiber failure. The second is the micro-segregation of alloying elements in aluminum alloy matrix around the whiskers or the particulates. This leads to the inhibition of the

growth of the brittle secondary phase onto the continuous fibers. The third is the chemical reaction between the continuous fiber and the unfavorable alloying element was controlled by the addition of whiskers or particualtes.

REFERENCES

(1) B. Blankenburg ; J. Austr. Inst. Met., 14 (1969), 236.
(2) M. F. Amateau ; J. Composite Materials, 10 (1976), 279.
(3) S. Towata and S. Yamada ; J. Japan Inst. Metals, 50 (1986), 336.
(4) S. Towata and S. Yamada ; Trans. JIM, 27 (1986), 709.
(5) J. A. Cornie, A. Mortensen, M. N. Gunger and M. C. Flemings ; Proc. of 5th Inernat. Conf. on Composite Materials, ICCM-V, (1985), 809.

Table 1 Strengths of Fiber Extracted from Composites and Strengths Predicted by ROM

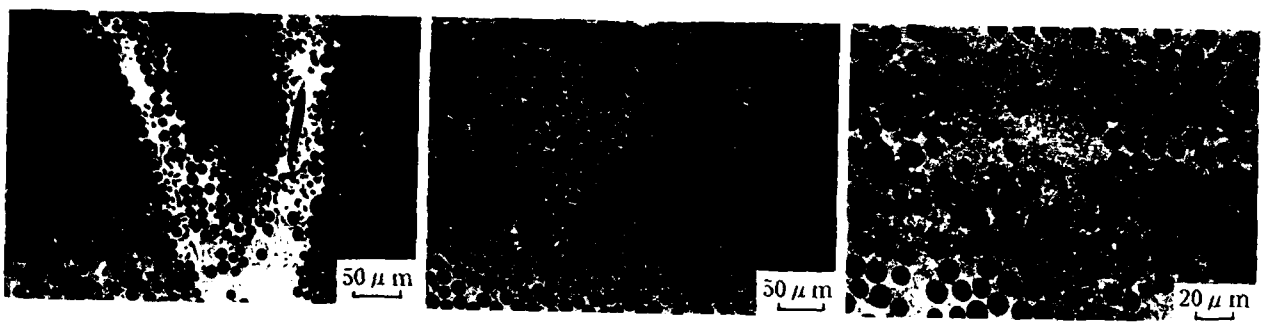
Specimen	V_f	σ_f	σ_m	σ_F	σ_{ROM}	σ_F/σ_{ROM}	Free Energy
As Received	-	2.42	-	-	-	-	-
Pure Al Non Hybrid	0.7	2.05	0.05	0.50	1.45	0.3	Al_2O_3; - 270 kcal/mol
Pure Al Hybrid	0.5	1.95	0.05	1.40	1.00	1.4	
Al-4%Cu Non Hybrid	0.7	1.10	0.19	0.45	0.83	0.5	Cu_2O; - 80 kcal/mol
Al-4%Cu Hybrid	0.5	1.62	0.19	1.00	0.91	1.1	
Al-3%Si Non Hybrid	0.7	0.87	0.13	0.35	0.65	0.5	SiO_2; - 200 kcal/mol
Al-3%Si Hybrid	0.5	1.36	0.13	0.60	0.75	0.8	
Al-5%Mg Non Hybrid	0.7	-	0.22	0.15	-	-	MgO; - 290 kcal/mol
Al-5%Mg Hybrid	0.5	0.40	0.22	0.40	0.31	1.3	

V_f : Volume fraction of fiber

σ_m, σ_f : Strength of matrix, fiber(GPa)

σ_F : Flexural strength of composite(GPa)

σ_{ROM} : Strength of composite by ROM(GPa)



70%Fiber/Al-4%Cu 50%Fiber+4%SiC_p/Al-4%Cu 43%Fiber+7%SiC_w/Al-4%Cu

Fig. 1 Scanning Electron Micrographs of Transverse Cross Section

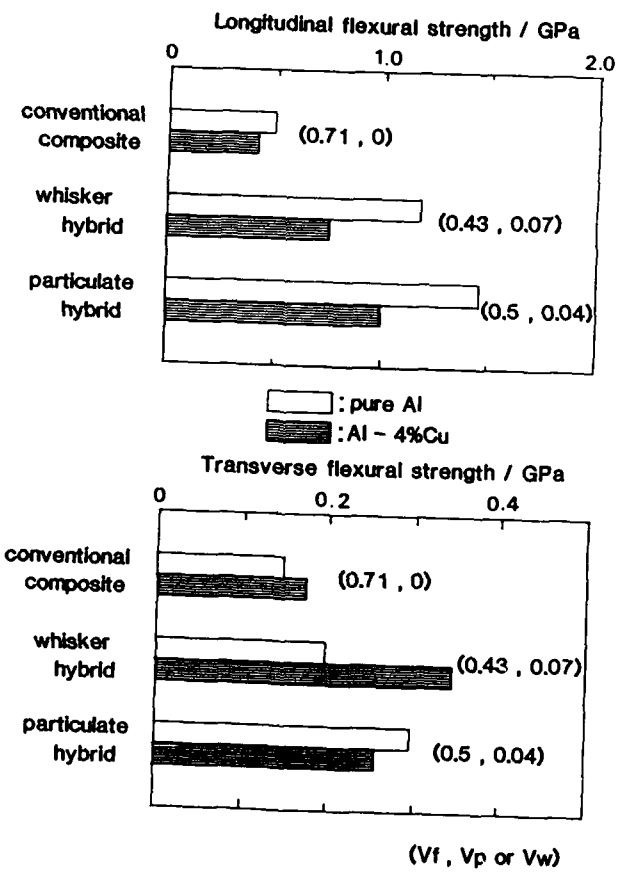
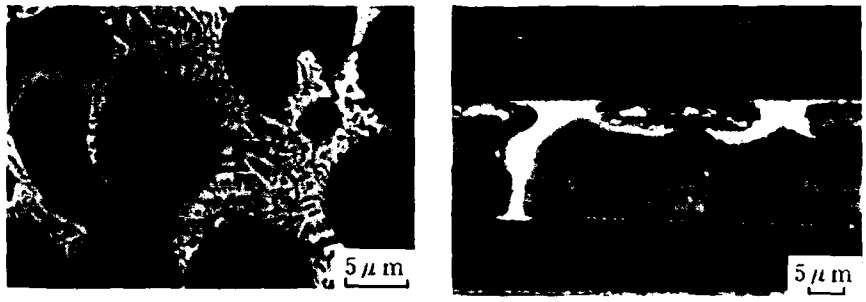
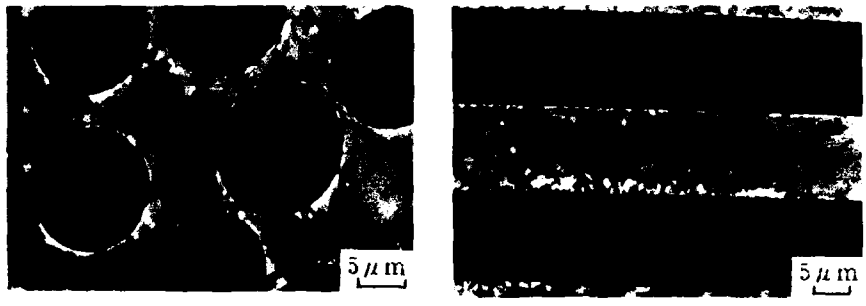


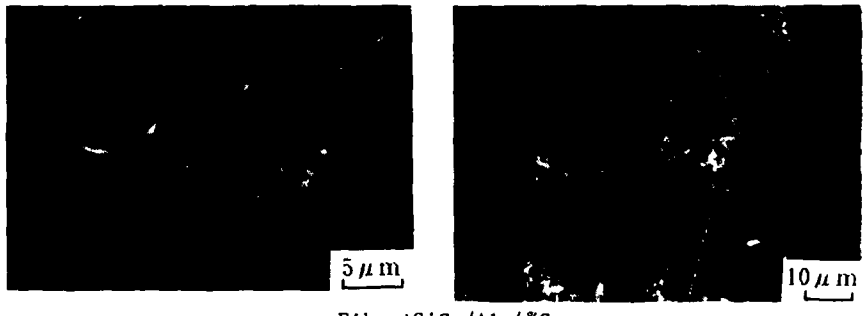
Fig. 2 Strength of MMCs



Fiber/Al-4%Cu



Fiber+SiC_p/Al-4%Cu



Fiber+SiC_w/Al-4%Cu

Fig. 3 Back-scattered Electron Images of Cross Section
(Bright image indicates Cu rich zone)

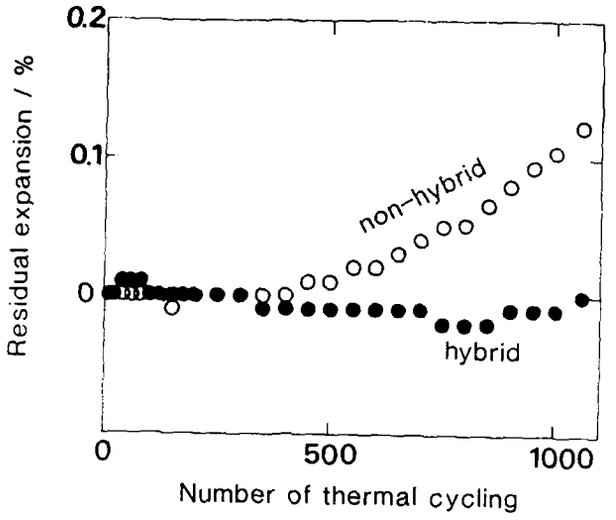


Fig. 4 Residual Expansion after Thermal Cycling (Transverse Direction)

MANUFACTURING OF COMPOSITES BY SQUEEZE CASTING

Suresh K. Verma, John L. Dorcic
IIT Research Institute
Chicago, Illinois 60616-3799 USA

ABSTRACT

Squeeze casting is the term designating solidification of liquid metal under pressure. Pressure during solidification helps achieve defect-free castings with improved metallurgical properties. Through the work described here, this process has been adapted to manufacture composite materials at affordable costs. A preheated, porous ceramic preform is placed in a die cavity, which is later filled with the liquid melt, and pressure is applied. The pressure, in this case, helps infiltrate the liquid metal into the pores of the ceramic preform, giving a sound metal-ceramic composite. These developments are discussed to show the usefulness of the squeeze casting process for manufacturing metal-ceramic composites economically.

THE EMERGENCE OF COMPOSITE MATERIALS with improved properties compared to those of conventional materials has raised hopes to manufacture complex-shaped components. However, cost remains a barrier to adopting these composites for noncritical applications. To make components at affordable costs, IITRI has developed a near net shape process, called squeeze casting, to manufacture ceramic-metal composites that offer economical and technological promise for a number of applications. The paper in particular explains the squeeze casting process and significant results that have led to the establishment of the squeeze casting process variables. It also provides details of the requirements for adapting squeeze casting to composite making. As expected, the quality and cost of the ceramic preform dictate the end use of the manufactured components. For this reason, a section on preform properties and currently available preforms is also provided. Finally, the available properties of the squeeze castings and composites are discussed to establish economical manufacturing routes for complex composite components.

SQUEEZE CASTING (1,2)*

With the current emphasis on reducing materials consumption through virtually net shape processing and the demand for higher-strength parts for weight savings, the emergence of squeeze casting as a production process has given materials and process engineers a new alternative to the traditional approaches of casting and forging. By forging liquid metals while they solidify, near net shapes can be achieved in sound, fully dense castings.

Squeeze casting has been successfully applied to a variety of ferrous and nonferrous alloys in traditionally cast and wrought compositions. Parts made to date include aluminum alloy pistons for engines and disk brakes; automotive wheels, truck hubs, barrel heads, and hubbed flanges; brass and bronze bushings and gears; steel missile components and differential pinion gears; and a number of parts in cast iron including ductile iron mortar shells.

Squeeze casting is simple and economical, efficient in its use of raw material, and has excellent potential for automated operation at high rates of production. The process has proved to generate the highest mechanical properties attainable in a cast product. The microstructural refinement and integrity of squeeze casting products is desirable for many critical applications.

PROCESS DESCRIPTION (3) - As shown in Figure 1, squeeze casting consists of metering liquid metal into a preheated, lubricated die and forging the metal while it solidifies. The load is applied shortly after the metal begins freezing and is maintained until the entire casting has solidified. Casting ejection and handling are done in much the same way as in closed-die forging.

The high applied pressure (typically 100 MPa or 15 ksi) is enough to suppress gas porosity

*Numbers in parentheses designate references at end of paper.

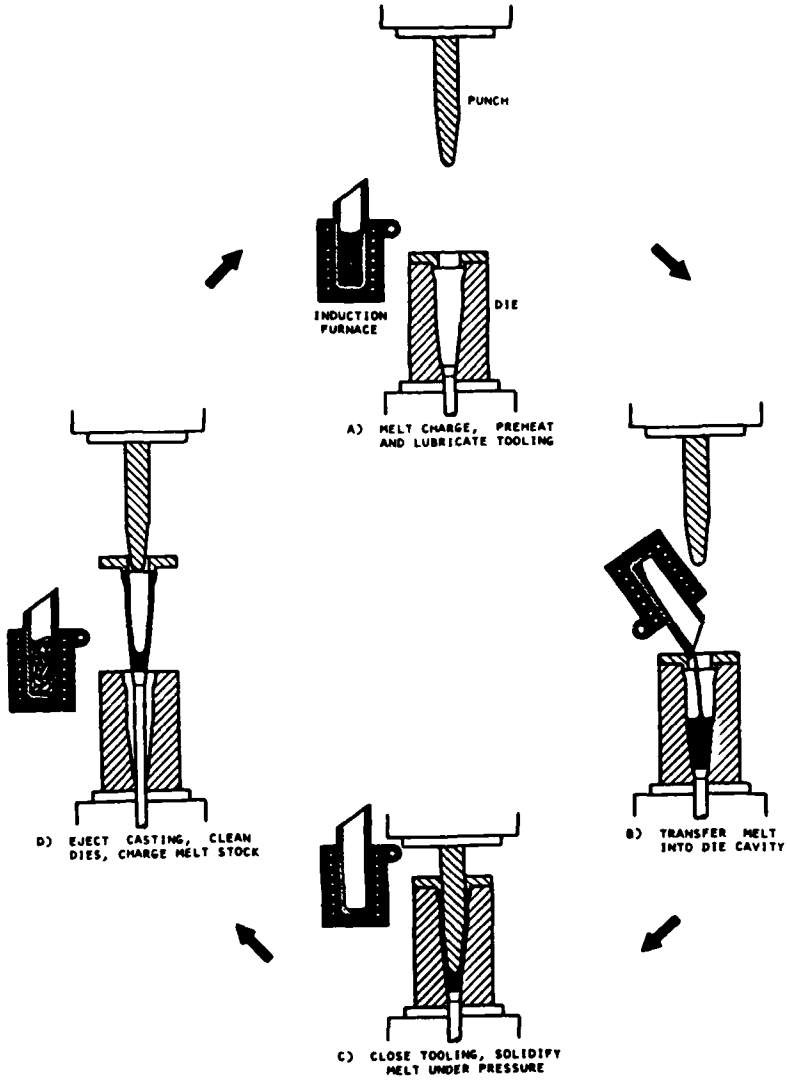


Fig. 1. Squeeze casting processing cycle, shown above for the ductile iron mortar shell seen to the extreme left in Fig. 2.[3]

except in extreme cases whereupon standard degassing treatments are used. The tendency towards shrinkage porosity is limited by using a bare minimum of superheat in the melt during pouring. This is possible in squeeze casting because melt fluidity--requiring high pouring temperatures--is not necessary for die fill, the latter being readily achieved by the high pressure applied. In heavy sections of the casting, which are particularly prone to the incidence of shrinkage porosity, the applied pressure squirts liquid or semi-liquid metal from hot spots into incipient shrinkage pores to prevent pores from forming. Alloys with wide freezing ranges accommodate this form of melt movement very well, resulting in sound castings with a minimum of applied pressure.

PROCESS PARAMETERS - While the relative importance of the following parameters may vary depending on the nature of the application, they all play an important role in ensuring the quality of the squeeze-cast part. It is important to precisely control the process parameters to maintain the quality of the manufactured parts.

The important process variables are:

- Melt quality
- Casting temperature
- Tooling temperature
- Time delay during die closing and pressure application
- Pressure level
- Pressure duration.

These variables are critical to the quality and reproducibility of the manufactured part, and can vary from component to component. Failure to control these variables can result in many defects, such as oxide inclusions, porosity, extrusion segregation, blistering, underfill, cold laps, hot tearing, sticking, case bonding, and extrusion bonding.

The squeeze casting process has been explored for a number of applications using various metals and alloys. The parts shown in Figure 2 include an aluminum dome, a ductile iron mortar shell, and a steel bevel gear. Other parts that have been tried are stainless steel blades, superalloy disks, aluminum automotive wheels and



Fig. 2. Squeeze-cast parts produced by IITRI.

pistons, and gear blanks made of brass and bronze. Squeeze-cast aluminum wheels are already commercially available, and high-strength aluminum pistons are expected to be commercialized by a number of U.S. manufacturers.

SQUEEZE CASTING ADVANTAGES (1-6) - Besides the densification achieved, there are several reasons why squeeze casting produces superior properties. The moderate applied pressure causes intimate contact between the solidifying casting and the die for a tenfold increase in heat transfer rate over permanent mold casting. This results in relatively fine grains in the casting. Fine grain size is also promoted by the large number of nuclei formed due to the low casting temperature and the elevated pressure. Further, since die filling in squeeze casting does not require high melt fluidity, a number of wrought alloys can be squeeze cast. Again, pressurized solidification with rapid heat transfer tends to minimize the segregation that wrought alloys are usually prone to.

The tensile properties reported by various sources for ferrous and nonferrous materials produced by squeeze casting show that, in the majority of cases, the properties (Table 1) are comparable to forgings (3-10).

In an analysis made by IITRI previously (3), a side-by-side comparison was made between squeeze casting and permanent mold casting for B-132 Al pistons. As seen in Figures 3 and 4, squeeze castings are sounder, with a pore-free, fine-grained, nearly equiaxed microstructure compared to permanent mold pistons. In particular, a thin case forms to 0.080 in. below the punch which is characterized by an unusually fine cast structure (Figure 4). This is caused by a combination of high pressure (resulting in undercooling and a greater number of nucleation sites) and rapid heat extraction into the punch.

The heat transfer rate was measured by Nishida and Matsubara (4) for squeeze casting and found to be approximately ten times as fast as in gravity permanent molding. Epanchintsev (5) measured a cooling rate of 140°C/s (250°F/s) when squeeze casting an aluminum alloy in steel dies heated to approximately 204°C (400°F). Spear and Gardner (6) documented the dendrite arm spacing for several commercial aluminum alloys. Extrapolation of their data would indicate that a melt cooled at the rate of 140°C/s would have a dendrite arm spacing of 8.94 μm or 0.00035 in. This is not far from the present observation of approximately 0.0002 in. size spacing near the head surface (see Figure 4) of the squeeze-cast pistons. This observation would, in fact, correspond to a cooling rate of 750°C/s (1350°F/s). This implies that the 0.080 in. "case" immediately below the punch, comprising melt poured at ∿650°C (∿1200°F), is quenched to the punch temperature of ∿204°C (∿400°F) in approximately 0.6 s.

In practice, squeeze castings made with ±0.030 in. tolerance on the as-cast head location can be machined to the finished tolerances and still retain in excess of 0.020 in. of the ultrafine-grained case. The benefits of this unique squeeze-cast structure, however, are yet to be properly utilized in industry.

METAL-CERAMIC COMPOSITES (11-12)

Metal-matrix composites (MMCs) offer promise in high technology areas where good strength at high temperature, good structural rigidity and dimensional stability, light weight, and ready fabricability are dominant requirements. The newly developed composites and their potential applications are shown in Table 2. Many MMCs have the structural capability of some metals, i.e., to withstand high temperatures, because of incorporation of fibers. Currently, research at IITRI and elsewhere is being focused on many lightweight composite metal systems, some of which are:

- Boron/aluminum (B/Al)
- Graphite/aluminum (Gr/Al)
- Graphite/magnesium (Gr/Mg)
- Aluminum oxide/aluminum (Al 0 /Al, FP/Al)
- Silicon carbide/aluminum (SiC/Al)
- Silicon carbide coated boron/titanium

Currently, the cost of composites may be excessive which prohibits their use in applications where economical materials are sought. It is, of course, expected that cost of raw materials (fibers) will be reduced with time as manufacturing processes are improved or as increased consumption enables higher volume production. Current and projected costs for fibers are shown in Figure 5. Cheaper preforms are also available but their potential has not been explored. It is realized that the cost of preforms or fibers would not change significantly immediately; the steps needed to convert the raw materials into usable composites, however, can be reduced significantly if squeeze casting is adopted over hot pressing.

COMPOSITE MAKING BY SQUEEZE CASTING (2) - Normally in metal-ceramic composites, fibers (continuous or short fibers, particles, or wires) are incorporated to reinforce a ductile matrix, and then the mixtures containing the required fibers (usually 10-35% fiber) are hot pressed to produce usable composites. Not only is the cost of processing prohibitive for many noncritical applications, but the properties of the compnents are not as predictable as desired because of a number of variables in the processing method (hot pressing) which cannot generally be precisely controlled.

The squeeze casting process, if adopted, will require a porous (fibers of different density) preform to be held in the casting mold by a fixture. The molten metal is forced into the mold at a predetermined pressure and held for a brief period. The fibrous preform is quickly and totally infiltrated by the molten metal resulting in a fiber-reinforced part. This process is much more economical compared to hot pressed composites and is in commercial use

Table 1 - Comparative Properties of Commercial Wrought and Cast Alloys (3,7-10)

Alloy	Process	Tensile Strength MPa	Tensile Strength ksi	Yield Strength MPa	Yield Strength ksi	Elongation, %
356-T6 Aluminum	Squeeze casting	309	44.8	265	38.5	3
	Permanent mold	262	38.0	186	27.0	5
	Sand casting	172	25.0	138	20.0	2
6061-T6 Aluminum	Squeeze casting	292	42.3	268	38.8	10
	Forging	262	38.0	241	35.0	10
CDA 377 Forging Brass	Squeeze casting	379	55.0	193	28.0	32.0
	Extrusion	379	55.0	145	21.0	48.0
CDA 624 Aluminum Bronze	Squeeze casting	783	113.5	365	53.0	13.5
	Forging	703	102.0	345	50.0	15.0
CDA 925 Leaded Tin Bronze	Squeeze casting	382	55.4	245	35.6	19.2
	Sand casting	306	44.4	182	26.4	16.5
357 S.S. (Annealed)	Squeeze casting	614	89.0	303	44.0	46
	Sand casting	400	58.0	241	35.0	20
	Extrusion	621	90.0	241	35.0	50
321 S.S. (Heat Treated)	Squeeze casting	1063	154.2	889	129.0	15
	Forging	1077	156.2	783	113.6	7



Fig. 3. Comparison of squeeze-cast and permanent mold E-132 Al pistons near open end of skirt. Microstructure of casting near the edge in contact with mold: (a) permanent mold casting, (b) squeeze casting. (Note: Preferred orientation of coarse columnar dendrites, voids, and segregation in permanent mold castings while squeeze castings show fine columnar dendrites resulting from effective constitutional supercooling.)



(a) (b)

Fig. 4. Comparison of squeeze-cast and permanent mold E-132 Al pistons near the edge in contact with the punch. Microstructure of (a) permanent mold casting, showing preferred columnar dendritic structure; (b) squeeze casting, showing ultrafine, equiaxed nondendritic structure.

Table 2 - Representative Metal-Matrix Composite Materials (12)

Matrix	Fiber	Potential Applications
Aluminum	Graphite	Satellite, missile, and helicopter structures
Magnesium		Space and satellite structures
Lead		Storage battery plates
Copper		Electrical contacts and bearings
Aluminum	Boron	Compressor blades and structural supports
Magnesium		Antenna structures
Titanium		Jet engine fan blades
Aluminum	Borsic	Jet engine fan blades
Titanium		High-temperature structures and fan blades
Aluminum	Alumina (FP)	Superconductor restraints in fusion power reactors
Lead		Storage battery plates
Magnesium		Helicopter transmission structures
Aluminum	Silicon Carbide	High-temperature structures
Titanium		High-temperature structures
Superalloy (Co-base)		High-temperature engine components
Superalloy	Molybdenum	High-temperature engine components
Superalloy	Tungsten	High-temperature engine components

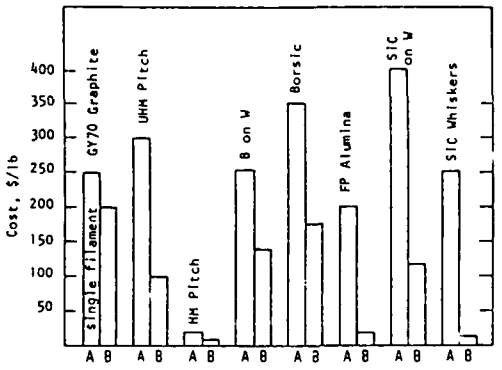


Fig. 5 - Current and projected costs for fibers (12). A = 1978; B = 1985-1990

(e.g., an improvement of 15 to 20% in room-temperature strength of an automotive piston has been noted over the permanent mold process for aluminum-silicon alloys of near-eutectic compositions).

CERAMIC FIBERS FOR COMPOSITE MAKING - Before discussing the composite making process in detail, it is appropriate to discuss the ceramic fibers--their composition, cost, and physical properties. Although various compositions of fibers are available on the market, an alumina-silica composition is taken to illustrate the processing of ceramic fibers and the advantages of using fibers for casting of composites.

Ceramic fibers of alumina-silica composition are made by several techniques (13,14). In one process the fiber is manufactured by melting the raw materials in an electric arc furnace at temperatures above 3600°F (200°C) to form a molten stream. The molten stream is then atomized using high pressure air impingement or spinning wheels. The discontinuous fibers generally have a composition of about 48% alumina and 52% silica. These fibers have an average mean diameter of 2.0 to 4.0 μm, depending on the exact chemistry of the material and whether they are spun or blown. The aspect ratio (the ratio of length to diameter) of the fiber ranges from 200 to over 1000. The particulate, called shot, is the unfiberized portion of the composition and normally represents 40 to 50% by weight. Means exist to remove the particulate so that it represents no more than 2% of the weight.

Another ceramic fiber process produces a discontinuous fiber of higher alumina content which offers greater temperature resistance and better physical properties affecting composite performance. This ceramic fiber is made by a chemical process where a fiber is drawn from a solution. The drawn chemical solution process results in a polycrystalline fiber whereas the melt-produced fiber is amorphous. The polycrystalline fiber has the chemistry that is referred to by ceramists as "mullite." Table 3 shows the typical chemistries of these basic ceramic fibers.

Table 3 - Typical Chemical Analysis of Ceramic Fiber (13)

Material	Fiberfrax Amorphous Ceramic Fiber	Fiberfrax Polycrystalline Ceramic Fiber
Al_2O_3	49.2%	72.0%
SiO_2	50.5	27.0
Na_2O	0.2	0.10
Fe_2O_3	0.06	0.02
TiO_2	0.02	0.001
Leachable chlorides	<10 ppm	<10 ppm

As would be expected, fiber properties depend on their manufacturing routes. A detailed study on the variance of mechanical properties of some fiber compositions from different manufacturing routes is not available, but the physical properties fundamental to composite and reinforcing applications are shown in Table 4. (For comparison, both carbon fibers and silicon carbide whiskers have also been included.)

The Fiberfrax and Fibermax ceramic fibers are discontinuous, and fiber length and diameter dimensions will vary. The length can be modified both in manufacturing and in subsequent processing. For example, the fibers can be modified to narrow the length distribution via chopping or can undergo a process beneficiation to remove much of the particulate. Coatings can be applied to enhance specific properties. In polymer composites, a silane or other coupling agents are often applied to the fibers to improve the fiber/matrix interface bonding.

PREFORM FOR COMPOSITE MAKING IN SQUEEZE CASTINGS - The fibrous preform is an important step in making metal matrix composites by the squeeze casting method. Preforms are made in near net shapes and, because they are made of ceramic fibers (Al_2O_3 and SiO_2), machining of the preform requires special skills. Preforms are designed to provide the needed performance at the lowest fiber concentrations in order to minimize costs. Ceramic fiber volume (percent of total part volume), chemical and physical characteristics of fiber(s), fiber direction or orientation, and binder levels affect the preform performance. These factors--as well as shape, tolerance, and volume--affect preform cost and final product costs. Preform composition, fiber volume, fiber type, and degree of fiber orientation are all essential to good metal matrix parts using the squeeze casting method. Figure 6 shows some typical preforms, and Figure 7 shows the dense structure of a Saffil structure penetrated by aluminum alloy with no porosity or gas bubbles.

Table 4 - Typical Physical Properties of Various Fibers (13)

Property	Fiberfrax	Fibermax (Mullite)	Carbon Fibers	Silicon Carbide Whiskers
Tensile Strength, ksi (MPa)	250 (1725)	120 (830)	550 (3800)	1200 (8300)
Young's Modulus, msi (GPa)	15 (105)	22 (150)	33 (230)	80 (550)
Density, lb/in^3 (g/cm^3)	0.10 (2.7)	0.11 (3.0)	0.06 (1.8)	0.11 (3.1)
Continuous Use Limit in Air, °F (°C)	2300 (1260)	3000 (1650)	600 (315)	2550 (1400)
Fiber Diameter, mils (μm)	0.10 (2.5)	0.12 (3.0)	0.28 (7.0)	0.01 (.3)
Fiber Length, mils (μm)	30 (762)	30 (762)	Continuous	4.9 (125)
Price, $/lb ($/kg)	1.00 (2.20)	16.00 (37.50)	21.00 (46.30)	300 (660)

The type and amount of fiber is based not only on cost but also on the need for wear resistance, seizure resistance, yield strength, tensile strength, fatigue strength, stiffness, dimensional stability, thermal resistance, vibration and acoustical characteristics, corrosion resistance, and the operating environment of the particular part. Fiber orientation indicates the direction in which the fibers are arranged in the preform. It is believed that for improved wear resistance in an aluminum part, fiber orientation is not essential; the fibers could either be normal or parallel to the surface being enhanced. Performance is a function of the fiber's basic properties, volume, and degree of orientation (11). In general, the higher the fiber volume, the better the performance. For most commercial applications, however, there are trade-offs in cost versus performance that a designer must take into account. As a compromise, for example, hybrid preforms using the alumina-silica Fibermax and Fiberfrax fibers may be possible. For improved wear resistance, a fiber volume of less than 10% is generally used; however, for high temperature fatigue resistance, cost-effective fiber volumes may be as high as 27%. A number of ceramic preforms are available; some of them are listed in Table 5.



Fig. 6 - Typical preforms used in study on composite making via squeeze casting.

PREFORM PREPARATION - In order to preserve the shape of the preform, pressure levels necessary to form sound castings can become critical and need careful control. Equally important is control of the preheating of the preform in order to avoid freezing of the liquid on the surface of the preform. This could result in incomplete infiltration in the final cast composite. Heating of the preform is often necessary to achieve sound casting of the composites.



Fig. 7 - Cross-section of an Al/Saffil composite. Note: Even the micron-size pieces are fully encased in aluminum with no microvoids or gas pockets.

Table 5 - Ceramic Fibers Available for Squeeze Casting Aluminum MMC Components

Trade Name	Composition, vol%	Manufacturer
Saffil	$95Al_2O_3$-$5SiO_2$	Chemical Industries, Ltd. (U.K.)
Kaowool 17C	$81Al_2O_3$-$19SiO_2$	Babcock & Wilcox
Kaowool 3000	$65Al_2O_3$-$35SiO_2$	Babcock & Wilcox
Kaowool 2600	$50Al_2O_3$-$50SiO_2$	Babcock & Wilcox
Kaowool--Blends of Saffil and Kaowool fibers		
Fibermax	$72Al_2O_3$-$27SiO_2$	Carborundum
Fiberfrax	$50Al_2O_3$-$50SiO_2$	Carborundum
FP/Fibers	99% Al_2O_3	DuPont
	Foamed Ceramic Preforms	
Durocel/SiC	99.9% β-SiC	ERG[a]
Durocel/SiN[b]	NA[c]	ERG
Durocel/BO_4	NA	ERG

[a]Energy Research and Generation, Inc.
[b]Available by special order.
[c]Data not available.

The shape and section thickness of the squeeze casting govern the duration of pressure necessary to ensure complete solidification under pressure. Beyond the minimum necessary duration, longer time delays have little benefit and can, in fact, cause wall cracking and punch retraction difficulty due to thermal contraction of the casting onto the rigid punch. The maximum duration of pressure, as a rule of thumb, is about 1 s/mm (0.04 in.) of section thickness.

PROPERTIES OF THE METAL-CERAMIC COMPOSITES (15,17)

The composites appear to be stable under long-term elevated temperature exposure. Apart from the difficulty experienced in conventionally machining these composites, and the implications of this on their wear and erosion resistance, the most notable features of the mechanical data collected are the excellent stiffness enhancement and the retention of tensile strength at elevated temperatures.

It has been found that a ceramic fiber preform composite can replace a Ni-Resist iron insert in an aluminum alloy diesel truck piston (15). Not only is the piston weight reduced by 5 to 10%, but the equivalent bond strength between the reinforced area and the piston alloy is superior to that of the Ni-Resist insert/aluminum alloy bond. Since the rate of heat transfer using a composite is decreased, the engine designer can move the upper piston rings closer to the crown or redesign the combustion chamber to operate at a higher temperature. **Composite technology could thus produce an engine that has significantly increased fuel economy as well as reduced emissions.**

Ceramic fiber composites in aluminum have also been evaluated for combustion bowls to eliminate thermal fatigue cracking due to high thermal cyclic compressive stresses, plastic deformation, and creep (14,16). Test results, as given in Table 6, show that better than a 90% improvement in yield strength is realized from using a ceramic fiber preform composite. In the future this may allow changes in combustion bowl design that achieves even better fuel usage.

Other data show similar results (14). Using a high-alumina ceramic fiber composite and a SiC whisker composite, the effect of fiber type and fiber volume can be observed. Although the yield strength of the two ceramic fiber types is much different, 20% ceramic fiber volume has about the same effect as 12% SiC whiskers at all temperatures (Table 7). However, the fiber cost difference is about 20:1.

The wear properties measured for squeeze cast composites and two other induction hardened steels show that wear properties are comparable. Dry sand/rubber wheel abrasion tests per ASTM G65, procedure B, were performed on two candidate BFV track shoe materials: an aluminum alloy A206-T7 with a reinforcement of an unknown reticulated ceramic foam and an aluminum alloy A206 with discontinuous fibers of Al_2O_3 and SiO_2. The currently used material, induction-hardened AISI 1345 alloy steel, was tested for comparison purposes. The results of the tests show that Al_2O_3-SiO_2 fiber metal matrix composite materials had abrasive wear resistance comparable to induction

Table 6 - Strength of Ceramic Fiber Reinforced Matrix F-332 Aluminum Alloy, T5 Condition (10)

Material	Room Temperature Interface Strength ksi	(MPa)	Tensile Strength ksi	(MPa)	0.2% Yield Strength ksi	(MPa)	Elongation, % (1 in. gauge)
Unreinforced	10.9	(75)	15	(103)	9	(62)	8
Ceramic fiber reinforced	25.5	(176)	21	(145)	18	(124)	1

Data from piston crown samples.

Table 7 - Yield Strength and UTS of Ceramic Fiber and SiC Whisker Reinforced Composites (10) (Al-Si-12Cu-Ni Alloy)

Fiber Volume	Strengths, ksi (MPa) 662°F (350°C) Y.S.	UTS	572°F (300°C) Y.S.	UTS	482°F (250°C) Y.S.	UTS
0%	10 (70)	17 (115)	-	10 (70)	5 (35)	8 (55)
12% Ceramic Fiber	-	-	-	-	10 (68)	11 (74)
12% SiC Whisker	29 (197)	33 (226)	22 (153)	26 (180)	14 (94)	18 (124)
20% Ceramic Fiber	27 (186)	29 (198)	22 (154)	22 (155)	16 (110)	16 (112)
20% SiC Whisker	39 (268)	41 (284)	30 (207)	34 (235)	24 (163)	26 (181)

hardened AISI 1345 steel. The detailed results are given in Table 8 and illustrated in Figure 8. Figure 9 presents additional data on the comparative wear properties of ceramic fibers with a SAE-242.0 and SAE-332.0 type aluminum composite (14). The data show a 70% improvement from the use of an alumina-silica ceramic fiber in the Toyota piston and an 80% improvement in the piston through the use of an alumina fiber. This improvement was achieved with only a small amount of fiber (5-7% fiber volume). A U.S. piston manufacturer (13) reports that a Ni-Resist cast iron insert can be replaced with a ceramic fiber insert resulting in equal performance and a 5-10% reduction in total piston weight. Even a small reduction in piston and connecting rod weights can have a significant impact on decreasing parasitic engine power losses. This is especially important in higher speed engines where inertial loads are critical. Unfortunately, the data base of ceramic-metal composites is very limited, and to realize the full potential of composites, a comprehensive data base is needed which could reveal many other applications.

SUMMARY

The review of squeeze casting and of composite making via squeeze casting reveals that this process is now acceptable to many corporations. Cost remains the issue for composite materials; however, the squeeze casting process provides an opportunity to take advantage of low-cost fibers and a well-defined, economical, net shape squeeze casting process. The interface problem between the fibers and matrix is not as critical as in hot-pressed composites because the porosity present in the preform (used for squeeze casting) is three-dimensional and is filled by liquid melt during casting. Because of the three-dimensional ceramic network in casting, properties of composites are improved considerably compared to hot pressed ceramic-metal compositions.

There is growing information that indicates ceramic fiber composites can provide needed performance and do so at costs which justify the

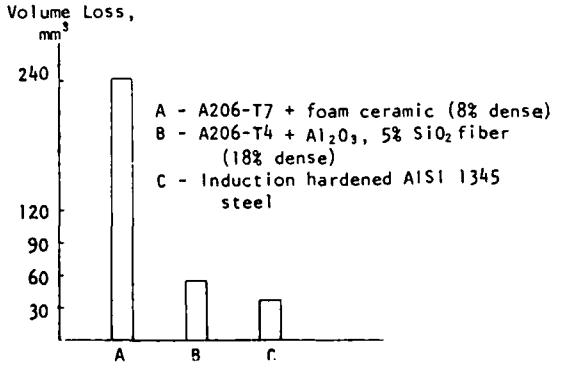
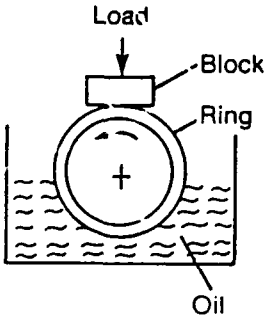


Fig. 8 - ASTM G65-B dry sand rubber wheel abrasion test on steel and ceramic fiber-reinforced aluminum.

Table 8 - Comparison of AISI 1345 and Squeeze Casting Composite Properties

Material	Specimen No.	Initial Weight, g	Final Weight, g	Weight Loss, g	Average Weight Loss, g	Average Volume Loss, mm
AISI 1345	1	114.4135	114.1204	0.2931	0.2779	35.4
	2	114.3513	114.0807	0.2706		
	3	114,3439	114.0739	0.2700		
A206-T7 + Ceramic Foam	1	43.7071	43.0129	0.6942	0.6885	242
	2	48.0881	47.4054	0.6827		
A206 + Al_2O_3 and SiO_2	1	47.6596	47.4943	0.1653	0.1653	55.9



TEST CONDITIONS

Block:	As noted
Ring:	Nodular C.I. HRC 43/45
Load:	150 lb (68 kg)
Surface Vel:	165 rpm (.3 m/s)
Lubricant:	10W40 Rotella T
Temperature:	375°F (190°C)
Duration:	5000 rev

Material	Orientation at Wear Face	Wear Scar Width, mils (mm)
332.0 Alloy	N/A	250 (6.3)
NiResist	N/A	80 (2.0)
CFR 332.0	Length	70 (1.8)
5% Al_2O_3-SiO_2	Ends	65 (1.6)
CFR 242.0	Length	65 (1.6)
5% Fiberfrax	Ends	65 (1.6)

Fig. 9. Wear property data comparison of aluminum versus composite.[14]

commercial use of metal matrix composites. The end-use composites would most likely be in the automotive industry (connecting rods, pistons), electronics, compressor blades, and various structural components where light weight, wear, and stiffness are key requirements. Many industries, however, should be able to use squeeze-cast composites for a variety of applications where economy and properties are key issues. Development of a data base is needed to identify other industrial applications for a range of metal-ceramic composites.

REFERENCES

1. S. Rajagopal, "Squeeze Casting: A Review and Update," J. Applied Metalworking, 1(4), 3-14 (1981).

2. M. A. H. Howes, "Ceramic Reinforced Metal Matrix Composites Fabricated by Squeeze Casting," paper presented at the Advanced Composite Conference, Dearborn, Michigan, December 2-4, 1985.

3. S. Rajagopal et al., "Squeeze Casting of Aluminum Alloy Heavy-Duty Pistons," Final Report No. IITRI-M08086-1, for Bohn Aluminum and Brass Corp., June 1981.

4. Y. Nishida and H. Matsubara, The British Foundryman, **69**, 274-278 (1976).

5. O. G. Epanchintsev, Russian Castings Production, May 1972, pp. 188-189.

6. R. E. Spear and G. R. Gardner, AFS Trans., 71, 209 (1963).

7. J. C. Benedyk, Trans. SDCE, **8**, Paper No. 86 (1970).

8. J. C. Benedyk, SME Paper No. CM71-840, 1971.

9. R. F. Lynch, R. P. Olley, and P.C.J. Gallagher, AFS Trans., **83**, 561-568 (1975).

10. R. F. Lynch, R. P. Olley, and P.C.J. Gallagher, AFS Trans., **83**, 569-576 (1975).

11. The Enigma of the Eighties, Environment, Economics, and Energy, Science of Advanced Materials and Process Engineering Series, Society for the Advancement of Materials and Process Engineering, Vol. 24, Book 2, (1979).

12. L. Rubin, "Applications of Metal-Matrix Composites, The Engineering Structural Materials," ibid., pp. 1236-1249.

13. E. J. Peters and P. Boymal, "Ceramic Fiber in Advanced Composites," paper presented at Impact '85, International Conference on Fiber Developments, Ft. Lauderdale, Florida, March 10-12, 1985.

14. E. J. Peters, "Ceramic Fiber Usage in Automotive Composites," paper presented at the 3rd LAVD Congress on Vehicle Design and Components, Geneva, Switzerland, March 1986.

15. M. Taoz and M. Smale, "Clevite's Advanced Technology for the Diesel Piston," Diesel Progress North America, 1985.

16. L. Ackermann, J. Charbonnier, et al., "Properties of Reinforced Aluminum Foundry Alloys," Proceedings of the Fifth International Conference on Composite Materials, The Metallurgical Society, Inc., Warrendale, Pennsylvania, August 1, 1985, pp. 687-698.

17. M. Bader, T. W. Clyne, G. R. Cappleman, and P. A. Hubert, "The Fabrication and Properties of Metal Matrix Composites Based on Aluminum Alloy Implanted Alumina Fiber Preforms," Composite Science and Technology, 23, 287-301 (1985).

HIGH PERFORMANCE METAL-MATRIX COMPONENTS MANUFACTURED BY SQUEEZE-CASTING

J. Charbonnier, S. Dermarkar, M. Santarini
Pechiney, Voreppe Research Center
Voreppe, France

J. Fages, M. Sabatie
Aérospatiale, 2 rue Béranger - BP 84
Châtillon s/s Bagneux, France

HIGH PERFORMANCE METAL-MATRIX COMPONENTS MANUFACTURED BY SQUEEZE-CASTING

J. Charbonnier, S. Dermarkar, M.Santarini,*J.M. Fages, *M. Sabatié

Pechiney, Voreppe Research Center, BP 27, 38340 Voreppe, France
*Aérospatiale, 2 rue Béranger, BP 84 92320 Châtillon s/Bagneux, France

ABSTRACT

The use of casting technologies offers many advantages for making fiber reinforced metallic components. Within a joint development program, Pechiney and Aerospatiale decided to use squeeze-casting technology to demonstrate the feasibility of a high performance cast component. The full program involved 3 steps :

1 - evaluation of the mechanical properties on unidirectional test samples,

2 - fabrication of reduced size test components after optimal fiber preform design,

3 - upscaling to full size fabrication.

This paper will present the results obtained after completion of steps 1 and 2. Improvements in strength and stiffness were demonstrated up to 500°C. Optimal preform design involved filament wound PCS-SiC continuous fibers and local SiC whiskers reinforcements.

The influence of the matrix alloy and the fiber on the mechanical properties will be discussed.

THE MATERIALS USED FOR BALLISTIC systems and advanced aircrafts are facing increased service temperatures as a result of higher cruise speeds.In addition, high specific strength and stiffness are necessary in order to reduce weight or to increase range.

The combination of light metallic matrices and ceramic fibers offers new materials to the component designers. Among the various routes for making such metal-matrix composites, we selected the infiltration of ceramic fiber preforms by liquid alloys under pressure, i.e., by squeeze-casting.

This paper describes a joint development program undertaken by PECHINEY and AEROSPATIALE to demonstrate the feasibility of this technology for making metal matrix components. The evaluation conducted on unidirectional samples illustrates the improvement of the mechanical properties obtained up to 350°C. The influence of the matrix alloy and the fiber on these properties will be discussed. The technical fabrication steps for making a reduced size component are then described, including fiber handling and metal infiltration.

UNIDIRECTIONAL SAMPLES

MATERIALS SELECTION - Polycarbosilane SiC (PCS-SiC) fibers were used in the form of yarns of 500 filaments. The fibers were supplied by Nippon Carbon (Nicalon). The fiber has a density of 2.55, a strength of 2450 to 2900 MPa and an elastic modulus of 170 to 195 GPa.

Two alloys were selected in order to assess matrix effects :
- commercial purity 1050 aluminium,
- Al-10%Si casting alloy.

EXPERIMENTAL PROCEDURE - The fibers are wound around an aluminium mandrel. The thickness of the fiber layer is 2 mm.Two sets of experiments were conducted, one with a symmetrical mandrel (Fig.1-a) and one with a non symmetrical mandrel (Fig. 1-c). In the case of a symmetrical mandrel, a layer of 3 mm of unreinforced molten metal is adjacent to the reinforced area on each side of the mandrel. In the case of a non symmetrical mandrel, the thickness of the molten metal layer is 8 mm on one side and 3 mm on the other side, in order to provide different solidification times on each side. In addition three levels of melt superheat over the liquidus of the alloys were used : 120°C, 160°C and 200°C.

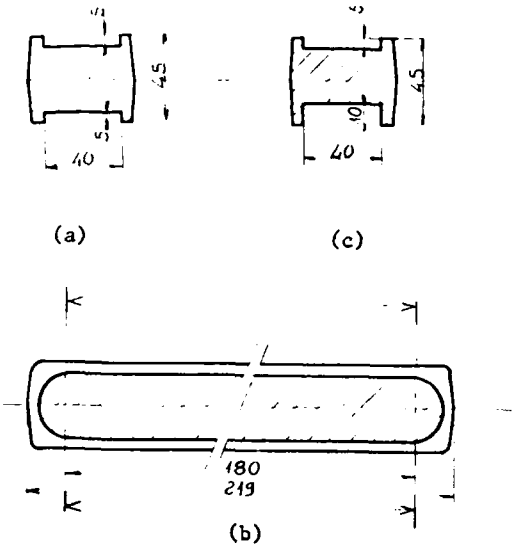


Fig. 1 - Schematic of the mandrel for unidirectional samples
(a) cross-section of a symmetrical mandrel
(b) longitudinal section of a symmetrical mandrel
(c) cross-section of a non symmetrical mandrel

The mandrel with the fibers is preheated at 550°C and introduced in the mold cavity (Fig. 2). The mould is then closed and the liquid metal poured in a holding chamber. The metal is forced into the mold cavity by the punch under a pressure of 50 MPa. After ejection, the layer of unreinforced metal is removed by machining and the reinforced areas are sawed.Three-point bending test samples of 80 mm x 15 mm x 2 mm are further machined for mechanical evaluation at room temperature and elevated temperatures. The elastic modulus was measured by a vibration method (dynamic modulus) and from the stress-strain curves (static modulus).

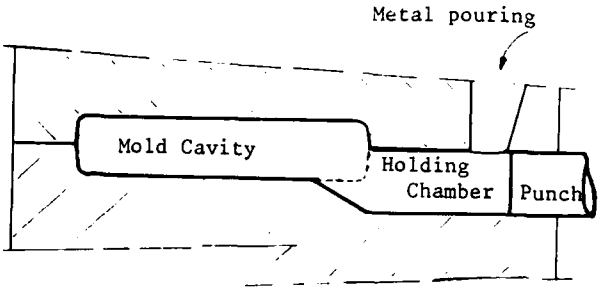


Fig. 2 - Schematic of the squeeze-casting system for unidirectional samples

RESULTS

The mechanical properties of Al-10%Si reinforced with 45% PCS-SiC fibers were measured at room temperature and up to 350°C after 15 minutes of holding at the test temperature (Table I). The variation of the flexural strength with temperature is represented in Fig. 3 for the matrix alloy alone and for the reinforced matrix. The strength remains almost constant for the reinforced matrix over the whole temperature range. The results however show a dispersion of about 10% of the mean strength value.

Fig. 4 illustrates the variation of the static and dynamic modulus with temperature. The variation of the dynamic modulus with temperature of titanium TA6V alloy is also represented in Fig 4. Although slightly lower at room temperature, the modulus of reinforced aluminium exhibits a better stability up to 350°C when compared with TA6V. This advantage is much higher in terms of specific stiffness, the density of the reinforced aluminium being 2.65 and the density of TA6V being 4.5.

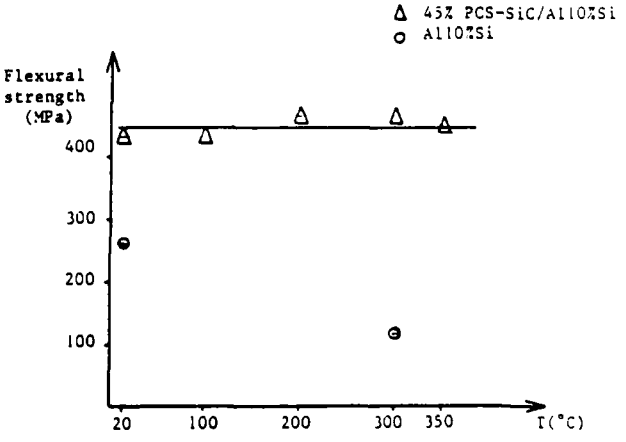


Fig. 3 - Flexural strength at different temperatures after 15 minutes holding time

Table I - Temperature Effect on Flexural Strength and Elastic Modulus
45% PCS-SiC/Al-10%Si unidirectional samples
(symmetrical mandrel, melt superheat = 160°C)

Test T° (PC)	Mean Flexural Strength (MPa)	Standard Deviation (MPa)	Mean Static Modulus (GPa)	S.D. (GPa)	Mean Dynamic Modulus (GPa)	S.D. (GPa)
20	430	45	95	4	109	6
100	430	18	90	3	107	7
200	467	39	87	4	106	6
300	467	13	78	9	102	6
350	450	30	72	2	100	4

The flexural strength of the Al-10%Si alloy cast in the same conditions is 257 MPa at R.T. and 124 MPa at 300°C.

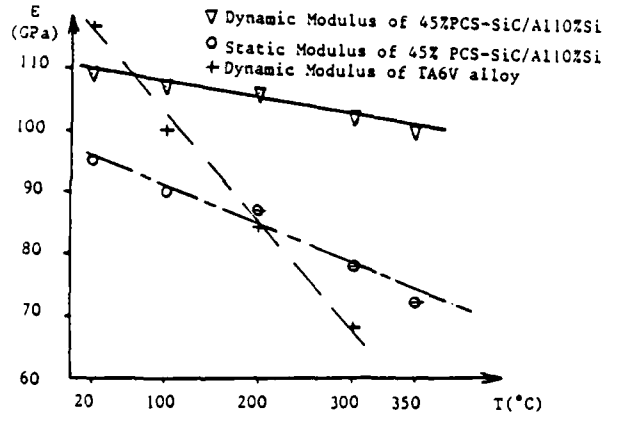


Fig. 4 - Elastic moduli for 45% PCS-SiC/A110%Si and TA6V at different temperatures after 15 minutes holding time

Table II - Flexural Strength at Room Temperature on unidirectional samples (symmetrical mandrel, melt superheat = 160°C)

	1050	Al-10%Si
Measured Values	918	582
	625	508
	582	488
	579	487
	484	453
	468	433
Mean Value (MPa)	609	491
Standard Deviation (MPa)	163	52

The influence of the matrix alloy was first considered through the flexural strength at room temperature (Table II). Six measured values are listed in this Table for each alloy. Higher values are quoted for the 1050 matrix, but the standard deviation is also higher.

Two additional parameters were also considered using non symmetrical mandrels: melt superheat (120°C and 200°C over the alloy liquidus) and solidification time. Solidification time is different on each side of non symmetrical mandrels and were computed from finite element analysis (1). The solidification time is 1.2 s. on the thin side and 4.2 s. on the thick side. The mean values and standard deviations in each case are listed in Table III. A statistical analysis was conducted on these results in order to assess if these parameters have a significant effect on the results (see ref. (2) for a detailed explanation of the statistical analysis). The following results were obtained :

1 - neither of the two parameters (melt superheat and solidification time) is significant in the case of the Al 10%Si matrix.

2 - in the case of the 1050 alloy, both parameters are significant. The melt superheat is "significant" (less than 5% error risk) while the solidification time is "very highly significant" (less than 0,1% error risk). Finally, the deviation in the case of low solidification times is significantly higher than in the case of large solidification times (with less than 1% error risk).

Table III - Flexural Strength from non symmetrical mandrels
Influence of solidification time and melt superheat
($\bar{x}$ mean value, s standard deviation)

	Melt Superheat = 120°C				MeltSuperheat = 200°C			
	solidification times				solidification times			
	1,2 s		4,2 s		1,2 s		4,2 s	
	$\bar{x}$	s	$\bar{x}$	s	$\bar{x}$	s	$\bar{x}$	s
1050+PCS-SiC	552	123	390	75	626	99	463	28
Al-10%Si + PCS-SiC	451	22	473	25	418	48	491	57

The test samples were also examined by optical metallography after polishing on cross-sections (Fig. 5). Although the fiber distribution is rather uniform, many fibers in contact are noticed in both cases. But the striking feature in Fig. 5-a is the random presence of silicon platelets in the 1050 matrix. In some areas of this micrograph, the surface fraction of Si platelets is as high as in the case of the Al-10%Si matrix (Fig. 5-b). This provides direct evidence of a strong interaction between the metal and the fiber and will be further discussed as a possible reason for the differences in mechanical behaviour between the two matrix alloys.

DISCUSSION

The melt superheat of 120°C and 200°C corresponds to casting temperatures of 780°C and 860°C for the 1050 matrix and 730°C and 810°C for the Al-10%Si matrix. The reactions between pure Al and an Al-Si alloy with PCS-SiC Nicalon fibers have been studied in detail by Viala and co-workers at 727°C (3).

In the case of a pure Al matrix, the major reaction at short holding times is

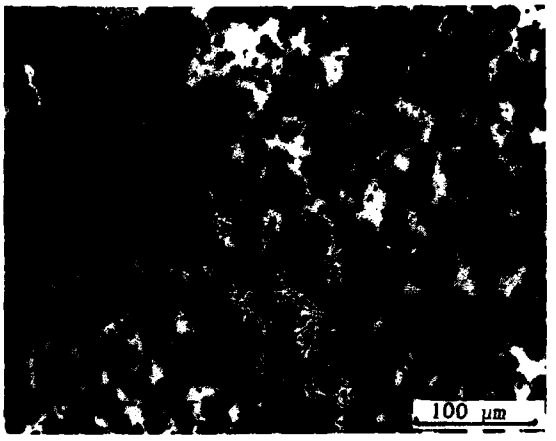
$$4Al + 3SiC \rightarrow Al_4C_3 + 3Si$$

Considering the short interaction time and non equilibrium conditions involved in our squeeze-casting tests, the presence of Si platelets in the 1050 matrix can hence be qualitatively explained.

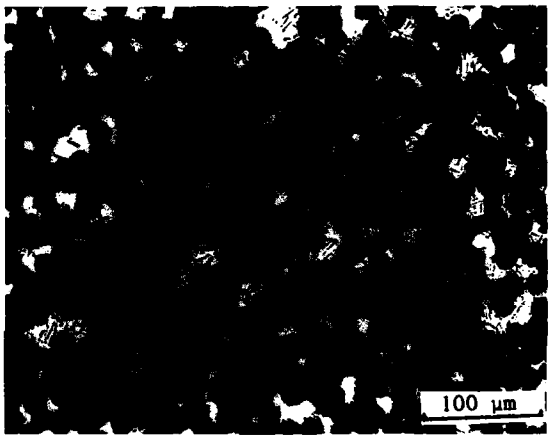
Conversely, the presence of silicon in the Al-10%Si matrix leads to the following major reaction

$$4Al + 3C \rightarrow Al_4C_3$$

$$Al_4C_3 + 3\,Si \rightarrow 3SiC + 4Al$$



(a)



(b)

Fig. 5 - Optical micrographs of unidirectional sample cross-sections :
(a) 1050 matrix
(b) Al10%Si matrix

However, the formation of in-situ SiC starts only after more than one hour holding time. Hence no significant change can be observed at the optical microscopy level in our tests. Consistently, none of the parameters, melt superheat and solidification time, has a significant effect on the mechanical properties in this case.

The mean values for flexural strength are higher in the case of the 1050 matrix than the Al-10%Si matrix (Table II), indicating the beneficial effect of a very ductile matrix around the fibers. However, a reaction between the 1050 matrix and PCS-SiC Nicalon fiber is occuring non uniformly through

the specimen thickness (Fig. 5-a), leading to a very large dispersion in mechanical properties (Table II). In addition, this dispersion in the mechanical properties is significantly higher for short solidification times than for longer solidification times. The exact reasons for the onset of the reaction need further investigation and may be related to minor variations in the fiber surface chemistry or in the local heat fluxes.

Practically, the following dilemna has to be considered :

1. The use of a casting Al-Si alloy leads to lower dispersion in mechanical properties.Thickness variations in a casting and hence variations in solidification times will not affect the results. However, the mean level of properties is rather low.

2. The use of pure aluminium provides better properties in some cases but the dispersion of the properties is very high. The uncontrolled reaction between the matrix and the PCS-SiC Nicalon fiber is suggested as a reason for this behaviour.

A less reactive fiber having a surface chemistry allowing a better control of the reaction with pure Aluminium is therefore needed.

Conversely, the effect of Si platelets on the MMC properties has to be further understood. This may lead to the design of casting alloys with improved mechanical behavior as matrices of metallic composites.

REDUCED-SCALE COMPONENT

COMPONENT DESCRIPTION - The reduced scale component is a hollow cylindrical body of 250 ± 0,5 mm and 120 ± 0,5 mm outer diameter (Fig. 6-d). The mean thickness is about 2 mm. The lower part of the component contains four reentrant arms. The component is machined on the outer surface only, the inner surface being left in the as-cast condition.

FIBER WINDING AND PREFORM DESIGN - A special core was designed for this fabrication, with a cylindrical body and two hemispherical ends (Fig. 6-a). This core is then used on a filament winding machine as a mandrel in order to deposit the continuous fibers by standard procedures. In the area corresponding to the four reentrant arms, it is not possible to introduce continuous fibers by filament winding. Hence preforms of SiC whiskers were manufactured and introduced inside the cavity of the core. The first layers of filament wound fibers helped to maintain these preforms in the requested position.

METAL INFILTRATION - The preform was preheated at 550°C - 1 hour before introduction in the open mold. The mold was then filled with liquid metal and closed (Fig.6-c). Pouring temperature was around 160°C above liquidus. After solidification, the component was ejected, the hemispherical ends were sawed and the core destroyed. Fig.7 shows the component after machining the outer surface.

A first set of 15 components was manufactured and is under evaluation by bending tests.

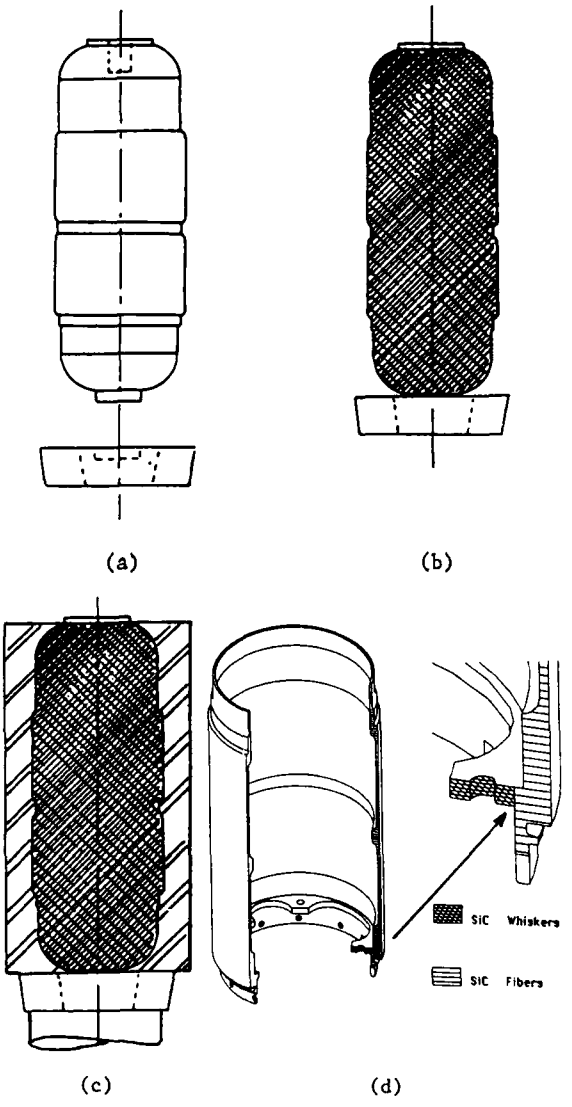


Fig. 6 - Principal stages in the fabrication of reduced scale component
(a) core fabrication
(b) filament winding of the fibers
(c) metal infiltration
(d) final component

CONCLUSION

This work demonstrated the advantages of squeeze-casting technology for making metal matrix components with reentrant non ejectable parts. The tests on unidirectional samples show a strong difference in terms of mechanical behaviour and reactivity between a 1050 matrix and a Al-10%Si alloy matrix. Improvements in infiltration conditions are easy to realize on a small scale and constant thickness test specimens. In view of industrial applications for making real complex components, there is a need for less reactive fiber, as well as for improved casting alloys.

ACKNOWLEDGEMENTS

The authors wish to express their acknowledgements to the Direction of Pechiney and Aerospatiale - Divisions Engins Tactiques, for permission to publish this work. They wish also to thank Mr. Burtin, for his help in the squeeze-casting operations and Mr. Mirand for the mechanical testing.

REFERENCES

(1) Hannart, B., Voreppe research Center, Internal report, (1988).

(2) Ackermann, L., Charbonnier,J., Desplanches G., Kolowski H.,ICCM V, 687-698, (1985).

(3) Viala, J.C., Bosselet, F., Forbier, P. and Bouix, J., ICCM VI & ECCM2, 2, 2.146-2.155, (1987).

EFFECT OF SQUEEZE CASTING CONDITIONS ON INFILTRATION OF CERAMIC PREFORMS

J. M. Quenisset, R. Fedou, F. Girot, Y. Le Petitcorps
Laboratoire de Chimie du Solide CNRS
Université de Bordeaux I - 33405 Talence, France

ABSTRACT

The effects of the squeeze casting conditions and physical parameters of the composite components on the ability of infiltrating fibrous ceramic preforms by light alloys have been approached by computing the general equations of heat and fluid flows with simplified boundary conditions. Taking into account the capillary effect and the possible occurence of heat sources within the preform during infiltration, the numerical results have shown a strong influence of the preform and liquid metal temperatures, the fiber volume fraction, the infiltration speed and the exothermic effect of a preform treatment, on the infiltration depth Also, the size of the fiber and the pressure required to achieve the infiltration. Finally, the consistency of the assumptions advanced in the model with the actual conditions of squeeze casting is discussed. Concluding remarks show the ability of such an approach for predicting the size of composite parts which can be processed or for adjusting the conditions of squeeze casting.

PROCESSING LIGHT ALLOY MATRIX COMPOSITES (LAMC) BY SQUEEZE CASTING is now well known for its suitability for mass production. As a consequence, a large amount of work has already been performed, mainly in industry, to improve the processing conditions and to extend the possibilities of squeeze casting [1-14]. However, the diversity of preform natures and part shapes as well as the conception of new processing techniques related to squeeze casting require many preliminary experiments which are particularly time consuming. Thus, the availability of a numerical model allowing the prediction of the effect of parameter changes, should be helpful to reduce expenses devoted to the optimization of processing conditions or the evaluation of new techniques dealing with liquid infiltration.

The aim of the present study is to show the potential of a numerical model for depicting the influence of each squeeze casting parameter on the infiltration depth of preforms and for evaluating the corresponding required pressure.

NUMERICAL SIMULATION OF INFILTRATION

SQUEEZE-CASTING CONDITIONS - The infiltration of fibrous preforms by a liquid metal is assumed to be performed at constant velocity so that the main parameters defining the squeeze casting procedure are as follows:

(1) the temperature T_m of the liquid alloy before infiltration (T_{Al} for pure aluminum),

(2) the temperature T_f of the fibers before infiltration,

(3) the infiltration speed U which can be controlled for example by the displacement velocity of a piston.

The resulting characteristics of the infiltration procedure are:

(a) the maximum infiltration depth z_M,

(b) and the minimum pressure P_m required to achieve the maximum infiltration depth.

As a matter of fact, the infiltration is assumed to have stopped when the temperature of the metal in the vicinity of the processing liquid front reaches the liquidus temperature of the alloy T_S.

PHYSICAL PARAMETERS OF THE COMPOSITE COMPONENTS - The characteristics z_M and P_m of the infiltration are expected to be dependent on the following physical parameters depicting the behavior of fibrous preforms and liquid alloys with respect to heat and fluid flows:

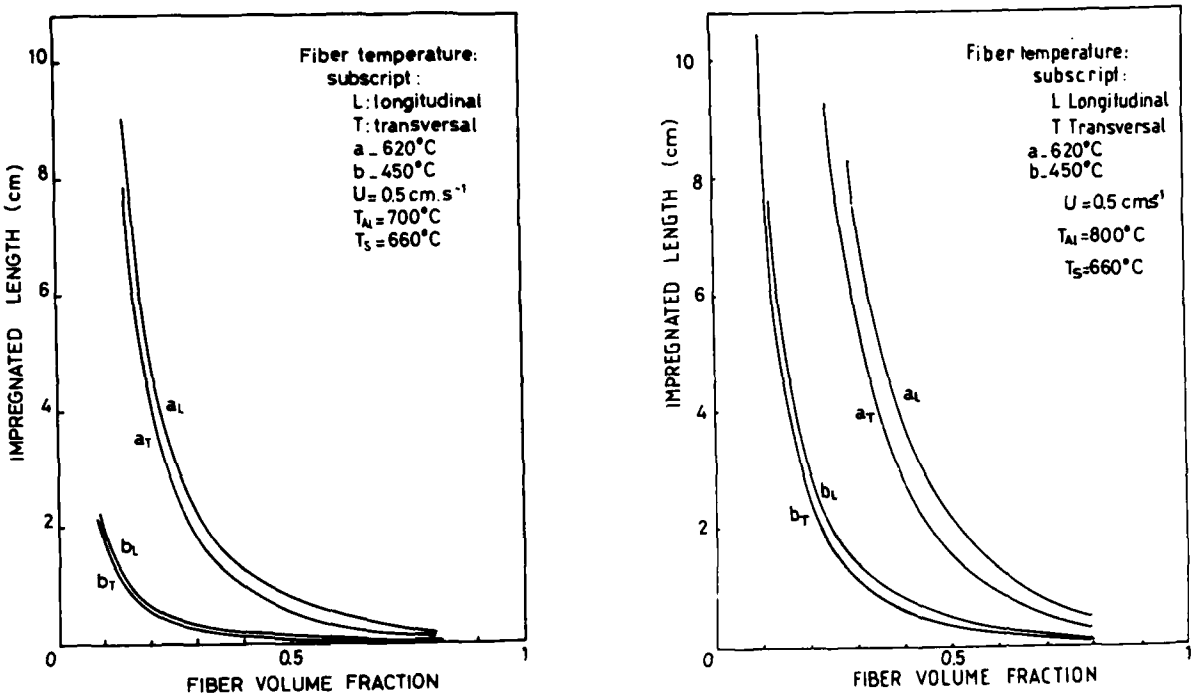
(1) the volume fraction of fiber V_f in the resulting composite,

(2) the densities of the components: d_m for metal, d_f for fibers,

(3) the specific heats C_m and C_f,

(4) the thermal conductivities λ_m and λ_f,

(5) the permeability K of the fibrous preform or the fiber diameter $\emptyset_f$,



(a) (b)

Fig.1: Influence of the fiber volume fraction, infiltration direction, fiber and liquid alloy temperatures on the impregnated length (SiC NICALON)
(a) - T_{Al} = 700°C (b) - T_{Al} = 800°C

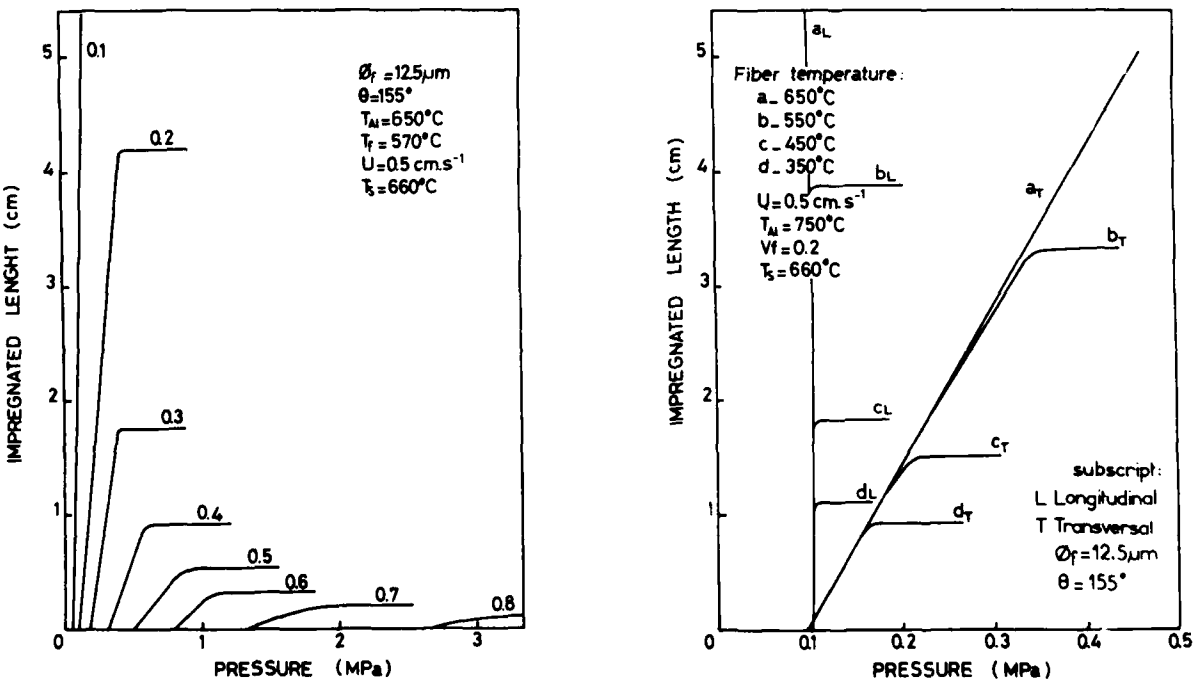


Fig.2: Influence of the fiber volume fraction on the pressure of infiltration (SiC NICALON)

Fig.3: Influence of the fiber temperature on the infiltration pressure (SiC NICALON)

(6) the liquid metal viscosity μ, versus temperature,

(7) the surface energy γ of the liquid alloy,

(8) the contact angle θ between the ceramic preform and the liquid alloy.

Only one of the above parameters is considered to depend on temperature (μ). Since the viscosity drastically changes in the vicinity of the solidification temperatures, it was thought to be necessary to take such evolution versus temperature into account. In fact, the results show a small effect of the viscosity increase on the infiltration depth related to a given pressure.

MODELLING - In order to propose a numerical approach of the general equations of heat and fluid flow according to a finite difference method detailed elsewhere, two models based on the following main assumptions have been used to simulate the preform infiltration [5, 14].

(1) the preforms are large enough to neglect any edge effect and to consider the infiltration as unidirectional,

(2) a rough assessment of the heat exchange kinetics between fibers and liquid alloys allows the interfacial heat transfer to be considered as instantaneous [2],

(3) the temperature of the liquid metal feeding the preform surface and that of the preform fraction which is not yet infiltrated remain constant during the infiltration,

(4) the temperature distribution is assumed to be independent of pressure,

(5) the preform morphology is defined as a regular hexagonal arrangement of continuous cylindrical fibers oriented either parallel (subscript L) or perpendicular (subscript T) to the infiltration direction.

RESULTS

The main features depicting the influence of the processing conditions and physical parameters on the maximum impregnated length z_M and the corresponding minimum required pressure P_m, have been derived from computations performed for pure aluminum.

FIBER VOLUME FRACTION - All of the results illustrated in figs. 1 and 2 show that the fiber volume fraction is one of the most important factors limiting z_M and increases the related value of P_m, whatever the direction of infiltration with respect to the fiber orientation (L or T).

DIRECTION OF INFILTRATION - The deviation between the values of z_M corresponding to the two directions of infiltration is only moderate as illustrated in fig.1. Thus, the impregnated lengths related to preforms with ramdomly oriented short fibers, are thought to be in the same range of values. On the contrary, the infiltration in a direction orthogonal to the fiber orientation requires much higher pressures than those allowing the infiltration in the fiber direction (fig.3).

TEMPERATURE - Raising the fiber temperature is most effective in increasing z_M as shown in figs. 1 and 3. As an example (in the case of pure aluminum reinforced by SiC (NICALON) fibers) an increase in T_f of 100°C enables an impregnation about six times deeper. As a consequence, the preform temperature is a major processing variable. Otherwise, figs. 2 and 3 clearly illustrate the very small dependence between the pressure required for a given impregnated length and T_f. Nevertheless, the minimum value P_m of the pressure required for the maximum impregnated length z_M depends strongly on z_M. As a result, the increase in P_m when T_f is raised is only related to a higher impregnated length. Also, fig.1 provides evidence that the influence of the alloy temperature T_m (T_{Al} for pure Al) is very similar to that of the preform temperature. However, the range of temperature in which T_m can be chosen is rather limited (700-800°C for most Al alloys).

IMPREGNATION SPEED - In contrast to the results already reported in the literature, the present analysis reveals a significant effect of the impregnation speed U on z_M as illustrated in fig.4 [2]. Since the alloy temperature at the surface of the preform is considered as remaining constant during the infiltration, the high thermal conductivity of the liquid metal enables an increase of z_M when U is decreased.

THERMAL CONDUCTIVITY - As long as the thermal conductivity of the fibers remains small compared to that of the liquid metal, an increase in λ_f gives rise to a moderate increase in the impregnation length as illustrated in fig 5. Nevertheless, preforms made of a high volume fraction (V_f = 60 - 65%) of very conductive high modulus carbon fibers could be infiltrated with reasonable processing conditions (T_{Al} = 750°C; T_f = 500°C; T_s = 660°C; U = 0.5 cm. s^{-1}) up to an impregnated length of about 3 - 5 cm. In a similar manner, smaller liquid metal conductivities lead to shorter impregnated lengths as shown in fig. 6. Otherwise, the sensivity of z_M to the metal density d_m is not negligeable particularly for low fiber volume fraction.

SOLIDIFICATION TEMPERATURE - A decrease in the solidification temperature T_s, for instance due to alloying elements, leads to a significant increase in the impregnation length. As an example, a deviation of 10°C corresponds to a change in z_M of about 25 pct.

CONTACT ANGLE AND SURFACE ENERGY - The beneficial effect of a good reinforcement wettability is more significant for longitudinal infiltration due to the lower fiber resistance to flow (Fig.8). In addition, the effect of θ is only effective for very small fiber sizes. Otherwise, the influence of the surface energy of liquid metal is not negligeable as illustrated in fig.9; a higher value of γ leads to an increase in z_M.

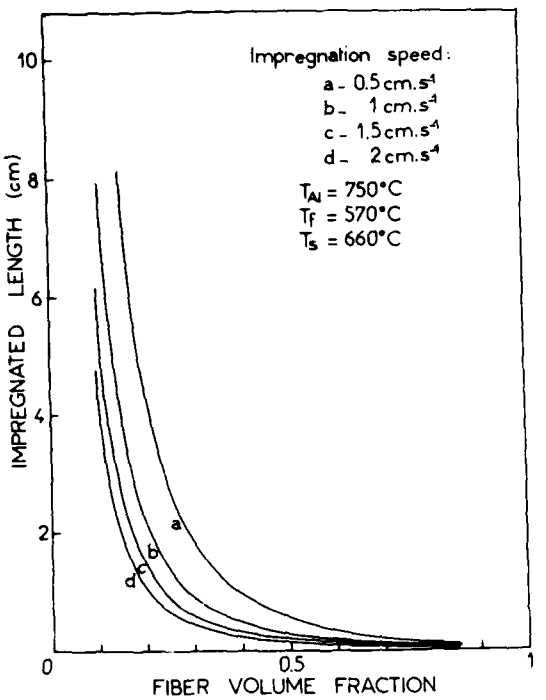


Fig.4: Influence of the infiltration speed in the fiber direction, on the impregnated length (SiC (NICALON)

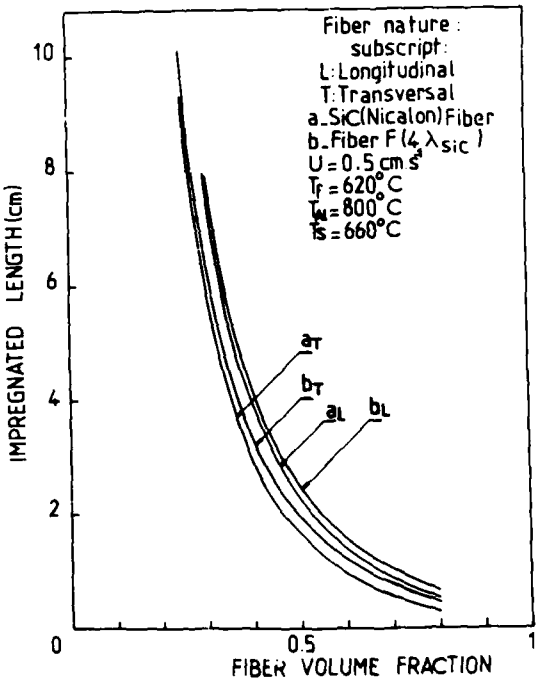


Fig.5: Influence of the fiber thermal conductivity on the impregnated length

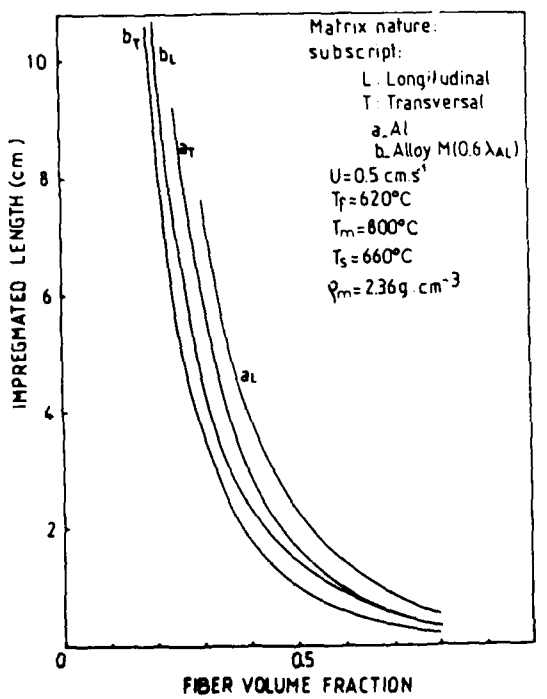


Fig.6: Influence of the liquid alloy thermal conductivity on the impregnated length (SiC NICALON)

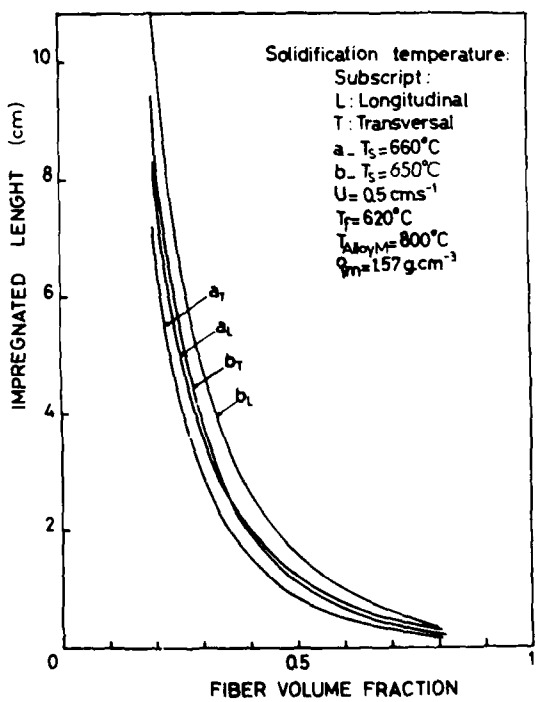


Fig.7: Influence of the solidification temperature of the alloy on the impregnated length (SiC NICALON)

FIBER COATING - Specific surface treatments of the fibrous preforms are able to improve the reinforcement wettability by reacting with the liquid metal and often giving rise to heat production |15|. As a result, such treatments can be very effective to increase the impregnated length depending on the reaction enthalpy ΔH (fig.9). As an example, a very thin continuous coating ($e \simeq 0.1$ µm) of zirconium hexafluoride should be sufficient to avoid any solidification of aluminum during the infiltration of SiC preforms ($V_f = 0.7$).

FIBER SIZE - When on one hand z_M is not dependent on the fiber diameter because the model assumes no partial solidification before reaching z_M, on the other hand P_m strongly depends on the fiber size. Hence, a preform made of filaments ($\emptyset$ = 140 µm) requires for a reinforcement volume fraction of 50 pct, a pressure about ten times less than that corresponding to fibers 15 µm in diameter and about a thousand times less than that for whiskers ($\emptyset$ = 0.5 µm). For example, infiltrating 10 cm of preform made of 20 vol pct of SiC whiskers requires pressures from 20 MPa up to 470 MPa depending on the infiltration direction.

DISCUSSION

The latter above remark shows that a more precise evaluation of the pressures required for preforms made of randomly oriented fibers needs the experimental measurement of the real preform permeability K, rather than calculating K from models of unidirectional preforms.

However, the model gives a range of impregnated lengths sufficiently narrow to allow the assessment of z_M whatever the fiber orientation in the preform. Nevertheless, a more accurate determination of z_M demands additional parameters to be taken into account such as the casting shape, the mold properties, as well as the cooling of the liquid metal which feeds the preform. The integration of these parameters in the numerical simulation is no more than an increase in the program complexity but one assumption remains questionable. The criterion which considers the limit of impregnation as corresponding to the liquidus temperature of the alloy enables the solidification heat to be ignored in the analysis of heat flows. While a partial solidification of a pure metal can be expected during the infiltration of unidirectional preforms made of large diameter filaments, the infiltration of randomly oriented whiskers by a liquid alloy must give rise to local segregation and remelting. These phenomena have to be clarified as liquid flow velocities can be rather high in the vicinity of the solidification surfaces. This could also increase heterogeneity in the composite so that it appears preferable to consider the impregnation as finished when solidification is about to occur. The above reasons allow the heat production related to solidification to be omitted although it has been shown that taking this effect into account, due for instance to a fiber coating, is not a difficulty for the numerical approach. Furthermore, assuming that a fraction of the liquid metal solidifies along the infiltration length, allows the calculation of the related pressures but such a model cannot provide a limit for the impregnated length since the equilibrium in heat transfer must lead to an infinite value of z_M |12|. It remains that more investigation has to be done to clarify the mechanisms related to the solidification of a liquid alloy flowing within a fibrous preform.

ACKNOWLEDGEMENT

The authors wish to thank CEGEDUR-PECHINEY for its financial support.

REFERENCES

1 Fukunaga, H. and Ohde, T., "Progress in Science and Engineering of Composites", p.1443, T. Hayashi, K. Kawata and S. Umekawa, Ed., ICCM IV, Tokyo (1982).

2 Fukunaga, H. and Kuriyama, M., Bul. JSME, 25 (203), 842 - 847 (1982).

3 Fukunaga, H. and Goda, K., Bul. JSME, 27 (228) 1245 - 1250 (1984).

4 Ackermann, L., Charbonnier, J., Desplanches, G., Koslowski, H., Proc. of ICCM V, p. 687, Jr. Harrigan, et al., the Metallurgical Society, Warrendale, PA (1985).

5 Girot, F., Rocher, J.P., Quenisset, J.M., and Naslain R., Proc. Conf. Eur. MRS, Strasbourg (1985).

6 Clyne, T.W., Bader, M.G. Cappleman, G.R. and Hubert, P.A., J. Mat. Sci., 20, 85 - 96 (1985).

7 Howes, M.A.H., J; of Metals, Applied Technology, March, 28 - 29 (1986).

8 Fujita, Y., Fukumoto, H., Proc. of ICCM VI and ECCM II, p. 340, F.L. Matthews, N.C.R. Buskell, J.M. Hodgkinson, J. Morton, Ed., Elsevier A.S. Vol.2, London (1987).

9 Fukunaga, H., Goda,K., Proc. of ICCM VI and ECCM II, p. 362, F.L. Matthews, N.C.R.Buskell, J.M. Hodgkinson, J. Morton, Ed., Elsevier A.S. Vol.2, London (1987).

10 Towata, S., Ikuno, H., Yamada, S., Proc. of ICCM VI and ECCM II, p.412, F.L. Matthews, N.C.R. Buskell, J.M. Hodgkinson, J. Morton, Ed., Elsevier A.S. Vol.2, London (1987).

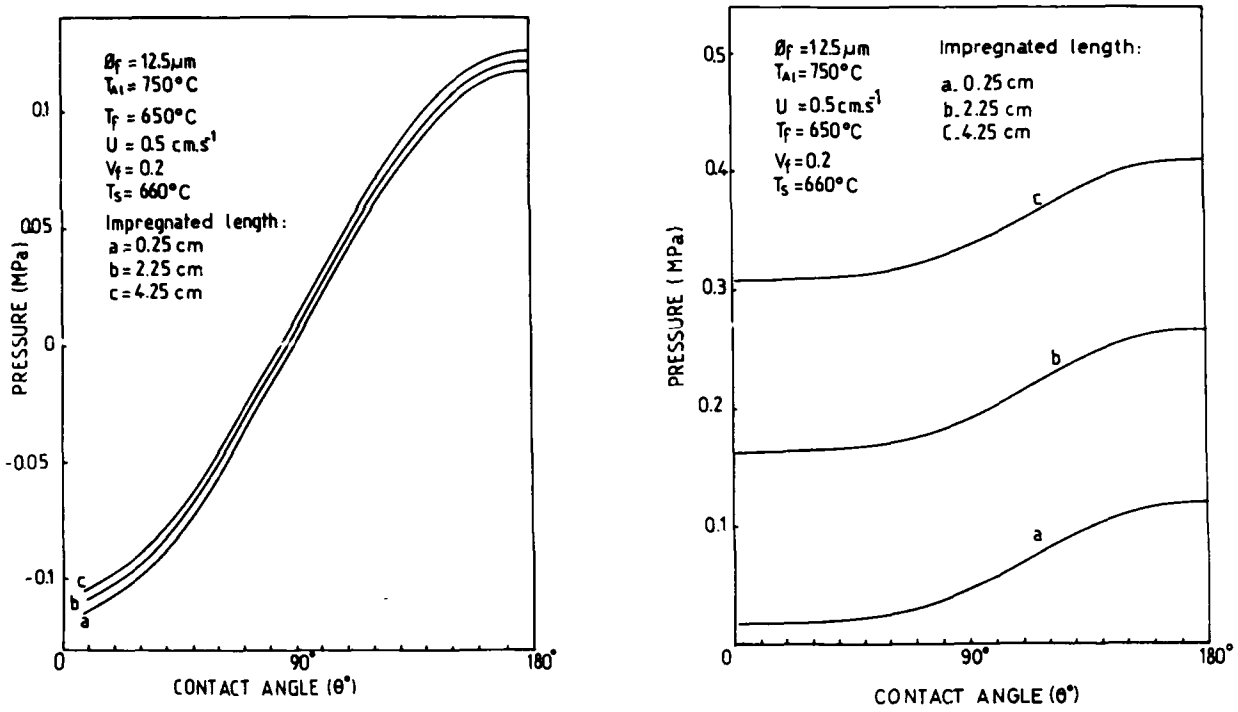
11 Clyne, T.W., Proc. of ICCM VI and ECCM II, p. 275, F.L. Matthews, N.C.R. Buskell, J.M. Hodgkinson, J. Morton, Ed., Elsevier A.S. Vol.2, London (1987).

12 Masur, L.J., Mortensen, A., Cornie, J.A., Flemings, M.C., Proc. of ICCM VI and ECCM II, p. 320, F.L. Matthews, N.R. Buskell, J.M. Hodgkinson, J. Morton, Ed., Elsevier A.S. Vol.2, London (1987).

13 Clyne, T.W. and Mason, J.F., Met. Trans A, 18A (8), 1519 - 1530, (1987).

14 Girot, F., Fedou, R., Quenisset, J.M. and Naslain, R., Proc. of the Am. S for Composites p.361, University of Delaware, (1987).

15 Rocher, J.P., Quenisset, J.M., and Naslain,R., J. Mat. Sci. Lett., 4, 1527 - 1529, (1985).



(a) (b)

Fig.8: Influence of the contact angle ceramic fiber-liquid metal on the pressure of infiltration (SiC NICALON)
(a)- in the fiber direction
(b)- in the direction perpendicular to the fibers

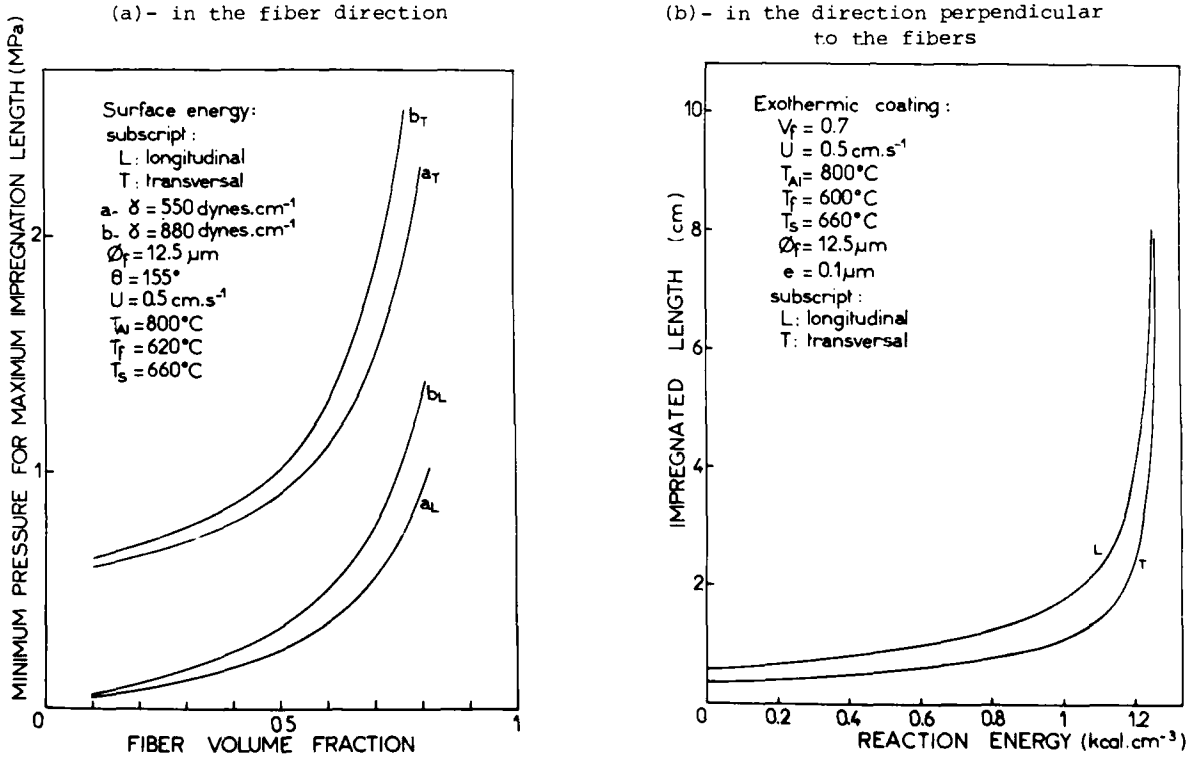


Fig.9: Influence of the surface energy on the minimum pressure required to achieve the maximum impregnated length (SiC NICALON)

Fig.10: Influence of an exothermic treatment of fibers on the impregnated length (SiC NICALON)

SOLIDIFICATION UNDER PRESSURE: ALUMINIUM AND ZINC ALLOYS CONTAINING DISCONTINUOUS SiC FIBRE

A. A. Das, A. J. Clegg
Loughborough University of Technology, UK

B. Zantout
Government of Syria
Damascus, Syria

M. M. Yakoub
University of Damascus
Damascus, Syria

ABSTRACT

Cast metal-matrix composites of an Al-base alloy (Al-4.5Cu) and a Zn-base alloy (Zn-27Al-3Cu), are explored with regard to some of their properties and structural features. The composites were fabricated by squeeze casting the liquid alloys containing up to 10 v% of chopped SiC fibre. A few squeeze-infiltrated samples of the Zn-27Al-3Cu alloy containing 18 v% fibre were also examined for comparison. Both alloys contain 2 v% or more copper and the EPMA line scans for both clearly indentify Cu-rich zones around the SiC fibre, except for the squeeze-infiltrated composites. The effect of fibre addition on the tensile properties of the alloys can be related, not only to the phase(s) occurring at the fibre/matrix interfaces but also to the stablility of the matrices. Given that fibre damage and/or degradation can be avoided during the process of fabrication, it is postulated that casting processes used for the production of the MMC's must ensure that (i) a controlled interaction takes place between the molten metal and the fibre, and (ii) the structure (as-cast) of the matrix is stable.

SQUEEZE CASTING of aluminium alloys, on a commercial scale, has become a reality in some western countries[1]. There is now also a great deal of interest in the fabrication of cast metal-matrix composites containing short inorganic fibre either in random orientation or aligned in appropriate ways for selective reinforcement[2]. The development of cast composites containing particulate reinforcement, such as SiC, is also being actively pursued.

Although squeeze infiltration methods have been widely used for fabricating cast metal-matrix composites, there is very little information available on the structure and properties developed by squeeze casting of composites. This paper is therefore concerned with the evaluation of the structure and properties developed by squeeze casting and to a lesser extent with squeeze-infiltrated castings of 'short fibre' MMC's. The methods used were aimed to provide a uniform distribution of fibre in random orientation.

BACKGROUND: There is some uncertainty and confusion in the literature when describing cast MMC's as far as 'squeeze-castings' and '*squeeze infiltrated castings*' are concerned. It is, therefore, important to clarify some of the important features of both.

(i) The distinctive feature of squeeze casting is that molten metal is subjected to a hydrostatic pressure during the liquid→solid transformation with virtually no movement of the molten metal.

For squeeze infiltrated castings, the liquid metal is initially under hydrodynamic pressure which changes to a hydrostatic pressure when infiltration is complete and consolidation begins. The extent of metal movement depends on the volume of fibre and/or fibre-preform to be infiltrated.

(ii) In squeeze casting the fibre or particles are introduced into the melt prior to casting, so that the contact time between the melt and the fibre at any one temperature can be controlled under preferred environmental conditions. For squeeze casting of aluminium base alloys the preferred casting temperatures are usually only 25°C to 50°C above the liquidus temperatures of the alloys.

In squeeze infilitration the molten metal comes into contact with the fibre or fibre preforms placed within the die cavity. The contact is of a transitory nature at any one temperature, due to the rapid cooling rate under pressure, and much higher casting temperatures are, therefore, required: usually 200°C or more of additional superheat.

(iii) In squeeze casting, preforms of the

reinforcement are not used and the fibre distribution and orientation in the solidified casting is the same as that obtaining in the melt.

Although the preforms used in squeeze infiltration processes could be prepared to provide the preferred density of population and orientation, in practice, the resistance of the preforms to collapse determines the outcome. The chemistry at the fibre/metal interface may also be changed because of the 'binders' used in the preforms.

Effect of Pressure: The effect of pressure on the solidification of metals has received attention in the past[3-10]. From the point of view of the fabrication of cast MMC's, the ductility of the matrix 'as cast', is of great importance. The factors that can improve the ductility are a fine grained equiaxed structure, matrix homogeneity, and freedom from voids and discontinuities, e.g. shrinkage cavities.

One effect of external pressure on alloy phase equilibria is to alter the melting (liquidus) temperature. It should be theoretically possible therefore (for alloys that shrink upon solidification) to solidify a melt of the alloy without lowering the temperature of the melt, if a sufficiently high pressure can be applied. Other effects may include shifts in the phase boundaries and in the eutectic point. For example, a nominally hyper-eutectic Al-Si alloy when solidified under pressure may show a refined hypo-eutectic structure, with the volume fraction of the α-phase increasing with increased pressure.

Another effect of pressure is to increase the heat flow from the casting through the die walls by a considerable amount compared to an equivalent casting at a pressure of 1 atmosphere and can, therefore, increase the potential for undercooling (supercooling) during solidification.

The application of pressure can effect the virtual elimination of shrinkage and other voids and discontinuities.

Under favourable conditions, therefore, pressure applied during the solidification of an alloy can result in a fine grained equiaxed macro-structure with the micro-structure being characterised by small dendrite arm spacing, small constituent particles and a more homogeneous distribution of structural components. The operative word, however, is 'favourable'. If the casting temperature is high, impracticably high pressures may be needed to obtain a 'refined' structure. The effect of casting temperature on the macro-structure of an Al-4Cu alloy[11] solidified under a pressure of 110 MPa with a die temperature of 210°C is reproduced in Fig.1 to illustrate the point.

On the other hand, if the casting temperature is below the liquidus temperature, e.g., as in rheocasting, both the macro-structure and the micro-structure would be influenced by the size and distribution of the solid particles already formed. The liquid which is the last to solidify (solute-rich) would appear as the continuous phase depending on the volume available. Solidification under pressure will not materially alter this situation[12], except for some marginal effect on the disposition of the solute-rich constitutent.

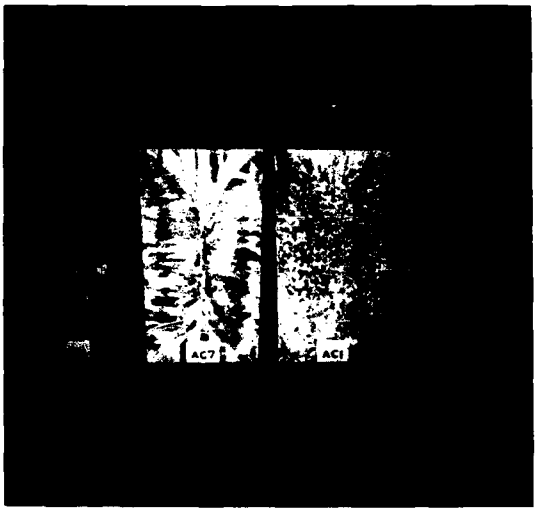


Fig.1 The Effect of Casting Temperature on the Macro-structure of an Al-4Cu Alloy Solidified Under a Pressure of 110 MPa.
Die Temperature 210°C
Legend: AC11 - Cast at 720°C (atmospheric pressure)
AC7 - Cast at 780°C (110 MPa)
AC1 - Cast at 700°C (110 MPa)
AC2 - Cast at 680°C (110 MPa)

Optimum temperatures and pressures during the consolidation stage of squeeze infiltrated castings should produce similar effects on the structure as in squeeze casting. In practice, however, the control of the conditions are much more complex. This is because (a) much higher temperatures need to be employed for the metal to successfully infiltrate through the fibre, and more so if the distance to be infiltrated is large (note: heating the fibre to excessively high temperatures can create 'hot spots' during solidification resulting in shrinkage defects in the casting), and (b) the dynamics of metal flow through the fibre mass or preform is influenced by a large number of variables such as fibre orientation, packing density, contact angle between fibre and metal, and changes in metal viscosity, even if gaseous reaction products at the fibre/metal interface can be precluded.

Fibre-Metal Interaction: Silicon carbide is highly susceptible to oxidation when heated in air. However, the oxide film initially formed (SiO_2) is protective in nature so that further oxidation takes place very slowly. This protective film can break down below a

critical oxygen partial pressure and rapid oxidation is thought to take place by a reaction[13] which yields the gaseous reaction products SiO and CO. At very low partial pressures the rate of oxidation slows down again.

Warren[13] also states that the reaction products most likely to form, when SiC is in contact with pure molten aluminium, are Al_4C_3 and Si. The dissolution and reaction of SiC in molten copper has been reported[14] as well. According to Kohara[15] the dissolution and reaction can be avoided (in Al-melt) if certain alloying elements are present. The presence of silicon is cited as an example. Webster[16] reporting on Al-Li/SiC composite states that there were no obvious signs of chemical interaction between the SiC whiskers and the Al-Li alloy matrix. It is not clear as to how long the whiskers were in contact with the liquid alloy and at what temperature.

Al-Cu Alloys and SiC Fibre: Initial investigations[17] with an Al-4Cu alloy containing small amounts of SiC whiskers, squeeze cast after intimate contact between the molten alloy and the whiskers, for periods of between 15 to 30 minutes, showed (a) that a stable bond was developed between the whiskers and the matrix, (b) that the individual whiskers were associated with the copper rich phase in the micro-structure and (c) that the minimum level of copper needed in the molten alloy to prevent whisker rejection and/or dissolution was approximately 2%. Fukunaga[18] working with squeeze infiltrated composites consisting of Al-Cu alloys and continuous SiC fibre found that for an Al-4% Cu alloy, there was a copper rich layer surrounding the fibre; for the Al-2% Cu alloy the fibre were only partially surrounded and for the Al-1% Cu alloy no Cu-rich layer was detected.

The utilisation of SiC fibre for the development of metal-matrix composites has been restricted due to its known chemical interactions with candidate matrices. Comprehensive data on the interactions with alloy matrices, however, are not yet available. Nevertheless, a number of alloy matrices including Al-base and Cu-base alloys are known to be compatible.

In the experimental work discussed in this paper, no attempt has been made to determine the chemical reactions involved in the composite systems examined. The choice of the matrix alloys were based on the following considerations/assumptions.

(i) In short fibre composites, the matrix is more responsible for the load transfer between fibres than it is in continuous fibre composites. The use of a strong but ductile matrix may improve the strengthening efficiency of the fibre.

(ii) The comparatively newly developed Zn-27Al-3Cu alloy shows excellent room temperature mechancial properties, but the creep properties in particular, are very poor even at a modest temperature of 80°C. An addition of a small volume % of fibre, it was thought might improve the properties.

(iii) The known compatibility of SiC with melts containing Al and Cu[19].

I EXPERIMENTAL PROCEDURE

1. Materials: The Al-4.5Cu alloy used in these experiments was prepared from commercially pure aluminium (99.7% Al) and electrolytically refined copper (99.4% Cu). The ZA-27 commercial alloy was supplied by Brock Metal Company Limited, U.K., with the following range of analyses: Al:26.07 to 26.79%; Cu:2.20 to 2.45%; Mg:0.017 to 0.018%; Fe:0.044 to 0.054%; Sn:0.0008 to 0.0011%; Pb:0.0001 to 0.0005%; Cd:0.0008 to 0.0015%; Zn:rem.

Typical properties of the Nicalon(R) silicon carbide fibre supplied by Nippon Carbon Co. Ltd., Japan are shown in Table I.

Table I

Mean fibre diameter	10-15μm
Mean fibre length	3mm
Cross-section	round
Filament per yarn	500
Density	$2.55 g/cm^3$
Tensile strength	$250-300 kg/mm^2$
Tensile modulus	$18-20 \times 10^3 kg/mm^2$
Maximum permissible temp	1250°C
Co-eff. of thermal expansion	3.1×10^{-6}/°C parallel to fibres.

2. Pretreatment of SiC: The fibre, as received, is in clumps and could not be dispersed uniformly into the melt in this state. Furthermore the 'sheen' on the as received fibre led to 'non-wetting' and fibre rejection from the melt. To obviate these problems the as received fibre had to be heated for 2 hours at a temperature of 900°C followed by passing the fibre through a specially designed mechanical device[20] (similar to those used in the textile industry to comb wool) before introducing the SiC to the melt or into the die where squeeze infiltration was employed.

3. Fabrication of Composite: The Al-matrix alloy was melted and degassed with dry nitrogen at a temperature of between 730-760°C. It was found from the initial experiments that to produce composites with the maximum tensile strength (for the volume of fibre added) the SiC fibre needed to be in intimate contact with the melt for 18 minutes $\pm$ 2 minutes, at 760°C, and this was adhered to during preparation of the test castings. A VORTEX was created in the melt by using a triple bladed stirrer (to provide maximum down- wash) and the requisite amount of fibre added through the separating device. The melt was contained in a mullite crucible and a shroud of dry nitrogen gas was used over the crucible during the 18 minutes the vortex was

maintained. Melts containing 0,2,4,6,8 and 10 v% SiC were prepared in this way and squeeze cast in a metal die (52mm dia x 72mm high):

Casting temperature	687 ± 5°C
Die Temperature	250 ± 3°C
Squeeze Pressure	140 MPa
Pressure Maintained	60-90 seconds

Six castings, from six separate melts, were made from each level of fibre addition.

For the Zn-alloy system, a somewhat different procedure was adopted:

(i) The fibre was pre-treated and introduced into an infiltration die (which had special venting channels) through a separating device (similar in design to the device used for the Al-alloy). The molten Zn-alloy, heated to a temperature of 560°C, was poured into the die and pressure applied via a punch on the free surface of the molten metal to obtain an infiltration speed of 0.127 m/minute.

(ii) The infiltrated ingot was allowed to solidify under a pressure of 110 MPa before ejection from the die.

(iii) The composite ingot produced was remelted and held at a temperature of 600°C ± 5°C for 10 minutes while being mechanically stirred. The crucible containing the melt was then removed from the furnace and the melt temperature allowed to come down to 535 ± 5°C with stirring. The melt was then squeeze cast as in the case of the Al-alloy, the temperature conditions being:

Casting temperature	535 ± 5°C
Die temperature	180 ± 3°C
Squeeze pressure	139 MPa

Squeeze cast composites containing, 0, 3, 6, and 10 v% SiC fibre were prepared in this way.

A group of squeeze infiltrated composites containing 18 to 20 v% SiC were also produced i.e., the final stage of remelting and squeeze casting was not carried through.

4. Metallography: Microscopic methods were used to study the composite structure, fibre orientation and fibre distribution. Fibre fracture (tensile fracture) was studied by scanning electron microscopy and the nature of the fibre/matrix interface by electron probe micro-analysis.

5. Mechanical Testing: Hounsfield No.18 and No.14 tensile test specimens were used for all tensile testing of composites (Note: No.18 has dia 12.8 to 12.85mm and gauge length of 45.4mm while the No.14 has dia 6.4 to 6.426mm and gauge length of 22.7mm). The testing provided data for Ultimate Tensile Strength, Proof Stress, Elastic Modulus, Percent Elongation and Percent Reduction in Area. Tests were carried out both at room temperature and at temperatures up to 300°C for the Al-alloy and 250°C for the Zn-alloy. Heat treated or temperature cycled specimens were tested at room temperature. All tests were carried out at a strain rate of $1.825 \times 10^{-4}.s^{-1}$.

Vickers Pyramid Hardness Testing and Brinell Hardness Testing followed heat treatment or temperature cycling of a number of test pieces.

Fatigue life (room temperature) was determined in a Wohler-type rotating bending machine (specimen dia 3.81mm). A reverse bending stress of 95 MPa was used for the Al-alloy and 200 MPa for the Zn-alloy.

6. Composite Stability: Due to the mismatch in the co-efficient of expansion between matrix and fibre, interest is focused not only at the fibre/matrix interface stability, but also at the stability of the matrix itself at different temperatures. A number of selected samples were heat-treated before tensile testing at room temperature.

(i) For the Al-alloy composite, specimens from some of the castings were solution treated at 545°C for 2 hours, water quenched (80°C), followed by 'ageing' at 180°C for 6 hours. Batches of castings were also subjected to temperature cycles between room temperature and 350°C; which consisted of holding in a furnace for 25 minutes at 350°C followed by quenching in air. The cycle was repeated up to 20 times.

(ii) For the Zn-alloy, dilatometric studies were made to determine the matrix stability (without fibre) at 95 ± 2°C for periods of up to 30 days (specimen dia 12.7 ± 0.005mm and length 59.9 ± 0.015mm) in an atmosphere of dry argon. Further batches were given a homogenisation treatment by heating at 320 ± 5°C for three hours followed by cooling in the furnace at an approximate rate of 0.5°C/minute, for subsequent testing at room temperature.

RESULTS AND OBSERVATIONS

Micrographs: Squeeze casting resulted in pore-free structures with uniform distribution of fibre in random orientation. No differences could be detected between longitudinal and transverse sections (with respect to the direction of travel of the punch). Gravity segregation was not detected in the castings examined. Typical micrographs of fibre distribution are reproduced in Figs.2 and 3.

The solution treated and aged composites of the Al-alloy system showed no signs of copper concentration near or next to the SiC fibre. (See Fig.10). However, the cast composite showed a distinct envelope of a copper-rich constituent around the fibre as did the castings undergoing temperature cycles.

In the case of the Zn-alloy, composite both the cast and the homogenised composites showed a copper-rich envelope around the fibre resembling a modified eutectic containing



Fig.2 Fibre Distribution in Al-4.5Cu Alloy Matrix, 10 v% SiC, Squeeze Cast x 50.



Fig.3 Fibre Distribution in Zn-27Al-3Cu Alloy Matrix, 10 v% SiC, Squeeze Cast x 40.

Cu, Zn and Al. The squeeze infiltrated castings, however, did not show any concentrations of Cu, either in the cast or the homogenised state. The micro-structure in the homogenised state is reproduced in Fig.4.

The inference to be drawn is that in the squeeze infiltrated castings either the duration of contact between liquid alloy and fibre or the temperature or both had been insufficient to allow any interactions to have taken place. (See Fig.12).

SEM: The fractured surfaces of tensile test pieces (tested at room temperature and at higher temperatures) confirmed that fibre degradation takes place when an optimum contact time between the molten alloy and fibre is exceeded (for any one temperature) as shown in Fig.5. On the other hand a shorter than necessary period of contact fails to develop a proper bond between fibre and matrix, illustrated in Fig.6.

For the Al-4.5Cu alloy the optimum time was found to be 18 minutes at 730°C and for the ZA-27 alloy 10-11 minutes at 600°C.

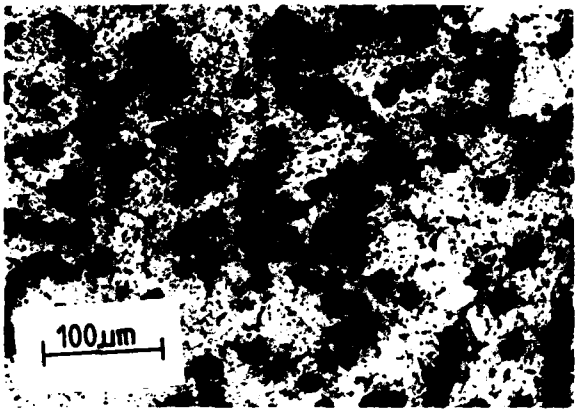


Fig.4 Micro-structure of Homogenised Composite Zn-27Al-3Cu Alloy Matrix, 20 v% SiC, Squeeze Infiltrated.

Squeeze castings produced after the optimum period of contact developed strong bonds and the fractured surfaces did not show any evidence of fibre pull-out when tested at room and elevated temperatures. The evidence for the Zn-alloy composite was not as clear cut as that for the Al-alloy illustrated in Fig.7.

The most important point to note is that controlled interaction between the fibre and the melt is necessary in the systems examined to develop stable and satisfactory bonds, and that the presence of Cu in both the Al-alloy and the Zn-alloy is instrumental in promoting the interaction. It may be no more than preferential nucleation of intermetallics such as $CuAl_2$ on a SiC or SiO_2 substrate.

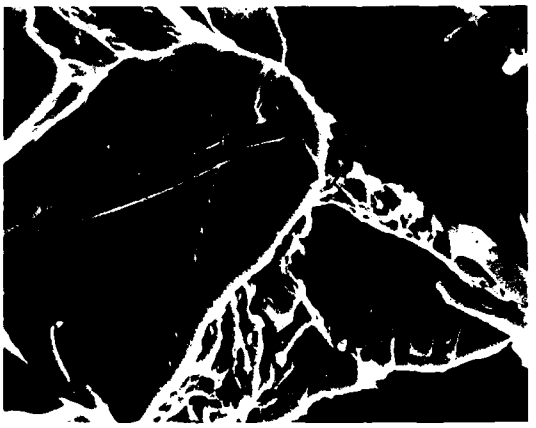


Fig.5 Fibre Degradation, 10 v% SiC in Al-4.5Cu Alloy Matrix. Contact Period 39 Minutes at 730°C SEM x 1.3K.

Mechanical Testing: The data for the Al-alloy composite containing 0, 6 and 10 v% fibre tested at 20°C and at 250°C are tabulated in Table II and for the Zn-alloy composite containing 0 and 10 v% fibre tested at 20°C and at 200°C are reproduced in Table III, together with values for the squeeze

infiltrated composite containing 18 v% fibre.

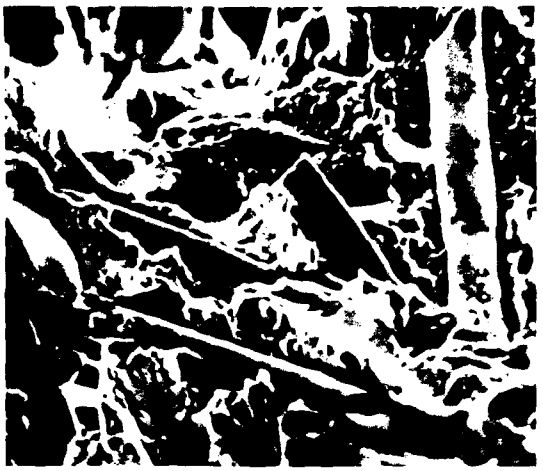


Fig.6 Poor Bonding: Fibre Pull-Out: 8 v% SiC in Al-4.5Cu alloy Matrix. Contact Period 8 minutes at 730°C SEM x 0.5K.

For the Al-alloy composite a steady improvement is observed in the values (except elongation) with increasing SiC content, but there is a deterioration in the values (except the elastic modulus) in case of the Zn-alloy composite with increasing SiC - the worst being for the squeeze infiltrated composites containing 18 v% SiC. Strengthening occurs, however, (comparative) for this system at 200°C.



Fig.7 Fractured Fibre: Tensile Test at 300°C: 8 v% SiC in Al-4.5Cu Alloy Matrix. Contact Time 18 Minutes SEM x 2.2K.

It is also interesting to note that an average deterioration (of about 20%) in the strength properties of the Al-alloy composite takes place in the heat treated castings,

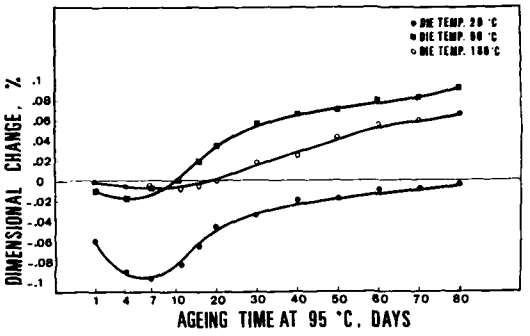


Fig.8 Dimensional Changes in Squeeze Cast Zn-Alloy Matrix as a Function of Ageing Time at 95°C.

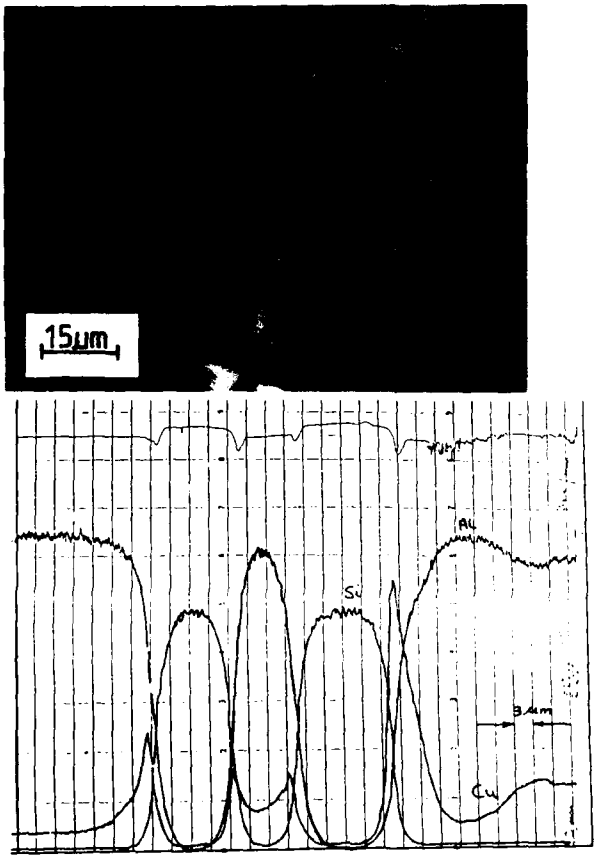


Fig.9 Scattered Electron Image and Corresponding EPMA Line Scan Pattern of SiC Fibre in Al.4.5Cu Alloy Matrix Squeeze Cast After 18 Minutes of Fibre/Melt Contact.

TABLE II Room and Elevated Temperature Tensile Properties of the Squeeze Cast Al-4.5Cu Matrix/SiC Fibre Composite (Average Values).

Testing Temp. °C	Volume % Fibre	UTS MPa	0.1% PS MPa	Elastic Modulus GPa	Elongation %	Reduction in Area %	Remarks
20	0	182	107	71	17	15	*20
20	6	192	153	78	5.1	4.5	cycles
20	10	198	184	82	3.5	2.5	through
*20	10	193	186	82	2.5	2.0	20-350°C
250	0	77	64	57	37	39	
250	6	96	90.2	68.2	14.7	12.5	
250	10	109	104	71.5	6	5.2	

TABLE III Room and Elevated Temperature Tensile Properties of the Squeeze Cast Zn-27Al-3Cu Matrix/SiC Fibre Composite (Average Values).

Testing Temp. °C	Volume %	UTS MPa	0.2% PS MPa	Elastic Modulus GPa	Elongation %	Reduction in Area %	Remarks
20	0	411	358	75.6	17	21	*squeeze
20	0	300		97.8	2	2	infil-
20	*18	265		95.90	1	1	trated
200	0	93	85	28	29	39	*squeeze
200	10	124	121	32	7	8	infil-
200	*18	118	115	31	6	9	trated

whereas cycling through from room temperature to 350°C has no apparent effect. The reason for this behaviour is linked to the absence of the Cu-rich 'envelope' in the heat-treated casting, whereas the envelope remains intact after temperature cycling up to 20 cycles. The age hardening treatment also reduces the ductility of the matrix which may be an additional reason for the observed deterioration in properties of the composite.

The behaviour of the Zn-alloy system can be clearly linked to the dimensional instability of the as cast matrix (determined by dilatometric methods, Fig.8).

It will be noted that the rate of return to equilibrium depends on the die temperature i.e. the overall cooling rate which affects the degree of non-equilibrium in the Al-rich and Zn-rich constituents of the as cast structure. The rapid cooling rate in squeeze casting also tends to give rise to a non-equilibrium copper-rich constituent which appears to remain stable even after homogenisation treatment at 320°C.

EPMA: The scattered electron images of SiC fibre in matrices of the Al- and Zn-alloys and the corresponding EPMA line scan traces are reproduced in Figs.9-12.

The point to note is the presence or absence of the copper-rich envelope around the SiC fibre. This when considered in conjunction with the results from mechanical testing (where the absence of the envelope is related to poor results) leads one to conclude that for the systems examined, copper plays a vital role in the development of fibre/matrix bond, and that the copper-rich zone is not dissipated in the Al-alloy at 350°C and the Zn-alloy at up to 320°C even after prolonged

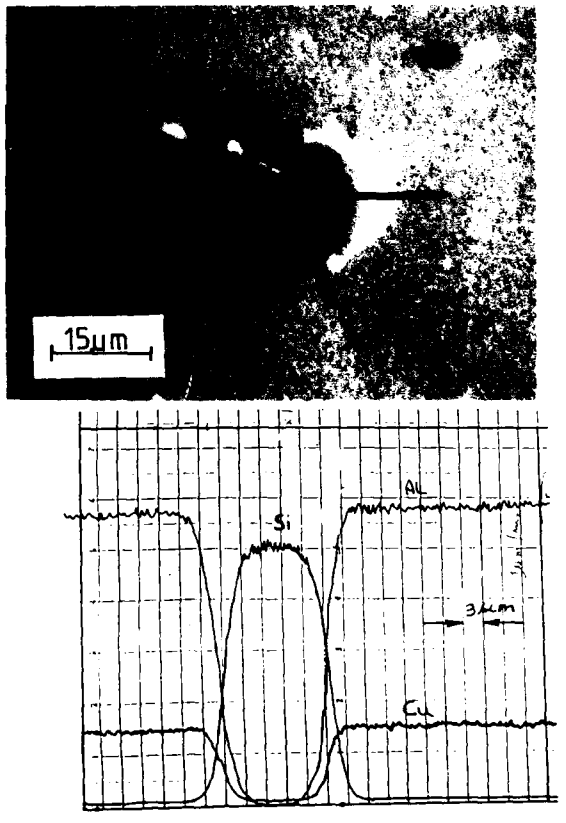


Fig.10 Scattered Electron Image and Corresponding EPMA Line Scan Pattern of SiC Fibre in Al-4.5 Cu Alloy Matrix. Age Hardened after Squeeze Casting.

treatment.

Fatigue Life: The room temperature fatigue life of both the Al-alloy and the Zn-alloy showed improvement with increasing fibre content:

Alloy	Fibre v%	Fatigue Life x 10^5
Al-4.5Cu	0	5.68
Al-4.5Cu	10	9.55
Zn-27Al-3Cu	0	2.48
Zn-27Al-3Cu	10	4.48

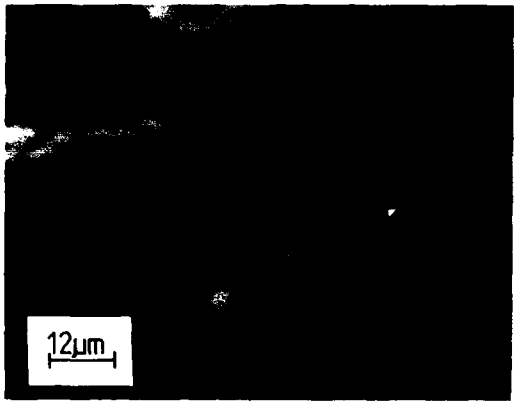
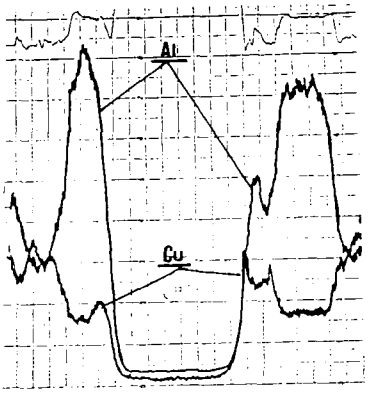




Fig.11 Scattered Electron Image and Corresponding EPMA Line Scan Pattern of SiC Fibre in Zn-27Al-3Cu Alloy Matrix. Homogenised After Squeeze Casting.





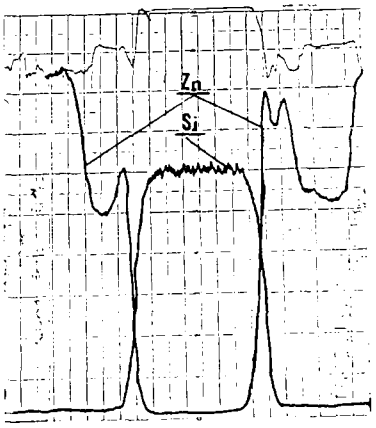


Fig.12 Scattered Electron Image and Corresponding FPMA Line Scan Pattern of SiC Fibre in Zn-27Al-3Cu Alloy Matrix. Homogenised After Squeeze Infiltration.

CONCLUSIONS

1. In the Al-4.5Cu and Zn-27Al-3Cu alloy composites the stability of the interface region depends on the nature of the Cu-rich zone at the fibre/matrix interface. It is suggested that preferential nucleation of $CuAl_2$ or $CuZn_4$ on the SiC or SiO_2 substrate cannot be ruled out; although no direct evidence has been presented.

2. When the 'as cast' matrix is not susceptible to structural modifications at room temperature or at higher temperatures (tested up to 350°C for the Al-alloy) the addition of even small amounts of SiC fibre can make measurable improvements in the tensile properties of squeeze cast composites. The strengthening effect is more marked at higher temperatures.

3. When the matrix structure 'as cast' is unstable as in the Zn-alloy, addition of SiC fibre has a deleterious effect on the room temperature tensile properties, except for the elastic modulus. The squeeze infiltrated castings showed the greatest deterioration in properties. When tested at higher temperatures e.g. 200°C the composites are stronger than the matrix alloy.

4. In the Zn-alloy composite(s) squeeze infiltration (under the conditions used) does not lead to a copper-rich zone around the SiC fibre (poor bonding) and exacerbates the damaging effect on the properties brought about by the unstable nature of the as cast matrix.

5. An almost linear increase in fatigue life is observed, for both composite systems, with increasing fibre addition. While this is to be expected in the Al-alloy, no such correlation exists with the other properties in the case of the Zn-alloy composites.

6. The stengthening efficiency of the fibre in both cases improves at higher temperatures i.e. related to higher ductility of the matrix.

ACKNOWLEDGEMENT

The authors gratefully acknowledge the financial support received for Dr. B. Zantout from the Syrian Government, and for Dr. M. M. Yakoub from the British Council. They also wish to thank the SERC for continuing support on the Zn-alloy project.

REFERENCES

1. Williams G., and K. M. Fisher, Metals Technology, 8, 263, (1981).
2. Feest E. A., M. J. Ball, A. R. Begg, and D. A. Biggs, Metal Matrix Composites Developments in Japan Report on OSTEM Visit to Japan, Harwell Laboratory, Oxfordshire, (1986).
3. Chatterjee S., and A. A. Das, The British Foundryman, 65, 420, (1972).
4. Chatterjee S., and A. A. Das, Ibid, 66, 118, (1973).
5. Epanchintsev O. G., Russian Casting Production, 34, (1972).
6. Lipchin T. N., and P. A. Bykov, Ibid, 109, (1973).
7. Oya S., J. Japan Foundrymen's Soc., 41, 29, (1969).
8. Aoki K., K. Kato, M. Nomoto, and H. Tokisue, J. Japan Inst. Light Met., 30, 212, (1980).
9. Lynch R. F., R. P. Olley, and P. C. J. Gallagher, AFS Transactions, 83, 561, (1975).
10. Lynch R. F., R. P. Olley, and P. C. J. Gallagher, Ibid, 83, 259, (1975).
11. Lee Ho-In, The Influence of Hydrostatic Pressure on the Macro- and Micro-structures of Al-4%Cu Alloys, M.Sc. Thesis, Loughborough University of Technology, Dec. (1976).
12. Gibson P. R., A. J. Clegg, and A. A. Das, Materials Science and Technology, 1, 559, (1985).
13. Warren R., and C. H. Andersson, Composites, 15, 101, (1984).
14. Bates H. E., F. Wald, and M. Weinstein, Advanced Fibrous Reinforced Composites, SAMPE, 10, E41-51, (1966).
15. Kohara S., Proc. Japan-US Conference on Composite Materials, Tokyo, Composite Materials K. Kawata and T. Akasaka, Ed., pp 224-231, (1981).
16. Webster D., Met. Trans. A, 13A, 1511, (1982).
17. Chatterjee S., Aluminium-Silicon Carbide Whisker Cast Composites: Some Observations on the Distribution, Bonding and Properties Developed, Ph.D. Thesis, Loughborough University of Technology, May (1973).
18. Fukunaga H., and K. Goda, Bulletin of JSME, 28, 1, (1985).
19. Imich G., United States Patent No.2,793,949, May (1957).
20. Zantout B., A. A. Das, and A. J. Clegg, Proceedings of the First National Conference on Productions Research, Kogan Page, pp. 345-352 (1986).

SQUEEZE CASTING AND PROPERTY EVALUATION OF ALUMINA FIBRE REINFORCED ALUMINIUM-SILICON ALLOY MATRIX COMPOSITE

Saeed Ahmed, V. Gopinathan, P. Ramakrishnan
Indian Institute of Technology
Bombay, India

ABSTRACT

Aluminium alloy metal matrix composites reinforced with ceramics like graphite, silicon carbide and alumina in fibre or particulate form have been used for various aerospace components, which are usually shaped by high cost fabrication techniques like vacuum hot pressing, diffusion bonding and controlled atmosphere liquid metal infiltration. The present investigation is concerned with the use of low cost squeeze casting process for the fabrication of alumina fibre reinforced aluminium alloy matrix composites.
Cylindrical saffil alumina fibre preforms were prepared from liquid slurry by vacuum filtration process using appropriate binders. Composites containing approximately 0.06,0.12 and 0.20 fibre volume fraction in matrix of aluminium - 12.5 wt% silicon alloy were prepared by squeeze casting under 50 MPa pressure. Microstructure of composite revealed a dense structure with no microporosities or segregated phase at fibre - matrix interfaces. The 0.20 fibre volume fraction composite exhibited a tensile strength of 224 MPa as compared to a value of 110 MPa for the unreinforced matrix alloy, squeeze cast under identical conditions. Fractographic examination revealed good fibre-matrix bonding and matrix deformation.

ALUMINIUM-SILICON ALLOYS ARE mainly used for castings of medium strength with good corrosion resistance because of their excellent castability. The presence of silicon imparts high fluidity and low shrinkage. The low thermal expansion of alloy is exploited for pistons and high hardness of silicon particles for wear resistance. The fluidity of these alloys is excellent and maximum at eutectic composition and also the range of solidification is very narrow. This tends to reduce segregation. These alloys are used for automobile components usually manufactured by permanent mold and die casting. Ceramic fibre reinforcement of these alloys can achieve very significant improvement of their critical properties. Alumina fibres are reported to exhibit high strength, thermal stability and wettability to aluminium (1-3). Characteristics of alumina fibres of different types are listed in Table 1.

Table 1 - Characteristics of different types of alumina fibres.

COMPARATIVE PROPERTIES OF ALUMINA FIBRES

	SAFFIL ①	DUPONT FP ②	SUMITOMO ③
1 GRADE	RF	FP	—
2 CHEMICAL COMPOSITION	96-97 % Al_2O_3 3-4 % SiO_2	—	85 % Al_2O_3 15 % SiO_2
3 TENSILE STRENGTH (MPa)	2000	1380 - 2070	1800
4 TENSILE MODULUS (GPa)	—	380	250
5 MELTING POINT °C	> 2000	2045	—
6 CRYSTAL PHASE	δ ALUMINA	α ALUMINA	SPINEL
7 DENSITY (g/cm³)	3.3	3.9	3.2
8 MEAN FIBRE DIAMETER (μm)	3	20	17
9 FIBRE TYPE	DISCONTINUOUS	CONTINUOUS	CONTINUOUS

① I C I Data sheet, I C I Metal division, Runcorn, Cheshire U K 1982
② A K Dhingra Chem Tech October 1981, P 600
③ Y Abe, S Hanlan K Funmuro, E Ichiki, Progress in Science and Engineering of composites Ed T Hayashi ICCM IV, Tokyo 1982 P 1430

Various aluminium alloy matrix compo-

sites reinforced with these fibres have been reported to exhibit high strength, tensile modulus, resistance to wear and fatigue in addition to elevated temperature properties (2-6). The suitability of these composites for automobile components is currently being investigated (7-12). The composite fabrication techniques such as vacuum hot pressing, liquid metal infiltration(3) and roll diffusion bonding (5) have not achieved mass production viability necessary for automobile components. Selectively reinforced aluminium matrix composites can be fabricated by the squeeze casting process in order to achieve tailored properties.

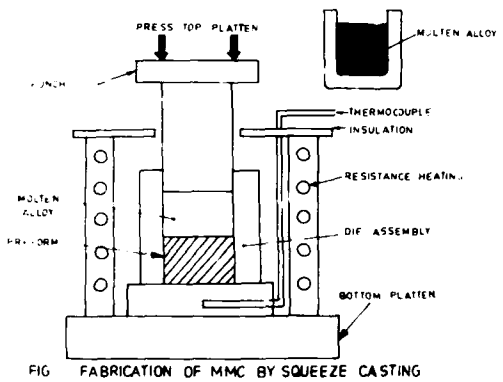


FIG FABRICATION OF MMC BY SQUEEZE CASTING

Figure 1-Schematic diagram of squeeze casting process.

In this process as illustrated in Fig.1, molten alloy is poured into a die containing ceramic preform with controlled fibre volume fraction. On application of pressures in the range of 25-75 MPa, the molten alloy infiltrates into preform and consolidation to solid shape is achieved. The advantages of squeeze casting metal matrix composites (MMC) are low cost, ease of fabrication, near net shape, feasibility of selective fibre reinforcement, complete microstructural homogeniety and good fibre-matrix bonding. In the present work aluminium - 12.5 wt % silicon alloy composites reinforced with random orientation δ alumina saffil fibres have been fabricated by squeeze casting and their characteristics evaluated.

EXPERIMENTAL WORK

DIE ASSEMBLY - For fabrication of composite specimens by squeeze casting, a three piece die was designed and fabricated from hot-die-steel. A photograph of the die assembly with the punch in position is shown in Figure 2.

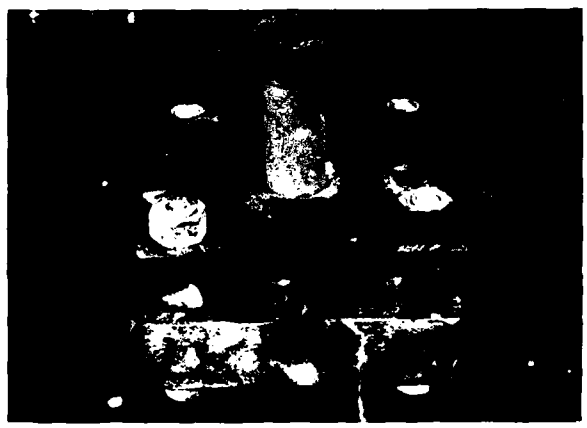


Figure 2-Assembled squeeze casting die system.

REINFORCING CERAMIC - Saffil - δ alumina fibres with random orientation have been used as reinforcing ceramic. The properties of these fibres are listed in Table 1.

MATRIX ALLOY - Aluminium - 12.5wt % silicon casting alloy has been used as composite matrix material. The chemical composition of this alloy is given in Table 2.

Table 2 - Chemical composition of matrix alloy.

Wt. percentage of elements				
Si	Fe	Cu	Mn	Al
12.500	0.250	0.050	0.003	Bal.

FABRICATION OF PREFORM - An aqueous slurry of alumina fibres with appropriate binder was prepared. Controlled ultrasonic agitation of slurry was used to ensure thorough mixing of the constituents. Cylindrical alumina fibre preforms were prepared by pouring measured quantities of this slurry into a split forming-mold and subsequently using vacuum filtration process. The density of alumina preforms was in the range of 0.68 - 0.76 g/cc.

COMPOSITE FABRICATION - The aluminium alloy was melted in a resistance furnace and maintained at 850°C. Alloy degassing was done by flushing nitrogen gas. The alumina preform was placed in the die cavity and this assembly was heated in a resistance furnace to 500°C Measured quantity of degassed molten

alloy was poured into preheated die cavity. The preheated ram attached to 50 Tonne hydraulic press was used to maintain 50 MPa pressure during alloy infiltration into preform and subsequent solidification into composite. This 50 MPa pressure for squeeze casting was maitained for 40 seconds. Specimens of unreinforced matrix alloy were also squeeze cast under idential conditions representing zero fibre volume fraction. The squeeze cast composite specimens were cylindrical in shape and had dimensions of 25 mm diameter x 50 mm length.

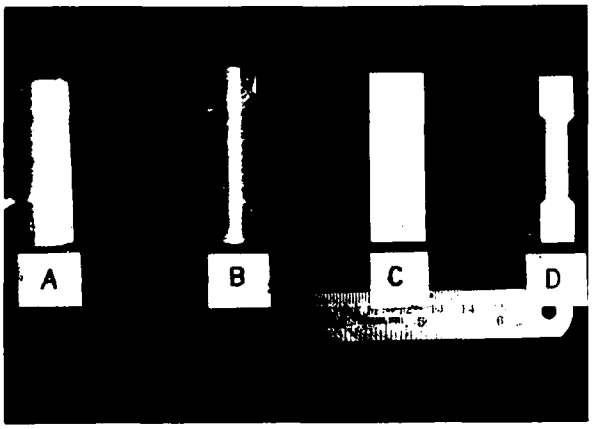


Figure 3-Photograph of (A) ceramic preform,(B) squeeze cast composite, (C) flat sectioned tensile specimen and (D) ASTM tensile specimen.

After retrieving the specimens from the die, standard tensile specimens of 4 mm thickness were prepared according to ASTM-E-8-66, section 4.2 specifications. Figure 3 shows photograph of fibre preform, squeeze cast composite and ASTM tensile specimen. The tensile tests were conducted on 40 Tonne Instron system. Metallographic observations were made on samples mounted in cold setting resin and etched with standard Keller's reagent. The fibre volume fraction was estimated using TAS-PLUS Image analysing system. Vicker's hardness was measured on Reicherter Vicker hardness machine using 1.0 kg load.

RESULTS AND DISCUSSION

FIBRE VOLUME FRACTION - The alumina reinforced aluminium - 12.5 wt % silicon alloy composites prepared by squeeze casting exhibited fibre volume fractions of 0.06, 0.12 and 0.20.

TENSILE STRENGTH - Figure 4 shows variation of composite tensile strength with alumina fibre volume fraction. For unreinforced alloy samples the strength is in the range of 95-110 MPa. For 0.20 alumina volume fraction composite, the maximum strength of 224 MPa has been observed. This represents 104 percent improvement in composite strength.

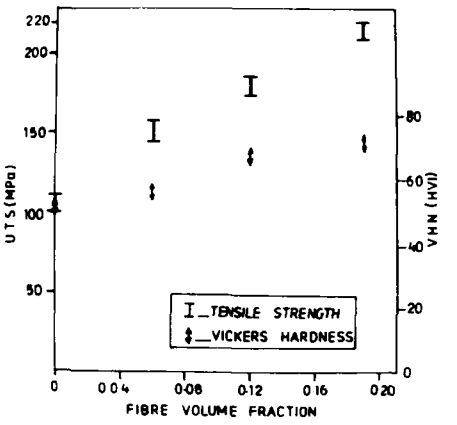


Figure 4-Tensile strength and hardness of alumina - aluminium + 12.5 wt % silicon alloy composites with varying fibre volume fraction.

HARDNESS - The Vicker hardness results are shown in Figure 4. Hardness of unreinforced matrix alloy is observed in the range of 50.3 to 53.6 VHN. For 0.20 alumina fibre volume fraction composites the hardness is in the range of 72.5 to 74.6 VHN. This represents an improvement of 39 percent in composite hardness compared to matrix alloy.

METTALLOGRAPHY - Figure 5 and 6 are optical metallographs showing the typical microstructures in the squeeze cast unreinforced matrix and 0.20 alumina fibre volume fraction composite respectively. The size and distribution of silicon and intermetallic ($FeSiAl_5$) phases in the squeeze cast matrix (Figure 5) are finer and more uniform than are generally observed in conventionally cast alloy. It can be observed from microstructure of composite (Fig.6) that the incorporation of alumina fibres has resulted in further improvement in the size and distribution of Si and $FeSiAl_5$ phases. The randomly oriented alumina fibres are mostly found to be distributed along grain boundaries. This can be attributed to the nucleation of matrix grains along fibre surfaces during liquid metal infiltration and rapid solidification under squeeze casting pressure. The unreinforced matrix and fibre reinforced composite

microstructures exhibit homogeneous and completely porosity free structure under the conditions of squeeze casting employed in the present investigation.

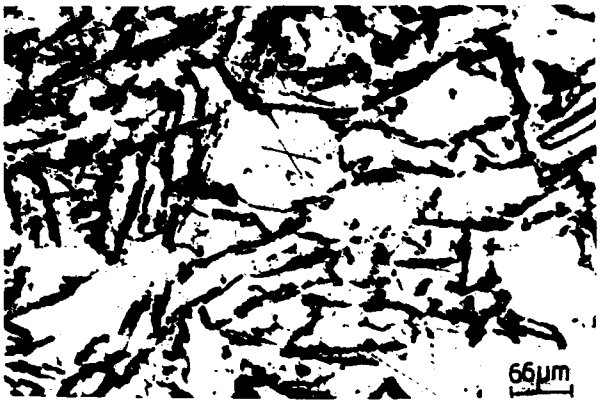


Figure 5-Optical micrograph of unreinforced aluminium + 12.5 wt % silicon alloy produced by squeeze casting.

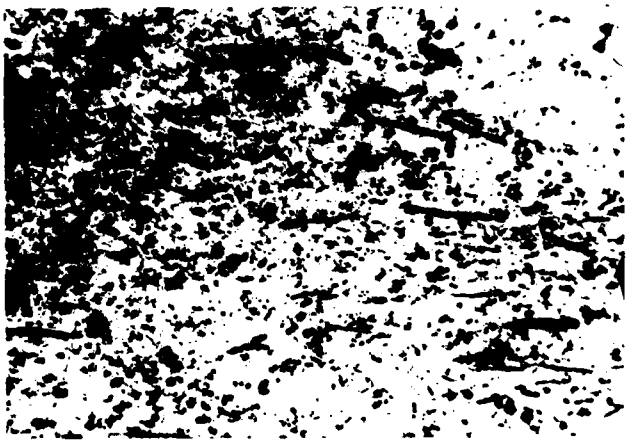


Figure 6-Optical micrograph of 0.20 alumina volume fraction aluminium + 12.5 wt % silicon alloy composite produced by squeeze casting.

FRACTOGRAPHY - The SEM fractograph of composite with 0.20 alumina fibre volume fraction is shown in figure 7. The fractured surface is found to be relatively smooth with no fibre protrusions. The deformation and flow pattern of the matrix indicate typical failure mode of composite. Failure appears to have occured simultaneously through matrix and fibres suggesting that squeeze casting technique has achieved good bonding between fibres and matrix. Substantial improvement in strength of composite with higher volume fractions of alumina can therefore be expected and investigations on these lines are currently in progress.

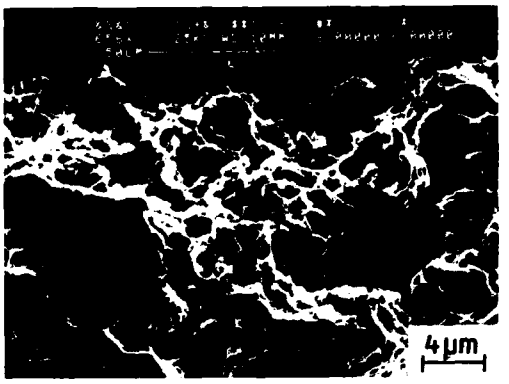


Figure 7 - SEM fractograph of 0.20 alumina fibre volume fraction aluminium + 12.5 wt % silicon composite fabricated by squeeze casting.

CONCLUSIONS

Composites of randomly oriented alumina fibre reinforced aluminium + 12.5 wt % silicon alloy could be successfully fabricated by squeeze casting using 50 MPa pressure. Maximum tensile strength of 224 MPa and a maximum hardness of 74.6 VHN have been achieved with 0.20 volume fraction alumina fibre reinforcement. The presence of alumina fibres in the squeeze cast composites resulted in considerable grain refinement as well as an improved distribution of silicon and intermetallic ($FeSiAl_5$) phases.

REFERENCES

1. I.C.I. data sheet on RF Saffil, I.C.I. Mond div., Runcorn, Cheshire, UK,(1982)
2. A.K. Dhingra, Chem. Tech., 600-608, Oct(1981)
3. Y.Abe, S.Horikiri, K.Fujimura, E.Ichiki, Progress in Science and Engg. of Composites, ICCM IV, Ed. T. Hayashi, K. Kawata, S.Umekawa, 1427-1434,(1982)
4. B.C.Bechtold, R.L.Beatty, J.L.Cook, ibid,113-120
5. H.Asanuma, A.Okura, ibid,1435-1442.
6. R.B. Aronson, Machine Design, 68-73, Aug 8, (1985)

7. M.A.H.Howes, Journal of Metals, 28-29, March (1986)
8. K.Ohori,H.Watanabe and Y.Takeuchi, Material Science and Tech.,Vol.3, 57-60, Jan (1987)
9. C.Milliere, M.Suery, Material Science and Tech., Vol.4, 41-51, Jan (1988)
10. T.W.Clyne, M.G.Bader, Fifth Intl. Conf. on Composite Materials, ICCM V, Ed.W.C. Harrigan Jr., J.Strife, A.K.Dhingra,TMS Pub., Warrendale, 755-771,(1985)
11. J.Dinwoodie, E.Moore,C.A.J. Langman and W.R. Symes, ibid, 671-685.
12. L.Akermann, J. Charbonnier, D. Desplanches and H.Koslowski, ibid, 687-698.

MICROSTRUCTURES AND PROPERTIES OF ZINC-ALLOY MATRIX COMPOSITE MATERIALS

J. A. Cornie
Massachusetts Institute of Technology
Cambridge, Massachusetts, USA

R. Guerriero, L. Meregalli, I. Tangerini
Nuova SAMIM - Centro Richerche Venizia
Venizia, Italy

Abstract

Among the new engineering materials, some of the most successful in terms of use outside the aerospace industry are Al-matrix composites discontinuously reinforced by powders or short fibers. Research aimed at producing analogous composites using a Zn-Al alloy matrix is being carried out by several groups.

A research program on discontinuously reinforced Zn-Al matrix composites using low-cost reinforcements and processing techniques is presented. The goal is to produce composites which are economically competitive with conventional engineering materials in the commercial sector.
The principal matrix alloy studied was Zn-Al27%-Cu2% (ASTM ZA-27) reinforced with SiC powders (abrasive grade) or short alumina fibers. Liquid metal infiltration of a reinforcement-filled die is used to obtain composites with reinforcement volume fractions of up to 50% SiC powder or up to 27% alumina short fiber. The former composites were remelted in a mixing apparatus and diluted with a quantity of matrix alloy in order to obtain composites with lower volume fractions of reinforcement.

Net-shape or near net-shape objects were produced by direct infiltration of a reinforcement-filled die or by deformation of the composite material in the semisolid state. Low concentration composites of both SiC and alumina were extruded in the form of wires and tubes or rolled.
Scanning electron microscopy and fractography revealed good bonding and wetting between matrix and reinforcement. In the extruded and rolled materials an alignment of the reinforcement in the direction of the plastic deformation was observed. Preliminary mechanical and physical characterization of the materials produced to date includes the modulus of elasticity, ultimate tensile strength, Brinell hardness and thermal expansion coefficient. Elasticity moduli from two to three times higher than the matrix of reference and tensile strength values similar or slightly higher were found. Preliminary wear resistance data show a tenfold increase.

PROJECT ENGINEERING REQUIRES, more and more, materials with better properties, lightweight characteristics, and competitive costs in comparison to traditional ones. With this incentive, metal matrix composite materials have been developed over the last few years. The matrix is primarily an aluminum alloy, the reinforcements may be either whiskers or long fibers. The production technology is sometimes very complex [1]. High quality products were derived, but unfortunately their production costs make them suitable only for aerospace applications.

More recently other metal matrix composites have been developed with different kinds of reinforcement and by more traditional and hence, less expensive. The matrix is generally an aluminum-base alloy, the reinforcements are abrasive-grade ceramic powders or short alumina base fibers. The manufacturing technology is derived from mixing and infiltration methods. In this field some commercial products are already known, e.g. pistons for diesel engines, partially reinforced with 5-27%v. short alumina fibers of different composition [2-3] and made by squeeze casting; piston rods and other shapes [4] derived from rolled, extruded, and forged materials with a SiC powder content of 15-25%v. Also reported are studies and prototype productions of magnesium alloys materials [5], reinforced by SiC powders up to 25%v. processed by compocasting.

ZINC MATRIX COMPOSITES

Along the line of the latter composite materials, research on zinc alloys based composites is carried on, in particular Zn-Al alloys (ZA Alloys), reinforced by powders or short fibers. The aim is to develop advanced materials with improved characteristics in comparison to those of the matrix alloys. This should be especially true for temperatures higher than room temperature, since zinc alloys show low properties which make them less suitable for higher performance applications. Until the last few years, only a few studies on zinc matrix composites have been published in literature and, among these, only one [6] concerning a Zn-Al matrix alloy composite reinforced with different kinds of ceramic powders. At present time, some industrial and university laboratories are studying the most convenient methods of manufacturing these composites, their technological properties and applications.

At the meeting of Toronto (Canada) on Zn alloys, held on August 1986, communications about this topic were presented. I.L.Z.R.O. (International Lead Zinc Organization) is investigating into zinc and zinc alloy matrix composites. On May 1987, I.L.Z.R.O. organized a workshop in Italy, at Centro Richerche Venizia-Nuovo SAMIM. At that time,

researchers were almost exclusively developing composites made commercial Zn-Al alloys, with a variable Al content in the Zn alloy matrix. Reinforcements were short alumina fibers, or abrasive grade SiC powders. Manufacturing methods are chiefly based on direct mixing of constituents, or on infiltration techniques.

The authors [10] are now carrying on a research program with the aim of developing composite materials with competitive costs compared to those of traditional materials.

COMPOSITE PREPARATION

MATERIALS- With reference to the above mentioned purpose of our research, we chose commercial low-cost materials as constituents. As the matrix we use hypereutectic zinc base alloys [11], in particular Zn-Al27%Cu2% (ZA-27) and Zn-Al11%-Cu1% (ZA-12) alloys, which show satisfactory melting ranges. These alloys are already applied to several mechanics and automotive fields.

In Table 1 some mechanical properties of alloys are shown; measurements were made on materials cast in the same conditions of composite preparation.

Casting Alloy	Melting Range °C	UTS MPa	E GPa	Elong %	HB
ZA-12	377-432	300	87	5	117
ZA-27	375-484	410	73	2	95

Table 1 - Some Physical and Mechanical Properties of as-cast ZA Alloys

We are testing several kinds of powders and fibers, as the reinforcement. We particularly considered abrasive-grade SiC powders. Three different grit sizes were considered: grit 100 (SiC100) with 125μm average diameter of particulates, grit 500 (SiC500) with 20 μm average diameter and gtit 1200 (SiC1200) with a 3 μm average particle diameter. Short alumina fibers, produced be I.C.I. and delivered under "Saffil" TM [13], with average diameter 3-4 μm and average length 500 μm are also included in the investigation. Of thes fibers some preforms of different shapes are also available and were applied in other kinds of metal matrix composites [14].

PREPARATION TECHNIQUES- The above mentioned composites are usually prepared making use of direct mixing of reinforcements with molten metal, or of a liquid metal infiltration into reinforcement-filled dies.

As a consequence of the poor reinforcement wettability and the boyancy of the reinforcements investigated in molten Zn. It was necessary to add the reinforcement to the matrix in the semisolid state under rapid stirring in order to increase the alloy's viscosity [5-6-15-16-17]. Pressure-assisted infiltration assures a better adhesion between the matrix and the reinforcement and insures the elimination of air from the interparticulate spaces and hence, was the most used technique [18].

We chose these methods for composite preparation because they satisfy economic considerations. The equipment, made and used by ourselves specifically for this project, were previously shown [7-10]. By these techniques we succeeded in mixing homogeneously up to 40%v. of SiC powder with up to 5%v. alumina fibers with molten metal.

We also infiltrated different kinds of reinforcements; SiC powders of different grain sizes, up to more than 50%v, and short alumina fiber (Saffil) preforms, in the range of 11-27%v. With the latter method we were able to prepare ingots, bars, and plates of various dimensions to 500 cm^3 total volume which corresponds to a weight of 20 N for a composite whose density is 4 Kg/dm^3.

DILUTION AND FORMING-Composite materials, produced by mixing or infiltration, can be remelted by heating the matrix at a temperature higher than melting range. Upon stirring, the composite becomes a semisolid slurry which can be extruded or forged.

Dilution can be achieved by adding new molten alloy to the semisolid slurry while stirring; the equipment is the same as for the previous mixing stage, even if dilution is normally easier than mixing because the reinforcement is already dispersed into the metal phase. This technique is particularly useful for composites derived through powders infiltration, in which the reinforcement content cannot be much lower than 50%v. Thus we produced composites with ZA-12 or ZA-27 alloy as the matrix, SiC500 10-12%v. as the reinforcement.

In order to produce net-shape composite materials, we followed two main approaches: 1st) is the direct infiltration by injection of liquid metal into suitable shaped molds, filled with reinforcement; 2nd) is material deformation in semisolid state. By the direct infiltration technique some objects were derived with a simple or a complicated shape as, for instance, small impellers whose molds were produced through the "lost-wax" method (Figure 1).

We applied the tixoforging technique [26-27] originally developed for metallic alloys to the slurries in which the solid phase is the reinforcement. By the backward extrusion technique on a slurry whose composition was ZA-27 alloy and SiC powders, we prepared small tubes (13 mm external diameter) with thin walls (Figure 2).This method was also used in order to obtain specimens for tensile strength measurements. The slurry was pressed between two graphite blocks of convenient shape. Thus, a plate was obtained from which it was possible to obtain flat specimens by parallel cuts made by a diamond wheel (Figure 3). It should be noticed that this forming technique decreased the composite's porosity, but resulted in an uneven distribution of the reinforcement if the material's flow is irregular.

finally, diluted composites, with ZA-12 or ZA-27 as the matrix and SiC as the reinforcement, in the range 10-20%v., were plastically worked for deriving wires, tubes, and sheets. The wires (Figure 4) were obtained by hot extrusion of small bars, from 10 or 16 mm diameter to 3.5 or 2 mm final diameter. After extrusion, the wires were straightened at 290°C for 1 h, under a tensile stress of 1 MPa and subsequently annealed at 300°C for 1 h and furnace cooled. The tubes shown in Figure 5 were produced by extrusion. Starting from castings of 20 mm external diameter and 10 mm internal diameter, we obtained thin tubes with 1 mm wall thickness, 12 mm external diameter and 10 mm interior diameter. The reduction ratio was approximately 85%. Finally we produced sheets (Figure 6), by rolling small plates of ZA-12 and ZA-27 matrix composite reinforcemed with SiC500 at the 10 and 20%v levels. The 10 mm plates were hot-rolled at 350°C to 1 mm thickness, with a 90% total reduction. For comparison, specimens with the unreinforced matrix were also extruded and rolled.

CHARACTERIZATION

SCANNING ELECTRON MICROSCOPY- SEM analysis was performed on all the composite materials: on those obtained by mixing or infiltration techniques, on those derived by dilution, and on plastically deformed materials. Fracture surfaces and cross-sections were examined, the latter after polishing and etching specificly for zinc alloys which dissolves the zinc phase of the matrix.

Figures 7 and 8, respectively, show a fracture surface and a section of a composite obtained by infiltration of ZA-27 alloy into SiC500 powders with an average grain size 20μm (approx. 50%v). Figures 9 and 10 show the fracture surface and the section of a composite having the same matrix but reinforced with 11%v alumina fibers.

SEM analysis revealed good bonding between matrix and reinforcement for all the materials examined this is clearly shown in fractographies where the alloy adheres to the SiC particulates and to the alumina fibers. good bonding can also be seen in high-magnification micrographs, where continuity between the matrix and the two kinds of reinforcement is evident (Figures 11 and 12).

The structures of diluted composites (Figures 13 and 14), show SiC particulates distribution; concentrations are 20 and 10%, matrices are ZA-12 and ZA-27, respectively. A good redistribution and a fairly even dispersion are evident, in spite of the reinforcement's tendency to segregate at the edge of dendrites during metal solidification. From above, the importance of careful control of matrix structure is noted which, in turn, depends on the kinds and contents of alloy chemistry and on the cooling conditions. These are related to grains size and, as a consequence, to the distance between the reinforcement particulates and their distribution.

A great influence on reinforcement redistribution in a composite material can be ascribed to forming under strong plastic deformation. The longitudinal section of an extruded wire of 16%v SiC500 in ZA-27 is shown in Figure 15. The reduction ratio was 98%. These structures can be considered typical for plastically deformed composites.

Generally, micrographs of specimens reveal an uniform distribution of the reinforcement into the matrix, lack of porosity and good adhesion between matrix and particulates Good adhesion between matrix and particulates was also observed in specimens produced at low reduction ratios. Local SiC aggregations, in case they should still be present after the dilution process, elongate along the extrusion direction and disaggregate. In all specimens we can see the alignment of particulates and their rotation to alling themselves with the extrusion direction. In additon, the deformation processed matrix structure is substantially different from those produced totally by solidification processing (infiltrated and diluted materials). mechanical working causes the primary phase elongation, which deminishes to dimensions comparable to those of reinforcement, whose distribution thus becomes homogeneous.

The orientation of reinforcement is much more evident in fiber containing composites. In micrographs of Figure 17, 18, and 19 the metallographic transverse and longitudinal sections are shown, in addition to a fractography of a 3mm diameter wire, obtained by extrusion of a composite, ZA-12 alloy and 20%v. alumina fibers, 98% reduction ratio.

TECHNOLOGICAL PROPERTIES- The different materials produced were characterized. The composite system with ZA-27 alloy as the matrix and SiC500 (20 μm) as the reinforcement was the most promising. The average values of the properties of the composite, obtained by infiltration and with 50%v reinforcement content, are shown in Table 2.

Some properties, such as density and thermal expansion, satisfy to the "rule of mixtures". Ohers are strongly dependent on the kind of composite. Even more noteworthy, increased values of elastic modulus, Brinell hardness and wear resistance were measured and compared to the matrix values. A lower tensile strength was observed as was already noticed by some other authors [8].

The mechanical properties of as cast composites lower reinforcement concentrations are shown in Table 3.

From the above values we can notice that Brinell hardness and elasticity modulus increase with the particulate fraction. However, tensile strength decreased and elongation value was reduced to nearly zero. The lower value of ultimate tensile strength of the composites, in comparison to the matrix value, is related to the high reinforcement content and to the poor plasticity of the matrix. Some tests, carried out on composites with a more plastic matrix (ZA-12 alloy) reinforced with SiC500 50%v, showed ultimate tensile strength values equal to those of the matrix.

The plastically deformed products were also tested, and, in order to have a comparison among the technological properties of different materials, wires and sheet of non-reinforced matrix were also prepared in the same conditions and with the same heat treatment as for composites. In Table 4 the properties of bars before extrusion and those of wires derived are shown.

We have obtained a comparison of the different kinds of materials: matrices and composites, cast and extruded. The composites as cast, even with a low reinforcement content, have a higher elastic modulus in comparison to their unreingorced matrices. However, their ultimate tensile strengths are lower. Extrusion improved their properties, increased the elastic modulus, but above all improved the ultimate tensile strength to values better than those of the as cast matrix. The matrix wire, when annealed, shows a lower tensile strength than the shell cast material and is comparable to a sand-cast alloy. The most enhanced improvement was observed for fiber reinforced wires, when the matrix was more plastic.

The noteworthy improvement of ultimate tensile strength of extruded materials may be ascribed to many factors, which however should be further examined. Among these, the following are extremely important:

- The elimination of defects caused by porosity or poor infiltration of metal through the reinforcement particulates.
- The reduction of inhomogeneties due to the presence of improperly dispersed reinforcement aggregates or to reinforcement segregations at he edges of dendrite grains.
- The reinforcement distribution into the matrix.
- The reinforcement alignment along the extrusion directions, which becomes that of tensile stress.
- The annealing conditions, with their effect on matrix recrystallization and on elimination of residual internal stresses.

The mechanical properties of composite sheet materials are compared to those of as-cast materials in Table 5.

In the case of composites with a more plastic matrix (ZA-12 alloy), the ultimate tensile strength and the elasticity modulus are improved by rolling and, even more, by reinforcement addition. with the less plastic alloy (ZA-27 alloy) only the modulus shows an improvement, on the contrary the ultimate tensile strength decreases either by the hot-rolling effect or by the reinforcement addition.

CONCLUSIONS

In our present research preparation techniques of composites materials with zinc-aluminum alloys in the matrix and reinforced by ceramic powders or fibers, were studied and evaluated. Our purpose was to improved materials properties utilizing costs competitive processes. The feasibility of forming by deformation in the semisolid state or by plastic deformation processes such as extrusion or rolling, was also verified.

Micrographic analysis showed satisfactory adhesion properties between matrix and reinforcement in infiltrated composites and a noteworthy reinforcement alignment in plastically deformed materials.

Preliminary evaluation of mechanical properties of different products show superior characteristics to those of the matrix and suggest the possibility for applications in fields where an enhanced wear resistance is required.

Materials	UTS MPa	E GPa	Elong %
ZA-12 (As Cast)	300	87	5
ZA-12 (Rolled)	350	115	22
ZA-12+SiC500 10%v	323	119	0
ZA-12+SiC500 20%v	373	129	0
ZA-27 (As Cast)	410	73	2
ZA-27 (Rolled)	393	85	16
ZA-27+SiC500 10%v	370	89	3
ZA-27+SiC500 20%v	349	102	0

Table 5 - Mechanical Properties of Rolled Composites.

Properties		Matrix	Composite
Density	kg/dm^3	5	4.1
Tensile Strength (UTS)	MPa	410	310
Elasticity Modulus (E)	GPa	73	220
Brinell Hardness	$HB_{2.5/62.5/30}$	117	225
Wear Resistence			>10 times
Thermal Expansion	$um\ m^{-1}\ K^{-1}$	26	12.9

Table 2 - Some typical Properties of Composites ZA-27 + SiC500 50%v.

MATERIALS	UTS MPa	E GPa	Elong %	HB
ZA-27 (Matrix)	410	73	2	117
ZA-27+SiC500 10%v	396	92	0	121
ZA-27+SiC500 20%v	330	110	0	159
ZA-27+SiC500 50%v	310	220	0	225

$HB_{2.5/62.5/30}$

Table 3 - Mechanical Properties of ZA-27+SiC500 as cast, with different concentrations of reinforcer

Materials			Inizial State As Cast				Final State Extruded		
Matrix	Reinforc. Kind	%v	Ø mm	UTS MPa	E GPa	Red. %	Ø mm	UTS MPa	E GPa
ZA-27	-	-	-	410	73	98	2	340	83
ZA-27	SiC	12	10	-	-	96	2	382	105
ZA-27	SiC	16	16	305	113	98	2	466	130
ZA-27	-	-	-	410	73	98	3	314	78
ZA-27	Saffil	20	20	220	76	98	3	382	100
ZA-12	-	-	-	300	87	98	3	313	102
ZA-12	Saffil	20	20	238	103	98	3	532	120

Table 4 - Mechanical Properties of Composites Extruded Wires.

BIBLIOGRAPHY

1) P. Appendino and M. Montorsi, "Materiali compositi con matrice in lega di alluminio," La Metallurgia Italiana, 78 (1986) pp. 743-758.
2) T. Donomoto, K. Funatari, N. Miura, and N. Miyate, "Ceramic Fiber Reinforced Piston for High Performance Diesel Engines," SAE Technical Papers 830252, March 1983.
3) E.J. Peters, "Ceramic Fiber Usage in Automotive Composites," Third I.A.V.D. Congress, Geneva, March 1986.
4) DACC, "Brochure of Products," San Diego, California
5) F.C. Bennet, T.E. Leontis and S.L. Couling, "Thixotropic Magnesium Alloy Products," Proc. Annual Meeting of the International Magnesium Assoc., 34 (1977) pp. 23-29.
6) F.A. Badia, "Dispersion of Oxides and Carbides in Al and Zn Alloy Casting," .Trans. American Foundry Soc. 79 (1971), pp. 347-350
7) R. Guerriero, J.B. Parse, and I Tangerini, "Metal Matrix Composites Utilizing Zn-Al Alloys," 25th CIM, Toronto, August 17-20, 1986, pp. 127-142.
8) P.N. Dent and S. Murphy, "Progress in the development of Inexpensive Composites with Zinc-Aluminum Alloy Matrix," Proc. International Symposium on Zinc-Aluminum (ZA) Casting Alloys, 25th CIM, Toronto, August 17-20, 1986, pp. 127-142.
9) A.A. Das, B. Zantout, M.M. Yakoub, and A.J. Clegg, "Squeeze Casting of Metal Matrix Composites," Proc. International Symposium on Zinc- Aluminum (ZA) Casting Alloys, 25th CIM, Toronto, August 17-20, 1986, pp. 213-228.
10) R. Guerriero, J.B. Parse, and I Tangerini, "Preparazione e caratteristiche di materiali compositi con matrice in lega di zinco," La Metallurgia Italiana, 80 (1988) pp. 205-212.
11) E. Gervais, R.J. Barnhurst, and C.A. Loong, "An Analysis of Selected Properties of ZA Alloys," Journal of Metals, 37 (1985), pp. 43-47.
12) R. Lyon, "High Strength Zinc Alloys for Engineering Applications in Motor Cars," Metals and Materials, Jan. (1985), pp. 55-57.
13) J. Dinwoodie, E. Moore, C.A.J. Langman, and W.R. Symes, "The Properties and Applications of Short Staple Alumina Fiber Reinforced Aluminum Alloys," Proc. Fifth International Conf. on Composite Materials, San Diego, California, 1985, pp. 671-685.
14) T.W. Clyne, M.G. Bader, G.R. Cappleman, and P.A. Hubert, "The Use of d-Alumina Fiber for Metal-Matrix Composites," J. Materials Science 20 (1985), pp. 85-96.
15) M.C. Flemings and R. Mehrabian, "Casting Semi-Solid Metals," Trans. American Foundry Society 81 (1973) pp. 81-88.
16) R. Mehrabian, R.G. Riek, and M.C. Flemings, "Preparation and Casting of Metal-Particulate Non-Metal Composites," Metallurgical Transactions 5 (1974) pp. 1899-1905.
17) P.K. Rohatgi, R. Asthana, and S. Das, "Solidification, Structures, and Properties of Cast Metal-Ceramic Particle Composites," Intern. Metals Review 31 (1986) pp. 115-139.
18) T.W. Clyne and M.G. Bader, "Analysis of a Squeeze-Infiltration Process for Fabrication of Metal Matrix Composites," Proc. Fifth International Conf. on Composite Materials, San Diego, California, 1985, pp. 755-771.
19) D.A. Pinsky, P.O. Charreyron, and M.C. Flemings, "Compression of Semi-Solid Dendritic Sn-Pb Alloys at Low Strain Rates," Met. Trans. B, 15B (1984), pp 173-181.
20) J.M.M. Molenaar, F.W.H. Salemans, and L. Katgerman, "Analysis of Process Limits for Continuous Thixotropic Slurry Casting," J. Material Science, 20 (1985) pp. 700-709.

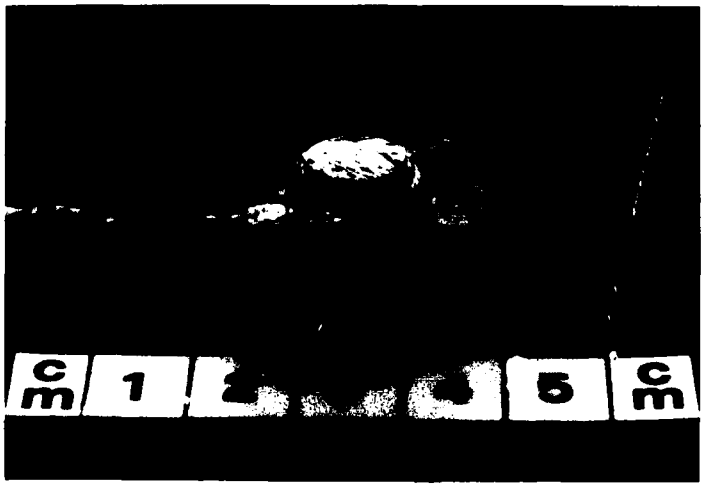


Figure 1 - Impeller formed in a proper shaped die.



Figure 2 - Small tube extruded from semi-solid slurry (3x).

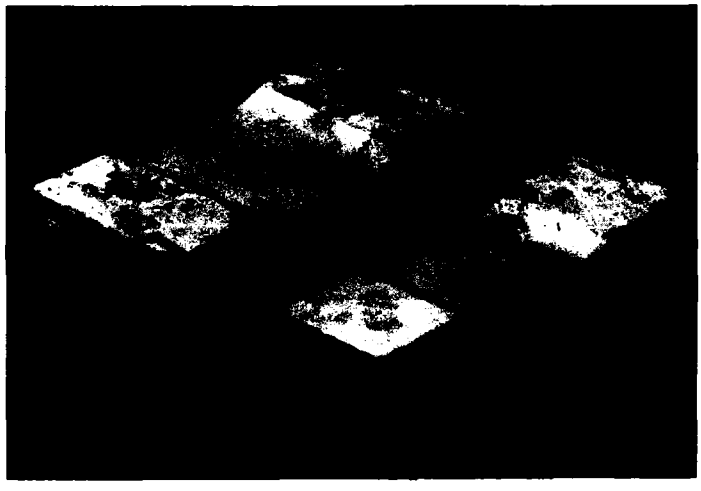


Figure 3 - Plate forged from semi-solid slurry for preparation of tensile test specimens (2/3 x).



Figure 4 - Wires obtained by plastic deformation (extrusion) of composites.

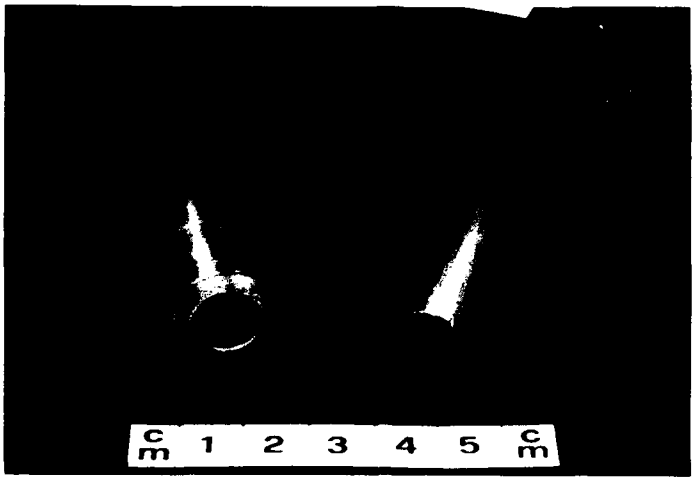


Figure 5 - Tubes obtained by plastic deformation (extrusion) of composites.

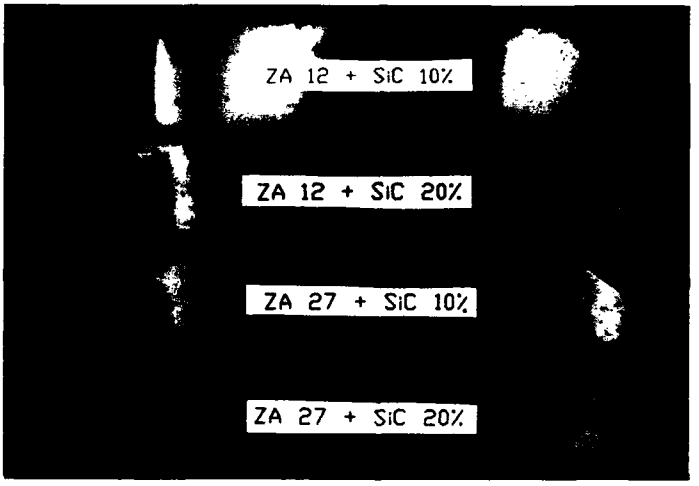


Figure 6 - Sheets obtained by plastic deformation (rolling) of composites.

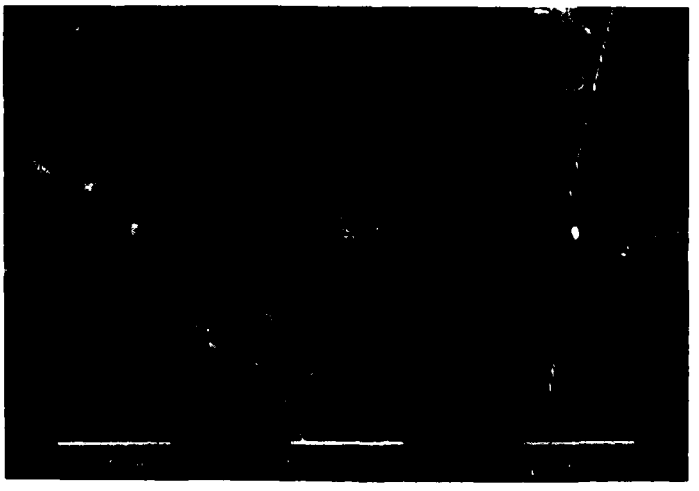


Figure 7 - Fractograph of ZA-27 + SiC500 50%v composite (2020x)



Figure 8 - Metallograph of ZA-27 + SiC500 50%v composite (1550x)



Figure 9 - Fractograph of ZA-27 + Alumina 11%v composite (2500x)



Figure 10 - Metallograph of ZA-27 + Alumina 11%v composite (600x)



Figure 11 - Metallograph of ZA-27 + SiC100 50%v composite (3100x)



Figure 12 - Metallograph of ZA-27 + Alumina 11%v composite (5000x)

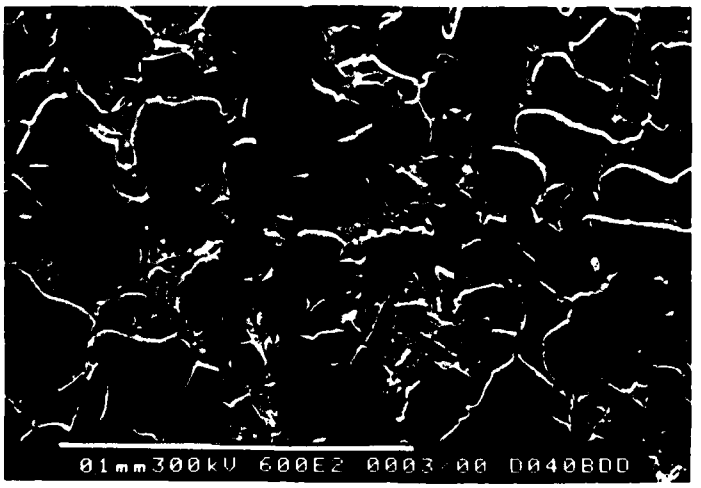


Figure 13 - Metallograph of ZA-12 + SiC500 20%v composite (600x)

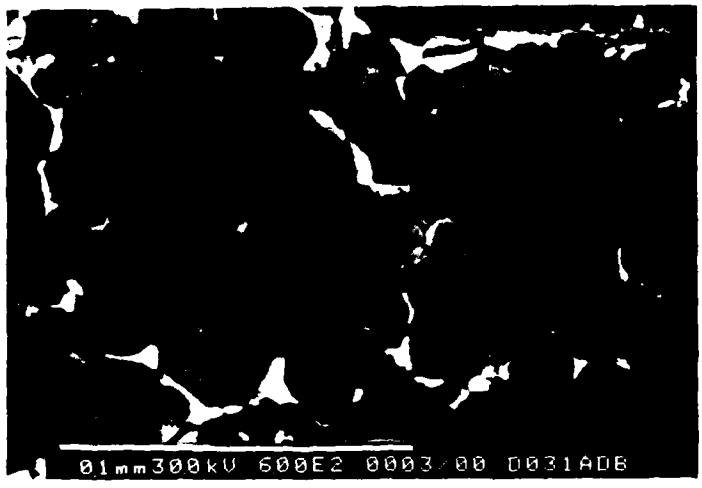


Figure 14 - Metallograph of ZA-27 + SiC500 10%v composite (600x)



Figure 15 - Metallograph of longitudinal section of extruded wire of of ZA-27 + SiC500 16%v composite (600x)

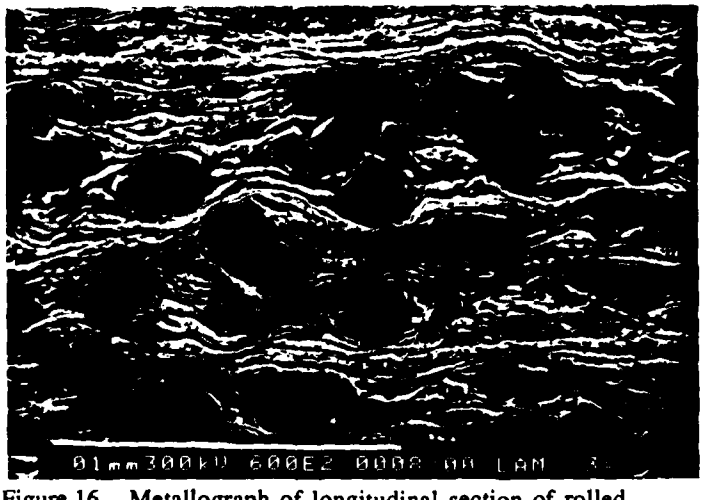


Figure 16 - Metallograph of longitudinal section of rolled sheet of of ZA-27 + SiC500 10%v composite (600x)

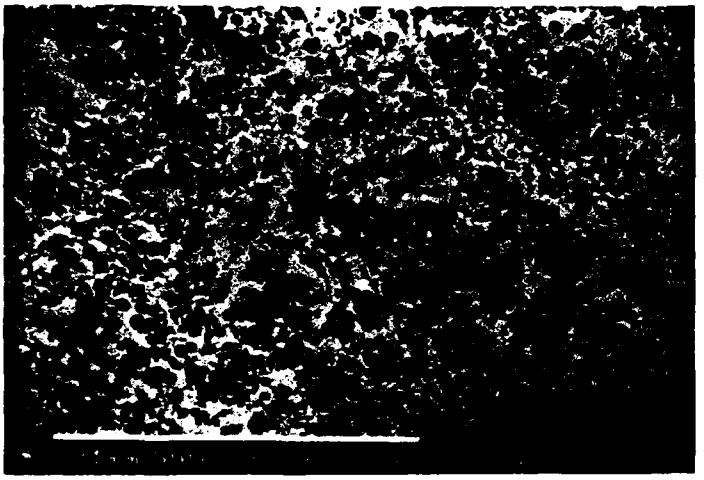


Figure 17 - Metallograph of transverse section of extruded wire of ZA - 12 + Saffil 20%v composite (625x)

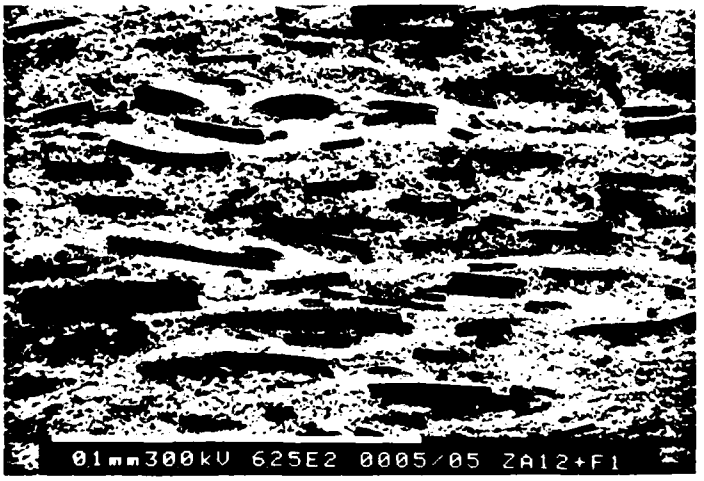


Figure 18 - Metallograph of longitudinal section of extruded wire of ZA-12 + Saffil 20%v composite (625x)

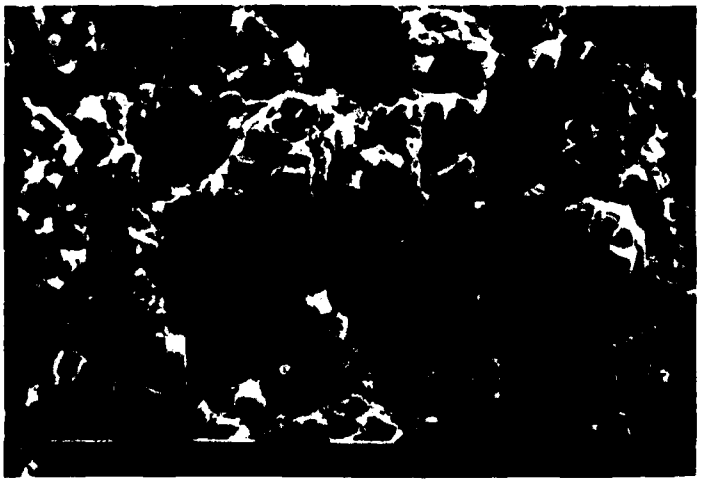


Figure 19 - Fractograph of extruded wire of ZA-12 + Saffil 20%v composite (1250x)

PARTIAL REMELTING AND FORMING OF Al-Si/SiC COMPOSITES IN THEIR MUSHY ZONE

M. A. Bayoumi,* M. Suéry
Institut National Polytechnique de Grenoble
E.N.S. de Physique de Grenoble
Génie Physique et Mécanique des Matériaux
BP 46- 38402- Saint Martin D'Heres, Cedex, France

*Present address: Department of Mechanical Engineering Al-Azhar University, Nasr City, Cairo, Egypt

Abstract

Composites of Al-Si alloys reinforced by SiC particles or various sizes were fabricated using the compocasting technique followed by squeeze casting in the fully liquid state. During isothermal partial remelting, transformation of the initial dendritic structure occurs into a globular one and it was shown to take place more rapidly in the composites than in the unreinforced matrix alloy. Compression tests performed in the mushy state at 585 °C when the structure has become globular, show that the stress needed to deform the material is much smaller than that required for compression in the fully solid state at 570°C. However, for the same holding time before compression, stress decreases with increasing SiC volume fraction up to a certain value, after which it increases slightly. This result is explained by considering the acceleration of the transformation and the refinement of the structure with the increase of SiC on one hand, and the increase of the total amount of solid particles with increasing SiC in the composite on the other. The experiments thus demonstrate the interest of using semi-solid forming for composite materials.

FORMING OF ALLOYS in their mushy zone after partial remelting is potentially interesting owing to the very low stresses involved in the forming process when the structure of the solid phase consists of small equiaxed globules surrounded by the liquid (1-4). Moreover with this structural morphology, deformation takes place with only limited liquid segregation in opposition to what happend if the structure is dendritic (1,3).

The advantages of semi-solid forming were demonstrated in various alloys but no detailed investigation was carried out until now on metal matrix composites(5,6). In addition to the previously mentioned interest, forming of MMC in their mushy state may overcome some of the problems encountered when deformation takes place in their fully solid state i.e. rapid tool deterioration and breakage of the reinforcing elements. The aim of this work is to give some preliminary answers concerning the advantage of semi-solid forming of MMC. The effect of isothermal partial remelting on the transformation of the initial dendritic structure of SiC reinforced Al-Si alloys is first considered. The paper deals thereafter with the deformation behavior in compression of these materials in their semi-solid state.

EXPERIMENTAL

MATERIALS - The aluminum matrix used in this investigation is an industrial Al-7 wt% Si alloys containing about 0.3 wt% Mg (AS7 G03 in the French designation). It was used with Sr addition to modify the silicon morphology during solidification. SiC particles of 7, 29 and 45 μm size were used as reinforcement in the as-received condition.

EXPERIMENTAL PROCEDURE -

Fabrication of the composite - The composites were prepared using the compocasting technique in which the reinforced elements are added to the semi-solid agitated alloy. The details of the procedure is given elsewhere (7,8). After complete addition of the elements, the melt was superheated to above its liquidus temperature and the liquid charge was transfered into the die of a squeeze casting apparatus which allows solidification to be performed under a pressure of 100 MPa, the temperature of the die being set at 300°C. Various volume fractions of particles were used in these experiments, essentially 8.5 and 17 % for all particle sizes. An ingot was prepared with 35 % particles of 29 μm. Ingots of the matrix alloy were also solidified at 100 MPa.

Partial remelting experiments - Specimens of 16 mm dia. and 35 mm height were cut from the ingot. They were put into a small graphite crucible which was induction heated at a rate of about 100°C/mn. They were maintained at 580°C. measured in the middle of the sample, for various times ranging from 5 to 60 mn. This temperature is about 3°C above the eutectic temperature.

After partial remelting, the specimens were water quenched in order to avoid structural evolution during cooling. Samples were thereafter prepared for microstructural observations.

Compression experiments - Specimens of 8 mm dia. and 12 mm height were used. The specimen is put between the two parallel plates of the compression apparatus preheated at the required temperature with a small electrical furnace. With this procedure, the required temperature of the specimen is reached within less than 10 mn which gives a heating rate of about 60°C/mn. It was checked that this difference in the heating rate compared to that used in the partial remelting experiments does not affect the structure. Various temperatures were used in the fully solid and the semi-solid state. The specimens were deformed up to 50 % engineering strain at a constant velocity of 7.2 mm/mn which gives an initial strain rate of 10^{-2} s^{-1}. The velocity was chosen such that the deformation takes a time (50 s) much shorter than the holding time before deformation (from 5 to 105 mn). After compression, the specimens were cooled rapidly with water.

RESULTS AND DISCUSSION

PARTIAL REMELTING - Figure 1 is a scanning electron micrograph of the structure of the matrix alloy after solidification. The structure consists of dendrites of the primary Al-rich phase and eutectic with fine globular Si due to Sr addition in the melt before squeeze casting. Figure 2 shows the modification of the structure as a function of the holding time at 580°C. Coarsening of the dendrites occurs initially (Fig. 2a) followed by globularization (Fig. 2b) which becomes almost complete for 30 mn holding time (Fig. 2c). In this morphology, many globules of the primary phase are surrounded by the the eutectic mixture which was liquid at 580°C.

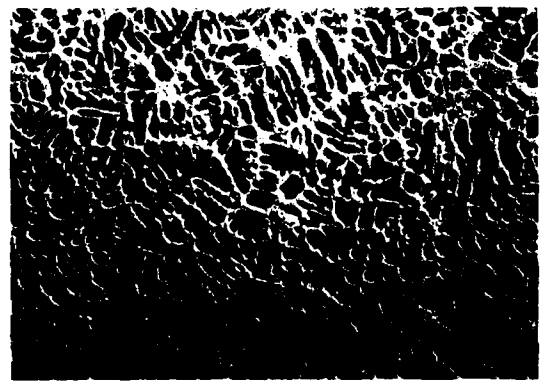


Fig.1 - SEM micrograph of the AS7 G03 alloy after squeeze casting (the primary Al-rich phase is dark, the eutectic mixture is light).

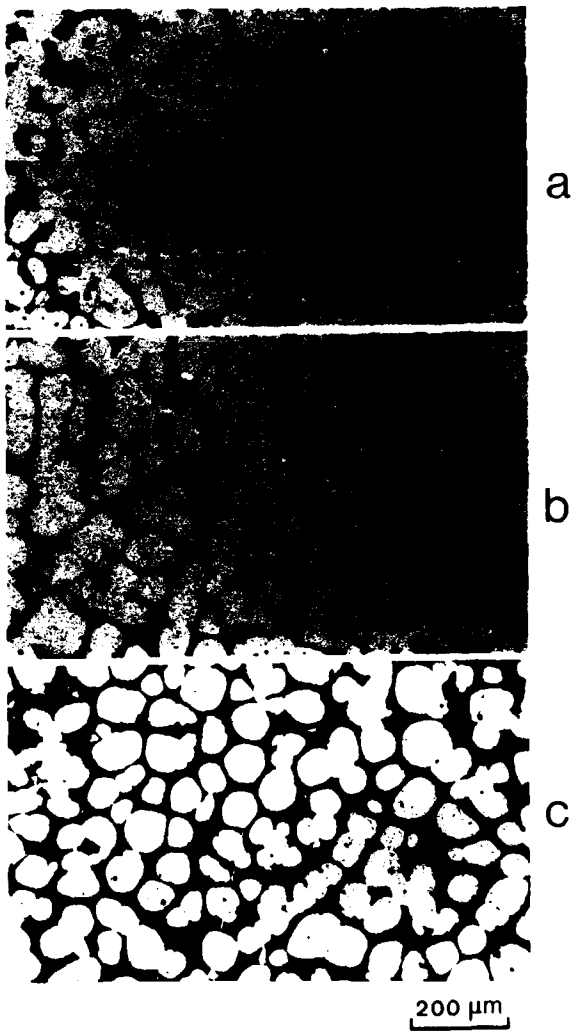


Fig.2 - Structures of the matrix alloy after partial remelting at 580°C for various holding times: a) 5 mn; b) 10 mn; c) 30 mn

Figure 3 shows similar results for a composite containing 8.5 % SiC particles of 20 µm. The initial dendritic structure of the composite (Fig.3a) is somewhat modified by the presence of the particles which are not homogeneously distributed due to their

rejection by the primary solid phase during solidification. After only 5 mn at 580°C, complete globularization of the dendrites fig.3b) has occurred after which coarsening is clearly observed (Fig.3c). For the composites containing 17 % SiC particles, the distribution of the particles is much more homogeneous (Fig. 4a) and transformation of the dendritic structure leads then to smaller globules which coarsen with increasing holding time(Fig.4b). The decrease of the size of the globules can be explained by the fact that the interparticle spacing decreases as the particle volume fraction increases which restricts the space available for the globules. It is to be noted that the particles are concentrated in the eutectic. Moreover no gravity segregation has occurred during partial remelting in opposition to what is observed during complete remelting (8).

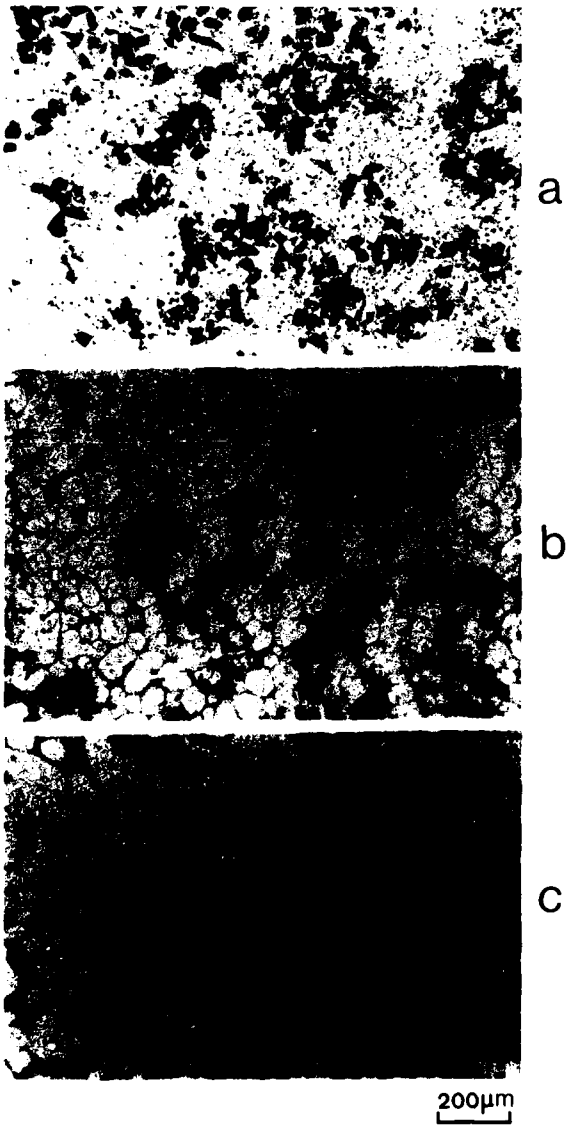


Fig.3 - Structures of the composites containing 8.5 % of 29 µm particles after partial remelting at 580°C for various holding times: a) 0 (as cast); b) 5 mn; c) 30 mn

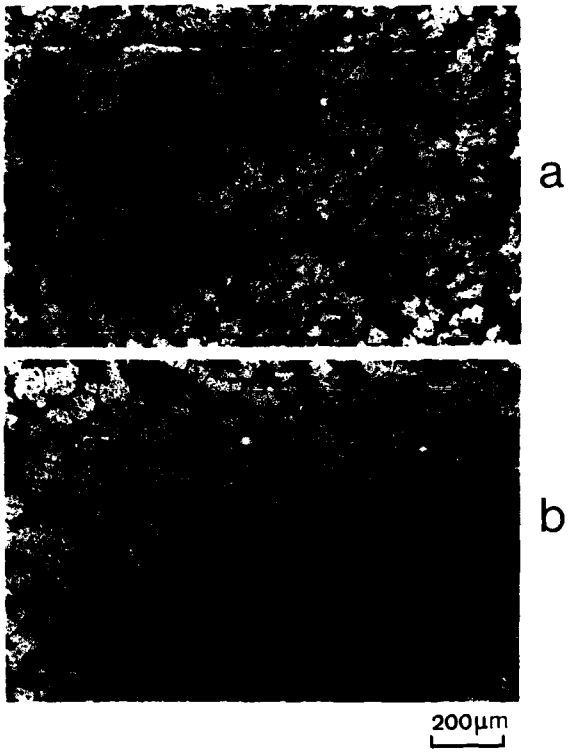


Fig.4 - Structures of the composite containing 17 % of 29 µm particles after partial remelting at 580°C for various holding times: a) 5 mn; b) 30 mn

Two explanations can be given for the acceleration of the transformation of the dendritic structure into a globular one in the composites compared to the matrix alloy :

- The initial dendritic structure is finer in the composite than in the matrix.
- Recrystallization can occur in the composite during heating due to the presence of a high density of dislocations in the vicinity of the particles(9,10). This recrystallization can lead to rapid globularization of the structure by melting of the grain boundaries as it was observed for Al-Si alloys predeformed by cold rolling(5). SiC particles act then as nucleation sites for recrystallization during heating of the sample.

COMPRESSION EXPERIMENTS - Specimens of the matrix alloy and the composites were used in these experiments. Figure 5 shows the variation of the compression stress with strain for the

matrix alloy deformed at various temperatures. The specimens were held for 5 mn at the required temperature before compression. As expected, stress decreases as temperature increases but a change in the material behavior is observed when the temperature is increased from 843K (570°C) to 848K (575°C). At the lowest temperature stress increases with engineering strain and this increase is partly due to the increase of the strain rate during the test (carried out at constant velocity) and to the friction between the specimen and the plates. At 575°C, some melting probably occurs and the stress remains almost constant. At this temperature, the stress increase is compensated by some degeneration of the dendritic structure.

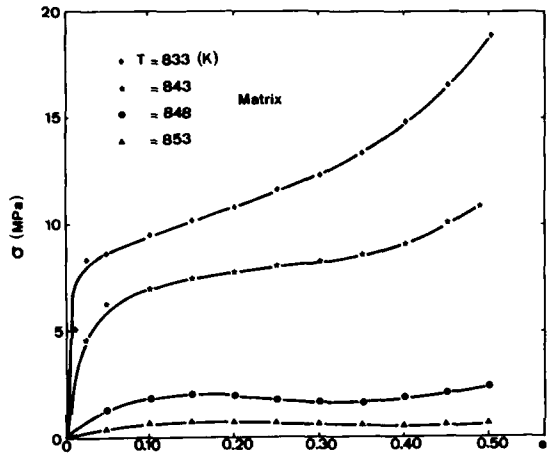


Fig.5 - Compression curves for the matrix alloy deformed at various temperatures after a holding time of 5 mn.

Figure 6 shows the variation of the compression stress (taken at 0.2 engineering strain) as a function of the deformation temperature. On the figure, is also plotted the compression stress measured in the range 20-300°C, the strain-rate being however smaller than that used for the compression at high temperature ($7x10^{-4}s^{-1}$ compared to $10^{-2}s^{-1}$). Stress normally decreases as temperature increases but a transition is clearly observed at 848 K (575°C) which indicates that the specimen begins to melt. This temperature is close to the eutectic temperature of the Al-Si alloy, the imprecision on the measurement being 2°C. For 580 and 585°C, the stress becomes very small due to the presence in the material of a liquid volume fraction of 50 %.

The previous result was obtained after an isothermal holding time of the specimen before compression of only 5 mn. Figure 7 shows the effect of this parameter on the compression stress of the matrix alloy at 585°C (858 K).

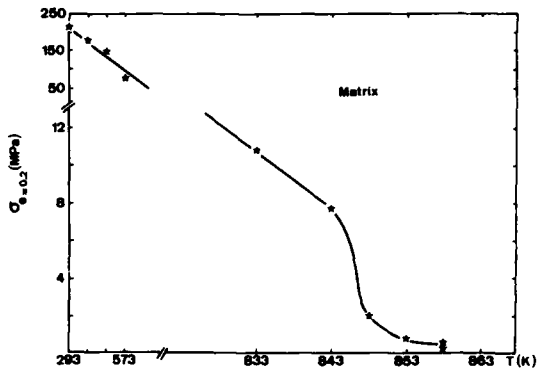


Fig.6 - Effect of temperature on the compressive stress (at 0.2 engineering strain) for the matrix alloy

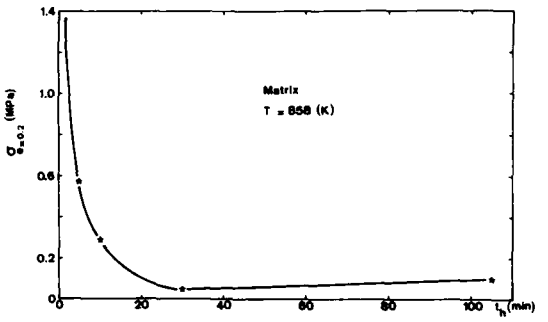


Fig.7 - Effect of the holding time before compression on the compressive stress (at 0.2 engineering strain) for the matrix alloy

Stress which was already small after 5 mn, decreases further up to 30 mn after which it seems to increase slightly. The decrease of the stress can be explained by the transformation of the structure into a globular one as demonstrated by the metallographic observations. The slight increase may be due to the coalescence of the globules.

Compression tests were performed at 585°C (858 K) with the composites after a holding time of 5 mn. Figure 8 shows the variation of the compression stress (taken at 0.2 strain) as a function of the particle volume fraction V_p for the various particle sizes. Stress decreases with increasing V_p whatever the particle size but the decrease is larger for the smaller particles.

For 17 % particles of 7 μm, the stress is only 20 % of that of the matrix alloy. This result seems to be non logical since the total volume fraction of solid (primary Al rich phase + SiC particles) increases as V_p increases, the specimen being deformed with the same volume fraction of primary Al. The behavior can, however, be explained by the structural

modification of the solid phase during partial remelting which takes place more rapidly in the composite than in the matrix alloy. Moreover, the structure of the composite is more globular than that of the matrix alloy for the same holding time in the semi-solid range (compare fig. 2a and fig. 3b or 4a). The same behavior was observed with composites reinforced with SiC fibers (fig. 9)(5). The lower stress observed for the small particles is probably due to the fact that they are able to move more easily than the big ones past one another during deformation.

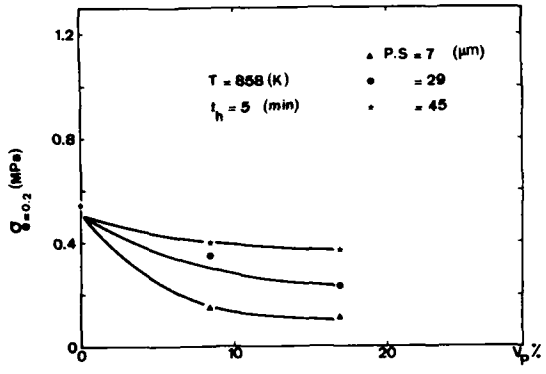


Fig.8 - Effect of particle volume fraction on the compressive stress (at 0.2 engineering strain) of composites with different particle sizes deformed after a holding time of 5 mn at 585°C.

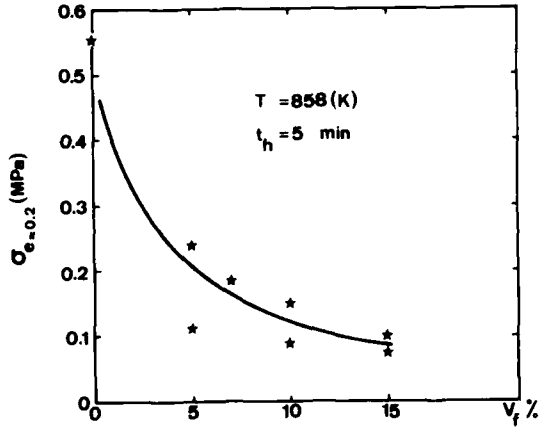


Fig.9 - Effect of fibre volume fraction on the compressive stress (at 0.2 engineering strain) of composites containing Nicalon SiC fibers deformed at 10^{-2} s^{-1} after a holding time of 5 mn at 585°C (From (5)).

As shown in figure 8, stress was observed to decrease with increasing V_p up to 17%. However, if V_p increases further, stress increases also and attains 0.8 MPa for 35 % particles. This result is shown in figure 10 for the 29 μm particles; it can be explained by considering the total volume fraction of solid which represents 68% of the volume of the material. It is to be noted that this stress is still very small which thus clearly demonstrates the interest of using semi-solid forming for composite materials.

For all the experiments reported in this work, compression was limited to 50 % engineering strain which does not lead to appreciable segregation of the liquid. Such a segregation is expected to occur at large strain which will thus limit the interest of semi-solid forming.

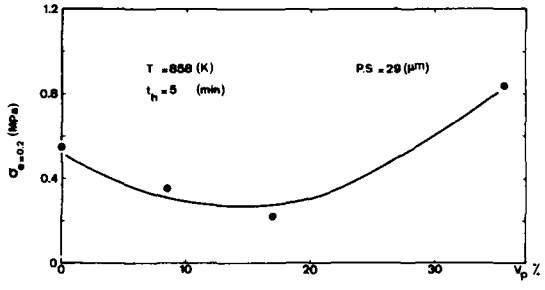


Fig.10 - Effect of particle volume fraction on the compressive stress (at 0.2 engineering strain) of a composite with a particle size of 29 μm deformed after a holding time of 5 mn at 585°C.

CONCLUSIONS

- Isothermal partial remelting of squeeze-cast Al-Si alloys leads to the transformation of the dentritic structure into a globular one with globules of the primary solid phase surrounded by the liquid phase.

- This transformation occurs more rapidly in the SiC reinforced alloy than in the matrix alloys with the formation of smaller globules.

- After transformation, the material can be deformed under very low stresses which demonstrates the interest of using semi-solid forming for composites.

REFERENCES

1. Suéry, M. and M.C. Flemings, Met. Trans. 13A, 1909-19 (1982)

2. Lehuy, H., J. Blain, G.L. Bata and J. Masounave, Materials Science and Eng. 67, L29-L32 (1984)

3. Seconde, J.F. and M. Suéry, J. Mat. Sci., 19, 3995-4006 (1984)

4. Lehuy H., J. Blain and J. Masounave, 2th Annual Conf. of Metallurgists, Toronto, Aug 17-20, 1986

5. Suéry, M., in "Formability and Metallurgical Structure" p.283-301, Ed. by A.K Sachdev and J.D. Embury, The Metallurgical Society of AIME, Warrendale (1987)

6. Kiuchi, M. and S. Sugiyama, Journal of the Japan Society for Technol. of Plasticity 23, 915-23 (1982)

7. Milliere, C. and M. Suéry, Materials Science and Technol. 4, 41-51 (1988)

8. Bayoumi, M., Thesis, Institut National Polytechnique de Grenoble (1987)

9. Mary Vogelsang, R.J. Arsenault and R.M. Fisher, Metall. Trans. 17A, 379-89 (1986)

10. Bayoumi, M.A., H. Ribes and M. Suéry, 9th RISO Internationnal Symposium on Metallurgy and Materials Science, Roskilde 5-9 Sept. 1988.

LIQUID PRESSURE FORMING OF ENGINEERED METAL MATRIX COMPOSITES

N. Mykura
Yeovil
Somerset, England

ABSTRACT

A new manufacturing method has been developed to produce metal matrix composites (MMC's) by using gas pressure to forcibly infiltrate reinforcing materials with molten metal. This process shows considerable promise due to the good quality of material produced, the wide range of reinforcing materials that can be used, and high production rates compared with most other processes. The required properties in the end product can be engineered by combining at an early stage material selection, component design and knowledge of the manufacturing technology.

INTRODUCTION

A great deal of research work has been undertaken on MMC's over the past three decades in efforts to establish a commercially feasible production process. The various methods can be split easily into two types, those that operate below the melting point (solid phase) of the metal and those that operate above (liquid phase).

Solid phase processes like diffusion bonding have proved successful to a certain extent with monofilament fibres such as boron and silicon carbide, but they are incapable of producing composites with multi-filament yarns such as carbon, alumina, and silicon carbide. Processing in the solid phase is restrictive in that only comparatively simple shapes can be manufactured, processing time is long and several discrete processing operations have to be carried out to produce a finished component.

Liquid phase processing has several inherent advantages over solid phase for the production of MMC's. The fluidity of the metal allows a wide range of fibre types to be infiltrated easily and offers the possibility of a one-shot process with high production rates and the capability to produce net shaped engineered components.

The main liquid phase production processes that have shown promise are squeeze casting, and gas pressurized infiltration. The vast majority of the work in both these processes has been on aluminium due to ease of processing and good mechanical properties. This paper aims to examine the gas pressurized infiltration process in detail and to establish its credentials as an alternative and advantageous method for the production of engineered reinforced metal components.

PRESSURIZED INFILTRATION

The manufacture of FRM's using molten metal requires that the reinforcing fibres are completely surrounded with a high quality matrix and that a good bond is established between the fibres and the matrix on solidification. There is a wide range of fibres suitable for use as reinforcement and the vast majority presently available tend to be of small diameter (4 - 17μm) and are normally supplied in multifilament tows. In this form the fibres are quite tightly packed together and the fact that liquid metals do not generally wet the fibres makes infiltration difficult. This lack of wettability can be overcome almost entirely by the application of external pressure to the system, so that forced infiltration results in the optimum bond at the matrix / fibre interface. This should be a continuous mechanical bond with no chemical reactions or interdiffusions taking place between the fibres and the matrix.

The external pressure can be applied by several different methods and using gas as the pressurizing medium is proving to be an eminently suitable solution to overcome manufacturing problems. The Liquid Pressure Forming (LPF) process is a high pressure gas infiltration process in which pressure is applied to a reservoir of the molten alloy allowing the metal to be forced into a cavity containing the fibres to be infiltrated.

REINFORCING MATERIALS

The LPF process is a net-shape process essentially and produces a component of or close to, the final required dimensions. To allow the fibres to be infiltrated they must be held in a die cavity that corresponds in shape to that of the component.

The fibres themselves will nearly always be formed into a preform that corresponds to the shape of the cavity. The exact shape and make up of the preform depends entirely on the engineering properties required in the final component. The process is not limited to the use of one type of reinforcement and is adaptable to the full range of the ceramic fibres available commercially as well as many particulate materials. This means that the component can be "engineered" to give the desired properties in the appropriate areas. Different fibres or combinations of fibres, can be put in different areas of the component to supply widely differing properties. In any given area the fibre layup can be varied almost infinitely from completely unidirectional through any angle or combination of angles. Figure 1 illustrates Nicalon/Al composite with a 0°/90° layup.

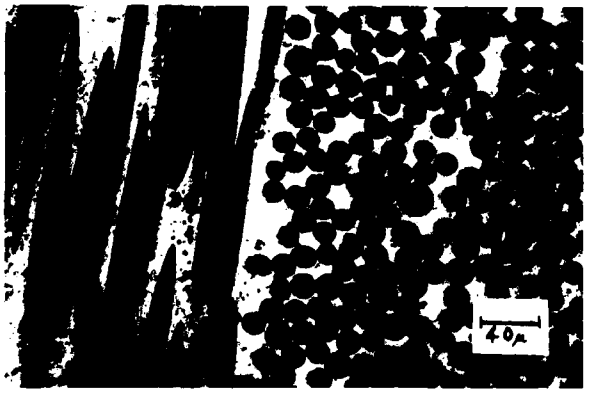


Fig. 1 - Nicalon/Aluminium composite with 0°/90° fibre layup.

Already a wide range of composites have been produced by the LPF process utilising reinforcement such as boron filament, SiC filament, SiC multifilament yarn, discontinuous random alumina, carbon yarn, semi-continuous random basalt fibre, alumina yarn, alumina particulate and SiC particulate. It is also possible to combine these reinforcements in a wide range of permutations to manufacture hybrid composites with two or more different types of reinforcement in the same component. For example a propulsor blade has been manufactured with unidirectional boron in the blade and random alumina in the integral root. The boron gives high strength and stiffness and the random alumina gives moderate strength and stiffness with relatively good machinability. A typical microstructure of a binary hybrid composite is shown in Figure 2.



Fig. 2 - Hybrid Random alumina/Nicalon/ aluminium composite. Alumina fibres to the right.

As well as varying the type of reinforcement within the component, the volume fraction (Vf) of fibre can be varied to alter the properties. With unidirectional fibres the process can produce composites from Vf=0 to Vf=0.55. Within a single component it is possible to have different volume fractions in different areas. Thus it is possible for example to vary the stiffness (or any other fibre dependent property) of the component from one region to another.

To maintain preform integrity and prevent fibre movement during processing, it is essential that the preform fibres are held in the required position. This can be done by several methods. The die itself can be used to locate and hold the fibres in the required position. This method will only work if the fibres are relatively stiff and will resist deflection due to metal flow during infiltration.

Fabrication of the fibres into tape form assists greatly in the manufacture of preforms. This can be done by weaving the fibre with itself or another suitable fibre that is an integral part of the preform and remains in position throughout the process and is incorporated into the component. Weaving increases the preform stability but decreases the maximum volume fraction achievable. It is not possible to weave the large diameter boron or SiC filaments due to their lack of flexibility although they can be held together as a tape with a small amount of flexible weft material. Once in tape form, the preforms are then built up layer by layer in the correct shape and orientations prior to insertion in the die. As can be seen in Figure 3, the weft material is incorporated into the microstructure of the composite.



Fig. 3 - Titanium weft material incorporated into boron/aluminium composite.

It is also possible to use a binder to hold the fibres in position, though this is only really feasible with the short discontinuous fibres, where a small amount of binder acting at point contact between the fibres can result in a strong preform without either interfering with metal flow during infiltration or affecting final material properties. In continuous unidirectional fibres a binder tends to act along line contacts between adjacent parallel fibres and cannot be restricted to point contacts. This tends to provide barriers to metal flow and results in a path of weakness between fibres in the final composite.

The manufacture of composites containing non-fibrous reinforcement also requires the use of a stable preform which is unaffected by metal flow on infiltration. As well as standard particulate materials such as silicon carbide it is also possible to infiltrate continuous ceramic structures such as an open network foamed ceramic. An example of alumina particulate reinforced aluminium is shown in Figure 4.



Fig. 4 - Aluminium (light) reinforced with with particulate alumina (dark).

The particulate materials are manufactured by first making a preform containing a small amount of inorganic binder to produce an open structure which can then be infiltrated. The binder acts at point contacts between the particles. A wide range of particle sizes can be used.

For a foamed ceramic to be suitable it must have an open network of interconnected pores to allow infiltration to take place, and this can be done with a wide variety of pore sizes.

MATRIX MATERIALS

As with most other MMC manufacturing processes, the majority of the work using the LPF process, has been undertaken with aluminium alloys for obvious reasons. A wide range of Al alloys have been used successfully including Al/Mg and Al/Si. Other alloys that have successfully been used in this process are a range of Zn alloys and some Pb alloys. Most of the alloys have been used with the full range of reinforcement materials.

PROCESS DESCRIPTION

The reinforcement (fibres, particles etc.) in the form of a preform are held in a cavity in a split metal (usually steel) die. The shape and size of the cavity and the die itself is dictated by the component that is being manufactured. The die is preheated to the process temperature prior to infiltration occurring. The die cavity is connected to a reservoir of molten metal by means of a tube which transports the metal during infiltration.

The reservoir of metal is held in a pressure vessel at the required temperature. Figure 5 illustrates the main steps in the LPF process sequence.

The split die can be opened to allow locating of the preform. (Fig. 5a.) This is a simple operation done by hand. Once the preform is in position the die is closed and then both the die and the pressure vessel are evacuated. (Fig. 5b.)

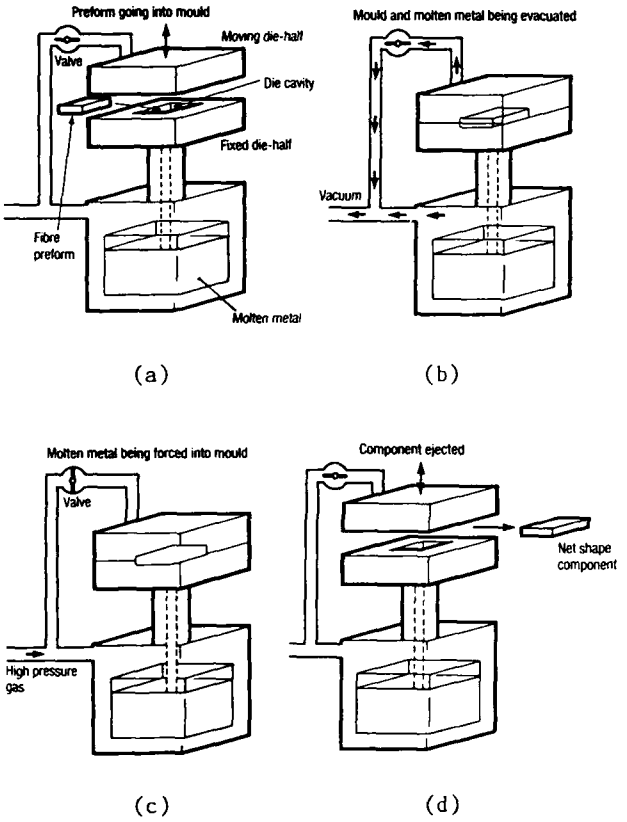


Fig. 5 - Diagramatic representation of LPF Process sequence. (a) placing of preform, (b) evacuation, (c) infiltration, (d) ejection.

The evacuation serves several purposes and greatly increases the quality of materials produced. It degasses the molten metal preventing the evolution of gas on solidification. It removes air in the die that may cause porosity and it allows faster cavity fill times as there is no back pressure, and therefore less resistance to metal flow through the preform. The ideal vacuum for the process is <1 mb.

The operating temperatures used in the process vary considerably depending on the alloy specification, the type and volume fraction of reinforcement being used, and the size and complexity of the component being produced. If the die temperature is too low, the fibre temperature will be low and this results in solidification prior to full infiltration and porosity in the casting. Normally die temperatures during processing are kept well below the solidus.

High die temperatures result in high fibre temperatures and cause excessively long solidification times and could result in reactions occurring at the fibre metal interface.

Ability to infiltrate also depends on two other factors, the melt temperature and pressure applied. As with squeeze casting, the melt temperature has a lesser effect on ability to infiltrate than the die temperature. Although increased melt temperatures supply more heat to the casting, the effect on viscosity above the liquidus is only slight. For most aluminium alloys, the melt temperature used in manufacture is approximately 100°C above the liquidus. Excessive melt temperatures result in longer solidification times, possibility of fibre/metal reaction and more rapid die erosion.

It has been found that fibres such as SiC and alumina are wetted relatively easily and that these fibres require a lower infiltration pressure than fibres which are more difficult to wet such as carbon. The infiltration pressure required is in general lower than those used in other pressure-casting systems such as squeeze casting. The majority of commercially available fibres can be successfully infiltrated with applied pressures of under 1000 psi.

The pressure is applied to the surface of the metal reservoir when all the main parameters (metal temperature, die temperature, vacuum and injection pressure) are at the required values. A valve prevents ingress of the high pressure gas into the evacuated cavity, ensuring that no gas can be trapped in the casting. (Fig. 5c.)

The molten metal is kept under pressure until the fibre preform is fully infiltrated and the metal has solidified. Care has to be taken at the die design stage to ensure that correct directional solidification and metal feeding occur. Metal feed is a much more severe and complicated problem than in conventional unreinforced castings because metal transport through the fibre preform is extremely difficult. Calculations on directional solidification are also more complex because solidification occurs more rapidly in reinforced areas than in unreinforced areas of a similar cross section.

Unreinforced sections can thus remain

molten after adjacent reinforced regions have solidified and if isolated as pockets can result in shrinkage. It is important to have even die temperatures during operations, and to ensure that the correct die temperature is maintained, it has been found necessary to use selective die heating. The die temperatures are constantly monitored and controlled. As with conventional die-casting the higher production rates result in a large heat input to the die from the molten metal and if this is excessive, die cooling is required.

At the completion of the solidification time, the gas pressure is removed by venting the pressure vessel containing the molten metal reservoir. Once the system is at atmospheric pressure, the die is opened. The die is designed so that the component is retained in the upper half of the die. This allows the metal in the molten metal supply pipe to fall back into the reservoir.

The component is then ejected from the upper portion of the die using vertically acting ejection pins mounted in the body of the die. Due to the additional strength of the material at high temperatures it is possible for the casting to be ejected shortly after solidification is complete, without damage occurring. (Fig. 5d.)

Further processing is seldom required as the amount of flash produced is minimal or non-existant. All that is necessary is the removal of any runners or gates used to feed metal to the casting.

All indications show that this process produces material equal to, if not better than, other MMC fabrication routes. Extensive microstructural studies of the composites produced have shown that within the normal range of production parameters there is no reaction occurring between the reinforcement and the matrix alloy. SEM studies failed to find any evidence of such a reaction in any of the composites produced by this method. There is however considerable evidence to show that a good mechanical bond is achieved between the alloy and the reinforcing material. This can be seen clearly in the fracture surfaces where there is little or no evidence of fibre pull out. (Fig. 6)

The size and complexity of components that can be produced by this method varies considerably. The largest unidirectional component manufactured to date is a solid strut 2m long. A good example of the larger components is the torpedo nose cone reinforced with alumina fibres shown in Figure 7.



Fig. 6 - Fracture surface of boron/Al composite.

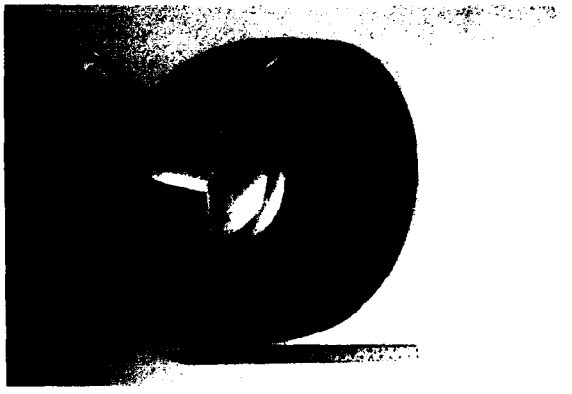


Fig. 7 - Alumina fibre reinforced torpedo nose cone produced by LPF process.

ENGINEERED MATERIALS

To obtain the greatest benefit from liquid pressure forming in terms of final component performance it is important to consider all aspects of the process. The development of the material, the design of the component shape and the manufacturing technology must all be combined at the initial design stage rather than treated separately.

By alteration of any or all of the important parameters such as, volume fraction, fibre orientation, fibre type, reinforcement location, alloy type, injection time, pressure and temperature, melt temperature, and component shape, it is possible to engineer a component to have specific properties in specific areas, within material limts. The specific properties that can be engineered in a

component include all the mechanical properties, such as strength, stiffness, fatigue limit, fracture toughness, impact strength as well as the co-efficient of thermal expansion, and wear resistance and many others.

SUMMARY

1. A new liquid metal infiltration process using gas pressure to force metal into fibrous and particulate preforms has been developed.
2. The process is capable of using nearly all commercially available reinforcing materials.
3. Good quality composite castings can be produced at relatively high production rates.
4. Accurate control of all casting parameters is essential to maintain quality.
5. A wide range of sizes and shapes can be manufactured from 2mm upto 2000mm.
6. No detrimental interfacial reactions between fibre and matrix have been found to occur.

HIGH PRESSURE SQUEEZE CASTING OF UNIDIRECTIONAL GRAPHITE FIBER REINFORCED ALUMINUM MATRIX COMPOSITES

Robert J. Sample, Ram B. Bhagat, Maurice F. Amateau
Applied Research Laboratory
The Pennsylvania State University
P.O. Box 30
State College, Pennsylvania 16804 USA

ABSTRACT

High pressure squeeze casting has been developed to fabricate unidirectional fiber reinforced metal matrix composites having a wide range of fiber volume fraction. The process development required innovative die-design in order to minimize the direct contact of molten metal with the metallic die, to prevent liquid metal escape from the die, to ensure fast infiltration and rapid solidification under high pressure. However, the application of high pressure causes certain difficulties, such as maintaining all fibers aligned in one direction and ensuring their uniform distribution in any cross section of the composites. This paper addresses the techniques used to overcome these difficulties.

Tensile test results for graphite fiber reinforced aluminum matrix composites are presented and discussed. Optical and scanning electron microscopy analysis of polished and fracture surfaces provide details of fiber/matrix interface characteristics and fracture mechanisms of the composites.

ONE OF THE MAJOR CONCERNS in the development of fiber reinforced metals has been the high cost of manufacturing. Fabrication techniques presently in use fall into two categories: variations involving infiltration by molten metal and powder metallurgy techniques. For example, in the fabrication of Gr/Al wires, the more common techniques involve the preliminary step of forming a coating, often by CVD, on the fiber surface in order to promote wetting of the fibers by the molten metal. This is necessary because the inorganic fibers that are commonly used for reinforcement in composites are not spontaneously wet by most molten matrix metals. DeLamotte and co-workers [1] used a nickel coating and other coatings include TiB, K_2ZrF_6 and K_2TiF_6. Chemical reactions between the fiber coatings and the matrix and also between the fibers themselves and the matrix can in extreme cases degrade the fibers and lessen the strength and the toughness of the reinforced metals.

Powder metallurgy techniques involve a solid state diffusion process that requires a relatively high temperature and considerable time [2]. Unfortunately, the same conditions that promote the densification of the metal also can lead to excessive interfacial reaction with consequential lower strength of the composites [3].

In order to develop a cost-effective manufacturing technique for composites, the ideal situation would be the elimination of the need for a fiber coating and the minimization of the contact time between the fibers and the molten metal. High pressure squeeze casting can be used to accomplish this goal. While the advantages of squeeze casting as a metal forming technique have been accepted for a number of years, squeeze casting has only recently attracted attention as a potential technique for the fabrication of metal matrix composites [4]. Squeeze casting can be used to circumvent the wetting angle requirement by force infiltrating molten metals into fiber bundles or preforms. In addition, the fiber-to-matrix contact time can be minimized by the complimentary effects of large under-cooling and increased rate of heat transfer out of the die cavity. Even with this great potential, there is very limited published research available on the squeeze casting of fiber reinforced metals [5-8]. It is imperative that further research work should be directed on process development to realize the full potential of the squeeze casting technique in fabricating near-net shape composites at a reasonable cost.

Therefore, the objectives of the present investigation are: (a) to demonstrate the ability to fabricate unidirectional continuous

fiber reinforced metals using high pressure squeeze casting, (b) to develop a technique for controlling the amount of interfacial reaction in the fabricated composites and (c) to characterize the composites by testing mechanical properties and by microscopic examination. The following section on the experimental work includes descriptions of the fiber and the matrix material, the equipment and the procedures used for the fabrication of fiber reinforced metals using high pressure squeeze casting; and testing and characterization of the composites.

EXPERIMENTAL WORK

The matrix material used was 6061 aluminum alloy. The fiber reinforcement used was pitch-based type P-55 graphite fibers in tow form. These fibers typically have a tensile strength of 2100 MPa and a stiffness of 379 GPa.

The die used for the casting in this investigation had a 6.9 cm internal diameter and was made from 1040 steel. The die assembly is shown in Fig. 1. The die cavity, bottom punch and the top punch, were case hardened to a maximum hardness of 55 Rc to a depth of 2.5 mm.

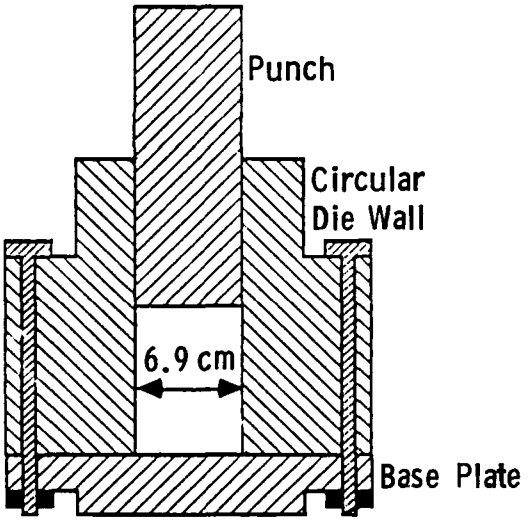


Fig. 1. Steel die used for squeeze casting of fiber reinforced metal matrix composites.

In order to fabricate unidirectional continuous fiber reinforced composites, a preforming technique was developed in which the tow fibers were arranged in such a manner that they will retain their parallel orientation during pouring of the metal and during the pressing. This preforming technique also insured uniform fiber distribution in a cross-section of the composites. A typical preform is shown in Fig. 2. Planar-random graphite fiber mats were used between the layers of the tow graphite fibers. For each casting, two identical preforms were used.

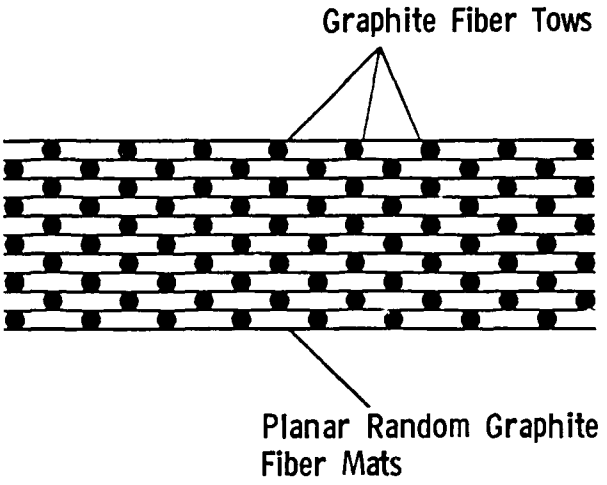


Fig. 2. Schematic of fiber preform.

The casting procedures were as follows. Approximately half the total amount of fibers to be used for a casting with a targeted fiber volume fraction was placed into the die cavity. Immediately after pouring the metal, the remaining fibers were placed into the die followed by the top punch. Pressure was applied within a few seconds to force the metal to infiltrate the fibers and was held until the metal had completely solidified and cooled to a low temperature. The fiber-to-molten metal contact time was approximately ten seconds.

Preliminary experiments were carried out to optimize the conditions of high pressure squeeze casting. The processing conditions include pouring temperature, pressure and time. The optimum values for both the pressure and the temperature were considered to be those that resulted in a minimum fiber-to-molten metal contact time while producing well infiltrated castings over a wide range of fiber volume fraction. Casting pressure and temperature were on the order of 250 MPa and 1100 K, respectively.

Some of the squeeze cast composites were heat treated to allow controlled metallurgical reaction between the fiber and the matrix in order to tailor the characteristics of the fiber/matrix interface. In a variation to the usual heat treatment procedure, squeeze cast composites were heated to a temperature a few degrees above the solidus of 6061 Al to effect a reaction between the carbon and the liquid aluminum. Similar procedure has been documented by Kim, et al., for FP-Al_2O_3/Al composites [9]. In the present investigation, the as-cast composite specimens were heated to the desired temperature in a rectangular metallic die. After a relatively short period of time, high pressure was applied on the composite in order to increase solidification temperature of the aluminum according to the

Clausius-Clapeyron equation; thus, solidifying the aluminum instantaneously and essentially preventing the liquid-solid reaction. The die was then allowed to cool in air and the pressure was released when the temperature fell well below the solidus temperature.

The ultimate tensile strength of the squeeze cast Gr/Al composites was measured using an Instron machine following standard procedures. Dog bone shape tensile specimens were made. Special care was taken in preparing the tensile specimens of the composites.

The fracture surfaces of the tensile tested composites were examined by Scanning Electron Microscopy (SEM). Polished cross-sections were examined by optical microscopy in order to characterize the fiber distribution and the degree of metal infiltration. Results from the microscopic examinations and the tensile tests are presented and discussed in the next section.

The microhardness of the matrix in the as-cast and heat treated condition, with and without reinforcement, was tested using a Vicker's diamond and a 0.030 kg load.

RESULTS AND DISCUSSION

The tensile strength of the unidirectional continuous fiber reinforced castings showed an expected behavior with an almost linear relationship with respect to unidirectional fiber volume fraction ranging from 4 to 52% (see Fig. 3).

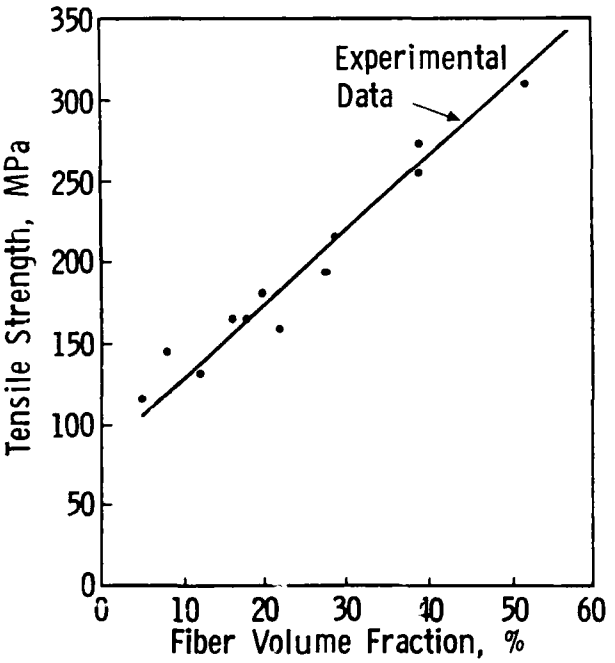
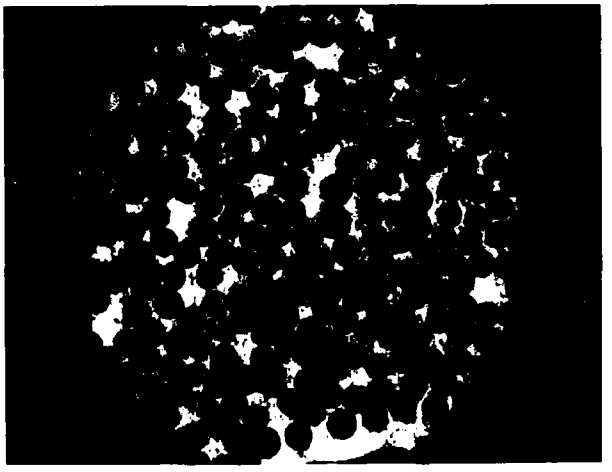


Fig. 3. Ultimate tensile strength of the squeeze cast graphite fiber reinforced aluminum matrix composites as a function of the unidirectional graphite fiber volume fraction.

Shown in Fig. 4 are optical micrographs of polished cross-sections near the fracture surface of a tensile tested composite with a fiber volume fraction of 25%. In Fig. 4(a), it can be seen that the overall fiber distribution is uniform. The degree of fiber infiltration into fiber bundles can be seen in Fig. 4(b). Virtually, each individual filament of the fiber tow is surrounded by the matrix metal.



(a)



(b)

Fig. 4. Optical micrographs of casting with unidirectional fiber volume fraction equal to 0.25 showing: (a) overall fiber distribution in the casting cross-section and (b) metal infiltration into a fiber tow.

Scanning Electron Microscope (SEM) micrographs of fracture surfaces of the tensile tested castings are given in Figs. 5 and 6. Figure 5 shows a fracture surface from as-cast unidirectional reinforced castings. The dominant mode of failure is apparently that of fiber pull-out, consistent with the relatively weak fiber-matrix interface. Pull-out can be

distinguished from debonding by the clean appearance of the fibers on the fracture surface, see Fig. 6(a). Although the vast majority of the fibers are very clean in appearance, there is some evidence of interfacial reaction on some fibers as shown in Fig. 6(b). Reaction products are shown extending outward from the fiber surface perpendicular to the axis of the fiber. The appearance of these reaction products is very similar to that shown in a study performed by Kohara and Muto [10].

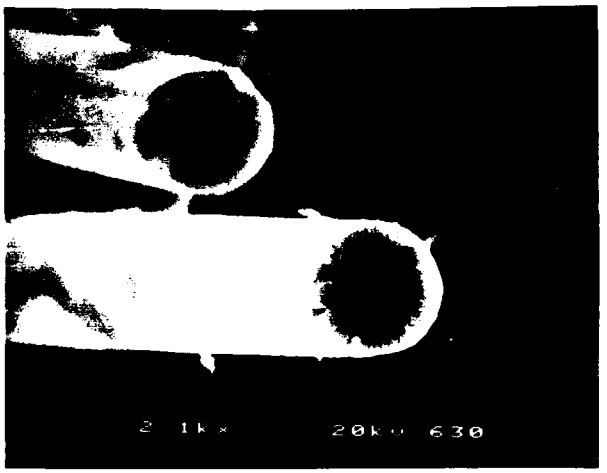


Fig. 5. SEM micrograph of unidirectional reinforced casting fracture surface showing high degree of fiber pull-out.

The Vicker's microhardness of the squeeze cast 6061 Al was measured to be 80 kg/mm^2. This is much higher than the known hardness of 6061-O Al (31 kg/mm^2) and 6061-T4 Al (57 kg/mm^2). It is likely that the squeeze cast 6061 Al undergoes limited precipitation hardening under the influence of high pressure on the just solidified aluminum alloy during



(a)



(b)

Fig. 6. SEM micrographs of fractured casting showing: (a) relatively clean appearance of pulled out fibers and (b) reaction products formed on a few of the fibers.

squeeze casting. The matrix hardness in the reinforced castings averaged 54 kg/mm^2 with considerable scatter (47 to 61 kg/mm^2) depending on where in the casting the measurement was taken. Thus, the hardness of matrix in the composite is lower than that of the matrix material alone processed identically. This may be attributed to the relatively reduced level of precipitation in the presence of fibers as affected by the processing conditions. The matrix hardness in the heat treated composites fell in general to a value around 34 kg/mm^2 which is close to the hardness of the 6061-O Al. This is believed due to the overaging of squeeze cast composites. The heat treated composites show evidence of enhanced reaction between graphite fibers and 6061 Al matrix. The details of the fiber/matrix interface characteristics and the tensile strength and stiffness of the heat treated composites are the subject matter of a forthcoming paper.

CONCLUSIONS

High pressure squeeze casting has been developed to fabricate unidirectional continuous graphite fiber reinforced aluminum matrix composites with the fiber volume fraction ranging from 4 to 52%. It has been demonstrated that during the casting process, the fiber tows are thoroughly infiltrated by the molten metal and rapid solidification is achieved. The fiber-to-matrix bonding in the squeeze cast composites is primarily of adhesion type; and there is very little evidence of interfacial reaction between the fiber and the matrix.

The composites show increased tensile strength with the increase in fiber volume

fraction. Microhardness data reveal limited precipitation hardening of 6061 Al matrix in the fabricated composites.

LIST OF REFERENCES

(1) DeLamotte, E., K. Phillips, A. Perry and H. Killas, Journal of Materials Science 7:346-349 (1972).
(2) Erich, D., International Journal of Metallurgy 23(1):45-54 (1987).
(3) Bhagat, R. B., Metallurgical Transactions A 16A:623-628 (1985).
(4) Bhagat, R. B., Developments in the Science and Technology of Composite Materials, ECCM I, A. R. Bunsell, P. Lamicq and A. Massiah, September 1985, Bordeaux, France, pp. 610-615 (1985).
(5) Fukunaga, H., S. Komatsu and Y. Kanoh, Bulletin Japan Society of Mechanical Engineers 26:1814-1819 (1983).
(6) Gibson, P., A. Clegg and A. Das, Foundry Trade Journal 152:253-263 (1982).
(7) Gelderloos, D. and K. Karasek, Journal of Materials Science Letters 3:232-238 (1984).
(8) Bhagat, R. B. and M. F. Amateau, High Pressure Casting of Metal Matrix Composites, Presented during Materials Week '87, Cincinnati, OH (October 1987).
(9) Kim, W., M. Koczak and A. Lawley, New Developments and Applications in Composites, TMS-AIME, pp. 40-53 (1979).
(10) Kohara, S. and N. Muto, Developments in Science and Technology Composite Materials, ECCM I, pp. 738-743 (1985).

SQUEEZE CAST METAL MATRIX COMPOSITES: EVALUATION OF THEIR STRENGTH, DAMPING CAPACITY AND CORROSION RESISTANCE

R. B. Bhagat, M. F. Amateau, J. C. Conway, Jr., J. M. Paulick, J. M. Chisholm, J. M. Parnell, D. G. Seidensticker
Engineering Science and Mechanics Department
The Pennsylvania State University
227 Hammond Building
University Park, Pennsylvania 16802 USA

ABSTRACT

Several graphite fiber reinforced (planar random) metal matrix composites employing copper, aluminum, tin and babbitt matrices were fabricated by a newly developed high-pressure squeeze casting method. The fiber volume fraction of these composites ranged from 5 to 55%. These composites had relatively weak fiber-to-matrix bonding because of the near-absence of interfacial reaction between fiber and matrix materials. The tensile strength of these composites increased with fiber volume fraction up to about 25% followed by a gradual decrease for higher fiber volume fractions.

Experiments were designed to evaluate various mechanical and physical properties of high pressure squeeze cast composites including the damping capacity and corrosion resistance. Measurements of logarithmic decrement values at resonant frequencies on cantilevered beam specimens have demonstrated that the damping capacity of the composites is much superior to that of wrought 6061-T6 Al and mechanically alloyed aluminum. Results on corrosion resistance of the composites in distilled water and 3.5% NaCl solution over a range of voltages and temperatures are presented and discussed.

THE PURPOSE OF THE PRESENT INVESTIGATION was to demonstrate the viability of high pressure squeeze casting method [1] of fabricating fiber reinforced metal matrix composites.

Fiber reinforced metal matrix composites are advanced engineered materials for demanding needs of high temperature, high performance reliable structures. In spite of significant progress made for fabricating quality metal matrix composites [2-29], it has been a technical challenge to develop a cost-competitive processing method with near-net shape capability for fiber composites. In a liquid infiltration technique, a suitable coating on the reinforcement fibers is a necessity for the fabrication of the composites. It is well known that the inorganic fibers, such as graphite, silicon carbide and alumina, which are of primary interest do not readily wet most molten metals. In view of this, a suitable coating on fibers serves two purposes: (a) it results in wetting and (b) it provides a diffusion barrier to minimize the formation of inter-metallic compounds at the fiber/matrix interface. Two early methods for liquid metal infiltration of graphite fibers include sodium pretreatment followed by infiltration and chemical vapor co-deposition of titanium and boron. Recently other investigators [30] have attempted to pretreat graphite fiber by SiO_2, K_2ZrF_6 and K_2TiF_6 and have claimed to have succeeded in thoroughly infiltrating fiber tows with molten aluminum or magnesium. This infiltration method results in precursor composite wires that must subsequently be hot pressed into structural shapes. An alternative to this dual processing is to carry out infiltration into simple shapes aided by pressure. The pressure is usually applied on the molten metal to force-infiltrate it into the fiber preform. As a corollary, suction can be applied to suck the molten metal into the fiber preform usually placed in a cylindrical ceramic tube. However, in these techniques, the composites are not completely free from shrinkage cavities, gas porosity and other usual casting defects. Besides, the contact time between molten metal and the fibers is not reduced to the extent that the reaction between fiber and molten metal can be significantly prevented. Even in those cases when fiber coating is used, the contact time is sufficient to dissolve the coating material thereby exposing the bare fiber to the molten metal.

In order to overcome these limitations, Bhagat and Amateau [1] employed a high

pressure squeeze casting (HPSC) approach for fabricating fiber composites. In this approach, conventional squeeze casting methods (also known as liquid forging, liquid pressing, extrusion casting and pressure crystallization) are modified to accommodate fiber preforms. Low pressure squeeze casting of metal composites have been previously used [23,31]. A brief overview of the squeeze casting method has recently been given by Bhagat [32]. The high pressure squeeze casting technique for fabricating composites uses a force-infiltrating molten metal into specially designed fiber preforms under sufficiently high pressure to effect rapid infiltration followed by rapid solidification. Recently Bhagat and Amateau [1] demonstrated that the high pressure squeeze casting technique can be used to fabricate fiber reinforced metal matrix composites free from shrinkage cavities and gas porosity without using any fiber coating. They also demonstrated that the fiber-to-matrix bonding was primarily of adhesion type and the interface was almost free from any reaction product.

The present investigation is, therefore, aimed at further extending the work on high pressure squeeze casting to demonstrate its viability by processing composites of planar isotropy using low to high melting metals as matrices and evaluating their strength, damping capacity and corrosion resistance.

EXPERIMENTAL WORK

The experimental work in the present investigation included fabrication of fiber reinforced metal matrix composites, tensile testing, low cycle fatigue, damping and corrosion. Characterization of the composites by optical and scanning electron microscopy (SEM) is also reported.

FABRICATION OF MMCs - The metal composites fabricated in the present work include matrices of copper, aluminum, babbitt and tin reinforced with bare or nickel coated planar random graphite fiber mats. The fabrication was done by high pressure squeeze casting previously described by Bhagat and Amateau [1]. In this technique, molten matrix metal is force-infiltrated into hand-made preforms of fiber mats in a metallic die without any need of preheating the die or the fiber preform. Infiltration is completed in less than ten seconds under a pressure ranging up to 500 MPa. Following the infiltration, the matrix metal rapidly solidifies. The rapid solidification is effected by the rapid application of high pressure which raises the solidification temperature of the matrix and increases the rate of heat dissipation through the die. Thus, the squeeze casting process minimizes the fiber-to-matrix reactions at the interface. Also, this process eliminates shrinkage cavities and porosity in the cast composites. The composites were fabricated with fiber volume fraction ranging from 5 to 55%. All the composites were fabricated in the form of disks with a diameter of 69 mm and 114 mm. The thickness of these composite disks was 3 mm (approximately).

TENSILE TESTING - The composites were tensile tested for their stiffness and strength. Tensile test specimens were prepared by first slitting composite disks into rectangular pieces followed by precision machining into dogbone specimens and hand-polishing with emery papers. The tensile tests were done at room temperature using an Instron machine with a 90 kN capacity load cell.

FATIGUE TESTING - Low cycle stress controlled fatigue tests were performed on hourglass shape composite specimens. These specimens were prepared by careful machining, paper-polishing and cloth-polishing ensuring smooth surface finish. All the specimens were tested at room temperature using an Instron machine at 25 Hz keeping the stress ratio R equal to 0.1 (tension-tension). The fatigue life was determined as the number of cycles to failure, designated as N.

DAMPING - Damping measurements were carried out on cantilevered beams which were clamped at one end and vibrated at the other end in the thicker dimension of the cross-section of the beams. The details of the experimental configuration are shown in Fig. 1. A signal generator produces a sinusoidal signal of varying frequency monitored by a frequency counter. This signal is amplified and sent to a switching box. This box splits the signal, sending it to an oscilloscope and to a copper coil which produces a varying electromagnetic force on a small cobalt-samarium magnet attached to the lower tip of the beam specimen (see Fig. 1). A small piece of aluminum foil is glued to the upper tip of the beam; the foil provides a reflective surface for the probe of a photoaccumulator device. This device provides the displacement of the beam as it vibrates by sending and receiving an optical signal through a fiber optic system. The vibration amplitude signal is sent through a band-pass filter which allows only a narrow range of frecuencies around a natural frequency of the beam to pass through. The filtered signal is sent to an oscilloscope where the signal is monitored to accurately establish a natural frequency. At this natural frequency, the current to the coil is cut-off simultaneously triggering the storage oscilloscope which records the pattern of the vibration decay. A photograph is made of the vibration decay and loss factor (η) is calculated using the following relationship:

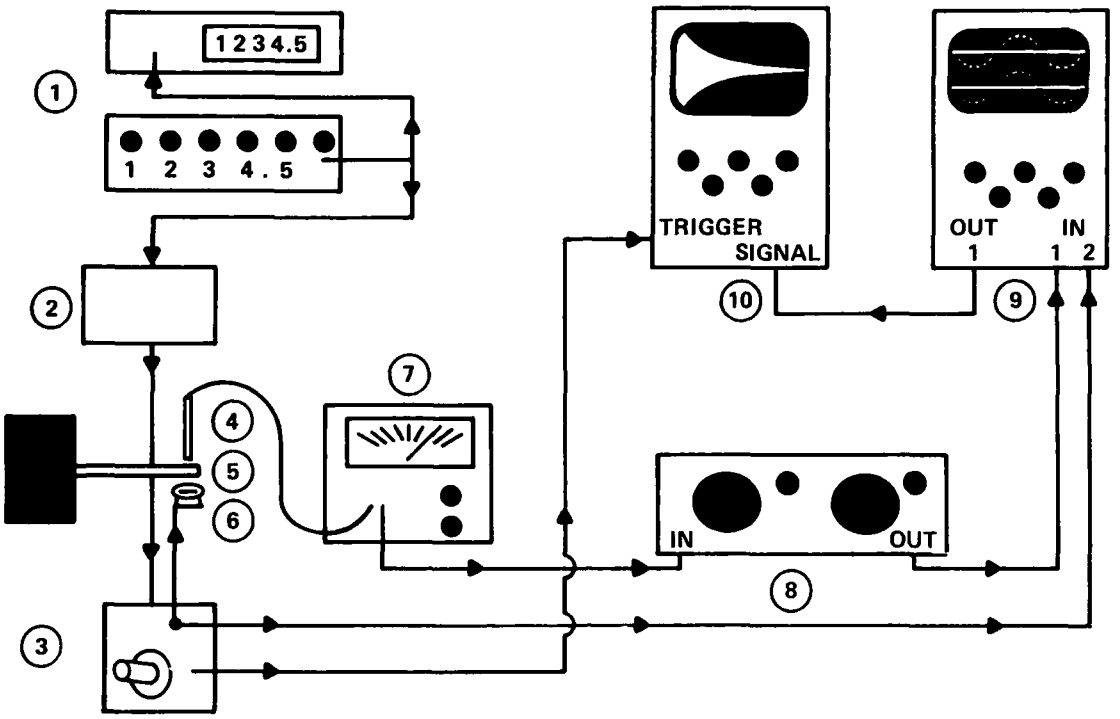


Fig. 1. Experimental configuration for damping measurements on clamped-free cantilevered beam specimens (adapted from an experimental setup used by Eckstein [33]): (1) signal generator and counter, (2) amplifier, (3) switching box, (4) probe of photoaccumulator device, (5) specimen, (6) coil, (7) photoaccumulator device, (8) frequency filter, (9) monitor oscilloscope and (10) storage oscilloscope.

$$\eta = \frac{1}{\pi n} \ln \frac{x_0}{x_n} \qquad (1)$$

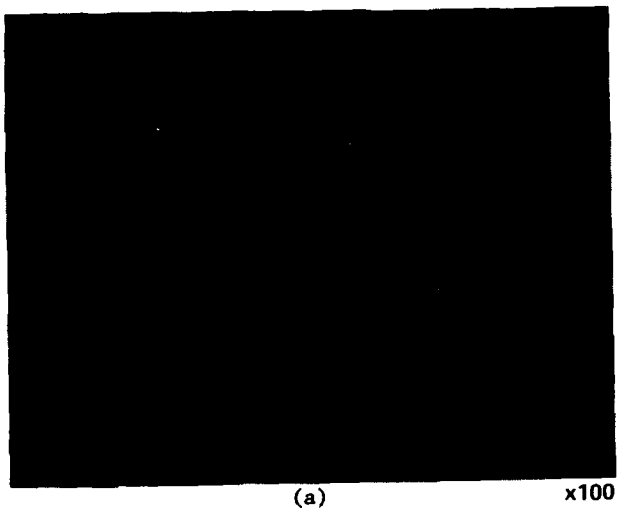
where x_0 is initial amplitude and x_n is amplitude after n cycles.

CORROSION - The corrosion testing of graphite fiber reinforced 6061 aluminum matrix was carried out over a range of voltages (.04 volt - 1.0 volt). The test specimens were used as anodes and the cathode was 304 type stainless steel; all the tests were carried out in a beaker containing 3.5% NaCl solution (pH = 6.60) or distilled water. The pH of the NaCl solution was monitored and maintained constant adding distilled water or salt. The tests were done at room temperature (295 K) and 365 K for time periods ranging from six hours to 24 hours.

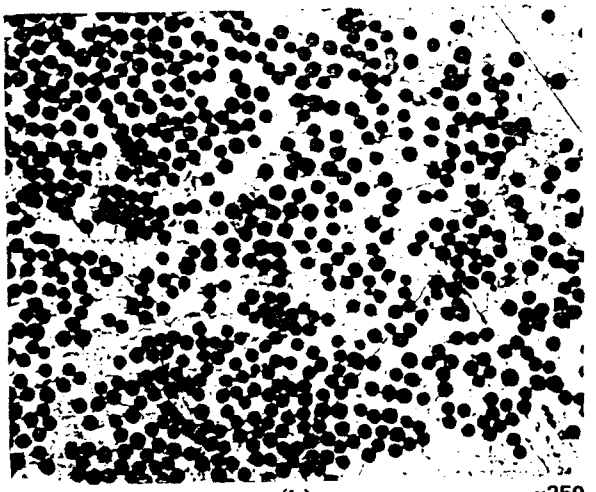
RESULTS AND DISCUSSION

Figure 2 shows typical micrographs of polished cross-sections of tensile test specimens of squeeze cast Gr/Cu, Gr/Al, and Gr/Sn composites. Fiber distribution is fairly uniform. The same is true for Gr(Ni)/Cu, Gr(Ni)/Al, Gr(Ni)/babbitt and Gr(Ni)/tin composites which were also fabricated in the present investigation.

Figure 3 shows that in the squeeze cast composites, the coating on the fiber remains intact. This is because of the nominal contact time between the coated fiber and the molten matrix metal in the squeeze casting process. Interfacial reaction between the coating and the matrix; and between fiber and matrix is almost nonexistent. It was demonstrated that the high pressure squeeze casting allows a thorough infiltration of molten metal in uncoated fiber preforms (see Fig. 2). Thus, the use of a coating on the fiber is not necessary for infiltration in the high pressure squeeze casting (HPSC) technique. Additionally, the HPSC technique provides a greater opportunity to tailor the properties of the composites by selecting a suitable coating (for example, a thermal barrier coating) for the fibers and retaining it intact in the fabricated composites. All the fabricated composites have primarily adhesion type bonding between the fiber and the matrix materials. The composites show improved strength as shown in Fig. 4. It is interesting to note that all the composites show peak strength at an optimum fiber volume fraction (V_{opt}) of about 25%. This general trend is expected for planar random fiber reinforced composites. We propose that the peak strength is reached when the



(a) x100

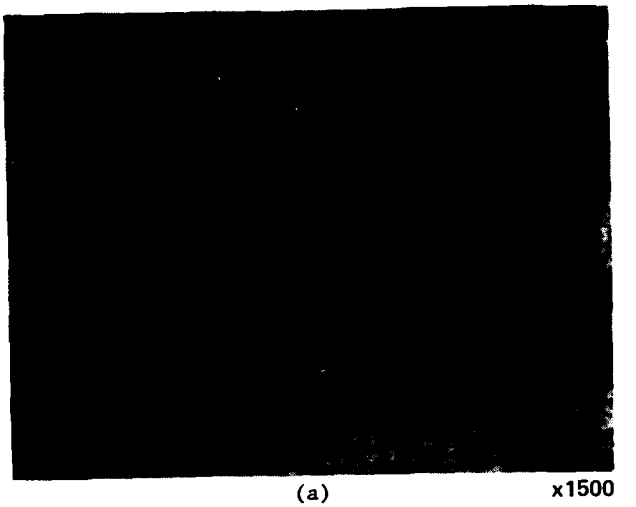


(b) x250

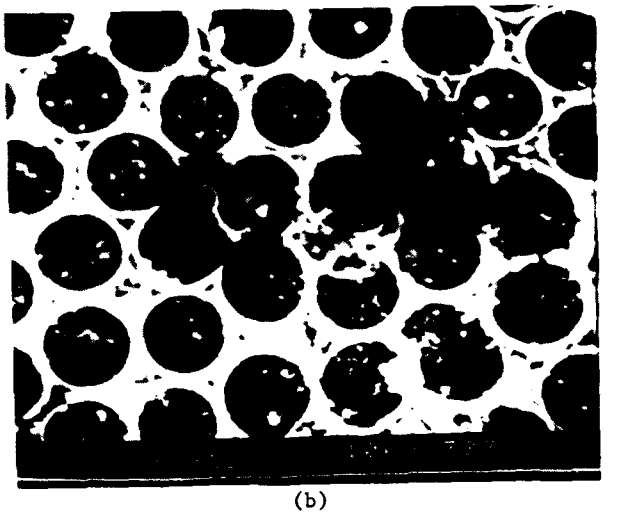


(c)

Fig. 2. Typical micrographs showing fiber distribution in planar random graphite fiber (bare) reinforced copper matrix (a), 6061 aluminum matrix (b), and tin matrix (c) composites.



(a) x1500



(b)

Fig. 3. Micrographs of Gr(Ni)/Al (a) and Gr(Ni)/babbitt (b) showing that the nickel coating remains intact in the high pressure squeeze cast composites.

strengthening effect of the fibers in the direction of the loading is balanced by the effect of stress concentration due to matrix cracking in the transverse direction of the loading. It should be noted that irrespective of the fiber volume fraction, all the composites failed by fiber pullout (for examples, see Fig. 5) as a consequence of the relatively poor interfacial bonding in the fabricated composites. Attempts are underway to improve the strength by improving the bonding between the fiber and the matrix by suitable heat treatment of the fabricated composites.

Figure 6 shows a plot for the dependence of the low cycle fatigue life, in terms of cycles to failure (N), on the fiber volume fraction of Gr(Ni)/Al composites. There is a significant increase in the fatigue life of

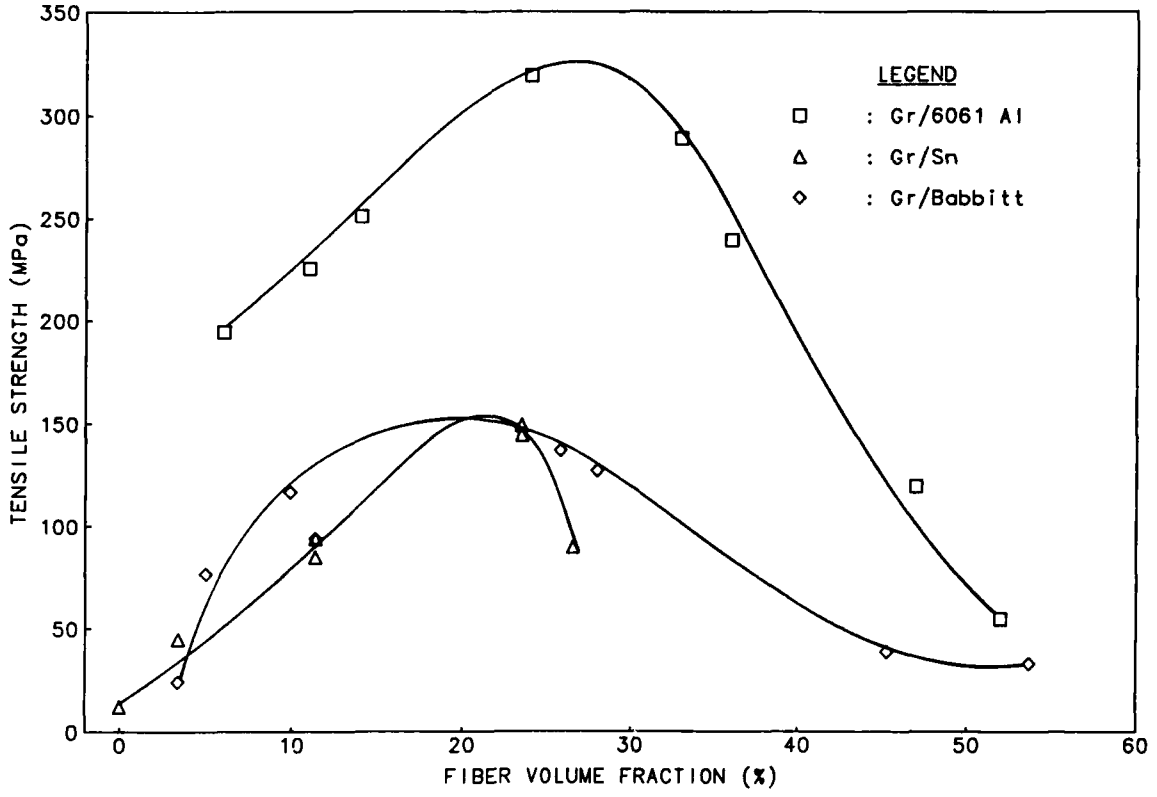


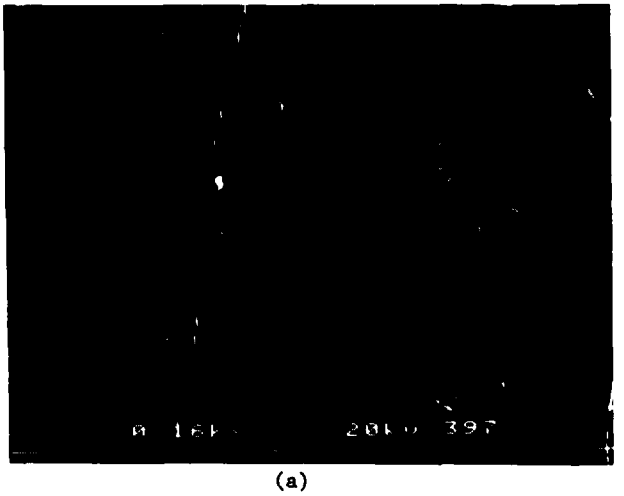
Fig. 4. Ultimate tensile strength of planar random graphite fiber reinforced metal matrix composites.

the composites at a relatively low fiber volume fraction of about 10% followed by almost constant life at higher fiber volume fractions (see Fig. 6). We propose that up to the fiber volume fraction of about 10%, the fibers bear most of the stress under the cyclic loading resulting in higher fatigue life compared to that of aluminum cast under identical conditions of high pressure squeeze casting. However, with an increase in fiber volume fraction beyond 10%, further increase in the fatigue life of the composites is not found because of two possible reasons:

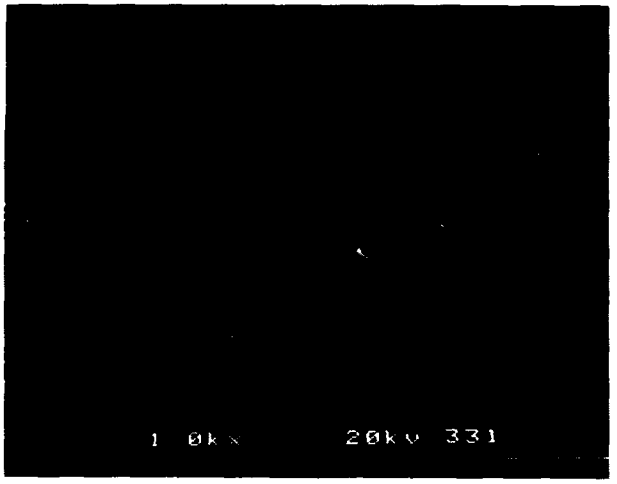
(a) Development of crack-like defects in the matrix because of the presence of increasing amount of fibers lying in directions other than the loading direction. This can happen at relatively low stress levels experienced by the matrix.

(b) Increased stress concentration leading to the local separation of the load bearing fibers from the matrix at the interface and eventual fracture of these fibers.

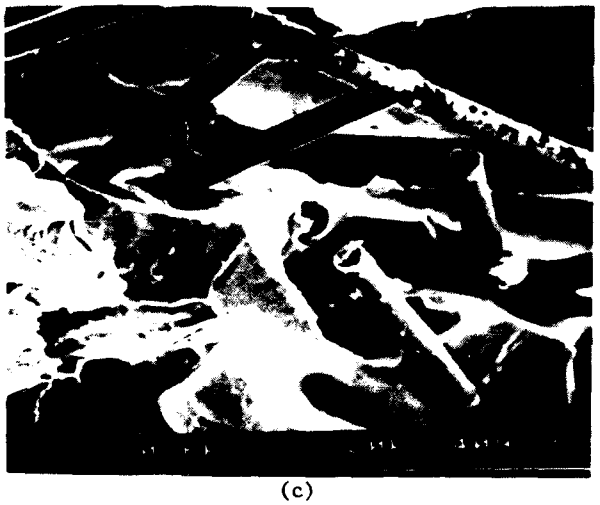
Damping capacity results were obtained for Gr/Al composites (V_f = 0.30), 6061-T6 Al and mechanically alloyed aluminum (4.0% Mg, 1.2% C, 0.8% O, balance Al). The composites were fabricated by high pressure squeeze casting as described earlier. The mechanically alloyed aluminum was provided by INCO Alloys International. The damping of 6061 Al and mechanically alloyed aluminum were found to be dependent on the resonant frequency ranging from ~ 300 Hz to ~ 12000 Hz. This broad range of resonant frequency includes first three modes of flexure vibration of clamped-free cantilever beams (see Fig. 7). The experimental data on loss factor (η) are well represented by the following relationships:



(a)



(b)



(c)

Fig. 5. SEM fractographs showing the nature of fracture under tensile loading -- (a) Gr/Al, (b) Gr(Ni)/Al and (c) Gr(Ni)/Sn composites.

$$\eta = 0.00567 - 0.00133 \log Fn \quad (2)$$
(for 6061-T6 Al)

$$\eta = 0.00506 - 0.00114 \log Fn \quad (3)$$
(for mechanically alloyed aluminum)

where η = loss factor as defined by Eq. (1) and Fn = resonant frequency (~ 300 Hz to ~ 12000 Hz). The experimental damping data for the fabricated Gr/Al composites (V_f = 0.30) when plotted against resonant frequency showed peaks at ~ 876.0 Hz and ~ 4362.5 Hz. The two damping peaks correspond to the vibration Modes I and II; existence of such a peak in Mode III could not be established because of the limited experimental data in Mode III. In Fig. 8, a comparison of the peak damping of the fabricated Gr/Al composites is made with the corresponding damping of 6061 Al and mechanically alloyed (M.A.) aluminum as

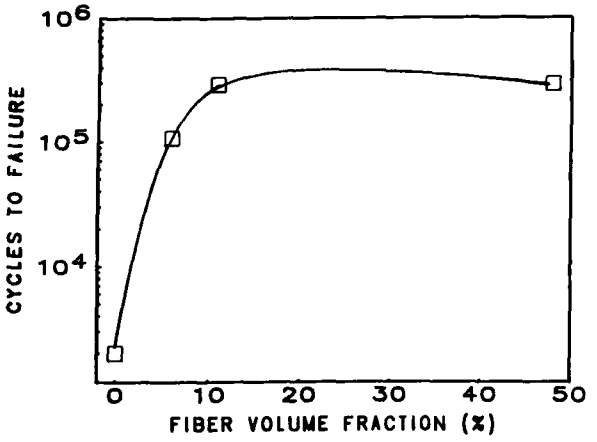


Fig. 6. Plot showing the low cycle fatigue life of nickel coated planar random graphite fiber reinforced 6061 aluminum matrix composites.

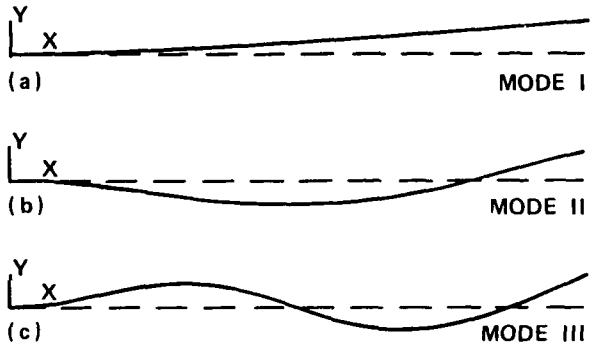


Fig. 7. Three modes of flexure vibration of clamped-free cantilever beams at resonant frequencies as predicted by finite element analysis (ANSYS).

predicted by Eqs. (2) and (3). It is found that the damping of the Gr/Al composites is up to 7.4 times that of the other two materials which have similar damping values.

Experimental results for the electrochemical corrosion of the fabricated Gr/Al and Gr(Ni)/Al composites are presented in Figs. 9 and 10. The following major observations are made based on the data of Figs. 9 and 10 and other similar results at voltages ranging from 0.04 volt to 1.0 volt:

(a) At a fixed voltage, the mass loss of the composites is, in general, linearly proportional to the time period of the corrosion.
(b) The mass loss increases with an increase in the fiber volume fraction of the Gr(Ni)/Al composites, fiber volume fraction ranging from 0.27 to 0.48. Similar trend is expected for Gr/Al composites.
(c) Corrosion rate for the Gr/Al composites is greater than that for the Gr(Ni)/Al composites.

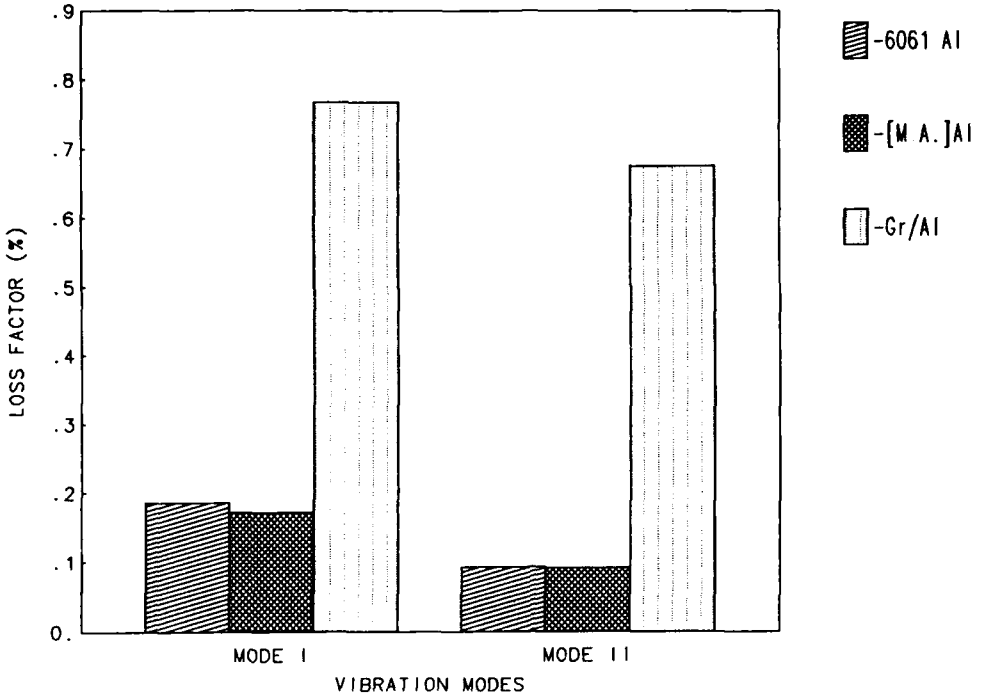


Fig. 8. Comparison of damping results for planar random graphite fiber reinforced aluminum matrix composites (V_f = 0.30), 6061-T6 Al, and mechanically alloyed aluminum. Vibration Modes I and II correspond to 876 Hz and 4362.5 Hz, respectively.

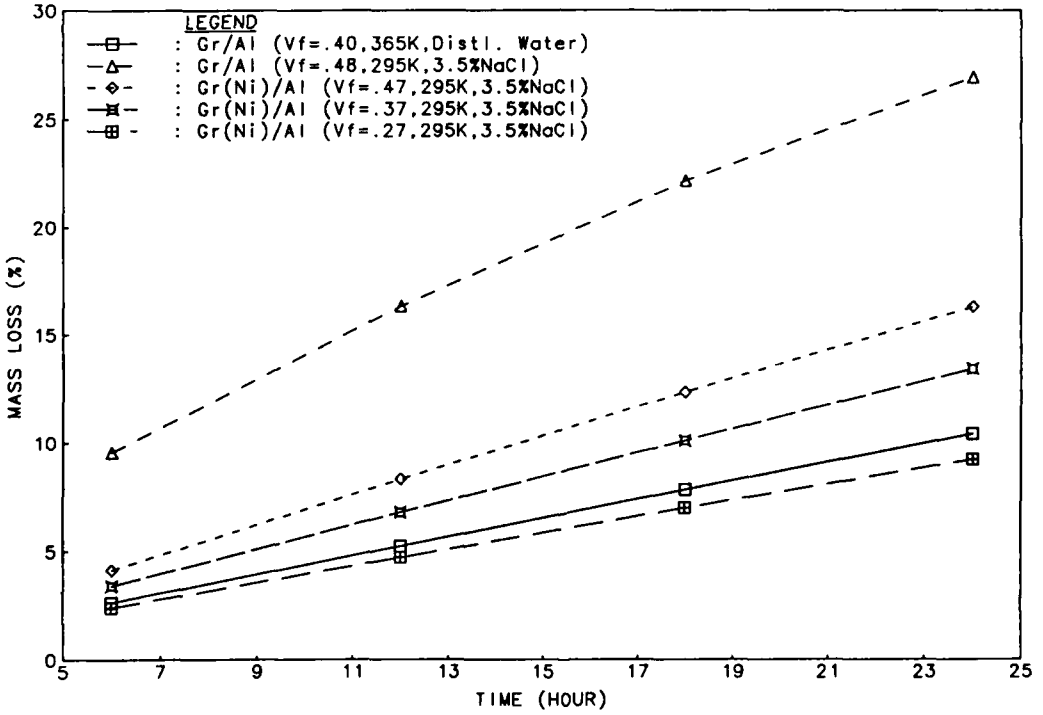


Fig. 9. Plots showing the increasing mass loss of composite specimens (anode) immersed in 3.5% NaCl solution (pH = 6.60) at 1.0 volt. Experimental results for corrosion in distilled water (365 K) are also included for comparison.

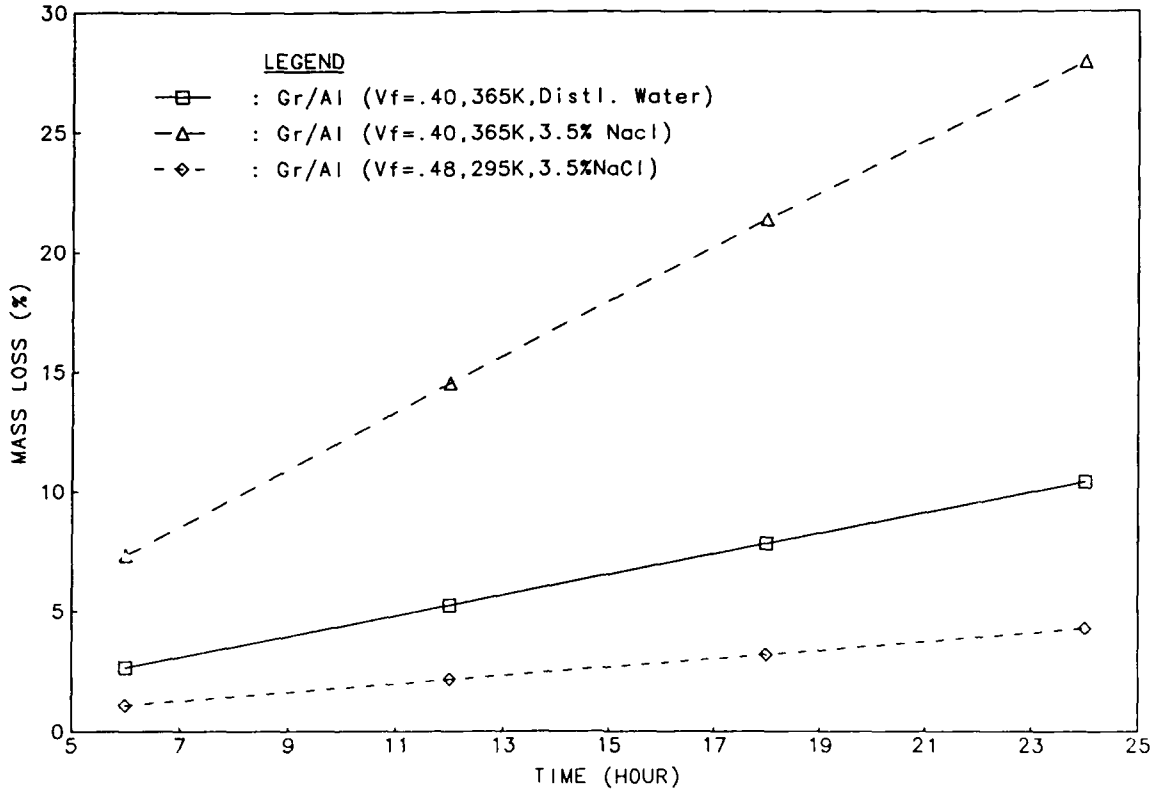


Fig. 10. Corrosion of Gr/Al composites in 3.5% NaCl (pH = 6.60) at room temperature (295 K) and 365 K; and at 0.6 volt. Also included is a plot for corrosion in distilled water (365 K) at 1.0 volt.

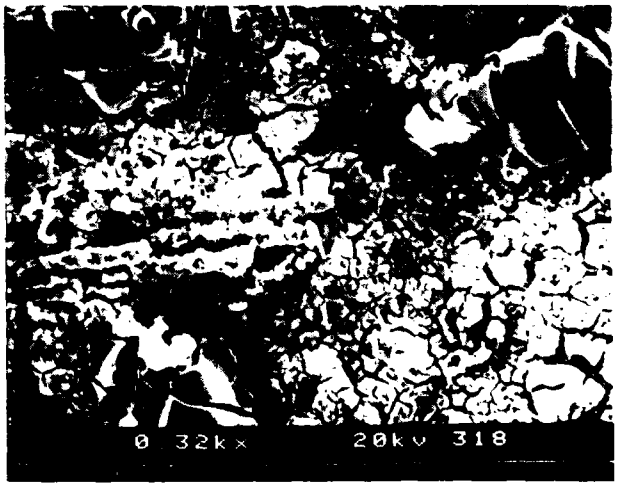
(d) Corrosion rate for the Gr/Al composites is higher at 365 K than that at 295 K.

The above findings on the electrochemical corrosion of the squeeze cast composites are consistent with our general expectation. The superior resistance to corrosion of the Gr(Ni)/Al composites is primarily because of the two factors:

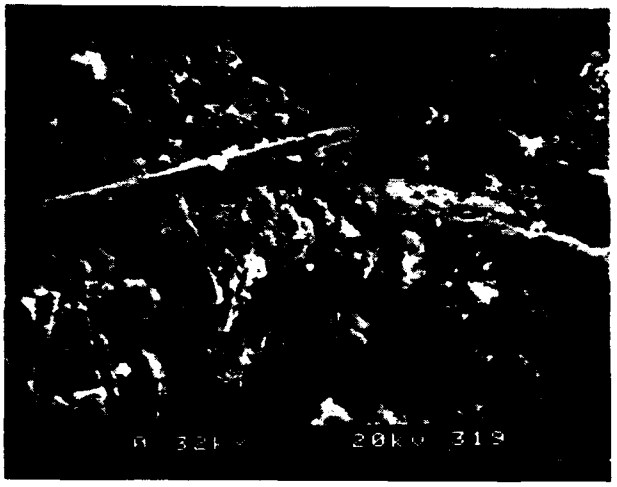
(a) The nickel coating on the fiber which remains intact during the fabrication of the composites ensures the absence of any aluminum carbide at the fiber/matrix interface. Thus in these composites, their corrosion by the hydration of Al_4C_3 into $Al(OH)_3$ is completely ruled out.

(b) The nickel coating on the fiber minimizes or even it eliminates the undesirable electrochemical coupling between the nobler graphite fiber and the active aluminum. This leads to the prevention of the galvanic corrosion.

Thus, the corrosion damage of the Gr(Ni)/Al composites is primarily by dissolution of matrix aluminum. However, besides the dissolution of matrix aluminum, galvanic corrosion also takes place in the Gr/Al composites. Additionally, the Gr/Al composites may degrade because of the hydration of Al_4C_3 at the fiber/matrix interface, notwithstanding how small in quantity it is present in the squeeze cast composites. Extensive damage, as it can be seen in Fig. 11(a) for Gr/Al composites in contrast to that observed in Fig. 11(b) for Gr(Ni)/Al composites, is a clear indication that the nickel coating is very effective in limiting the corrosion damage.



(a)



(b)

Fig. 11. SEM micrographs showing the damage of (a) Gr/Al and (b) Gr(Ni)/Al composites immersed in 3.5% NaCl solution for 24 hours at 0.6 volt.

SUMMARY AND CONCLUSIONS

High pressure squeeze casting has been demonstrated as a very viable technique of fabricating fiber reinforced metal matrix composites. For planar random bare and nickel coated graphite fiber reinforcement ($0.05 \leq V_f \leq 0.55$) into copper, aluminum, tin and babbitt matrices, near-absence of interfacial reaction products has been achieved. The bonding between the fiber and the matrices is primarily of adhesion type. These composites have uniform fiber distribution. For nickel coated graphite fiber, the coating remains intact in the composites. High tensile strength and fatigue life of these composites are limited to optimum fiber volume fractions of ~ 0.25 and ~ 0.10, respectively.

Logarithmic decrement measurements on clamped-free cantilevered beams have been carried out at resonant frequencies. Gr/Al composites ($V_f = 0.30$) shows damping peaks of 0.767% and 0.675% (in terms of loss factor, η) at 876.0 Hz and 4362.5 Hz of resonant frequencies, respectively. It is demonstrated that the superior damping of the Gr/Al composites is up to 7.4 times that of 6061-T6 Al and mechanically alloyed aluminum which exhibit similar damping values over a frequency range of ~ 300 Hz to ~ 12000 Hz.

Electrochemical corrosion study of Gr/Al and Gr(Ni)/Al composites in 3.5% NaCl solution has revealed that the presence of nickel coating on the fibers in the fabricated composites significantly reduces the damage of the Gr(Ni)/Al composites. This is in contrast to the extensive damage suffered by Gr/Al composites because of the cumulative effects of dissolution of aluminum, hydration of Al_4C_3 into $Al(OH)_3$ and galvanic coupling between Gr and Al. The latter two mechanisms are almost non-existent in Gr(Ni)/Al composites.

REFERENCES

1. Bhagat, R. B. and M. F. Amateau, "High Pressure Casting of Metal Matrix Composites," presented at Materials Week '87, Cincinnati, OH (October 1987).
2. Amateau, M. F., "Progress in the Development of Graphite/Aluminum Composites using Liquid Infiltration Technology," J. Composite Materials 10, 279-296 (October 1976).
3. Erich, D., International Journal of Metallurgy 23(1), 45-54 (1987).
4. Bhagat, R. B., Metallurgical Transactions A 16A, 623-629 (1985).
5. Fukunaga, H., S. Komatsu and Y. Kansh, Bull. Japan Soc. Mech. Eng. 26, 1814-1819 (1983).
6. Gibson, P. R., A. J. Clegg and A. A. Das, Foundry Trade Journal 152, 253-263 (1982).
7. Bhagat, R. B., "Squeeze Casting Fiber Reinforced Aluminum Matrix Composites," Developments in the Science and Technology of Composite Materials, ECCM 1, A. R. Bunsell, P. Lamicq and A. Massiah (eds), First European Conference on Composite Materials and Exhibition, Bordeaux, France, 610-615 (September 1985).
8. Gelderloos, D. G. and K. R. Karasek, J. Mater. Sci. Lett. 3, 232-238 (1984).
9. Pepper, R. T. and R. A. Penty, "Mechanical Properties of Aluminum-Graphite Composites Prepared by Liquid Phase Hot Pressing," J. Composite Mater. 8(1), 29-33 (1974).
10. Dhingra, A. K., "Metal Matrix Composites Reinforced with Fiber FG (Al_2O_3)," Phil. Trans. Royal Soc. London A294, 559-564 (1980).
11. Signorelli, R. A., "High-Temperature Composites -- Status and Future Directions," Progress in Science and Engineering of Composites, Proc. of the Fourth International Conference on Composite Materials, T. Hayashi, K. Kawata and S. Umekawa (eds), Japan Society for Composite Materials, 37-45 (1982).
12. Fishman, S. G., "Processing Metal Matrix Composites - The State of the Art," ASTM News, 46-49 (October 1986).
13. Howes, M. A. H., "Ceramic-Reinforced MMC Fabricated by Squeeze Casting," Journal of Metals 38(3), 28-29 (1986).
14. Petrasek, D. W., D. L. McDanels, L. J. Westfall and J. R. Stephens, "Fiber-Reinforced Superalloy Composites Provide an Added Performance Edge," Metal Progress, 27-31 (August 1986).
15. Signorelli, R. A. and J. A. DiCarlo, "High Temperature Metal and Ceramic

Composites," Journal of Metals 37(6), 41-42 (1985).
16. Schuster, D. M., M. Skibo and R. Yep, "SiC Particle Reinforced Aluminum by Casting," Journal of Metals 39(11), 60 (November 1987).
17. Xizngun, L., Z. Hanlin and W. Renjie, "The Effect of Long Period Heat-Treatment on Carbon Fiber Reinforced Aluminum Composite," Fifth International Conference on Composite Materials, ICCM V, W. C. Harrigan, Jr., J. Strife and A. K. Dhingra (eds), The Metallurgical Society of AIME, 623-629 (1985).
18. Baty, D. L., J. P. Price and B. G. Coleman, "Selective Properties of Aluminum Alloys Reinforced with Alumina-Silica Fibers," Metal Matrix Composites '87, Philadelphia, PA, Society of Manufacturing Engineers, Dearborn, MI (16-17 September 1987).
19. Hack, J. E., R. A. Page and R. Sherman, "The Influence of Thermal Exposure on Interfacial Reactions and Strength in Aluminum Oxide Fiber Reinforced Magnesium Alloy Composites," Met. Trans. A. 16A, 2069-2072 (1985).
20. McMinn, A., R. A. Page and W. Wei, "The Effect of Processing Parameters on the Tensile Properties of Alumina Fiber Reinforced Magnesium," Met. Trans. A. 16A, 273-281 (1987).
21. Girot, F. A., R. Fedon, J. M. Quenisset and R. Naslain, "On the Squeeze Casting Conditions of Aluminum Matrix Composite Materials," Proc. Second Technical Conference, American Society for Composites, University of Delaware, Newark, DE, 361-370 (23-25 September 1987).
22. Quigley, B. F., G. J. Abbaschian, R. Wunderlin and R. Mehrabian, "A Method for Fabrication of Aluminum-Aluminum Composites," Met. Trans. A. 13A, 93-100 (1982).
23. Chou, T. W., A. Kelly and A. Okura, "Fiber-Reinforced Metal Matrix Composites," Composites 16(3), 187-206 (1985).
24. Zantout, B., A. A. Das and J. R. Franklin, "Squeeze-Cast Aluminum-Matrix Composite: Strength at Higher Temperature," Spring Residual Conference No. 20 of the Institute of Metallurgists, Loughborough University, 215-221 (March 1983).
25. Gibson, P. R., A. J. Clegg and A. A. Das, "The Production of Cast Aluminum-Silicon Alloys Containing Graphite," Spring Residual Conference No. 20 of the Institute of Metallurgists, Loughborough University, 208-214 (March 1983).
26. Yajima, S. and K. Okamura, "High-Temperature Strength of Aluminum Composite Reinforced with Continuous SiC Fiber," J. Materials Science 16, 3033-3038 (1981).
27. Cappleman, G. R., J. F. Watts and T. W. Clyne, "The Interface Region in Squeeze-Infiltrated Composites Containing δ-Alumina Fiber in an Aluminum Matrix," J. Materials Science 20, 2159-2168 (1985).
28. Skarmaki, K., M. Hamada and M. Hasegaeva, Fracture Behavior of Aluminum Composites Reinforced with Fiber," Met. Abstracts on Light Metals and Alloys, Vol. XVIII, 58-60 (December 1985).
29. Murakami, Y. and K. Nakao, "Effect of Interfacial Conditions on the Tensile Strength of Carbon Fiber-6061 Aluminum Alloy Composites," Met. Abstracts on Light Metals and Alloys, Vol. XVIII, 44-46 (December 1985).
30. Personal Communication, Howard Katzman, Aerospace Corporation, El Segundo, CA.
31. Mortensen, A., M. N. Gungor, J. A. Cornie and M. C. Flemings, "Alloy Microstructures in Cast Metal Matrix Composites," J. of Metals 38(3), 30-35 (1986).
32. Bhagat, R. B., "High Pressure Squeeze Casting of Stainless Steel Wire Reinforced Aluminum Matrix Composites," to appear in Composites (September 1988).
33. Eckstein, F. D., On the Specially Orthotropic Free-Free-Free-Free Square Plate in Resonance, M.S. Thesis, Department of Engineering Science and Mechanics, The Pennsylvania State University (1986).

SYSTEM OPTIMIZATION FOR SQUEEZE CAST COMPOSITES

C. R. Cook, D. I. Yun, W. H. Hunt, Jr.
Alcoa Laboratories
Alcoa Center, Pennsylvania 15069 USA

ABSTRACT

A wide range of reinforcement/matrix combinations are possible using the squeeze casting process of composite manufacture. In order to optimize the properties of a given system, an understanding of component properties and various fiber/matrix interactions is needed. The matrix alloy selection influences the composite through inherent properties such as strength, ductility, and thermal stability. In addition, results from recent research show that short alumina fibers alter the physical metallurgy and segregation patterns during solidification of an Al-Cu-Mg matrix. The nature of these interactions influences the fiber/matrix interfacial bond, required thermal practices, and resultant composite properties such as fracture behavior. Improvements needed to produce higher quality squeeze cast composites will be discussed.

MANY MATERIAL AND PROCESSING OPTIONS are available to produce composite structures which satisfy design criteria that are not satisfactorily met by a monolithic material. This flexibility in design is most successful when property-limiting factors are identified and addressed. A knowledge of process-structure-property relationships is needed to achieve the best combination of properties for a given composite system.

Room and elevated temperature tensile properties were identified as targets for improvement through careful consideration of process and component material selection in the present work. Concurrent improvements of other properties (such as modulus, fatigue, CTE, and wear resistance) were expected, but were not used as primary target properties.

Specifically, this paper discusses important factors related to the design and production of squeeze cast Al-Cu-Mg alloys reinforced with discontinuous Saffil (96% alumina-4% silica) fiber preforms. Matrix alloy selection was seen as the key aspect to influence composite properties.

Several generations of composites were cast and evaluated to demonstrate the capability of this method to produce high quality castings. Defects related to processing and fiber preforms were identified and corrected when possible. Results of investigations of the influence of process parameters, reinforcement quality, and matrix compositions on resultant composite strength follow.

FABRICATION METHOD

The squeeze casting process has been employed to incorporate a variety of reinforcements in aluminum alloys. The process consists of placing a porous, rigid ceramic preform into a die chamber and introducing molten metal into the die on top of the preform as shown in Figure 1. The die is closed and pressure is applied by a hydraulic piston, forcing the metal into the preform. As with conventional castings, incomplete filling can occur if solidification blocks liquid from feeding shrinkage. Therefore, process variables such as superheat, preform temperature, die temperature, and pressure application rate and level have a strong influence on composite structure and final properties[1].

The use of pressure in squeeze casting allows the selection of alloys not normally considered for casting purposes. Therefore, alloy selection can include wrought as well as casting compositions since the increased pressure overcomes the need for high fluidity in the alloy itself. Final selection of an alloy can be made depending upon the properties desired in the composite[1-3]. Property improvement over conventional castings are also seen due to increased solidification rates and a refined microstructure[1-4] Additional benefits of squeeze casting include the ability to produce near-net shape parts.

COMPONENT MATERIALS

REINFORCEMENT - A variety of reinforcement types have been successfully infiltrated with aluminum alloys using the squeeze casting process[3]. Generally, preforms are required to maintain a desired distribution of reinforcement during the infiltration process. Preforms have been constructed from silicon carbide, boron carbide, and alumina-silicates in a variety of morphologies, including particulate, whisker and short fiber. Continuous fibers may be woven into three dimensional fabrics or ropes and infiltrated to provide more directional properties.

Preforms of alumina-silica chopped fibers were chosen for evaluation from various manufacturers based on their moderate cost and general availability. Fiber compositions range between 55% to 96% alumina with the balance silica.

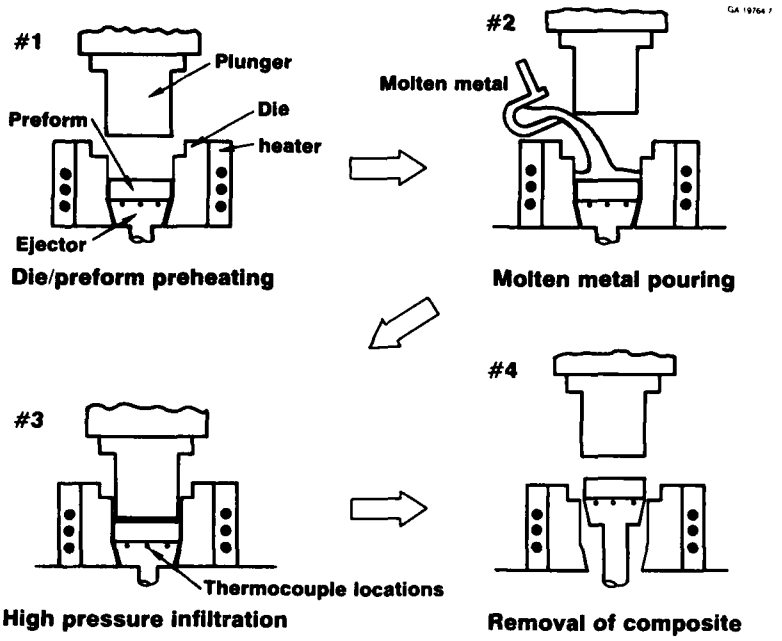


Fig. 1 - Schematic illustration of squeeze casting process

Although improvements in preform quality are in progress, at the time of testing the 96% alumina preforms (trade name Saffil) preforms were the most consistent in fiber uniformity, and were exclusively used throughout the remainder of the work.

The preforms are provided as planar random mats with fibers oriented in the plane of the preform. Large boards are available, and can be machined to desired geometries for either complete or partial reinforcement of a squeeze cast component. Preform strength during handling and infiltration is achieved by use of a colloidal silica binder. Individual Saffil fibers are 3-5 microns in diameter, an average of 500 microns long, has a tensile strength of approximately 2000 MPa and a tensile modulus of 300 GPa. The fiber density is slightly higher than aluminum alloy matrices at 3.29 X 10^3 kg/m^3 (0.119 lb/in^3) compared to 2.7 X 10^3 kg/m^3 (0.100 lb/in^3) for a typical Al alloy. Preforms are generally supplied in fiber volume fractions between 5% and 27%[5].

Important considerations in preform selection are property-volume fraction tradeoffs, and the qulaity of the preform. Failure of a composite at low strains can be caused by defects in the preform as well as high reinforcement levels. Composites fabricated with preforms that contained large inclusions (Figure 2) or preform cracks exhibit low tensile properties and a large amount of property scatter. Weak preforms were found to fail during the squeeze casting process when the colloidal silica binder level was decreased to very low levels in one experiment, leading to non-uniform fiber distribution.

MATRIX ALLOY - In a continuously-reinforced composite, the matrix acts to transfer loads to the fibers and the influence of the matrix properties as determined from the rule of mixtures is usually small in the direction of reinforcement. The matrix plays a more important role in composites reinforced with discontinuous fibers, however.



Fig. 2 - Large inclusion in alumina fiber preform

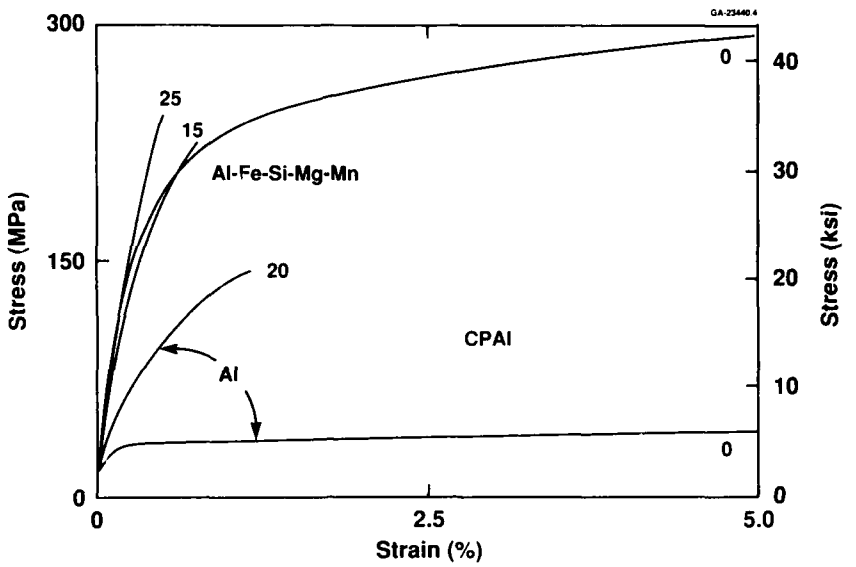


Fig. 3 - Influence of matrix alloy on composite properties

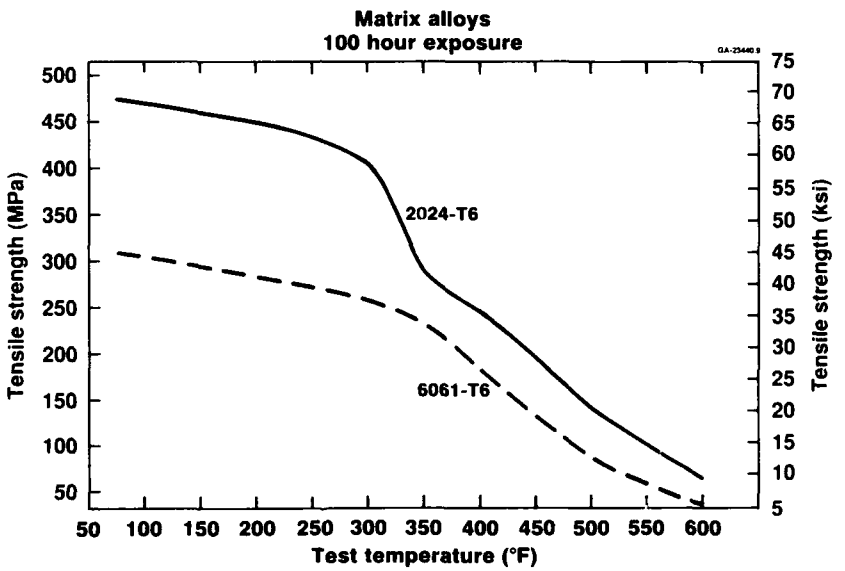


Fig 4 - Comparison of 2124 and 6061 matrix alloy strength levels at various temperatures

As seen in Figure 3, composite strength is strongly dependent upon matrix properties as well as fiber reinforcement levels[6]. Although a low-strength matrix may result in low composite properties, the percentage improvement in mechanical properties may be significantly larger than in a high-strength matrix.

Wrought alloy compositions were considered because of the decreased importance of fluidity in squeeze casting. This is beneficial in these composites because a higher strength alloy with reduced amounts of undissolved second phase is possible. Commonly reinforced systems include the 2XXX, 6XXX, and 7XXX aluminum alloy series, which reach peak strength levels by precipitation reactions.

A comparison of 2124 and 6061 matrix tensile strength as a function of exposure to elevated temperatures is given in Figure 4. A clear advantage in strength exists for 2124 up to about 300°F. Based on inherent strength and elevated temperature stability, 2124 was initially selected as a wrought matrix alloy composition.

COMPOSITE SYSTEM SELECTION

Composite strength and ductility are influenced by both matrix alloy and reinforcement level, and the optimum combination is often found experimentally. Generally, the addition of reinforcement to a low strength matrix causes a large improvement in strength. Higher strength matrices show a smaller strengthening effect, although the resulting composite strength may be high. At a certain level of reinforcement, the composite fails by brittle fracture at low strains, and the strengths achieved are limited. Therefore, an optimum level exists for a given matrix which, if exceeded, strength and ductility suffer. In several matrix compositions investigated (shown in Figure 5) the peak room temperature strength was obtained with 20% Saffil fibers; lower strength matrices showed maximum strength at 27%.

Certain properties display relatively linear relationships with increasing volume fraction reinforcement, such as shown in Figure 6 for tensile compressive modulus and coefficient of thermal expansion. If maximum modulus or minimum CTE were desired with little need for ductility, a high level of reinforcement would produce optimum properties.

An example of the difficulty in selecting optimum conditions for multiple property criteria is demonstrated by Figure 7 which shows the elevated temperature yield strength for a 2124 squeeze cast matrix and composites reinforced with 15% and 27% Saffil fiber preforms. The highly reinforced composite has lower properties at room temperature, but provides optimum strength at elevated temperatures. Selection of a reinforcement level usually represents a compromise of several important properties.

MICROSTRUCTURE-PROPERTY CHARACTERIZATION

Metallographic analyses of castings produced early in the investigation indicated that a 2124 matrix reinforced with Saffil preforms was modified by the presence of the fibers in significant ways, as reported by a number of researchers[7-9]. Solidification started in interfiber channels, and growing dendrites rejected solute-rich liquid to fiber surfaces, which were the last locations to solidify. As shown in Figure 8, Mg also segregated to fiber surfaces, which is generally believed to promote good bond strength through limited chemical reaction. Another observation was that standard solutionizing heat treatments were not successful in dissolving the eutectic phases.

Results of the above analysis provided input to the selection of the next generation of matrix alloys which were intentionally modified for composite systems based on the above microstructural observations. Matrix strength was believed to be limited by the loss of alloy additions to fiber surfaces; to produce a stronger matrix, higher Cu and Mg levels were studied than were practical from a solubility standpoint. As summarized in Table 1, Cu levels were varied from 4.5% to 7.5% and Mg from 0.2% to 3.0%. (Casting alloy A206 contains 4.5% Cu-0.2% Mg, and 2124 contains 4.5% Cu-1.5% Mg.)

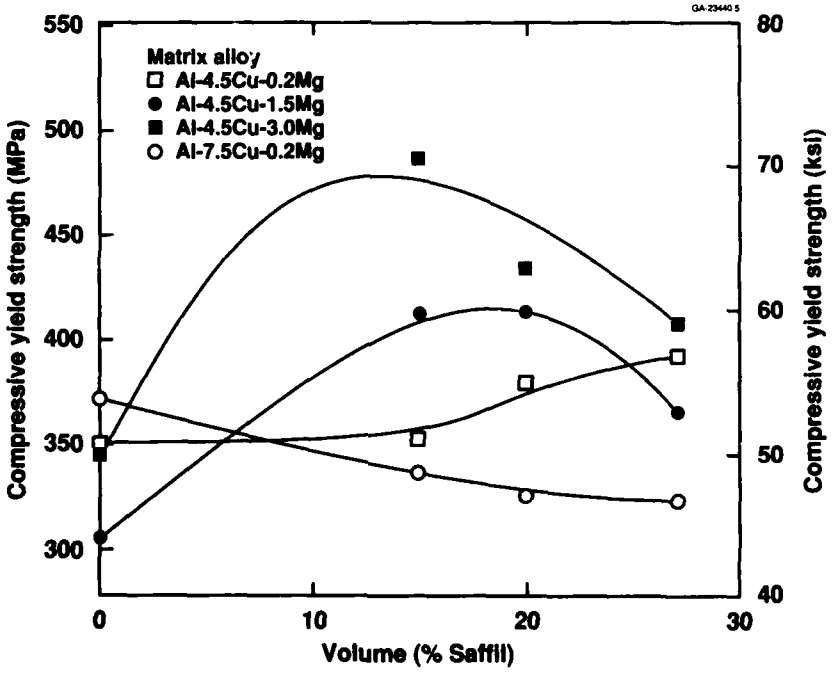
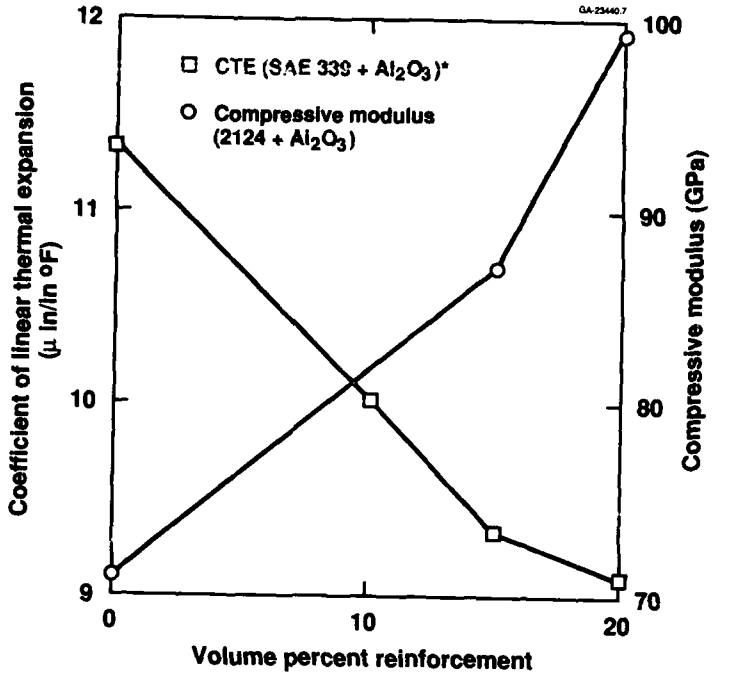


Fig. 5 - Variation in compressive yield strength with volume fraction reinforcement for various matrix alloys



* Reference: Spengler, Young - SAE 860162 pg 19-22

Fig. 6 - Variation in coefficient of linear thermal expansion and compressive modulus with volume fraction reinforcement

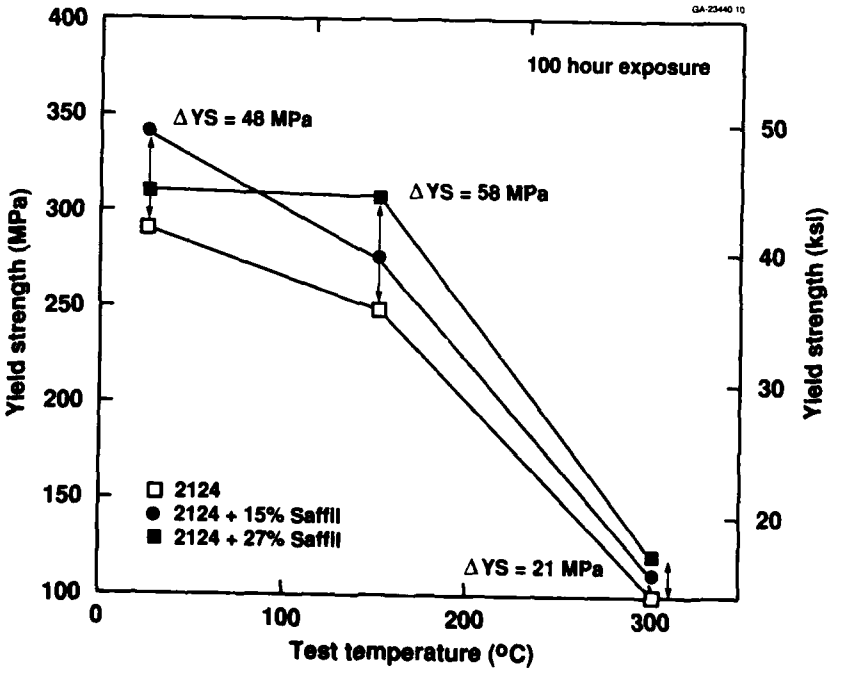


Fig. 7 - Variation in yield strength at various temperatures

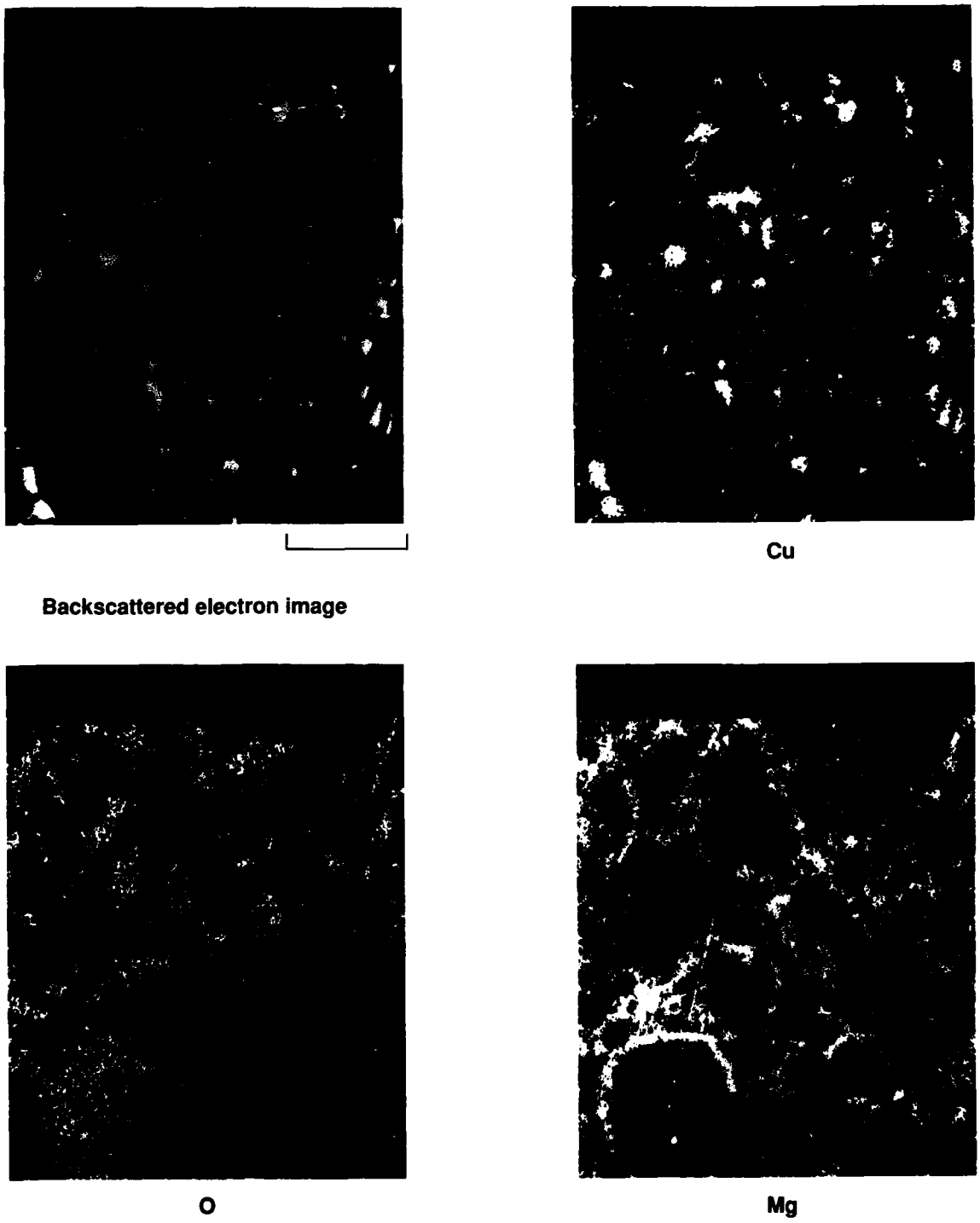


Fig. 8 - Distribution of Cu, O, and Mg in Al-Cu-Mg matrix/Saffil fiber cast composite

Selected yield strength data for various reinforcement levels previously shown in Figure 5 indicate that higher Mg content improves properties, while increasing copper has the opposite effect. TEM studies have confirmed the formation of approximately 1000-5000 Å thick $MgAl_2O_4$ spinel phase at the fiber/matrix interfaces. Increasing levels of Mg are expected to improve composite properties by both aiding in this limited chemical interaction at fiber surfaces, and by increasing matrix strength. Higher levels of undissolved copper-bearing second phases are located mainly at fiber surfaces, were seen to have a negative influence on composite strength and also to produce greater scatter in properties. The brittle nature of these composites can be seen in the fracture surface in Figure 9, in which only limited regions in the matrix demonstrate ductile fracture.

A final set of castings were produced for more extensive testing based on the above analysis. Two variations of the original 2124 composition were studied to focus on matrix compositions which were expected to result in high composite strength and lower property variability: a high Mg version (Al-4.5 Cu-3.0 Mg) and a low copper, high Mg combination (Al-3.0 Cu-3.0 Mg), reinforced with 20 v/o Saffil. Average mechanical properties of each composition for ten specimens are given in Table 2.

As expected from the previous consideration of the influence of undissolved eutectics on strength and fracture, lower average properties and greater scatter were seen for the system containing higher amounts of copper. These composites typically failed before a 0.2% offset yield stress could be measured. The average yield strength resulting from the addition of 20 v/o Saffil increased by less than 30 MPa (4 ksi) and ultimate strength decreased by 7 MPa (1 ksi). The combination of lower Cu and higher Mg resulted in an unreinforced matrix with higher yield and lower ultimate strength than the unreinforced 2124 squeeze cast matrix, but with marked improvement in composite strengths: the addition of 20 v/o Saffil fibers to Al-3.0 Cu-3.0 Mg improved average yield strength and ultimate strength between 55-65 MPa (8-10 ksi).

Fatigue properties were determined for reinforced and unreinforced specimens with the Al-4.5 Cu-3.0 Mg matrix (due to a greater availability of this composition). Although the composite has a small yield strength property advantage, the axial stress fatigue life (R=-1) was greater, as shown in Figure 10.

Table 1 - Summary of Matrix Compositions Studied

	Cu	Mg
	3.0	3.0
(A206)	4.5	0.2
(2124)	4.5	1.5
	4.5	3.0
	6.0	1.5
	7.5	0.2
	7.5	3.0



500X

Fig. 9 - Fracture surface of Al-Cu-Mg/Saffil composite showing brittle nature of failure

Table 2 - Mechanical Properties

Matrix Alloy	Volume Fraction Saffil Reinforcement	UTS MPa (ksi)	YS MPa (ksi)	Percent Elongation	Modulus GPa (Msi)
Al-3.0Cu-3.0Mg	0	345 (50.0)	319 (46.3)	1.2	71.7 (10.4)
	20	401 (58.2)	385 (55.9)	0.8	88.9 (12.9)
Al-4.5Cu-3.0Mg	0	376 (54.6)	344 (49.9)	1.2	66.2 (9.6)
	20	375 (54.4)	371 (53.8)	0.8	88.6 (12.8)

Greater attention was given to matrix characterization of the reinforced and unreinforced castings, and included chemical analysis, X-ray phase identification, and differential scanning calorimetry traces to the melting point. Between 0.5%- 1.5% Si was measured in the matrix for both compositions by atomic absorption chemical analysis; the source was the soluble preform binder. Mg levels varied throughout the casting, probably due to the flow of enriched fluid in the final stages of solidification.

As a result of the modification of the matrix composition by the reinforcement, the phases produced upon solidification were altered. Unreinforced cast 2124 or 3.0 Cu- 3.0 Mg contains only the S phase (Al_2CuMg), as predicted from the equilibrium phase diagram. Due to interactions with the preform during solidification, the composites contained theta ($CuAl_2$), Mg_2Si, and Q ($Al_4CuMg_5Si_4$). These results can be explained by the Al-Cu-Mg phase diagram for a 0.6% Si level, as shown in Figure 11, after adjusting the actual Mg level in the matrix downward due to depletion to fiber surfaces. Calorimetry results from the composite indicated higher volume fractions of second phases for the higher-copper alloy, and provided information to develop a more optimum multi-step thermal treatments to dissolve a greater amount of second phase during solution heat treatment.

MICROSTRUCTURE-BASED SYSTEM OPTIMIZATION

An outline of recommendations to optimize the squeeze cast composite system Al-Cu-Mg/Saffil fibers follows with the objective of high tensile strength accompanied by low variability. Conclusions from the preceding experiments are incorporated into these considerations.

Ideally, matrix selection takes into account modifications in composition due to interaction with the preform, and provides high strength and good ductility with a minimum of undissolved second phase. Although matrix strength is important, minimizing brittle eutectic phases which limit composite ductility (and therefore potential strength levels) is critical. Off-the-shelf alloys are often not ideal for composite matrices due to modification of composition by the preform (increased Si, reduced Mg in this study). Thermal treatment adjustments are also necessary in many cases to obtain optimum composite properties.

Previous work suggests an property advantage of a Al-3.0 Cu-3.0 Mg matrix over the 2124 composition. Further adjustments to the matrix composition to account for Mg depletion to fiber surfaces and the addition of Si to the matrix from the preform binder may be necessary. The Al-Cu-Mg phase diagram shown in Figure 11 for a 0.6% Si level may indicate the approximate Cu-Mg combinations to produce S, Q, or theta in addition to the unavoidable Mg_2Si for strengthening. Unless an alternate binder which does not contain silicon (or other elements which would alter the equilibrium phase diagram), alloy optimization of a 2XXX series is perhaps limited by Mg_2Si formation.

Another essential step is to eliminate all known causes of poor properties resulting from the fabrication process or preforms. Processing conditions should be reviewed to

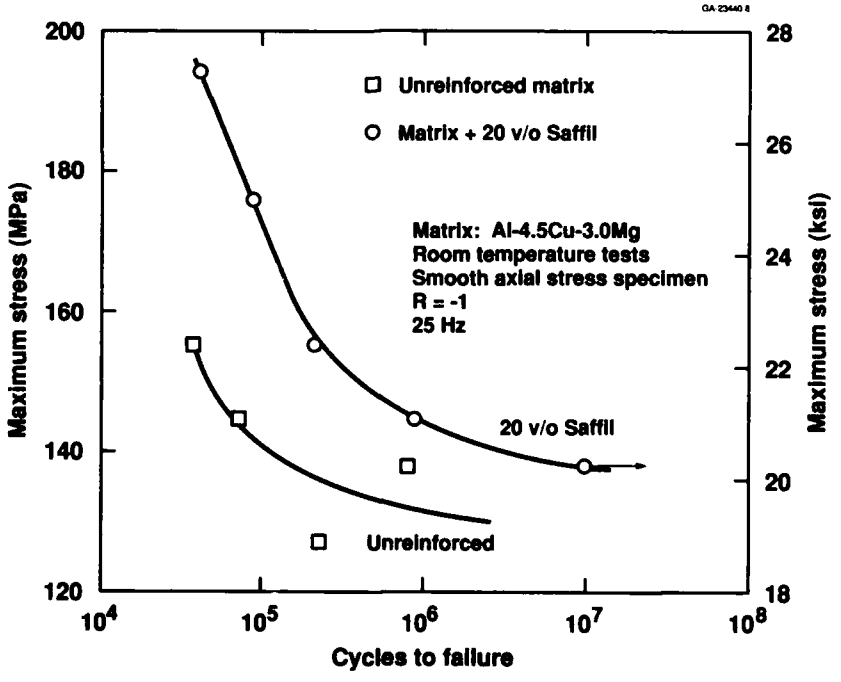
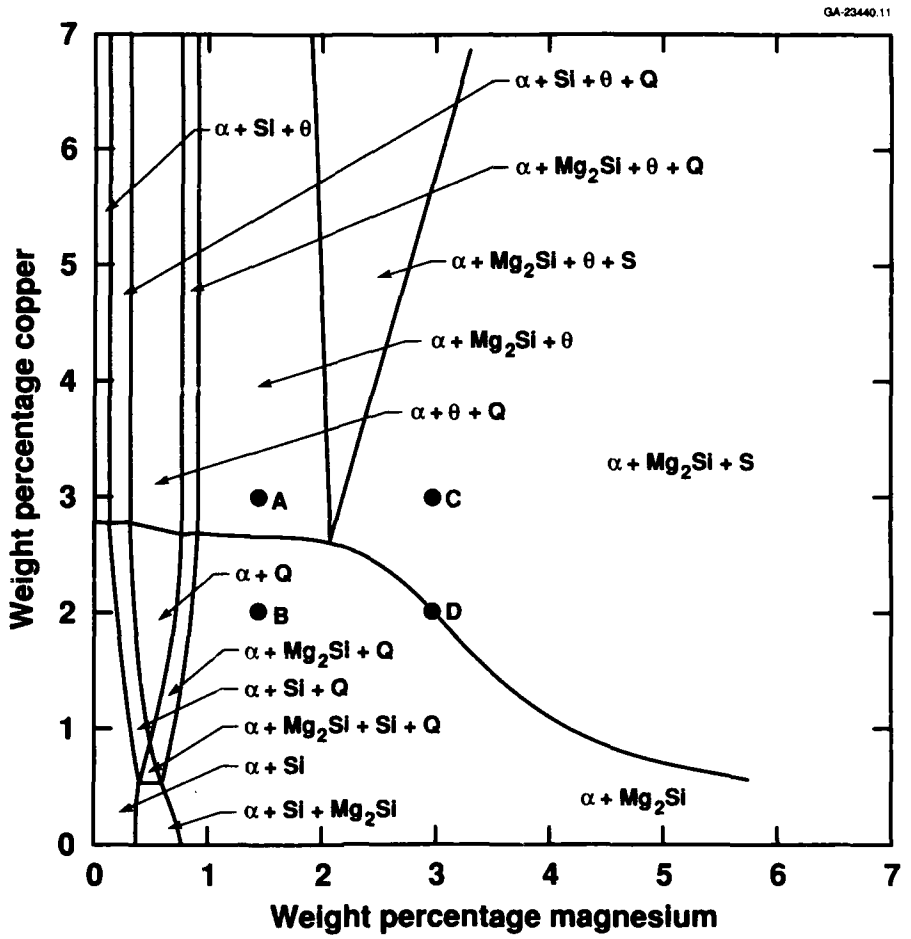


Fig. 10 - Axial stress fatigue response for unreinforced and reinforced Al-Cu-Mg matrix



H. J. Axon: J. Inst. Metals, p. 450, vol. 81, 1953

Fig. 11 - Equilibrium Al-Cu-Mg phase diagram for 0.6% silicon at 460°C

produce a sound, porosity-free composite. The preforms should be screened by SEM to assure that adequate binder exists for preform strength, that shot and fiber diameter variability are acceptable, and that the distribution of fiber volume fraction is uniform (although many times these defects can only be detected after infiltration). The optimum level of reinforcement may be adjusted along with matrix composition to obtain peak benefits at room or elevated temperatures.

CONCLUDING REMARKS

The approach outlined in this study assumed that optimized strength requires a matrix alloy containing inherent room temperature and elevated temperature strengths, but with as much ductility as possible. The addition of high strength-high modulus fibers improves the baseline matrix properties. Although processing and preform quality are an issue, the work focused on improvements in composite strength through matrix alloy composition. Interactions between specific alloy additions and the fibers resulted in further modifications to improve ductility and strength. Better understanding of microstructure-property relationships are needed to explain the mechanisms of flow and fracture so that specific property targets can be met for a variety of applications.

REFERENCES

1. Cornie, J. C., Y-M Chiang, D. R. Uhlman, A. Mortenser, and J. M. Collins, Ceramic Bulletin, 65(2), 293 (1986).
2. Howes, M. A. H., "Ceramic-Reinforced Metal Matrix Composites Fabricated by Squeeze Casting," Proceedings from Advanced Composites Conference, ASM/ESD, 223 (1985).
3. Verma, S. K. and J. L. Dorcic, Advanced Materials and Processes, 48 (1988).
4. Mortensen, A., M. N. Gungor, J. A. Cornie, and M. C. Flemings, Journal of Metals, 30 (1986).

5. Dinwoodie, J., E. Moore, C. A. J. Langman, and W. R. Symes, "The Properties and Applications of Short Staple Alumina Fibre Reinforced Aluminium Alloys," paper presented at the 5th International Conference on Composite Materials, San Diego CA (1985).
6. Harris, S. and T. E. Wilks, Developments in the Science and Technology of Composite Materials, ECCM 1, Bordeaux, France, 595 (1985).
7. Clyne, T. W. and J. F. Mason, Met Trans A, 18A, 1519 (1987).
8. Bader, M. G., T. W. Clyne, G. R. Cappleman, and P. A. Hubert, Composites Science and Technology, 23, 287 (1985).
9. Cappleman, G. R., J. F. Watts, and T. W. Clyne, Journal of Materials Science, 20, 2159 (1985).

MECHANICAL PROPERTIES OF SiC WHISKER REINFORCED ALUMINUM ALLOYS FABRICATED BY PRESSURE CASTING METHOD

Toshiro Kobayashi, Masaki Yosino, Hiroyoshi Iwanari, Mitsuo Niinomi
Department of Production Systems Eng.,
Toyohahsi University of Technology, Toyohahsi 440 Japan

Kunji Yamamoto
Tokyo Yogyo Co., Ltd., Tajimi 507 Japan

ABSTRACT

Microstructures and mechanical properties of SiC whisker (SiCw) reinforced aluminum alloys fabricated by pressure casting method are investigated. The SiCw reinforced aluminum alloys fabricated under the pressure of 90 MPa are superior to those fabricated under lower pressure conditions in mechanical properties. The fracture of SiCw reinforced aluminum alloys is associated with the failure of SiCw and the interface decohesion between whiskers and matrix. It is shown that these composites are strengthened by increasing interface bonding between SiCw and matrix, i.e. the interface cohesion is strengthened by accelerating the interface reaction adequately. The addition of the highly reactive lithium to aluminium matrix makes the interface cohesion tight and results in lower density and greater strength composites.

PRESSURE CASTING METHOD is considered to be superior to other methods like powder metallurgy and hot press methods in the productivity of metal matrix composites because of shorter composing time and less necessity of secondary machining though it requires higher temperature for composing [1]. Therefore, microstructures and mechanical properties of SiCw reinforced aluminum alloys fabricated by the pressure casting method with varying pressure were investigated in order to establish the most suitable fabricating condition of composites. Then, the effects of volume fraction of SiCw and lithium (Li) addition to aluminum matrix on the mechanical properties of SiCw reinforced aluminum alloys were examined.

EXPERIMENTAL

SiC whiskers produced by Tokai Carbon Ltd., of which properties [2] are shown in Table 1, were used for reinforcements, and 99.9 mass% purity aluminum was used for matrix.

SiC whiskers were preformed at first into 15 mm thick in the metallic mold of the experimental equipment shown in Fig.1 for the fabrication of composites. The melt of pure aluminum was poured on the preform at 1073 K when the temperature of metallic mold came to be 823 K, and was pressurized for 3 minutes. Then, the casting was taken out from the mold and water cooled. In addition, aluminum lithium matrix SiC reinforced composites were also fabricated in the same manner as described above.

Vickers hardness test, tensile test and dynamic fracture toughness test using the specimens shown in Fig.2 were carried out on these composites. Tensile test was carried out at a cross head speed of 0.5 mm/min using an Instron type machine. Dynamic fracture toughness test was carried out at an impact speed of 1.13 m/sec using a 14.7 J capacity instrumented

Table 1 - Properties of SiC Whisker Used.

Density:	3.19×10^{3} kg/m^3
Diameter:	0.1-1.0μm
Length:	30-100μm
Tensile strength:	3-14GPa
Elastic modulus:	400-700GPa
Crystal structure:	β-SiC
Chemical analysis:	SiC>98.00
	SiO_2<0.1
	Ca<0.05
	Co<0.05
	Fe<0.05

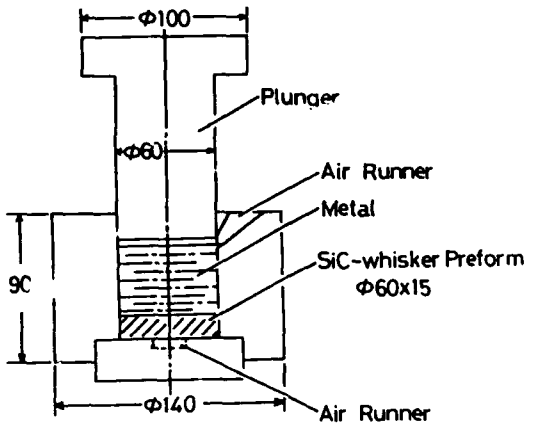


Fig.1 - Schematic drawing of the apparatus used.

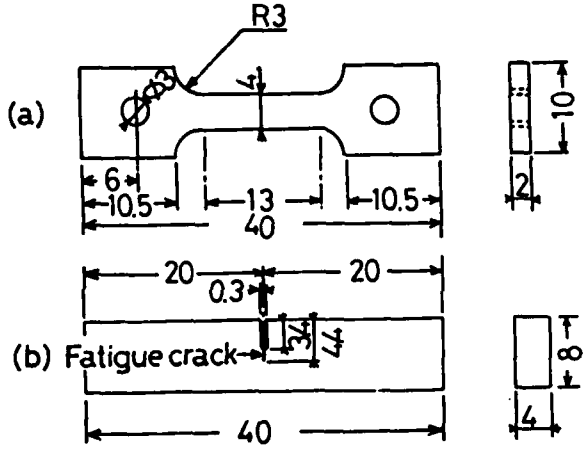


Fig.2 - Geometry of specimens.
(a) Tensile specimen
(b) Fatigue cracked Charpy specimen for dynamic fracture toughness test

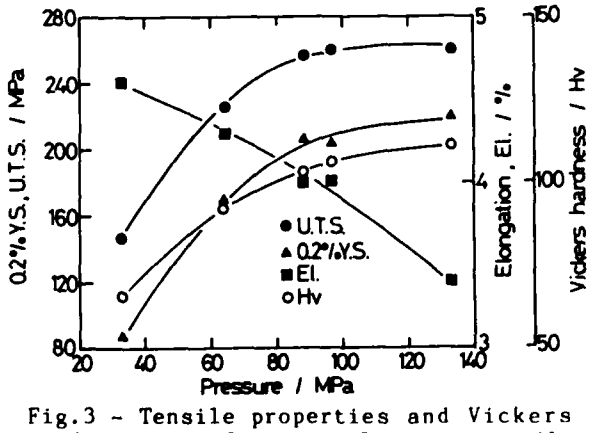


Fig.3 - Tensile properties and Vickers hardness as a function of pressure in Al-20%SiCw composites(0.2%Y.S.: 0.2% proof stress, U.T.S.: ultimate tensile strength).

Charpy impact testing machine on fatigue precracked specimen of its a/W (a:initial crack length, W:specimen width) was 0.55. Then, the dynamic elastic-plastic fracture toughness value was calculated using the CAI (Computer Aided Instrumented Charpy Impact Testing) system [3].

Each material was etched by 5 % HF solution. Then, the microstructural observation was performed. Fracture surfaces of tensile and dynamic fracture toughness tested specimens were characterized using a scanning electron microscope (SEM), and Auger electron spectral analysis were carried out on the whisker-matrix interface. Microstructural phases in composites were identified by X-ray diffraction analysis.

EXPERIMENTAL RESULTS AND DISCUSSION

EFFECT OF APPLIED PRESSURE ON MECHANICAL PROPERTIES-Tensile properties and Vickers hardness of aluminum matrix SiC whisker reinforced (Al-SiCw) composites which contain 20 % SiCw are shown in Fig.3 against the applied pressure. Vickers hardness, tensile strength and 0.2 % proof stress increase, and elongation decreases with the applied pressure. Fig.4 shows the variation of J_d value with the applied pressure. J_d value decreases with the increase in pressure. Hardness, tensile strength, 0.2 % proof stress and J_d value have a tendency to approach to a constant value at around 90 MPa pressure. Over 90 MPa pressure, porosities were scarcely observed and SiC whiskers came to distribute uniformly. The amount of whisker pullout was recognized to decrease with the applied pressure from the observation of the fracture surface. Tensile strength is greater in the highly pressurized composites because the stress transfers better to whiskers. Namely, it is considered that the bonding strength is improved because the interface reaction between whiskers and matrix is more activated with the increase in the applied pressure.

Therefore, EDX analysis was performed on the whisker-matrix interface. The results are

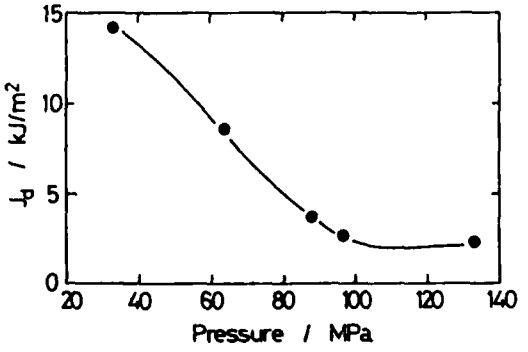


Fig.4 - Dynamic fracture toughness (J_d) as a function of pressure in Al-20%SiCw composites.

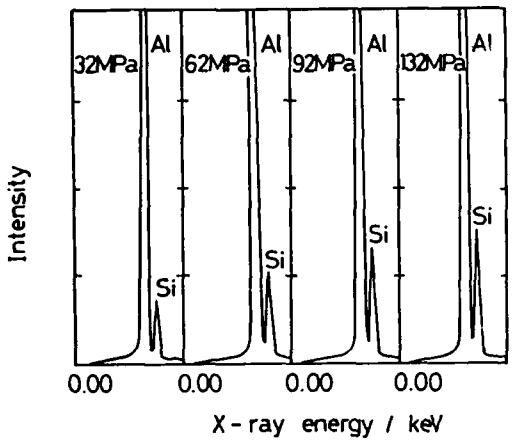


Fig.5 - EDX analysis for the whisker-matrix interface of pressure cast Al-20%SiCw composites.

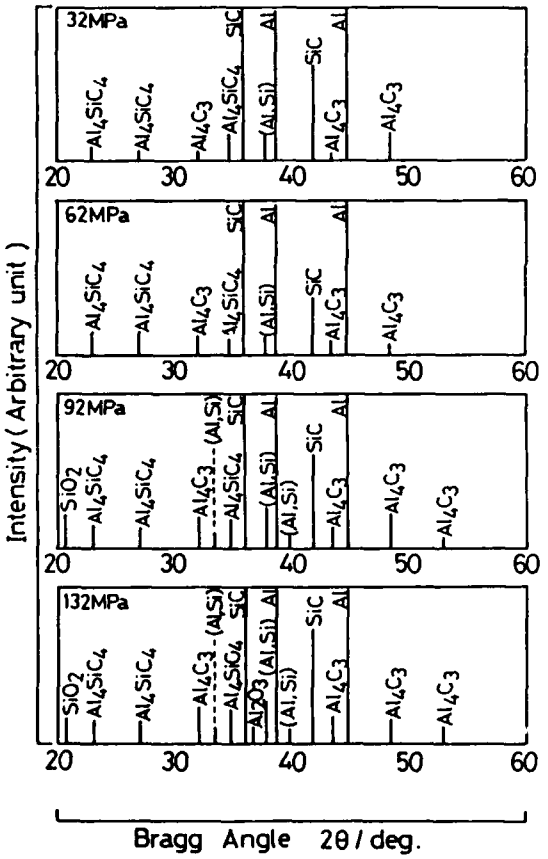


Fig.6 - X-ray diffraction patterns of the pressure cast Al-20%SiCw composites.

shown in Fig.5. The intensity of Si peak is clearly greater wih increasing the applied pressure comparing with that of Al. A reaction quantity is considered to increase with the increase in the applied pressure. Fig.6 shows the X-ray diffraction patterns of the pressure cast Al-20%SiCw composites. The intensity and number of Al_4C_3, (Al,Si) and Al_4SiC_4 phases, which are considered to be formed by the interface reaction, are recognized to increase with the increase in the applied pressure.

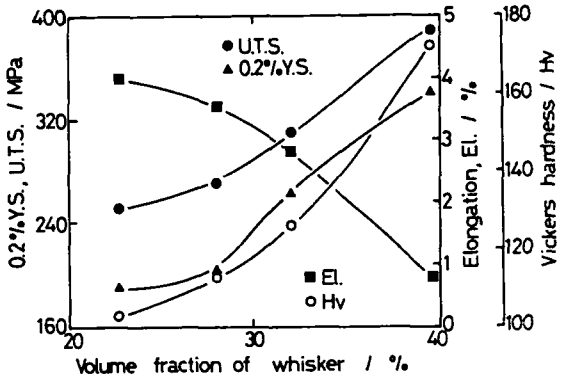


Fig.7 - Change in tensile properties and Vickers hardness of 92MPa pressure cast Al-SiCw composites with volume fraction of whisker(0.2%Y.S.: 0.2% proof stress, U.T.S.: ultimate tensile strength).

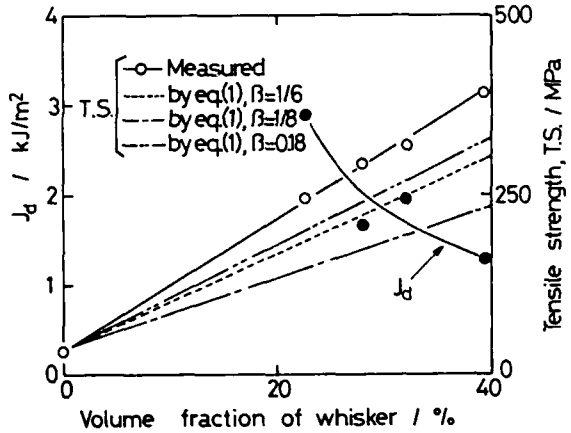


Fig.8 - Change in dynamic fracture toughness (J_d) and tensile strength of 92MPa pressure cast Al-SiCw composites with volume fraction of whisker.

EFFECT OF VOLUME FRACTION OF SiC WHISKERS ON MECHANICAL PROPERTIES-Mechanical properties of Al-SiCw composites fabricated by the pressure casting method under the constant pressure of round 90 MPa with varying the volume fraction of SiC whiskers were examined. The change in tensile properties and Vickers hardness of cast Al-SiCw composites fabricated at 92 MPa pressure with volume fraction is shown in Fig.7. Hardness and strength characteristics increase and elongation decreases with the volume fraction of whiskers. The relationship between the dynamic fracture toughness and the volume fraction of whiskers is shown in Fig.8. J_d value decreases

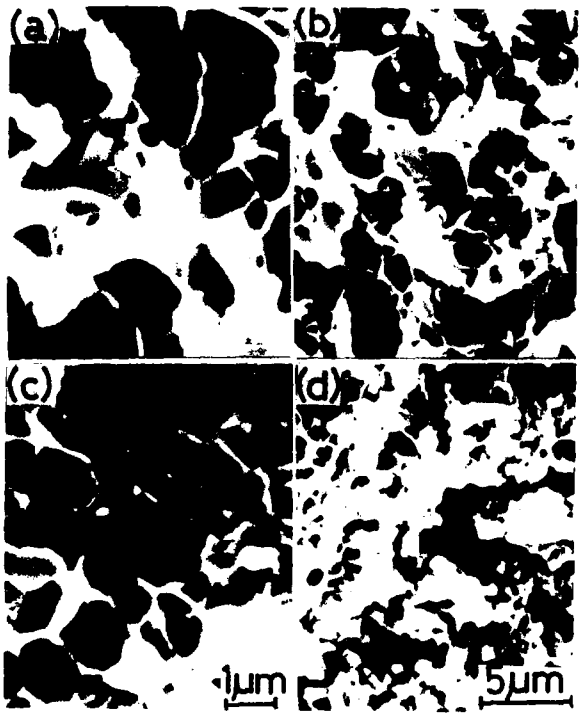


Fig.9 - SEM micrographs of fracture surfaces of 92MPa pressure cast Al-SiCw composites with different volume fraction of whisker after dynamic fracture toughness test.
(a).(b) 22%-SiCw (c),(d) 39%-SiCw

with the volume fraction of whiskers.

The strength of composites, of which reinforcements are short fibers, can be presented by the following equation [4]:

$$\sigma_c = \beta\sigma_f(1-l_c/2\bar{l})V_f + \sigma_m(1-V_f) \qquad (1)$$

where σ_c is the strength of composites, σ_f is the strength of fibers, l_c is the critical length of fibers, $\bar{l}$ is the average length of fibers, V_f is the volume fraction of fibers and β is the orientation factor of which value is reported as 1/6, 1/8 or 0.18 for the completely random orientation. Fig.8 shows the measured tensile strength values and calculated ones by eq.(1) where β=1/6 [5], 1/8 [6] and 0.18 [7] using the measured σ_m and average σ_f value of 8.5 GPa against the volume fraction of whiskers. The measured tensile strength of Al-SiCw composites in this study increases linearly with the volume fraction of whiskers. In this case, assuming that $\bar{l}=l_c$, β was obtained to be 0.22 from eq.(1). This value is larger than the aforementined values, i.e. β=1/6,1/8 and 0.18. Millière [8] et al. have reported that the measured tensile strength of SiC reinforced Al-Si alloys is greater than the calculated one by eq.(1) because the matrix microstructure becomes finer and the residual stress close to the interface increases with V_f. The reason why β in this study is larger than the reported values is assumed to be similar to that reported by Millière et al. in Al-Si matrix SiC reinforced composites. However, a further investigation is necessary to clarify this point. Anyhow, since the strength of this composites can be estimated from eq.(1), the fabricating method and condition of Al-SiCw composites in this study can be concluded to be sufficiently suitable.

SEM micrographs of fracture surfaces of Al-SiCw composites with different volume fraction of whiskers, which were fabricated at a pressure of 92 MPa, after dynamic fracture toughness test are shown in Fig.9. The edge and cross section of whiskers are observed in dimples. Small voids with decohesion like appearance or whiskers pulled out are also observed. Therefore, the following two fracture mechanisms of whisker reinforced composites can be considered:
(1)The stress transfers effectively to whiskers, and then the failure of whiskers occurs.
(2)Whisker pullout occurs because of the interface decohesion between whisker and matrix. Nutt et al. [9] have reported that the interface

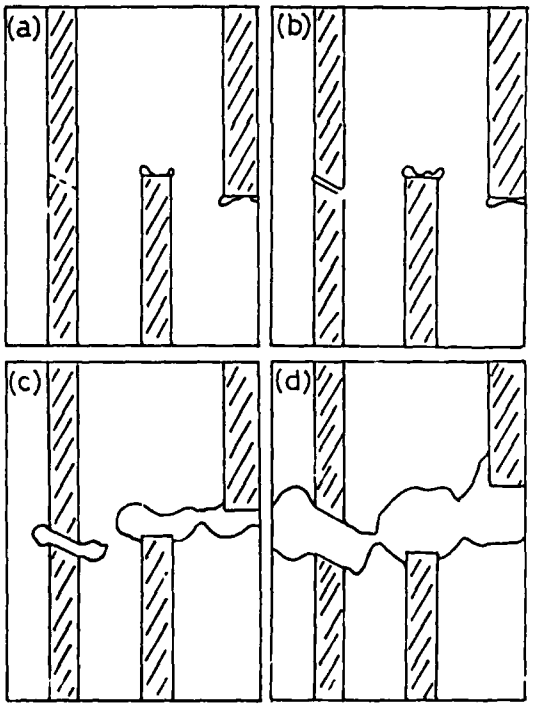


Fig.10 - Fracture mechanism of Al-SiCw composites.
(a) Void initiation at short whisker end and long whisker fail at critical length.
(b) Void growth and coalescence at whisker end.
(c) Interface decohesion at whisker end.
(d) Al-SiCw composites fracture by coalescence of large voids.

decohesion is apt to occur at the edge, in particular at the corner of whiskers.

The fracture mechanism of whisker reinforced composites would be presented schematically as shown in Fig.10 by summarizing the above stated result from the fracture surface observation and report. It is considered to be important for increasing the strength of whisker reinforced composites to increase the bonding strength of whisker-matrix interface in order to prevent the interface decohesion.

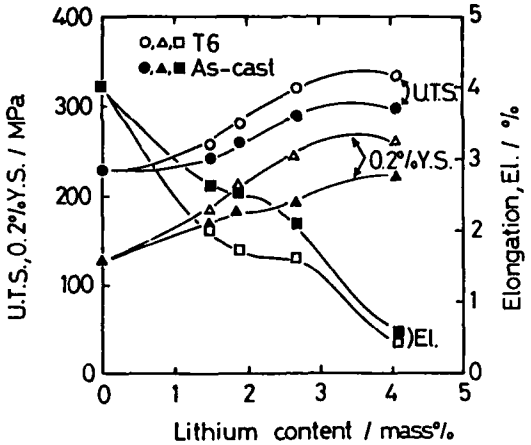


Fig.11 - Tensile properties as a function of lithium content in Al-Li-20%SiCw composites(0.2%Y.S.: 0.2% proof stress, U.T.S.: ultimate tensile strength).

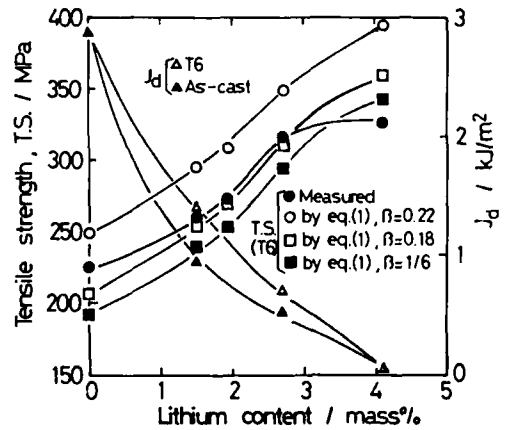


Fig.12 - Change in tensile strength and dynamic fracture toughness (J_d) of 92MPa pressure cast Al-Li-SiCw composites with lithium content.

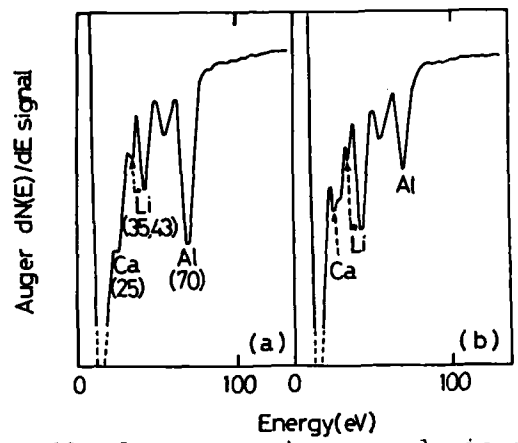


Fig.13 - Low energy Auger analysis on whisker-matrix interface and matrix of Al-4.1%Li-20%SiCw composites.
(a) matrix (b) whisker-matrix interface

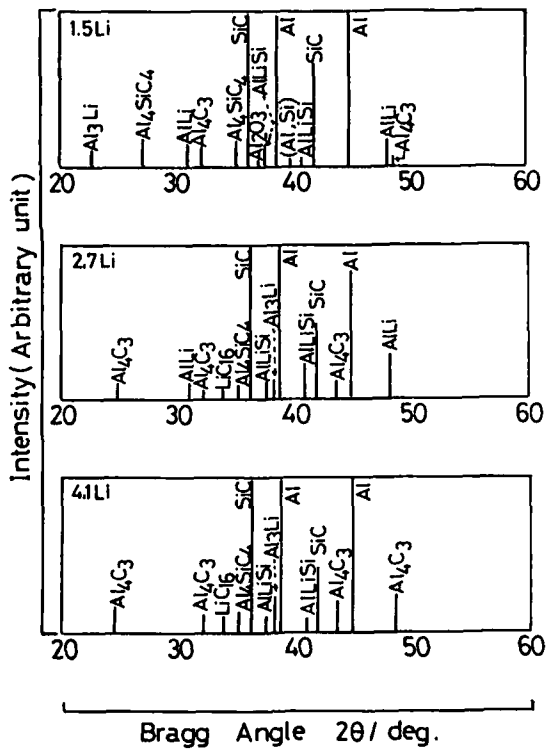


Fig.14 - X-ray diffraction patterns of 92MPa pressure cast Al-Li-20%SiCw composites (T6).

EFFECT OF LITHIUM ADDITION ON MECHANICAL PROPERTIES-It is considered to be effective in increasing the cohesion force of the aluminum-SiC whisker interface to increase the quantity of the interface reaction adequately by adding the highly reactive elements like magnesium or lithium to matrix [10]. The increase in the specific strength and elastic modulus is also expected by adding lithium because a greater decrease in density is expected.

Therefore, the aluminum lithium matrix SiCw composites with 1.5-4.1 mass% lithium contents

were fabricated and their mechanical properties were investigated in this study. Tensile properties of as cast and T6 treated Al-Li-20%SiCw composites are shown in Fig.11 against lithium content. The strength characteristics increase and the elongation decreases with the increase in lithium content. The measured tensile strength and the calculated ones by eq.(1) putting 0.22 which has been obtained in the pure aluminum matrix composites in this study, 0.18 and 1/6 into β are shown in Fig.12. The measured value is a little greater when using β=0.22, almost equal when using β=0.18 and a little smaller when using β=1/6 than the calculated one until round 2.7 mass% lithium content. However the measured value is considerably smaller than the calculated one at 4 mass% lithium. The relationship between lithium content and dynamic fracture toughness J_d is also shown in Fig.12. J_d value decreases rapidly with the increase in lithium content. Fig.13 shows the low energy Auger analysis on the whisker-matrix interface and matrix of Al-4.1%Li-20%SiCw composites. The intensity of Li and impurity Ca peaks is greater at the whisker-matrix interface. Fig.14 shows the X-ray diffraction patterns of 92MPa pressure cast Al-Li-20%SiCw composites with different lithium contents. LiC_{16} is detected in the Al-Li-SiCw composites of which lithium content is over 2.7 mass%. Therefore, the brittle carbide phases and impurties will increase because of the over reaction at the matrix-SiC whisker interface and the brittle fracture occurs over 2.7 mass% lithium although satisfied interface strength could be obtained until 2.7 mass% lithium contents as stated above.

CONCLUSION

Mechanical properties of aluminum and aluminum lithium matrix SiCw reinforced composites fabricated by the pressure casting method were investigated and the following results were obtained.

(1)The best aluminum matrix SiC whisker reinforced composites could be fabricated at an applied stress of round 90 MPa by the pressure casting equipment in this study. The strength characteristics of aluminum matrix SiC reinforced composites fabricated under the aforementioned condition increased with the increase in the volume fraction of whiskers although the elongation and dynamic fracture toughness decreased.

(2)The fracture of aluminum matrix SiC reinforced composites is caused by the failure of whiskers, the void formation at the interface decohesion at the edge of whiskers or the pullout of whiskers associated with the decohesion at the whisker-matrix interface. The brittle fracture caused by the interface decohesion was recognized in the lithium added composites.

(3)The strength characteristics was improved by adding lithium to matrix within 2 mass%. Al-Li matrix SiC reinforced composites were expected to be more effective in the future because the decrease in density and the improvement in the specific strength and elastic modulus is expected by adding lithium.

REFERENCES

[1] H.Asanuma and K.Hirohashi, Kinzoku, 57, 35 (1987).

[2] "SiC whisker", Catalogue of Tokai Carbon Ltd., (1987).

[3] T.Kobayashi, M.Niinomi, I.Yamamoto and M.Kamimura, Proc. Int. Conf. Impact Loading and Dynamic Behavior of Mat.,Bremen, (1987), to be published.

[4] W.H.Bower, M.G.Bader, J. Mater. Sci., 7, 1315 (1972).

[5] H.L.Cox, Brit. J. Appl. Phys., 3, 72 (1952).

[6] H.Fukuda, T.W.Chou, J. Mater. Sci., 17, 1003 (1982).

[7] J.C.Fisher, General Electric Report, RL-450, (1950).

[8] C.Millière, M.Suèry, Materials Science and Technology., 4, 41, (1988).

[9] S.R.Nutt, J.M.Duva, Scripta Metallurgica, 20, 1055 (1986).

[10]D.Webster, Advances in Composite Materials, 2, 1165 (1980).

TENSILE AND CREEP MICROSTRUCTURES OF CAST 2014 Al/20 v% SiCp COMPOSITE

Mehmet N. Gungor, P. K. Liaw, M. G. Burke
Westinghouse Research and Development Center
Pittsburgh, Pennsylvania 15235 USA

ABSTRACT- Microstructures of elevated tensile and steady-state creep tested cast 2014 Al 20v% SiCp composite have been examined. Cast composite material was hipped, extruded and heat treated prior to mechanical testing. The composite material was tensile and creep tested at and above 423 K. Subsequent material characterization has indicated that the composite material fails via a mechanism of void nucleation which initiates within the matrix and at the matrix/SiC interface.

INTRODUCTION- Ceramic particle reinforced metal matrix composite systems, particularly Al/SiC, have been developed and implemented in a numb : of industrial applications. Although th: se materials have not yet found widespread ac~eptance, recent improvements in processing, microstructure and properties have drawn attention of various industrial laboratories to develop the potential of these materials for product applications. In order to employ these materials in real life applications, however, they must be shown to have reproducible and clearly defined microstructures and properties.

To assist in developing this technology, the Westinghouse R&D Center has been evaluating the microstructures and properties of commercially available Al and Mg based SiC particulate reinforced metal matrix composite materials (1-6). In this particular paper, we report the results of a research program concerning the elevated temperature tensile and steady-state creep microstructures of a commercially available cast 2014 Al /20 v% SiC composite.

EXPERIMENTAL WORK- The composite material that was evaluated was prepared by a commercial vendor using a casting and solidification approach. The cast composite billets were hipped, extruded with an 11:1 ratio and heat treated to T-6 condition. Tensile and steady-state creep tests were performed on button-head specimens that were machined from the extruded bars, with the loading direction of the specimens being parallel to the bar extrusion direction. Tests were conducted in air at elevated temperatures between 473 K and 673 K.

Microstructures of the tensile and creep tested materials were studied using scanning electron microscopy (SEM) and analytical electron microscopy (AEM). Fracture surfaces were carefully examined in order to characterize the fracture morphology. In addition, the fractured specimens were subsequently nickel-plated to preserve the details of the fracture path. The specimens were then sectioned along the longitudinal direction and diamond-polished for further SEM characterization. Specimens for transmission electron microscopy were prepared from 3 mm diameter discs punched from mid-section slices which were parallel to the tensile and creep loading directions in the failed samples. These specimens were were subsequently dimpled to a thickness of approximately 35 microns prior to ion-milling in a Gatan dual ion mill equipped with a liquid nitrogen cold stage.

AEM examination was performed using a Philips 400T analytical electron microscope operated at 120 kV and equipped with a Kevex EDS system. Microstructural information concerning the Al/SiC interface, precipitates, dislocation structures and void formation was obtained via high resolution SEM /TEM/STEM/EDS analysis.

RESULTS AND DISCUSSION- The microstructures developed during the elevated temperature (523K) tensile and creep tests are presented in Figures 1 through 5. SEM examination of the tensile fracture surfaces (Fig. 1a) revealed the presence of dimples, characteristic of ductile failure in the matrix. Figures 1a and 1b also show localized separation at the matrix/SiC interface and alloy second phases. Although some similar microstructural features were observed in the creep specimens, additional discrete second phases were also found at the matrix/SiC interface (white features in Figures 1c and 1d).

Supplementary microstructural data concerning deformed specimens were obtained via the examination of the ion-milled specimens using the SEM mode of of the S/TEM. Of particular interest was the location and extent of the void formation in the deformed composites. Typical features observed in the deformed composites are presented in Figure 2. The elevated temperature tensile deformation resulted in the formation of voids within the matrix and also at the matrix/SiC interface. Figure 2a shows several large voids in the vicinity of the SiC particulates. A very fine void located away from the SiC particulate is evident in Figure 2b. A substantially larger number of voids were observed in the creep specimens. Figures 2c and 2d show both coarse and fine voids located at the matrix/SiC interface. Also, a relatively coarse ($\sim$ 0.5 μm) darkly-imaging second phase was detected at some matrix/SiC interfaces (Figure 2c). EDS analysis revealed that this phase contained Al, Cu and small amount of Mg.

The matrix of the deformed materials was characterized by the presence of fine and coarse precipitates. These precipitates were identified by electron diffraction as θ' and θ, respectively. In addition, a small proportion of S' precipitates were detected in these samples. Typical microstructures are presented in Figure 3. The larger precipitate size in the creep specimens indicated that significant precipitate coarsening had occurred during the test. In both the elevated temperature tensile and the creep specimens, dislocations were found to be associated with the precipitates, TEM examination also revealed evidence of dislocation pinning by these precipitates. Moreover, no significant variation in dislocation density or substructure was noted between ceramic particulate-free regions and areas near the matrix/particulate interface.

Coarse θ precipitates ($\sim$ 0.5 μm) were observed at the matrix/SiC interface in both materials (Figure 4a). Finer precipitates were also detected at the Matrix/SiC interface in the creep specimen (Figure 4b), which suggests that additional precipitation may have occurred during the creep test. The major microstructural difference between the tensile and creep specimens was, however, the presence of numerous sub-grains in the creep failed specimen as shown in Figure 5. The sub-grain

size ranged from approximately 0.5 μm to several microns. No such features were observed in the specimens deformed by tensile testing. This indicates that polygonization/ recovery occurred only during during the creep-rupture test.

In summary, the elevated temperature tensile and steady-state creep microstructures of the cast 2014 Al/20 v% SiC composite has been characterized by SEM fractography and AEM. In both tensile and creep testing, the material failed via a mechanism of void nucleation, growth and coalescence which resulted in interface separation and matrix tearing. The matrix/SiC interface integrity was preserved during the tensile and creep tests although creep exposure promoted additional precipitation of alloy second phases at the matrix/SiC interface. Also, the dislocation distribution (in the tensile and creep specimens) and subgrain distribution (in the creep specimens) were found to be relatively uniform indicating no preferential enhancement of the dislocations at the matrix/SiC interface. Thus, while great similarities exist between the features of high temperature tensile and creep fractured materials, the differences in terms of second phase precipitation, dislocation structure and matrix void formation indicate that the long term high temperature mechanical performance of Al-SiC composites may be controlled by different factors than those that influence tensile test behavior. The quantitative impact of the various factors on longer time higher temperature behavior requires more detailed study of the structures of the matrix and SiC-matrix interface regions that are produced by controlled creep conditions.

ACKNOWLEGEMENTS- This work was sponsored by Westinghouse internal funds. We are thankful to many individuals who contributed to this work. Among them are C. M. Fox, T. A. Manion, A. Karanovich, T. J. Mullen, R. T. Blackham and J. J. Haugh.

REFERENCES-

1. M. N. Gungor, P. K. Liaw, W. A. Logsdon, M. A. Burke, Proc. of the MRS-TMS meeting on "High Temperature Structural Composites: Synthesis, Characterization and Properties", May, 1987.
2. M. G. Burke, M. N. Gungor and P. K. Liaw, Proc. of 46th Annual EMSA Conference, ed. G. W. Bailey, 1988, San Francisco (in press).
3. W. A. Logsdon and P. K. Liaw, Engrg. Frac. Mechs., 24, no. 5, 1986, p. 737.
4. P. K. Liaw, G. G. Greggi and W. A. Logsdon, J. Mat Sci., 22, 1987, p. 1613.
5. G. Mott and P. K. Liaw, " Correlation of Mechanical and Ultrasonic Properties of Al/SiC Metal Matrix Composites," Met. Trans. (in press).
6. M. N. Gungor, P. K. Liaw, J. M. Wells, J. Nunes, H. L. Gegel and J. T. Morgan, Proc. of 10 Annual MMC Working Group Meeting, MMCIAC, Park City, Utah, Jan. 1988.

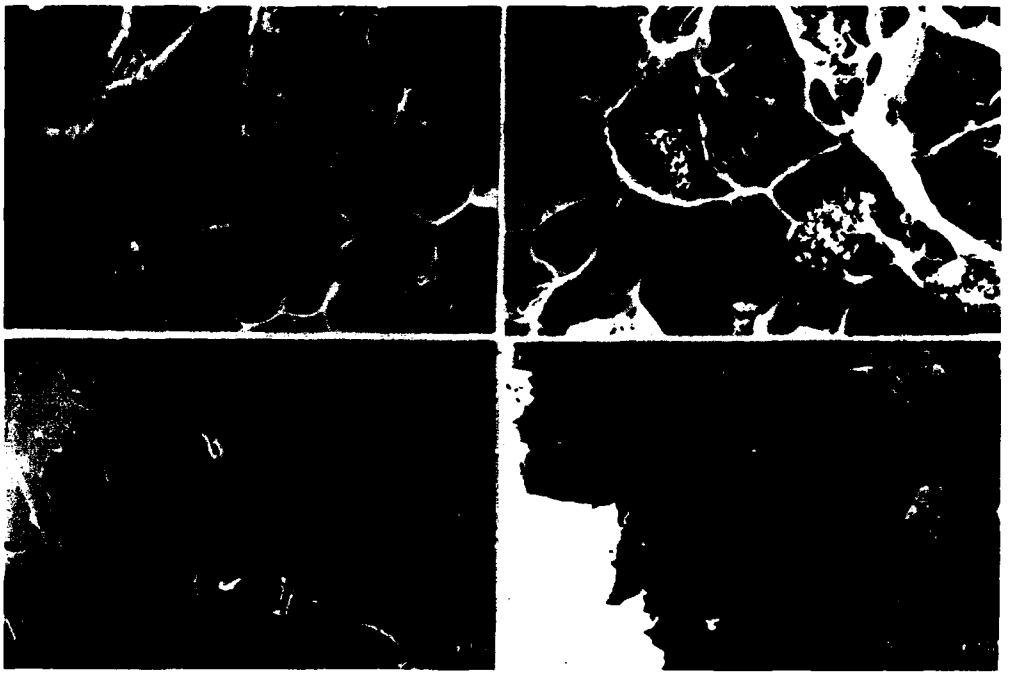


Figure 1. The elevated temperature (523 K) tensile (A and B) and steady-state creep (C and D) fracture surfaces. Notice the dimples in the matrix (A and C) separation of the matrix/SiC interface (B and D) and the presence of the alloy second phases (white features, particularly in C).

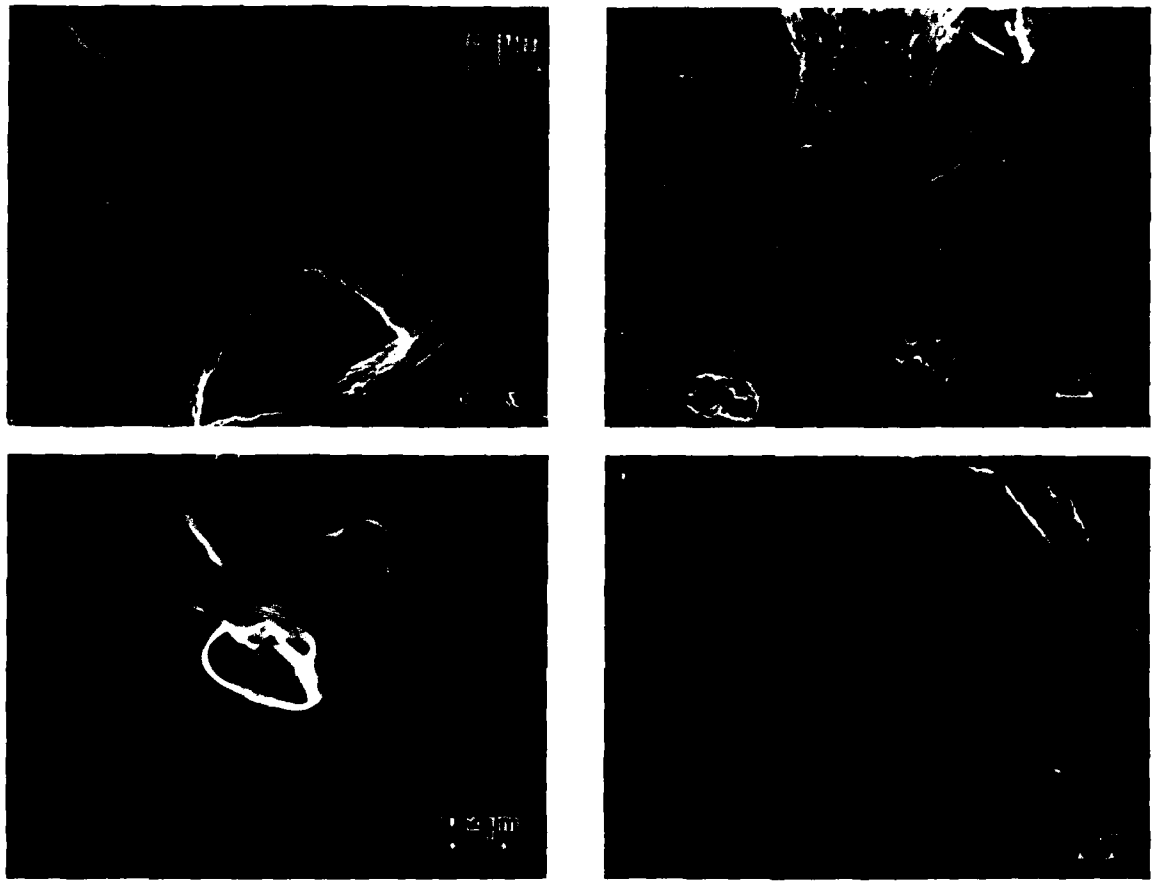


Figure 2. SEM micrographs of the TEM specimens prepared from the elevated temperature (523 K) tensile samples (A and B) and from the steady-state creep samples (C and D). Note the presence of voids in the vicinity of the SiC particulate (A) and within the matrix (B) after tensile deformation. Coarse voids and limited Al/SiC interface decohesion (arrowed) are evident in the specimens deformed by creep (C and D).

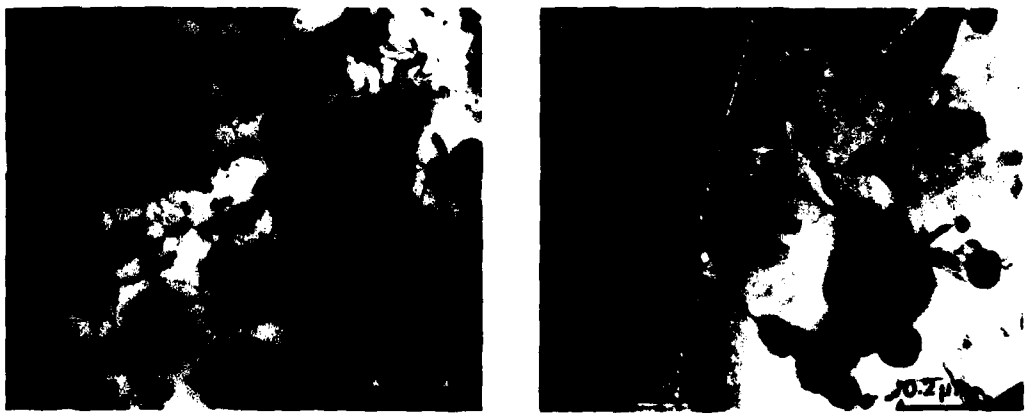


Figure 3. TEM micrographs of the matrix of the elevated temperature (523 K) tensile specimen (A) and the creep specimen (B). Note the coarser θ precipitates in the matrix of the creep sample (B).

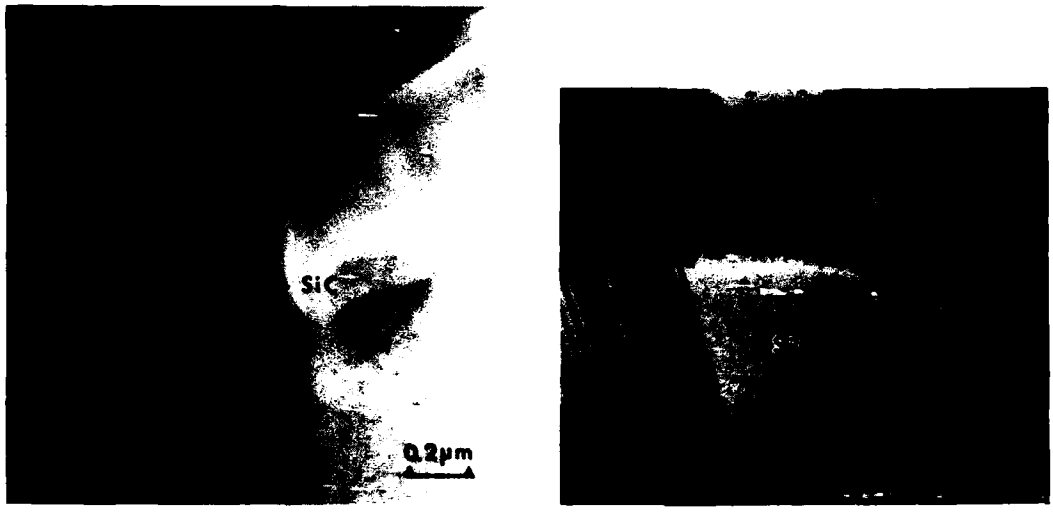


Figure 4. STEM micrograph of the matrix/SiC interface in the elevated temperature (523 K) tensile specimen (A), and TEM micrograph of the the matrix/SiC interface in the creep specimen (B). Note the preferential precipitation of θ.



Figure 5. TEM micrographs of the creep specimen showing the general deformation structure, dislocations and subgrains.

ENHANCEMENT IN THE PROPERTIES OF A SQUEEZE-CAST ALUMINIUM MAGNESIUM ALLOY CONTAINING DELTA-ALUMINA FIBRE

A. A. Das, A. J. Clegg
Loughborough University of Technology
Loughborough, Leicestershire, UK

B. Zantout
Government of Syria
Damascus, Syria

ABSTRACT

The ductility of most aluminium alloys can be greatly enhanced by squeeze casting. The improved ductility can be used to advantage for reinforcing the matrix of the alloys with ceramic fibre.
In this paper the properties of a squeeze-cast Al-3.75 Mg alloy, tested in tension, are first considered. This is followed by examinations of the alloy composites containing up to 10 v% of delta alumina fibre. To obtain a fine homogeneous and equiaxed matrix with uniformity of fibre distribution in random orientation, a slurry consisting of the short fibre dispersed in molten alloy is squeeze cast under a pressure of 140 MPa.
Improved ratios for composite/matrix properties are noted for UTS, Proof Stress and Young's Modulus, even with small v% of fibre added. The ratios are higher for tests carried out at higher temperatures; up to 300°C .
The room temperature fatigue life increases with increasing fibre content.
For the metal-matrix composite system investigated, the concept of a minimum (critical) volume fraction of fibre needed for strengthening is not substantiated.

INFILTRATION OF LIQUID METAL into metal dies containing preformed inserts of inorganic fibre has been widely used as a method to fabricate metal-matrix composites; not only for experimentation in the laboratory[1-7] but also for commercial developments[8-11]. The summaries of publications and reports from the MIT Center for the Processing and Evaluation of Metal Matrix Composites[12] have raised a number of questions regarding the process parameters for fabrication by squeeze infiltration and their effect on the structure and properties derived in the solidified shape.

The main areas of uncertainty associated with squeeze infiltration may be summarised as:

Reaction Time: In order to develop a satisfactory and stable bond between matrix and fibre, e.g., between aluminium alloys and Al_2O_3 or SiC fibre, it is necessary to promote some interaction between the molten alloy and the fibre. There is evidence to suggest that the type of interaction at any one temperature may be strongly influenced not only by the availability of oxygen at the interaction zone[13] and the composition of the alloy and fibre[14], but also by the length of time the molten metal and fibre are in contact[15]. The available empirical data[16] for an Al-4.5 Cu alloy/SiC fibre system strongly points to an optimum time of contact between 15-18 minutes at a temperature of 760°C $\pm$ 5°C. Longer periods of holding at this temperature result in progressive fibre degradation. The control of the contact time during squeeze infiltration would appear to be impractical unless the alloy and fibre are heated to undesirably high temperatures.

Reaction Temperature: Because of the rapid cooling during squeeze infiltration, it is necessary, in most cases, to preheat both the alloy and the fibre to temperatures much higher than those used for normal casting operations. For aluminium alloy composites, temperatures as high as 1000°C have been reported[17]. Heating aluminium alloys to these temperatures can cause oxidation to an undesirable degree and can change the nature of the interactions at the fibre/metal interface. A high starting temperature for infiltration is also likely to give rise to steep temperature gradients in the solidifying shape and depending on the alloy system, could result in a columnar structure in the fibre-free areas of the matrix (assuming selective reinforcement). Either normal or inverse segregation could also occur depending on the temperature conditions. The matrix structure in the infiltrated regions would be influenced by the heat capacities and conductivities of

the fibre i.e., these regions would remain liquid for a longer period compared to the fibre-free matrix, which could lead to shrinkage defects.

A further point to note is that the binders used to prepare the fibre preforms can lead to interactions with the metal. For example, the silica normally present in preforms of alumina fibre can give rise to the following reaction[18] at about 900°C, $4[Al]_{melt} + 3SiO_2 = 2Al_2O_3 + 3[Si]_{melt}$. Organic binders may give rise to gaseous products at the temperatures involved.

Infiltration Pressure: Controlled (possibly variable) pressure is applied during infiltration, for two main reasons: (i) to ensure that complete infiltration takes place through the fibre preforms through capillary spaces against 'surface tension' forces (the infiltration channels may be more or less tortuous depending on fibre orientation) and, (ii) to prevent shrinkage cavities appearing within the cast shape during the liquid → solid transformation. There are, therefore, a very large number of factors that can affect the infiltration pressure apart from the temperature and heat flow conditions. These are: packing density and orientation of fibre; casting configuration; distance of the fibre inserts from the pressure application zone; contact angle between fibre and molten alloy; mechanical properties of fibre preforms and the nature of the interaction between fibre and alloy. Theoretical predictions regarding the level of pressure needed for a particular application are, therefore, extremely difficult. A blockage occurring in the infiltration channels due to solidified metal or any other cause can give rise to pressure build-up leading to the collapse or cracking of the fibre insert. Although, under favourable conditions, infiltration can take place at comparatively low pressures, e.g. 30MPa, those needed to avoid shrinkage defects in the solidifying casting are generally higher e.g. about 100MPa for aluminium alloys. Optimum pressures needed for infiltration are not necessarily suitable for consolidation to prevent voids and discontinuities.

It will be clear from the foregoing considerations that the fabrication of selectively reinforced castings by the squeeze infiltration process may be extremely complicated and that at present the uniformity of fibre distribution (short fibre) within the entire body of the casting is not practicable.

Squeeze Casting: Earlier studies[19,20] on squeeze casting had shown that one of the main advantages to be gained is the remarkable improvement in the ductility properties of commercial alloys, as Table I will show, where the ductilities of some squeeze cast Al-alloys are compared with the ductilities of the same alloys when gravity die cast in the same die.

Subsequent studies[21] reported later[22] established that an Al-4.5Cu alloy can be successfully squeeze cast after dispersing whiskers of SiC in the alloy melt. The report also pointed to the role of Cu in the alloy in preventing the rejection of whisker during melt preparation and the micrographs from the casting clearly associated the whiskers with the copper-rich constituent. The method of introducing and dispersing the whiskers in the melt remained the main objection due to the complexity of the procedure.

Table I - Comparisons of 'as cast' elongation %

BS:1490 Alloy	% Elongation Gravity Die Cast	Squeeze Cast
LM4	2.40	8.00
LM5	7.75	18.50
LM6*	7.58	17.35
LM6	4.00	10.10
LM11	7.00	17.10
LM24	1.82	4.80

* Sodium modified

The availability of chopped fibres of SiC (NICALON), allowed a simple VORTEX method to be used to disperse the fibre in an Al-4.5Cu melt[15] followed by squeeze casting. Delta alumina fibre (SAFFIL), however, is readily available and much less expensive. A number of investigators including Meherabian and co-workers[14,23] have reported on the interaction of Al_2O_3 fibre (in this case α-Al_2O_3 Dupont FP fibre) with aluminium alloys. According to Mehrabian et al, interaction between α-Al_2O_3 and Al-Mg alloys resulted in a magnesium-rich region around the individual fibres, which was thought to provide a strong and stable bond, provided that the contact time between metal and fibre was adequate.

Considerations on the strengthening mechanisms of fibre reinforcement pointed to the ability of the matrix to transfer load to the fibre when the composite is under stress, and to accommodate any mismatch in the expansion characteristics with the fibre and/or interface reacted zone. A ductile matrix, at room and elevated temperatures, is therefore a principal requirement.

In the fabrication of MMC's using short fibre in combination with aluminium alloys, squeeze casting (as separate from squeeze infiltration) provides the following advantages:

(i) The fibre is dispersed in the melt before squeeze casting so that the temperature of the melt and contact time between fibre and melt can be closely controlled to develop a stable interface zone and thus a suitable bond.

(ii) The casting temperatures are usually only 30-50°C above the liquidus temperatures of the alloys so that oxidation damage to the metal due to high melt temperatures can be avoided. The lower casting temperature also promotes rapid solidification of the casting throughout its cross-section, resulting in a fine equiaxed grain structure.

(iii) The fibre in the melt is subjected to hydrostatic pressure (without any movement of liquid) so that high pressures, e.g. 150 MPa, can be used for consolidation of the casting without causing damage to the fibre. This helps to eliminate macro and micro-shrinkage and ensures a sound matrix free from voids and other discontinuities — the main reason for improved ductility.

(iv) A uniform distribution of randomly oriented fibre (in the matrix) can be achieved due to the rapid cooling and solidification of the casting which prevents gravity segregation and/or directional alignment of fibre.

(v) The entire casting is reinforced and shows properties which are isotropic.

(vi) Suitable for mass production.

The main disadvantages of the process are (a) the inability to provide selective reinforcement and (b) special melt preparation methods are normally needed (i.e. not simple vortex) if the fibre content exceeds 12-15 volume %.

The purpose of the investigation was to determine the suitability of the squeeze casting process for fabricating composites from an Al-3.75 Mg alloy and δ-Al_2O_3 fibre and to evaluate the casting properties.

MATERIALS AND METHODS

1. Materials: The alloy used was B.S.;1290 LM5 with the following chemical composition Al (Rem); Cu (0.01); Mg (3.75); Si (0.02); Fe (0.27); Mn (0.47); Ni (0.01); Zn (0.02); Pb (0.01); Sn (0.01); Ti (0.10).

The average properties of the Saffil alumina fibre grade RF, supplied by ICI Limited (UK) is given below:

Mean diameter	3 m
Mean length	0.5 mm
Density	$3.3/cm^3$
Tensile strength	2000 MPa
Tensile modulus	300 GPa
Max oper temp	1600°C
Crystal phase	mainly delta alumina
Impurities	mainly SiO_2 up to 4%

2. Methods: The 'as received' fibre is in 'clumps' and cannot be dispersed uniformly in the melt. A pretreatment is therefore necessary. Fibres were dispersed and pickled for 5 minutes in hydrochloric acid (15%) diluted with deionized water. The dispersion was then filtered and the residue washed off three times by dispersion in deionized water followed by filtration. The dispersion was carried out in a glass vessel fitted with a mechanical stirrer. The final residue was dried off at 160-175°C. This procedure produced a fluffy mass of the fibre. However, to ensure that the fibre did not stick to each other while entering the melt the requisite mass of fluffy fibre was passed through a specially designed[15] separating device. It is also better to use the fibre immediately after the drying out operation to eliminate any moisture going into the melt.

The alloy was melted and held at a temperature of 730°C $\pm$ 10°C in an electrical resistance heated vertical tube furnace. Alumina crucibles were used. A triple bladed graphite stirrer, driven by a variable speed motor, when immersed in the melt, made a tilt angle of 15°, which made a strong enough VORTEX to draw and disperse the fibre into the alloy melt. The optimum time of contact between fibre and melt had been previously determined during initial experimentation and found to be 15.5 minutes at 730 $\pm$ 10°C. Since the VORTEX was maintained for this entire period, oxidation could be a problem since freshly exposed metal at the surface would not have any cover. To obviate this problem a dry nitrogen gas stream was used to provide a shroud over the VORTEX. After the elapsed time the crucible was removed from the furnace and the contents poured into a metal die, 52mm dia x 72 mm height, and pressure applied to the free surface of the casting via a punch. The casting was ejected after 90 seconds. A series of test castings were made with 0, 2, 4, 6, 8 and 10 volume percent of fibre. The casting details are:

Die Temperature	250°C $\pm$ 5°C
Squeeze Pressure	140 MPa
Pouring Temperature	682°C $\pm$ 10°C
Pressure Maintained	60-90 seconds

3. Evaluation : Metallographic methods were used for examining the uniformity of fibre distribution and the randomness of fibre orientation. Electron probe microanalysis was carried out to examine the fibre-matrix interface region, and scanning electron microscopy to examine the fractured surfaces of the test pieces (after tensile testing) for signs of fibre pull-out.

Room Temperature Tensile Test: All tests were carried out using Hounsfield No.18, tensile specimens (gauge length 45.4 mm and diameter 9.05-9.09 mm). Specimens were tested for ultimate tensile strength, 0.1% offset proof stress, modulus of elasticity, percent elongation and percent reduction in area. All tests were carried out at a strain rate of $1.835 \times 10^{-4}.s^{-1}$. Average values were taken from a minimum of three test specimens. Test specimens were prepared from both the longitudinal and transverse directions of the test casting to test for anisotropy.

Higher Temperature Tensile Test: Composite castings were tested at temperatures of 20°, 150°, 200°, 250° and 300°C. Test conditions, except for temperature, were as for tests carried out at room temperature. Temperature differences along the length of the specimens were within acceptable limits, i.e., 2-4°C at 150°C, 4-7°C at 250°C and 5-8°C at 300°C which is $\pm$ 3% of the test temperature.

Fatigue Testing: A Wohler-type (rotating bending) machine was used. Specimen diameter

= 3.8100 mm ± 0.0125 mm and reverse bending stress = 95 MPa which corresponds to M (the bending moment) set at 0.561 Nm. The rotating speed of the machine allowed 1.71 x 10^5 stress reversals per hour.

Thermal Stability: To test the stability of the interface and bond between matrix and fibre, specimens containing up to 10v% fibre were thermally cycled between room temperature and 300°C. Specimens were heated in a furnace for 25 minutes and then quenched in air. This procedure was repeated up to 20 cycles before carrying out tensile tests at room temperature.

RESULTS AND DISCUSSIONS

1. Metallography: Fig.1, shows the fibre distribution and orientation in two perpendicular planes, i.e., parallel and perpendicular to the direction of travel of the punch used to apply pressure. It will be noted that no differentiation is possible between the two micrographs indicating that the application of pressure did not produce vertical and horizontal components of different magnitude.

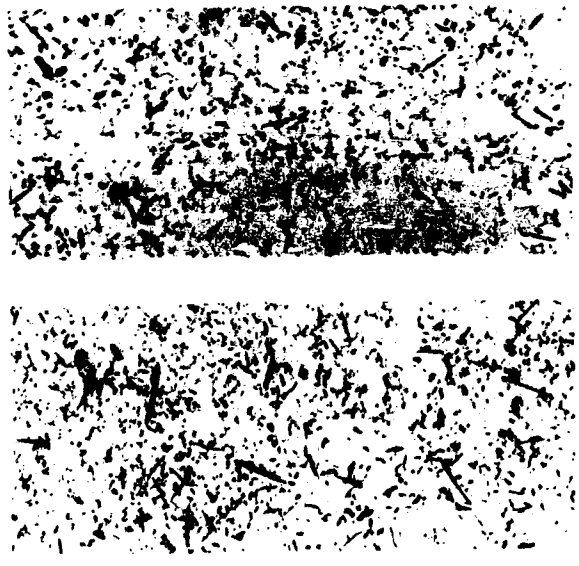


Fig.1 Fibre Distribution in Two Perpendicular Planes 8 v% Fibre x100.

2. EPMA: Fig.2, is a reproduction of a typical EPMA line scan across a fibre, approximately corresponding to a scattered electron image. Compared to the results reported by Levi et al[14], there was no sign of any concentration of Mg-rich constituents around the fibre. This may be due to the fact that the δ-Al_2O_3 used in these experiments is different from α-Al_2O_3 used by Levi. δ-Al_2O_3 contains up to 4% SiO_2 and it is likely that the Mg in the metal reacted with SiO_2 which precluded reactions of the type suggested in the work with α-Al_2O_3. It is also possible that since the interaction time was strictly controlled in the experiments reported here (although the temperatures were higher) the rapidity of solidification by squeeze casting did not allow the lower melting magnesium rich constituent to accumulate round the fibres as it would have done at the much lower temperatures used by Levi et al.

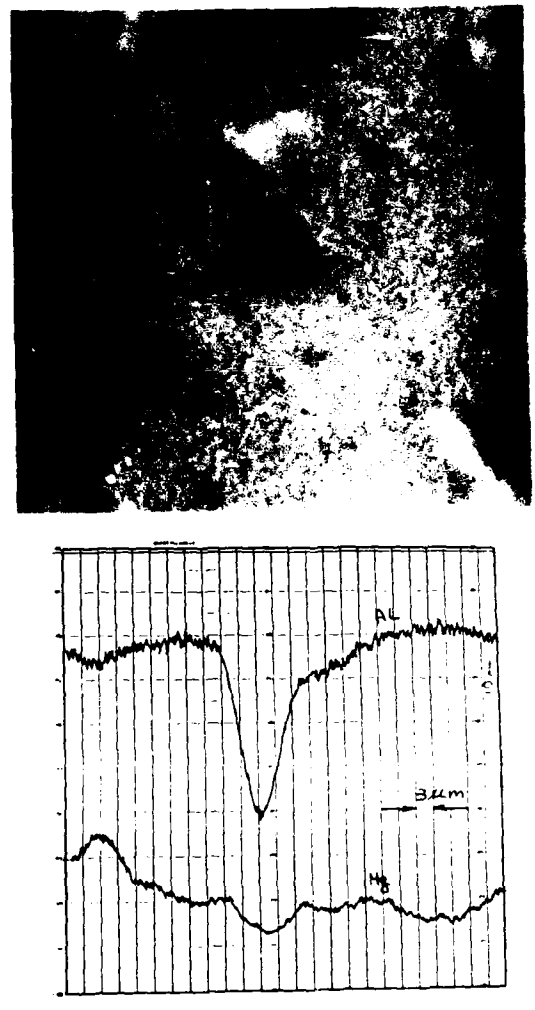


Fig.2 Scattered Electron Image x1K and Corresponding EPMA Line Scan for a Fibre in the Matrix Alloy.

3. Scanning Electron Microscopy: Figs.3 and 4 are representative views of the fractured surfaces after tensile testing at room temperature and at 250°C respectively for composites containing 10 v% fibre. All surfaces examined showed complete absence of any signs of fibre pull out which would tend to indicate that the fabrication process did not damage the fibre, at least, not sufficiently to reduce the lengths below the critical length.



Fig.3 SEM of Tensile Fracture at Room Temperature 8 v% Fibre x10K.

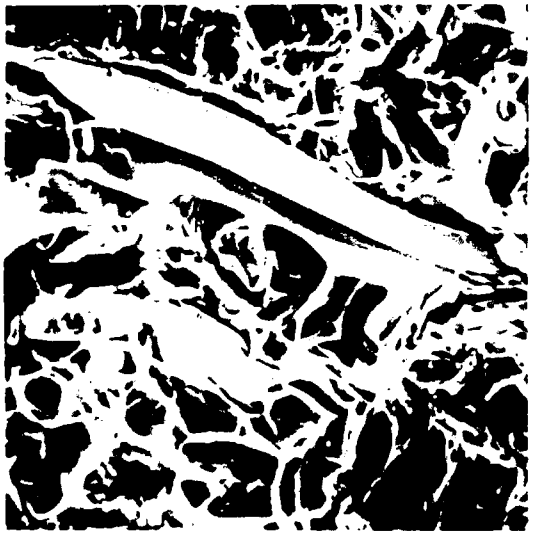


Fig.4 SEM of Tensile Fracture at 250°C 10 v% Fibre x1.6K.

4. Room Temperature Tensile: The effect of the squeeze pressure on the tensile properties of the matrix alloy (without fibre) is shown in Fig.5.

It will be noted that the values become more or less constant beyond a certain level of pressure. These initial experiments were carried out to determine the suitability of the alloy for fibre reinforcement and to determine the optimum pressure levels to be employed while fabricating the composites. The improvement in the % elongation values are quite remarkable.

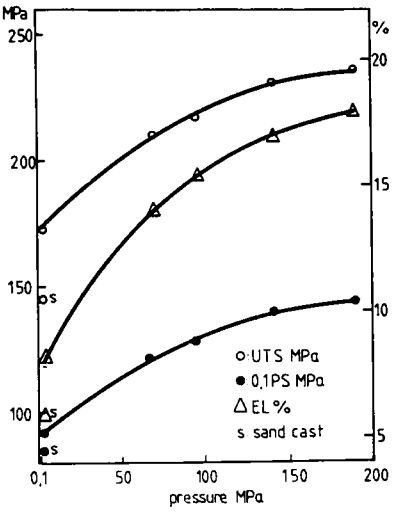


Fig.5 Effect of Solidification Pressure on the Tensile Properties of the Matrix Alloy.

5. High Temperature Tensile: The ratios of the properties of composite/fibre are shown against increasing volume of fibre content for three different temperatures of testing. Fig.6 shows UTS ratios, Fig.7 the proof stress, Fig.8 elastic modulus, and Fig.9 % elongation and % reduction in area.

It will be noted that the improvement in properties takes place even at low volume % addition of fibre (except of course for the ductility properties) and that the strengthening effect is more pronounced at higher temperatures. The decrease in the absolute values of proof stress is gradual up to 250°C but more rapid at 300°C. Decrease in the absolute values of UTS was more marked. It is important to note, however, that at 250°C, the composite systems containing 10 v% fibre have proof stress and elastic modulus values comparable to the squeeze cast matrix alloy (without fibre) tested at room temperature. The only moderate improvement in the UTS for the composite reinforced with up to 10 v% fibre is no surprise, since this is just about at the borderline of the minimum volume fraction (theoretical prediction). What is significant is that inspite of the 3D random orientation of chopped fibre, some strengthening is observed even with 2-4 v% fibre. This calls into question the concept of a minimum critical volume fraction of fibre needed for strengthening. The strengthening efficiency, with 10 v% fibre was at a maximum at 200°C.

A further point to note is that Fukuda and Chou[24], theoretically predicted the value of the orientation factor (for 3D random orientation) to be 1/8 while Cox[25] and Christensen[26] predicted a value of 1/6. For the Al-3.75 Mg/δ-Al_2O_3 composite system the theoretical value of UTS, (Rileys[27] solution),

for 10 volume % fibre was calculated at 234 MPa whereas the actual measured average value was 243 MPa. An orientation factor of 1/6 was used for these calculations. It is also useful to note that the room temperature UTS and 0.1% offset proof stress of squeeze cast composites containing 10 v% fibre are 41% and 104% higher respectively, than the gravity die casting of the same alloy (without reinforcement).

The foregoing considerations point to the fine grained, homogeneous and highly ductile matrix of the squeeze cast alloy to be the main contributing factor for the improvement.

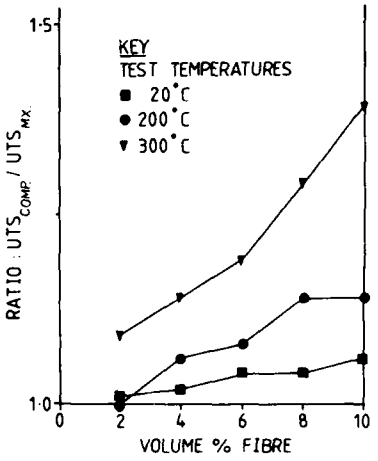


Fig.6 Effect of Fibre Volume % on Composite/Matrix UTS Ratio.

6. Temperature Cycling: The result of temperature cycling between room temperature and 300°C for composites containing 10 v% fibre is shown in Table II.

Table II: 10 v% Fibre Average Values

No of Cycles	UTS MPa	0.1% P.S. MPa	Elastic Modulus GPa
0	243	186	76
5	238	184	75.5
10	235	183	75.3
20	237	187	75.9

Inspite of the mismatch in the expansion characteristics between fibre and matrix, the thermal shock during cycling did not appear to affect the fibre properties in any way, which would indicate that the ductility of the matrix is sufficient to accommodate unequal expansion and contraction without damaging the interface zone.

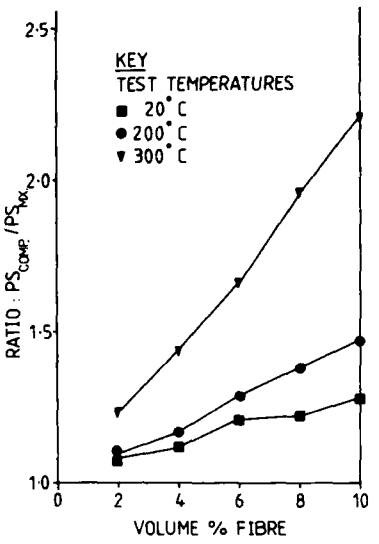


Fig.7 Effect of Fibre Volume % on Composite/Matrix Proof Stress Ratio.

Fatigue Life: Table III gives the fatigue life of composite compared to the sand cast and gravity die cast matrix alloy. The steady increase in the average fatigue life with increasing fibre content provides reassurance that the composite is free from voids and discontinuities, i.e. those that can give rise to rapid deterioration in fatigue life. The role of the fibre in preventing rapid crack propagation cannot be neglected either.

Table III

Fibre v%	Average Fatigue Life (Reversals x 10^5)
0 (Sand Cast)	5.86
0 (Gravity Die Cast)	6.63
0 (Squeeze Cast)	7.1
2	6.97
4	7.61
6	8.70
8	9.51
10	10.15

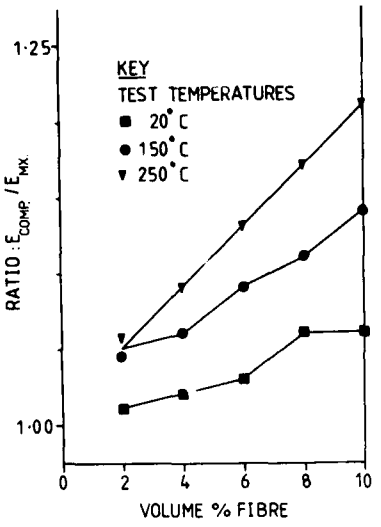


Fig.8 Effect of Fibre Volume % on Composite/Matrix Elastic Modulus Ratio.

III CONCLUSIONS

The work reported here confirms that delta alumina fibre can be used to reinforce an Al-3.75 Mg commercial alloy, via the squeeze casting route provided that the fibre is allowed to interact with the molten metal for a predetermined length of time at a predetermined temperature. The results show that:

(i) Stable bonds are developed between fibre and matrix which can withstand cycling between room temperature and a temperature of 300°C, without deterioration.

(ii) The EPMA failed to detect any concentration of magnesium-rich constituents around the fibre.

(iii) At room temperature the tensile strength properties increase approximately linearly with increasing fibre content.

(iv) The strengthening efficiency is higher at higher temperatures.

(v) The fatigue life, at room temperature, is significantly increased with modest increases in fibre content.

(vi) SEM of tensile fracture surfaces (testing at temperatures up to 300°C) did not show any loosely bonded and/or pulled out fibre which indicates that fibre damage, during fabrication, is minimal - if at all.

(vii) The better than expected results obtained for the very modest amounts of fibre added, are attributed to the defect free and ductile matrix resulting from squeeze casting and the uniformity of distribution and randomness of fibre orientation.

(viii) For 3D randomly oriented short fibre composite of the system examined, the concept of a minimum (critical) volume fraction (following analyses of continous aligned fibre systems) is not applicable.

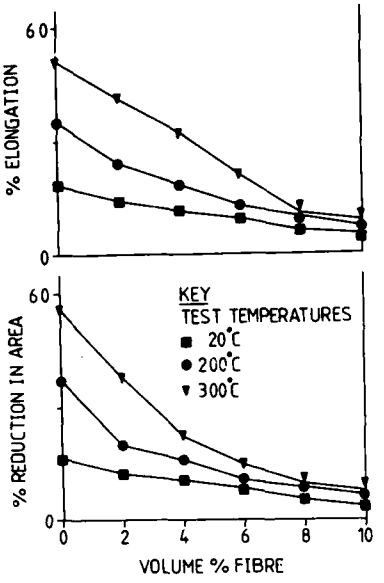


Fig.9 Effect of Fibre Volume % on Percent Elongation and Reduction in Area of Composite.

ACKNOWLEDGEMENT

The authors acknowledge with thanks the financial support provided by the Syrian Government to Dr B Zantout. They also wish to thank Mr J Dinwoodie of ICI Limited, for the gift of Saffil fibre used in the experiments.

REFERENCES

1. Mehan R. L., Metal Matrix Composites, ASTM STP, vol 438, pp. 29-58, (1968).
2. Mehan R. L., Comps. Mater., vol 4, p. 90, (1970).
3. Noone M. J., E. Feingold and W. H. Sutton, Interfaces in Composites, ASTM STP, vol 452, p.90, (1969).
4. Mortensen A., M. N. Gungor, J. A. Cornie and M. C. Flemings, Journal of Metals, vol 38, pp. 30-35, (1986).

5. Cornie J. A., Y. M. Chiang, D. R. Uhlman, A. Mortensen and J. M Collins, Ceramics Bulletin, 65(2), pp. 293-297, (1986).
6. Cornie J. A., A. Mortensen, M. N. Gungor, and M. C. Flemings, Proc. ICCM/5, pp. 809-823, (1985).
7. Clyne T. W. and J. F. Mason, Metal. Trans. A, vol 18A, p. 621, (1987).
8. Fukunaga H., and M. Kuriyama, Bull. of JSME, vol 25, No. 203, pp. 842-847, (1982).
9. Toyota Motor Corporation and Isolite Babcock Refractories Ltd., J P Pat. 8393847, (1981).
10. Toyota Motor Corporation and Art Metal Ltd., J P Pat. 5848648, (1983).
11. Toaz M. W., Selective Fibre Reinforcement: A New Frontier in Casting Technology, AFS Trans., vol 94, p. 312, (1986).
12. Booth S. E., M. J. Ball, A. J. Clegg, N. S. Hurd and R. Savery, Report on an OSTEM Visit to USA, March/April 1987, BNF 6.103.0, pp. 186-208, (1987).
13. Warren R., and C. H. Anderson, Composites vol 15, No. 2, pp. 101-111, (1984).
14. Levi C. G., G. J. Abbaschian and R. Mehrabian, Metallurgical Transactions A, vol 9A, pp. 697-711, (1978).
15. Zantout B., A. A. Das and A. J. Clegg, Proc. of the First National Conference on Production Research, Kogan Page, pp. 345-352, (1986).
16. Zantout B., The Production and Evaluation of Squeeze Cast Al-alloy Mattrix-Short Ceramic Fibre Composites, PhD Thesis, Loughborough University of Technology (1986).
17. Jolly M. R., and G. Haour, Third International Conference, Solidification Processing, pp. 505-509, (Preprint 1987).
18. Feest E. A., M. J. Ball, A. R. Begg and D. A. Biggs, Report on an OSTEM Visit to Japan, October 1986, Harwell Laboratory, Oxfordshire, UK (1986).
19. Chatterjee S. and A. A. Das, The British Foundryman, vol 65, p. 420, (1972).
20. Chatterjee S. and A. A. Das, Ibid, vol 66, p. 118, (1973).
21. Chatterjee S., Aluminium-Silicon Carbide Whisker Cast Composites: Some observations on the Distribution, Bonding and Properties Developed, PhD Thesis, Loughborough University of Technology, pp. 1-74, (1973).
22. Das A. A. and Chatterjee S., The Metallurgist and Materials Technologist, vol 13, pp. 137-142, (1981).
23. Quigley B. F., G. J. Abbaschian, R. Wunderlin and R. Mehrabian, Metallurgical Transactions A, vol 13A, pp. 93-100, (1982).
24. Fukuda H. and T. Chou, J. Mater. Sci., 17, p. 1003, (1982).
25. Cox H. L., Brit. Jnl. Appl. Phys., 3, p. 72, (1952).
26. Christensen R. M., and F. M. Waals, J. Compos. Mater., 6, p. 402, (1972).
27. Riley V. R., J. Compos. Mater., 2, p. 436, (1968).

EFFECT OF MANUFACTURING VARIABLES ON THE STRUCTURE AND PROPERTIES OF SQUEEZE CAST C/Al MMC's

Ashish P. Diwanji
Materials Science Program
University of Delaware
Newark, Delaware, USA

Ian W. Hall
Department of Mechanical Engineering
University of Delaware
Newark, Delaware, USA

INTRODUCTION

In continuous fiber reinforced metal matrix composite materials (MMCs) the structure and properties of the fiber-matrix interface control most of the mechanical properties of interest, including the axial and transverse strengths and fracture resistance (1). In each of the above loading conditions, transfer and distribution of the externally applied load are achieved through the matrix and take place through the generation of shear or tensile stresses at the fiber-matrix interface. For the case of axial loading, several theoretical and experimental studies have shown that brittle reaction zones reduce strength and fracture resistance (2,3) because of the stress concentrations caused by cracks in this zone. Also, it is becoming clear that, even in the absence of any reaction zone, a very strong fiber/matrix bond is undesirable since propagating cracks are not blunted in such cases (4,5) and catastrophic failure occurs as soon as a weak fiber breaks. The blunting effect is dependent on the ease of debonding and pull-out of fibers from the matrix during crack propagation. Figure 1 schematically summarizes the dependence of tensile properties of a unidirectionally reinforced composite on the shear strength of the interface. If the interface shear strength is zero (for theoretical considerations only), then no load is transferred to the fibers and the composite has very low strength. At the other extreme, if the interface shear strength is greater than that of the matrix a strong bond results which, as mentioned above, leads to lower strengths. Thus, the optimum interface is one wherein the shear strength is high enough to load up the fibers but not too high to prevent debonding and fiber pull-out (4).

Interfaces can be classified into two extreme types, a mechanical interface and a chemical interface, depending on the type of interaction between the matrix and fiber. Generally the load transfer in a mechanical interface is a purely frictional type of interaction whereas in a chemical interface the load transfer is a consequence of the strength of the chemical bond. An optimum interface as suggested by Fig. 1 may be a combination of a mechanical and a chemical interface (4).

The final form of the interface in any composite system depends on the manufacturing conditions. The present study focusses on the C/Al system. Prasad *et al.* (6) have achieved pressure induced improvement in interfacial bonding between graphite and aluminum in graphitic-aluminum particle composites. Shindo (7) and Honjo *et al.* (8) have suggested the use of various SiC, TiC or TiN coatings on carbon fibers so as to achieve R.O.M. strengths in C/Al composites. Investigations of Kimura *et al.* (9) suggest that the

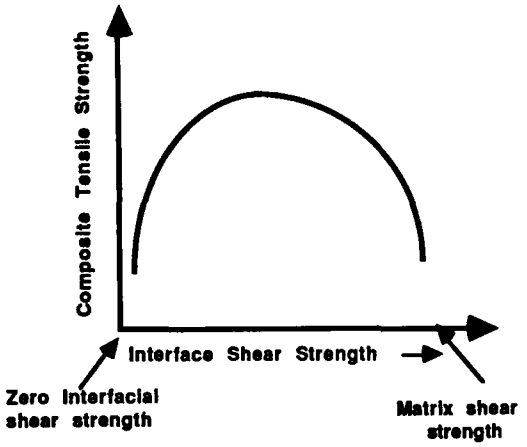


Fig.1:Schematic representation of the dependence of tensile properties of a composite on its interfacial shear strength

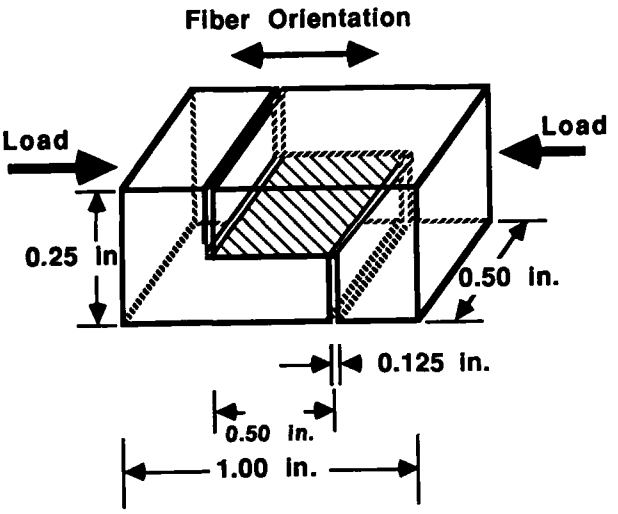


Fig.2: Shear strength test specimen geometry

wettability and adhesion between carbon fibers and aluminum are significantly improved by small alloying additions of indium, lead or thallium. In order to tailor interfaces to yield specific properties, it is necessary to identify the structure and type of the interface which produces the desired properties and then to determine how these structures may be reproducibly generated by systematic control of manufacturing parameters.

The present study addresses the effect of manufacturing parameters on the properties of continuous carbon fiber aluminum metal matrix composites. These MMCs have been squeeze cast under systematically varied manufacturing conditions. Interest centers upon the mechanical properties and, in particular, how manufacturing conditions affect the fiber-matrix interface. In a comprehensive on-going research program at the University of Delaware the effects of the following variables on high modulus carbon fiber reinforced aluminum composites are being investigated: type of carbon fiber, surface treatments of fibers, matrix alloy variation, liquid metal superheat, fiber preform temperature, fiber distribution and fiber volume fraction and heat treatment. This paper reports the effect of variation in fiber preform temperature, matrix alloying and heat treatment on the mechanical properties and fiber-matrix interactions in C/Al composites.

EXPERIMENTAL

The composites investigated in this program were squeeze cast by Honda R & D Co. Ltd, Wako-Shi, Japan. The basic composite system, against which all variations are compared, is aluminum alloy A356 (Al-7Si-0.3Mg-0.3Fe), reinforced with the high modulus M40 carbon fiber using a preform temperature of 600°C and melt temperature of 780°C: the nominal fiber volume fraction is 35%. The experimental parameters used for the composites reported in this paper are summarized in Table 1, along with the mechanical properties.

Cylindrical tensile samples with cross-sectional area of 19.4 mm^2 and gage length of 12.7mm were machined from each of these composites and tested in a static Instron machine at a strain rate of $2x10^{-3}sec^{-1}$. Rectangular double notched samples as shown in Fig. 2 were machined from each of the composites and tested so as to evaluate their shear strength and also attempt to calculate the interfacial shear strength. The sample geometry is similar to that used in ASTM D3846-79 (10), for the shear testing of polymer composites. Vickers Microhardness testing of the matrix was done using a Buehler Micromet II test machine. Optical metallography was performed on each composite to provide details of the solidification process and the effect of heat treatment on the

microstructure. Extensive T.E.M. analysis of each of these composites, using a Philips EM400T, is currently under way in order to characterize the fiber/matrix interface and initial results are presented below.

RESULTS

Table 1 presents the tensile test, shear test and microhardness results for the as-cast and heat treated composites and several features are worthy of particular note. Firstly, it is clearly seen that heat treatment leads to an apparent reduction in tensile strength and an increase in elastic modulus.

Secondly, the tensile strength increases as the fiber preform temperature is lowered. It must be mentioned that almost none of the above composites failed in pure tension. The dominant failure mechanism was a longitudinal shear failure along fiber tow boundaries. This type of fracture is strongly indicative of a low fiber-matrix interfacial shear strength. In order to investigate this belief shear testing of some of the composites was carried out using the sample geometry suggested in Fig.2. These tests resulted in fairly consistent values and the failure in each case was predominantly along the fiber-matrix interface.

The microhardness data indicate that the heat treatments were successful in altering the matrix properties and these strongly influence the composite properties. Similarly, temperature variations of the preform led to matrix property changes.

Figures 3(a) and(b) show the decrease in grain size of the A356 matrix between the tow regions as the fiber preform temperature is decreased from 650°C to 450°C. Optical metallography also shows that the fibers are pushed ahead by matrix dendrites and increasing amounts of second phase Si surround the fibers as the preform temperature is decreased. Optical metallography therefore confirms that the solidification ends at the fiber surface even in samples where the preform temperature was as low as 450°C. The matrix structure of the Al-Mg-Zn alloys is essentially single phased, however, as shown in Figure 4 there is coring within each grain. The heat treatments substantially reduced the coring noticed in the as-cast grains.

TABLE 1

Each composite listed below has been reinforced by high modulus M40 fibers.

ALLOY	PREFORM TEMP. (°C)	HEAT TREATMENT		U.T.S. MPa	Young's Modulus GPa	Shear Strength MPa	VHN
		Solution Treatment	Aging Treatment				
A356	600	----	----	855	165	---	127
Al-5Mg	600	----	----	782	180	54	135
Al-7Mg-2.5Zn	600	----	----	948	142	24	198
Al-3Mg-2Zn	600	----	----	1110	160	31	160
A356	600	24hrs-450°C	1hr-200°C	745	218	---	100
Al-5Mg	600	1hr-350°C	2hr-180°C	655	230	---	159
Al-7Mg-2.5Zn	600	1hr-410°C	1hr-250°C	565	230	---	228
Al-3Mg-2Zn	600	1hr-330°C	1hr-200°C	432	218	---	137
A356	650	----	----	902	152	---	93
A356	550	----	----	796	160	---	134
A356	450	----	----	1025	171	---	136

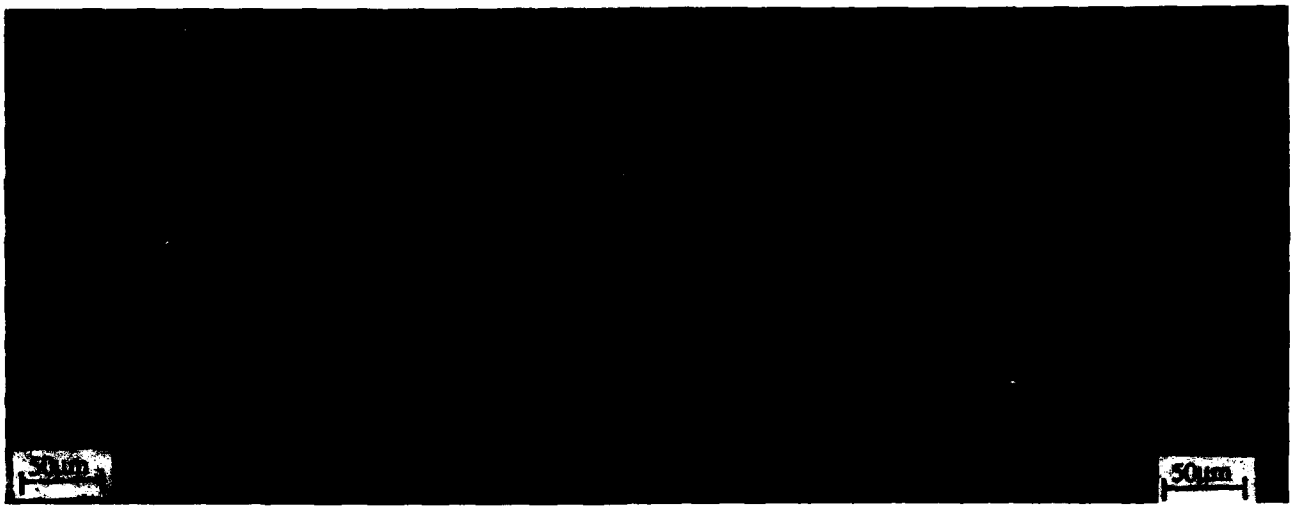


Fig.3 As-cast matrix microstructure in the tow region in M40/A356 showing a decrease in grain size as the fiber preform temperature is decreased from (a) 650°C to (b) 450°C.

Extensive T.E.M. analysis of all the above composites is currently underway to characterize the fiber-matrix interface. Figures 5, 6 and 7 show the typical appearance of the fiber/ matrix interfaces in M40/A356, M40/Al-5%Mg and M40/Al-7%Mg-2.5%Zn composites. These observations show the presence of carbides to varying degrees at the interface in all the composites mentioned in Table 1. However, an exhaustive T.E.M. analysis of the interfacial area in the various alloy matrix composites showed that, relatively, there are more carbides present in Al-Mg-Zn alloy matrices than in the A356 alloy matrix composites. The Al-Mg-Zn matrix composites showed a variety of second phase particles at the interface such as $Mg_{17}Al_{12}$ and Al_3MgZn_3 . EDS line scans of the matrix between two fibers confirm concentration gradients of magnesium and zinc towards the fibers in Al-Mg-Zn alloys and silicon towards the fiber in A356 alloy matrices. As shown in Fig.5, a large portion of the interface area in A356 matrix composites was covered by second phase silicon.

Convergent beam diffraction patterns and micrographs taken under lattice imaging conditions



Fig.4. As-cast matrix microstructure in tow region of M40/Al-3%Mg-2%Zn showing coring in each grain.



Fig.5. Typical appearance of an interface in M40/A356 showing the highly twinned secondary phase, Si, covering the fiber surface.



Fig.6. Interface in as-cast M40/Al-5%Mg showing an essentially single phase matrix and a relatively large amount of carbides (arrow marked).

Fig.7. Regularly spaced second phase (Al_3MgZn_3) particles at the interface and secondary precipitates in as-cast M40/Al-3%Mg-2%Zn.

of the carbides seen in all the composites indicate that they are Al_4C_3. Figure 8 shows an Al_4C_3 particle in lattice imaging conditions. However, a substantial number of similarly sized particles arising from the aging treatments was present in addition to the fine carbides in many cases.

The above T.E.M. observations lead to the conclusion that, apart from the formation of carbides, there is no other chemical reaction between the M40 fibers and the various matrices. The varying amounts of carbides in the alloy matrices and the presence of second phase at the interface suggests that Si restricts carbide formation at the interface.

DISCUSSION

Table 1 clearly shows the effect of manufacturing parameters on the final mechanical properties of C/Al composites. These variations in the mechanical properties are a consequence of the dependence of fiber-matrix interface properties on the manufacturing parameters. Since the failure mode in the tensile tests was by shear failure along the tows, it is clear that the shear strength of the interface in these composites is not large enough to load the fibers to their ultimate tensile strengths. Thus, these composites must lie on the left half of Fig.1. Improving the fiber-matrix interface shear strength in these composites to the point where the fibers are loaded to their maximum strength would lead to a composite with higher tensile strength.

T.E.M. observations reveal the presence of varying amounts of aluminum carbides in these composites, however, there is no other chemical reaction seen at the interface which suggests that the interface in these C/Al composites is mostly a mechanical interface. In a mechanical type of interface the load transfer in the axial direction across the interface occurs due to friction, and for a fixed fiber surface, the magnitude of this frictional force depends on the transverse compressive residual stresses. If the transverse residual stresses are high the frictional load transfer is better than the case where these compressive residual stresses are low.

The disparate thermal expansion properties of the fiber and matrices coupled with the huge difference in elastic modulii ($E_f/E_m \geq 100$) lead to the build up of residual stresses during fabrication (11,12). Thus, a rationale for the tensile data presented in Table 1 is that the micro-residual stresses at individual fibers increase with the decrease in preform temperature, leading to a higher interfacial shear strength, whereas, heat treatment of the matrix alloys leads to the decrease in

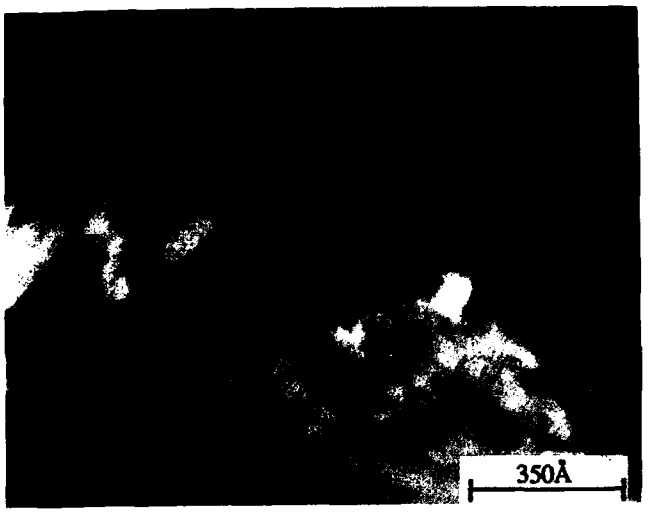


Fig.8. (111) planes in Al4C3 with an inter-planar spacing of 8.2Å latticed imaged in M40/Al-5%Mg.

compressive residual stresses at the interface. Interfacial shear tests to measure the interface shear strength are to be carried out using one of the following methods: the fiber indentation or push-out, single fiber pull-out or the double notched specimen of Fig.2. Residual stress determination at the micro- and macro- level using an X-ray technique is to be carried out in the second stage of this research program to confirm the above hypothesis.

CONCLUSION

This initial phase of a detailed research program at th University of Delaware has shown that the mechanical properties of a continuous carbon fiber aluminum composite depend on the interface properties and that the interface properties in turn depend on the manufacturing parameters. In general, the interface shear strength in continuous carbon fiber aluminum composites is weak, hence, there is an inefficient transfer of load to the fibers resulting in weaker composite. T.E.M. observations suggest that the interface in these composites is mostly a mechanical interface as defined in the introduction. Consequently, the efficiency of load transfer in a mechanical type of interface depends on the value of the compressive residual stresses, which may be dependent on the manufacturing parameters.

ACKNOWLEDGEMENTS

The authors are grateful to Honda R. & D. Co. Ltd., Wako-Shi, Japan for the financial support for this work. Use of the facilities of the University of Delaware Engineering Research Center for Composites Manufacturing Science and Engineering is also gratefully acknowledged.

REFERENCES

1)G.A. Cooper and A. Kelly, "Role of the Interface in the Fracture of Fiber-Composite Materials," pp. 90-106 in Interfaces in Composites, ASTM STP 452, American Society for Testing Materials, 1969.

2)S. Ochiai and Y. Murakami, "Tensile Strength of Composites with Brittle Reaction Zones at Interfaces," Journal of Materials Science 14 (1979) pp. 831-840.

3)M.K. Shoshorov, L.M. Ustinov, A.M. Zirlin, V.I. Olefirenko and L.V. Vinogradov, "Brittle Interface Layers and the Tensile Strength of Metal-Fibre Composites," Journal of Materials Science 14 (1979) pp.1850-1861.

4) A.P. Diwanji, Master's Thesis, Materials Science Program, University of Delaware, 1987.

5)Y. Murakami, K. Nakao, A. Shindo, K. Honjo and S. Ochiai, "Effect of Interfacial Conditions on the Tensile Strength of Carbon Fiber-6061 Aluminum Alloy Composites," in Proc. Conf. International Conference on Composites Structures, Eds. T.T. Loo and C.T. Sun, Beijing 1987 pp.1045-1050

6)B.K. Prasad, T.K. Dan and P.K. Rohatgi, "Pressure induced improvement in interfacial bonding between graphite and aluminum in graphitic-aluminum particle composites," Journal of Materials Science Letters, 6 (1987) pp. 1076-1078.

7)A. Shindo, "Chemical Property of Carbon Fiber Surface and Interfacial Compatibility of Composites," Composite Interfaces, eds. H. Ishida and J.L. Koenig, Elsevier Science Publishing Co., Inc. 1986. pp.93-100.

8)K. Honjo and A. Shindo, "Interfacial Behavior of Aluminum Matrix Composites Reinforced with Ceramics-Coated Carbon Fibers," Composite Interfaces, eds. H. Ishida and J.L. Koenig, Elsevier Science Publishing Co., Inc. 1986. pp. 101-107.

9)Y. Kimura, Y. Mishima, S. Umekawa and T. Suzuki, "Compatibility between Carbon Fibre and Binary Aluminium Alloys," Journal of Materials Science 19 (1984) pp. 3107-3114.

10)"In Plane Shear Strength of Reinforced Plastics," ASTM Standard D3846-79.

11)J.A Nairn and P. Zoller, "Matrix Solidification and the Resulting Residual Thermal Stresses in Composites," Journal of Materials Science 20 (1985) pp. 355-367.

12)H.T. Hahn and J.N. Pagaro, "Curing Sresses in Composite Laminates," Journal of Composite Materials, Vol. 9, Jan 1975, pp.91-101.

THE STRENGTHENING OF PM VS. MELTED SiC/Al COMPOSITES

R. J. Arsenault, S. B. Wu
Engineering Materials Group
University of Maryland
College Park, Maryland 20742-2111 USA

ABSTRACT

Discontinuous metal matrix composites can be produced by several different techniques, and it has been suggested that the reason for increased strength of powder metallurgical (PM) produced composites is that during processing a high dislocation density and a small subgrain size are introduced and the reinforcement prevents their removal. An investigation was undertaken to compare PM vs. melted SiC/Al composites, and one conclusion which can be obtained from the results is that the PM processing does not account for the strengthening.

THE CONTROVERSY CONCERNING the strengthening mechanism of discontinuous metal matrix composites still exists. It has been suggested that the reason for the increased strength of discontinuous metal matrix composites is due to the powder metallurgical (PM) processing which is used in the production of most of the discontinuous metal matrix composites (1). The presumed reason for this assumption is that during the PM processing a high dislocation density and a small sub-grain size could be introduced, and recrystallization is prevented by the reinforcement, and therefore, this accounts for the high strength of the PM-produced discontinuous metal matrix composites. Implicitly, it was assumed by Nardone and Prewo (1) that if the composites were made by melting the matrix, the high dislocation density and the small sub-grain size would not exist and that the strength of melted composites would be less than that of PM composites. This actually assumes that the high dislocation density and small sub-grain size are not due to the difference in thermal coefficient of expansion between the SiC and Al (2-5).

There have been a few investigations in which a comparison was undertaken of PM and melted discontinuous metal matrix composites. Kloucek and Singer (6) found that melt infiltrated SiC whisker composites were weaker than PM produced composites. However, they observed significant segregation of the SiC whiskers in the melt infiltrated composite. Laiw and Gungor (7) have compared melted and PM produced SiC/Al composites, and found the melted composite approximately 25% weaker than PM produced composite. As in the other investigation (6) there was significant segregation in the melted produced composite, and secondly, the particle size used in melt produced composites was 2.5 times larger than that in the PM composite.

In order to make a valid comparison of melted vs. PM produced composites and to check the supposition of Nardone and Prewo (1), it is necessary that the reinforcement be of the same size (and obviously same volume fraction) and have the same distribution, i.e. no segregation of the reinforcement. Also, the density of voids in both composites should be the same.

Along with the controversy of PM vs. melted composites there are other additional aspects of the strengthening controversy. Of the many, two are related to the effect of particle size on strengthening and particle size on dislocation density. An investigation was undertaken in order to compare the strength of PM vs. melted SiC/Al composites in which the reinforcement size and distribution was the same.

EXPERIMENTAL PROCEDURE

The production of discontinuous metal matrix composites with a melted matrix by casting generally results in the segregation of the SiC and the formation of voids. After numerous attempts of producing

*This research was supported under a grant from the Office of Naval Research (N00014-85-K-0007).

SiC/Al composites by a casting procedure, this procedure was abandoned because a uniform distribution of SiC and void-free conditions were not obtained. It was found that a reasonable distribution and a reasonable void density could be obtained by starting with a material which was initially produced by PM processing and then melting this material in small quantities under controlled conditions. Extruded or as-pressed rods of the PM material, (12.5 μm dia. by 100 μm long) were placed in graphite boats in a vacuum furnace and the temperature was slowly increased to ~ 848 K. The rods were held at this temperature for 24 hours to remove as much hydrogen as possible from the rods prior to melting, and thereby reducing as much as possible the probability that hydrogen would produce voids in the melted composite. Finally, the temperature was increased to 948 or 1023 K for 0.5 hours, and then the rods were slowly cooled to room temperature under vacuum.

Commercial purity Al (1100 grade) was chosen as the matrix in order to minimize the reaction between molten Al and SiC. If an alloy, e.g. 6061 Al alloy is used, then the SiC has to be "coated "* and this induced other complications. Therefore, by using 1100 Al, the coating can be elimated..

The above described procedure was found to be unacceptable when larger particle size (70 - 100 μm) billets which were made by blending SiC with Al powder were extruded. The SiC particles were fractured into very small particles. Therefore, an alternate technique was investigated. The blended powder was initially vacuum-hot composted at 823 to 873 K at a pressure of ~ 28 MPa. The reason for the low pressure was to reduce the probability of fracturing the SiC particles. Then the composted rod (13 mm in dia.) was melted in a horizontal rotating mold. The mold was rotated at ~ 10 rpm.

After melting, the rods were machined into tensile specimens in the same configuration as described elsewhere (2). The same machining procedure was used for the PM rods. After machining, all of the samples were annealed at 803 K in air for 12 hours and furnace cooled. The samples were then tested in the INSTRON testing machine at a strain rate of 5 $x10^{-2}$ per minute. After tensile testing, metallographic observations of longitudinal and transverse sections were conducted to determine the distribution of the SiC and the void density of the PM vs. the melted composites. Also, a TEM investigation was undertaken to determine if there were differences in dislocation densities in the PM and melted composites.

EXPERIMENTAL RESULTS

As stated in the introduction, in order to make a valid comparison between melted and PM composites the size and distribution of the reinforcement should be the same in the both cases, along with the same void density. The degree that these conditions were satisfied depended upon the particular composite. In the case of whisker and spherical SiC/Al composites, there may be a slight tendency for segregation of SiC in the melted composite (e.g.. comparing Fig. 1a and Fig. 1b), but the major difference was the presence of a few large voids in the melted composite (Fig. 1b). If we consider the 250 μm SiC particulate reinforced composite,- grain boundaries are evident in the melted composite (Fig. 2a and Fig. 2b). The segregation of SiC particulate is readily evident in the melted 250 μm SiC/Al composite (comparing Fig 2a

The following is a list of the various different matrices and composites tested.

1. 0% ⟶ Matrix (1100 Al) that was produced in the same manner as the whisker and spherical SiC composite, but containing zero volume fraction of whiskers.
2. 0% P ⟶ Matrix (1100 Al) that was produced in the same manner as the particulate SiC composite, but containing zero volume fraction of 250 μm particulate.
3. 20% 250 μm whisker ⟶ Twenty volume percent SiC particulate 250 μm dia. in an 1100 Al matrix.
4. 20% 0.5 μm whisker ⟶ Twenty volume per cent SiC whisker 0.5 μm dia. (average) and ~ 2-3 μm long in an 1100 matrix.
5. 20% 0.5 μm spherical ⟶ Twenty volume percent SiC spherical particles 0.5 μm in an 1100 Al matrix.

*DURAL process which is proprietary.

and Fig 2b). A TEM investigation was also undertaken to determine if there were any differences in the dislocation densities between the melted and the PM composites. In the case of the 250 μm SiC particulate composite, the dislocation density and arrangement around the SiC particulate was the same in the PM and melted composites. However, the average density (the density of dislocation averaged over the entire volume of the matrix) of the melted composite is lower than the PM composite, and this is due to the segregation of the SiC particulates. If the whisker and spherical SiC/Al composites are considered, then there is no difference in the dislocation densities, locally or on average between the melted and PM composite (Fig. 3a and 3b.)

As expected, there is correlation between the microstructural differences between the PM and melted composites and differences in strength between the PM and melted composites. In the smaller size SiC reinforced Al composite (spherical and whisker SiC) there was only a small difference between the microstructure of the PM and melted composite and there is a small, i.e. 3%, difference in the strength (Table I). If we consider the 250 μm particulate



Fig. 1 - An optical micrograph of 20 V% spherical (0.5 μm dia.) SiC in an 1100 Al PM composite.



Fig. 1b - An optical micrograph of 20 V% spherical (0.5 μm dia.) in an 1100 Al matrix melted composite.

Table I
The Yield and Ultimate Strengthof Melted and PM SiC/Al

Condition & Volume Fraction	SiC Morphology	Yield Strength 0.2% MPa	Ultimate Strength MPa
0% P PM		37.3	85.6
0% P Melted		25.6	93.2
0% W PM		31.6	68.4
0% W Melted		21.3	65.6
20% PM	250 μm particle	56.0	86.9
20% Melted	250 μm particle	47.9	71.9
20% PM	0.5 μm dia. whisker	167.0	298.8
20% Melted	0.5 μm dia. whisker	151.6	302.4
20% PM	0.5 μm dia. spherical	172.6	250.5
20% Melted	0.5 μm dia. spherical	167.1	237.1



Fig. 2a - An optical micrograph of 20 V% 250 μm particulate SiC in an 1100 Al matrix PM composite.



Fig. 2b - An optical micrograph of 20 V% 250 μm particulate SiC in an 1100 Al matrix melted composite.

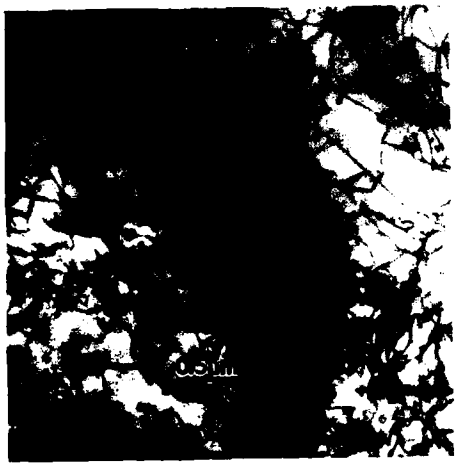




Fig. 3 - Transmission electron micrographs from 20 V% whisker SiC-1100 Al matrix composites. Fig. 3a is from the PM composite and Fig. 3b is from the melted composite.

SiC/Al composite, then the melted SiC/Al composite is 15% weaker then the PM composite.

The largest difference in strength occurs upon melting the 0 V% alloy. In this case, the yield strength of the 0 V% melted alloy is 30% less than the 0 V% PM alloy. Finally, the difference in yield strength of the composite and the matrix (0 V% alloy) $\Delta \sigma_y = \sigma_y$ composite - σ_y matrix. Then, $\Delta \sigma_y$ is larger for the melted composites as compared to the PM composites, e.g.. in the case of the SiC spherical composite, $\Delta \sigma_y$ for the melted case is 145.8 MPa whereas in the PM case, $\Delta \sigma_y = 141.0$ MPa.

It was found that by rotation of the mold at speeds at which the centrifugal force was small compared to that gravitational force that a reasonable distribution of SiC particulates could be maintained. In other words, the degree of segregation was reduced due to the rotation.

DISCUSSION

If the size, volume fraction and distribution of the reinforcement in both powder metallurgical (PM) and melted composites are the same, then the strengths of the PM and melt produced composites are the same. The observations of differences in the strength between PM and melted SiC/Al composites are due to segregation in the melted composite and the increased void density of the melted vs. PM composites.

The present results also indicate that the dislocation arrangement and density are the same in the PM and melted composites if the size, volume fraction and distribution are the same in the PM and the melted composites. This result would be expected if a good bond existed between the SiC and Al in both the PM and melted composites, for the presence of dislocation in these composites is due to the difference in thermal coefficient of expansion between the SiC and Al (2-5).

It is suspected that the lower strength of the "coated" SiC/Al melted composites (7-8) as compared to a comparable PM composite is due to lack of bonding, for the number of dislocations generated, i.e. the magnitude of the plastic zone about SiC particles, is significantly reduced in the "coated" SiC/Al composites. As a result of the reduction in dislocation generation the strength of these coated SiC/Al melted composites is lower than the comparable PM composites. In the investigation by Kloucek and Singer (6), they observed a difference in strength between liquid metal infiltrated SiC whisker and PM SiC whisker Al matrix composites. The reduced strength of the melted composite was due to the distribution, i.e. segregation of the SiC whiskers.

CONCLUSIONS

There is no difference in strength between the PM and melted discontinuous metal matrix composites if the comparison is made between composites that are comparable; in other words, if the bonding between the reinforcement and matrix is the same, and with the same size, distribution and volume fraction of the reinforcement.

ACKNOWLEDGEMENTS

The authors wish to acknowledge the assistance of C. R. Feng and L. Wang with the TEM investigations. Also, the authors acknowledge the continued support of Dr. S. Fishman of the Office of Naval Research.

REFERENCES

1. Nardone, V. and C. Prewo, Ninth Annual Discontinuous Metal Matrix Composite Report, (Jan 1987), to be published.
2. Arsenault, R. J., Met. Sci. & Eng., 64, 171 (1984).
3. Arsenault, R. J. and N. Shi, Mat. Sci. & Eng. 81, 175 (1986).
4. Arsenault, R. J. and B. Wu, Mat. Sci. & Eng. 96, 77 (1987).
5. Vogelsang, M., R. J. Arsenault and R. M. Fisher, Mat. Trans., 17A, 379 (1986).
6. Kloucek, F. and R. F. Singer, SAMPE Proc., 31, 1701 (1986).
7. Laiw, P. and M. Gungor, Tenth Annual Discontinuous Metal Matrix Composites Report (Jan. 1988) to be published.
8. Garrett, R.,Tenth Annual Discontinuous Metal Matrix Composites Report (Jan 1988) to be published.

DENDRITIC SEGREGATION IN PARTICLE-REINFORCED CAST ALUMINUM COMPOSITES

John W. McCoy, Franklin E. Wawner
Materials Science Department
School of Engineering and Applied Science
University of Virginia, Charlottesville, Virginia 22901 USA

Abstract

Dendritic segregation of particles is a serious problem in the casting of discontinuously reinforced aluminum matrix composites. Even though reinforcing particles may have been ...etted and uniformly dispersed in a liquid metal, they may become segregated into dendrite interstices during solidification. In some cases, this segregation causes severe agglomeration and interparticle contact, but in others, it is not observed at all. The factors believed to influence this effect are the dendrite arm spacing of the matrix (proportional to the dendrite growth rate), the size of the particles, the relative thermal conductivities of the matrix and particles, and the difference in contact angles between a particle/liquid and a particle/solid interface.

In this study, a set of experiments was performed to determine what combinations of these factors produce this effect. A matrix alloy of Al-3Mg was used in combination with particles of SiC, B_4C, TiB_2, Al_2O_3, and ZrB_2. Particle size was varied between 3 and 25 microns. A mold was designed which produced a range of secondary DAS between 5 and 50 microns. The composites cast in this mold were sectioned, polished and photographed in an SEM. The photographs were digitized into a computer, and the inter-particle spacings were statistically analyzed. The results indicate wide variations in segregation behavior among different types of particles, probably due to differences in particle/solid contact angle. Segregation is most severe at the lower end of the particle size range studied, and at the upper end of the DAS range studied.

During the course of experimentation on the compocasting of 3 micron silicon carbide/aluminum castings, particle distributions like that shown in figure 1 were repeatedly encountered. This was at first attributed to poor dispersal of particles in the liquid metal due to inadequate agitation or to agglomeration. Soon, however, it was recognized that these distributions possesed a spatial periodicity that could not be explained in this way. One can notice a spacing of about 25 microns that occurs repeatedly throughout figure 1. A metallographic analysis of this casting confirmed that 25 microns was also the average secondary dendrite arm spacing. This made it clear that the non-uniform distribution of particles was produced during solidification of the composite and not during mixing. Evidently, particles which may have been quite uniformly dispersed in the liquid were being pushed by the growing dendrite arms into the last-frozen regions during solidification.

This type of uneven distribution of particles does not provide adequate composite strengthening and is unacceptable for any engineering material. Anyone concerned with the casting of particle-reinforced composites must be aware of the conditions which lead to this dendritic segregation so that it can be avoided. It would be useful to the advancement of composites casting technology to establish the relative importance of solidification rate, contact angle, thermal conductivity, alloy composition, and particle radius in defining the limits of castable composite systems. This was the goal of this study.

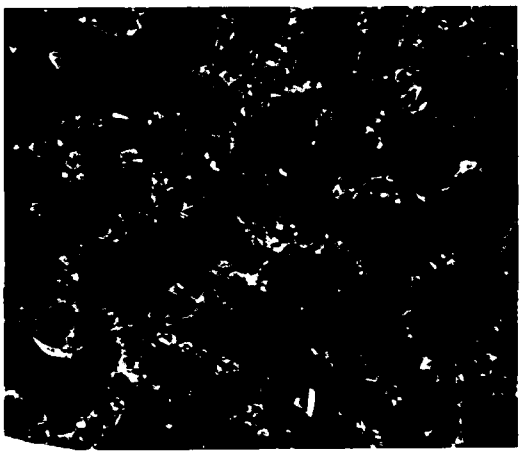


Figure 1 - An example of dendritic segregation in 3μm SiC reinforced Al.

Background

When a reinforcing particle which is dispersed in liquid metal encounters a growing solidification front, it may be either rejected and pushed along ahead of the advancing front, or it may adhere to the solid and be engulfed by it, remaining stationary as the solidification front sweeps past it through the matrix. In the case of cast metal-matrix composites, this solidification front will be in the form of a growing dendrite arm which is lengthening and swelling simultaneously. If particle pushing occurs, then the reinforcing phase will become segregated into the last-frozen, interdendritic regions of the matrix.

The interaction between a particle and a solidification interface has been discussed quite extensively in the scientific literature for the case of a planar solidification front. To date, however, only a few sketchy empirical observations[1] and no theoretical discussion have yet been published on the subject of particle pushing during dendritic solidification. The two phenomena undoubtedly share the same basic principles, and the simpler case of the planar solidification front is the logical starting point for studying the latter. Numerous theoretical treatments of this subject have appeared in the literature over the past twenty-five years.[1-11] They have established that the following factors all play a role in determining V_c, the critical velocity for engulfment.

surface energy - This is the most important factor influencing rejection versus engulfment[2,3]. If $\gamma_{ps} > \gamma_{PL} + \gamma_{LS}$ then there will be a disjoining pressure which will push the particle ahead of the advancing solidification front unless the velocity is high enough that viscous drag forces overcome the disjoining force. The disjoining pressure is proportional to $\gamma_{ps}-(\gamma_{PL}-\gamma_{LS})$.[4]

particle radius - Small particles can be pushed to higher velocities before being engulfed than can larger particles of the same material. This is because of the higher viscous drag force on the larger particle.[5]

thermal conductivity - If the thermal conductivity of a particle is lower than that of the surrounding liquid, the temperature gradient around it will be altered so that the particle shields the front behind it from some of the heat flow. This produces a cooler spot in the front which leads to faster growth. A bump will thus be created in the front behind the poorly conductive particle. The viscous drag exerted on this particle will be reduced compared to a particle pushed by a planar front or by a concave depression in a planar front. The lower viscous drag leads to a higher rejection velocity. Conversely, if the conductivity of the particle is higher than that of the surrounding liquid, a depression will form in the front beneath it and it will be more easily trapped.[6,7]

heat diffusivity - This quantity, $\sqrt{\lambda c_p \rho}$, is proposed by Surappa and Rohatgi[8] as a criterion for rejection versus engulfment. No theoretical basis for this suggestion has yet been published.

viscosity - A high viscosity liquid will exert a greater viscous drag force on a particle being pushed by a solidification front. This will promote trapping at low velocities[9].

concentration of solutes - A dissolved impurity in the liquid will have a melting point lowering effect, and will be rejected by the advancing front. The impurity will be concentrated in the gap between particle and front and cause a local decrease in melting point. This will slow front growth and make the depression deeper, leading to easier trapping. [10]

These concepts were developed only for the case of planar solidification fronts. It is not clear which principles will carry over to dendritic solidification and which may not. Since dendritic growth will involve faster growth velocities and higher solute concentrations, one might expect that trapping would be more likely. On the other hand, the convex shape of the soldification front during dendrite growth might make particle pushing easier because of easier feeding of the parent melt to the front behind the particle.

Experimental Procedure

A series of nine composite castings was prepared in order to study the effects of particle size, particle composition, and solidification rate on the phenomenon of dendritic segregation. The target matrix composition was Al - 3.0%Mg - .004%Be for all of these castings. The actual composition fluctuated somewhat because of the loss of magnesium during long periods of melt agitation. The compocasting process for producing these composites has been described elsewhere.[11]

These composites were cast into a mold which was water-cooled on the bottom and insulated on the sides. This produced a range of solidification times which increased from bottom to top. Within a single vertical section of this casting, one could observe the particle distribution as a function of dendrite arm spacing, which varied linearly with vertical position.

Quantitative metallographic measurements yielded interparticle spacing data at regular intervals along this vertical section. The analysis of these spacing distributions led to a criterion for quantifying the degree of segregation. This makes it possible to graphically represent the degree of segregation as a function of DAS, particle size, or other parameters.

Materials The matrix alloys were prepared from commercial "pure" aluminum by adding carefully weighed quantities of Al-5%Be master alloy and pure magnesium immediately before adding the reinforcement. The rationale for the Al-3Mg-.004Be composition is as follows. Earlier experiments with several common alloying elements showed that magnesium was the only one which markedly improved wetting without causing other problems[11]. Less than two percent of magnesium in the alloy proved to be inadequate to provide complete wetting of some of the reinforcements. Since very tight control of the final magnesium concentration was not possible given the small volume and the long agitation time, the concentration needed to be well above this perceived minimum, and 3% proved to be satisfactory. Beryllium was added in the concentration recommmended by Whitaker[12] to produce a thin, protective oxide layer to reduce the oxidation rate of the magnesium.

The reinforcing particles came from numerous sources which are listed in table 1.

Table 1 - Reinforcing Powders

Material	Size (μm)	Source
Aluminum Oxide	3 5 12.5 17.5 25	A. Buehler Ltd.
Silicon Carbide	4.5	Superior Graphite Inc.
Titanium Diboride	6	Union Carbide
Zirconium Diboride	5	American Matrix Inc.
Boron Carbide	5	Advanced Refractory Technologies Inc.

This combination of powders makes it possible to produce one set of five castings holding composition constant (Al_2O_3) while varying size, and another set of five holding size constant (5μm) while varying composition.

Measurement of Dendrite Spacings The cooling characteristics of the insulated, bottom-chilled mold were determined by making an un-reinforced reference casting of Al-3Mg-.004Be at the same carefully controlled 700C pouring temperature used for the composites. The casting was water-quenched immediately after solidification was complete to minimize homogenization of the magnesium. A vertical section was cut, polished and etched. A potassium permanganate etch was used to reveal the dendrite structure.

Reference lines were inscribed on the specimen parallel to the bottom surface at 5mm intervals to indicate distance away from the chill plate. Optical micrographs were taken directly beneath each reference line near the center of the section. Secondary dendrite arm spacing measurements were made from the micrographs using the oriented line intercept method[13]. The DAS was found to vary linearly with vertical distance above the chill plate, ranging from about 5 microns at a distance of 5mm above the bottom to about 50 microns at 50mm above the bottom. The relationship between dendrite spacing and position in the casting was firmly established so that new DAS measurements were not needed for each casting.

Measurement of Inter-Particle Spacings The composite castings were sectioned, polished, and scribed in the same manner as the DAS specimen. The polished section was put in the SEM, and two micrographs were taken at each of the 5mm reference lines. An enlargement of each electron micrograph was mounted on a computer digitizing panel, a grid was laid over it, and the particle and matrix intercept lengths were digitized into the computer according to the conventions of lineal analysis[14]. For each micrograph, the computer recorded a file containing each matrix intercept length and each particle intercept length crossed by a grid line. On average, the grid would intercept 350 particles per micrograph. A number of computer programs were written to analyze these lists of spacing data in different ways. A more detailed explanation of this measurement method can be found in the dissertation of McCoy[15].

Results and Discussion

The series of SEM micrographs in figure 2 was made from a casting containing 3 micron Al_2O_3 particles. There is one micrograph for every 10mm interval above the chill plate. A reference bar next to each photograph indicates the dendrite arm spacing expected at that position in the casting. Upon inspection of these photos, one will observe that there are particle-free expanses in the matrix of approximately the same width as the reference bars. this effect is most prominent for the largest arm spacings. One may also observe that the particles are tightly clustered into strings around the peripheries of these bare expanses. There is quite a lot of direct inter-particle contact in these clustered strings, especially towards the top of the casting. This particular casting is the most extreme example of dendritic segregation among the series of nine composites that were solidified in this mold.

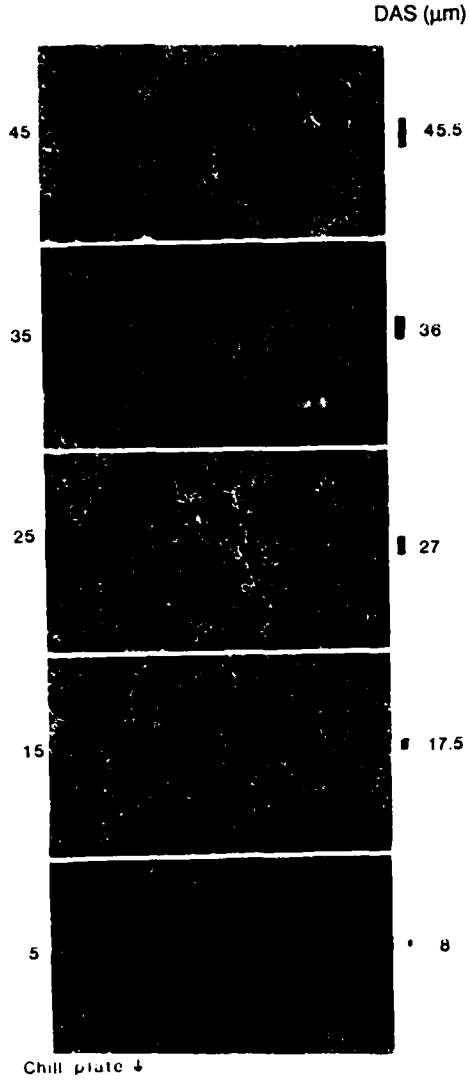


Figure 2 - SEM micrographs of segregation in a casting containing 3μm alumina particles shown at increasing distances from the chill plate.

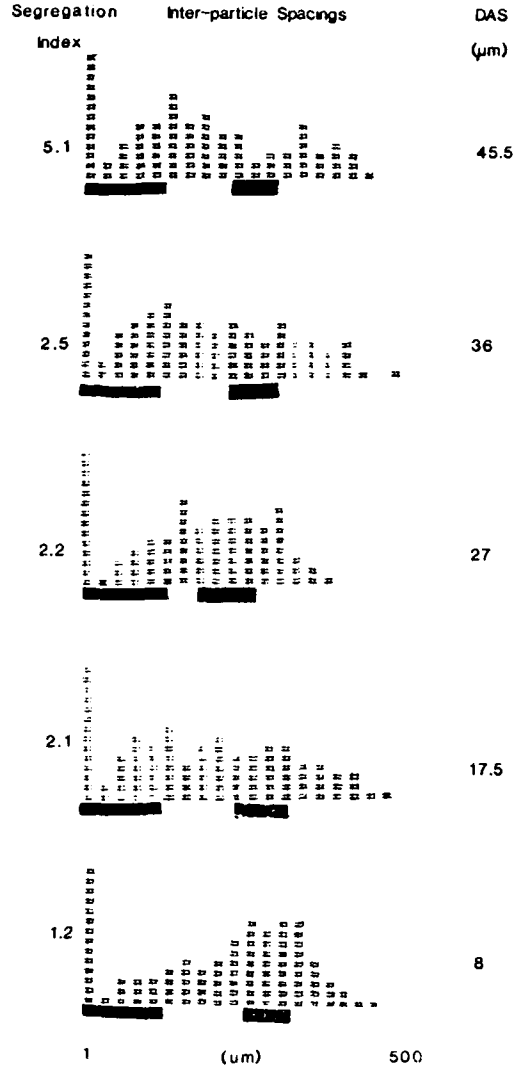


Figure 3 - Histograms of the distribution of inter-particle spacings at different locations in the casting.

Quantifying Segregation One of the first goals of this work was to develop a means of quantifying the amount of dendritic segregation in a particular micrograph. What is needed is a dimensionless segregation index which would be calculated from the list of inter-particle line intercept distances that are collected by digitizing each photograph into the computer. Ideally, such an index would equal zero when the particle distribution was perfectly uniform (not the same as a *random* distribution), and should increase as the inter-particle spacings are displaced from lengths which correspond to uniform spacing.

A formula was found empirically which combines two observations about how the distribution changes as segregation increases. This formula is the ratio of the number of very closely spaced particles, $N_{<D}$, to the number of particles spaced at lengths near the mean free path, N_{λ}.

$$\frac{N_{<D}}{N_{\lambda}}$$

The close spacings were counted as everything smaller than the mean particle intercept length. This is an arbitrary cutoff point approximately equal to the average particle diameter. It would be a mathematically complex task to actually calculate the average diameter of irregularly shaped particles based on line-intercept data. Using particle size as a reference length for defining closeness of particle spacing makes the criterion independent of scale. That is, any photograph of a discontinuous phase dispersed in a continuous phase could be digitized and analyzed by this method without ever knowing the size of the particles or the magnification of the photograph. Both the mean particle intercept length and the mean free path are calculated individually for each micrograph. A width factor, α, was used to define a window around the mean free path from λ/α to $\lambda\alpha$. A value of α=1.6 was empirically determined to produce a segregation index with a minimum of scatter.

The segregation index is depicted graphically in figure 3. Under each histogram are two black bars. The left bar is centered on the mean free path and extends from λ/α to $\lambda\alpha$. The right bar extends from a length equal to the mean particle intercept length down to the bottom of the histogram. The number to the left of each histogram is the quotient of the number of counts over the left bar divided by the number of counts over the right bar. By examining these histograms, one can see that at the bottom of the casting where there is very little segregation, the distribution of spacings is evenly centered about the mean free distance. As one moves up the casting, the distribution becomes almost bimodul, with a gap centered at the mean free distance. This corresponds to particles being pushed away from their natural positions by the intrusion of dendrites.

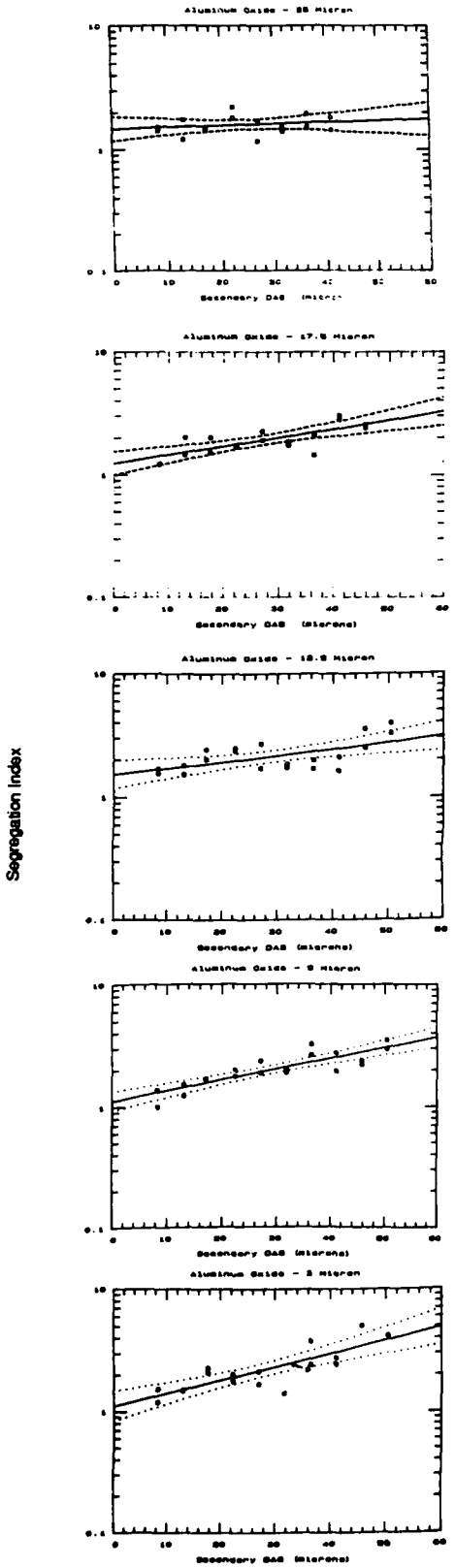


Figure 4 - Segregation index versus dendrite arm spacing for 5 castings of different size alumina particles

This segregation index could theoretically vary between zero and infinity. If particles were perfectly uniform in their distribution, and the volume fraction was low enough that the mean free path divided by α is larger than the average particle intercept length, then there would be no matrix intercept lengths falling into $N_{<D}$, so the segregation index would be zero. Conversely, if all the particles were clustered into a single contiguous mass surrounded by an expanse of matrix, then all the spacings would fall into $N_{<D}$ and none would fall into N_{λ}, so the index would go to infinity.

Diameter Dependence The first test of this segregation index was to apply it to the data collected from digitizing micrographs of the alumina particle composites of five different diameters. Figure 4 shows the segregation index plotted against dendrite arm spacing for the five alumina particle composites. Each point on a graph represents the segregation index computed from one micrograph. Each micrograph generated approximately 350 matrix intercepts (interparticle spacing lengths). Two micrographs were taken at every 5mm interval from 5mm to 50 mm above the chill plate. A total of 20 micrographs and about 7000 particles are represented by each graph. The points are fitted to a line of the form $y=e^{(a+bx)}$ which was chosen after comparing equations of several different types to the data. There is considerable scatter in the fit of the data to the lines, but this is consistent with the photographs which also show significant variability. One may notice from these plots that there is no evidence of a discontinuity in the slope which might be interpreted as indicating a critical growth velocity above which particles are no longer pushed.

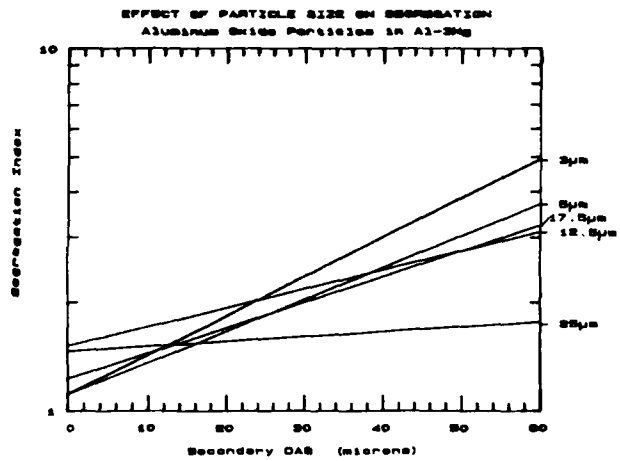


Figure 5a - Fitted lines from figure 5 plotted together to illustrate the dependence of segregation on particle size.

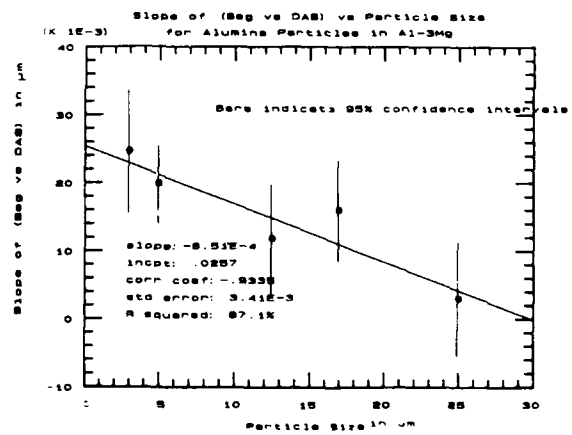


Figure 5b - The slopes of the lines from figure 6a plotted against diameter.

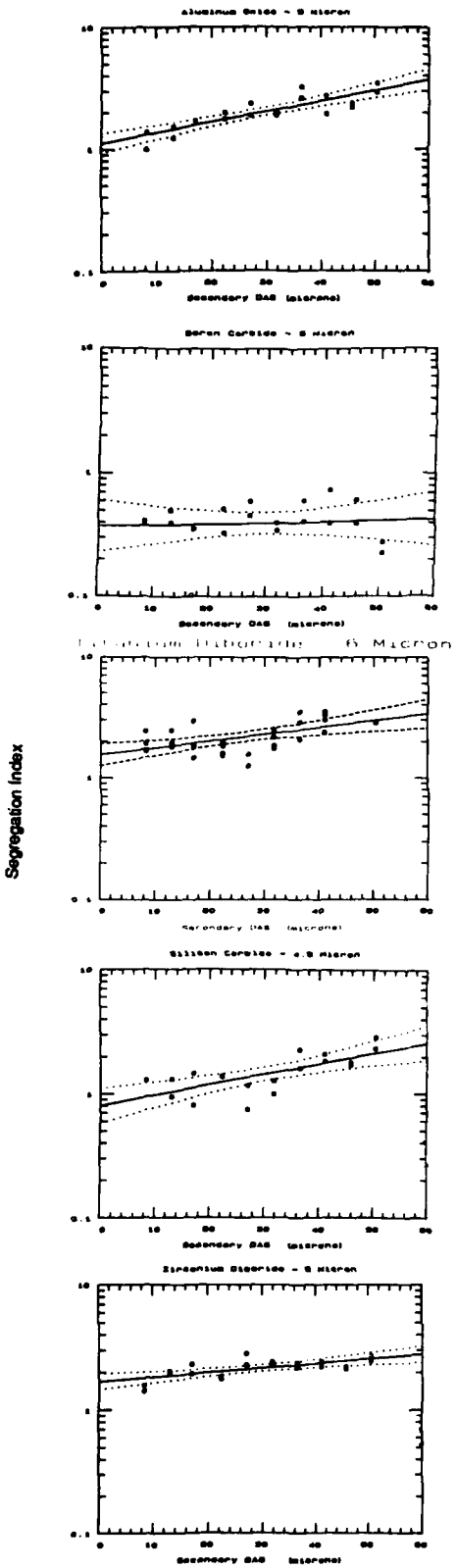


Figure 6 - Segregation index versus dendrite arm spacing for 5 micron particles of different compositions

The most salient feature of these plots is the clear dependence of slope on the particle diameter. This is more clear in figures 5a&b. In figure 5a, the fitted lines from the plots in figure 4 are plotted together on the same graph. The slope of these lines is probably the best indicator of dendritic segregation. The vertical displacement or intercept of the lines is an indicator of some other kind of non-uniformity in the particle distribution which is unrelated to dendrite growth. In 5b, the slope of each line is plotted against particle diameter. A straight line of the form y=a+bx fits the points reasonably well as shown.

Composition Dependence The set of experiments to be described next was aimed at separating out the effect of particle composition on dendritic segregation. To accomplish this, five different types of ceramic powders, all of approximately 5 micron diameter were used to prepare composites. The materials were Al_2O_3,B_4C, SiC, TiB_2, and ZrB_2. All of these particles were easily wetted and dispersed by the compocasting process. The boron carbide produced a mixture that was much more viscous than the others. It required the prodding of a ceramic rod to flow out of the crucible and into the mold when it was time for casting. Such a high viscosity was quite unexpected for a mixture which only contained five volume percent solids. The significance of this observation is not known. The boron carbide casting was also unusual in that it was more difficult to cut than any of the other composites. The castings were all sectioned with a rubber-bonded silicon carbide blade. The hardnesses of all the reinforcements were similar, so the difficulty in sawing might be due to higher interfacial strength between the boron carbide and its matrix.

The segregation behavior of each of the five castings is presented in figure 6. The fitted lines from these graphs are plotted together in figure 7. There is considerable variation in both the slope and the intercept of these lines. The most interesting feature of this comparison between materials is the dramatically lower position of the boron carbide. There is absolutely no indication of dendritic segregation at all in this casting. Evidently, as soon as a particle encounters a growing dendrite, it adheres to it, and the dendrite grows around the particle and captures it.

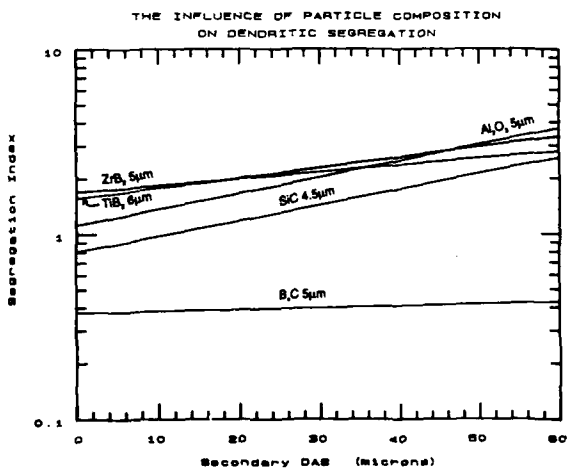


Figure 7 - Combined plot of segregation for reinforcing particles of five different compositions

By describing segregation in terms of slope and intercept, we essentially divide the effect into dendritic and non-dendritic components. The non-dendritic component probably arises from residual agglomeration from the mixing process. The dendritic component is the chief concern of this study. This component, the slope of the segregation versus DAS plot, is listed in table 2 next to the material it represents. The five different materials are listed in order of decreasing slope. The other columns of the table contain data about certain properties of the reinforcements which might influence the segregation behavior. It is clear from this table that neither thermal conductivity nor heat diffusivity bear any relationship to segregation. The wetting angle data was taken from sessile drop experiments where a drop of pure aluminum rests on a flat ceramic substrate of the material in question and the contact angle is measured by light projection. These particular data were taken at 900°K in an argon atmosphere. These values are so close together that they do not differentiate the materials very well in the first place, but no relationship between slope and angle appears to exist. Two columns list the magnesium and silicon concentrations measured for each sample. These measurements were made with an inductively coupled plasma spectrometer. It is unfortunate that the Mg composition varies so widely from the target composition of 3%, but this is probably inevitable in a melt that is agitated for 45 minutes. The data table shows no apparent correlation between magnesium concentration and slope. The silicon concentrations may be somewhat more informative, however. No silicon was deliberately added to the castings. Some silicon would be expected in the silicon carbide casting, but the high silicon content of the boron carbide casting is unexpected. Perhaps this is related to the unusually low segregation index of this composite.

	Slope b	Thermal Conductivity λ	Specific Heat c_p	Density ρ	Heat Diffusivity $\sqrt{\lambda c \rho}$	Silicon Concentration [Si]	Magnesium Concentration [Mg]	Wetting Angle θ
	x10⁻⁴ μm					wt %	wt %	degrees
Al_2O_3	20	0.021	0.29	3.9	0.15	.43	2.6	114
SiC	19	0.047	0.28	3.2	0.20	.73	3.1	112
TiB_2	13	0.16	0.25	4.4	0.43	.25	2.6	114
ZrB_2	8.4	0.15	0.15	6.0	0.36	.12	2.8	107
B_4C	2.2	0.035	0.41	2.5	0.19	1.6	2.7	118
Al (Eq)		0.23	0.62	2.4	0.58			

Table 2 - A listing of the reinforcing materials in order of decreasing segregation sensitivity and a comparison with properties that may influence this sensitivity. Wetting angle is measured against pure aluminum in argon.

Summary and Conclusions

The first conclusion that was reached using this method resulted from plotting the segregation index against dendrite arm spacing. These plots always resulted in a fit to a single continuous line. If there had been a discontinuity in this line, it might have indicated a critical arm spacing that represented a dividing line between particle pushing and particle entrapment during dendrite growth. It is still possible that such a critical DAS exists for every matrix/particle combination, but that it lies below the range of spacings which the mold used in this study would produce. This would probably place the critical DAS outside of the reach of conventional solidification technologies for many types of small particle reinforcement. It is also possible that there is no critical dendrite arm spacing for dendritic segregation. Perhaps certain ceramic particles will always be pushed by growing dendrites, no matter how fast their growth rate. In this case, the segregation might be kept to a harmless low level by solidifying as rapidly as possible in a water-cooled mold to create a dendrite arm spacing which is very small.

The clearest result from this study was in establishing the relationship between particle size and tendency for segregation. The slope of the segregation index versus DAS plot might be thought of as the dendritic segregation sensitivity. In figure 5b, one sees that this sensitivity is a linear function of particle diameter and has a negative slope. This piece of information should be useful to anyone trying to cast particle-reinforced composites.

It might seem reasonable to speculate that if the secondary dendrite arm spacing is smaller than the average particle diameter, then segregation would not happen. This turns out not to be the case. Evidently, if the secondary arms are too closely spaced for a particle to fit between, then the particle will be pushed by the entire dendrite.

The results from the composition dependence experiments are the most difficult to interpret. There are large differences in the segregation sensitivities of the different ceramic materials, but these differences do not correlate with any properties of the materials which would appear to be relevant and which can be obtained from reference books. There is one property which is extremely relevant, but which cannot be looked up or easily measured. That property is the free energy change of engulfment γ_{PS}-γ_{PL} . The literature on particle pushing by planar solidification fronts suggests that this is the overriding factor which determines rejection or engulfment [2]. The reason that contact angle was included in table 2 was that this quantity should bear some relationship to the free energy change. Unfortunately, sessile drop data is not very reliable. A single atomic monolayer on a solid surface can drastically alter its free energy. These experiments do succeed, however, in demonstrating that neither thermal conductivity nor heat diffusivity is a reliable predictor of segregation sensitivity.

The interaction of boron carbide particles with growing dendrites was completely different from the behavior observed in the other materials. The B_4C displayed absolutely no tendency to be pushed by the dendrites. This behavior may be related to silicon impurities in the powder which was evidenced by a 1.6% Si content that showed up when an alloy chemistry analysis was performed on the composite. The only boron carbide used in this study was manufactured by Advanced Refractory Technologies Inc.. It is not known whether other makes of boron carbide would exhibit the same behavior. Based on these observations, it appears that boron carbide ought to be more widely considered as a reinforcement for cast aluminum composites.

Acknowledgment This work was funded by the Virginia Center for Innovative Technologies.

References

1 C. E. Schevzov and F. Weinberg; *Metall Trans* 16B: 367 (1985).
2 S. N. Omenyi, A. W. Neumann, and C. J. van Oss; *J. Appl. Phys.* 52(2):789 (1981).
3 S. N. Omenyi and A. W. Neumann; *J. Appl. Phys.* 47(9):3956 (1976).
4 D. R. Uhlmann, B. Chalmers, and K. A. Jackson; *J. Appl. Phys.* 35(10):2988 (1964).
5 S. N. Omenyi, A. W. Neumann, W. W. Martin, G. M. Lespinard, and R. P. Smith; *J. Appl. Phys.* 52(2):796 (1981).
6 A. A. Chernov and A. M. Melnikova; *Sov. Phys. Cryst.* 10(6): 672 (1966).
7 A. M. Zubko, V. G. Lobanov, and V. V. Nikonova; *Sov. Phys. Cryst.* 18(2): 239 (1973).
8 M. K. Surappa and P. K. Rohatgi; *J Mat. Sci. Lett.* 16:562 (1981).
9 G. F. Bolling and J. Cissé; *J. Cryst. Growth* 10:56 (1971).
10 D. E. Temkin, A.A. Chernov, and A.M. Melnikova; *Sov. Phys. Cryst.* 22(1):13 (1977).
11 J. W. McCoy, C. C. Jones, and F. E. Wawner; *SAMPE Quart.* 19(2):37 (1988).
12 M. Whitaker; *J. Inst. Metals* 82:107 (1953).
13 K. J. Oswalt, and M. S. Misra; *Trans. Am. Foundrymens Soc.* 80-51:845-862 (1977).
14 Ervin E. Underwood; **Quantitative Stereology**, Addison-Wesley, Reading,Mass., (1970) pp 11 and 24-25 .
15 John W. McCoy, Ph.D. Dissertation, University of Virginia, May 1988.

MODIFICATION AND REFINEMENT OF SILICON IN CAST Al-Si-GRAPHITE PARTICLE COMPOSITES

S. Das, S. V. Prasad, T. K. Dan
Regional Research Laboratory
C.S.I.R., Bhopal, India

P. K. Rohatgi
Materials Department
University of Wisconsin-Milwaukee
Milwaukee, Wisconsin, USA

ABSTRACT

Modification of eutectic silicon and refinement of primary silicon in a hypereutectic Al-Si alloy-graphite particle composite produced by solidification processing was studied for various sequences of additions of elemental sodium and phosphorus, and graphite particles in the melt prior to casting. Metallographic examination revealed that best results were achieved when sodium was added prior to the addition of graphite particles. The usual aluminum halo structure present in the unmodified hypereutectic matrix alloy does not appear in the presence of 3 wt.% graphite. These modification and refinement effects resulted in a 14% increase in the tensile strength and a 23% decrease in the wear rate of the composite.

INTRODUCTION

ALUMINUM-SILICON ALLOYS are extensively used in internal combustion engines as pistons. Recently, there have been some attempts to utilize hypereutectic aluminum-silicon alloys as cylinder blocks in IC engines in place of cast iron, in order to reduce the weight of the piston-cylinder assembly [1,2]. However, aluminum-silicon alloys have a tendency to seize where they come in contact with similar material even under fairly satisfactory lubrication conditions. In order to overcome this problem, three techniques have been adopted. The first is an electrochemical technique [1,3], wherein the aluminum matrix of the hypereutectic alloy of the cylinder block is completely etched away leaving protrusions of primary/eutectic silicon. It has been reported [1,3] that the etched surfaces of hypereutectic aluminum-silicon alloy cylinder blocks provide better resistance to seizure. The second technique involves electroplating with harder materials [1]. The third technique involves dispersion of solid lubricants like graphite [4-6] in order to achieve the same objective. In recent years there has been considerable success in synthesizing various aluminum alloys with graphite particle dispersions by inexpensive foundry technique [7]. It has also been reported that graphite particle dispersion in aluminum alloys improves the machineability and damping capacity of the alloys [8]. Matrix microstructure also plays an equally important role in governing the physical and mechanical properties of the composite metals.

In hypereutectic aluminum-silicon alloys, silicon is present as large cuboids of primary silicon and needles or platelets of eutectic and near eutectic silicon. These morphologies of silicon largely control the mechanical strength and fracture behavior of these hypereutectic alloys. With a view to controlling the undesirable growth of eutectic and primary silicon, alloying elements as modifiers [9-12] and refiners [13,14] are added to the melt prior to the onset of solidification. It is well known that the additions of phosphorus and sodium in hypereutectic aluminum-silicon alloys [15] tend to refine the primary silicon and modify the eutectic silicon respectively. Mascre [16] has reported that sodium has a tendency to reduce the effectiveness of phosphorus, when both are added in the melt at the same time. In contrast, the work of Sugiyama et al. [17] has indicated that the simultaneous introduction of phosphorus and sodium promotes refinement and modification of primary and eutectic silicon respectively.

In earlier work, it has been shown that when graphite particles are added to hypoeutectic Al-Si alloys, primary α aluminum dendrites push the graphite into the last freezing interdendritic region. In addition, in eutectic alloys, the presence of graphite particles did partial modification of eutectic silicon; sodium could be added as a supplemental refiner of silicon in Al-Si-graphite alloys.

EXPERIMENTAL

MATERIALS PREPARATION - Five sets of experiments were conducted with various sequences of sodium, phosphorus and graphite additions to the matrix alloy. In the first heat about 10 Kg alloy was melted in a graphite crucible using a coke fired pit furnace. After degassing with dry nitrogen, the melt was cast in a 22 mm diameter mould. The second heat involved the addition of 0.028 wt.% P to the aluminum-silicon alloy melt, after it was degassed with dry nitrogen. In the third heat, 0.028 wt.% P was added to the melt after it was degassed. After a lapse of 5 minutes, 0.288 wt.% Na was added. In the fourth heat, phosphorus and sodium were added in the same sequence described in the third set and, after this, melt was stirred to create a vortex and 3 wt.% graphite particles were dispersed in the melt. In the fifth and final heat, 0.028 wt.% P was added after the melt was degassed. The melt was then stirred to create vortex and 3 wt.% graphite particles were dispersed in the melt. Just prior to casting, 0.028 wt.% Na was added. In all cases, the melt was cast in a 22 mm cast iron finger mould.

MATERIAL TESTING - The specimens were polished according to standard metallographic procedure, etched with Keller's reagent and examined using Leitz optical microscope. Tensile tests were carried out using an Instron machine at a cross head speed of 2 mm/min. Wear test was carried out using a Cameron-Plint pin-on-disc wear test apparatus. A sample, in the form of an 8 mm cylindrical pin, was held against a rotating EN25 steel disc (heat treated to a hardness of 32 RC), at an applied load of 53 N. Before commencement of the test, the disc was polished to a standard finish of 1 μm CLA. The disc was rotated at 800 rpm and a 40 mm wear track was employed, corresponding to a sliding speed of 1.674 m/sec. Iron-constantan thermocouple was inserted into the sample 1.5 mm away from the mating surfaces, in order to measure the rise in the test temperature. The wear rate was computed from weight loss measurements.

RESULTS

Figure 1 shows a typical microstructure of hypereutectic aluminum-silicon alloy from sequence 1, wherein no sodium and phosphorus additions were made. The microstructure consists of large cuboids of primary silicon of 100 μm average size, primary aluminum dendrites of average secondary dendrite arm spacing of the order of 20 μm, and eutectic silicon. The plate shape of eutectic silicon in the interdendritic region of primary aluminum and the needle shape of eutectic silicon can be seen in Figs. 2 and 3 respectively. It is noted that primary silicon crystal grows in different shapes, for instance platelike, as shown in Fig. 1, or a combination of plates originating from a central nucleation site as shown in Fig. 4. A halo or primary α aluminum phase is frequently observed around the primary silicon (Figs. 4 and 5).

Phosphorus in elemental form was added to hypereutectic aluminum-silicon alloy with a view to refining the primary silicon crystals. A typical microstructure from sequence number two is shown in Fig. 6. It can be noted that the addition of phosphorus leads to considerable refinement in the shape of primary silicon. A histogram showing the size distribution of primary silicon phase in refined sequence (no. 2) and unrefined sequence (no. 1) is shown in Fig. 7. It can be seen that the average size of primary silicon is reduced from 100 μm to about half due to the addition of phosphorus. However, eutectic silicon appears to be unaffected as shown in Fig. 8. The microstructure produced with sequence number 3, when phosphorus and sodium were added, is shown in Figs. 9 and 10. It can be clearly seen that the primary silicon was refined and the eutectic silicon was modified.

Microstructures of LM30-graphite particle composites produced in sequence number 4 are shown in Fig. 11.

Although the size of the primary silicon is considerably less compared to unrefined structure shown in Fig. 1, the shape of the eutectic silicon is not modified to the extent desirable. The microstructure of LM30-graphite particle composites produced in the fifth sequence (Fig. 12) shows both modification of eutectic silicon as well as refinement of primary silicon. In this heat initially phosphorus was added followed by stirring of graphite. Sodium was added just prior to pouring of the casting. This appears to be a promising sequence and shows both modification of eutectic silicon as well as refinement of primary silicon. The wear rates and tensile strength of some of the alloys are shown in Table 1. There was a marginal difference in both tensile strength and wear rates of LM30 alloy due to the addition of phosphorus. However, the sequential addition of phosphorus and sodium to the melt,

TABLE 1

No.	Alloy and Sequence of Additives	Wear Rate x 10^3	Tensile Strength (MPa)	% Elongation
1	LM30	1.73	141	1.30
2	LM30 + P	1.72	145	1.30
3	LM30 + P + Na	1.33	162	1.40
4	LM30 + P + Na + graphite	--	107	1.0
5	LM30 + P + graphite + Na	--	--	--

which resulted in both modification of eutectic silicon and refinement of primary silicon, had a significant effect on both tensile strength and wear rates. For instance tensile strength was increased by about 14% and the wear rate was decreased by 23% due to the refinement of primary silicon and modification of eutectic silicon as shown in Table 1. It is, therefore, possible to add phosphorus, graphite, and sodium to hypereutectic Al-Si alloys in such a manner that the matrix has refined primary silicon as well as modified eutectic silicon. The sequence of addition should be phosphorous prior to graphite addition, and sodium added after dispersion of graphite just prior to casting.

DISCUSSION

The microstructural features described so far illustrate the need to add phosphorus and sodium in a preferred sequence to achieve a combination of refinement of primary silicon and modification of eutectic silicon in Al-Si-graphite particle composites. There have been several reports in the literature describing the use of phosphorus and sodium to refine and modify the primary and eutectic silicon respectively. Mascre [16] has reported that sodium tends to drop the effectiveness of phosphorus when both are added in the melt at the same time. However, Sugiyama et al. [17] have shown that simultaneous additions of phosphorus and sodium promote refinement of primary silicon and modification of eutectic silicon respectively.

Results of this work show that if phosphorus, graphite and sodium are added in a proper sequence, one can get refinement of primary silicon as well as modification of eutectic silicon in the matrix, along with dispersion of graphite particles. It is also interesting to note that in several instances primary silicon is found to preferentially nucleate around graphite particles (Fig. 13). This is in contrast to the fact that primary α-aluminum dendrites do not nucleate around graphite particles. In fact, primary α-aluminum dendrites push graphite particles into last freezing interdendritic liquid. If graphite with selected morphology, size and habit is dispersed in the alloy, more nucleation of primary silicon can be promoted. One can achieve partial modification of primary silicon by suitably dispersed graphite particles.

Another interesting feature which is generally observed around the primary silicon phase is the formation of Al halo [18,19]. It is generally understood that after nucleation of primary silicon, the liquid composition in the vicinity of silicon crystals is enriched in aluminum, so that the liquid composition moves down along the metastable extension of phase diagram liquidus, and primary aluminum is formed around primary silicon due to the higher growth rate at that composition and temperature. Yilmaz and Elliot [20] have estimated the critical growth rate required for halo formation in directionally solidified hypereutectic Al-Si alloys. However, in the presence of graphite particles, the formation of α-aluminum halo around primary silicon crystals is suppressed as shown in Fig. 12. Apparently, the dispersed graphite particles do not allow thermal and compositional changes to take place to an extent which would promote formation of Al halo around primary silicon in Al-Si alloy-graphite particle composites.

CONCLUSIONS

1. Sequential addition of P and Na to the hypereutectic Al-Si (LM30) alloy melt was found to refine and modify the primary and eutectic silicon respectively.
2. Tensile strength of LM30 alloy was increased by 14% and the wear rate was decreased by 23% as a consequence of modification of eutectic Si and refinement of primary silicon.
3. In hypereutectic Al-Si-graphite alloys, refinement of primary silicon and modification of eutectic silicon in the matrix can be obtained along with dispersions of graphite particles by choosing the proper sequence for the addition of graphite, sodium and phosphorus.
4. In case of hypereutectic Al-Si alloys (LM30) - 3 wt.% graphite particle composites, aluminum halo formation was found to be suppressed and primary silicon was found to nucleate preferentially around graphite particles.

REFERENCES

1. Bruni, L. and P. Iguera, Automotive Engineer, 29, February/March (1978).
2. Sarkar, A. D., Friction and Wear, Academic Press, 204-025.
3. Eyre, T. S., Wear Resistance of Metals, Treatise on Materials Science and Technology, Douglas Scott, Ed., 13, 406.
4. Gibson, P. R., A. J. Clegg and A. A. Das, Foundry Trade Journal 152, 253-256, 262-263 (1982).
5. Pai, B. C., P. K. Rohatgi and S. Venkatesh, Wear 30, 117 (1974).
6. Rohatgi, P. K. and B. C. Pai, Wear 59, 323 (1980).
7. Rohatgi, P. K., R. Asthana and S. Das, Int. Met. Rev. 31, 119 (1986).
8. Rohatgi, p. K., N. Murali, H. H. Shetty and R. Chandrashekhar, Mater. Sci. Engrg. 26 119 (1976).
9. Hanna, M. D., Shu-Zu Lu and A. Hellawell, Met. Trans. 15A, 459 (1984).
10. Glenister, S. M. D. and R. Elliot, Metal Science, 181, April (1981).
11. Elliot, R., Int. Met. Rev. 219, 161 (1977).
12. Kim, C. B. and R. W. Heine, J. Inst. Metal 92, 367 (1963-64).
13. Shingu, P. H. and Jin-Ichi Takamura, Met. Trans. 1, 2339 (1970).

14. Jorsted, J. L., Trans. THS, AIME 242 1219 (1968).
15. Shimizu, Y., Y. Kaot, S. Hashimoto and N. Tsuchiya Nagano, Aluminium 276, April (1986).
16. Mascre, C. Foundry Trade Journal 25, 725 (1953).
17. Sugiyama, M., J. Sato, J. Jpn. Foundrymen's Soc. 37, 209 (1965).
18. Rohatgi, P. K. and C. M. Adams, Jr., Met. Trans. 239, 1737 (1967).
19. Barelay, R. S., P. Niessen and H. W. Kerr, J. Cryst. Growth 20, 175 (1973).
20. Yilmaz, F. and R. Elliot, Metal Science 18, 362 (1984).

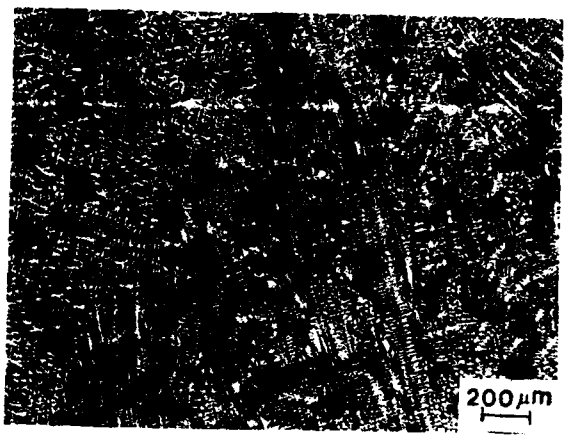


Fig. 1. Microstructure of die cast LM30 alloy



Fig. 2. Plate like primary silicon between primary Al dendrites

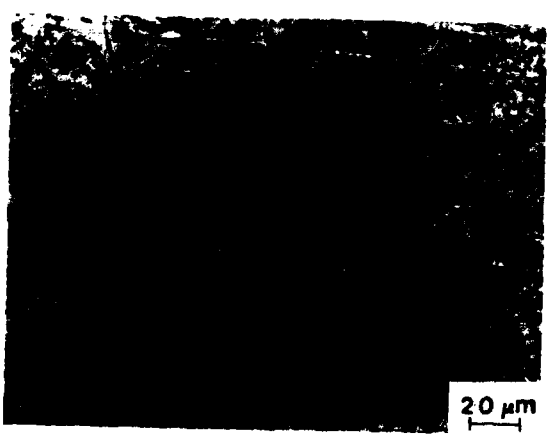


Fig. 3. Eutectic silicon needles in LM30 alloy

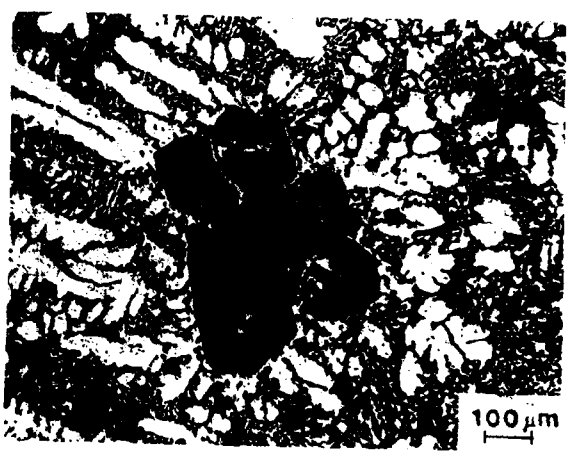


Fig. 4. Al halo around primary silicon emanating from a central nucleus

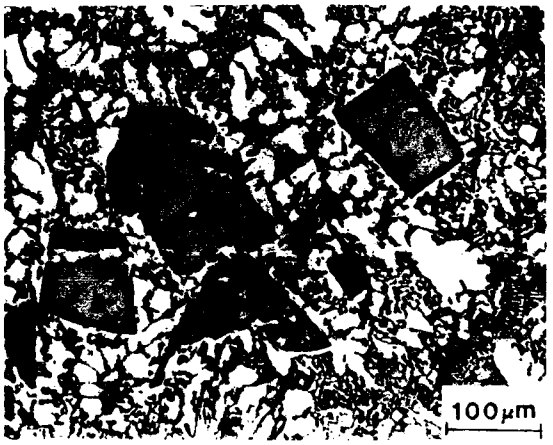


Fig. 5. Al halo around silicon crystal in LM30 alloy

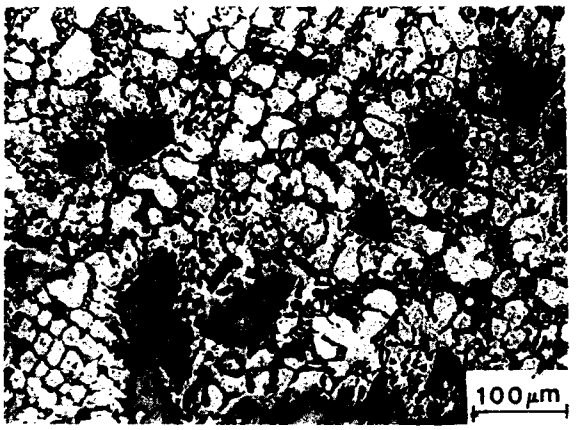
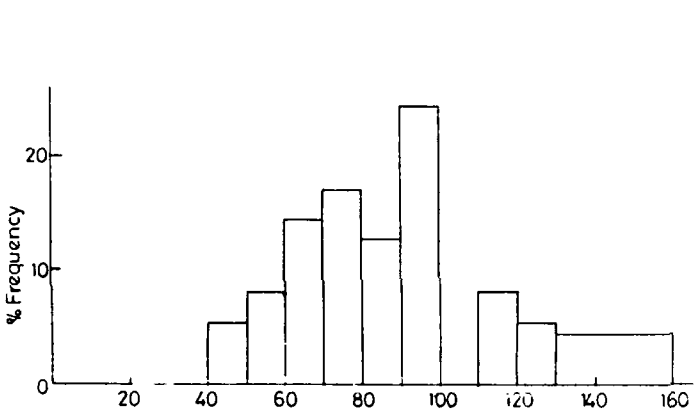


Fig. 6. Refined primary silicon in LM30-Phosphorous



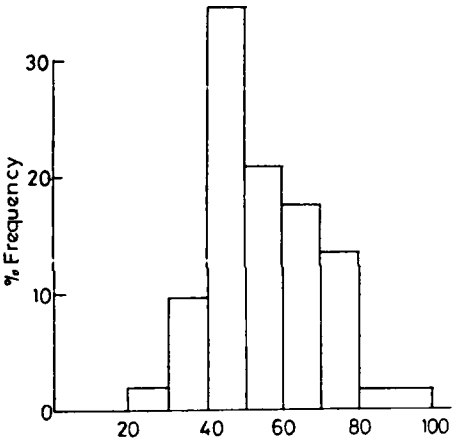


Fig. 7. Silicon size distribution before and after refinement

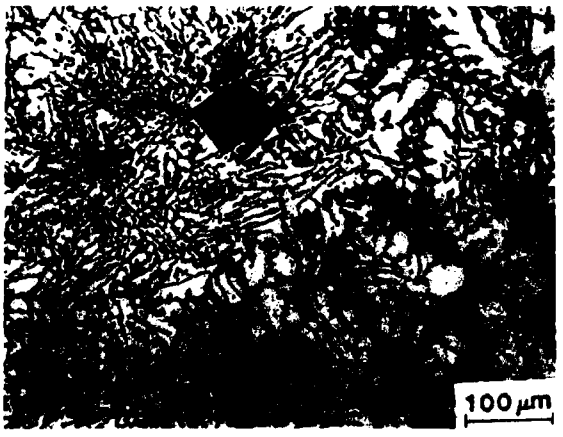


Fig. 8. Eutectic Silicon needles in LM30-Phosphorus



Fig. 9. Refined primary silicon and modified eutectic in LM30.



Fig. 10(a) Modified eutectic silicon in LM30-P-Na alloy



Fig. 10(b) Modified eutectic silicon between primary Al dendrites in LM30-P-Na



Fig. 11(a) LM30-P-Graphite-Na alloy (Na added after Gr addition)



Fig. 11(b) Off eutectic plate shaped Si in LM30-P-Gr-Na composites



Fig. 12. Modified eutectic and absence of primary Al halo in LM30-P-Na-Gr

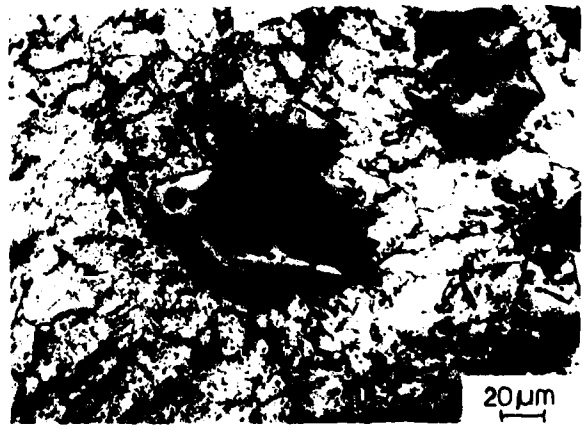


Fig. 13. Preferential concentration of primary silicon on graphite

INFLUENCE OF SOLIDIFICATION CONDITIONS ON SEGREGATION OF ALUMINUM-SILICON CARBIDE PARTICLE COMPOSITES

P. K. Rohatgi, F. M. Yarandi, Y. Liu
Materials Science Department
University of Wisconsin-Milwaukee
Milwaukee, Wisconsin 53201 USA

ABSTRACT

In this paper results of melting, isothermal holding of the melt and subsequent solidification of Al-SiC particle composite have been reported. The effects of remelting and holding time on the distribution and segregation of silicon carbide particles in the cast matrix have been examined. Remelted samples have been solidified at different rates and effects on dendrite structure and distribution of silicon carbide particles have been studied. Redistribution of silicon carbide particles during unidirectional solidification, multi-directional solidification and rapid solidification has been investigated. The interactions between silicon carbide particles and moving solid-liquid interfaces have been analyzed in view of current theories of particle pushing and observed microstructure.

INTRODUCTION

ALUMINUM-SILICON CARBIDE particle composites are being manufactured commercially by liquid metallurgy and powder metallurgy techniques. Distribution of Silicon Carbide particles in aluminum matrices controls the as cast properties of the composites prepared by liquid metallurgy techniques. Therefore it is important to study the influence of holding time and solidification conditions on distribution and segregation of Silicon Carbide particles in the aluminum matrix. Useful information on prediction of particle entrapment or rejection by the moving solid-liquid interface during solidification will provide the understanding of particle distribution and mechanical properties of aluminum-SiC Composites.

Segregation of SiC particles in the final casting is due to:

a) flocculation of SiC particles in the original powder.
b) flocculation and segregation of SiC particles during and after injection into the melt.
c) movement of particles in the melt.
d) segregation of SiC particles during original solidification.
e) segregation of SiC particles during the first remelt and final solidification.

In this study, the principal objective is to study segregation of SiC particles during remelting, holding and resolidification under multidirectional, unidirectional and rapid solidification. This study was initiated to understand the structure formation and distribution silicon carbide particles in cast-aluminum-silicon carbide composites.

EXPERIMENTAL PROCEDURE

The experiments of settling of SiC particles were conducted in a tubular resistance furnace. A graphite crucible was used to melt the aluminum-SiC Composite. A K-type thermocouple was used to record the temperature during the experiments. Material used to remelt was dural aluminum-SiC particle composites (Al 357 and 15% by volume SiC particles). Specimens were cut in (0.4" x 0.4" x 4.0") dimensions. Melting and settling took place inside the crucible. An Argon gas "blanket" was used to reduce the oxidation and dross formation of aluminum during the melting. Aluminum-SiC Composite was held in molten state at 700° C for 0 and 120 minutes respectively. Then it was air cooled. Settling of heavier SiC particles took place due to holding the molten metal at 700° C for different periods of time.

A unidirectional solidification experiment was conducted by remelting of Dural Al-SiC Composites (Al 357 matrix with 15% by volume SiC) in a similar resistance furnace. Al-SiC melt was heated up to 700° C. An Argon gas blanket was also provided to reduce the oxidation of

aluminum during melting. The remelted sample was poured at 700° C into a well insulated plaster mold. The plaster mold was heated to 800° C and was placed on a water-chilled copper plate. Unidirectional solidification experiment of the composite was carried out from the bottom up, counter to gravity. Rapid solidification of aluminum-SiC particle composites was conducted by means of either water quenching droplets of molten Al-SiC Composite or by splat quenching the droplets on a water cooled copper chill. Microstructure of solidified castings were examined to study the effect of holding time, and solidification conditions.

THEORETICAL PREDICTION OF SETTLING

The primary information required for remelting and casting is, whether, the distribution of particles remain the same when recast. If the original distribution of particles in the melt was perfectly uniform, theoretical prediction of settling can be made by using simple Stoke's law (2) which assumes: 1) the particles to be spherical and 2) no interactions between particles.

Stokes predicts the settling rate of a particle by:

$$V_p = \frac{2 R_p^2 (\rho_p - \rho_m) g}{9 \mu} \qquad (1)$$

where:

V_p = settling velocity of the particle
R_p = particle's radius
ρ_p = particle's density
ρ_m = matrix density
μ = viscosity of molten metal

Applying Eq. (1), for a 20 μ particle size of SiC, settling velocity was found to be of the order 8.41 x 10^{-3} cm/sec for molten aluminum temperature at 700° C. However, when several particles are present there is hindered settling. This affects the settling velocity. In addition any flocculation of Silicon Carbide will affect the rate of settling. Effects of flocculation and clustering will depend on the degree of flocculation and the size of clusters.

DISCUSSION OF EXPERIMENTAL RESULTS

PARTICLE SETTLING EXPERIMENTS - The results of settling experiments indicate that SiC particles show a definite tendency of segregation as a result of settling. As the holding time in the molten state increases, the particle settling increases. This is shown in Figs. (1) and (2). In general, as the distance from the bottom of the casting increases, the average size and the number of particles decreases, since coarse particles tend to settle to the bottom of the crucible. In addition much greater clustering of particles is seen near the bottom of the crucible. Large alpha aluminum

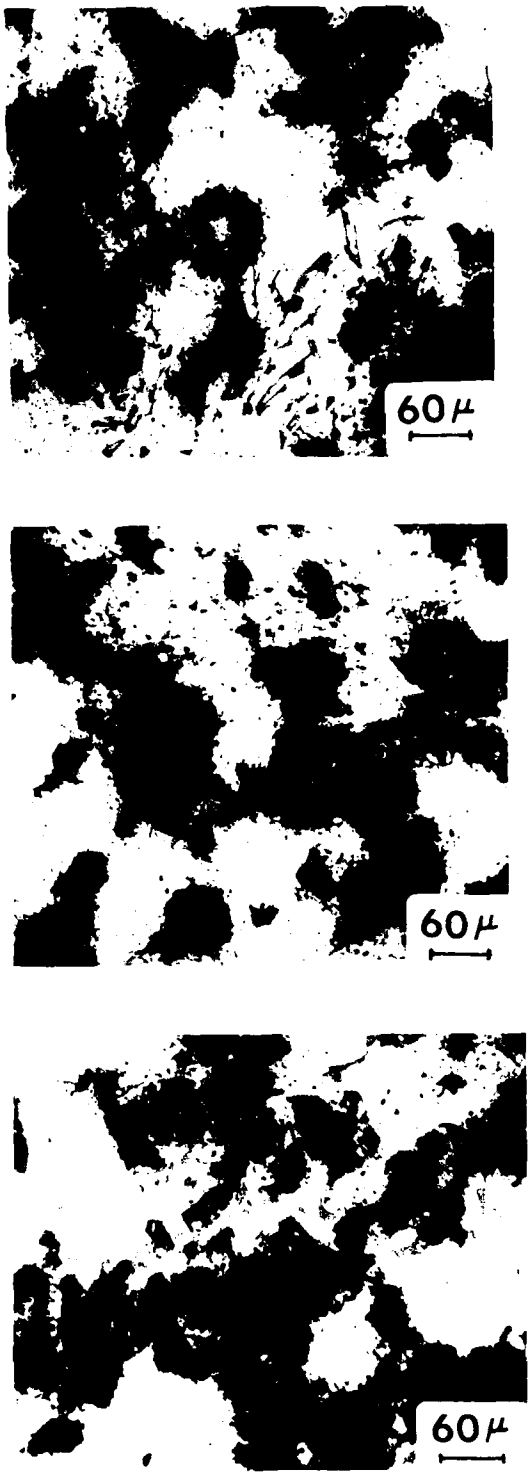


Fig. 1. Distribution of SiC particles when the composite was held at molten state (700° C) for zero minutes and air cooled. a) 1.60 cm from bottom
b) 2.54 cm from bottom
c) 4.12 cm from bottom.



Fig. 2. Distribution of SiC particles when the composite was held at molten state (700° C) for 120 minutes and air cooled. a) 1.60 cm from bottom
b) 2.54 cm from bottom
c) 4.12 cm from bottom.

dendrites apparently have pushed the particles to the interdendrite boundaries. Due to this pushing the particles have accumulated in interdendrite boundaries. In certain locations near the bottom of the casting where a large number of SiC particles have accumulated, one sees nucleation of primary silicon around silicon carbide particles; this is shown in Fig. (3).

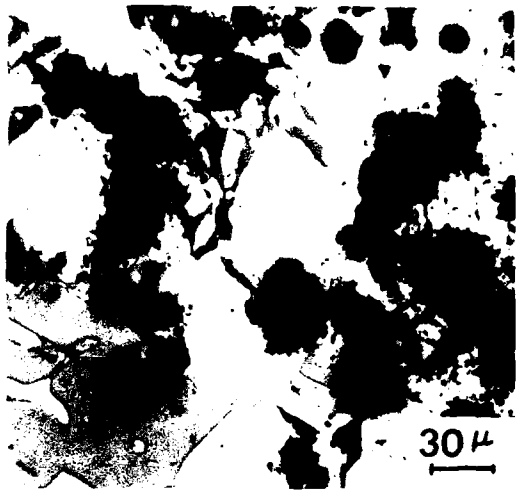


Fig. 3. Higher magnification of figure (2) showing nucleation of primary silicon around silicon carbide.

Results of unidirectional and rapid solidification experiments are presented in Table I. Experimental data were obtained for different distances from the water chill. At the bottom where the cooling rate is high and local solidification time is very small (approximately 6 seconds) some particles are randomly entrapped in the interdendrite regions, even though by and

Table 1
UNIDIRECTIONAL SOLIDIFICATION EXPERIMENT DURAL (Al 357, 15% SiC)

Distance From Water Chill (in.)	Average Arm Spacings (μm)	Local Solidification Time (sec)	Cooling Rate (C/sec)	Local Interface Velocity (μm/sec)	Number of Particles per mm²
0 - 0.5	20	6.30	8.08	1.59	< 1000
1 - 1.5	32.77	22.50	2.47	0.73	< 100
2 - 2.5	49.53	93.22	0.59	0.26	< 100
3 - 3.5	52	107.34	0.51	0.24	< 100
4 - 4.5	60.31	166.64	0.33	0.18	< 100
5 - 6.0	71.87	280.50	0.20	0.13	2240
Copper Quenched	10.5	0.931	59.63	5.63	----
Water Quenched	13.5	1.96	28.30	3.44	----

large the particles have been pushed by growing α-aluminum dendrites. As the distance from the water chill increases the cooling rate decreases.

Figure (4) shows the particle pushing process during the directional solidification. As it is shown in this figure, most particles are pushed to the top of the casting during solidification.

In essence counter gravity pushing of silicon carbide particles is observed during unidirectional solidification of aluminum alloy from bottom up. Due to the pushing of the particles by α-aluminum dendrites one can see the clusters of particles around the α-aluminum dendrites. In addition to single particles, clusters of silicon carbide particles are pushed by growing α-aluminum dendrites. Figure (5) shows the change in dendrite arm spacing as the distance from the water chill increased. Average arm spacing increases as the distance from the chill has increased. This is due to increase in solidification time and decrease in cooling rate from bottom (near the chill) to the top. The presence of silicon-carbide particles has not significantly affected the variation of dendrite arm spacing with cooling rate.

Figures (6) and (7) show the microstructure of rapidly solidified (water quenched and splat quenched on copper substrate respectively) Al-SiC composites. In these microphotographs the dendrite spacing is still finer due to faster cooling rate. Due to the finer dendrite spacing the number of silicon carbide particles which are accommodated at each dendrite boundaries is less compared to the case where dendrites are larger at slower cooling rates and more particles are accommodated at each interdendrite boundary. For the same initial distribution, above a certain minimum dendrite size equal to surface interparticle spacing, the greater the dendrite spacing the greater will be segregation due to particle pushing. Rapidly solidified structures therefore give best distributions of silicon carbide particles.

COMPARISON OF PREDICTION OF MODELS ON PARTICLE PUSHING

A review of earlier models on particle pushing phenomena and a comparison of these models with experimental results during the solidification of Al alloy-SiC particle composites is presented in the following section.

THE UHLMAN, CHALMERS AND JACKSON (U.C.J.) MODEL (3,4,10) - This model is a kinetic approach to particle pushing. It assumes that a particle is pushed in front of the solid-liquid interface and is incorporated into the solid if liquid can not diffuse sufficiently rapid to the growing solid behind the particle. A repulsion between the particle and the solid occurs when the sum of the particle-liquid and liquid-solid interfacial free energies is less than the particle-solid interfacial free energy. The U.C.J. model has introduced a theoretical crit-

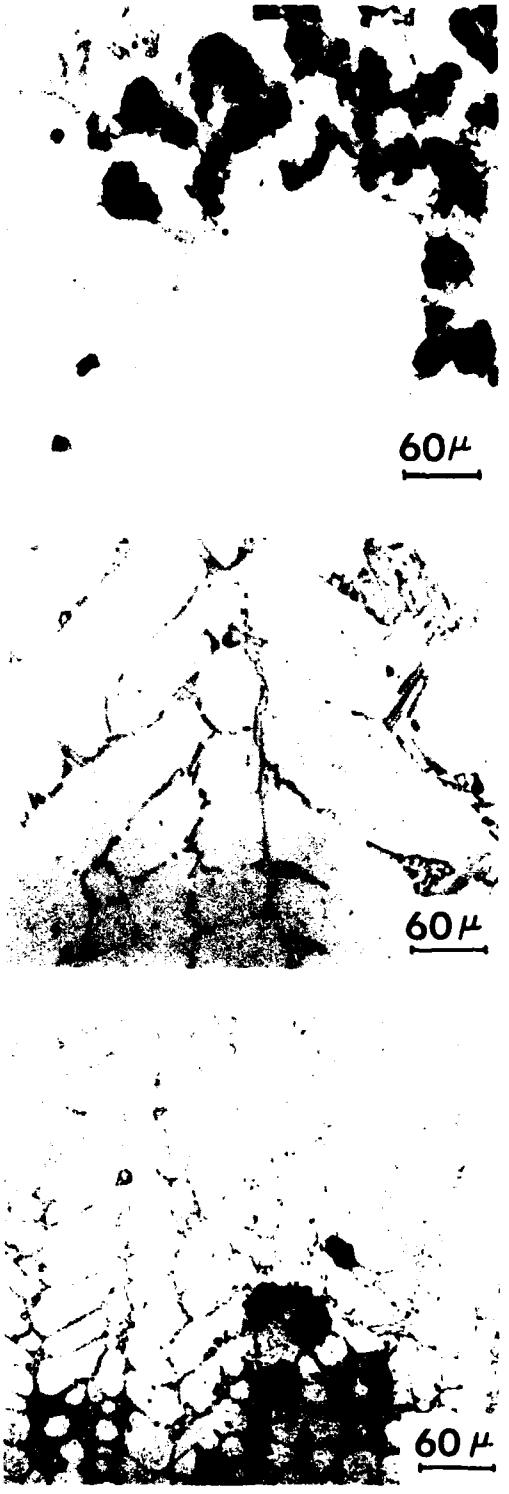


Fig. 4. Microstructure of unidirectionally solidified Al 357 and 15% by volume SiC particle composites.
a) Bottom 0.5" from the chill
b) Middle 3.5" from the chill
c) Top 6.0" from the chill

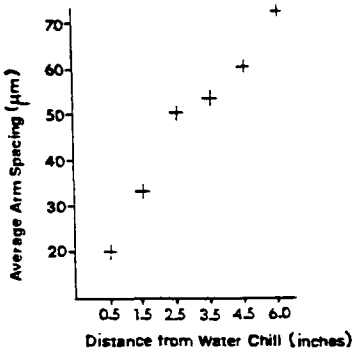


Fig. 5. Average arm spacing vs. distance from the water chill in unidirectionally solidified Dural (Al 357, 15% SiC particle) composite.

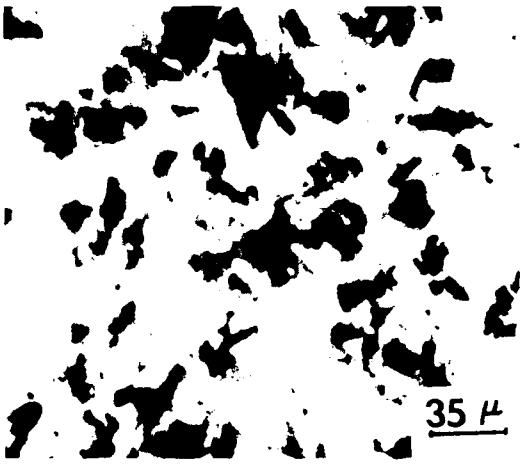


Fig. 6. Rapidly solidified (water quenched) microstructure of Dural (Al 357, 15% SiC particel) composites.

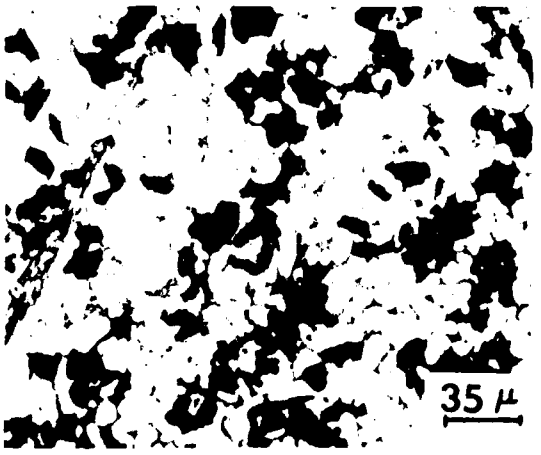


Fig. 7. Rapidly solidified (splat quenched on copper substrate) microstructure of Dural (Al 357, 15% SiC particle) composite.

ical velocity above which the particles should be entrapped and below which the particles are rejected by the moving solid-liquid interface.

The theoretical critical velocity is given in Eq. (2)

$$V_c = \frac{1}{2}(n+1)\ LA_oV_oD/KTR^2 \qquad (2)$$

V_c = theoretical critical velocity
L = latent heat of fusion per unit volume
A_o = atomic spacing
V_o = atomic volume
D = diffusion coefficient of liquid
KT = Boltzman factor
R = particle radius

n is a constant approximately equal to 5.0 (3).

The theoretical critical velocity for aluminum-silicon carbide particle composite (20 μm particle size) using the U.C.J. model is 0.187 μm/sec. Experimental measurements for actual solid-liquid interface velocity for aluminum-silicon carbide particle composite of the same size was obtained to be 0.377 μm/sec. Since the critical velocity of the interface front predicted by the U.C.J. model is less than the actual experimental measurement of solid-liquid front velocity, prediction of the U.C.J. model is the entrapment of silicon carbide particles by the growing solid-liquid front. However, experimental observations show that the particle rejection has occurred. Therefore, the U.C.J. model fails to correctly predict the entrapment of silicon carbide particles by the moving solid-liquid aluminum front, as observed in the present experiment.

BOLLING AND CISSE MODEL (5,6,7,11) - Bolling and Cisse have proposed a model that mainly concentrates on the shape of the solid-liquid interface behind the particle. An expression for the viscous drag upon a body at the interface has been developed. Initially, it is considered that the particle is separated from the growing interface and impressed upon by a small force (i.e., gravity or viscous drag) that promotes the contact. Then the particle must be forced in the direction of interface motion until the steady state configuration of particle and interface is formed. This model has proposed the theoretical critical velocity of entrapment for smooth particles by the following relationship:

$$V_c = \left(\frac{4\psi(\alpha,\beta)}{9\pi\eta^2 R^3}\right).\ KT\gamma a_o)^{1/2} \qquad (3)$$

where:

V_c = critical velocity is a specified function
ψ = $\alpha(1-\alpha)^3/(1-3\alpha)$
α = interface shape factor and a function tion of β
β = $\ln\alpha + (1-\alpha)/(1-3\alpha)(11)$, β is some characteristics of melt and particle properties and is assumed to be unity
KT = Boltzman factor

η = viscosity
R = Particle radius
γ = specific solid-liquid surface free energy
a_o = atomic spacing

The theoretical critical velocity for aluminum-silicon carbide particle composite (20 μm particle size) using the Bolling and Cisse model (Equation 3) is calculated to be 4.24 μm/sec. This value is larger than experimental velocity measurement of interface velocity (0.377 μm/sec). Prediction of Bolling and Cisse model (i.e., the rejection of particle by the moving solid-liquid interface) agrees with the experimental observations. This model concludes that the larger the particle diameter (regardless of the particle type), the lower is the critical velocity for particle entrapment. The model also proposes that the critical trapping velocity is lower when the viscosity of the liquid is higher for the same particles.

ZUBKOV ET AL. MODEL (8) - The Zubkov model is an empirical relation for prediction of entrapment or rejection of particles in a freezing melt. In this model, it is proposed that when the thermal conductivity of the particle is less than the thermal conductivity of the liquid, that is:

$$\lambda_p/\lambda_l < 1 \qquad (4)$$

(where λ_p and λ_l represent the thermal conductivities of particles and liquid respectively) the interface growth rate increases. A protuberance appears on the interface and the particle can not be captured by the growing crystal. If the thermal conductivity of the particle is greater than the thermal conductivity of the m elt, that is, $\lambda_p/\lambda_l > 1$, the interface growth rate decreases and a crater is developed on the interface, and this will result in the entrapment of the particles.

For Aluminum-Silicon carbide particle composites, the ratio of thermal conductivity values of Silicon Carbide to that of Aluminum is 0.29. This ratio is less than unity, therefore Zubkov prediction of Silicon Carbide particle rejection by the glowing solid Aluminum during the solidification is in agreement with the experimental observations. Zubkov model assumes that the ratios λ_p/λ_l for room temperature are also applicable for the temperature of the interaction of the particle with the growing crystal.

Rohatgi and Surappa (1,9) have proposed an empirical relation similar to the one proposed by Zubkov to predict particle entrapment during solidification. This model is a heat diffusivity criterion, according to which

$$\left(\frac{\lambda_p C_p \rho_p}{\lambda_l C_l \rho_l}\right)^{1/2} \begin{cases} > 1 \text{ for capture} \\ < 1 \text{ for rejection} \end{cases} \qquad (5)$$

where

C = heat capacity
λ = thermal conductivity
ρ = density

subscripts p and l represent the properties for particles and liquid respectively.

When the heat diffusivity of the particle is greater than that of the surrounding liquid metal, a crater is formed in the solid-liquid interface, thus, enhancing the entrapment of the particle. When the diffusivity of the liquid is greater than the ceramic particle, a mound is formed at the interface and the particle is rolled-off the interface, leading to particle rejection. This model is valid at small growth rates and it is assumed that the body forces do not overtake the heat flow effect.

The square root of heat diffusivity ratio for Al-SiC is 0.614 which is less than unity. This model predicts rejection of the SiC particles by the growing solid aluminum during the solidification which is in agreement with the actual observations.

Table (2) provides the summary of predictions made by some of the models described above.

Table 2
COMPARISON OF PREDICTION OF MODELS ON PARTICLE PUSHING WITH ACTUAL EXPERIMENTAL OBSERVATIONS DURING THE SOLIDIFICATION OF 2014 ALUMINUM AND SiC PARTICLES.

Experiment	Interface Velocity Va(μm/sec)	Experimental Observation	U.C.J. Prediction	Cisse-Bolling Prediction	Zubkov Prediction	Rohatgi-Surappa Prediction
1	0.362	Rejection	Entrapment	Rejection	Rejection	Rejection
2	0.260	Rejection	Entrapment	Rejection	Rejection	Rejection
3	0.363	Rejection	Entrapment	Rejection	Rejection	Rejection
4	0.319	Rejection	Entrapment	Rejection	Rejection	Rejection
5	0.322	Rejection	Entrapment	Rejection	Rejection	Rejection
6	0.512	Rejection	Entrapment	Rejection	Rejection	Rejection
7	0.503	Rejection	Entrapment	Rejection	Rejection	Rejection

DISCUSSION AND CONCLUSION OF THE PARTICLE PUSHING - Over the wide range of freezing rate studied in this work the silicon carbide particles appear to be rejected by the growing alpha aluminum. A review of critical velocity calculation by using several models, and comparison with the actual experimental results for aluminum-silicon carbide is presented, in Table (2).

Results show that the U.C.J. model has failed to predict the particle pushing for Aluminum-SiC system. Therefore, this model in its present state of development is not a suitable model for prediction of entrapment of SiC particles in Al-SiC system. This model may have to be expanded to include the effect of particle properties.

Prediction of Cisse and Bolling model for particle entrapment agreed with the experimental observations. This model may be a good candidate for prediction of particle entrapment for Aluminum-SiC composites. However, more solidification data are needed to check the validity of this model for dendrite front. This model also needs to be modified to include the effect of thermophysical properties of the particle.

Predictions of Zubkov's and Surappa and Rohatgi's model, which are empirical relations, agree with the actual observation as shown in Table (2). These models however, disregard thermal convection, body forces, and breakdown of the front, and at best, represent the interactions for very short times prior to attainment of steady state condition.

There obviously is a need for development of a new analytical model which can predict the entrapment of rejection of ceramic particles by liquid metals where thermal parameters are different. Attempts should be made to include the effect of interface curvature, solute transport, particle chemistry, particle shape and interface characteristics. Such a model could then be used to design solidification conditions to get rejection or entrapment of particles as well.

SUMMARY

1. Remelting of Aluminum-Silicon carbide particle composites followed by solidification leads to settling of Silicon Carbide particles to the bottom of the crucible. In general, large size particles have a higher settling rate.
2. The number of Silicon Carbide particles settling to the bottom of the crucible increases as the holding time in molten state increases. Holding the melt for two hours resulted in denudation of particles from the top of the casting.
3. During the counter-gravity unidirectional solidification of Aluminum-Silicon Carbide particle composites, most of the SiC particles are pushed to the top of the casting. This counter gravity segregation is due to pushing of individual particles and clusters of particles ahead of growing alpha aluminum dendrites.
4. Comparison of theoretical predictions of particle pushing models with actual experimental observation showed that the U.C.J. model may not be a suitable model to predict the particle entrapment or rejection of Aluminum-Silicon Carbide composites.
5. Results of Bolling and Cisse as well as Zubkov's and Rohatgi-Surappa's models for predicting the particle entrapment of rejection of Aluminum-Silicon Carbide particle composite agree with the actual observation. These models may be good candidates to predict the particle pushing in Aluminum-SiC systems.
6. Rapid solidification of composites leads to better distribution of silicon carbide particles.

ACKNOWLEDGEMENT

The authors wish to acknowledge the General Motors Corporation for their support of this work, and Dural Aluminum Co. in providing the samples. They would also thank Mr. C. Vaidyanathan for his help in conducting the settling experiment.

REFERENCES

(1) Rohatgi, P. K., R. Asthana and S. Das, Solidification, structures, and properties of cast metal-ceramic particle composites, International Metals Reviews, 31 (3) (1986).

(2) Geiger, G. H. and D. R. Doirier, Transport Phenomena in Metallurgy, Addison-Wesley Publishing Co. (1973).

(3) Uhlman, D. R., B. Chalmers and K. A. Jackson, Journal of Applied Physics, 35 (10) Oct. (1964).

(4) Chernov, A. A. and A. M. Melinikova, Soviet Physics - Crystallography, 10 (6) May-June (1966).

(5) Bolling, G. F. and J. Cisse, Journal of Crystal Growth, 10, (1971).

(6) Cisse, J. and G. F. Bolling, Journal of Crystal Growth, 10 (1971).

(7) Cisse, J. and G. F. Bolling, Journal of Crystal Growth, 11 (1971).

(8) Zubkov, A. M., V. G. Labanov and V. V. Nikonova, Soviet Physics Crystallogr., 18 (1973).

(9) Surappa, M. K. and P. K. Rohatgi, Journal of Materials Science Lett., 16 (1981).

(10) Stefanescu, D. M., B. K. Dhindaw, S. A. Kackar and A. Moitra, "Behavior of Ceramic Particles at the Solid-Liquid Metal Interface in Metal Matrix Composites," Castings: Metals Handbook (ASM), 15, 9th ed. (1988).

(11) Aubourg, P. F., "Interaction of Second-Phase Particles with a Crystal Growing from the Melt," Ph.D. Thesis at the Massachusetts Institute of Technology, June (1978).

STRUCTURE AND PROPERTIES OF LIQUID METAL PROCESSED SiC REINFORCED ALUMINUM

M. Skibo
Dural Aluminum Compsites Corporation
San Diego, California 92121 USA

P. L. Morris, D. J. Lloyd
Alcan International Ltd
Research & Development, Kingston, Ontario, Canada

ABSTRACT

During the fabrication of liquid processed silicon carbide reinforced metal matrix composites, silicon carbide particulate is introduced and dispersed into molten aluminum alloys and subsequently cast into billets or ingots for further processing. When the particles are in contact with certain aluminum alloys in liquid form, it is possible for a reaction to occur between the particles and the matrix. This may result in the degradation of the mechanical and physical properties of the solidified composite. The kinetics of this reaction are presented and a simple method of establishing quantitatively the extent of the interaction discussed. The influence of the reaction products on the matrix microstructure and composite properties is also considered. If appropriate measures are taken to minimize this interaction, microstructure and properties are improved. Some examples of recent materials processed to minimize this reaction are discussed.

METAL MATRIX COMPOSITES have been the focus of intense development by government and private laboratories for over a decade. The improvements in stiffness and strength as well as many other physical properties are well accepted by applications engineers throughout the industry. Of these materials, the discontinuous ceramic reinforced aluminum composites appear to have the greatest commercial potential. Although this type of composite may be fabricated by many techniques, the low cost liquid-metal-process may be the first to achieve large scale production. In this process ceramic particulate (e.g. silicon carbide or aluminum oxide) is introduced into liquid aluminum by a proprietary process and cast either to final shape, as in near net shape casting, or billet for further processing. The mechanical and physical properties of metal matrix composites are a strong function of the ceramic particle-matrix interaction and its effect on the physical characteristics of the interface. Most interfacial studies have been performed on powder processed composites where aluminum alloy powders and ceramic fibers or particulate are blended and hot pressed in the solid state to achieve composite forms. The emerging liquid phase composite processing technology may involve extended contact between liquid aluminum and ceramic reinforcement. The object of this work is the study of the reaction between liquid aluminum and silicon carbide particulate reinforcing phase.

MATRIX REINFORCEMENT INTERACTION

The specific details of molten metal processing of silicon carbide reinforced composites are proprietary and will not be presented here. This process does, however, involve the introduction of ceramic particulate into molten aluminum alloys followed by agitation to achieve uniform distribution and subsequent casting and solidifying into final form. Under certain circumstances, the particles may be in contact with the molten aluminum alloy for extended periods of time. An example of this may be in foundries where production casting cycles could necessitate the holding of molten composite for many hours. Aluminum is well known as an active and aggressive metal. Although silicon carbide refractories have been used in the aluminum industry for many years without significant fear of unwanted chemical reaction pure, untreated silicon carbide is thermodynamically unstable in many molten aluminum alloys. When small particles (between 5 and 40 microns) are brought into intimate contact with liquid aluminum they begin to react and dissolve. (1-5)

The reaction between molten aluminum and silicon carbide is given by the equation:

$$4\ Al + 3\ SiC \rightarrow Al_4C_3 + 3\ Si \qquad (1)$$

where the Al_4C_3 forms a stable compound in the melt and the solidified composite and the excess Si becomes alloyed with the matrix.

This reaction is of concern for numerous reasons. The excess Si added to the matrix is not detrimental to all alloys but in certain high strength wrought alloys the modification of the chemical composition by the addition of Si significantly degrades the matrix properties. The Al_4C_3 particles usually form at the SiC - aluminum interface as illustrated in Figure 1 which shows a 20 v/o SiC reinforced 6061 after holding at 900°C for 1 hour.

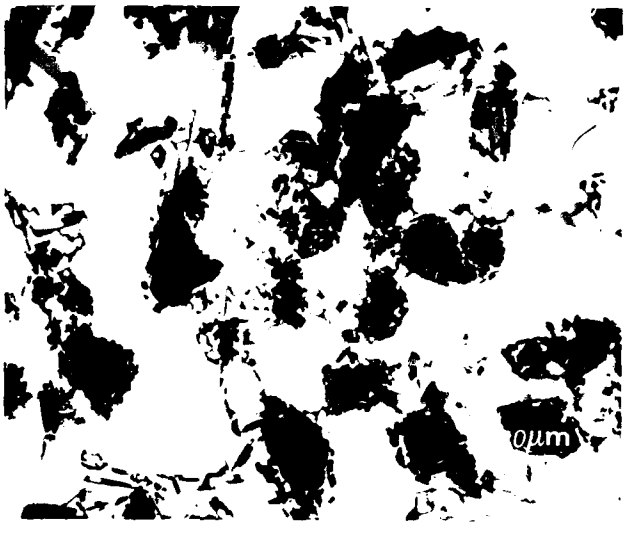


Fig. 1 - 20 v/o SiC 6061 held at 900°C for 1 hour

Their presence in the melt complicates processing and in the solidified composite they may serve at sites for corrosion. There is also some indication that the presence of Al_4C_3 at the SiC boundaries may interfere with the effective transfer of stress between matrix and reinforcement leading to a degrading of mechanical properties. Clearly this reaction must be controlled in order to maintain composite integrity and maximize composite properties.

ANALYSIS OF EXTENT OF REACTION

One method of monitoring Al_4C_3 formation is through X-ray diffraction and the measurement of Al_4C_3 and Si peak intensities in the solidified composite. An alternative for alloys where the influence of Si concentration on the liquidus is known, is to follow the changes in liquidus reflecting the increasing Si content as reaction occurs (6). A billet of 20 v% SiC in 6061 was prepared using standard methods. The billet was cut into small pieces, remelted and held for 1 hour at 675,800 and 900°C. The samples were then solidified and the liquidus temperatures measured using differential scanning calorimetry. The results in Figure 2 show that the liquidus decreased with increasing temperature, and this can be converted to increasing Si content with the extent of reaction, as shown in Figure 3. Knowing the initial Si content of the alloy, and the SiC content of the composite, the percentage SiC converted to Al_4C_3 can be calculated (6), and this is also shown in Figure 3.

It is apparent from these results that the low Si alloys can react with untreated SiC very rapidly with the formation of aluminum carbide and the release of silicon into the matrix.

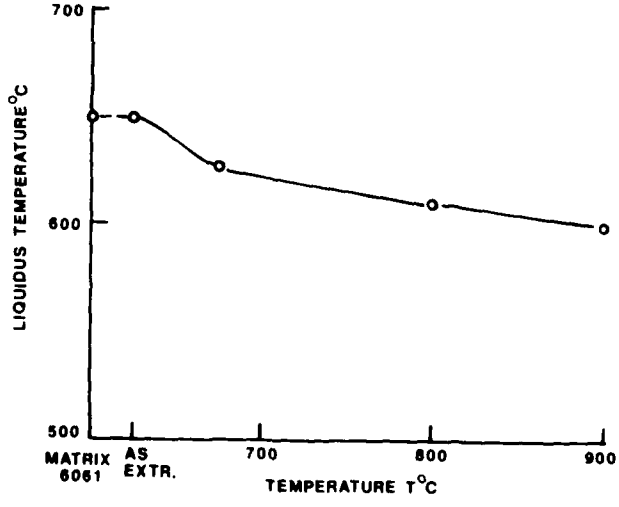


Fig. 2 - Changes in the liquidus after holding for 1 hour at different temperatures.

Only the control of the kinetics of the reaction through the use of thermodynamics or protective coatings which reduce reaction rate can prevent the degradation of matrix and hence composite properties.

MECHANICAL PROPERTIES

If the interaction between the matrix and the ceramic particles can be minimized, the silicon carbide particulate reinforced aluminum composite will demonstrate enhanced properties. Billets of 10 and 20 v/o SiC in 6061 were prepared using liquid metal processing techniques. Using standard extrusion practice, the billets were extruded to rectangular bar at a reduction ratio of 23 to 1. The microstructure of the cross section of the 20 v/o 6061 extrusion is shown in Figure 4. Note the even distribution of the SiC throughout the cross section and the lack of Al_4C_3 at the interfacial regions.

The age hardening response of the composite extrusions, together with that of the unreinforced alloy, is shown in Figure 5. It can be seen that considerable strengthening is obtained in the composite, and the age hardening response is maintained in the composite.

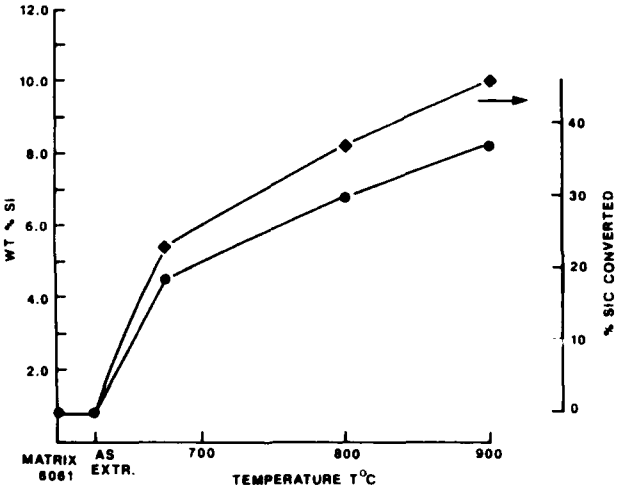


Fig. 3 - Wt% of Si and the calculated % SiC converted after 1 hour at different temperatures.

Table 1 is a summary of the T6 properties obtained in the 6061 reinforced matrix. Stiffness and strength are significantly increased with SiC content as anticipated. Although there is the expected decrease in tensile elongation in the composites, it still remains at a useful level.

Figure 6 shows the microstructure of a similarly processed 2014 with 15 v/o SiC.

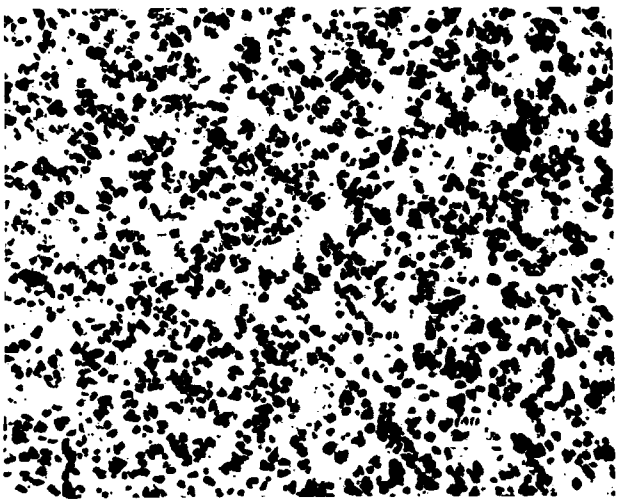


Fig. 4 - 20 v/o SiC 6061 extruded and heat treated to T6 temper.

2014 is an alloy with less tolerance for excess silicon than 6061, however the tensile properties given in Table 2 indicate that with correct processing significant increases in strength and modulus are achieved.

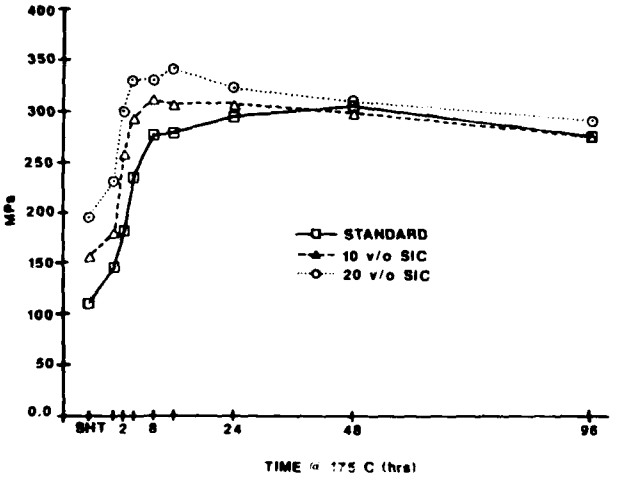
SUMMARY

The increasing commercial acceptance of liquid phase processed silicon carbide reinforced metal matrix composites necessitates the understanding of matrix - ceramic interactions. When SiC particulate and molten aluminum are brought into intimate contact, in the processing of metal matrix composites, it is possible for a reaction between the matrix and the SiC to occur. This reaction yields the formation of Al_4C_3 and free Si. Their presence may be detrimental to the physical and mechanical properties of the composite. The extent of the reaction and the dissolution of the SiC can be monitored by changes in the liquidus temperature of the composite.

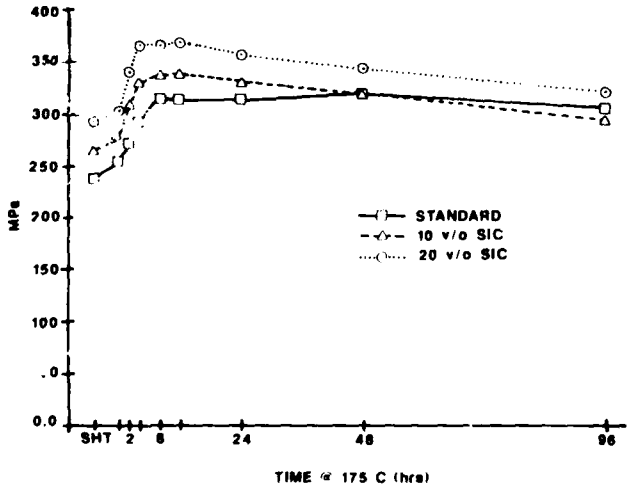
Through careful composite processing, the extent of matrix-particle reaction can be minimized yielding a composite showing improved modulus and strength.

Table 1 - Tensile Properties of 6061 Extruded Bars in the T6 Temper

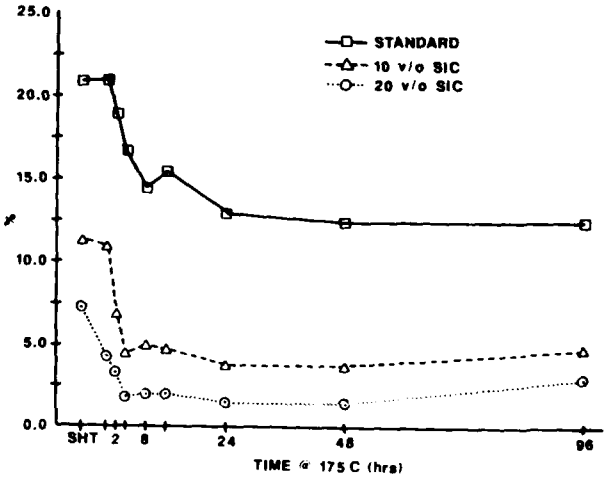
Vol % SiC	0.2% YS MPa	UTS MPa	Elongation on 50 mm %	Modulus GPa
0	308	326	15.1	67.6
10	321	351	7.5	78.6
20	343	377	2.8	97.2



(a) Yield Stress



(b) UTS



(c) Elongation

Fig. 5 - Ageing response of 6061 and 6061 - SiC composite.

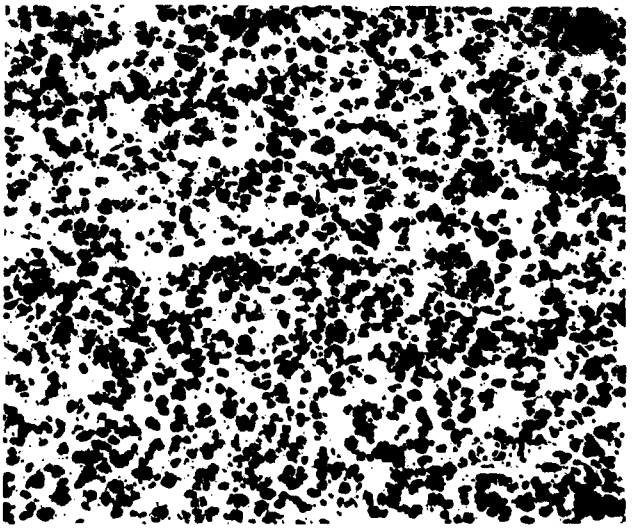


Fig. 6 - 15 v/o SiC 2014 extruded and heat treated to T6 Temper.

Table 2 - Tensile Properties of 2014 Extruded Bars in the T6 Temper

Vol % SiC	0.2% YS MPa	UTS MPa	Elongation on 50 mm %	Modulus GPa
0	414	409	10	72.4
15	462	473	4	95.2

REFERENCES

1. Warren, R., and Andersson, C.H., Composites 15, 16-24, (1984).
2. Warren, R., and Andersson, C.H., Composites 15, 101-111, (1984).
3. Baes, H.E., Wald, F., and Weinstein, M., "Advanced Fibrous Reinforced Composites", (SAMPE, 1966), 10, E41-51.
4. Naidich, Y.B., and Nevodnik, G.M., Bull Acad Sci USSR - Inorganic Metals 5, 2066-2070, (1969).
5. Lloyd, D.J., Composite Science and Technology, 1988.
6. Iseki, T., Kameda, T., and Maruyama, T., J. Mater. Sci. 19, 1962, (1984).
7. Viala, J.C., Fortier, P., Berhard, C., and Bouix, J., "First European Conf. Comp. Matls., 583-588, (1985).
8. Murray, J.L., and McAlister, Bull, A.J., Alloy Phase Diag. 5, 74 (1984).
9. Bhagat, R.B., "Interfaces in Metal-Matrix Composites", Metl. Soc. Aime., 169 (1986).

PROPERTIES OF SHAPE CAST Al-SiC METAL MATRIX COMPOSITES

David J. Lloyd, B. Chamberlain
Alcan International Limited
Kingston Research and Development Centre
Box 8400, Kingston, Ontario, Canada K7L 4Z4

ABSTRACT

A variety of solidification factors influence the microstructure and properties of cast Al-SiC composites. Since SiC is thermodynamically unstable in many Al alloys, unprotected SiC has a tendency to react with molten aluminum to form aluminum carbide. The kinetics of this reaction in different alloys is considered and alloy compositions which limit reactivity are discussed. during holding in the liquid state SiC particulates tend to settle due to differences in density between aluminum and the reinforcement. The extent of settling in a typical casting alloy is considered. During the solidification itself the SiC is rejected at the miniscus and pushed to the interdendritic regions. This effect is a function of the solidification rate. Directional solidification experiments are discussed which show the influence of solidification rate on the microstructures obtained in different alloys. Finally, the mechanical properties obtained in castings of A356 alloy reinforced with SiC are presented.

INTRODUCTION

PARTICULATE METAL MATRIX composites (MMCs) offer potentially higher strength, higher modulus, and higher wear resistance material than is currently available by conventional alloying. In the past these materials have been processed by powder metallurgy, and as a result, have only been available in wrought product form. The development of the Dural Aluminum Composite Corporation (DACC) technology, which is a molten metal mixing method, enables these materials to be cast to shape. In this paper consideration is given to some of the metallurgical and physical factors involved in shape casting these materials, together with the properties obtained.

A variety of reinforcements can be used, but SiC has specific property advantages over most commercially available ceramic particles, and SiC in an A356 matrix will be considered in this work.

In a typical foundry operation incoming ingot is first remelted, then, after holding for some time above the liquidus, is cast to shape, and the final shape casting is heat treated to obtain the optimum properties. A MMC has to be processed as closely as possible to this route, and this means that it has to satisfy certain criteria:

(1) It has to be remeltable, and able to be held for a reasonable time above the liquidus without degradation of the reinforcement.

(2) It has to have good casting fluidity to fill the intricate passages of the mould.

(3) The shape casting has to have a good degree of integrity and a suitable microstructure.

(4) The mechanical properties of the final casting have to be superior to the unreinforced casting.

Each of these will be considered in turn.

REMELTING

The main problems with remelting are the stability of SiC in the melt, segregation of reinforcing particles in the melt, and the subsequent fluidity of the molten composite. The fluidity is also important in terms of casting the final shape, and will be considered in the next section.

Previous work on the Al-Si-C phase diagram(1) has shown that SiC is thermodynamically unstable in molten Al, and work on SiC fibres have confirmed this(2).

At temperatures above the liquidus SiC reacts with Al to form Al_4C_3:

$$4Al + 3SiC \rightarrow Al_4C_3 + 3Si \quad (1)$$

From this equation it is seen that, in addition to Al_4C_3, Si is produced, and if the Si content is sufficiently high the reaction will tend to go to the left ie. the SiC will be stable in the matrix and not react. The required Si levels at different temperatures can be calculated(3), and at typical casting temperatures 10 to 12wt% Si is required for complete thermodynamic stability. However, in practice it is the kinetics of aluminium carbide formation which has to be considered. In practice melt holding times can be many hours, depending on the foundry, and for very long times the equilibrium Si levels will be needed. However, for holding times of 2 to 4 hours, which is viable for most casting operations, much lower Si levels are sufficient to prevent extensive Al_4C_3 formation. With a common hypoeutectic Al-Si-Mg casting alloy, which contains 6-7wt%Si, 4 hours at 750C produces barely detectable Al_4C_3, and even at 800C the rate of Al_4C_3 formation is quite slow, as seen from Fig. 1.

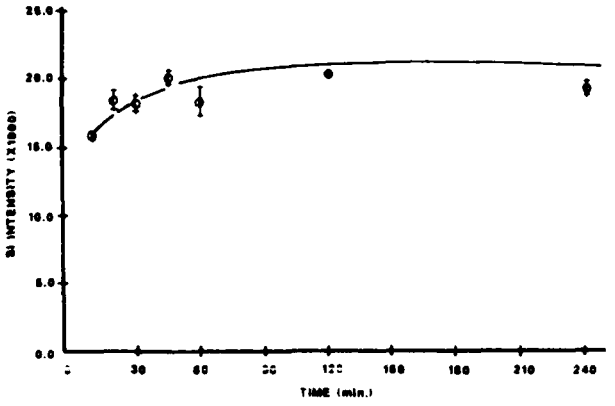


Fig. 1. X-Ray diffraction results for A356 + 15 v/o SiC at 800°C

A356-15v% SiC held for 2 hours at 750C shows clean interfaces at the particle-matrix boundary, Fig. 2.



Fig. 2. Silicon carbide particulate in A356 alloy microstructure after holding 2 hours at 750°C.

So the Si level required to limit Al_4C_3 formation will depend on the particular foundry practice, the higher the melt temperatures and the longer the holding times involved, the higher the required Si level. A good practice is to minimise superheat and holding times as much as possible - which is normal, good foundry practice.

Segregation of reinforcing particles in the melt arises because the density of liquid Al is 2.3 g/cc, while that of SiC is 3.2 g/cc, and settling due to gravity occurs. This settling results in the top of the melt becoming denuded of SiC, and the extent of the denuded zone increase with time, Fig. 3.

The majority of the settling occurs rapidly in the first hour, and after this subsequent settling occurs slowly. Settling in melts containing a high volume fraction of particles occurs slower than the Stoke's velocity, and is given by (4)

$$V_h = V_s(1-C)^{4.65} \quad (2)$$

where Vs is the Stoke's velocity

C is the particle concentration

For SiC in molten Al this gives a settling velocity of about 0.002 cm/sec for 10 micron particles, which is consistent with the settling results in the first hour, shown in Fig. 3.

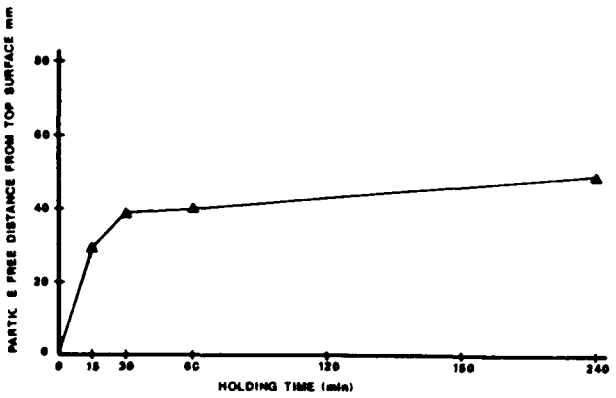


Fig. 3. Settling of silicon carbide particulate in a melt of A356 matrix alloy.

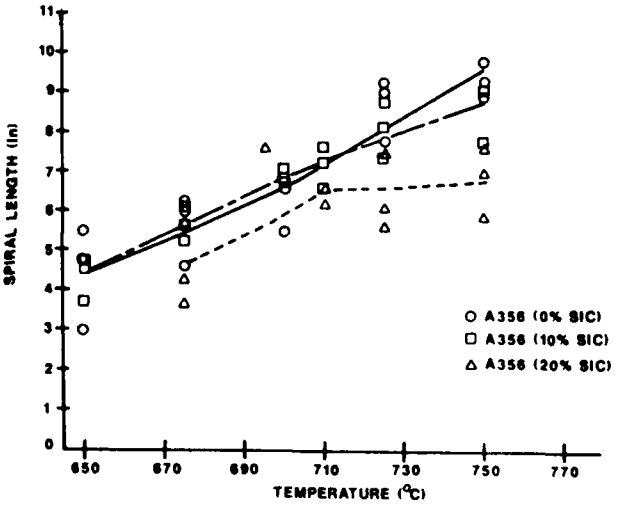


Fig. 4. Foundry fluidity of A356 matrix alloy with different SiC particulate content.

For longer times the settling decreases because the SiC content below the denuded zone increases and hinders further settling. The extent of settling will be influenced by particle size and particle shape, finer particles settling more slowly, as will platelike rather than blocky particles.

Since settling occurs so rapidly, it is essential that the melt is stirred prior to shape casting, and conventional stirring methods that minimise surface disturbance are adequate to maintain the particulate well distributed in the melt.

CASTING FLUIDITY

Casting fluidity is usually assessed by measuring the distance the melt will flow before it solidifies, so it involves both rheological and solidification factors. Typically melts are cast from different temperatures into a spiral mould, and Fig. 4 shows the results of such a test.

The spiral lengths obtained in A356-2 with 10v% SiC are comparable to those of the matrix alloy, and increase with increasing temperature. The 20v% composite shows shorter spiral lengths at higher temperatures. The viscosity of the melt is expected to increase with increasing particle content(5), however, there is no data for metallic melt at the particle loadings of interest that the authors are aware of.

Considering that the decrease in spiral length occurs in the high volume fraction composite at high temperatures, the most likely explanation is that reaction to form Al_4C_3 is occuring and this leads to an increase in viscosity. This is consistent with the finding that in the wrought matrix composites, the casting fluidity decreases to a very low value as Al_4C_3 is formed(6).

It can, therefore, be concluded that these metal matrix composites should have adequate casting fluidity provided an appropriate melting and casting practice is used.

MICROSTRUCTURE

In unreinforced alloys the microstructure is dependent on the solidification rate ie. the cooling rate of the casting. Solidification rate is particularly important in composites because the distribution of the reinforcing particles is dependent on the cell size of the casting. The cooling rate dependence of the cell size is the same in the composite as in the matrix alloy, Fig. 5, and it obeys the equation:

$$DR^a = K \qquad (3)$$

where D is the cell size, R is the cooling rate, and "a" and K are constants, and "a" has a value of 0.36-0.38.

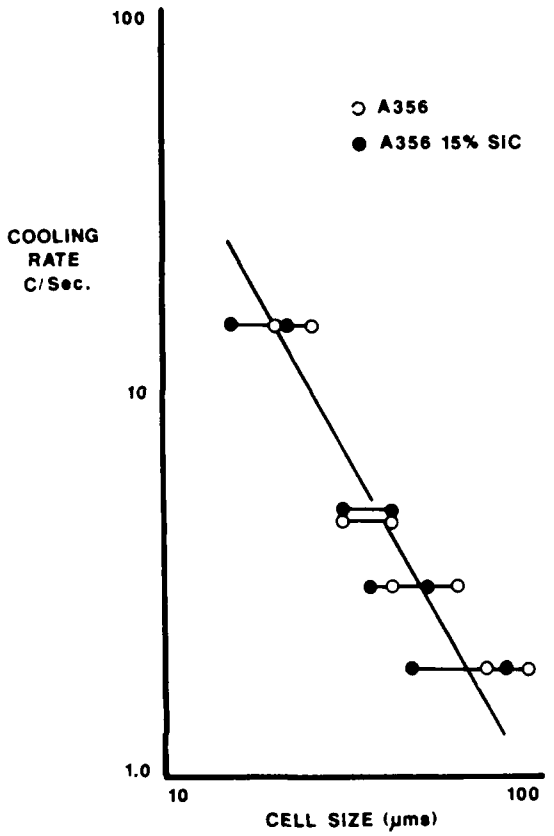


Fig. 5. Cell size vs cooling rate for A356 with 0% and 15% SiC

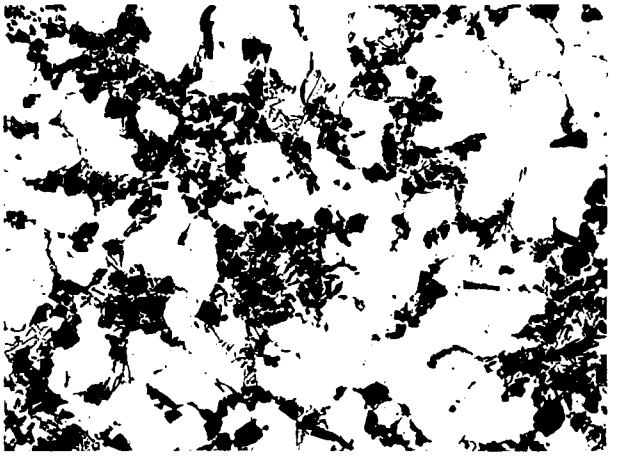
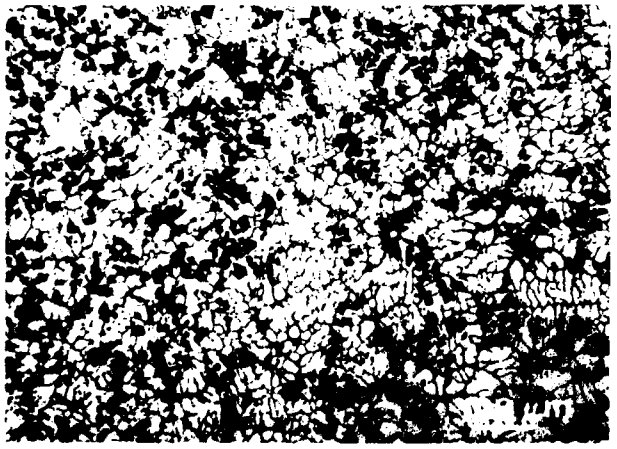


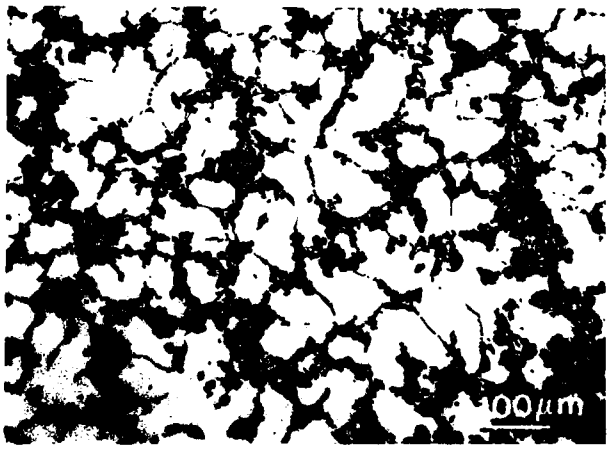
Fig. 7. Ceramic concentration in intercellular regions.



(a)

Cooling rate of

75°C/sec



(b)

Cooling Rate of

1°C/sec

Fig. 6. Effect of solidification rate on microstructures.

Fig. 6 shows the microstructures after solidifying at cooling rates of (a) about 75C/sec and (b) 1C/sec. Note that the SiC particles are rejected ahead of the solidification miniscus and trapped by converging dendrites in the intercellular regions.

This is shown in more detail in Fig. 7. Since the particles are pushed to the intercellular regions, the distribution of SiC becomes more clustered as the solidification rate decreases. The SiC particles do not act as solidification nuclei, nor do they appear to significantly influence the size of the intercellular Si plates. Transmission electron microscopy, Fig. 8 shows that the particle-matrix interface is free of any reaction product, and the SiC is often associated with Si particles, which is expected since both are inter-cellular.

Particle entrapment by a solidifying interface has been considered for non-metallic systems. The energetic models(7,8) suggests that for the present composite, entrapment should occur for solification front velocities beyond about 0.1 microns/sec, which is much smaller than the velocities in the present experiments, yet the experiments show that rejection is occuring. Other models based on differences in the thermal conductivities(9), or thermal diffusivities(10), also indicate that entrapment would be expected. Obviously, this is an area where present models are inadequate.

Commercially, A356 alloys are modified with strontium or sodium to refine the eutectic Si, and this can also be done in the composite. Fig. 9 shows the microstructure after modifying with 0.005 wt%Sr. The composite can also be grain refined if necessary.

Porosity in castings can have a major effect on properties, and normal gating and casting practices are required to prevent shrinkage porosity. Microporosity can occur in the composite castings. Fig. 10 shows the microporosity in a small investment casting. The pores are surrounded by SiC particles. Microporosity can be removed by hot isostatic pressing at 520°C, as shown in Fig. 11.

From the above considerations, it can be seen that the solidification rate of the casting is very important in controlling the distribution of the reinforcement. The most uniform particle distribution is obtained at high solidification rates, such as those obtained in permanent mould castings.

In general, normal practices for obtaining optimum properties in unreinforced castings also apply to composite castings.



Fig. 8. SiC/Si/Al Interfaces

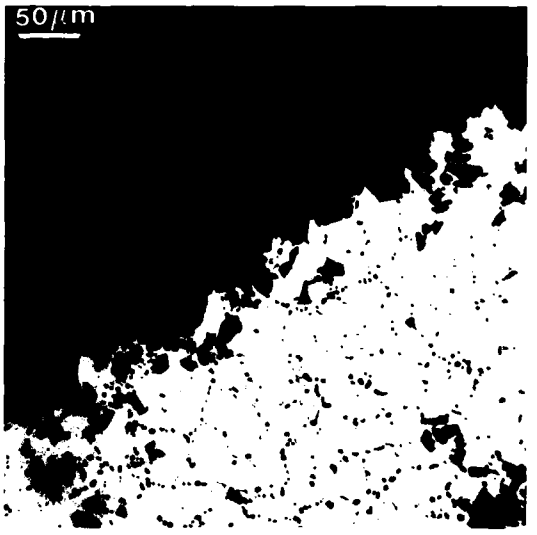


Fig. 9. Modified Si Eutectic

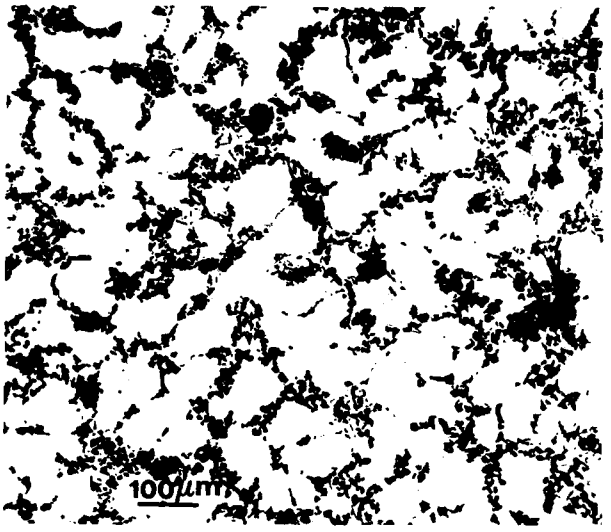


Fig. 10. As cast showing porosity.

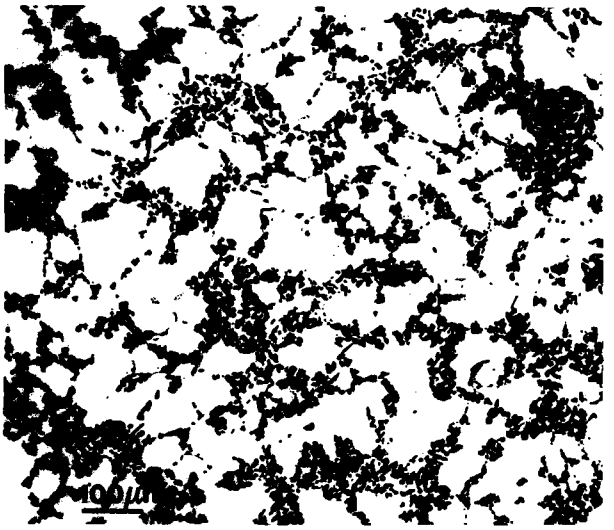


Fig. 11. Hipped material.

Figs. 10 & 11. Microstructure of investment cast test bars.

MECHANICAL PROPERTIES

The mechanical properties obtained at different ageing times, after solution treating at 540°C, hot water quenching, holding at room temperature for 1 hour and furnace ageing at 155°C, is for two different composite melts with the compositions shown in Table 1, together with a cast of commercial A356-2. In all cases the results are from standard permanent mould cast test bars (ASTM B108) of 50.8 mm guage length.

Table 1 - Chemical Composition of Separately Cast Tensile Test Bars.

	Cu%	Fe%	Mg%	Si%	Ti%
Composite #1	0.02	0.09	0.65	7.0	0.09
Composite #2	0.02	0.09	0.66	7.1	0.10
AA A.356.2	0.01	0.09	0.34	7.1	0.07

Fig. 12 shows that the composite properties are comparable in the two melts and show the normai age hardening response. The composite is considerably stronger than the unreinforced alloy, but it should be noted that some of this enhanced strength could be due to the higher Mg content in the composites. The modulus is as much as 20GPa higher than the commercial alloy, but the tensile elongation is significantly reduced, at 1% in the aged condition.

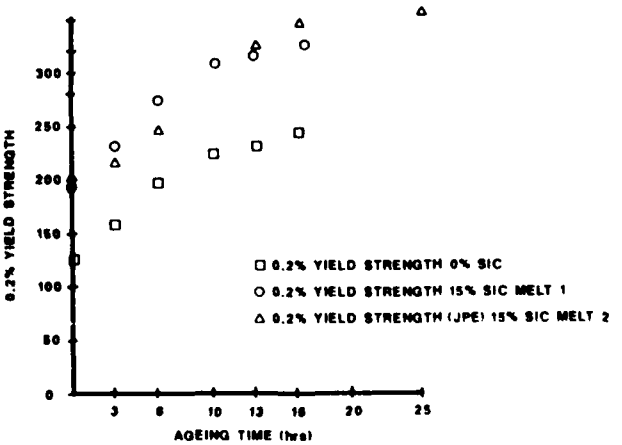


Fig. 12. 0.2% Yield strength with ageing time for commercial A356 and two melts of MMC.

SUMMARY

These experiments have shown that SiC particulate reinforced Al-Si alloys can be remelted with good casting fluidity and without significant loss or degradation of reinforcement. Provided appropriate melting and casting practices are followed, high quality castings with improved strength and modulus can be obtained. To date only permanent mould casting has been examined in any detail and further work needs to examine other casting methods, in addition to exploring methods of improving the tensile elongation.

ACKNOWLEDGEMENTS

The authors are grateful to Alcan International and DACC for permission to publish this work. They would also like to acknowledge the assistance of their colleagues at KRDC for their contributions to many areas of this work.

REFERENCES

(1) R. Warren and C.H. Andersson, Compos., 1984, Vol. 15, p. 101.
(2) W.C. Moshier, J.S. Ahearn and D.C. Cooke, J. Mater. Sci., 1987, Vol.22, p.115.
(3) E.W. Dewing and D.J. Lloyd - to be published.
(4) J.F. Richardson and W.N. Zaki, Chem. Eng. Sci., 1954, vol. 3, p. 65.
(5) M.K. Surappa and P.K. Rohatgi, Met. Trans., 1981, vol. 12B, p. 327.
(6) D.J. Lloyd - to be published.
(7) D.R. Uhlmann, B. Chalmers and K.A. Jackson, J. Appl. Phys., 1964, vol. 35, p. 2986.
(8) S.N. Omenyi and A.W. Neumann, J. Appl. Phys., 1976, vol. 47, p. 3956.
(9) A.M. Zubko, V.G. Lobanov and V.V. Nikonova, Sov. Phys. Cryst. 1973, vol. 18, p. 239.
(10) M.K. Surappa and P.K. Rohatgi, J. Mat. Sci. Let., 1981, vol. 16, p. 562.

EFFECT OF MATRIX STRENGTHENING AND FIBER ORIENTATION ON THE MECHANICAL BEHAVIOR OF CAST BORON-MAGNESIUM COMPOSITES

A. K. Dhingra
DuPont Co.
Wilmington, Delaware, USA

L. B. Gulbransen
Washington University
St. Louis, Missouri, USA

ABSTRACT

Cast composites with uniform periodic distribution of boron fibers in magnesium matrix were developed using casting techniques.

The effect of strengthening the magnesium matrix by using pure Mg and higher strength alloys on the mechanical behavior of Boron Magnesium composites was studied. The measured mechanical properties of composites at various fiber orientations including 30, 45 and 90 degrees showed excellent agreement with theoretical micromechanics analysis. The matrix transverse and shear strengths of the composites were found to be 2 to 3 times higher than the corresponding strength of the similarly cast bulk matrix. This increase in the strength was attributed primarily due to ultra fine grain size of the matrix in the composite obtained by rapid cooling. On strengthening the magnesium matrix three distinct types of composite failures were observed: (a) matrix failure, (b) combined matrix and fiber failure, (c) predominant fiber failure. Each of these failure mechanisms operated progressively as the strength of the matrix was increased by alloying.

* The pioneering research in cast metal composites reported here is part of the author's unpublished D.Sc. dissertation with L. B. Gulbransen at Washington Unversity, St. Loius, Missouri, USA.

COMPOSITE FABRICATION

There are several methods to combine fibers with metals in order to produce fiber reinforced metal composites. Some of the methods of fabrication include: liquid infiltration of molten metal into fiber bundle or preform, powder metallurgical techniques, diffusion bonding, directional solidifcation of eutectic alloys, plasma spray, hot pressing of fibers precoated with matrix, electroforming, extrusion, swaging or drawing, etc.

The fabrication of fiber reinforced metal composites by infiltration of molten metal into a fiber bundle, mat, or fiber preform has some fundamental advantages:

- It is relatively simple and economical
- It has all the basic advantages which the casting techniques offers over other methods of production
- There is no limitation on the size of the sample, as compared to powder metallurgical techniques where the size of the sample is limited by the capacity of the press
- Complicated shapes are relatively easy to produce
- Once the equipment is properly set up, the rate of production of samples is much faster than diffusion bonding or hot pressing.

The basic disadvantage of the method is that the fibers may be degraded because of reaction between molten metal and fibers. This, however, can be prevented by using suitable coatings on the fibers and controlling processing conditions. Considering the above factors, it was decided to make samples by liquid infiltration.

BORON - MAGNESIUM COMPOSITES

Magnesium, is the lightest structural metal used with the density of 1.74 gms/cc. The aerospace metals titanium (density 4.5 gms/cc) and aluminum (density 2.7 gms/cc) are 2.6 and 1.55 times heavier than magnesium. It has a hexagonal close packed crystal structure, with the M.P. of 651°C and approximately 4% increase in density on freezing.

Because of the above interesting characteristics, and particularly low melting point and density, magnesium was selected as the

matrix material.

Boron fibers, obtained from Texaco were about 4 mil in diameter with estimated tensile strength of 400,000 psi and Young's modulus of about 50×10^6 psi.

Boron - Magnesium composites rods (1/8" x 3" long for flexural and torsion/shear testing) dog bone shaped tensile bars (4" long with gage length of 2". The diameter at gage was about 1/16" and diameter at grips 1/8") plates (3" x 2" x 3/32" for flexural testing at 30°, 45° and 90°) containing 70% volume loading of boron fibers were cast using liquid infiltration techniques. Processing techniques and conditions were developed to obtain pore free composites with controlled hexagonal packing of boron fibers as shown in Figure 1.

The wetting behavior of the matrix was studied by examining the fracture surface of the composite under a scanning electron microscope. Figure 2 shows that the fibers are not pulled out of the matrix, but are broken to fracture. The projecting fibers are completely surrounded by matrix material, indicating excellent wetting and bonding.

To determine the effect of matrix alloying on the mechanical behavior of Boron - Magnesium system unidirectional test specimens with four different magnesium matrix strengths (pure magnesium, alloy AZ31B, alloy ZK and precipitation hardened alloy called HZK) and boron content of about 70% in all cases were cast in the form of rods, dog boned shaped tensile bars, and plates. For comparisons the properties of the matrix were determined by casting the matrix alloys under similar conditions and sizes as composites.

MECHANICAL PROPERTIES

Longitudinal (0°) tensile and flexural, transverse (90°) flexural, and longitudinal torsion (for shear properties) tests were performed to characterize the Boron - Magnesium composites system with four different matrix strengths as shown in Table 1. Data in Table 1 shows the average strength and modulus values from 6 to 10 samples with 90% confidence limits. For example the transverse flexural properties of composites (Table 2) are average of 8, 7, and 10 samples for Mg-B, AZ-B and HZK-B composite system.

Table 1

BORON FIBER MAGNESIUM MATRIX COMPOSITES

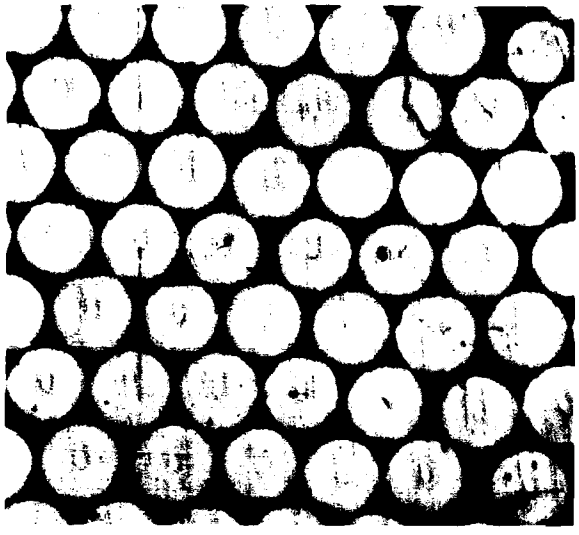
	Composite System			
	Mg-B	AZ-B	ZK-B	HZK-B
Longitudinal Tensile Strength (K.S.I.)	153	--	152	158
Longitudinal Young's Modulus ($\times 10^6$ P.S.I.)	40	--	43	43.5
Longitudinal Flexural Strength (K.S.I.)	337	327	255	259
Longitudinal Young's Modulus ($\times 10^6$ P.S.I.)	42.9	41.3	39.9	39
Transverse Flexural Strength (K.S.I.)	24.2	36.9	--	41
Transverse Young's Modulus ($\times 10^6$ P.S.I.)	17.6	18	--	20.7
Longitudinal Shear Strength (K.S.I.)	17.5	24	19	23.2
Longitudinal Shear Modulus ($\times 10^6$ P.S.I.)	7.1	7.0	7.4	8.7
Tensile Strength of Matrix - Wrought (K.S.I.)	25	35	--	40
Shear Strength of Matrix - Wrought (K.S.I.)	17	23	19	22
Young's Modulus of Matrix ($\times 10^6$ P.S.I.)	6.5	6.5	6.5	6.5
Shear Modulus of Matrix ($\times 10^6$ P.S.I.)	2.4	2.4	2.4	2.4

Table 2

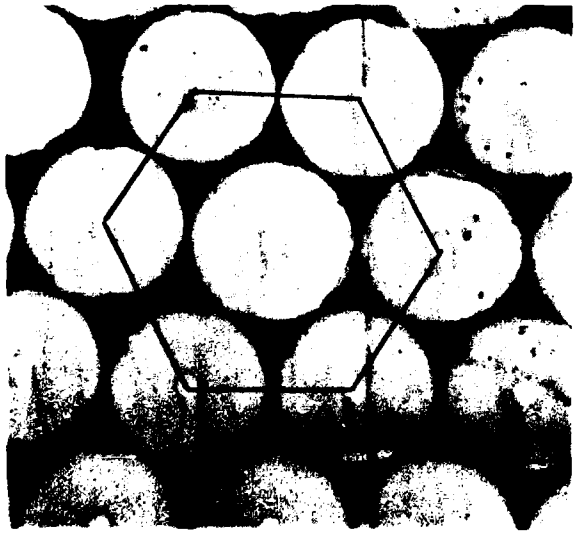
TRANSVERSE FLEXURAL PROPERTIES

Subject	Particulars	Composite System		
		Mg-B	AZ-B	HZK-B
Sample Size	No. Off	8	7	10
Transverse Flexural Strength (K.S.I.)	Mean	24.2	36.9	41
	S.D.	3.2	5.2	4
	90% Confidence Limits	±2	±3.7	±2.3
Transverse Modulus ($\times 10^6$ P.S.I.)	Mean	17.6	18	20.7
	S.D.	0.6	1	1.1
	90% Confidence Limits	±0.4	±0.7	±0.7
Deflection (Inches)	Mean	0.0065	0.0086	0.0089
	S.D.	0.0026	0.001	0.0008
	90% Confidence Limits	±0.0017	±0.0007	±0.0005
Matrix	Strength (K.S.I.)	25	35	40
	Modulus ($\times 10^6$ P.S.I.)	6.5	6.5	6.5

Figure 1



Boron Fibers Showing Periodic Distributions in the Composite, 112x

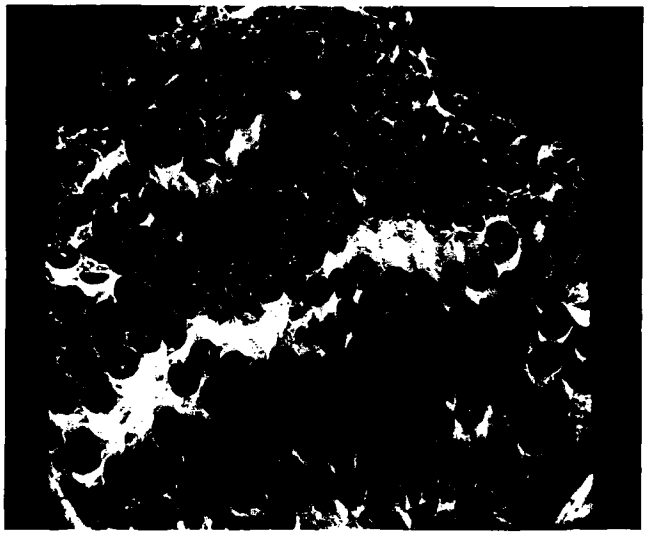


Hexagonal Packing of the Boron Fibers in the Composite, 230x

Figure 2



Scanning Electron Micrograph of the Tensile Fracture Surface, 16x



Scanning Electron Micrograph of the Tensile Fracture Showing That the Fibers Are Not Pulled Out of the Matrix, Indicating Strong Interfacial Bonds, 40x

EFFECT OF MATRIX STRENGTHENING

One of the main problems encountered in the utilization of fiber reinforced composite materials to structural applications is the poor transverse and shear properties. The strength of the matrix does not significantly affect the longitudinal properties; however, the transverse and shear strength of the composite can be appreciably increased if the matrix strength is improved (Figure 3).

The longitudinal flexural strength of the composite increases with the ductility of the matrix. This is because the ductiliy matrix can arrest any crack more efficiently by plastic deformation. The effect of matrix strengthening on the mechanical properties of the magnesium - boron system is summarize in Figure 4. It should be noted that the matrix grain size in a high volume fraction fiber reinforced composite fabricated by liquid infiltration techniques is much smaller than the grain size in a similarly cast bulk matrix. The strength and ductiliy of a metal increases with the decreasing grain size and the mechanical properties of hexagonal magnesium are more dependent on grain size than those of the cubic structure metal.

Some investigators have reported that the transverse and shear properties of the composites may be slightly higher than the corresponding strength of the bulk matrix because of the constraint provided by the fibers to the flow of matrix. However, in the case of cast magnesium - boron composites, the shear strength is found to be about 3 times and the transverse strength of the composite about 2 times the corresponding strength of cast bulk magnesium. This substantial improvement of matrix strength in the composite is primarily due to the effect of strong grain refinement, the evidence of which was supported by metallographic observations. It must be remembered that this grain refinement will occur in high volume fraction composites fabricated by liqiud infiltration techniques and rapid quenching.

FAILURE MECHNANISM

Under transverse loading, the mode of composite failure is changed from matrix failure to fiber failure as the matrix strength is increased. The three types of failure observed by transverse flexural loading of the composites were: (a) failure to the matrix; (b) failure of the matrix and the fiber; (c) failure of the fiber. Each of the above failures of the composite occurred progressively as the strength of the matrix was increased (Figure 5). It was found that under transverse flexural loading, Mg-B composites with lowest matrix strength (25,000 psi) failed by failure of the matrix and interface.

The failure of the matrix was accompanied by the formation of a network of cell-like structures. This may suggest that at high volume fractions of fibers the transverse failure of the composite occurs by the shear flow of the matrix rather than the tensile flow, as is generally believed. The AZ-B composites with intermediate matrix strength (35,000 psi) failed by failure of both matrix and fiber, indicating that the transverse strength of the fibers and the matrix strength are about the same and the failure occurs at relatively weaker fibers and at points of stress concentrations in the matrix. HZK-B composites, which possessed the strongest matrix (40,000 psi), failed by the failure of fibers. The tungsten core of the fractured boron filaments in this can is clearly seen in Figure 5.

EFFECT OF FIBER ORIENTATION

The effect of fiber orientation on the flexural strength of the composite is shown in Figure 6. Theoretical curves based on maximum stress, maximum stress as maximum work distortional critera are alsc shown in Figure 6.

Up to about 10°, the failure of the composite occurs by failure of the fiber, whereas between 10° and about 60°, the shear failure of the matrix or interface is the controlling failure mechanism (Figure 7). Between about 60° and 90° fiber orientation, the composite fails by failure of the matrix.

It is seen that the predications of maximum stress theory are higher than the maximum distortional work theory. The maximum strain curve and the maximum stress curve coincide with each other between 0° and 63°, the prediction of maximum strain theory is ever higher than maximum stress theory.

It is noticed from Figure 6 that the experimental results agree best with the maximum distortional work theory. The maximum

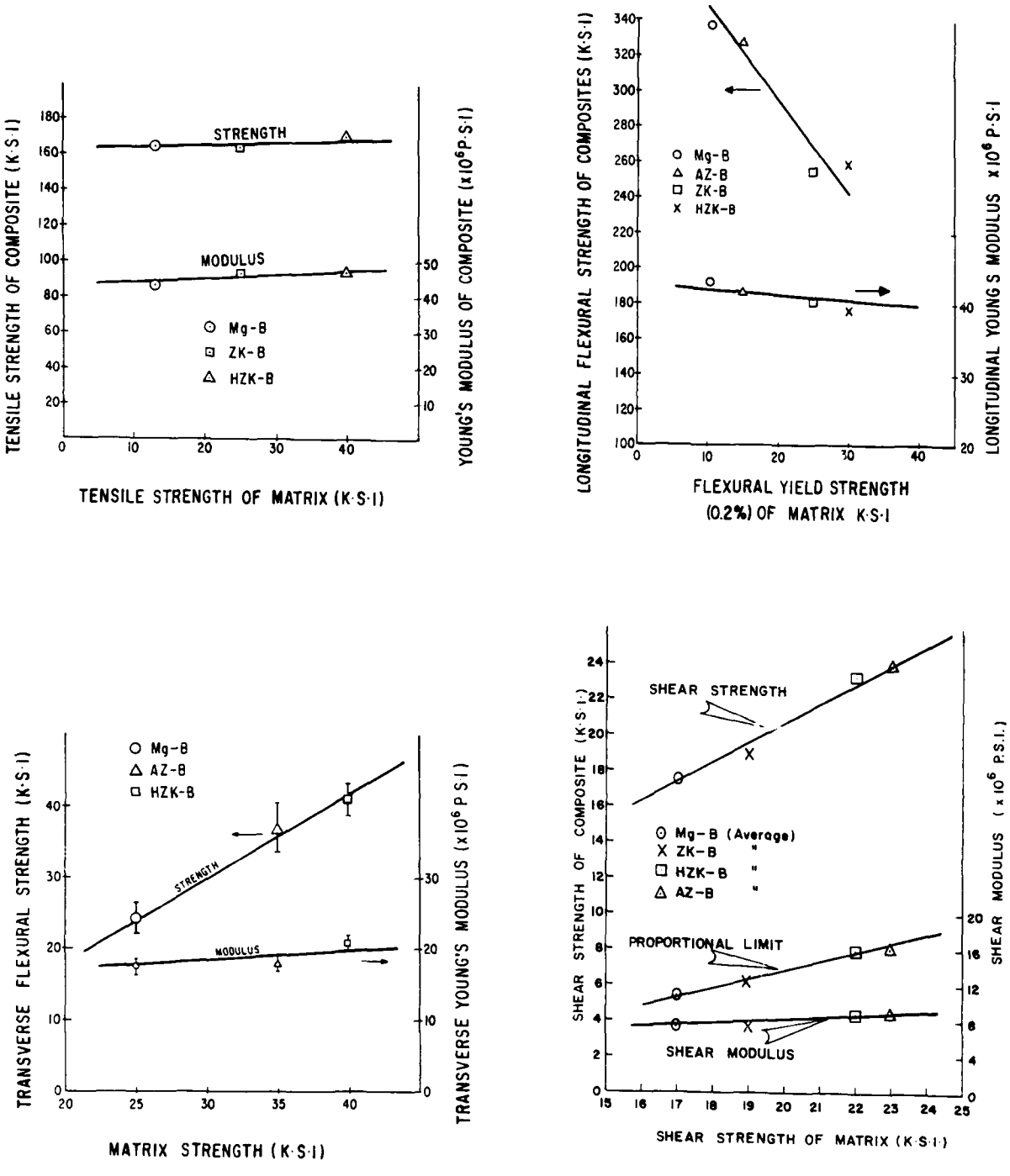


Figure 3 Effect of Matrix Strengthening on the Mechanical Behavior of Boron - Magnesium Composites.

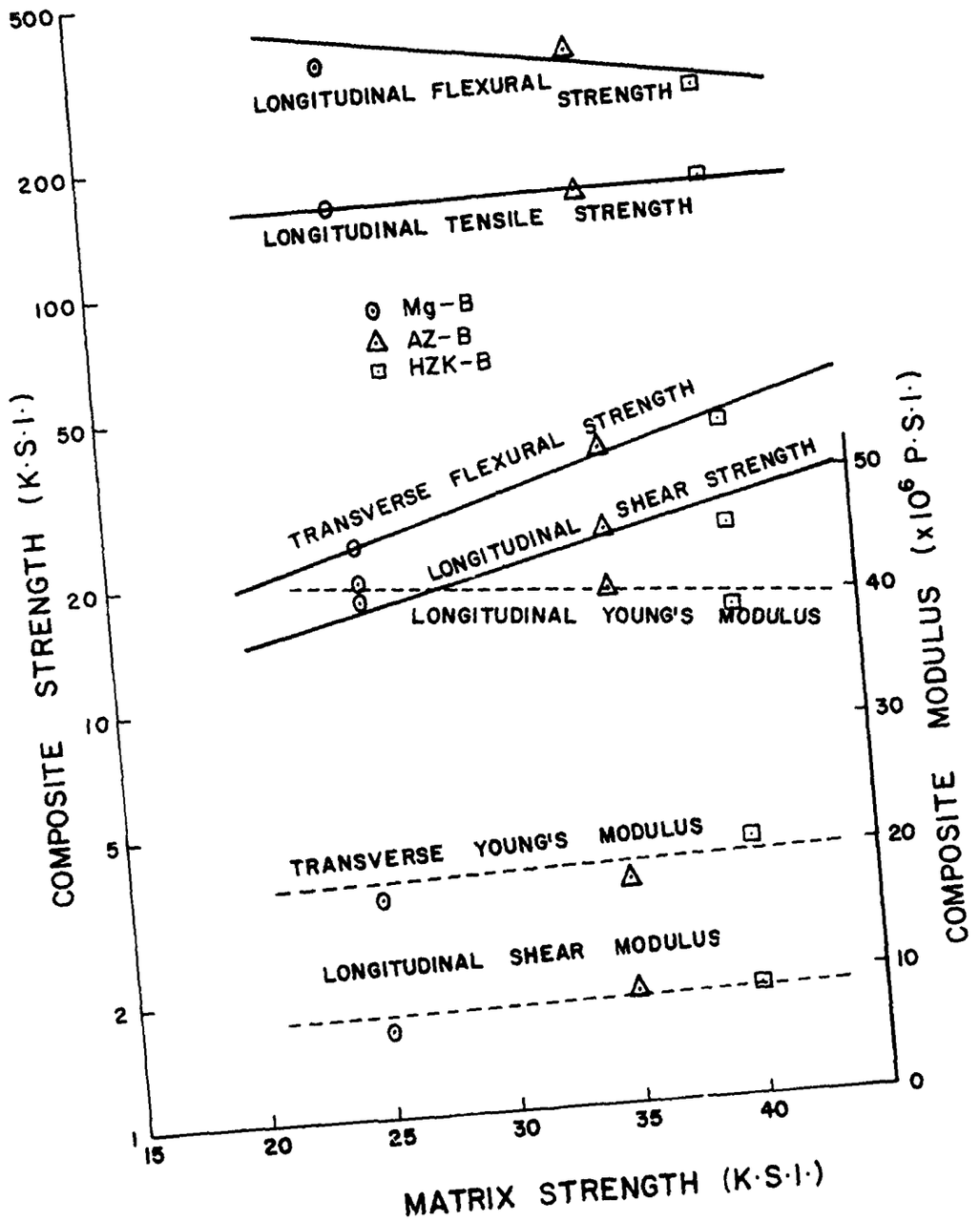
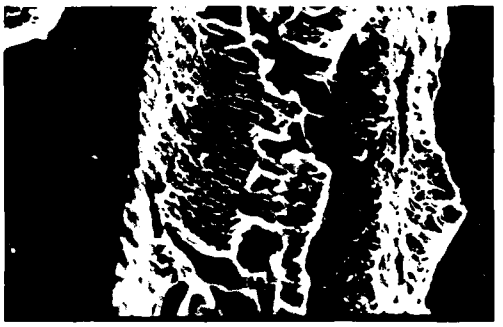

500
200
100
50
20
10
5
2
1
COMPOSITE STRENGTH (K·S·I·)
LONGITUDINAL FLEXURAL STRENGTH
LONGITUDINAL TENSILE STRENGTH
Mg-B
AZ-B
HZK-B
TRANSVERSE FLEXURAL STRENGTH
LONGITUDINAL SHEAR STRENGTH
LONGITUDINAL YOUNG'S MODULUS
TRANSVERSE YOUNG'S MODULUS
LONGITUDINAL SHEAR MODULUS
50
40
30
20
10
0
COMPOSITE MODULUS (x10⁶ P·S·I·)
15
20
25
30
35
40
MATRIX STRENGTH (K·S·I·)

Figure 4



160x

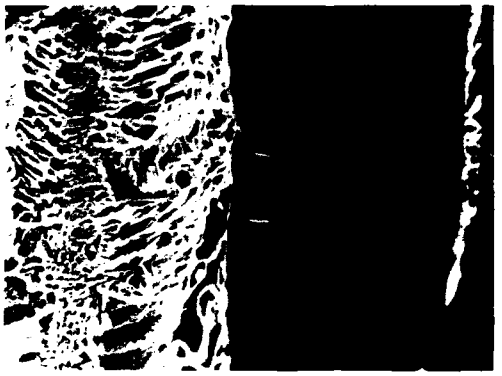


400x

Scanning Electron Micrographs of the Fracture Surface of Magnesium Matrix Composite Under Transverse Flexural Loading Showing Matrix and Interface Failure

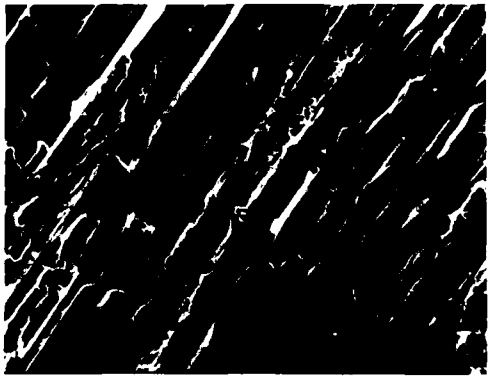


40x



400x

Scanning Electron Micrograph of the Fracture Surface of AZ31B Alloy Matrix Composite Under Transverse Flexural Loading Showing Fiber and Matrix Failure



80x



800x

Scanning Electron Micrograph of the Fracture Surface of Alloy HZK Matrix Composite Under Transverse Flexural Loading Showing Fiber Failure

Figure 5

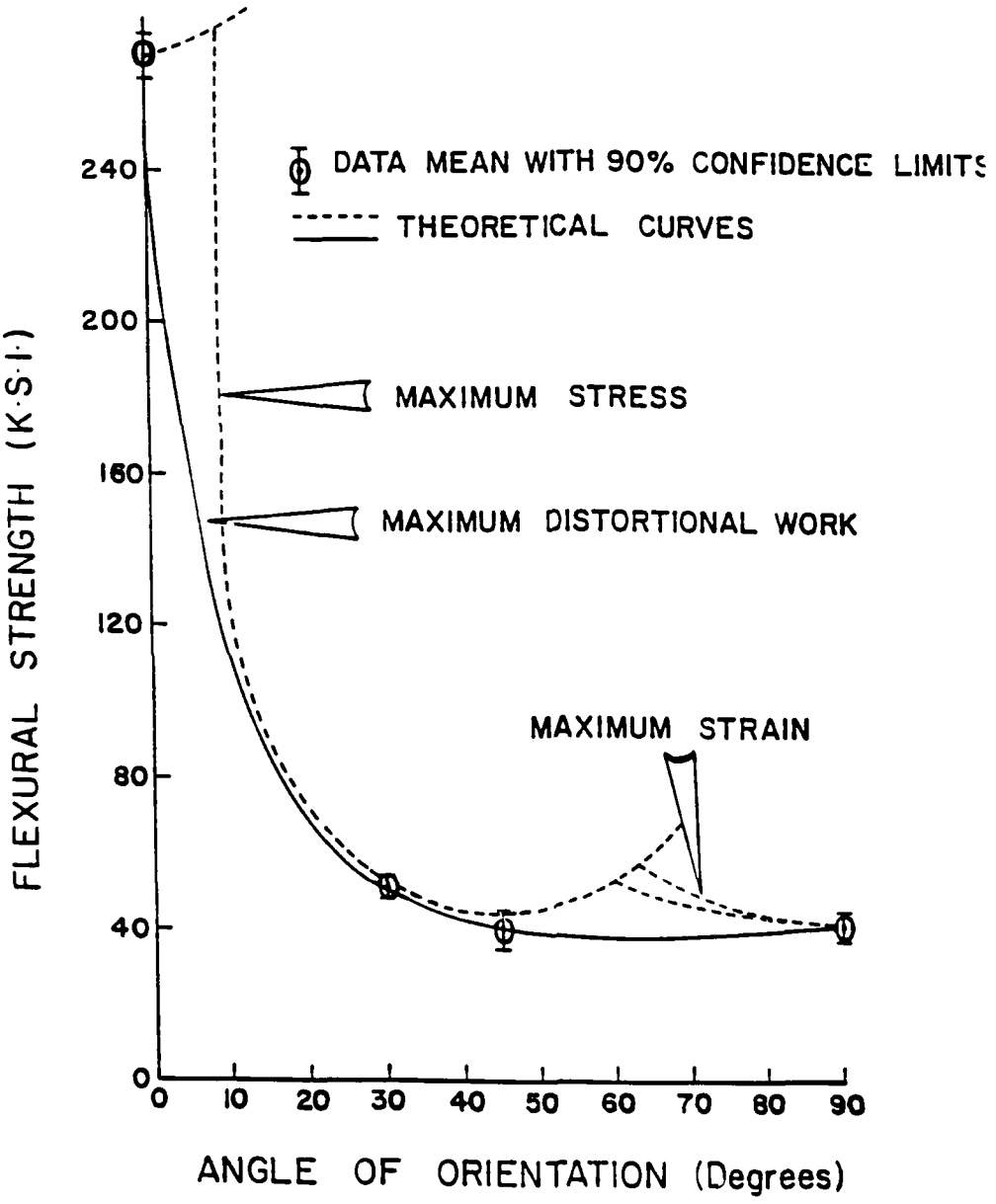
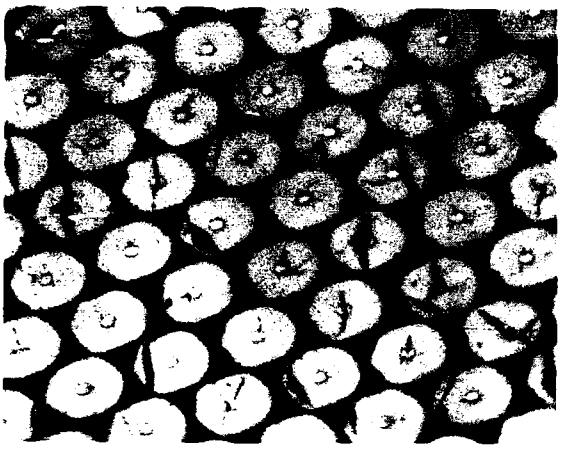
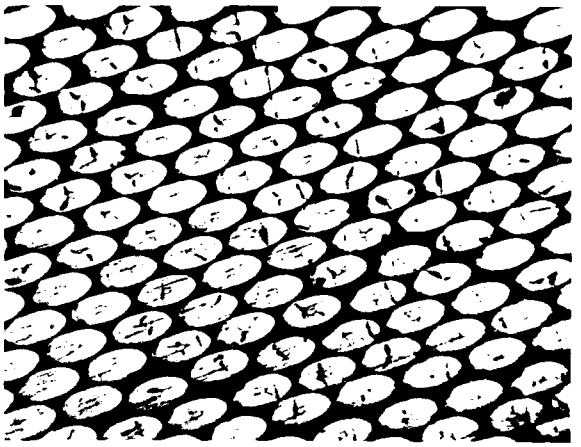


Figure 6. Comparison of Theory with Experimental Results for Flexural Strength of HZK-Boron Composite as a Function of Fiber Orientation (Volume fraction of boron equal to 70%.)



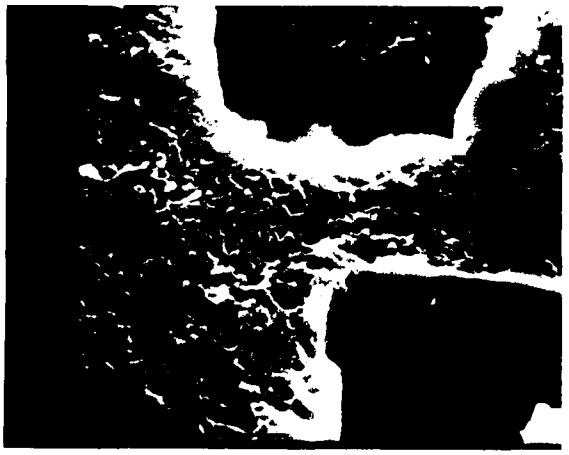
100x

Photomicrographs of Composite with Fiber Orientation of 30° Showing Distribution and Spacing of Fibers



50x

Photomicrographs of Composite with Fiber Orientation of 45° Showing Distribution and Spacing of Fibers



(b) 4000x

Scanning Electron Micrographs of the Fracture Surface of the Composite with Fiber Orientation of 30° Showing Shear Failure of the Matrix



80x

Scanning Electron Micrographs of the Fracture Surface of the Composite with Fiber Orientation of 45° Showing Matrix and Interface Failure

Figure 7

stress and maximum strain theories predict higher strengths. This is due to the fact that in the maximum stress and maximum strain theories, the three failure mechanisms, are assumed to operate rather independently,whereas the maximum distortional work criterion takes into consideration the interaction among the basic material strengths.

Based on experimental data at fiber orientation of 45° and 30°, it may be concluded that the anisotropic strength of cast Mg-B composites is best predicted by maximum distortional work theory.

Reference

"Effect of Matrix Strengthening and Fiber Coating on the Boron - Magnesium Composites", A. K. Dhingra, D.Sc. Dissertation Material Science and Engineering, Washington University, St. Loius, Missouri., 1969.

MECHANICAL PROPERTIES AND MICROSTRUCTURE OF C/Mg COMPOSITES SUBJECTED TO THERMAL EXPOSURE AND THERMAL CYCLING

Susan J. Swindlehurst, Ian W. Hall
University of Delaware, Newark, Delaware, USA

ABSTRACT

Samples of unidirectionally reinforced C/Mg metal matrix composites have been subjected to a variety of thermal and thermomechanical treatments followed by tensile testing at room temperature. It was found that the residual room temperature tensile strength was strongly dependent upon the precise combination of fiber and matrix and upon the treatment applied: thermal cycling led to a decline in tensile properties in most cases, while isothermal exposure in argon caused little property degradation. The thermal treatments were found to lead to the formation of an oxide layer at the fiber/matrix interface. Creep was not found to be a significant phenomenon in these materials at short times and temperatures up to ~ 350°C.

INTRODUCTION

The primary use for C/Mg metal matrix composites (MMC's) to date has been in high performance space structures and antenna systems. These applications take advantage of the light weight, high stiffness, and near zero coefficient of thermal expansion obtainable with high modulus pitch-based fiber systems, and which provide the necessary dimensional stability. C/Mg systems offer advantages over Gr/epoxy, which has dimensional stability problems due to such factors as outgassing in space, moisture absorption, microcracking, and a higher susceptibility to radiation damage (1). Additionally, the high specific strength and stiffness available through the use of such a low density matrix are now of increasing interest to the automotive industry. To the emphasis on dimensional stability is added a concern over how this system will behave in an environment in which composites are exposed to stress at elevated temperature and under thermal cycling-type conditions.

Whilst corrosion generally poses problems for magnesium alloys and composites, recent advances in magnesium alloy technology have significantly reduced susceptibility to corrosion (2) and there are applications where normal atmospheric corrosion would not be a major or limiting factor. Under these circumstances interest centers upon the mechanical properties at room and moderately elevated temperatures, and upon how these are affected by isothermal exposure, thermal cycling and creep. This paper reports some results of such a study.

EXPERIMENTAL

The composites used in this investigation were prepared by a squeeze casting technique by Honda R.&D. Co. Ltd, Wako-shi, Japan. High strength T300 PAN-based carbon fibers were used as the unidirectional reinforcement: they were used either in an untreated, unsized condition (designated -99) or in a surface treated condition (designated -90). Titanium powder particles were incorporated into the fiber preform in an attempt to promote a uniform fiber distribution. The nominal volume fraction of fibers was 35%; the matrix was either commercially pure magnesium (c.p.Mg) or a Mg-4%Al alloy. The squeeze casting process as used here appears to provide good infiltration and bonding between the matrix and reinforcement

without the need for a coating to enhance wetting. Some comparison testing and metallographic examinations have also been performed with samples reinforced with high modulus M-40 fibers.

The composites were subjected to isothermal exposure or thermal cycling and then tensile tested at room temperature. Some specimens were also creep tested. The microstructural changes accompanying these thermal treatments were observed by optical and transmission electron microscopy (TEM); scanning electron microscopy (SEM) was used to characterize the fracture surface morphology. TEM samples were prepared such that the fiber axes lay in the plane of the foils; this gave samples in which large interfacial areas lay almost perpendicular to the electron beam. Isothermal exposure was carried out at 325°C for up to 1000 hours in argon, or 216 hours in air. Thermal cycling experiments were conducted in air in a system comprising two fluidized baths; the hot bath was maintained at 325°C and the cold bath at 20°C. The dwell time was 2 minutes in each bath, and tests were run for a maximum of 1300 cycles. Creep tests were performed in air in the temperature range 300-350°C, at loads corresponding to approximately 50 or 75% of the room temperature ultimate tensile strength. These tests ran from 120 to 200 hours.

Room temperature tensile tests were conducted on an 1125 Instron machine at a constant cross-head speed of 1.3 $mm.min^{-1}$. The samples had a cylindrical reduced gage length of 25.4mm and a cross sectional area of $26.4mm^2$. Each sample was fitted with two strain gages for tensile testing.

RESULTS

MECHANICAL PROPERTIES - The results of all the tensile tests are presented together in Table 1. It should be noted firstly that the tensile strength of as-fabricated samples was markedly reduced by the fiber surface treatment, and substantially increased by the addition of 4%Al to the matrix alloy.

The environment in which thermal exposure treatments were performed was found to be of great importance in affecting the residual tensile strength. After treatments of up to 1000 hours in Ar there was no significant difference in the tensile properties of any of the samples tested. However, treatments for shorter times, 216 hours, in air caused remarkable changes in the residual tensile strength. The strengths of composites containing untreated fibers (-99) were reduced by more than 20% in comparison to their as-fabricated values while the strength of surface treated fiber composites (-90) was increased.

Thermal cycling also affected the residual tensile strength and again the environment is be-

Table 1. Mechanical Property Data

Sample type	Treatment	Tensile Strength (MPa)	Young's Modulus (GPa)
T300-99/c.p.Mg	As fabricated	498	80
T300-90/c.p.Mg	As fabricated	382	
T300-99/Mg-4Al	As fabricated	638	76
T300-99/c.p.Mg	Th. exp. 216h	390	80
T300-90/c.p.Mg	Th. exp. 216h Th. exp. 1000h	511 422	71 92
T300-99/Mg-4Al	Th. exp. 216h Th. exp.1000h	510 650	85 152
T300-90/c.p.Mg	Th. cycl. 1300x	644	86
T300-99/Mg-4Al	Th. cycl. 1300x	469	76

lieved to be an important factor as will be described below. Cycling reduced the strength of untreated fiber composites even further than isothermal treatment but, in contrast, the strength of surface treated fiber composites was correspondingly increased.

No appreciable creep deformation was noted during the 120-200 hour creep tests. The small initial strains noted rapidly decayed and are believed to be attributable to fiber straightening. Nor was there any apparent change in the residual tensile strength when the crept samples were tested at room temperature.

FRACTOGRAPHY - The mechanical property variations noted above were accompanied by the following changes in fracture surface morphology. In general, the as-fabricated T300-90/c.p.Mg samples showed surfaces which were rather flat and in which large areas of fibers had failed in stepped colonies without appreciable pull-out. Composites containing T300-99 fibers exhibited rather rougher surfaces in which fiber pull-out was more in evidence. These observations emerge as a general trend for all specimens in that as the strength decreases the fracture surface becomes macroscopically flatter and, conversely, as it increases the surface becomes rougher.

Isothermal exposure in argon caused relatively little change apart from an increased tendency for whole fiber tows to fail as a single microstructural unit in T300-99/Mg-4Al% samples, Fig. 1.

After thermal exposure in air for 216 hours the fracture surface of T300-90/c.p.Mg composites had become macroscopically rougher, showed more matrix ductility between fibers and also showed some fiber pull-out, Fig. 2. However, T300-99/c.p.Mg and T300-99/ Mg-4Al samples now both had very flat surfaces, Fig. 3.

Thermal cycling produced fracture surfaces consisting of areas of bundle failure interspersed with occasional fiber pull-out. The most remarkable feature of these samples though was that, for the first time, the Ti particles used to obtain good fiber distribution were clearly visible. Some of these are indicated in Fig. 4 and they are believed to be exerting a dominant influence over the final fracture event in these samples.

METALLOGRAPHY - Optical microscopy revealed that the initial dendritic as-cast structure gave way to a more regular grain structure after heat treatment at 300°C. Also some fiber misalignment had occurred during the casting process. These features and the dispersed Ti particles are seen in Fig. 5. Microcracking was occasionally noted in the matrix at the tow boundaries of thermally cycled samples.

TEM examination of as-fabricated T300-99/c.p.Mg samples revealed an almost totally featureless fiber/matrix interface in which, as reported elsewhere (3), contact was excellent and no reaction products were found. When

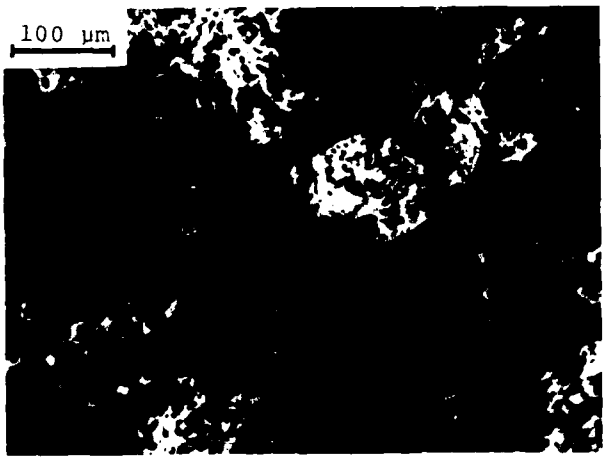


Fig. 1. T300-99/Mg-4Al, thermally exposed for 1000h in Ar showing tendency for tow pull-out.

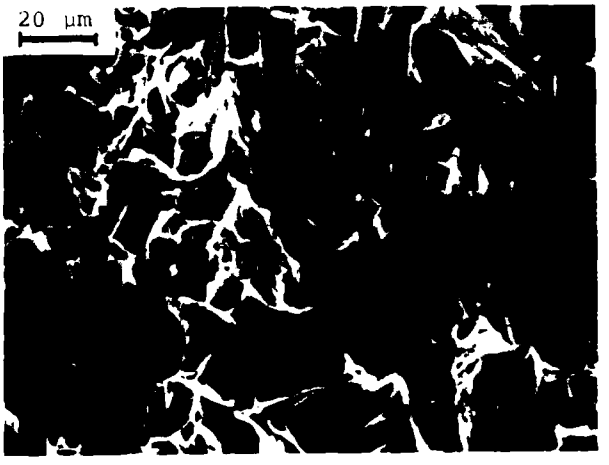


Fig. 2. T300-90/c.p.Mg, thermally exposed 216h in air showing some fiber pull-out and matrix ductility.

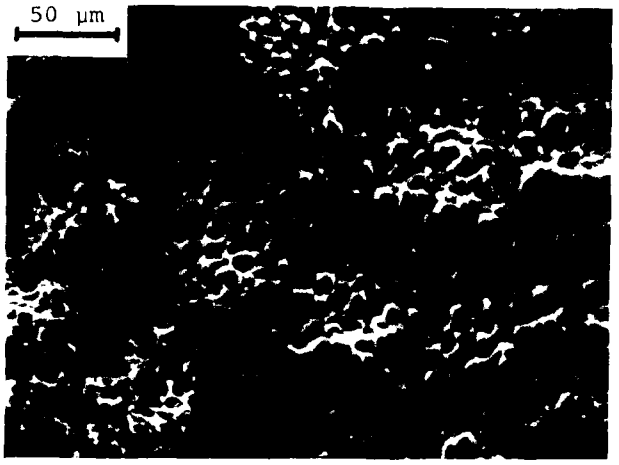


Fig. 3. T300-99/c.p.Mg, thermally exposed for 216h in air showing fiber bundle failure giving flat fracture surface with no fiber pull-out.

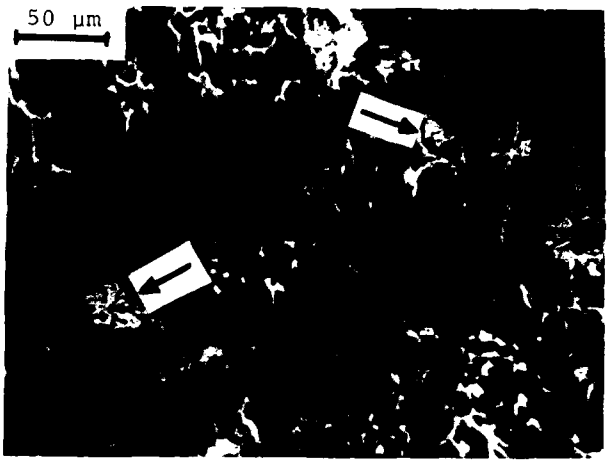


Fig. 4. T300-90/c.p.Mg, thermally cycled, showing bundle failure and Ti particles indicated on the fracture surface.

aluminum was present in the matrix, numerous fine carbides were found at the interface, as seen in Fig.6, along with occasional small $Mg_{17}Al_{12}$ particles. This micrograph shows a section in which the plane of the foil contains the fiber/matrix interface. In the T300-90/c.p.Mg case, however, a thin interfacial layer was noted uniformly distributed along the fiber. The layer was generally amorphous in appearance and gave a very diffuse ring electron diffraction pattern.

Isothermal exposure in argon caused no microstructural alteration at the interface as far as the carbides were concerned but did lead to the appearance of a thin interfacial layer in places. In the T300-90/c.p.Mg samples the layer was more microcrystalline in appearance than in its as-fabricated counterpart, though not noticeably thicker, Fig. 7(a). In the T300-99/ Mg-4Al samples, the layer was discontinuous and much finer: evidently the layer has only just begun to nucleate in this sample, Fig. 7(b).

Thermal exposure in air caused the layers to achieve much greater thicknesses in all cases and thermal cycling proved even more effective in this respect. Even in the crept T300-99 samples an incipient layer was noted at the interface.

Samples reinforced with M40 fibers were also examined by TEM and were found to be exceptionally susceptible to the formation of an interfacial layer upon thermal exposure or thermal cycling. The layer frequently reached thicknesses of the order of 0.5microns. Under these circumstances the layer was amply thick enough to obtain sharply defined powder diffraction patterns in the TEM and from these, using the single crystal matrix pattern as an internal calibration standard, it was found that the layer consisted of MgO, Figs. 8 (a)&(b). This is consistent with EDS analyses which only show Mg in these layers (elements lighter than F being undetectable in our system).

DISCUSSION

The present work has shown that, while the room temperature mechanical properties of the composites are strongly dependent upon long term exposure to high temperature or to thermal cycling, there is little evidence as yet that creep deformation occurs as a result of short term (<200 hour) tests.

The changes in tensile properties and fracture morphology for the T300-99 systems, at least, correlate well with the simple interface model proposed by Ochiai and Murakami (4). A sufficiently strong interface can serve as a stress raiser and lead to notch effects. The presence of a brittle reaction zone may also serve as a stress raiser for the fiber, since it will fracture at small strains and form a circumferential notch around the fiber. If the interface is strong enough to allow the notch to extend into the fiber, fracture will rapidly follow whereas a weak interface would debond and cause blunting of the crack tip. The interface may rely upon mechanical



Fig. 5. T300-99/Mg-4Al, crept 200h @ 300°C. Note dispersed Ti particles and quite good fiber alignment.



Fig. 6. T300-99/Mg-4Al as-fabricated. Fiber/matrix interface showing $Mg_{17}Al_{12}$ particles (arrowed) and fine needle-like carbides.



Fig. 7(a). T300-90/c.p.Mg, thermally exposed for 1000h in Ar showing microcrystalline layer at fiber/matrix interface.

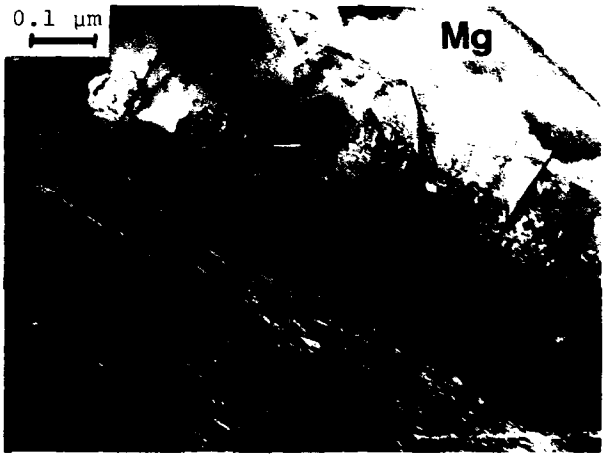


Fig. 7(b). T300-99/Mg4Al, thermally exposed 1000h in Ar showing the discontinuous reaction layer and interfacial carbides.

interlocking or chemical bonding, or a combination of the two, for load transfer from the matrix to the fibers. The interfacial shear strength is thus variable in nature and system specific.

The effect of the brittle zone is thickness dependent. If it is very thin, fiber flaws will dominate fracture; as the zone thickens, the interface increasingly begins to dominate the behavior until a critical point where the fiber fractures simultaneously with the brittle zone. Beyond this critical thickness, the zone becomes weaker since it will contain more defects. Ochiai and Murakami (4) calculated that the critical reaction zone thickness for carbon fibers was ~170nm.

In the composites studied here, a reaction zone is formed as a result of the fabrication process only for surface treated (-90) fibers but subsequent thermal treatments have been shown to lead to the formation of such a layer in all samples. The layer has been shown to consist of microcrystalline MgO and its presence contributes an increasing component of chemical bonding to the fiber/matrix interfacial shear strength which is otherwise mainly mechanical in character. Hence, for surface treated samples, the strain at which notch effects occur in the fibers is less than the strain at which debonding occurs and low composite strength is measured. Samples which do not contain an interfacial oxide layer, have a lower interfacial shear strength and measured strengths are higher.

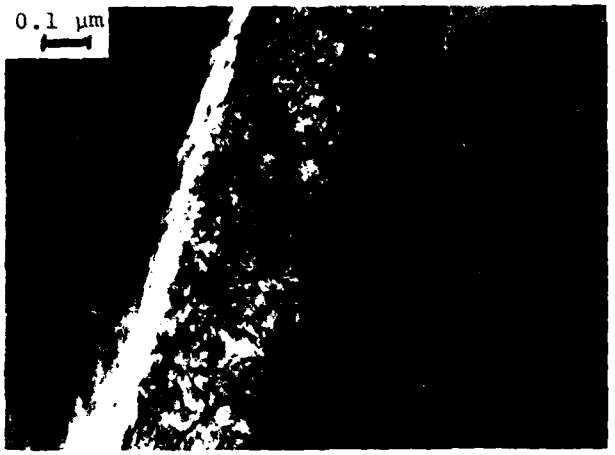


Fig. 8(a). M40-99/c.p. Mg, thermally exposed for 1000h in argon showing oxide layer between fiber (F) and matrix (M).

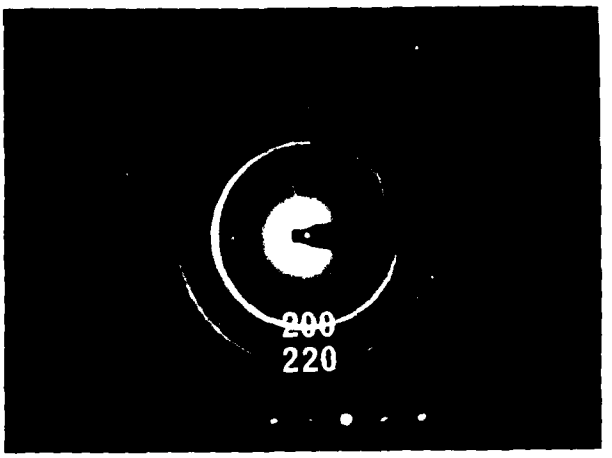


Fig. 8(b). Ring diffraction pattern from oxide layer of (a) along with spot pattern from Mg matrix.

The treatment applied to the -90 fibers produces a highly reactive surface which itself forms a thin oxide layer even during fabrication. Many workers have reported that surface treatments increase the concentration of oxygen on the fibers (5,6) as well as increasing the surface roughness. Untreated fibers do not contain enough adsorbed oxygen or reactive groups to form a complete layer during fabrication but prolonged exposure to high temperature allows diffusion of oxygen along the fiber/matrix interface. Treatments which allow easy access of oxygen, and possibly moisture, and which promote mechanical stresses and debonding at the interface to aid diffusion will maximise oxide layer formation. Thermal cycling is clearly the most effective in this respect since it has been noted that microcracking occurred after thermal cycling due to the differing coefficients of thermal expansion of fiber and matrix. The titanium particles also proved efficient sites for crack nucleation and in future work specimens will not contain these potential stress raisers.

It must be noted that the oxide layer present in these samples is either amorphous or microcrystalline and cannot be assumed to behave in the same manner as a monolithic reaction layer. In particular, since there is a volume contraction of ~19% when MgO forms from Mg, significant tensile stresses can be expected to occur within the layer as it thickens. The layer will, therefore, undergo internal cracking and will further complicate the tensile response.

The oxide thickness depends on the treatment and the particular fiber/matrix system but certainly constitutes a brittle zone which has an increasing effect on the fracture morphology as it increases in thickness. Cracks, unblunted by the brittle zone, run across the fibers, leading to their fracturing in bundles and hence the flat, step-type appearance of the surface found in samples with oxide layers. The T300-99 samples in their as-fabricated state have a weaker bond which relies principally upon mechanical interlocking and leads to an extensive amount of fiber/matrix debonding and fiber pull-out and, hence, higher strength. As the oxide layer forms in these systems during the various thermal treatments, the fracture becomes more and more interface dominated, and results in the noted flattening of the fracture surface and decrease in strength.

Since the oxide layer thickness varies from one region to the next it is not possible to give an accurate estimate of it after any specific treatment. However, the range of thicknesses, 2-200nm, corresponds closely to the range over which effects on strength are to be expected (4).

CONCLUSIONS

For the PAN-based T-300/Mg composite system studied:

1. Creep at temperatures below 300°C was found to be insignificant at stresses up to 75% of

U.T.S. for times less than 200 hours.

2. Thermal treatments led to the formation of an interfacial layer: thermal cycling was the most severe treatment, thermal exposure in air next, and thermal exposure in argon least severe.

3. The interfacial layer was identified as MgO.

4. Room temperature mechanical properties are markedly dependent upon the thickness of the interfacial oxide layer.

ACKNOWLEDGEMENT

The authors gratefully acknowledge the provision of the material used in this study by Honda R. & D. Co., Ltd., Wako-shi, Japan. Financial support was provided by the Center for Composites Manufacturing Science and Engineering.

REFERENCES

1. Martin Marietta Technical Report N00024-84-C-5306, Nov. 1985.

2. Proc. World Magnesium Conf., Tokyo, 1987, in press.

3. A. P. Diwanji and I. W. Hall, Proc. ICCM-VI, (F. L. Matthews, N. C. R. Buskell and J. M. Hodgkinson eds.) Elsevier, London, 1987, p. 2.265.

4. S. Ochiai and Y. Murukami, J. Matls. Sci., 14 (1979) p.831.

5. A. Shindo, Y. Sawada and Y. Nakanishi, *"Composites '86: Recent Advances in Japan and the United States"* (K. Kawata, S. Umekawa and A. Kobayashi, eds.) Tokyo, 1986, p.727.

6. T. Norita, J. Matsui and H. Matsuda, *"Composite Interfaces"* (H. Ishida and J. L. Koening eds.) Elsevier, New York, 1986, p.123.

MECHANICAL BEHAVIOR OF HIGH-CONDUCTIVITY IN-SITU ULTRAFINE MICROCOMPOSITIES

R. W. Hayes, J. L. Yuen, N. E. Paton, G. Schnittgrund
Rockwell International/Rocketdyne Division
Canoga Park, California, USA

Abstract

The mechanical behavior of three Cu-based in-situ processed ultrafine microcomposites has been studied by means of the determination of activation energies for the flow stress as a function of the processing true strain and alloy composition. In addition, the strain-hardening behavior as a function of the processing true strain and the alloy composition has also been determined. The in-situ microcomposites studied were Cu-15 v/o Nb, Cu-2 v/o Ag-15 v/o Nb, and Cu-3.3 v/o Mo-11.2 v/o Nb. Based on the activation energies and the strain-hardening characteristics, it is proposed that the dominant aspect of the strengthening achieved in the in-situ-formed microcomposites is a transition in deformation mode from Stage III hardening back toward Stage II hardening in the Cu matrix with increasing processing true strain. This transition from Stage III back toward Stage II hardening occurs as a result of the decreasing Nb ribbon spacings with increasing true strain during heavy mechanical working. As the ribbons approach a spacing of about 1 μm, they become short-range dislocation obstacles acting to suppress further Stage III hardening and, thus, promote the transition back toward Stage II linear hardening. It is further proposed that it is the transition from Stage III back toward Stage II hardening with true strain that leads to the positive deviation from rule of mixture strength predictions observed in the heavily deformed in-situ ultrafine microcomposites.

RECENTLY, AN INCREASED EFFORT has been devoted to the development, processing, and fundamental characterization of a class of materials that have become known as the in-situ processed ultrafine microcomposites. These materials consist of a continuous high-purity face centered cubic (FCC) Cu matrix with the addition of low-volume fractions of body centered cubic (BCC) metal elements such as Fe or the BCC refractory elements Nb, Mo, Ta, V, W, or Cr as the second-phase constituents. The name in-situ ultrafine microcomposites has been coined by virtue of the means by which they are processed. Generally, the processing of these materials consists of machining grooves into a high-purity Cu rod and then inserting strips of the high-purity BCC metal into the machined grooves. The Cu rod with the inserted BCC strips is then consumable arc melted into an ingot consisting of a high-purity Cu matrix with the BCC element appearing as isolated dendrites upon completion of ingot solidification. One basic requirement for this type of "as-cast" microstructure is that the Cu matrix possesses a very limited solubility for the selected BCC second-phase constituent. The fine ribbon morphology of the second phase, typical of the final microcomposite microstructure is developed by heavy mechanical working to very high processing true strains defined as $\eta = \ell n (t_o/t)$ where t_o and t are the initial and final thicknesses, respectively. The mechanical working can be achieved by either rolling into sheet or foil or drawing into rod or wire.

At the present time, there still remains an uncertainty over the fundamental mechanisms by which these materials achieve their high strengths with increasing processing true strains (generally at $\eta > 4$). These high strengths are manifested by a positive deviation from "rule of mixture" (ROM) strength predictions common to the in-situ-processed ultrafine microcomposites.

In a previous study, Spitzig, Pelton, and Laabs[1] correlated the microstructural evolution with the strength level of Cu-12 v/o Nb and Cu-20 v/o Nb as a function of the processing true strain. Detailed transmission electron microscope (TEM) examination of specimens deformed to various processing true strains indicated that during deformation, the Cu matrix undergoes a deformation-dynamic recovery-dynamic recrystallization cycle. Concurrently, the BCC Nb phase undergoes a transition from a dendritic to a filamentary morphology with increasing

RESULTS

FLOW STRESS - All flow stress data presented in this study are given in terms of the shear stress τ defined for polycrystals as tensile stress σ divided by 2. The material reductions are given in terms of the processing true strain η. The fundamental dislocation mechanisms controlling the deformation and strengthening of the in-situ microcomposites of the present study are defined by characterizing the shear stress as a function of temperature and strain rate. The temperature-strain rate dependence of the shear stress is presented in Fig. 1 through 3. From these data, the activation energies for plastic flow were obtained by plotting log $\dot{\epsilon}$ at constant τ ($3\%\epsilon$) against the reciprocal of the absolute temperature. The activation energy for the shear stress is obtained from the Arrhenius equation relating the strain rate ($\dot{\epsilon}$) and temperature (T) to the shear stress written in the form

$$\dot{\epsilon} = A\, e^{-\Delta H/RT} \qquad (1)$$

where $-\Delta H$ is the activation energy for the shear stress. Rewriting Eq. (1) and solving for ΔH gives

$$-\Delta H = 4.6 \left(\frac{10g\ \dot{\epsilon}}{1/T} \right)_{\tau}$$

where 4.6 = R/log e and τ is constant. The activation energies obtained from the data in Fig. 1 through 3 are summarized in Table 1. In examining the data in Table 1, it is seen that there is a substantial decrease in the activation energy for the shear stress of the Cu-15 v/o Nb with increasing true processing strain. For the Cu-3.3 v/o Mo-11.2 v/o Nb, the activation energy for the shear stress at processing true strains of 4.1 and 5.7 are approximately equal and both well above 1.0 eV while at a processing true strain of 6.7, the activation energy has decreased to 1.0 eV. In contrast to the two above alloys, the activation energy for the Cu-2.0 v/o Ag-15 v/o Nb is consistently below 1.0 eV at all three true strains and also appears to be independent of processing true strain. The summary of activation energies presented in Table 1 suggest that for the Cu-15 v/o Nb and the Cu-3.3 v/o Mo-11.2 v/o Nb microcomposites, the rate-controlling deformation mechanism is a function of the true processing strain while the rate-controlling deformation mechanism of the Cu-2.0 v/o Ag-15 v/o Nb remains constant and, thus, independent of true processing strain. Recently, Olivares and Sevillano[5] have shown activation energies for dislocations cutting the forest (i.e., linear Stage II hardening) in polycrystalline Cu ranging from 0.5 to 0.9 eV

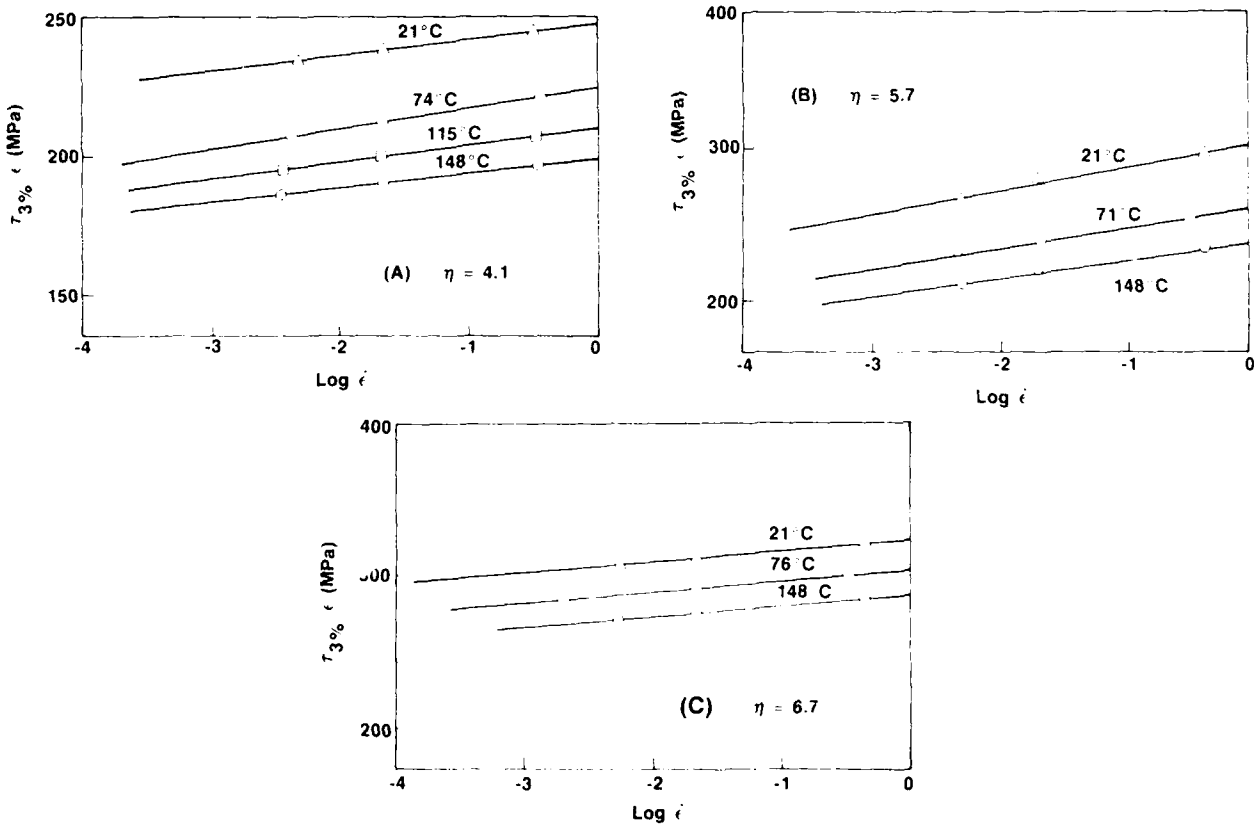


Fig. 1 - Effect of temperature and strain rate on the flow stress of Cu-15 v/o Nb as a function of true strain (η)

deformation and both the spacings and the thicknesses of the Nb filaments decrease. The dynamic recovery and recrystallization of the Cu matrix allows continuous deformation of the microcomposite matrix without the need for intermediate annealing cycles. It was proposed by Spitzig et al.[1] that the strength achieved in their Cu-Nb microcomposites was in the effectiveness of the Nb ribbons acting as planar barriers to the movement of dislocations within the Cu matrix. The increase in tensile strength correlated with the decrease in Nb ribbon spacings in accordance with a Hall-Petch relationship.

In another study conducted on heavily deformed two-phase materials, Funkenbusch and Courtney[2] proposed that the dominant strengthening achieved in the Cu-BCC-phase microcomposites (such as Cu-Fe, Cu-Cr, Cu-Nb, etc.) arises from the difference in strain hardening characteristics of the FCC Cu matrix and the BCC filaments. In their study, the Cu matrix is assumed to undergo a deformation-dynamic recovery cycle (as does unalloyed high-purity Cu). However, the BCC filaments undergo linear hardening and, thus, continue to gain in dislocation density and strength with increasing processing true strain. The basis for their model is that additional geometrically necessary dislocations are generated during deformation of the two-phase materials in order to maintain strain compatibility at the interface. With increasing disparity between the plastic flow behavior of the two phases, the greater the excess strength achieved for the overall matrix due to the high density of interfacial dislocations generated. Thus, the greatest composite strengths are predicted to occur in systems in which dynamic recovery processes are minimal[2]. The strength contribution from the interfacial dislocations is an outgrowth of Ashby's original concept for the work hardening of polycrystalline materials.[3] This concept has been modified by Funkenbusch and Courtney[2] to take into account the continuously decreasing interphase spacing with continued deformation that occurs during heavy mechanical working of the microcomposites.

In the present study, the dislocation mechanisms controlling the microcomposite deformation process are defined in terms of the activation energy for the flow stress and from the strain-hardening characteristics as a function of processing true strain and alloy composition. The results obtained from this study are then compared to previous strengthening mechanism models proposed for the in-situ ultrafine microcomposites.

EXPERIMENTAL

MATERIAL AND SPECIMEN FABRICATION - Three in-situ processed ultrafine microcomposites were selected for a study of the fundamental mechanisms leading to the strengthening of these materials. The materials selected for this study were Cu-15 v/o Nb, Cu-2 v/o Ag-15 v/o Nb, and Cu-3.3 v/o Mo-11.2 v/o Nb. The materials were initially arc cast into 76.2-mm-diameter ingots. The ingots were then sectioned into three 101.6-mm-length billets for subsequent mechanical reduction. One of the 101.6-mm billets from each alloy composition was mechanically worked by cold rolling to produce sheet material with processing true strains of 4.1, 5.7, and 6.7, respectively. The cold rolling was performed at room temperature with the rolling being continuous (e.g., no annealing treatment between rolling passes) until the desired reduction was obtained. The arc casting and mechanical processing of the sheet was performed at Ames Laboratory, Iowa State University, Ames, Iowa.

Flat-sheet tensile specimens were fabricated from the rolled material by milling. The tensile specimens consisted of a reduced section 25.4 mm long by 12.7 mm in width. Specimen fabrication procedure was identical for all three process thicknesses. The material thickness corresponding to the true processing reductions was 1.27 mm for $\eta = 4.1$, 0.254 mm for $\eta = 5.7$, and 0.083 mm for $\eta = 6.7$.

MECHANICAL TESTING - A series of uniaxial tension tests were performed in the temperature range of 21 to 148°C. The temperature range was narrow in order to minimize the possibility of microstructural changes occurring in the specimen during the test. The uniaxial tension tests were conducted on a Tinus Olsen 20 kip screw-driven testing machine of rigid construction. The strain rates were varied from 8.3×10^{-5} sec^{-1} up to 5.0×10^{-3} sec^{-1}. All tests conducted at temperatures above 21°C were performed in an argon atmosphere. The specimens for elevated temperature testing were placed in a Satec Systems 3 zone resistance heating furnace in an open-end retort sealed with temperature-resistant Kaowool. All temperatures were maintained to within ± 3°C of the desired test temperature. Upon reaching temperature, the specimens were allowed a 5-min equilibration soak to ensure complete temperature uniformity throughout the specimen gage section. All test temperatures were monitored by means of a Chromel-Alumel type-K thermocouple attached directly to the specimen gage section. All specimen strain measurements were obtained by attachment of a high-temperature extensometer directly to the specimen gage section. The temperature-strain rate dependence of the flow stress was obtained by conducting incremental strain rate changes on a single specimen at each of the test temperatures. The flow stress as a function of temperature and strain rate was measured at a constant strain of 3%. It has been shown by Basinski[4] and others that this experimental method does provide a sound approach to defining the fundamental rate-controlling dislocation mechanisms for the plastic deformation and the strengthening behavior of both single and polycrystalline metallic materials.

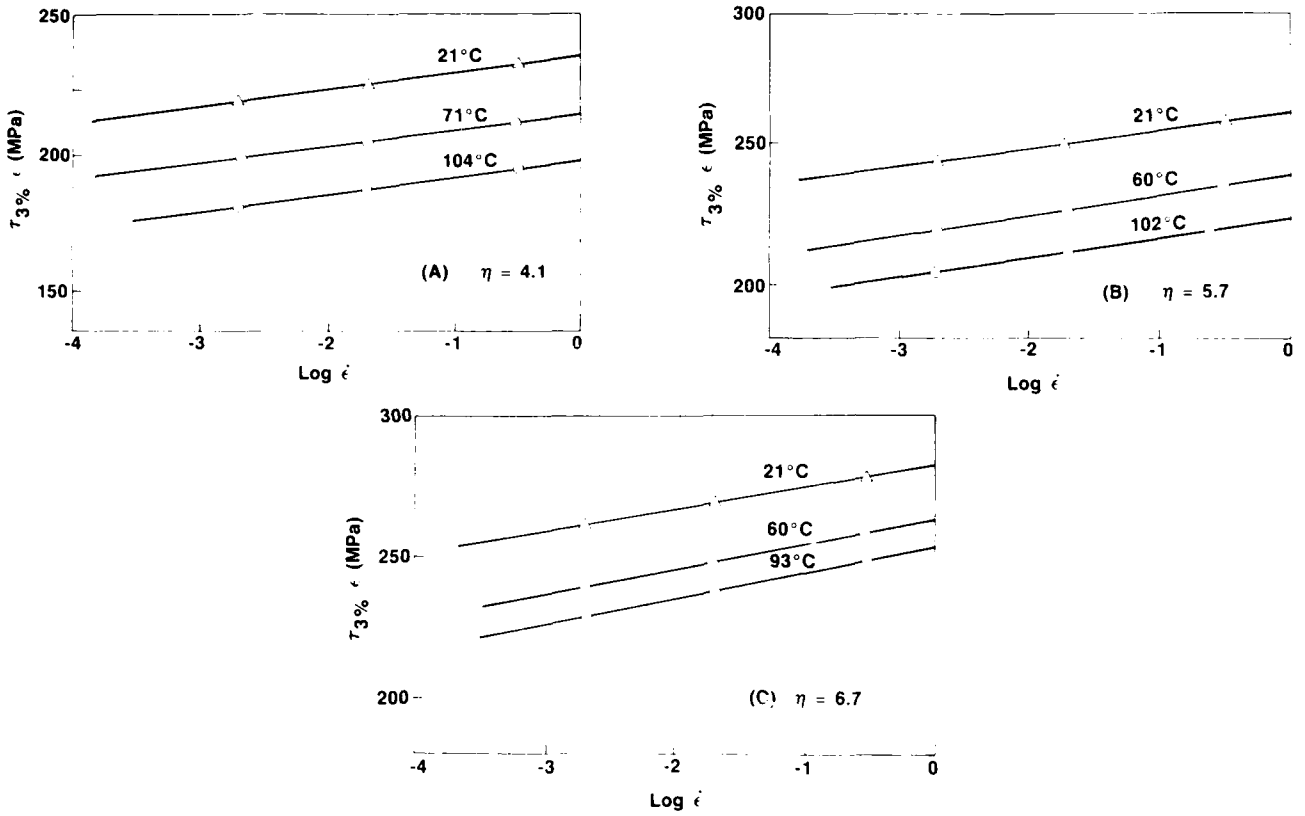


Fig. 2 - Effect of temperature and strain rate on the flow stress of Cu-3.3 v/o Mo-11.2 v/o Nb as a function of true strain (η)

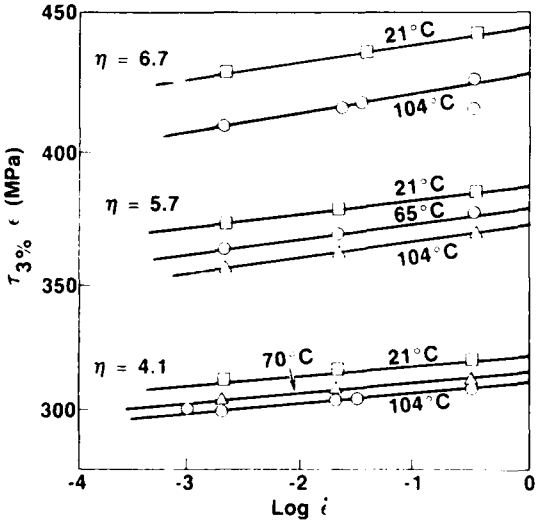


Fig. 3 - Effect of temperature and strain rate on the flow stress of Cu-2 v/o Ag-15 v/o Nb as a function of true strain (η)

for deformation at 326°K. Previously, Feltham and Meakin[6] have shown activation energies for cross slip (i.e., Stage III hardening) in polycrystalline Cu ranging from 1.21 to 1.40 eV. It is well established that the cross-slip mechanism is the primary mechanism by which Cu undergoes dynamic recovery (Stage III hardening) during deformation centering around 300°K. In comparing the activation energies obtained from the in-situ ultrafine microcomposites to those reported in the literature for high-purity polycrystalline Cu, it appears that at low-processing true strains (η < 4), the controlling deformation mechanism is cross slip, while at processing true strains greater than 4, dislocations cutting the forest (i.e., Stage II linear hardening) controls the deformation behavior.

It will be shown that a comparison of the two-phase ultrafine microcomposite deformation mechanisms to those of high-purity polycrystalline Cu is indeed a valid comparison. Further, it will also be shown that the primary role of the second-phase BCC filaments is in influencing the deformation mode and work-hardening characteristics of the continuous FCC Cu matrix.

STRAIN-HARDENING CHARACTERISTICS - In view of the fact that the activation energies for the Cu-15 v/o Nb and the Cu-3.3 v/o Mo-11.2 v/o Nb showed a strong dependence on the processing true strain, it seemed appropriate to examine the fundamental strain-hardening behavior as a function of processing true strain as well. The strain-hardening rates ($\theta = \Delta\sigma/\Delta\epsilon$) would then be correlated with the activation energy values in an overall attempt to gain an enhanced

understanding of fundamental in-situ microcomposite deformation and strengthening mechanisms. A summary of the strain-hardening rate θ as a function of processing true strain and composition for the in-situ microcomposites of the present study are also included in Table 1. For comparison of strain-hardening rates of the present in-situ microcomposites to OFHC Cu deformed in Stage II, Jaoul's[7] data are also included in Table 1.

Table 1 - Summary of Activation Energy and Strain-Hardening Rate Values of In-Situ Processed Microcomposites

Alloy	Processing True Strain $\ell n(t_o/t)$	ΔH (eV)	θ (MPa)
Cu-15 v/o Nb	4.1	1.50	510
	5.7	0.84	1471
	6.7	0.94	1382
Cu-3.3 v/o Mo-11.2 v/o Nb	4.1	1.63	549
	5.7	1.79	--
	6.7	1.00	672
Cu-2.0 v/o Ag-15 v/o Nb	4.1	0.78	1039
	5.7	0.70	1190
	6.7	0.70	--
ΔOFHC Cu			1177
ΔData from Jaoul (Ref. 7)			

DISCUSSION

It is clear from the experimental results that the activation energies and the strain-hardening rates of the Cu-15 v/o Nb and the Cu-3.3 v/o Mo-11.2 v/o Nb show a strong dependence on the true processing strain. It is also shown that, although the activation energy for the shear stress of the Cu-2.0 v/o Ag-15 v/o Nb remains constant, the strain-hardening rate increases with increasing true processing strain. A most interesting observation is that with increasing processing true strains, the activation energies for shear stress decrease, while strain-hardening rates increase (Table 1).

These results present a direct contrast to the strengthening mechanism of two-phase microcomposites proposed by Funkenbusch and Courtney.[2] If the strengthening of the in-situ microcomposites was controlled by the strength of the BCC filaments as proposed by Funkenbusch and Courtney,[2] it would be expected that both the activation energies and the strain-hardening rates would be constant over the range of true processing strain investigated. This is in keeping with their view that the BCC phase does not undergo dynamic recovery within the range of processing true strains of 4 to 7.

Based on the results obtained in the present study, it is proposed that the dominant strengthening of the two-phase in-situ microcomposites arises from a transition in deformation mode from Stage III hardening back toward Stage II hardening in the Cu matrix with processing true strains exceeding 4. This concept is illustrated in Fig. 4. In Fig. 4A, the ultimate tensile stress as a function of processing true strain for Cu-15 v/o Nb, Cu-12 v/o Nb[1] and Cu-2.0 v/o Ag-15 v/o Nb are shown. Also included in Fig. 4A are data for high-purity polycrystalline Cu[1] showing the typical transition from Stage II hardening to Stage III hardening resulting from the onset of dynamic recovery (i.e., cross slip) with increasing processing true strain. The dotted line in Fig. 4A shows an extrapolation of Stage II hardening of high-purity Cu assuming no transition to Stage III.

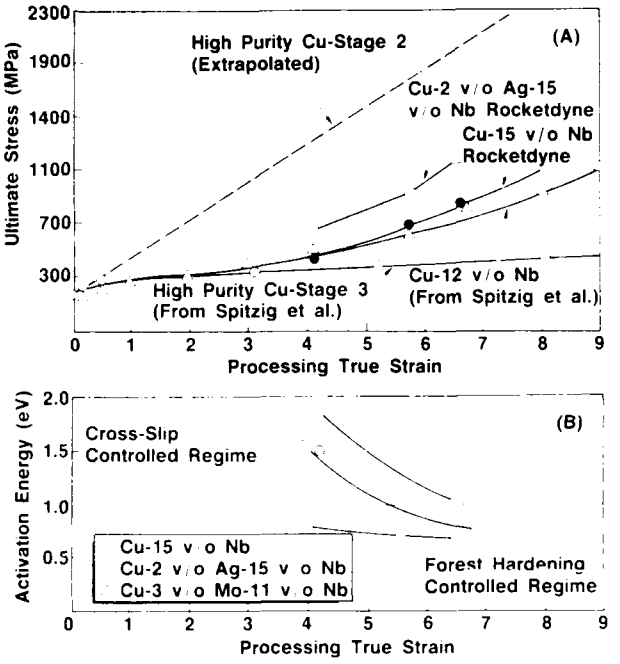


Fig. 4 - Ultimate tensile stress and activation energy for shear stress as a function of processing true strain

It is significant to note that at low-processing true strain ($\eta < 4$), the microcomposites follow roughly the same deformation path as does high-purity polycrystalline Cu. However, at processing true strains exceeding 4, the microcomposites deviate considerably from the deformation path of high-purity Cu. That is, the strength level per unit strain increases significantly for the microcomposites as processing true strain exceeds 4, where as high-purity Cu remains relatively constant with lower strain-hardening rate. In Fig. 4B, it can be seen that, as the true processing strain exceeds 4, the activation energy values decrease significantly and, as indicated, the plastic flow deviates from

Stage III hardening back toward Stage II hardening as cross slip in the Cu matrix becomes inhibited with increasing processing true strain (decreasing Nb ribbon spacings).

Previously, in comparing the activation energies and strain-hardening characteristics of the ultrafine microcomposites to those of high-purity polycrystalline Cu, the assumption that the microcomposite deformation was controlled by the deformation in the Cu matrix was made. To validate this, the thermal component can be separated from the nonthermal component of the flow stress. A specimen from the Cu-15 v/o Nb was given a recrystallization anneal at 649°C for 10 hours. After separation of the thermal from the nonthermal component,[8-10] the temperature dependence of the thermal component of the flow stress of the Cu-15 v/o Nb was determined.

The temperature dependence of the thermal component of the annealed Cu-15 v/o Nb is then compared to that of annealed high-purity polycrystalline Nb and annealed high-purity polycrystalline Cu. Temperature dependence of the thermal component of Cu-15 v/o Nb, high-purity Nb and high-purity Cu is presented in Fig. 5. It is readily seen that the Cu-15 v/o Nb microcomposite exhibits a minimum temperature dependence of the thermal component at low temperatures and indeed falls along the high-purity polycrystalline Cu curve. The small temperature dependence of the thermal component of high-purity Cu at 77°K is expected and in agreement with the fact that FCC materials do not possess a high Peierls stress at these temperatures.[8-9] Further, the fact that the Cu-15 v/o Nb microcomposite falls closely to that of high-purity Cu at 77°K indicates that it is the dislocation glide in the FCC Cu matrix

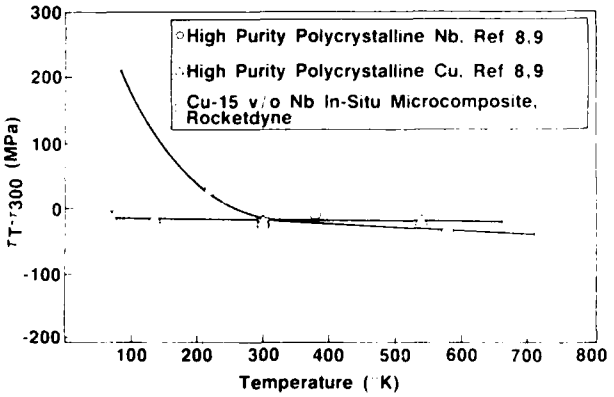


Fig. 5. - Temperature dependence of thermal component yield stresses of annealed high-purity Nb, Cu, and a Cu-15 v/o Nb in-situ microcomposite

that controls the overall deformation and strengthening of the in-situ ultrafine microcomposites.

Further support of the decreasing Nb ribbon spacing promoting the Stage III to Stage II deformation mode transition can be shown by examining the Cu-3.3 v/o Mo-11.2 v/o Nb alloy. Referring to Table 1 and Fig. 4, it is shown that the activation energies reflect the values for Stage III hardening at all three processing true strains. Also note the concurrent low strain-hardening rates for this material compared to those for the Cu-15 v/o Nb and Cu-2.0 v/o Ag-15 v/o Nb. Preliminary metallographic examination by optical and scanning electron microscopy (SEM) indicated a distinct lack of microstructural refinement (i.e., decreasing Nb-Mo ribbon spacing) with increasing processing true strain. This would correspond to the fact that sufficient obstacles to cross slip were not developed in the Cu-3.3 v/o Mo-11.2 v/o Nb system at higher processing true strains (at least in the range investigated in this study). As a result, typical Stage III deformation persists as manifested by the higher activation energies ($\Delta H > 1.0$ eV) and lower strain-hardening rates. In contrast to the Cu-3.3 v/o Mo-11.2 v/o Nb microcomposite, the activation energies and strain-hardening rates obtained for the Cu-2.0 v/o Ag-15 v/o Nb indicate a consistent Stage II deformation mode at all three true processing strains. Although a quantitative assessment of this behavior pattern has yet to be made, a speculation on the role of the Ag in promoting this behavior pattern can be presented. The amount of Ag present (2 v/o) will be completely dissolved in the Cu phase, thus promoting solid solution strengthening of the Cu phase. It is possible that the 2.0 v/o Ag in solution in the Cu may lower the stacking fault energy (SFE) of the Cu phase, thus acting to inhibit Stage III hardening (dynamic recovery) at the lower true processing strains. Concurrently, the Nb ribbon spacings decreasing with increasing processing true strain provide the obstacles responsible for dynamic recovery inhibition at the higher processing true strains as discussed previously. Thus, a complete suppression of Stage III hardening might be expected if the contribution to Stage III suppression imparted by the Ag solid solution strengthening effects at lower true strains ($\eta > 4$) were to overlap the microstructural refinement contribution to Stage III inhibition at higher true strains ($\eta > 4$). In Fig. 4, it is shown that the Cu-2.0 v/o Ag-15 v/o Nb microcomposite does indeed possess the highest room temperature strength of all three ultrafine microcomposites. These results indicate that a combination of solid solution strengthening coupled with the microstructural refinement (i.e., second-phase

distribution) accomplished through mechanical processing may provide an interesting and useful class of materials for future high strength-high conductivity applications.

CONCLUSIONS

The strengthening of the in-situ ultrafine microcomposites is attributed to the decreasing Nb ribbon spacing with increasing processing true strain. When the Nb ribbons approach a spacing of approximately 1 m, they become sufficient obstacles that act to suppress further cross slip in the Cu matrix. At this point, the transition from Stage III hardening (dynamic recovery) back toward Stage II (forest hardening) occurs.

Evaluation of the temperature dependence of the thermal component of the flow stress of annealed Cu-15 v/o Nb supports the results of this study, which indicate that the overall deformation and strengthening mechanisms of the in-situ ultrafine microcomposites is controlled by the deformation mechanisms in the Cu matrix.

Solid solution strengthening of the Cu matrix in combination with the strengthening imparted by the microstructural refinement accomplished by the mechanical working appears to be additive in contributing to the in-situ microcomposite strengthening.

ACKNOWLEDGMENT

This work was funded by the Defense Advanced Research Projects Agency (DARPA) under Contract No. N00014-86-C-2224, Dr. C. R. Crowe, Naval Research Laboratory, Contract Monitor.

REFERENCES

1. Spitzig, W. A., A. R. Pelton, and F. C. Laabs, Acta Met, 35, 2427-2442 (1987).

2. Funkenbusch, P. D. and T. H. Courtney, Acta Met, 33, 867-922 (1985).

3. Ashby, M. F., Phil Mag, 21, 339 (1970).

4. Basinski, Z. S., Phil Mag, 4, 393-432 (1959).

5. Olivares, F. Hernandez and J. Gil Sevillano, Acta Met, 35, 631-641 (1987).

6. Feltham, P. and J. D. Meakin, Acta Met, 7, 614 (1959).

7. Jaoul, B., and R. W. K. Honeycombe, "Plastic Deformation of Metals," p. 233, 2nd ed., Edward Arnold, ASM (1984).

8. Conrad, H. and W. Hayes, Trans Quart., 56, 249-262 (1963).

9. Conrad, H. and W. Hayes, Trans Quart., 56, 125-134 (1963).

10. Nix, W. D., Private Communication, Stanford University, Stanford, California (1988).

STUDY OF ACOUSTIC EMISSION DUE TO THE MULTIPLE FIBRE FRACTURE IN A SINGLE SiC (CVD) FILAMENT-ALUMINUM MATRIX MODEL COMPOSITE

T. Boniface, P. Fleischmann, R. Fougeres, P. F. Gobin, D. Rouby
Groupe d'Etude de Metallurgie Physique et de Physique des Matériaux,
U.A. C.N.R.S. N 341, France

F. Lonca-Hugot, M. Boivin
Laboratoire de Mécanique des Solides
I.N.S.A. De Lyon, F 69621 Villeurbanne, France

IN ORDER TO UNDERSTAND the mechanical behaviour of metal matrix composites, basic knowledges are needed about the effect of fibre-matrix interface on reinforcement and damage processes. These basic problems have to be studied on simple model systems such as tensile specimens containing a single filament. Concluding considerations can thereafter be extended to real composites reinforced either with one or multidirectional continuous fibres or with whiskers. Several basic problems can be understood as follows :

i) Cooling after processing leads to internal stresses in fibres, which modify the relation between the applied stress and the stress actually supported by fibres. As a result of equilibrium conditions internal stresses are also present in the matrix. They can induce changes in the yielding and in the hardening behaviour of the matrix. In addition internal stresses are gradually reduced as the plastic deformation of the matrix is increased.

ii) Tensile fracture of an uncoated fibre is governed by preexisting surface flaws, described by a weibull statistics, with an average fibre strength increasing as the test length decreases. When a fibre is embedded in a matrix, the distribution of fibre breaks with applied stress is probably altered due to the effect of stress transfer conditions between fibre and matrix. Stress transfer problems are linked with internal stresses, plastic deformation of the matrix and dynamic interfacial effects occuring during the pull-back of fractured fibre ends. Therefore, effective parameters of the stress-transfer requiere to be identify. The final multiple fracture situation of a single filament specimen can be characterized by the mean length D of the remaining fibre segments corresponding to experimental conditions for which fibre-end effects are overloped (Fraser et al., 1983). The D value depends on several parameters specially on the critical interface shear stress τ^c, that characterizes the fibre-matrix interface.

The aim of this paper is to present preliminary results about basic problems listed above, in the case of a model composite having a single SiC filament embedded in an aluminium alloy matrix. Results are concerned with theoritical considerations on both statistics fracture distribution and internal stresses and with experimental characterizations of fibre fractures using acoustic emission (A.E.) measurements. As a matter of fact A.E. measurement permit the localization of fibre breaks along the fibre axis and in the tensile stress-strain curve. Moreover, quantitative analysis of A.E. signals leads to very useful informations about dynamic interfacial effects.

EXPERIMENTAL PROCEDURE

The tensile speciments used are of dog-bone shape (figure 1) and consist of a single axial AVCO SiC filament of 140 µm in diameter, processed by C.V.D. and embedded in a 6061-T6 aluminium alloy. Model composite specimens have been processed by PECHINEY - France, using the squeze-casting technique ; they have been after machined in the final shape and then heat treated (T6). The fibre volume fraction is $v_f \approx 0.003$.

The specimens are stressed by a M.T.S. Machine (model 810) at constant cross-head speed (strain rate $\approx 30 \times 10^{-6}\ s^{-1}$). As shown on figure 1, an A.E. transducer is fixed at each end of the specimen, in order to localize fibre breaks along the fibre axis. The sensitive element of the A.E. transducer is a thick piezoelectric piece (PZT, ϕ 10 x 10 mm^3) which provides an electrical voltage directly proportional to the displacement carried out by the A.E. wave (Rouby et al. 1983). The A.E. signal due to the breack of the single fibre is a spike of very high energy ; so it is not necessary to amplify the signal. The very energetic characteristic of break A.E. signals permits very easy break counting without any doubt. For each channel, the signal provided by the transducer is only procesed by a high imput impedance preamplifier (gain : 1) and then put into the transient recorder (TEKTRONICS, model 2430-A) which works on two channels with a sampling frequency of 100 MHz (sensitivity : 100 mV, trigger level : 10 mV). Recorded signals are also counted as a function of the specimen elongation.

Figure 2 gives an example of recorded signals coming from the same source event.

RESULTS AND DISCUSSION

Before describing A.E. results obtained on single fibre specimen, two types of theoritical considerations are given :

- first, the calculation of internal stresses, due to the heat treatment of composite specimens and of internal stress modifications with the plastic deformation of the composite matrix.
- secondly, the simulation of multiple fibre fractures, of the embedded single fibre from the fracture distribution obtained on uncoated fibres.

INTERNAL STRESSES - Internal stress calculation have been analytically carried out inside the model composite using the method of successive elastic solutions proposed by A. Mendelson (1968) . Main hypothesis are the following :

- the specimen cooling is assumed to be slow enough to considere that the effect of the temperature gradient inside the specimen is negligible.
- due to the great length of the specimen compared to its diameter the axial deformation of the sample is considered as remaining at the same value at each point of the matrix and of the fibre.
- during the cooling, the fibre is ascribed to be kept in the elastic stress field. Thermal expansion coefficient and YOUNG modulus are taken equel to 4×10^{-6} K^{-1} and 500 GPa respectively.
- for the matrix, mechanical and thermal characteristics are given by Habachou et al (1985).

At the beginning of the cooling specimen, the difference of thermal coefficients between the fibre and the matrix leads to plastic deformation of the matrix in the surrounding of the fibre. Subsequent internal stress field is reported on figure 3. Following remarks can be made :

- the fibre is submitted to a very high level of compressive stress (σ_z = - 5 200 MPa, $\sigma_r = \sigma_\theta$ = - 190 MPa).
- the plastic deformation is confined in a small region around the fibre (approximatively 0.2 mm of thickness). Beyond this region, internal stresses exhibit a very small level.

In addition, calculations have been also made in order to determine the evolution of the internal stress field by a subsequent tensile loading. On figure 4, the value of the VON MISES equivalent stress in the fibre, including both tensile stress and internal stress values, is reported as a function of the total deformation of the composite model. It is noticed that the equivalent stress reaches a minimum value at approximatively 1 % of total deformation, corresponding pratically to an annihilation of the internal stress field.

SIMULATION OF MULTIPLE FIBRE FRACTURES - Tensile tests on uncoated SiC (CVD) filaments have been performed at PECHINEY (Jarry), with 50, 100 and 200 mm gauge length. Results concerning the scattering of strength values and also the effect of gauge length can be described with the following WEIBULL expression, giving the failure probability P_F :

$$P_F = 1 - \exp\left[- L \left((\sigma - \sigma_u)/\sigma_0\right)^m\right] \quad (1)$$

with σ_u = 1 200 MPa, σ_0 = 1 950 MPa and m = 6.6, where L is the gauge length of tested uncoated fibre.

From this statistics law, we have now to simulate the successive fibre breaks along an uncoated fibre of length equal to the useful length of the single fibre model composite. For this simulation the fibre is considered to be cut into N elements of length equal to the diameter of the fibre ($2r$). We considere that each element exhibits the whole spectrum of preexisting defects, that means that defects are assumed to be very numerous along the fibre axis. Using the MONTE-CARLO method, the "local" strength of each element has been distributed on the basis of the Weibull statistics given by the relation (1).

In order to determine the statistics distribution of fibre breaks of the embedded fibre in the matrix it is assumed that the stress transfer is carried out according to the KELLY's model (Kelly, 1965). In a given fibre segment the tensile stress, σ_f, increases linearly (slope = $2\tau^*/r$) from zero at the end of the broken segment to a plateau stress value, $\sigma_{f\ max}$, given by the mixture rule under uniform strain conditions. If, at a given point along the fibre segment, the fibre stress profile exceeds the local fibre strength, the segment will be broken again. The multiple fibre fracture process stops when the length of remaining segments is shorter than the critical one i.e. the length for which the stress profile of the fibre segment becomes too low for further breaking.

The curve (a) of the figure 5 shows a typical result of simulation obtained from MONTE-CARLO method and with τ^* = 115 MPa. This last value corresponds to the yield shear stress of the 6061-T6 matrix. It is assumed to be independant of the magnitude of the plastic deformation.

This hypothesis is very debatable because strain hardening occurs during the plastic deformation of the matrix. However, credible information on the locale yield shear stress is very difficult to obtain up to now. So, this very simple hypothesis has been considered.

First breaks occur between 3 000 and 4 000 MPa i.e. between 0.75 and 1 % of deformation. The total number of fibre fractures is closed to 40 (39 to 43), giving a mean length of remaining segments of 1.5 mm.

ACOUSTIC EMISSION - An example of tensile curve and A.E. event counting is shown on figure 6. The strain value at which first fractures occur is much lower than 1 %, value for which internal stresses in the fibre just becomes annihilated (see § Internal stresses). This result indicates that the fibre could be damaged during the squeeze-casting process, introducing changes in the WEIBULL distribution of flaws and reducing locally the internal stress level. However, the most A.E. signals are recorded for strain values higher than 2 %, illustrating the shift of apparent fibre strength due to compressive internal stress. The total count is not very significant because the specimen can fail before the multiple fibre fracture is saturated. The A.E. results are also reported on figure 5 (curve (b)). The curve (b) is obtained by assuming that the fibre strain in the plateau stress region , equals the average strain of the specimen determined from the tensile curve.

At high fibre stress the difference between the two curves (a) and (b) is maintened in despite of the fact that internal stresses are strongly reduced (see § Internal stresses). The shift maintenance between the two curves could be due to the difference of POISSON's coefficients between the fibre and the plastic matrix leading to a "ferrule phenomenon" on the fibre. In order to compare more precisely simulation and experimental results, we have to study the relation between the applied load to the

specimen (or the elongation) and the stress profile actually applied to fibre segments. This relation is very complicated because there is matrix yielding (this problem has been studied by Ochiai and Osamura , 1986). The initial compressive fibre stress relaxes as the matrix elongates plastically (see § internal stresses)and as fibre segments become shorter . More works must be done on this scape for clarifying the effect of parameters controlling the stress transfer phenomenon.

Source locations along specimen axis are determined from the delay between the two signals recorded (Δt on figure 2). The accuracy of location is of the order of 0.5 mm. An example of localization is given on figure 7. As shown on this example, fibre breaks occur seemingly first at one end of the gauge length and then propogate to the other end ; this phenomenon is not understood at this time.

According to the A.E. source model (Rouby et al., 1983), the displacement carried out by the A.E. wave (measured with the "thick piezotransducer") is proportional to the crack opening velocity of the source, i.e. the velocity of the pull-back of the two fibre ends after fracture. As shown on figure 2, the acoustic signal is serrated, probably due to slip-stick displacement during pull-back (a negative signal corresponds to a dilatational A.E. wave).

CONCLUSIONS

The preliminary results given in this paper show that A.E. in a very powerful tool for studying the multiple fracture process in a single filament model composite. Results can be analyzed in terms of interface characteristics and compared with statistics distribution of uncoated fibre fractures if theoritical considerations are taken into account. In order to progress in this way, the stress transfer phenomenon have to be more studied

Fraser W.A., Ancker F.H., Dibenedetto A.T. and Elberly B, Polymer Composites 4, 238-248.(1983)

Rouby D., Fleischmann P. and Duvergier C, Philos. Mag. 47, 677-688.(1983)

Mendelson A., "Plasticity : Theory and applications", the Mac-Millan Company. (1968)

Habachou R. et Boivin M., Journal de Mécanique Théorique et Appliquée. vol 4,n°5, 701-723.

Jarry P., Private communication.

Kelly A. and Davies G.J., Metall. Rev., 10, 1 (1965)

Ochiai S. and Osamura K. - Z. Metallkde, 77, 249-254 (1986)

Rouby D., Fleischmann P and Duvergier C. - Philos. Mag., 47, 689-705 (1983)

ACKNOLEDGEMENT

The authors are very grateful to the Office Public Régional Rhône-Alpes for the financial support and to the Centre de Recherche de VOREPPE-PECHINEY - France for supplying specimens.

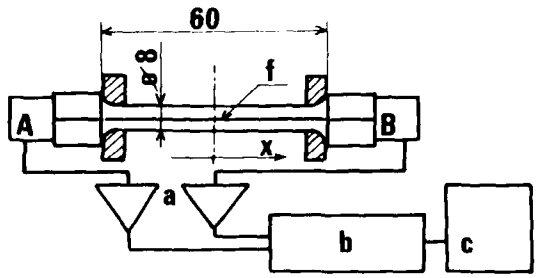


Fig. 1 : Specimen and acoustic emission set-up
f : filament ; A and B : transducers ;
a : preamplifiers; b : transient recorder ;
c : computer

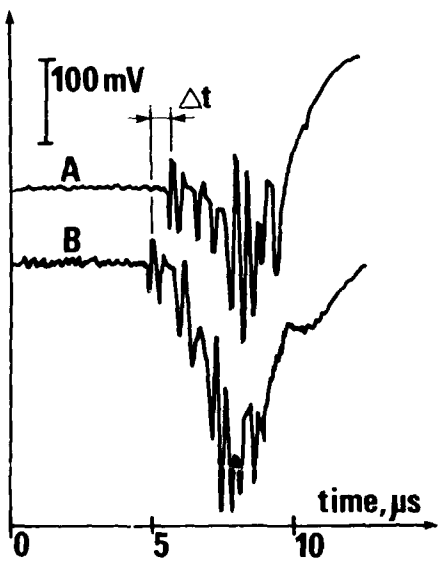


Fig. 2 : Recorded A.E. signals (channels A and B) due to a fibre fracture

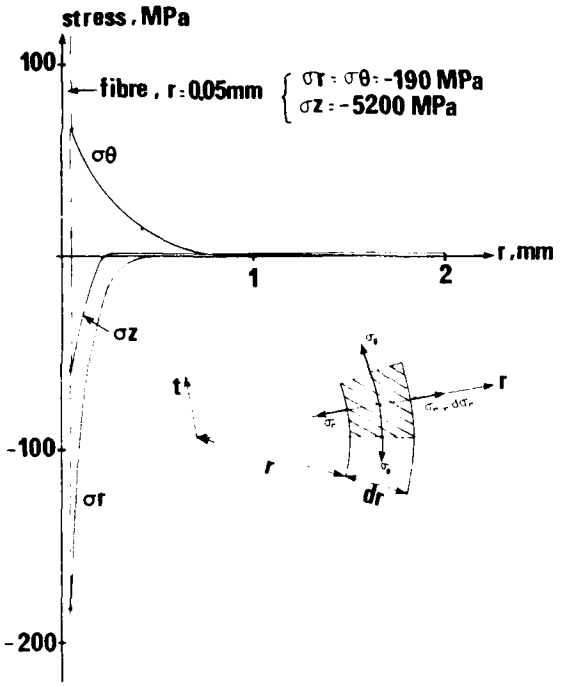


Fig 3 Calculated internal stress values versus the radius of the model composite.

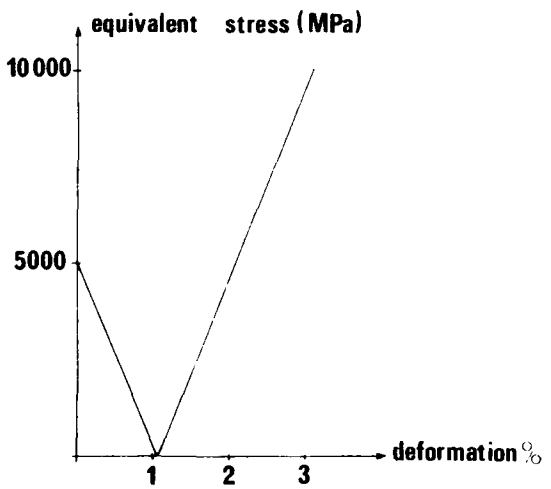


Fig. 4 Variation of the VON MISES equivalent stress in the fibre with the amplitude of the tensile strain applied to the model composite.

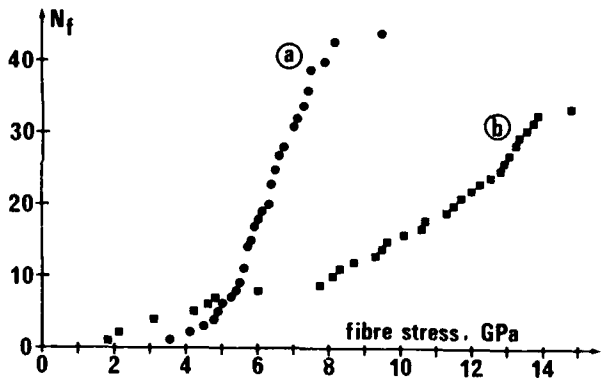


Fig. 5 : Number of fibre breaks (N_f) versus embedded fibre stress.
a : calculated by simulation ; b : experimental.

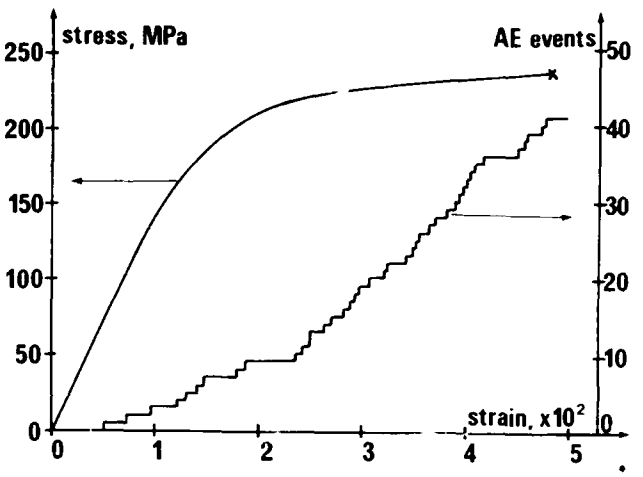


Fig. 6 Single filament composite. Applied stress and A.E. event count versus specimen elongation

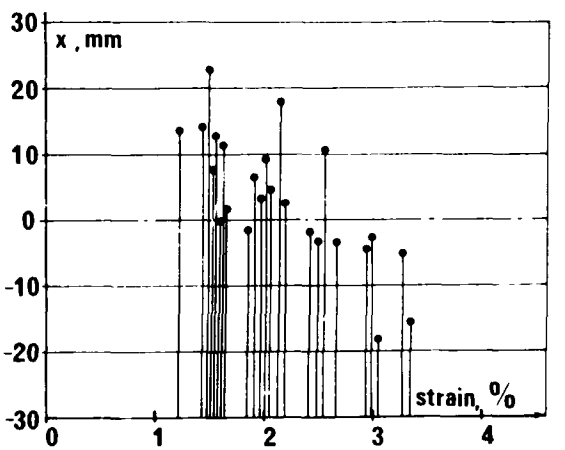


Fig. 7 : Example of fibre break locations versus specimen elongation. X is the distance from the A.E. source to the middle of the gauge length. Wave velocity : 6 000 m/s.

THERMAL CYCLING OF ALUMINA(FP)/MAGNESIUM ALLOY COMPOSITE

C. S. Lee
Dept. of Met., Mech., & Materials Sci.
Michigan State University
East Lansing, Michigan 48824 USA

K. K. Chawla
Dept. of Materials & Met. Eng.
New Mexico Institute of Mining and Technology
Socorro, New Mexico 87801 USA

J. M. Rigsbee
Dept. of Materials Sci. & Eng.
University of Illinois
Urbana, Illinois, USA

M. Pfeifer
Dept. of Materials Sci. & Eng.
Northwestern University
Evanston, Illinois 60201 USA

INTRODUCTION

As-cast alumina (FP)fiber/ZE41A magnesium alloy containing 35% volume fraction of unidirectionally aligned fibers were characterized microstructurally. Samples of composites were subjected to thermal cycling between 30 and 300°C and isothermal exposure of 300°C. The objective of this study was to evaluate the effects of thermal treatments on microstructure and mechanical behavior of this composite system. TEM samples were prepared by slicing thin foils from the bulk samples and mechanically polishing them to 90 μm thickness. Three mm disks punched out from these were mechanically thinned to 25 μm. These were subjected to ion-milling until electron transparency. Four point bend tests were done on the thermally cycled and isothermally treated samples. Other experimental details can be found in Ref. 1.

RESULTS AND DISCUSSION

The interfacial zone in this system was made up of MgO as determined by X-ray diffraction analysis (Fig. 1) and TEM (Fig. 2). The thickness of the reaction zone varied between 0.1 and 0.2 μm, and it remained stable when subjected to thermal treatments describe above.

Void formation at interface was observed in samples cycled 500 times and more. This was attributed to high vacancy concentration obtained on cycling and the resultant thermal stress induced creep cavitation. The thermal stresses had origin in the thermal mismatch between the fiber and the matrix ((2,3).

Microhardness profiles of the as-fabricated and thermally cycled samples (Fig. 3) showed that the matrix near the interface was much harder than the matrix far away from the interface. As the number of cycles increased, the matrix hardness increased in the beginning and then dropped in the later stages. The initial hardness increase in matrix was due to work-hardening of the matrix while severe void formation and precipitate coarsening the later stages led to the hardness decrease.

As the time of isothermal treatment was increased the hardness at the interface did not drop significantly, while the hardness in the matrix did (Fig. 4). The hardness decrease in the matrix was attributed to precipitate coarsening.

The flexural longitudinal and transverse strengths dropped monotonically with increasing cycles, Figs. 5 and 6. Scanning electron microscopic observations showed the phenomena of void formation at the interface which led to a lower interfacial bond strength, Fig. 7. This was the prime reason for strength loss in cycled samples.

On isothermal treatment, the longitudinal and transverse strengths dropped monotonically but less than that in the case of thermal cycling, Figs. 5 and 6. Matrix hardness measurements (Fig. 4) indicated that the matrix softening was the prime contributor to strength loss after isothermal treatments. There was no thermal stress induced work hardening of the matrix or void damage in the isothermal case because it involved only one thermal cycle.

CONCLUSIONS

The interfacial zone in this composite consisted of MgO and was stable under the thermal treatments given.

Void formation at interface was observed in samples cycled 500 times and more. This was due to the extremely high vacancy concentration available in thermally cycled samples and the thermal stress induced creep cavitation.

Microhardness profiles of the as-fabricated and thermally cycled samples showed the matrix near the interface was much harder than the matrix far away from the interface. As the number of cycles increased, the matrix hardness increased in the beginning and then dropped in the later stages. The initial hardness increase was due to thermal stress induced work-hardening of the matrix. On continued cycling, severe void formation and the precipiate coarsening in the matrix occurred which led to the drop in the hardness as well as flexural strength. In the case of isothermal exposure, the matrix hardness and flexural strength dropped monotonically with the exposure time. This was because of the matrix softening due to the precipitate coarsening, which was the prime contributor to the loss of hardness.

ACKNOWLEDGMENTS

We thank DuPont Co. for providing the composite samples.

REFERENCES

1. C.S. Lee and K.K. Chawla, in Proc.: Adv. Mater. Conf., TMS-AIME, Warrendale, PA, 1987, p. 289.

2. K.K. Chawla, Metallography, 6 (1973) 155.

3. K.K. Chawla, Phil. Mag., 28 (1973) 401.

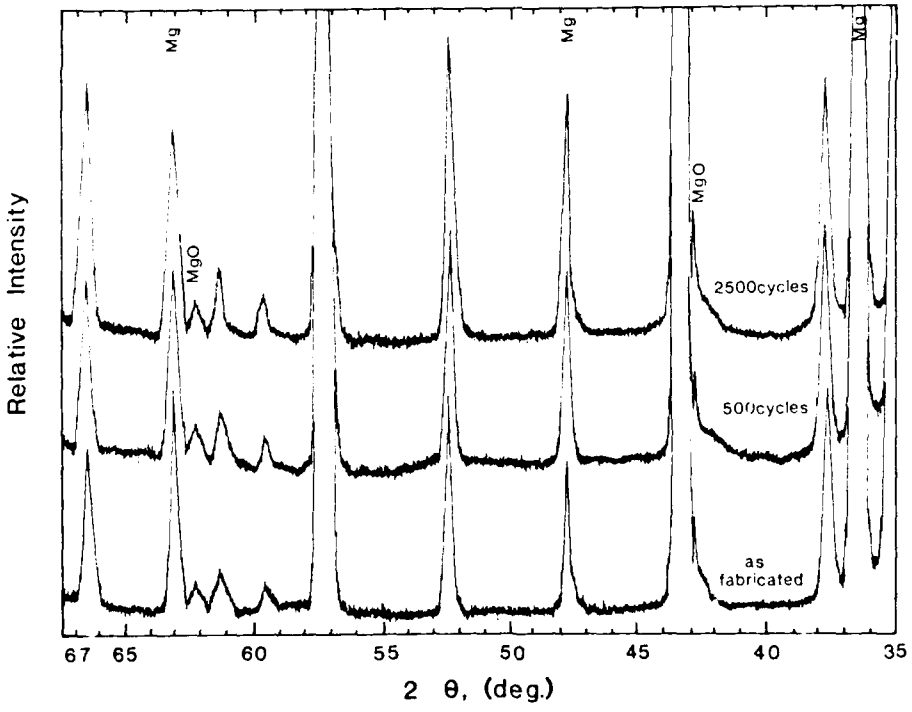


Figure 1. X-ray diffraction data showing the reaction product MgO at the interface in the as-fabricated state and after thermal cycling.

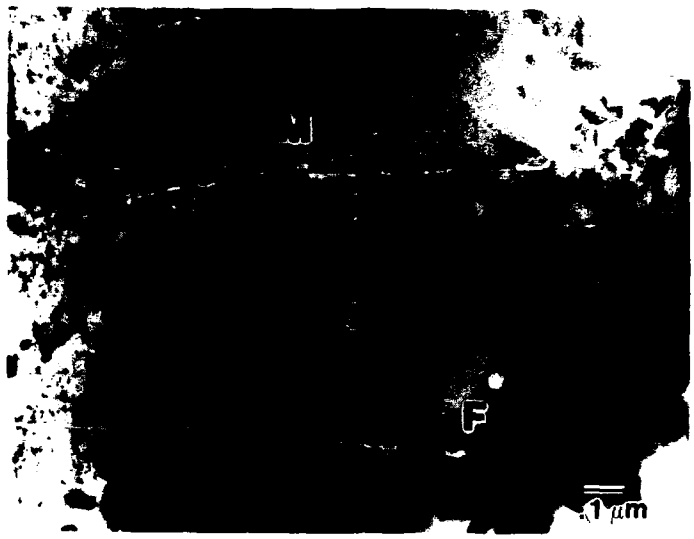


Figure 2. A bright field TEM micrograph showing the matrix (M), the fiber (F), and the reaction zone (arrow).

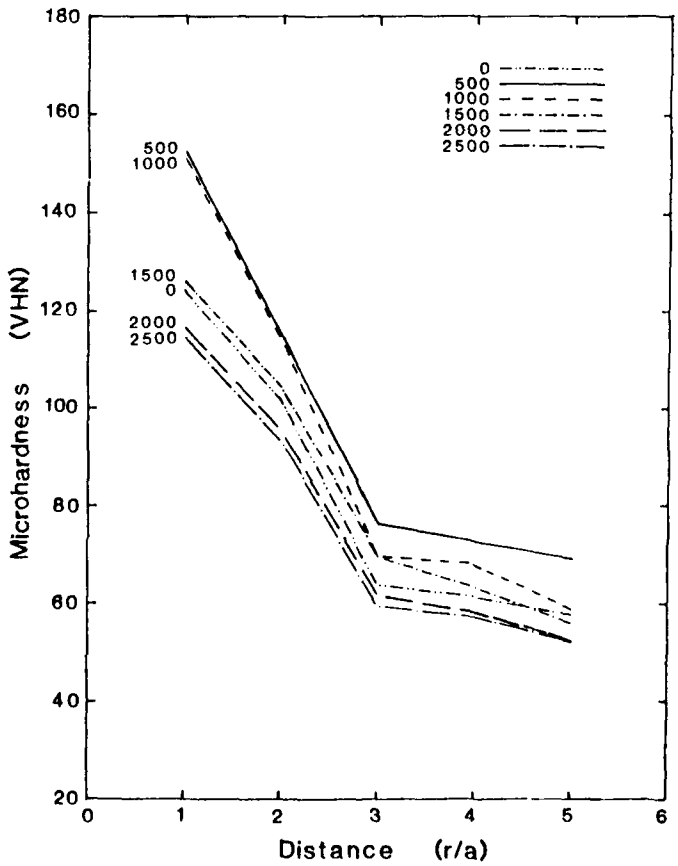


Figure 3. Microhardness profiles of the as-fabricated and thermally cycled samples. a is the radius, r is the distance from the fiber center, and r/a = 1 respresents the interface.

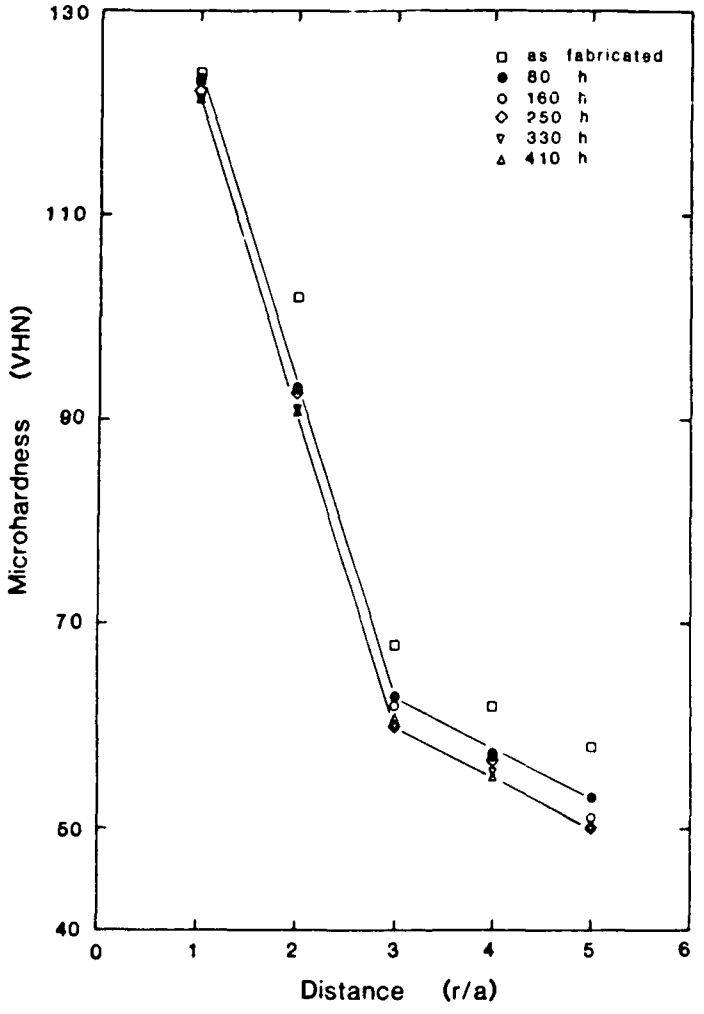


Figure 4. Microhardness profiles of the as-fabricated and isothermally treated samples.

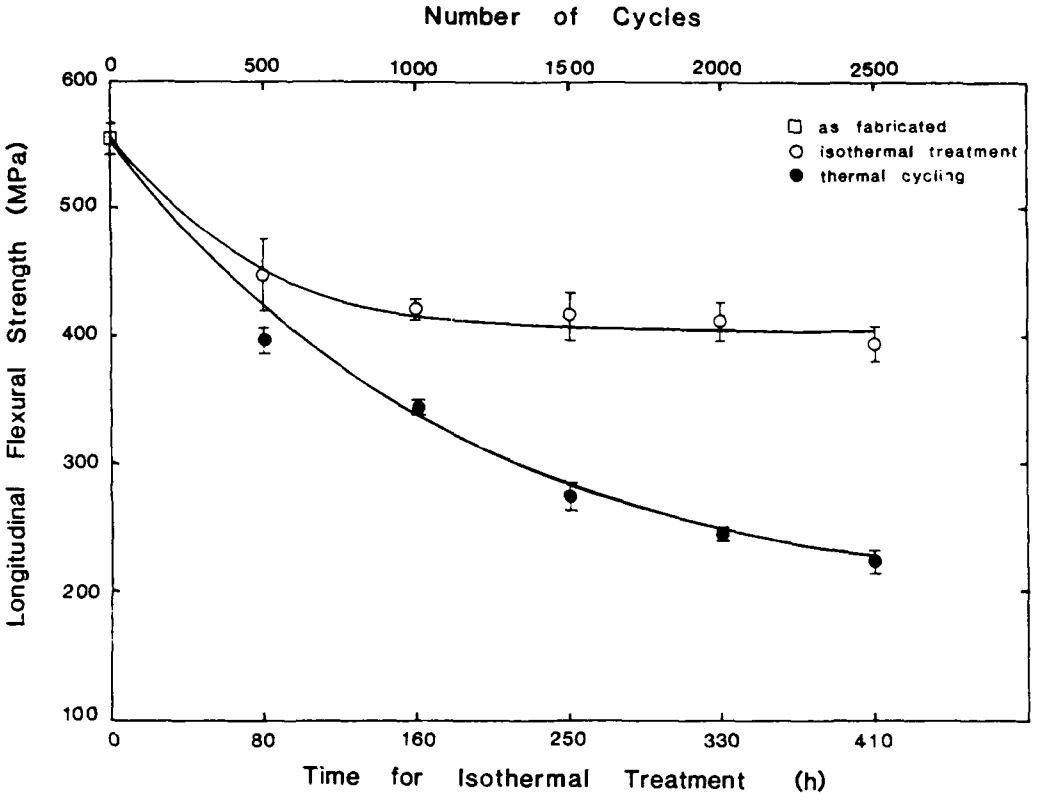


Figure 5. Longitudinal flexural strength of thermally cycled and isothermally treated samples.

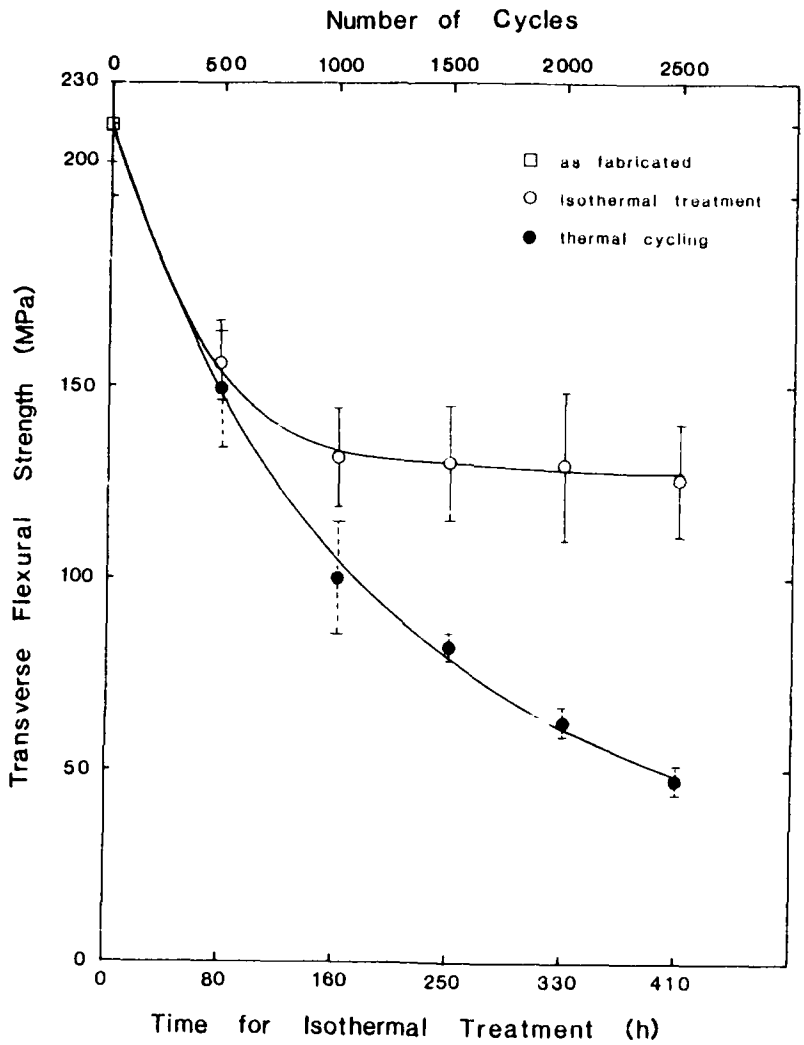


Figure 6. Transverse flexural strength of thermally cycled and isothermally treated samples.

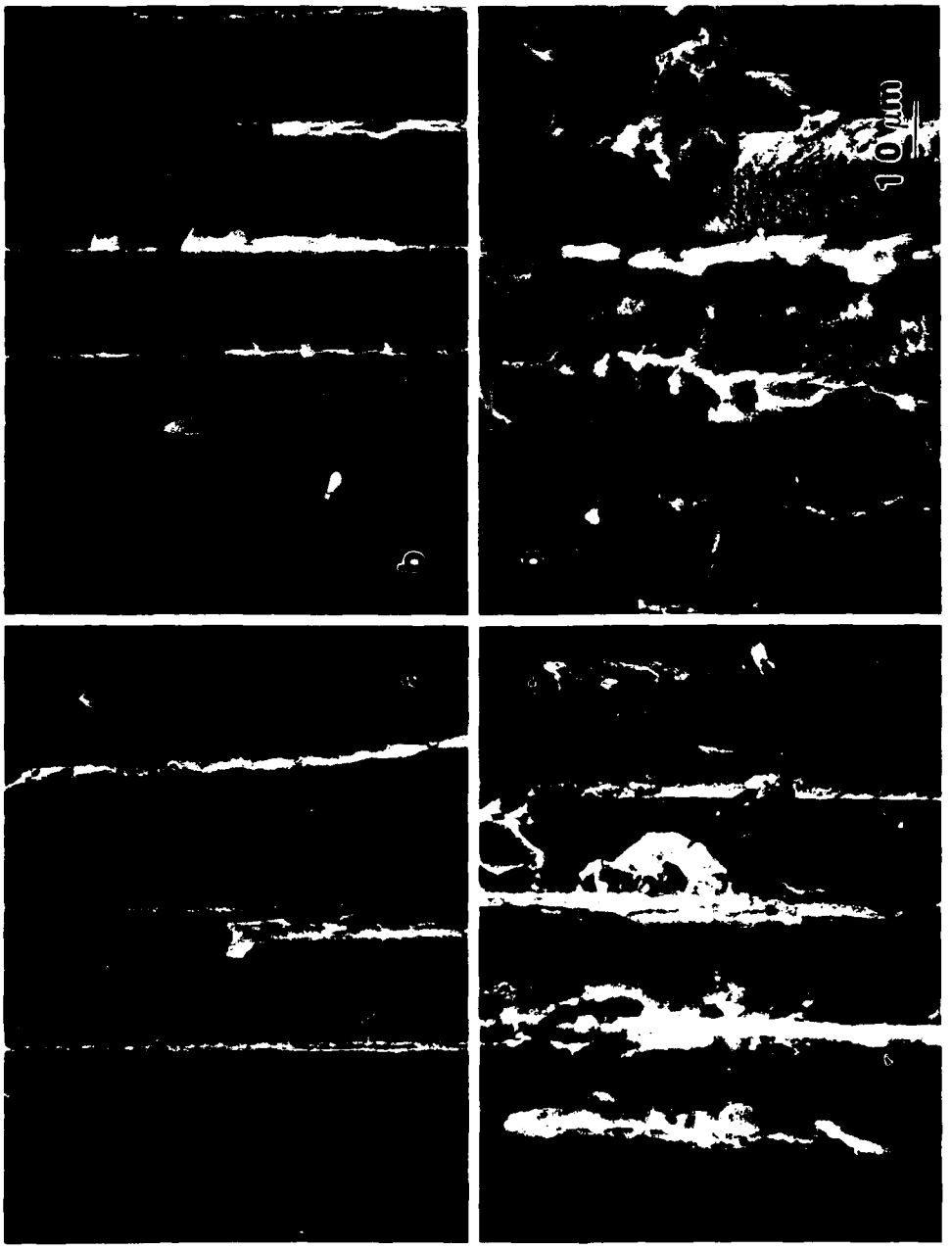


Figure 7. Fracture morphology showing incidence of cavitation and increasing size of cavities with the number of cycles. (a) 500 cycles; (b) 1000 cycles; (c) 1500 cycles; (d) 2000 cycles.

THE EFFECT OF FIBRE/MATRIX INTERFACES ON THE AGE-HARDENING CHARACTERISTICS OF δ-ALUMINA FIBRE REINFORCED AA6061

C. M. Friend, I. Horsfall, S. D. Luxton, R. J. Young
Materials Technology Group, Royal Military College of Science (Cranfield)
Shrivenham, Swindon Wilts
SN6 8LA England

ABSTRACT

This paper presents the results from an experimental investigation into the age-hardening response of short δ-alumina fibre reinforced AA6061 produced by a liquid metal infiltration process. It is shown that there are a number of effects which degrade the age-hardening characteristics of these composites. These can be broadly classified into two categories, (i) chemical and (ii) physical effects. It is shown that both effects depend on the nature of the interface between the δ-alumina fibres and the alloy matrix. Chemical effects degrade the age-hardening response of the composites through subtle interactions between the active alloying elements and the surfaces of the δ-alumina fibres. Even when such chemical effects are minimised however age-hardening can still be impaired by further physical phenomena. It is shown that physical degradation of age-hardening results from an interaction between the non-equilibrium vacancies quenched into the alloy following solution treatment and the fibre/matrix interfaces. Chemical and physical effects degrade the age-hardening potential of the alloy matrix and reduce the peak-hardness attainable from both the matrix alloy and the composite.

CURRENTLY THERE IS CONSIDERABLE TECHNOLOGICAL INTEREST IN METAL MATRIX COMPOSITES (MMC) since materials reinforced with high strength fibres represent a unique method for tailoring properties to particular applications. Most work however has concentrated on composites with light alloy matrices (in particular those of aluminium) and the optimisation of composite properties by changing the type of fibre, its size, and orientation. Whilst this is extremely important little consideration is usually given to the properties of the matrix and how these contribute to the final composite properties.

It is now clear (1,2) that in short fibre reinforced light alloys the matrix properties play a significant role in controlling the strength of the resulting MMC. The matrices of MMC can also constitute 'metallurgically active' components (3) which can be used to alter the final properties of the composite by heat-treatment. Such 'active-matrices' are usually age-hardenable alloys and it is therefore of some importance to identify any changes which may arise in the structure and properties of heat-treated matrices due to the presence of a fibre array.

When heat-treating age-hardenable MMC it is generally assumed that the matrix heat-treats in a manner identical to the unreinforced alloy. Little consideration is therefore given to the effect of the fibre array on the structure and properties of the heat-treated matrix. However a fibre array must have a significant effect on the microstructure and properties of liquid metal processed MMC.

During liquid metal processing of MMC significant segregation can occur during solidification of the matrix. This results from the constraint the fibre array imposes on the solidifying metal. Alloying elements in the melt are swept or the solidification front until the alloy-enriched residual liquid finally solidifies at the fibre/matrix interface. This results in variation in alloy concentration across the matrix (4) and even the formation of unexpected second phases at the fibre/matrix interfaces (5). In addition to these segregation effects chemical inhomogeneities can also develop in the matrix due to reactions between the fibre surfaces and matrix alloying elements. The nature and extent of such reaction depends on the actual composite system but always results in lower alloying element concentrations in the matrix.

Segregation and reaction therefore result in considerable variations in alloy content throughout the matrix of a liquid metal processed MMC. Since the formation of hardening precipitates requires a critical ratio of the active alloying elements such compositional variations should significantly alter the age-hardening response of matrix alloys.

There is little published data describing the age-hardening response of alloys containing fibre arrays. The evidence that does exist suggests that age-hardening is impaired in MMC (6,7). Rack (6) has shown that the presence of SiC whiskers can considerably influence the age-hardening of AA6061, and Abis and Donzelli (7) have observed similar effects in aluminosilicate fibre reinforced Al-Cu alloys. The latter also suggest that this degradation in hardening results from a change in the precipitation sequence so that the fibre reinforced matrix effectively becomes rapidly overaged. This behaviour is similar to the age-hardening of SAP (8,9) and suggests that the degradation in age-hardening is produced by 'physical' rather than chemical effects.

The available evidence therefore suggests that the heat-treatment response of an alloy containing fine ceramic fibres should be significantly different from that of the unreinforced matrix alloy due to a combination of chemical and physical interactions. The present work was therefore undertaken to identify the nature and magnitude of such effects in short δ-alumina fibre reinforced AA6061.

EXPERIMENTAL PROCEDURES

The composites employed in this investigation were based on a heat-treatable matrix of AA6061 (Al-1%Mg-0.6%Si-0.5%Cu-0.2%Cr) reinforced with 'Saffil' (ICI trademark) which is a 3 micron diameter short δ-alumina fibre containing a small proportion of silica. The composites were manufactured by a pressure infiltration route (10) using fibre preforms with volume fractions (V_f) of 0.08 and 0.26. The preforms were preheated to 750°C and infiltrated with AA6061 superheated to 1,000°C using a pressure of 25MPa applied for one minute. Excess alloy was used in order to obtain a sample of unreinforced matrix alloy cast under identical conditions to those employed for the composite. Specimens were machined from both the unreinforced and fibre reinforced regions of the casting for testing and microscopy.

All specimens were heat-treated in two stages (i) solution-treated at 529°C for either one or eight hours followed by water quenching and (ii) aged either isochronally or isothermally. Hardness and resistivity measurements were carried out following solution treatment and the microstructures were characterised by microscopy. The specimens were then isochronally or isothermally aged. Specimens were isochronally aged for 30 minutes at temperatures between 20 and 300°C and isothermally aged at room-temperature (natural ageing) and 140°C. The hardness and resistivity of the specimens were measured following isochronal ageing and these properties were monitored during isothermal ageing. Hardness measurements were systematically conducted at fixed points within the composite following each heat-treatment stage and also through the thickness of the composite. Hardness was characterised by the Vickers Hardness of the composite. The resistivity of the composites was measured by a four point DC technique and their heat-treatment behaviour was characterised by the resistivity change relative to the solutionised condition. Microscopy was carried out using optical, transmission (TEM) and scanning electron (SEM) microscopes and the distribution of alloying elements in the composite matrices was characterised by microprobe analysis.

RESULTS AND DISCUSSION

The unreinforced matrix alloy exhibited a normal age-hardening response throughout the heat treatments described above, with peak hardness developed following ageing for 30 minutes at a temperature between 180 and 190°C. However the composites exhibited significantly impaired hardening. Fig.1 shows a series of hardness traverses through the thickness of a $0.26V_f$ composite in the as-cast, solutionised, and peak-aged conditions. This data shows that when such a composite was solutionised (and also subsequently aged) a gradient in hardness developed with a normal solutionising and hardening response at the top of the composite, but severely impaired hardening at the base. The magnitude of this phenomenon was also strongly dependent on the solutionising time as can be seen in fig 2. As the solutionising time was increased from 1 to 8 hours impaired hardening developed throughout the composite thickness. The absence of a significant hardness gradient in the as-cast condition and its development following solutionising suggests that this phenomenon was not due to local variations in the microstructure (particularly in the fibre volume fraction). This was confirmed by optical microscopy which showed no significant differences in V_f or matrix microstructure through the thickness of the composite in any of the heat-treated conditions. The development of the gradient following solutionising does however suggest that the hardness gradient was due to variations in solid solution alloy content. This effect was confirmed by extensive microprobe analysis and

digimapping of the composites. In composites solutionised for one hour, microprobe analysis showed a significant interaction between the fibres and matrix alloying elements. Magnesium enrichment was observed at the fibre/matrix interfaces in regions exhibiting impaired hardening, with less obvious interaction in the regions exhibiting normal age-hardening response. Such data provides strong evidence that a chemical interaction was responsible for the observed variations in age-hardening response.

It is now well established (11,12) that δ-alumina fibres have silica-rich surfaces which show a strong affinity for magnesium and will remove magnesium from a matrix alloy to form a fine-scale reaction product (13). The phenomenon observed in fig 1 appears to result from such an effect. During liquid metal pressure infiltration the matrix alloy at the infiltration front spends a considerable length of time in the presence of the fibre array as the front passes through the preform and past the fibre surfaces. Conversely the liquid metal at the top of the preform spends the least residence time in the vicinity of the fibres. As a result of interaction between the fibre surfaces and matrix alloy significant removal of magnesium can occur in the liquid alloy during infiltration and result in a gradient of magnesium content from a low level at the base of the composite (the original infiltration front) to a normal concentration at the top of the composite. Since the magnesium content of the alloy is low the effect of such a gradient on the as-cast microstructure and properties is small. However a gradient of this type has a significant effect on both the solutionised hardness of the matrix and its age-hardening response. The decreasing amount of free magnesium towards the base of the composite means that on solutionising decreasing amounts of magnesium enter solid solution. This is reflected in the low solutionised hardness at the base of the composite (fig 1) and the gradient in hardness which develops between the composite's base and top. This variation in magnesium content has a significant effect on subsequent ageing. The formation of the age-hardening intermediate precipitate in AA6061 (β^{1}-Mg_2Si) requires a narrow alloy stoichiometry. Therefore if there is insufficient magnesium in solid solution the formation of β^{1} is inhibited and age-hardening impaired. The gradient in magnesium content following solutionising therefore produces a gradient in the aged condition with a low peak hardness at the base of the composite and a normal response at the top.

Further evidence for such a chemical interaction comes from the effect of extended solutionising. Fig 1 shows that solutionising for one hour produced a gradient in hardness due to variation in solid solution magnesium through the thickness of the composite. One hour was therefore a sufficient time to solutionise the composite but insufficient to allow diffusion and reaction between the fibre surfaces and magnesium. However, extending the solutionising time (eg 8 hours, fig 2) clearly allowed sufficient time for both solutionising and extensive interaction between the magnesium and fibre surfaces. This is shown by both the impaired hardening which developed throughout the thickness of the composite (fig 2) and also by the increased concentration of magnesium observed at the fibre matrix interfaces.

This shows that chemical interactions play a significant role in the heat-treatment response of δ-alumina fibre reinforced AA6061. Subtle chemical interactions occur during both liquid metal infiltration and solutionising which result from the strong affinity of the fibre surfaces for magnesium. This results in the formation of a fine-scale reaction product at the fibre/matrix interfaces and impaired age-hardening in the matrix due to the removal of magnesium which is an active alloying element in AA6061.

Fig 3 shows the isochronal age-hardening response of the unreinforced matrix alloy, and 0.08 and $0.26V_f$ composites following solutionising for one hour and ageing for 30 minutes. The hardness data for these composites was generated from a localised region ~8mm from the top of the composite and therefore shows the age-hardening response of a material at a single point along the hardness gradient in fig 1. The composites exhibited a behaviour which deviated from that of the unreinforced alloy, with the magnitude of the deviation dependent on the volume fraction of reinforcement. This data is interesting since it shows that the hardening kinetics were substantially altered in the composites. This suggests that in addition to chemical effects caused by interaction at the fibre surfaces, the fibre array also significantly alters some physical process which further impairs the age-hardening response. This can be seen more clearly by comparing the hardness and resistivity changes of the unreinforced alloy and composites following isochronal ageing. Typical data of this type is shown in fig 4 for the unreinforced alloy. A cross-plot of this type can be used to identify the individual stages of age-hardening. It is clear from fig 4 that there were three distinct stages in the age-hardening of unreinforced AA6061 (I, II and III). The intermediate stages in the age-hardening of AA6061 are now well established (14) and Stages I to III clearly coincide with the three documented stages of precipitation. Stage I therefore represents the formation of GP zones, II the formation of the intermediate precipitate β^{1}-Mg_2Si and III overageing and Ostwald ripening of the equilibrium β-Mg_2Si. Fig 5

shows a similar cross-plot for a $0.26V_f$ composite. This showed a completely different ageing response. Stage I was absent which suggests that the δ-alumina fibre array had a considerable effect on GP zone formation. This observation is supported by the cross-plotted natural ageing data in Fig 6. The naturally aged unreinforced alloy exhibited GP zone formation with a characteristic increase in resistivity and some age-hardening. However in the $0.26V_f$ composite GP zone formation was inhibited, suppressing the increases in both hardness and resistivity. The magnitude of this GP zone suppression was also volume-fraction dependent, increasing with higher fibre fractions. This shows that in reinforced matrices there are additional physical phenomena which also degrade the age-hardening response of the alloy matrix.

The development of significant levels of hardness is AA6061 is associated with the formation of β^1-Mg_2Si. However the level of hardening also depends on the size and spacing of the β^1 precipitates. The latter is controlled by the nature of the β^1 nuclei (which are normally GP zones) and their temperature of formation. The absence of GP zone formation in the composites therefore has a significant effect on the size and morphology of the β^1 precipitates and the resultant age-hardening. Fig 7 shows a resistivity/hardness cross-plot for an isothermally aged (140°C) $0.26V_f$ composite. It is clear that suppression of GP zone formation occured during the early stages of artificial ageing. This meant that no nuclei were produced for β^1 formation until considerably later stages of the ageing process. This had a number of consequences. Firstly β^1 precipitation was supported solely by the equilibrium thermal vacancy concentration and secondly there were no fine nuclei which enabled the intermediate β^1 precipitate to form in a morphology which caused significant hardening. It is clear from TEM observations that the latter effect was most significant. Fig 8 shows the microstructure of a peak-aged matrix in a $0,26V_f$ composite. The material contained β^1-Mg_2Si in a coarse Widmanstatten morphology quite unlike the fine-scale, nearly irresolvable homogeneously nucleated precipitate in the peak-aged unreinforced alloy.

This inhibition of GP zone formation and its effect on age-hardening is similar to observations in aluminosilicate fibre reinforced Al-Cu (7) and SAP alloys (8,9) where this phenomenon has been attributed to a lack of quenched-in vacancies. The observations in the current work suggest that a similar mechanism is responsible for the inhibition of GP zone formation in the matrices of δ-alumina fibre reinforced AA6061 composites. There are a number of possible sources for the low quenched in vacancy concentration. Vacancies could be soaked up by (a) α-phase grain boundaries, (b) matrix dislocations and/or (c) fibre/matrix interfaces. In SAP the matrix grain-size is very fine and grain boundaries therefore play a significant role in soaking-up non-equilibrium quenched-in vacancies. In liquid metal processed MMC however, there is insufficient refinement of the matrix grain-size for this to be a feasible mechanism. Abis and Donzelli (7) have suggested that in MMC the presence of lattice defects produced by the thermal expansion mismatch between the reinforcement and matrix may be the active vacancy-sinks. In the present work however TEM showed that there was no significant difference in dislocation density between the composite and unreinforced matrix alloy. This suggests that the fibre/matrix interfaces must play the most significant role in this physical phenomenon. The driving force for this vacancy sinking must therefore be the reduction in elastic strain-energy associated with the fibre/matrix interfaces.

CONCLUSIONS

The age-hardening of AA6061 reinforced with δ-alumina fibres is significantly impaired when compared to the age-hardening characteristics of the unreinforced alloy. A number of effects combine to degrade the age-hardening response of these composites. These can be broadly classified into (i) chemical and (ii) physical effects.

Chemical effects degrade the age-hardening response through a subtle interaction between the δ-alumina fibre surfaces and the active alloying elements. This interaction removes active alloying elements such as magnesium from the matrix alloy which suppresses the formation of the age-hardening β^1 precipitates.

In addition to chemical effects age-hardening can be further impaired by physical effects. The most important physical effect is the suppression of GP zone formation. The most probable cause of this phenomenon is the lack of quenched-in vacancies following solution treatment due to the availability of large numbers of vacancy sinks at the fibre/matrix interfaces. The inhibition of GP zones alters the precipitation sequence in the matrix alloy with the result that age-hardening is significantly impaired.

REFERENCES

1. Friend, C.M. J.Mat.Sci. 22, 3005 (1987)
2. C.M. Friend, 'Proc. ICCM6' Vol.2 p402, Elsevier Applied Science, London (1987)
3. England, J. and I.W. Hall, Scripta Met. 20, 697 (1986)

4. Clyne, T.W, 'Proc ICCM6' Vol 2 p.275, Elsevier Applied Science, London (1987)
5. R. Trumper, presented at 'Metal Matrix Composites: Structure and Property Assessment', The Royal Aeronautical Society, London, November (1987).
6. H.J. Rack, 'Proc ICCM6' Vol 2 p.382, Elsevier Applied Science, London (1987)
7. Abis, S. and G. Donzelli, J.Mat.Sci Let 7, 51 (1988)
8. Ceresara, S. and P. Fiorini, Powd.Met. 1, 1 (1979)
9. Ceresara, S and P Fiorini, Powd.Met 4, 210 (1981)
10. Clyne, T.W, M.G. Bader, G.R. Cappelman and P.J. Hubert, J.Mat.Sci. 20, 85 (1985)
11. S. Fox and H.M. Flower, presented at 'Metal Matrix Composites: Structure and Property Assessment', The Royal Aeronautical Society, London, November 1987.
12. Dinwoodie, J. and I. Horsfall, 'Proc ICCM6' Vol 2 p.390, Elsevier Applied Science, London (1987)
13. Cappleman, G.R, J.F. Watts and T.W. Clyne, J.Mat.Sci. 20, 2159 (1985)
14. I.J. Polmear, 'Metallurgy of Light Metals' p.15, Edward Arnold, London (1981)

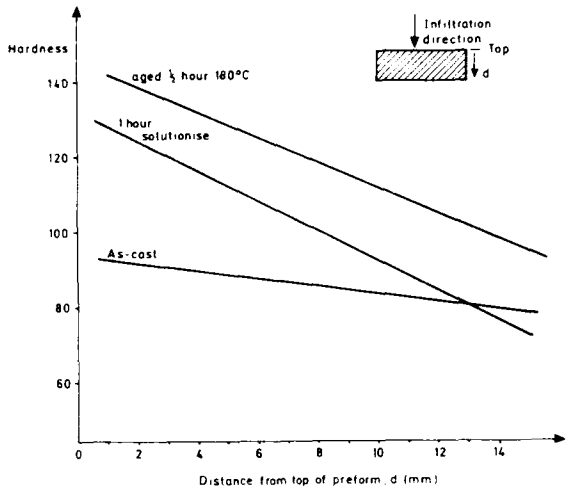


Fig.1 - Through-thickness hardness traverses in a 0.26 V_f composite (solutionised 1 hour).

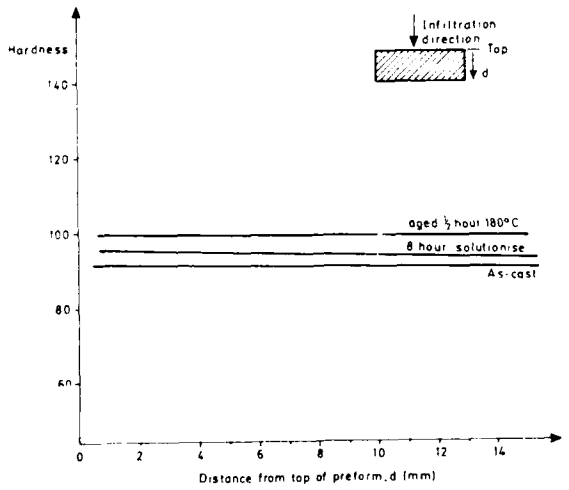


Fig.2 - Through-thickness hardness traverses in a 0.26 V_f composite (solutionised 8 hours).

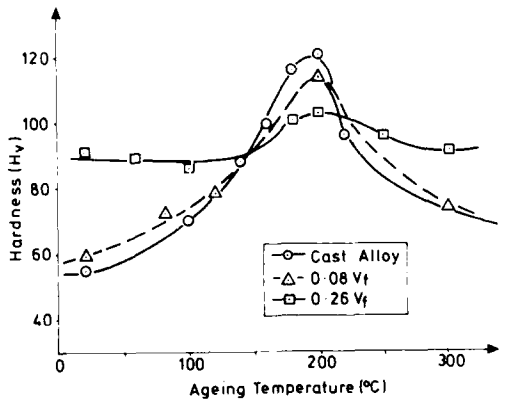


Fig.3 - Isochronal age-hardening characteristics of the unreinforced alloy, and 0.08 and 0.26 V_f composites.

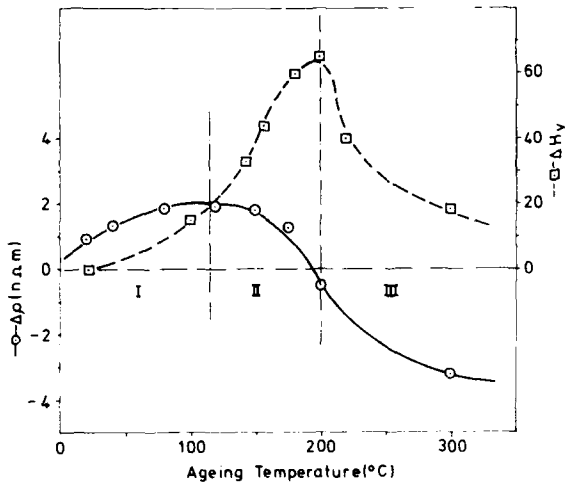


Fig.4 - Cross-plot of the hardness and resistivity changes following isochronal ageing of the unreinforced alloy.

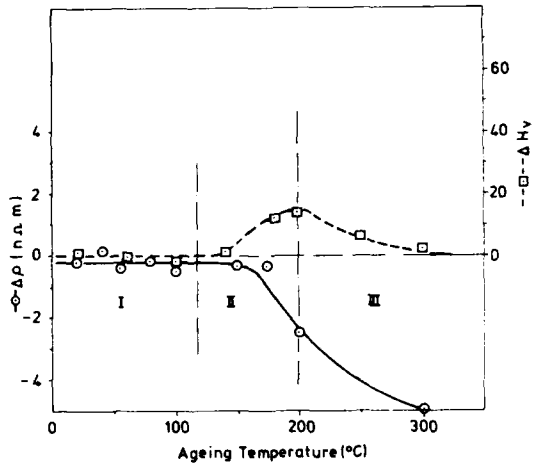


Fig.5 - Cross-plot of the hardness and resistivity changes following isochronal ageing of a 0.26 V_f composite.

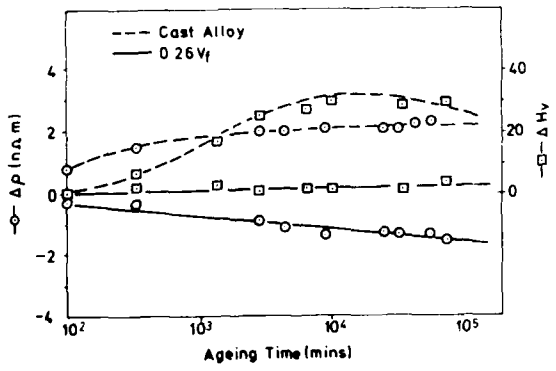


Fig.6 - Cross-plot of the hardness and resistivity changes for the unreinforced alloy and a 0.26 V_f composite during natural ageing.

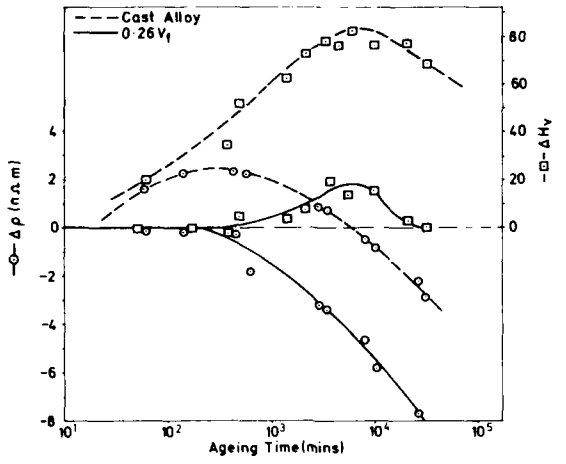


Fig.7 - Cross-plot of the hardness and resistivity changes for the unreinforced alloy and a 0.26 V_{f_0} composite during artificial ageing at 140°C.



Fig.8 - TEM micrograph of the matrix of a peak-aged 0.26 V_f composite.

RESIDUAL STRESSES IN CONTINUOUS GRAPHITE FIBER Al METAL MATRIX COMPOSITES

Hun Sub Park, Gui Sheng Zong, Harris L. Marcus
Center for MS&E, The University of Texas at Austin
Austin, Texas 78712 USA

UNIDIRECTIONALLY REINFORCED FIBROUS composites respond to changes in temperature quite differently from the behavior of monolithic materials. For isotropic monolithic materials nonuniform temperature distribution between the center and surface of a sample can be the source of thermal residual stress. Composites, on the other hand, have a built - in constraint even for spatially uniform temperature changes.[1] The combination of graphite fibers with slightly negative coefficient of thermal expansion (CTE) and aluminum matrix with high positive CTE leads to large internal stresses in the constituents and plastic flow in the matrix after slight temperature changes.[2] The axial coefficient of thermal expansion of the graphite fiber, α_{FL}, is -1.2×10^{-6} °C^{-1} for P 100 graphite fibers ; the corresponding figure for the aluminum, α_{Al}, is approximately 23×10^{-6} °C^{-1}. For a change in temperature, ΔT, of 400 °C, longitudinal residual stress as much as 400 MPa in the matrix which is far beyond the yield stress of aluminum has been predicted by a finite element analysis.[3] The fibers are assumed to remain perfectly elastic throughout the fabrication and processing cycles, and they may be treated as being anisotropic - transversely isotropic. The matrix material is assumed to be isotropic and is allowed to undergo plastic flow when its stress state reaches the yield surface. Transverse residual stresses are much less than longitudinal residual stresses because the fiber's transverse expansion coefficient approaches that of the matrix.

EXPERIMENT

The actual residual stresses in the Gr / Al composites with various thermal histories were measured using x - ray diffraction methods. X - ray diffraction stress analysis is based on the determination of lattice strains by precise measurements of the interplanar spacings in different directions of the sample.[4] The lattice spacings and the 2 θ peak for the (422) planes of aluminum were measured using Cu K_α radiation at six ψ tilts between 0 and 45°. The x - ray sampling depth is approximately 50 μm which corresponds to several layers of fibers. Unidirectional P 100 graphite fiber ($E_{FL} \cong 690$ GPa $\cong$ 100 Msi) reinforced 6061 aluminum MMC plates with a fiber volume fraction of 0.4 were used for the experiment. The plate consists of two - ply P 100 Gr / Al 6061 precursor wires and 6061 aluminum overlayers. Prior to measurement of the residual stresses with x - ray the 6061 aluminum overlayers were electrochemically removed.

RESULT AND DISCUSSION

In order to calibrate the relationship between stress magnitude and lattice spacing shift, samples of Al 6061 were loaded at varying stress levels in a three - point bend fixture while the stresses were simultaneously determined by x - ray diffraction techniques and by strain gages attached to the surface of the specimen.[5,6] The results of this calibration experiment are shown in Figure 1 ; the stresses determined by the x - ray techniques closely match those determined by the strain gages. The slope of the line corresponds closely to the 70 MPa modulus of the aluminum alloy. Using these calibrations, the longitudinal residual stresses of P 100 Gr / Al 6061 composites were measured for various heat treatments and the results are shown in Table 1.

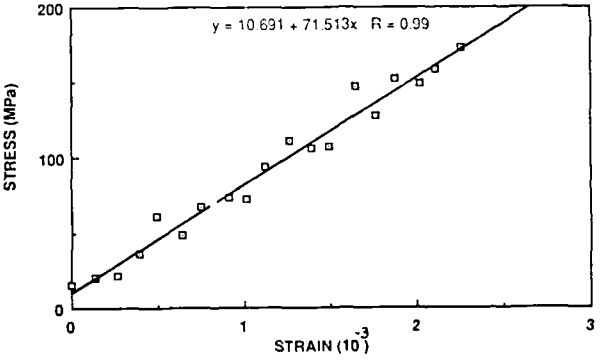


Fig. 1 - X - ray stress vs. strain from strain gage for Al 6061 alloy. The stresses determined by the x - ray techniques closely match those determined by the strain gages.

Table 1 - Longitudinal Residual Stresses of P 100 Gr / Al 6061 Composites for Various Heat Treatments.

Specimen	Thermal History	Longitudinal Residual Stress of Al Matrix
1	Solutionized at 530 °C for 1 Hr and water quenched to room temperature	149.2 MPa
2	Solutionized at 530 °C for 1 Hr, quenched into liquid nitrogen, aged at 205 °C for 1.5 Hr and water quenched to room temperature	270.1 MPa
3	Solutionized at 530 °C for 1 Hr, quenched into liquid nitrogen, aged at 205 °C for 1.5 Hr, quenched onto dry ice (- 78.5 °C) and back to room temperature	68.9 MPa
4	Solutionized at 530 °C for 1 Hr, quenched into liquid nitrogen, aged at 205 °C for 1.5 Hr, quenched into ethanol at its ice point (-117 °C) and back to room temperature	-30.2 MPa
5	Solutionized at 530 °C for 1 Hr, quenched into liquid nitrogen, aged at 205 °C for 1.5 Hr , quenched into liquid nitrogen (- 196 °C) and back to room temperature	- 86.9 MPa

Residual stresses of specimen 1 and 2 were found close to yield stresses of Al 6061 T 4 and T 6, respectively. The stress on cooling to room temperature was tensile in the matrix and reverted to a residual compressive state during subsequent heating to room temperature after cooling below room temperature (specimen 4 and 5). In - situ measurements of residual stresses at different temperatures are now under way to fully describe thermal cycling of the unidirectional graphite - aluminum composite.

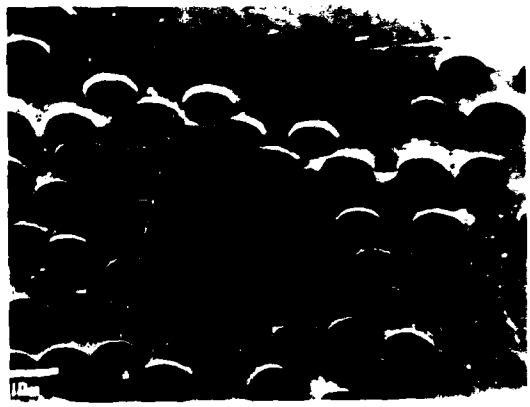
The differences between predicted residual stresses by finite element analysis and measured ones suggest some form of stress relaxation mechanism in these composites. In an attempt to determine the mechanisms of stress relief, P 100 Gr / Al 6061 composites were thermal cycled from room temperature to 300 °C and back in - situ in the SEM.[7] Fiber extrusion / intrusion phenomena were observed at a polished cross sectional surface during the cycling. Figure 2 are the SEM photomicrographs showing intrusion and extrusion of fibers in the P 100 Gr / Al 6061 unidirectional composite.



(a)



(b)



(c)

Fig. 2 - SEM photomicrographs showing intrusion and extrusion of fibers in the P 100 / 6061 unidirectional composite. (a) at room temperature before heating ; (b) at 300 °C, the peak temperature ; (c) at room temperature after cooling.

Over a limited range of temperatures and thermal cycles, the process was reversible (within experimental precision). No difference in the SEM micrographs of the cross section of the composites occured before and after a thermal excursion of 150 °C was applied. Additional heating led to the intrusion / extrusion of the fiber. Further study is now in progress on microstructural changes at the fiber - matrix interface during thermal cycling and a more detailed x - ray residual stress determination as a function of thermal history.

ACKNOWLEDGEMENT

This research was supported by a DNA subcontract ATP Dtd from S - Cubed Corporation and NASA grant NAG - 9-205.

REFERENCES

1. G. Garmong, Met. Trans., 5, 2183 (1974).
2. S. D. Tsai, D. Mahulikar, H. L. Marcus, J. Ismail, and J. B. Cohen, J. Mat. Sci. Eng. 47, 145 (1981)
3. M. H. Rice and G. A. Gurtman, "Residual Stresses and Thermo- mechanical Behavior of Metal Matrix Composites," Report prepared by S - Cubed Corporation (#SSS-R-84-6534) and submitted to the Naval Research Laboratory (1984).
4. J. B. Cohen, Power Diffraction 1, 15 (1986)
5. R. Zhong, I. Noyan and J. Cohen, Adv. in X-ray Anal., 29, 17 (1986)
6. A. Esquival, Adv. in x-ray Anal., 12, 269 (1969)
7. Y. M. Cheong and H. L. Marcus, Scripta Metallurgica 21, 1529 (1987)

DEFORMATION MECHANISM MAPPING OF SiC/Al METAL MATRIX COMPOSITE MATERIALS

Floyd R. Tuler, James T. Beals, Chrysanthe Demetry, Dan Zhao
Worcester Polytechnic Institute
Worcester, Massachusetts, USA

David J. Lloyd
Alcan International Limited
Kingston, Ontario, Canada

ABSTRACT

Compression tests were performed on as-cast 10 and 20 volume percent silicon carbide particle-reinforced 6061 aluminum composite materials over a range of temperatures from 300 to 550 C and strain rates from 10^{-3} to 160 sec^{-1}. Deformation mechanism maps were developed, and microstructural analysis was conducted to determine the operative metallurgical processes controlling the deformation. Dynamic recrystallization occurs at the higher strain rates and temperatures, nucleating in the vicinity of silicon carbide particle clusters.

METAL MATRIX COMPOSITE MATERIALS are currently being produced by a modified ingot metallurgy process followed by conventional metalworking and heat treatment. To optimize the fabrication process, the relationship among flow stress, microstructure, temperature, and strain rate needs to be determined. This paper describes the experimental results of such a study on composite materials produced by casting of 6061 aluminum containing 10 and 20 volume percent silicon carbide particulate reinforcement.

EXPERIMENTAL PROCEDURE

The composite materials were supplied by Dural Aluminum Composites Corporation in the as-cast condition using commercial grade aluminum alloy 6061 and SiC particles with an average size of 12 microns. Cylindrical compression specimens, approximately 1 cm in diameter and 1.5 cm long, were machined from the ingots and tested in uniaxial compression on a servohydraulic machine for the true strain rate range from 0.001 to 1 sec^{-1}, and on a cam plastometer for the true strain rate range from 5 to 160 sec^{-1}. The temperature range examined was from 300 to 550 C, and the deformation was continued to a true total strain of 0.45. All specimens were quenched in water in less than 10 seconds after deformation was completed.

EXPERIMENTAL RESULTS AND DISCUSSION

Typical stress-strain curves for the 10 volume percent composite material at high and low strain rates at 500 C are show shown in Figure 1.

In all cases the flow stress decreases with increasing temperature, as shown in Figure 2 for three representative strain rates. Figure 3 shows the increase in flow stress with increasing strain rate. The slopes of these logarithmic plots give the strain rate sensitivities, m, presented in Table 1. Values of m for the composite materials range from 0.06 at 300 C to 0.17 at 550 C, comparable to values for unreinforced alloy 6061.

To determine the activation energy of the microstructural mechanisms controlling the deformation, the logarithm of the flow stresses have been plotted against inverse temperature, as shown in Figure 4. These results can be used to construct the three-dimensional maps, shown in Figure 5, of activation energy as a function of temperature and strain rate. Figures 4 and 5 indicate that more than one deformation mechanism is controlling the behavior of the composite materials over the ranges of temperature and strain rate examined.

Microstructural examination of the

deformed samples can be related to the activation energy maps of Figure 5. At 300 C and 0.03 sec^{-1} the initial cast structure can still be identified in Figure 6, while at 550 C and 0.001 sec^{-1} a well-recovered structure with the occasional region of recrystallization is observed, as shown in Figure 7. Furthermore, Figure 8 shows that complete recrystallization has occurred in specimens tested at 500 C and 160 sec^{-1}. A summary of the microstructural observations is given in Table 2, showing that dynamic recrystallization takes place at the higher temperatures and strain rates. Careful examination of the microstructures suggest that, as shown in Figure 9, recrystallization nuclei occur in the regions of SiC particle clusters.

Table 1 - Strain Rate Sensitivity for As-Cast SiC Particle-Reinforced 6061 Aluminum Composites

Temperature C	10 vol %	20 vol %
300	0.06	0.06
350	0.08	0.09
400	0.10	0.11
450	0.13	0.13
500	0.16	0.15
550	0.17	0.17

CONCLUSIONS

The flow stresses and microstructures of as-cast 10 and 20 volume percent SiC particle-reinforced 6061 aluminum composite materials were determined over a broad range of temperatures and strain rates. The following conclusions concerning the deformation of these materials can be drawn from the results:

1) The variation of activation energy of deformation over the range of test conditions examined indicates that more than one microstructural mechanism is controlling the deformation.
2) Recovery occurs at the higher temperatures and lower strain rates (corresponding to the longest deformation tim at temperature).
3) Dynamic recrystallization occurs at the higher temperatures and strain rates.
4) Recrystallization appears to nucleate in the aluminum matrix in the vicinity of SiC particle clusters.

ACKNOWLEDGMENTS

The authors are grateful to Alcan International Limited and Dural Aluminum Composites Corporation for permission to publish this work, and to Dr. D.L. Baragar, Physical Metallurgy Research Laboratory, Ottawa, Canada, for arranging the cam plastometer tests.

Table 2a - Summary of Microstructural Observations for As-Cast 10 vol % SiC Particle-Reinforced 6061 Aluminum Composite Deformed to Strain = 0.45

Temperature C	Strain Rate sec^{-1}	Recrystallized Structure
450	5	No
450	160	No
500	5	Beginning/elongated
500	80	Not complete
500	160	Yes

Table 2b - Summary of Microstructural Observations for As-Cast 20 vol % SiC Particle-Reinforced 6061 Aluminum Composite Deformed to Strain = 0.45

Temperature C	Strain Rate sec^{-1}	Recrystallized Structure
450	5	Beginning at clusters
450	160	Not complete
500	5	Yes
500	160	Yes

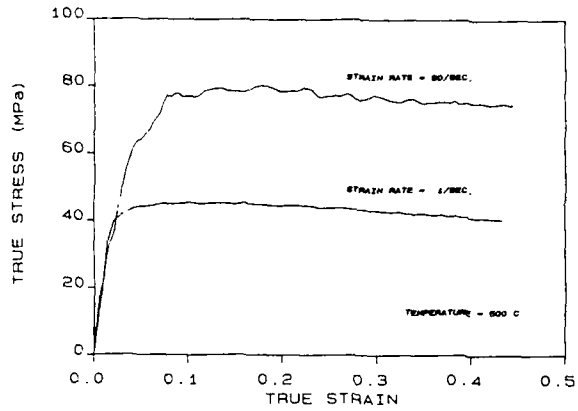


Figure 1 - Typical Stress-Strain Curves for As-Cast 10 vol % SiC Particle-Reinforced 6061 Aluminum Composite

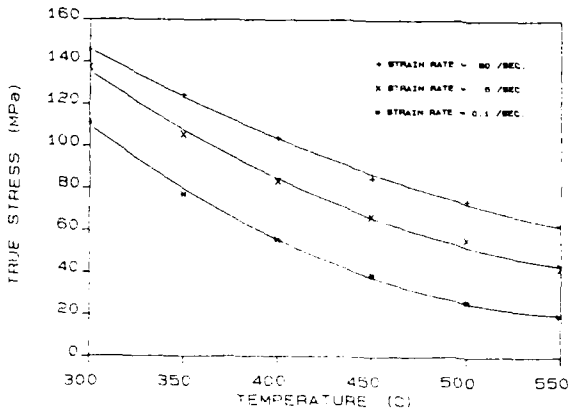


Figure 2a - Effect of Temperature on Flow Stress at 0.45 Strain for As-Cast 10 vol % SiC Particle-Reinforced 6061 Aluminum Composite

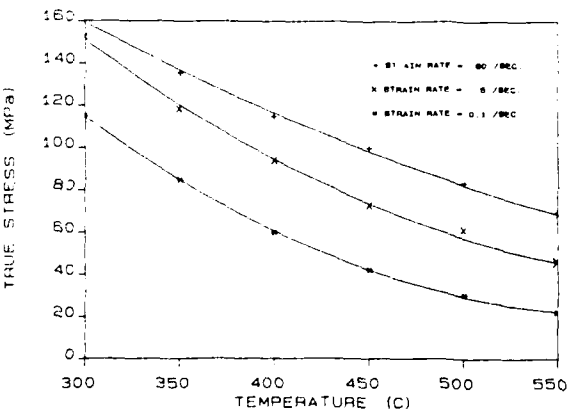


Figure 2b - Effect of Temperature on Flow Stress at 0.45 Strain for As-Cast 20 vol % SiC Particle-Reinforced 6061 Aluminum Composite

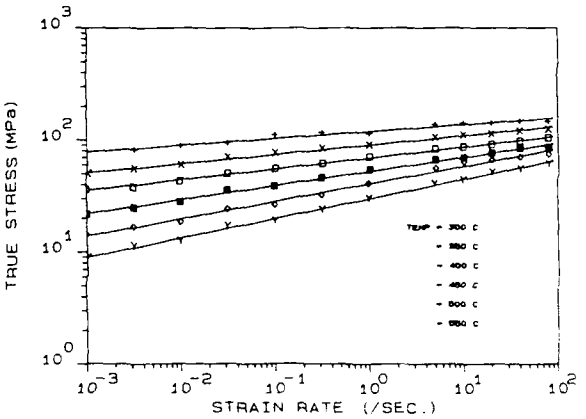


Figure 3a - Effect of Strain Rate on Flow Stress at 0.45 Strain for As-Cast 10 vol % SiC Particle-Reinforced 6061 Aluminum Composite

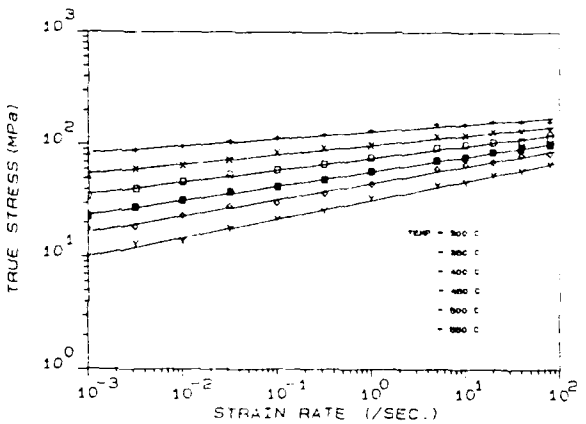


Figure 3b - Effect of Strain Rate on Flow Stress at 0.45 Strain for As-Cast 20 vol % SiC Particle-Reinforced 6061 Aluminum Composite

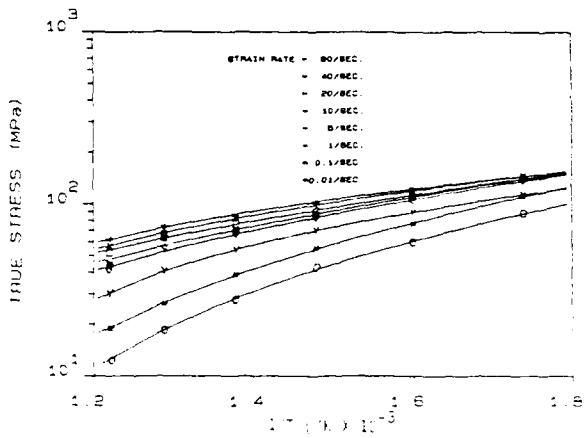


Figure 4a - Flow Stress (at 0.45 Strain) vs Reciprocal Temperature for As-Cast 10 vol % SiC Particle-Reinforced 6061 Aluminum Composite

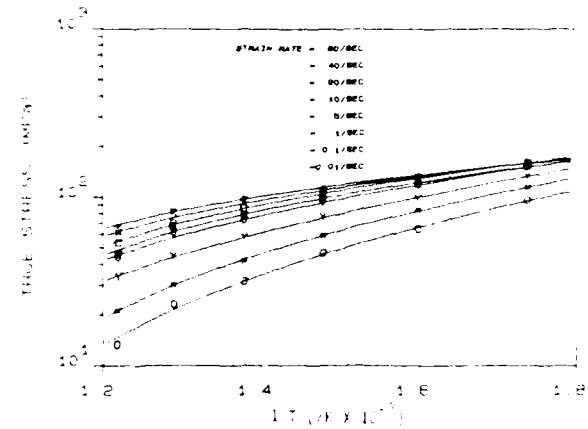


Figure 4b - Flow Stress (at 0.45 Strain) vs Reciprocal Temperature for As-Cast 20 vol % SiC Particle-Reinforced 6061 Aluminum Composite

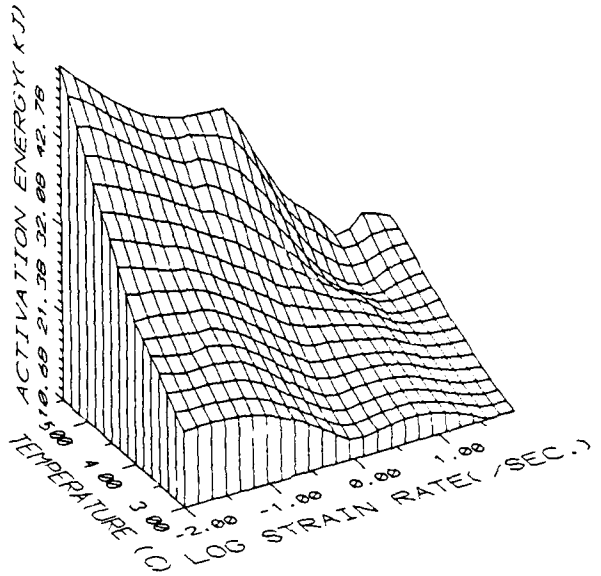


Figure 5a - Activation Energy Map for As-Cast 10 vol % SiC Particle-Reinforced 6061 Aluminum Composite

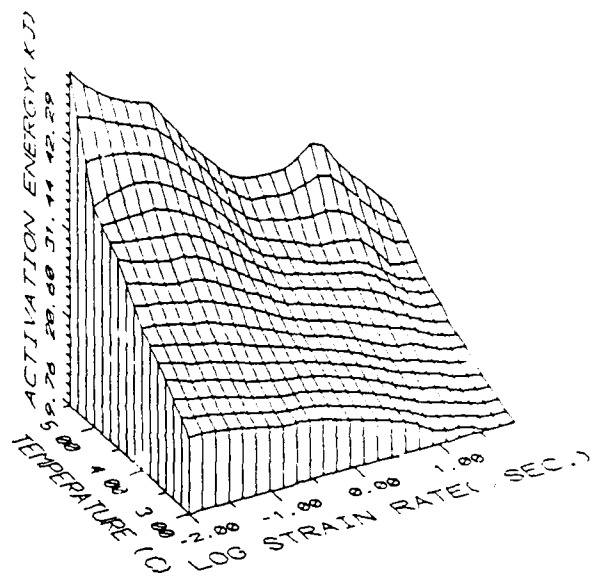


Figure 5b - Activation Energy Map for As-Cast 20 vol % SiC Particle-Reinforced 6061 Aluminum Composite

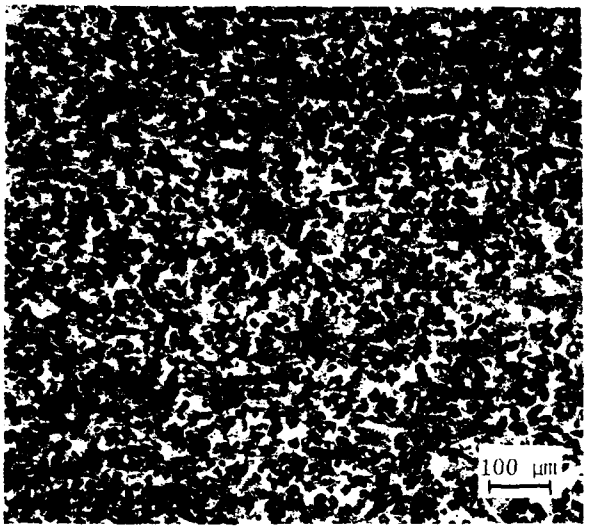


Figure 6 - Quenched Microstructure of As-Cast 20 vol % SiC Particle-Reinforced 6061 Aluminum Composite Deformed to Strain = 0.45 at T = 300 C and Strain Rate = 0.03 sec^{-1}

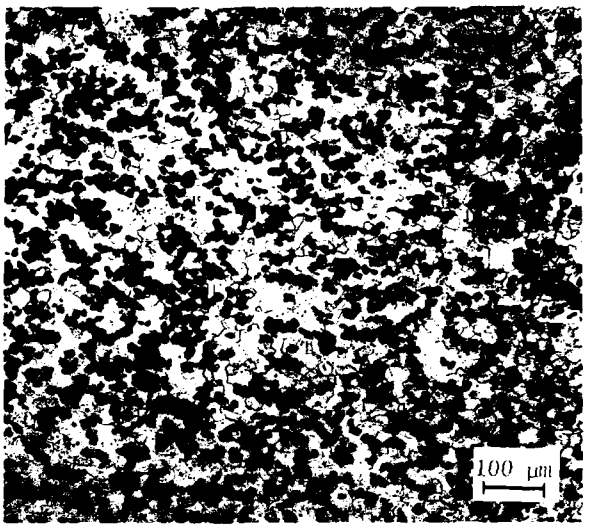


Figure 8 - Quenched Microstructure of As-Cast 20 vol % SiC Particle-Reinforced 6061 Aluminum Composite Deformed to Strain = 0.45 at T = 500 C and Strain Rate = 160 sec^{-1}

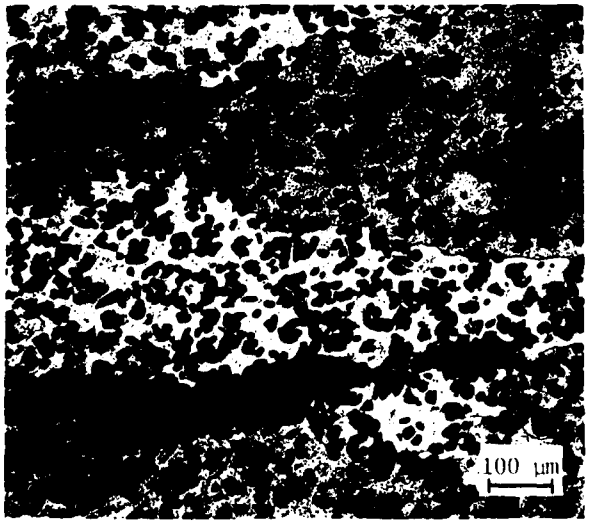


Figure 7 - Quenched Microstructure of As-Cast 20 vol % SiC Particle-Reinforced 6061 Aluminum Composite Deformed to Strain = 0.45 at T = 550 C and Strain Rate = 0.001 sec^{-1}

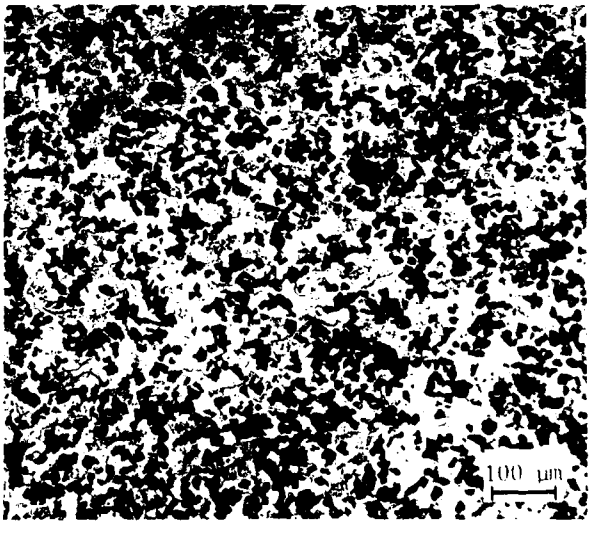


Figure 9 - Recrystallization Nuclei in Regions of Particle Clusters in As-Cast 20 vol % SiC Particle-Reinforced 6061 Aluminum Composite Deformed to Strain = 0.45 at T = 450 C and Strain Rate = 5 sec^{-1}

EFFECT OF RAPID SOLIDIFICATION ON MICROSTRUCTURE AND PROPERTIES OF CAST SiC_p/Al METAL MATRIX COMPOSITES

W. R. Loué, W. H. Kool
Faculty of Metals Science and Technology
Delft University of Technology
Rotterdamseweg 137
2628 AL Delft, The Netherlands

ABSTRACT

In this study, the effects of rapid solidification on microstructure and mechanical properties of SiC/Al metal matrix composites were investigated. For this purpose both compocast and rapidly solidified SiC/Al composites were produced with particle contents up to 10 wt.%. The average diameter of the SiC particles was 3 μm. The precipitation hardenable AlMg1Si1 alloy was selected as matrix material, in order to investigate the effect of matrix heat treatment on composite properties.
Clear microstructural differences between compocast and rapidly solidified composites, such as grain size or distribution of intermetallic phases, were not observed. The distribution of the SiC particles was generally homogeneous. However, the observed strengthening effect by the SiC addition was considerable for the rapidly solidified composites, whereas for the compocast composites hardly any strengthening effect was observed. Ductility loss with increasing particle content was less severe for the rapidly solidified composites than for the compocast composites.
Fracture surface analysis indicated that bonding between SiC and the Al alloy matrix was good for both the compocast and rapidly solidified composite. It appeared that, independent of heat treatment, the fracture surfaces of the rapidly solidified composites were finer dimpled than those of the compocast composites. This indicates that the homogeneity within the matrix is better after rapid solidification processing which might account for the observed differences in strengthening effects.

SILICON CARBIDE has been one of the most successful reinforcement materials for Al alloys up to now since it has very high strength, stiffness and hardness and it is chemically compatible with Al alloys up to 500°C. Improvements in strength at room temperature or higher temperatures, Young's modulus and wear resistance of SiC/Al composites on Al alloys have been reported [1,2].

However, SiC/Al composites usually show bad ductility and fracture toughness which makes them, despite the above mentioned advantages, less favourable to use in certain critical applications. The presence of coarse intermetallic phases, inhomogeneous distribution of the reinforcing phase and void initiation at the reinforcement-matrix interface, resulting from a weak interfacial bond, are mentioned as possible origin of low ductility and toughness [1,2].

Only recently, mention is made of rapid solidification processing (RSP) of some metal matrix composites [3-6] and Al matrix composites [7,8]. Kimura et al. [3] prepared, using meltspinning, Ni-based metallic glasses containing WC particles, which showed improved yield strength compared to the matrix alloy. Zielinski et al. [4-6] incorporated other particles and fibres (like SiC, TiC, C) in the same matrix alloy. Singer et al. [7] used a spray codeposition technique to prepare particle reinforced Al matrix composites. In their study they introduced various reinforcing materials, like SiC, Al_2O_3, Fe and C, ranging in size from 75 to 120 μm, into the atomized stream of molten metal. In this way they were able to build up a spray cast strip which contained the reinforcing phase with a fairly uniform dispersion within the rapidly solidified Al matrix. The authors claim that bonding of the reinforcing phase to the matrix was by mechanical interlocking. Ductility was generally poor. Probably, the short contact time with the liquid metal inhibited the formation of good interfacial bonding. Ehrström et al. [8] produced rapidly solidified SiC/Al composites by meltspinning molten composite material. Consolidation of the composite ribbons or flakes produced was done by hot extrusion. AlMg5Si(0-7wt.%) casting type alloys were used as matrix alloy. The SiC particles used were either 3 μm or 20 μm in diameter. It was observed that meltspinning of composite melts provided strong bonding between SiC and the Al matrix. In most cases no reinforcing effects were found for the 20 μm SiC/Al composites as the particles appeared to fracture first under load, but strong reinforcing effects were found for the 3 μm SiC/Al composites, coupled with a very low loss in ductility.

The aim of this study is to further investigate the effects of rapid solidification processing on microstructure and properties of SiC/Al composites. The improved homogeneity and ductility of a rapidly solidified matrix should be profitable for the properties of the composite material. Moreover, as the particles are found to be pushed, at normal solidification rates, by the solidification front into the last freezing regions , the segregation of solute elements near the SiC particles should be less pronounced after rapid solidification. SiC/AlMg1Si1 composite billets, with SiC particles of 3 μm average diameter in contents up to 10 wt.%, were prepared by compocasting. One part of the billet was extruded directly, whereas the other part was meltspun and subsequently extruded. Any difference in structure and properties between both kinds of composites might therefore directly be attributed to rapid solidification effects.

SiC particles of 3 μm average diameter were used because they were found to provide a strong reinforcing effect in SiC/Al composites [8]. The choice of the medium-strength AlMg1Si1 matrix alloy was made because this alloy offers the possibility of influencing matrix properties by heat treatment. Furthermore, ample literature deals with the SiC/AA 6061 composite system [9-11], for which the matrix composition is similar to the one used in this work.

EXPERIMENTAL PROCEDURE

COMPOSITE PRODUCTION - The AlMg1Si1 matrix alloy was made starting from pure Al (99.99%), pure Mg, and AlCu-, AlMn- and AlSi-master alloys of known composition. The composition of the matrix alloy, as determined by X-ray fluorescence analysis, is listed in table 1, along with the nominal composition of the AA 6061 alloy.

Table 1 Chemical composition (wt.%) of the AlMg1Si1 matrix alloy and the nominal composition of AA 6061 [12].

	Mg	Si	Cu	Fe	Mn	Cr	Al
AlMg1Si1	1.0	0.8	0.3	0.2	0.15	<0.01	bal.
AA 6061	0.8-1.2	0.4-0.8	0.15-0.4	<0.7	<0.15	0.04-0.35	bal.

The apparatus used for the production of the compocast Al matrix composites is schematically shown in Fig. 1. Basically, the apparatus consists of an electrical resistance heated furnace containing a graphite crucible connected to a water cooled steel mould. Particle introduction, using Ar as carrier gas, takes place while the matrix alloy is stirred in the semi-solid state. A stopper assembly separates the crucible from the mould during composite production; lowering the stopper allows casting of the stirred composite into the mould. This apparatus is quite similar to the one used by Hosking et al. [13]. The production of the composites

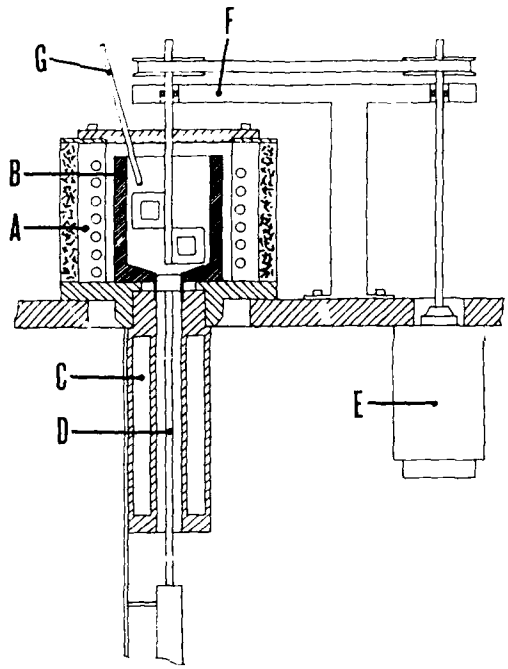


Fig.1 Compocasting apparatus used for the production of the SiC/AlMg1Si1 composites. A: electrical resistance furnace; B: graphite crucible; C: water cooled steel mould; D: stopper assembly; E: motor; F: stirrer assembly; G: particle injection.

started with melting the matrix alloy (approx. 400 g) in the crucible and then cooling the melt, while stirring, to the lowest temperature in the solidus-liquidus range at which good stirring was still possible. This temperature was 4-5°C below liquidus-temperature and was kept constant during the addition of the ceramic particles. The particles were preheated at 400°C and, using a vibrating dispenser and an Ar flow, directedto the surface of the vigorously agitated semi-solid slurry. The SiC particles were thus entrapped in the melt while the mechanical interaction between particles and the high viscosity matrix slurry promoted wetting. After completion of the particle addition, which took about 10 to 15 minutes depending on the amount of particles charged, the slurry was remelted and heated to a temperature high enough to ensure good fluidity. Then, still under continuous stirring, the stopper was lowered and the composite flowed into the mould and solidified, resulting in a composite billet of 30 mm diameter and about 200 mm length. The entire processing was performed in an Ar atmosphere to prevent the stirred melt from oxidizing as much as possible.

A part of the billet was extruded directly, whereas about 50 grams of the billet was melted again, using induction heating, in a graphite crucible positioned above a melt-spinning wheel. After complete melting and heating to a

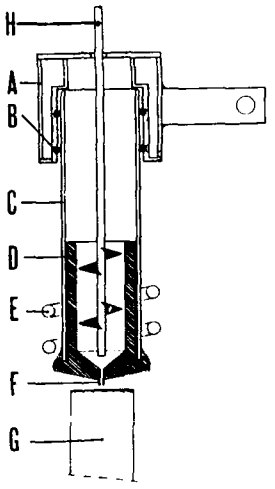


Fig. 2 Details of the meltspinning equipment. A: water cooled tube holder; B: rubber fastening ring; C: quartz tube; D: graphite crucible; E: induction coil; F: ceramic orifice; G: copper wheel; H: spiral shaped stirrer.

sufficiently high temperature, the composite was stirred some minutes to ensure a homogeneous particle distribution. Then, under continuous stirring in Ar atmosphere, the composite was ejected from the crucible and meltspun on a fast rotating copper wheel. Details of the equipment are schematically shown in Fig. 2. The composite ribbons obtained were then chopped into flakes of about 2 mm length and width.

After preheating for 10 minutes at 420°C, both the compocast billets and the rapidly solidified composite flakes were extruded at 450°C in a 60 tons laboratory extrusion press. The extrusion ratio was 35:1. Starting from a billet of 30 mm diameter and about 60 mm length, rectangular strips of 2 mm thickness, 10 mm width and about 150 cm length were produced, from which tensile specimens were machined. After extrusion, the composites were tested both in the as extruded condition and in the T6 condition. The T6 heat treatment comprised 15 and 40 minutes of solution heat treating at 530°C for the rapidly solidified and compocast materials respectively, followed by water quenching and ageing at 175°C for 8 hours.

MICROSTRUCTURAL AND MECHANICAL INVESTIGATIONS - The microstructures of the compocast composites, the rapidly solidified composite ribbons and the extrudates were examined by optical microscopy, while the examination of fracture surfaces of both the compocast and the rapidly solidified tensile specimens was performed with a scanning electron microscope (SEM). The mechanical properties of the extruded products were determined using a 5 tons Instron tensile testing machine.

RESULTS

PROCESSING - The particle content in the rapidly solidified composite was limited by the viscosity of the composite melt during meltspinning. SiC/Al composite melts containing up to 10% of SiC particles could be meltspun. The maximum particle content in the rapidly solidified composites produced here, using particles of 3 μm, is higher than reported elsewhere. Kimura et al. [3] and Zielinski et al. [4] introduced 2 to 7 wt.% reinforcement in amorphous alloys using meltspinning. Ehrström et al. [8] introduced at most 5 wt.% of 3 μm SiC particles in AlSi7Mg5 matrix alloys, also using meltspinning.

OPTICAL MICROSCOPY - On a macroscopic scale relatively uniform particle distributions were observed in all compocast composites produced. On a microscopic scale, the structure was characterized by some local variations in particle content. It was observed that most particles were present between the individual dendrite arms or at grain boundaries, indicating that there was no nucleation of primary Al on the SiC particles and that the particles were pushed by the advancing solidification front into the last freezing regions. Consequently, most particles are surrounded by large intermetallic phases (probably Mg_2Si, also containing some Fe and Cu), as can be seen in Fig. 3. Particle distributions found in compocast composites known from literature were generally less homogeneous [13-15]. In these studies, clusters of 1 to 5 μm particles, if formed, were found not to break up at all, even when only 5% of particles was added.

A typical microstructure of the compocast composite after extrusion, is shown in Fig. 4. The particle distribution transverse to the direction of extrusion appears to be quite homogeneous (Fig. 4a). Hardly any clustering is observed.



Fig. 3 Micrograph of the compocast SiC/AlMg1Si1 billet, containing 5 wt.% of SiC. Arrows indicate intermetallic phases, formed at the matrix/particle interface. Oblique illumination. —— 5 μm

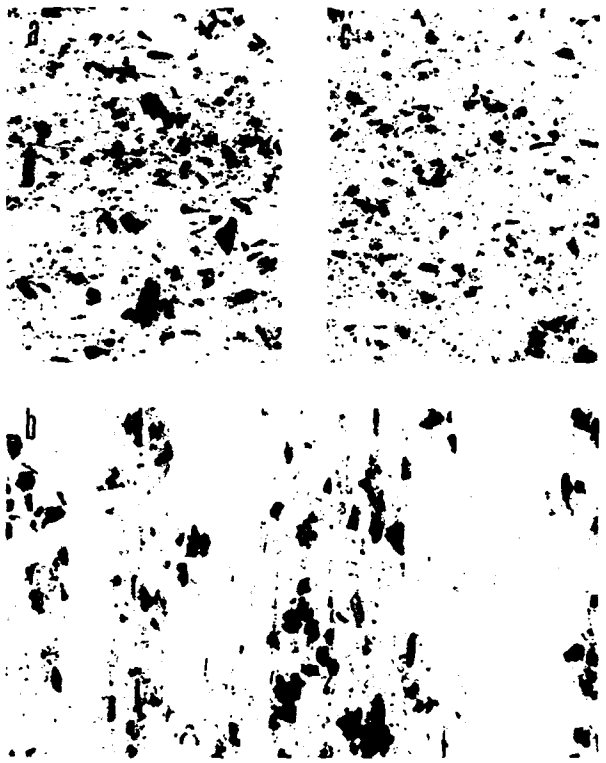


Fig. 4 Micrographs of the SiC/AlMg1Si1 composites, containing 5 wt.% SiC, after extrusion and T6 heat treatment. a) compocast, section transverse to the direction of extrusion; b) compocast, section parallel to the direction of extrusion; c) rapidly solidified, section transverse to the direction of extrusion. —— 20 µm

In the direction parallel to extrusion, the presence of particle-free zones was observed (Fig. 4b). These zones are, on the average, about 300 µm in length and 50 µm in width. The presence, on a macroscale, of elliptic zones in the extruded profile with higher and lower particle concentrations, as reported in ref. [16], was not observed. Grain sizes in the as extruded composite were about 6 µm in length, being only slightly elongated in the direction of extrusion. In regions with higher particle concentrations, grains were equiaxed with sizes of about 3 to 4 µm. Probably these SiC particles pinned the grain boundaries. After the T6 heat treatment the grains were elongated, about 200 µm in length and 40 µm in width.

Except for thickness, the rapidly solidified composite ribbons did not differ very much from meltspun matrix ribbons. The average thickness of the meltspun composite ribbons was in the range of 70 to 140 µm with the ribbons getting thicker as the particle content increased. The width of the meltspun composite ribbons was a little less and the surface was less smooth than the corresponding matrix alloy ribbons. The particle content in the ribbon varied locally along the longitudinal direction, as can be seen in Fig. 5. Almost no clustering of particles was observed in the ribbons. A periodic variation of the particle content along the longitudinal direction, as reported in ref. [6], or segregation of particles to the upper part of the ribbon, as reported in ref. [8], was not observed. Large intermetallic phases as found in the compocast microstructures were not observed.

The microstructure of the rapidly solidified composite after extrusion is also given in Fig. 4. As with the compocast composite, this composite is also characterized by a homogeneous SiC distribution transverse to the direction of extrusion (Fig. 4c) and the presence of particle-free zones in the direction of extrusion. These zones had in general similar dimensions as in the extruded compocast composites. In the as extruded condition, grains were about 2 µm in section, which is considerably less than in the corresponding compocast composite. After heat treatment, grains of about the same size as in the corresponding compocast material (elongated, 200 µm in length, 40 µm in width) were encountered, which, in this case, were alternated with zones where the grains were still about 5 µm in size. In these latter zones, the presence of the particles prevented the structure from recrystallization.

In both the compocast and rapidly solidified composites, any presence of large intermetallic phases near the SiC matrix interface after extrusion was not observed by optical microscopy. After the T6 heat treatment of the compocast and rapidly solidified composites, no porosity could be observed, indicating that gas entrapment during processing was limited.

Grains in both the compocast and rapidly solidified matrix alloys, without SiC particles, were slightly elongated in the as extruded condition (10 µm) and stronger elongated after the T6 heat treatment (700 µm in length; 100 and 50 µm in width respectively). The distribution of precipitates in the rapidly solidified matrix alloy seemed to be slightly more homogeneous. Comparing the grain sizes of the matrix alloys with the corresponding composites, it appeared that grain sizes were smaller in the composites. The SiC particles apparently hindered grain growth.



Fig. 5 Micrograph of the SiC/AlMg1Si1 composite ribbon, containing 5 wt.% of SiC. Oblique illumination.

TENSILE TESTING - The results of the tensile tests are summarized in table 2. From this table it can be concluded that both yield strength and ultimate tensile strength of the rapidly solidified matrix alloy are, in both conditions, not very much different from those of the compocast matrix alloy. However, the elongation of the rapidly solidified matrix alloy was found to be independent of heat treatment, whereas in the case of the compocast matrix alloy the elongation was strongly reduced after heat treatment.

The presence of SiC particles does not give an increase in ultimate tensile strength of the compocast composites for both the as extruded and T6 condition, whereas in the rapidly solidified composites the tensile strength is raised considerably by SiC particle additions. In the as extruded state, the yield strength of the rapidly solidified composites seems to increase with increasing particle content to the same extent as in the compocast composite. However, in the T6 condition the rapidly solidified composites show a considerable increase in yield strength with SiC particle content whereas in the compocast composites no increase in yield strength is observed. In general, the elongation of the composites is lowered with increasing particle content but the effect is less severe for the rapidly solidified composites than for the compocast composites.

In general terms, it can be concluded that with increasing particle content the mechanical properties of the compocast composites deteriorate, whereas the mechanical properties improve in the case of the rapidly solidified composites. Matrix alloy properties were found to be comparable for both the rapidly solidified and compocast matrices.

Table 2 Mechanical properties of compocast (CC) and rapidly solidified (RS) SiC/AlMg1Si1 composites.

SiC content (wt.%)	Condition	U.T.S. (MPa)	Y.S. (MPa)	elongation (%)
0	CC, as extr.	169	91	18
	CC, T6	294	276	7
	RS, as extr.	165	100	13
	RS, T6	303	280	12
5	CC, as extr.	172	96	13
	CC, T6	308	279	5
	RS, as extr.	201	115	13
	RS, T6	356	304	9
10	CC, as extr.	164	113	3
	CC, T6	286	277	1
	RS, T6	384	339	5

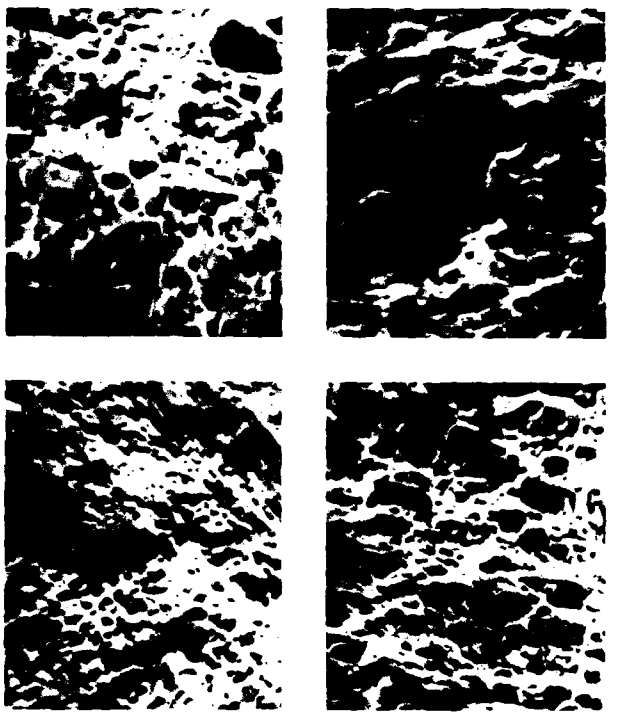


Fig. 6 SEM micrographs of fracture surfaces of the extruded SiC/AlMg1Si1 composites, containing 5 wt.% SiC. a) compocast, as extruded; b) compocast, T6 condition; c) rapidly solidified, as extruded; d) rapidly solidified, T6 condition. ——10 μm

FRACTURE SURFACE ANALYSIS - The influence of rapid solidification and matrix condition on the fracture behaviour was studied at the fracture surfaces of the composites containing 5% of SiC particles. In these composites hardly any clusters of SiC, which could influence the fracture by providing easy crack initiation, were present.

The fracture surface of the as extruded compocast composite was characterized by the appearance of dimples (about 3 μm in diameter), which is typical for a ductile mode of fracture by void initiation and growth (Fig. 6a). No particles were seen at the fracture surface. However, the distribution of Si at the same spot of the fracture surface, using X-ray imaging, showed that some SiC was present near the fracture surface. Direct comparison of the SEM micrograph with the corresponding Si X-ray image did still not reveal clearly distinguishable SiC particles. With the accelerating voltage applied (10 kV), the information depth, from which the X-ray photons are generated, is about 1 μm. This means that the SiC present near the fracture surface had to be covered with an Al matrix layer, at most 1 μm in thickness, indicating that good bonding between the matrix and the SiC particles existed. Furthermore, this indicated that fracture initiation did not occur at the matrix-particle

interface itself. After T6 heat treatment, the fracture surface of the extruded compocast composite was more coarsely dimpled (dimple diameter of about 6 μm - Fig. 6b). The Si X-ray distribution at the fracture surface revealed that more SiC was present than in the as extruded condition. Reminding that the particle distribution transverse to the direction of extrusion was quite homogeneous, this difference cannot be explained by local variations in particle content only. When comparing the fracture surface with the corresponding Si X-ray distribution, some SiC particles could be recognized. These particles were always found at the bottom of a dimple, indicating that void initiation took place at the matrix-particle interface.

In the as extruded condition, the fracture surface of the rapidly solidified composite displayed a finer dimpled structure (dimple diameter approx. 1 μm - Fig. 6c) than that of the corresponding compocast composite. The matching Si X-ray distribution showed that there was hardly any SiC present near the fracture surface. Again, this indicates that good bonding between matrix and SiC had been achieved. After T6 heat treatment, the fracture surface became more coarsely dimpled (dimple diameter approx. 3 μm - Fig. 6d) but still the dimples were finer than in the case of the compocast composite in the same condition. The matching Si X-ray distribution showed that the amount of SiC present near the fracture surface increased considerably. Again, the difference in Si distribution at the fracture surface between the as extruded condition and the heat treated condition is too big to be explained by local particle content variations. Again, the particles retrieved were found at the bottom of a dimple.

In all cases, no intermetallic phases at the matrix-reinforcement interface were observed. In general, the fracture surfaces of the rapidly solidified composites were, for both conditions, finer dimpled than those of the corresponding compocast composites. It also appeared that in both the rapidly solidified and the compocast composites heat treatment drastically changed the amount of SiC present near or at the fracture surface. After T6 heat treatment, the SiC content, derived from the Si X-ray distribution, roughly corresponded with the actual concentration of SiC. SEM investigation of longitudinal sections near the fracture surface of the tensile tested compocast as well as rapidly solidified composites revealed that before heat treatment the fracture path proceeded through the material independent of the position of the SiC particles whereas after heat treatment the fracture path followed matrix-particle interfaces. This confirms the earlier observation that more SiC particles were distinguishable near the fracture surface after T6 heat treatment. Due to the stronger matrix, the deformation will be concentrated more near these hard ceramic particles.

DISCUSSION

From table 2 it is clear that for the rapidly solidified composites the ultimate tensile strength strongly increases by the addition of particles, whereas less or no reinforcement effect is observed for the compocast composites. Ductility loss in the rapidly solidified composites was found to be less severe than in the compocast composites. The results also indicate that, in general, addition of SiC raises the yield strength of the composite materials, but the effect is stronger in the rapidly solidified composites. However, clear microstructural differences between the compocast and rapidly solidified composites were not observed by optical microscopy. The particle distributions in both kinds of composites were rather homogeneous and they did not contain many clusters. Differences in grain sizes, although observed, were not very large and could not account for the observed differences in mechanical properties. Large intermetallic phases at the particle-matrix interface were not observed. Analysis of fracture surfaces indicated that bonding was good. After the T6 heat treatment, no gas porosity could be observed in both cases.

Yet, fracture surface analysis revealed that, independent of the matrix condition, fracture surfaces were finer dimpled for rapidly solidified composites than for compocast composites. This suggests that the rate of void growth in the rapidly solidified composites was lower. The stronger reinforcement effects found in the rapidly solidified composites might therefore be due to improved matrix homogeneity which reduces strain localization and results in better reinforcement-matrix interaction. However, clear microstructural differences confirming this statement were not observed yet.

From literature, it can be deduced that the deformation behaviour of the matrix alloy plays an important role in the effectiveness of the reinforcing phases. For instance, the reinforcement effect on the tensile strength in the rapidly solidified SiC/AlSi7Mg5 composites investigated by Ehrström et al. [8], containing 3 μm particles, is stronger (with 3.5% SiC, as extruded: 74 MPa) than in the rapidly solidified SiC/AlMg1Si1 composites investigated in this study (with 5% SiC, as extruded: 36 MPa; after T6 heat treatment: 53 MPa). Also, the loss in ductility is lower for the rapidly solidified SiC/AlSi7Mg5 composite system. It is noted that the rapidly solidified AlMg1Si1 matrix alloy used in this study showed lower strain hardening than the rapidly solidified AlSi7Mg5 matrix alloy used by Ehrström. On the other hand, comparison of the results of the as extruded and T6 heat treated SiC/AlMg1Si1 composites indicates that the stronger reinforcement effect is obtained for the condition with lower strain hardening. Friend [17] also found the reinforcement effect to depend on matrix strain hardening in short alumina fibre reinforced Al metal matrix composites. Alloy matrices were found to fall into two families exhibiting significantly different fiber strengthening response. Using a rule of mixtures strength analysis, it was proposed that for optimum reinforcement the matrix alloys should exhibit a low rate of strain hardening. The large influence of the matrix on the reinforcement effects is apparent.

Combination of the effects of particle addition on yield strength and ultimate tensile strength should provide insight in the effect of particle addition on composite deformation behaviour. In Fig. 7 the differences in ultimate tensile strength between composites and their matrices are plotted versus the corresponding differences in yield strength. From the figure, it can be concluded that, in most cases, an

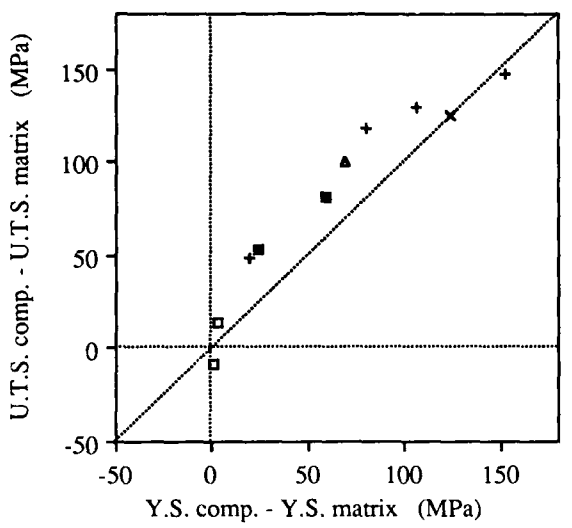


Fig. 7 The reinforcing effects in U.T.S. and Y.S. for compocast (CC), rapidly solidified (RS) and P/M SiCp/AA 6061 T6 composites; comparison between present data and literature data. Dotted line at 45° corresponds with strengthening before yielding only.
❑ : CC, 5-10% SiC, present result;
■ : RS, 5-10% SiC, present result;
+ : P/M, 15-40% SiC, ref. [9];
x : P/M, 20% SiC, ref. [10];
Δ : P/M, 25% SiC, ref. [11].

observed increase in tensile strength is mainly caused by a similar increase in yield strength. Apparently, the addition of particles mainly provides strengthening before yielding of the material and, to a lesser extent, deformation resistance during plastic flow. The present results obtained with the rapidly solidified SiC/AlMg1Si1 are comparable with those of the P/M composites with corresponding SiC content [9-11]. Also ductility loss is comparable. However, it is noted that the use of rapid solidification techniques does not have a strong effect on 6xxx alloy properties. The origin of the small effect of particle addition on the properties of the compocast composites is not understood yet and will be further investigated.

CONCLUSIONS

The effect of rapid solidification on microstructure and mechanical properties of 3 μm particle reinforced SiC/AlMg1Si1 composites has been studied. It is concluded that:

1. Both the compocast and rapidly solidified composites exhibit strong bonding between SiC and the Al matrix.
2. The reinforcement effects found in the rapidly solidified composites are stronger than those found in the corresponding compocast composites.
3. Ductility loss with increasing particle content is less severe for the rapidly solidified composites than for the compocast composites.
4. The observed differences in mechanical properties between compocast and rapidly solidified composites might be attributed to improved matrix homogeneity after rapid solidification processing, which reduces strain localization.

ACKNOWLEDGEMENTS

The authors would like to thank H. Kleinjan for his helpful contributions and stimulating discussions as well as P. de Ruiter for his invaluable technical assistance. We are indebted to Dr. J. Bouvaist and Ph. Jarry (Voreppe Research Centre of Cégédur Péchiney, Voreppe, France) for supplying the SiC particles.

REFERENCES

[1] S.V. Nair, J.K. Tien and R.C. Bates, Int. Met. Rev., **30** (1985) 275.
[2] Y. Flom and R.J. Arsenault, J. Metals, **38** (1986) 31.
[3] H. Kimura, B. Cunningham and D.G. Ast, in "Proceedings of 4th International Conference on Rapidly Quenched Metals", Sendai, January 1981, eds. T. Masumoto and K. Suzuki (Japan Institute of Metals, Sendai, 1982) p. 1385.
[4] P.G. Zielinski and D.G. Ast, J. Mater. Sci. Lett., **2** (1983) 495.
[5] *Idem*, Scripta Metall., **17** (1983) 291.
[6] *Idem*, in "Proceedings of the MRS Symposium on Rapidly Solidified Metastable Materials", Boston, November 1983, eds. B.H. Kear and B.C. Giessen (Elsevier, New York, 1984) p. 189.
[7] A.R.E. Singer and S. Ozbek, Powder Metall., **28** (1985) 72.
[8] J.C. Ehrström and W.H. Kool, *Production of rapidly solidified Al/SiC composites*, J. Mater. Sci., in press.
[9] D.L. McDanels and C.A. Hoffman, NASA Techn. Paper 2302 (NASA, Cleveland, 1984).
[10] R.J. Arsenault, Mater. Sci. Eng., **64** (1984) 171.
[11] C.R. Crowe, R.A. Gray and D.F. Hasson, in "Proceedings of the 5th International Conference on Composite Materials", San Diego, July-August 1985, eds. W.C. Harrigan, J. Strife and A.K. Dhingra (Metallurgical Society, Warrendale, 1985) p. 843.
[12] H.E. Boyer and T.L. Gall (Eds), Metals Handbook, Desk Edition, ASM, 1985.
[13] F. Hosking, F. Folgar Portillo, R. Wunderlin and R. Mehrebian, J. Mater. Sci., **17** (1982) 477.
[14] R. Mehrebian, R.G. Riek and M.C. Flemings, Metall. Trans., **5** (1974) 1899.
[15] A. Sato and R. Mehrebian, Metall. Trans. B, **7B** (1976) 443.
[16] J.C. Ehrström and W.H. Kool, *Migration of particles during extrusion of metal matrix composites*, J. Mater. Sci. Lett., in press.
[17] C.M. Friend, J. Mater. Sci., **22** (1987) 3005.

EFFECT OF MAGNESIUM CONCENTRATION ON THE SHEAR STRENGTH OF UNIDIRECTIONAL ALPHA-ALUMINA/ALUMINUM COMPOSITES

William D. Johnston
Materials Science Program
Center for Composite Materials
University of Delaware
Newark, Delaware 19716 USA

Irwin G. Greenfield
Department of Mechanical Engineering
Center for Composite Materials
University of Delaware
Newark, Delaware 19716 USA

ABSTRACT

Magnesium was added to aluminum alloy matrices to promote wetting and to vary the interfacial shear strength of squeeze-cast composites reinforced with unidirectional α-Al_2O_3 fibers. Shear strength measurements for composite and equivalent matrix alloys were used to evaluate the effect of magnesium concentration on the mechanical properties of the fiber-matrix interface. The area of the shear surface of the composites was calculated by accounting for the undulations observed on the shear-fracture surface due to the presence of the fibers. This analysis can be used to determine the composite shear strength and also the interfacial shear strength when it is less than the shear strength of the matrix. The shear strength of the composites tested was the same as that of the matrix alloy. From the data it was concluded that the shear strength of the interface is greater than or equal to the shear strength of the matrix alloy for each composite composition investigated.

The dependence of interfacial microstructure on magnesium content was observed in the transmission electron microscope (TEM), and scanning transmission electron microscope (STEM) with energy dispersive x-ray analysis (EDS) techniques.

INTRODUCTION

The microstructure and mechanical properties of the fiber-matrix interface were varied systematically in squeeze-cast aluminum-magnesium alloy, α-Al_2O_3 fiber composites by varying the amount of reactive magnesium in the matrix. Magnesium enhances the wetting of aluminum oxide fibers by aluminum alloys and contributes to interfacial bonding through chemical reaction at the fiber surface (1). The adhesion and distribution of reaction phase at the interface can be varied to achieve a desirable degree of fiber-matrix interaction or to tailor the material for a specific application.

EXPERIMENTAL

The materials systems investigated were selected for their practical usefulness, purity, and consistency. Polycrystalline α-Al_2O_3 fiber (Fiber FP, manufactured by Dupont) without sizing or surface treatment, and high-purity binary aluminum-magnesium alloys prepared by Reynolds Aluminum were used in these experiments. The as-received alloys were analyzed by spark emission spectroscopy (Table 1) to confirm their compositions.

Alloy (as-received)	Mg	Si	Fe	Others
	(Weight Percent)			
Al-99.99%	<0.001	0.004	0.005	<0.005
Al-0.96% Mg	0.96	<0.01	<0.01	<0.01
Al-4.82% Mg	4.82	0.02	0.01	<0.01

Table 1 - Composition of as-received alloys determined by spark emission spectroscopy.

Alloys of intermediate composition for the metal matrices were prepared by combining portions of the as-received materials, Al-4.82% Mg and Al-99.99%. Because part of the magnesium content of the alloys is lost to a magnesium-rich dross during melting, the matrix composition of the squeeze-castings was

analyzed by a wet chemical technique, DC Plasma spectroscopy. Although energy dispersive x-ray analysis in the SEM was readily available, the method gave inconsistent results, and thus was not used to obtain absolute compositions.

COMPOSITE FABRICATION - Aluminum-magnesium alloy metal-matrix composites were produced by a low-pressure vacuum squeeze-casting method. The apparatus developed for this process (Figure 1) was mounted in a screw-driven Instron testing machine.

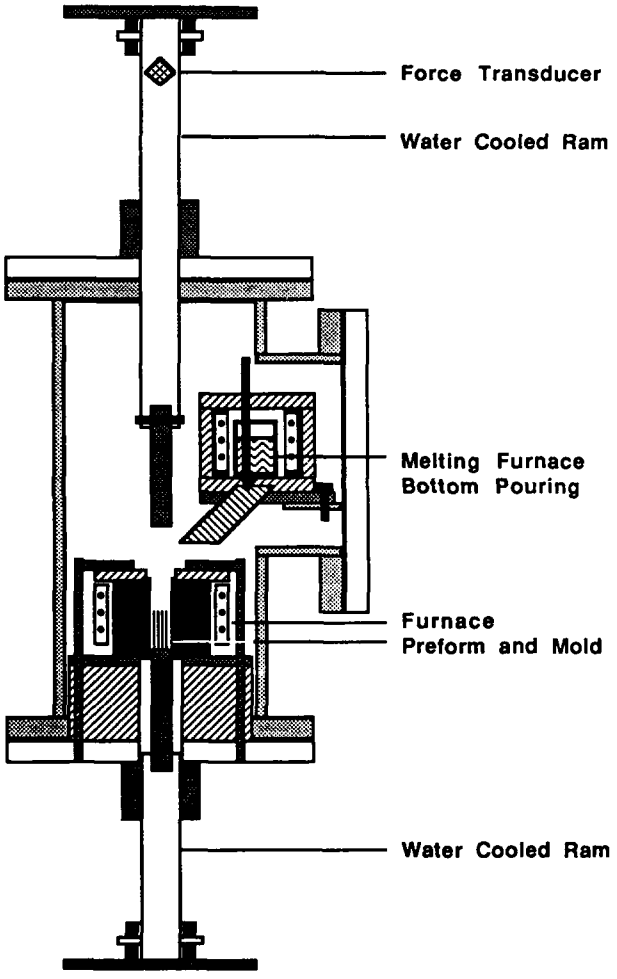


Figure 1 - Experimental apparatus developed for low-pressure squeeze-casting.

Four castings of a given matrix composition were simultaneously made in a graphite mold with cylindrical chambers preloaded with longitudinally oriented fibers. The mass of continuous fiber inserted into each cavity was adjusted to result in a 38% fiber volume fraction.

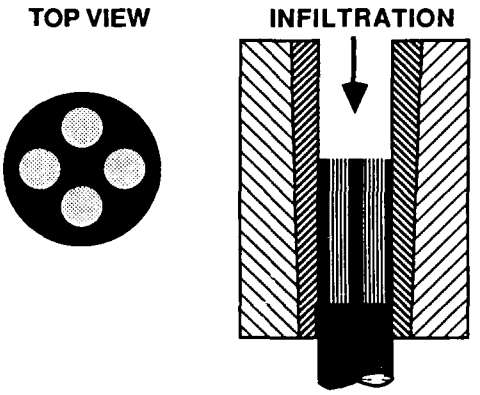


Figure 2 - Top view of four chamber graphite mold used to support fibers and placement in graphite lined tool steel die. Each chamber is 9 mm in diameter and 50 mm long.

Temperatures of the melting crucible and mold wall were continuously recorded using chromel-alumel thermocouples. The infiltration force was measured during pressure casting with a full-bridge strain-gauge transducer attached to the upper ram.

After heating the preform to 645 °C, the matrix alloys were melted in a boron-nitride coated graphite crucible. The melting crucible was heated to 800 °C in a separate resistance furnace and held for ten minutes before the melt was bottom poured into the mold. This pouring technique was used to exclude dross from the squeeze-casting.

Matrix Mixture (before melting)	Mold Temperature °C	Die Temperature °C
Al-1% Mg	647 ± 3	799 ± 3
Al-2.3% Mg	646 ± 3	796 ± 3
Al-3.6% Mg	642 ± 3	799 ± 3
Al-4.8 % Mg	644 ± 3	809 ± 3

Table 2 - Summary of processing temperatures.

The bottom-poured molten alloy was introduced into the die cavity via an aluminum oxide launder. After a volume excess to that needed to fill the preform was added to the die, the upper punch was rapidly lowered and the preform was infiltrated at a speed of 1 in/min, (25.4 mm/min). The pressure measured during infiltration was less than 5 MPa, and the ram motion was stopped when a sharp increase was noted indicating the beginning of solidification. The mold was then ejected from the hot zone and cooled by opening the chamber and circulating air through the apparatus.

SHEAR TESTING - A blanking shear test (2) was adapted for the composite specimens with the fibers oriented parallel to the shear surface (Figure 3). Disk-shape, cross-section test specimens were cut from the 4 mm cylindrical composite castings using a diamond-grit impregnated abrasive saw and a fixture designed to keep the work-piece perpendicular to the wheel without clamping. To attain the final thickness and to remove the surface damage from sawing, the specimen was hand lapped with a 600 grit abrasive.

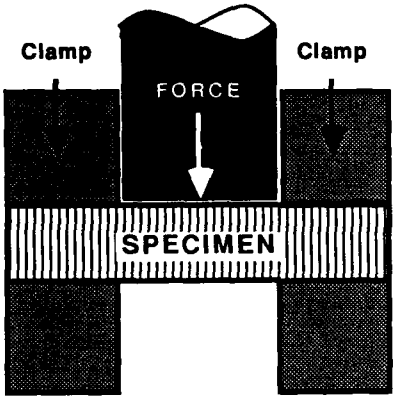


Figure 3 - Portion of the blanking shear test fixture showing specimen with thickness 1.6 mm, punch diameter 3.2 mm, and fiber orientation normal to surface. Shear tests were conducted at a crosshead speed of 0.01 in/min (0.254 mm/min).

MICROSCOPY - Scanning and conventional transmission electron microscopy with energy dispersive x-ray analysis were performed in a Phillips EM 400T analytical electron microscope. Specimens for TEM were prepared by a slow, fine abrasive polishing (dimpling) in preparation for final cold-stage ion-milling at 6 KV and 12° tilt. Scanning electron microscopy was performed in a Phillips 501 SEM.

SHEAR DATA INTERPRETATION - Observation of the fracture surfaces in the SEM revealed corrugated shear surfaces that avoid the fibers. To account for the increase in fracture surface area due to the wavy fracture path, the area of the shear-fracture surface was determined. For a uniform distribution of unidirectional fibers, the fiber spacing λ, is inversely proportional to the square root of the fiber volume fraction.

$$\lambda = K\sqrt{1/V_f} \qquad (1)$$

The constant K is a factor associated with the geometrical pattern of the fibers. For a hexagonal array of fibers of radius r,

$$K_{hex} = \sqrt{\frac{\pi r^2}{\sin(\pi/3)}} \qquad (2)$$

The model for the corrugated shear surface is based on the diagram in Figure 4.

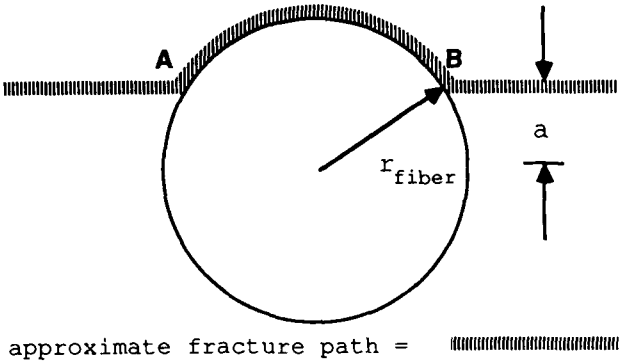


Figure 4 - Increase in path length, arc AB - chord AB, due to interference by a fiber.

It is assumed that the propagating shear crack couples with a fiber at A, and follows its surface until B and then continues through the matrix until it interacts with the next fiber. The random distance between chord AB and the center of the fiber is called a, such that $0 < a < r$. The shear surface area is obtained by averaging an expression for the length of the undulating fracture path and multiplying by the sample thickness t.

The average shear-fracture path length per intersected fiber, δL, is given by averaging the path length over a.

$$\delta L = \frac{\int_0^r \left[2r\cos^{-1}(a/r) - 2\sqrt{r^2 - a^2}\right] \cdot da}{r} + \lambda$$

$$= \frac{r(4-\pi)}{2} + \lambda = 0.43r + \lambda \qquad (3)$$

The true composite shear surface area A_C, is calculated by multiplying δL by the number of intersected fibers and the specimen thickness. For the shape of the blanking specimen, the composite shear surface area is

$$A_c = \delta L \cdot \frac{\pi D}{\lambda} \cdot t \qquad (4)$$

where D is the diameter of the specimen and t is its thickness. The composite shear strength, τ_c, is then assumed to be equal to the maximum force divided by the shear surface area.

$$\tau_c = \frac{F_{max}}{A_c} \qquad (5)$$

Application of this model to composites depends on the fibers being aligned in the shear direction.

RESULTS

MACROSCOPIC PROPERTIES - No evidence of porosity or infiltration failure was detected in specimens prepared for optical metallography or by density measurements.

DISTRIBUTION OF MAGNESIUM - Samples for analysis were taken from several locations within the composite and the unreinforced riser. A lower magnesium content in the riser indicates that solidification initiated at the surface of the upper punch, and magnesium was rejected as the solidifying front advanced toward the preform.

Matrix Mixture (before melting)	(Weight % by DC Plasma Spectrocopy) Composite	Riser
Al-0.96% Mg	0.97	0.51
Al-2.3% Mg	2.27	1.11
Al-3.6% Mg	2.17	1.40
Al-4.82% Mg	4.06	2.04

Table 3 - Average magnesium content of matrix alloy in composite and riser parts of castings.

SHEAR TEST RESULTS - The relationship between shear strength and magnesium content is presented in Figure 5. From the maximum load and thickness of each specimen, shear strengths were calculated by calculating the contribution of fibers to the shear surface areas. These data show that the shear strengths of the composites and matrix alloys are the same for the same composition. The presence of off-axis fibers bridging the shear surface substantially increases the load to failure.

MICROSTRUCTURE AND COMPOSITION OF INTERFACE - Transmission electron microscopy revealed a magnesium-rich reaction product phase at the interface in all specimens examined. An Al-Mg ratio of approximately 1:2 in the reaction product was measured by EDS under convergent beam conditions. Owing to the small grain size of the reaction product, its crystal structure could not be identified by electron diffraction. Qualitative analysis of the EDS spectra indicates, however, that the principle reaction product phase is likely $MgAl_2O_4$.

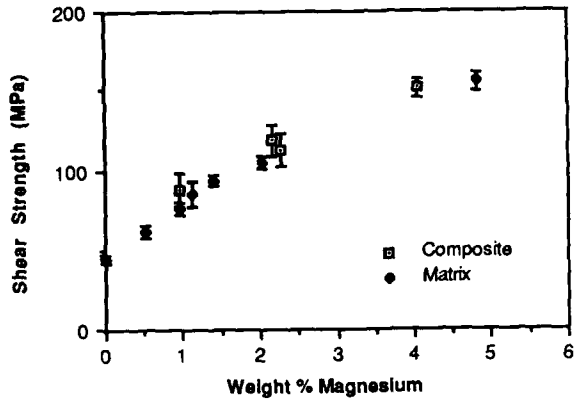


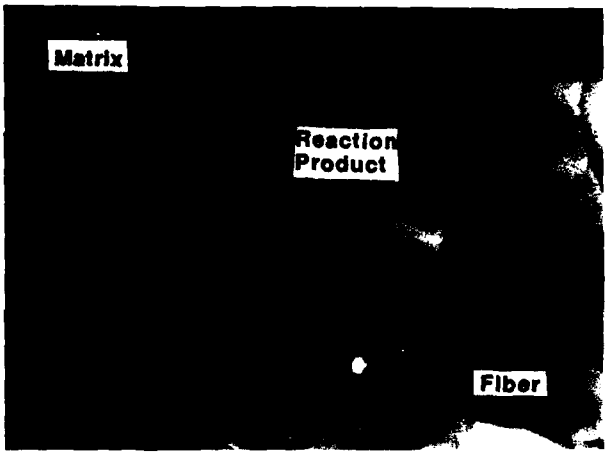
Figure 5 - Shear strength versus magnesium concentration.

This compound at the interface was previously reported (1) for a slurry-cast Al-Mg alloy, α-Al_2O_3 fiber composite.

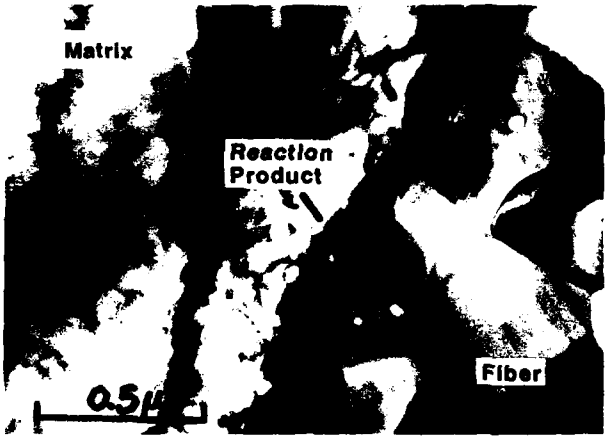
TEM micrographs (Figure 6) illustrate the location and distribution of the reaction product phase for composites with 0.97%, 2.27%, and 4.06% magnesium content in the matrix alloys. Rarely, large (about 1 μm) particles of Mg_2Si were found near the interface. Figure 7 shows a magnesium silicide particle large enough to be identified by electron diffraction and EDS in the 4.06% Mg matrix composite.

EDS elemental mapping indicated that an excess of magnesium was present at the fiber-matrix interface. This was most pronounced for the 4.06% Mg matrix composites and was observed irrespective of the presence of a reaction product in the 0.96% Mg matrix composite.

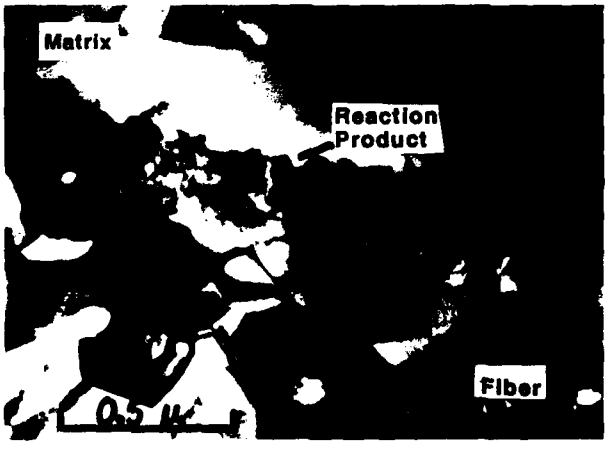
SHEAR-FRACTURE SURFACES - The morphology of the shear-fracture surfaces was dependent on magnesium content. For the 1% Mg composite (Figure 8) the grain structure of exposed fibers and partially debonded matrix fragments are evident on the fracture surface. In the 4.06% Mg matrix composite (Figure 9), however, a thin layer of matrix covers the fibers, and heavily dimpled matrix regions are observed between fibers. The 2.17% Mg and 2.27% Mg specimens exhibited intermediate fracture surface characteristics.



(a)



(b)



(c)

Figure 6 - TEM micrographs showing the reaction product phase formed at the fiber-matrix interface for matrix alloys with (a) 0.96%Mg, (b) 2.27%Mg, and (c) 4.06%Mg.

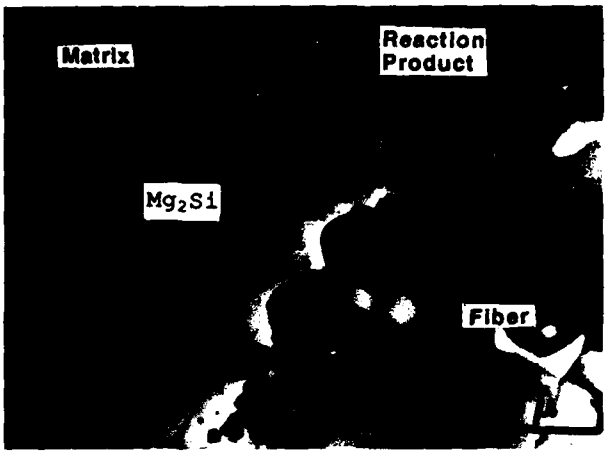


Figure 7 - TEM micrograph showing a particle of Mg_2Si at the interface in the 4.06% Mg matrix composite. Mg_2Si was observed infrequently at the interface in the binary Al-Mg alloy matrix squeeze-cast composites.



Figure 8 - Shear-fracture surface of a 0.96% Mg matrix composite showing matrix debonding and the grain structure of exposed fibers.



Figure 9 - Shear-fracture surface of a 4.06% Mg matrix composite showing a matrix layer covering fibers and dimpled matrix between fibers.

DISCUSSION

When the shear strength of the composite interface is less than that of the matrix alloy, fracture occurs by debonding at the fiber-matrix interface and shear failure of the matrix between fibers. The method used above can be used to determine the interface shear strength, τ_i, since the area fractions of matrix, A_m and interface, A_i, can be calculated. Thus,

$$\tau_i = \frac{\tau_c \cdot A_c - \tau_m \cdot A_m}{A_i} . \quad (6)$$

When the shear strength of the composite is less than the shear strength of the matrix alloy, the interface shear strength can be measured by shear testing. Shear strength measurements have been used by Diwanji (3) to explain interface-dominated mechanical property effects in graphite fiber-reinforced metal-matrix composites in which weak fiber-matrix adhesion is commonly observed.

The composite shear strengths are the same as that of the unreinforced matrix alloys for the composite compositions investigated, indicating that the shear strengths of the interfaces are equal to or greater than those of the respective matrix alloys.

The quantity and distribution of reaction product observed at the fiber-matrix interface changes systematically with increasing magnesium content. In the 0.96% Mg matrix composite, a small number of reaction-product grains formed preferentially at grain boundary junctions of the fiber. The fibers are completely covered with reaction product in the 2.27% Mg matrix composite. In the 4.06% Mg composite the reaction layer is typically thicker, but the grain size of the reaction product appeared to be similar to that of the lower magnesium content composites.

CONCLUSION

Aluminum matrix composites reinforced with unidirectional α-Al_2O_3 fibers were prepared by a low-pressure vacuum squeeze-casting process. The microstructure of the fiber-matrix interface depended strongly on the magnesium content of the matrix alloys. The extent of fiber coverage and the quantity of reaction product phase observed at the fiber-matrix interface increased with increasing magnesium content of the matrix alloy.

The shear strength of the fiber-matrix interface in the composite specimens was greater than or equal to the shear strength of the matrix alloys with equal magnesium content. Observation of the shear-fracture surfaces show a trend toward greater fiber-matrix adhesion with increasing magnesium content.

ACKNOWLEDGEMENTS

The work was supported by the Engineering Research Center for Composites Manufacturing Science and Engineering at the University of Delaware. The authors would like to thank the following corporations for providing materials: Reynolds Metals Company, KB Alloys, Inc., Stackpole-Ultra Carbon, and E.I. Dupont de Nemours, Inc.

REFERENCES

1) Quigley, B.F., Abbaschian, G.J., Wunderlin, R., and Mehrabian, R., "A Method for Fabrication of Aluminum-Alumina Composites", Metallurgical Transactions A, 13A, 93-100, (1982).

2) Metals Handbook, Ninth Edition, Volume 8, Mechanical Testing, ASM, Metals Park, OH, 64-5, (1985).

3) Diwanji, A.P., Structure-Property Characterization in Squeeze-Cast Carbon Fiber Reinforced Metal-matrix Composites, M.S. Thesis, Materials Science Program, University of Delaware (1987).

ULTRASONIC TECHNIQUES IN EVALUATION OF METAL MATRIX PARTICULATE COMPOSITES

P. K. Rohatgi
Materials Department
University of Wisconsin-Milwaukee
Milwaukee, Wisconsin 53201 USA

S. Raman
Indian Institute of Technology
Madras, India

B. S. Majumdar
Battelle Memorial Institute
Columbus, Ohio, USA

A. Banerjee
Materials Science
Institute für Metallforschung
W. Berlin, FRG

ABSTRACT

Gravity and pressure die cast Al alloy-ceramic particle composites containing dispersions of alumina and zircon particles were characterized by using a pulse echo ultrasonic technique. Good agreement was obtained between the experimental and theoretical values of longitudinal ultrasonic velocities and moduli in the case of low (< 1%) porosity composites. By suitably controlling the casting conditions to reduce porosity levels below 1%, these ultrasonic measurements can be used for rapid determination of volume percent particles in a production unit.

1. INTRODUCTION

METAL MATRIX PARTICULATE COMPOSITES form a class of new generation tailor made materials with the capability to suit such diverse combinations of properties as high modulus, strength, hardness, toughness, wear resistance and low thermal expansion coefficients. They consist of a metal matrix in which particulates such as graphite, silica, silicon carbide, alumina, zircon, are dispersed primarily by mechanical means. Particle sizes generally vary from a few microns to about 150 μm, and the particles are introduced either by a powder metallurgy or by a liquid metallurgy route. In the latter case the particles are dispersed by stirring them in the liquid melt.

The present work involves study of the elastic properties of aluminum-based ceramic particulate composites, prepared y a liquid metallurgy technique. Elastic constants have been determined by ultrasonic velocity measurements, as well as by tensile testing, and are compared with theoretical estimates. In an earlier investigation [1] on an Al-Al_2O_3 system, considerable discrepancy was observed between theoretical and experimental values of modulus, and this was attributed to particle and casting porosity, as well as to poor particle-matrix bonding. The present study is an extension of that work, using mainly cast aluminum matrix-zircon particulate composites. It is observed that suitable alloy additions, which impart good particle matrix wettability, and the use of appropriate particle treatment and casting conditions provide improved agreement between theoretical and experimental values of the moduli. This gives confidence to the reasoning that, assuming casting conditions are suitably controlled to reduce the porosity level to below 1%, then ultrasonic measurements could be used as a viable technique in a production unit for rapid determination of volume fraction particulate in various batches of production. In addition, the measurements can also yield rapid data regarding the nonuniformity of particle concentrations in various regions of a casting. Such nonuniformities are indeed problems with composites since particulates are generally added by mechanical means.

The evaluation of composite casting techniques by ultrasonic measurements where porosity levels in castings were higher than 1.5% is the subject matter of another study [2]. It is shown there how by using nondestructive ultrasonic measurements it is possible to determine the nature of a particle matrix interface, as to whether pores are associated with such interfaces. Porosity associated with particles would diminish the strengthening effect of particles, even though by and large particle-matrix wettability may be good, and modulus, strength, and ductility would be reduced to well below theoretical estimates. The same analysis could eventually be extended to composites prepared by powder metallurgy routes.

2. EXPERIMENTAL PROCEDURE

Particulate composites consisting of zircon ($ZrSiO_4$) particles (approximately 100 μm size) in Al-alloy matrices were prepared by a liquid metallurgy route [3,4]. The two alloy compositions were Al-3 Mg and Al-11.8 Si - 3 Mg, where

Mg was introduced for improved bonding (wettability) between particles and matrix. After the normal mixing of zircon particles in the molten aluminum alloys, the composite suspensions were poured in moulds, cast ingots were prepared by one of the following pouring techniques: a) top pouring (TP) of the melt into molds using ladle; b) bottom pouring (BP) where the melt, while being stirred, was poured into a mold through an opening at the bottom of melting crucible; and c) pressure die (PD) casting.

Ultrasonic measurements of longitudinal (V_L) and shear (V_S) velocities were made by pulse-echo and the through-transmission technique at a frequency of 1.25 MHz. Standard transducers were used, and the accuracy of measurements was within $\pm$ 0.05 Km/sec. Since particulate composites can be treated as statistically homogeneous and isotropic [5], the results of ultrasonic measurements of wave velocities were interpreted within the framework of the theory of elasticity of isotropic and continuous media. Young's modulus (E), bulk modulus (K) and shear modulus (G) were thus determined from the ultrasonic velocity data. In some cases the Young's moduli were determined from stress-strain plots generated from regular tensile tests carried out on an Instron testing machine with suitable extensometer.

The microstructure of the composites were observed using optical and scanning electron microscopes. X-ray microprobe analyses were also conducted to determine elemental segregation near particles.

3. RESULTS AND DISCUSSION

Ultrasonic velocities depend not only on particle volume fraction, but also on percent porosity, the ultrasonic attenuation increasing with increasing porosity. The extent of porosity depended on the casting technique employed, as well as on particle pretreatment. In this paper low (< 1.5%) porosity composites have been analyzed. A more complete analysis of both low and high porosity composites has been made elsewhere [2].

3.1 COMPOSITES WITH LOW POROSITY

3.1.1 Pressure-Die-Cast Composites - Composites of system Al - 11.8 Si - 3 Mg - zircon, prepared by a pressure- die-casting technique, had low porosities (< 1%). The elastic moduli were determined from longitudinal (V_L) and shear (V_S) velocities using standard relationships given below:

$$K = \text{Bulk Modulus} = \rho \left(V_L^2 - \frac{4}{3} V_S^2\right) \quad (1)$$

$$E = \text{Young's Modulus} = \rho \left(\frac{3V_S^2 V_L^2 - 4V_S^2}{V_L^2 - V_S^2}\right) \quad (2)$$

$$G = \text{Shear Modulus} = \rho V_S^2 \quad (3)$$

For comparison with theoretical results, the data were compared with upper and lower bounds of moduli, predicted by Hashin and Shtrikman [6] as follows:

$$K_L = K_m + \frac{V_p}{\frac{1}{K_p - K_m} + \frac{V_m}{3K_m + 4G_m}} \quad (4)$$

$$K_U = K_p + \frac{V_m}{\frac{1}{K_m - K_p} + \frac{3V_p}{3K_p + 4G_p}} \quad (5)$$

$$G_L = G_m + \frac{V_p}{\frac{1}{G_p - G_m} + \frac{6(K_m + 2G_m)V_m}{5G_m(3K_m + 4G_m)}} \quad (6)$$

$$G_U = G_p + \frac{V_m}{\frac{1}{G_m - G_p} + \frac{6(K_p + 2G_p)V_p}{5G_p(3K_p + 4G_p)}} \quad (7)$$

$$E = \frac{9KG}{3K + G} \quad (8)$$

Table 1 gives the results for a pressure-die-cast Al - 11.8 Si - 3 Mg - 12.5 vol.% zircon composites. In calculating Hashin-Shtrikman's (H-S) theoretical modulus, the following properties were used for the particle and matrix: K_m = 69.5 GPa, K_p = 156 GPa, G_m = 28.6 GPa, G_p = 89.3 GPa, E_m = 75.5 GPa, E_p = 225 GPa, m = 2.65 gm/c.c., ρ = 4.6 gm/c.c.

It may be observed that the agreement is excellent between the values of the modulus obtained from tensile test measurements and ultrasonic measurements, and that the results fall well within the theoretical bounds predicted by Hashin and Shtrikman [6]. In the case of other pressure-die-cast samples, the agreement was not as good. Though experimental densities indicated porosities below 1%, there was considerable attenuation of shear waves, which made the determination of shear velocities rather inaccurate. Accordingly, emphasis was focussed on the determination of longitudinal velocities, and correlating them with volume fraction particles. The theoretical bounds of longitudinal velocities were calculated using Hashin and Shtrikman's [6] equations.

Figure 1 is a plot of longitudinal velocities (V_L) versus volume percent zircon, for pressure-die-cast Al - 11.8 Si - 3 Mg - zircon composites. In addition to the experimental data, the theoretical lower and upper bounds of longitudinal velocity are also plotted. Here, too, the experimental results fall well within the theoretical bounds. This provides confi-

dence that longitudinal velocity measurements may be sufficient to determine volume fraction particles, especially where shear wave attenuation is high.

Figure 2 is an optical micrograph of an Al - 11.8 Si - 3 Mg - 48 wt% zircon pressure-die-cast composite. The good distribution of particles is clear from the micrograph. Elemental X-ray microprobe analyses [7] indicated an excess concentration of Mg at the periphery of the particles, suggesting that Mg was instrumental in providing good wettability. As already mentioned, density measurements indicated that porosities were limited to below 1%. In spite of these favorable factors, shear waves were greatly attenuated, so that emphasis had to be focussed only on longitudinal velocities.

3.1.2 Composites Prepared by Bottom-Pouring Technique - Composites of system Al - 3 Mg - zircon, prepared by bottom-pouring technique, also had porosities below 1.5%. Optical micrographs [7] have shown particle distribution and embeddability similar to Figure 2 for pressure-die-cast samples. Density measurements verified low porosity levels. In this system, however, the modulus was measured from the linear elastic region of stress-strain curve, obtained from tensile tests. Figure 3 is a plot of Young's modulus E versus volume percent zircon. Also plotted are the H-S theoretical bounds on moduli obtained assuming K_m = 70.4 GPa, K_p = 156 GPa, G_m = 23.97 GPa, and G_p = 89.3 GPa. Within the accuracy of modulus measurements, the experimental data lie close to the bounds of moduli. It is not clear at present why the experimental data exceeded the upper bound values at high volume fraction zircon. It could be due to a change in effective properties of the matrix constrained and solidified between zircon particles.

For comparison, the moduli data for a SiC particle reinforced 6061 Al-alloy [8] composite is shown in Figure 4. These composites were prepared by the powder metallurgy route and were extruded. The theoretical upper and lower bound values were calculated using a Young's modulus of 650 GPa [9] and a shear modulus 273 GPa for SiC particles. The 6061 Al-alloy matrix properties were E_m = 69 GPa and G_m = 26.5 GPa. It may be observed from Figure 5 that the elastic moduli for the powder metallurgically prepared Al-SiC composites fall well within theoretical bounds, similar to the Al-zircon composites prepared by liquid metallurgy route. In other words, provided that porosity levels are held low, the metal matrix particulate composites (containing particles as large as 150 μm) do yield elastic properties, which are bounded by theoretical results for particulate systems.

This has been shown to be due to pore - particle interactions [2] which would reduce the strengthening effect of particles.

4. CONCLUSIONS

By using a pulse-echo type ultrasonic apparatus, it is shown that measurements of longitudinal velocities can be used to advantage for characterization of composites. It is observed that by suitable alloy additions for imparting particle-matrix wettability, and by using appropriate particle treatment and casting conditions, good agreement is obtained between theoretical and experimentally determined ultrasonic velocities and moduli in cast Al-Si-zircon particle composites. The good agreement between theoretical and experimental velocities gives confidence to the reasoning that if casting conditions are suitably controlled to reduce porosity levels below 1%, then ultrasonic measurements could be used as a viable tool for rapid determination of volume percent particles.

REFERENCES

1. Madhava, M. R., S. Raman, P. K. Rohatgi, and M. K. Surappa, Scripta Met. 15, 1191 (1981).
2. Rohatgi, P. K., S. Raman, B. S. Majumdar and A. Banerjee, Materials Science and Engineering (communicated) (1988).
3. Banerjee, A. and P. K. Rohatgi, J. Mat. Sc. 17, 335 (1982).
4. Banerjee, A., M. K. Surappa, and P. K. Rohatgi, Met. Trans. 14B, 273 (1983).
5. R. M. Fulrath and J. A. Pask (Ed), Ceramic Microstructures, p. 313, Robert Krieger Publishing Co., Huntington, N.Y. (1976).
6. Hashin, Z. and S. Shtrikman, J. Mech. Phys. Sol. II, 126 (1973).
7. Banerjee, A., M.E. Thesis, University of Kerala, India (1982).
8. DWA Composite Specialities, Chatsworth, California, USA, Private Communication, (1987).
9. Decker, R. F., Met. Trans. 4, 2495 (1973).
10. Madhava, M. R., S. Raman, P. K. Rohatgi, M. K. Surappa and V. C. Padaki, Acoustic Lett. 4, 41 (1980).
11. Mackenzie, J. K., Proc. Phys. Soc. B 63, 2 (1950).

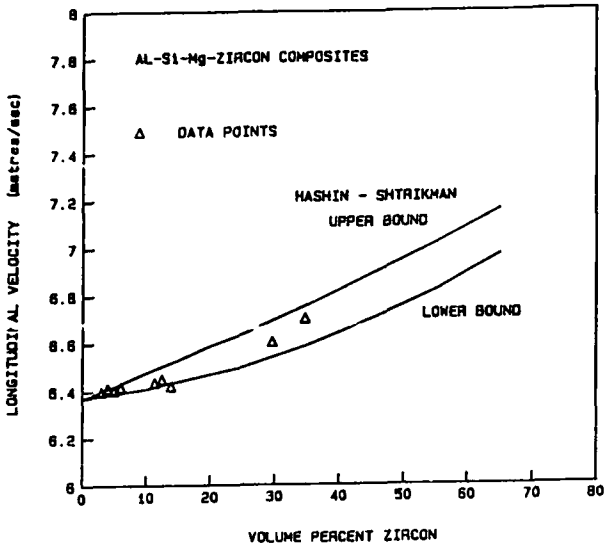


Fig. 1 Longitudinal velocity vs. vol. % zircon for Al-11.8 Si-3 Mg.-zircon composites. The solid lines represent Hashin-Shtrikman's upper and lower bounds.

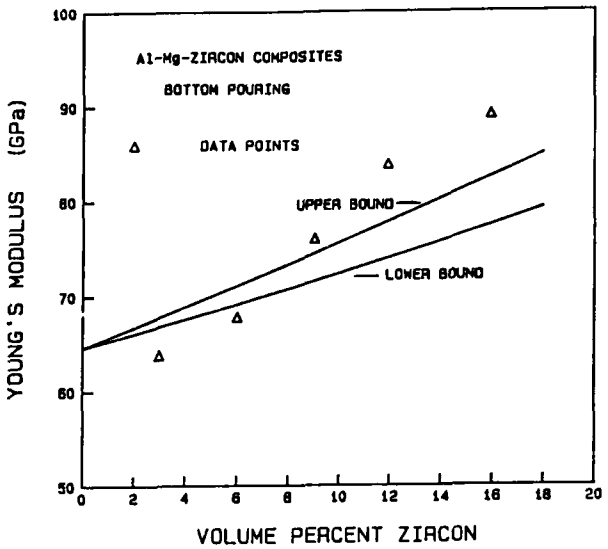


Fig. 2 Young's Modulus vs. vol % zircon for Al-Mg-zircon composites. The solid lines represent Hashin-Shtrikman's upper and lower bounds on Young's Modulus.



Fig. 3 Microstructure of Al-Si-Mg-48% zircon composite showing uniform particle distribution. (X 100)

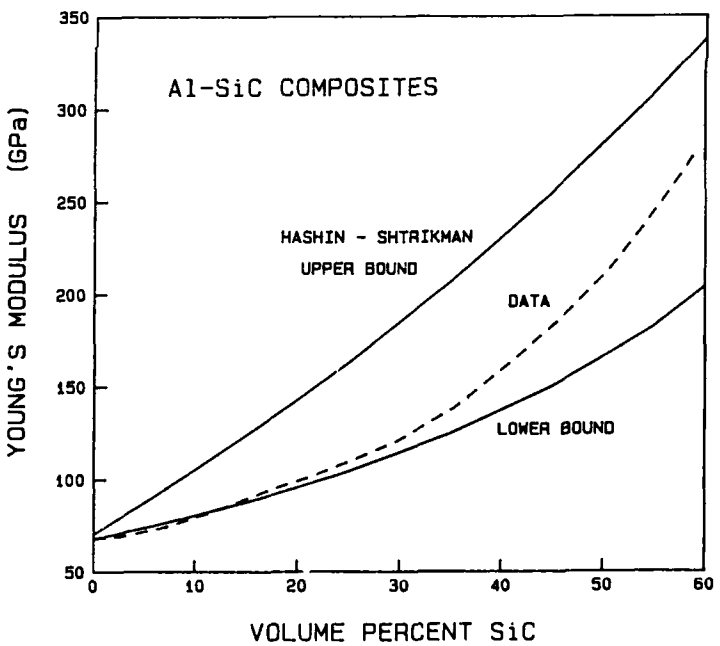


Fig. 4 Young's Modulus vs. vol. % SiC for 6061 Al-SiC composite. Solid lines represent Hashin-Shtrikman's upper and lower bounds.

TABLE I

Modulus Values for an Al-Si-Mg-Zircon Composite.

Composition	Specific Gravity	Experimental Velocities		Experimental Modulus, E, GPa		Hashin-Shtrikman's Modulus, E, GPa	
		V_L Km/sec.	V_S Km/sec.	Ultrasonic	Tensile Test	E_U	E_L
Al-11.8Si - 3Mg + 12.5 vol.% zircon	2.85	6.45	3.4	86	85	88	75

E = Young's Modulus

FRICTION, WEAR AND INTERFACIAL TEMPERATURES IN METAL-GRAPHITE COMPOSITES

Doris Kuhlmann-Wilsdorf, David D. Makel
Department of Materials Science
University of Virginia
Charlottesville, Virginia 22901 USA

Neal A. Sondergaard, David W. Maribo
David Taylor Naval Ship Research and Development Center
Annapolis, Maryland 21402 USA

ABSTRACT

The tribological behavior of silver-graphite (and by implication other metal-graphite) composites is characterized by changing roles of the two constituents from relatively low to high temperatures. An analysis of the wear debris, together with computations of the flash temperatures at the interface, indicates that the decisive parameter is water adsorption on the graphite. If present, it acts like a glue between the basal plane of graphite and the metals, and also it permits extensive plastic shear deformation of graphite on the basal plane whereas without an adsorbed water film, the graphite appears not to deform. The lower-temperature regime, called mode I, has correspondingly a coefficient of friction of about 0.15 to 0.2, the same as for graphite, while in the higher temperature mode II, when water is desorbed from the graphite, the coefficient of friction becomes that of silver. The existence of two major wear modes, namely cutting wear and wedge formation, is documented. In mode I the wedges, or resulting "pads", consist of parallel lamellae of silver and graphite, in mode II they are composed almost only of silver lamellae, probably with some embedded, virtually undeformed graphite particles. Cutting wear is believed to be due to fragments of graphite whose basal plane is steeply inclined to the interface. All of the observations can be explained, or at the least rationalized, by means of a simple model.

INTRODUCTION - Typically, composites are designed for a combination of light weight and mechanical properties, but in some cases, the present included, for lubrication and wear reduction. Best known in this connection are self-lubricating bearing metals which rely on a system of interconnecting pores for supplying liquid lubricants to the interface, and/or incorporate soft inclusions such as lead or graphite. In the latter case, after "running-in", lubrication comes about by the formation of a transfer film based on the softer constituent which serves as a solid lubricant.

Composites find wide application also for contact materials. Evidently, this is a most suitable area for tailor-making composites which combine wear resistance with high electrical conductivity wherein self lubrication for reducing friction heat may or may not be used also. A pertinent survey of composites for electrical contacts was given by D. Stöckel (1) with emphasis on metal/metal composites. Most widespread among the composites used for sliding electrical contacts are, however, metal-graphite composites with varying amounts of metals, typically between 50% and 90%. Copper-graphite with an optional minority addition of other metals is inexpensive and gives excellent results, while silver-graphite is the best in terms of very low achievable bulk and contact resistance but is, of course, more expensive.

The most basic experimental research as well as relevant theoretical interpretation is available for the silver-graphite system with a particular focus on 70w/o silver. This is about the optimal, technologically most widely used composition. In connection with the present paper, the most impor-

tant previous publications on silver-graphite include those by Johnson and coworkers (2-4) and from the University of Virginia (5-9).

In terms of tribological properties of the composite, which result from the interplay of the properties of the components, scientific interest focuses on two peculiar aspects. Firstly, and quite generally, effective graphite lubrication requires moisture to be present in the ambient atmosphere at temperatures low enough that water is not desorbed (see for example refs. 10 and 11). Secondly, it is known for silver-graphite composites and is presumed to apply generally to metal-graphite composites of similar structure, that friction and wear shows two regimes dubbed mode I and mode II, which depend on the existence of two different transfer films. Mode I operates at low temperatures and exihibits low friction and wear, and mode II operates at a higher temperature with higher friction and wear.

It had been surmised from the very beginning (7), and will be further substantiated in this paper, that the two above effects are related, in that mode I operates in the presence of adsorbed water films, and mode II sets in once these are desorbed from the graphite. It follows that the decisive parameter determining whether mode I or mode II operates, i.e. which of the two transfer films form, depends on the local temperature at the contact spots, i.e. on the flash temperature. The concern of the present paper will be the changing roles of the silver and graphite in the transition from mode I to mode II and vice-versa, and the role that water vapor plays therein.

METHODS OF INVESTIGATION AND EARLIER RESULTS - In both mode I and mode II the transfer film is not continuous but is present in the form of islands on the substrate on which the metal-graphite composites slide (2-4). In all of the previous investigations this substrate has been polished copper or a Cu rich alloy, as will generally be the case also in practical applications. The surface of the silver-graphite composites, during sliding, becomes relatively enriched in silver, the more so the higher the interfacial temperature, and the graphite is relatively recessed.

The micro-geometry thus insures that the load-bearing contact spots are predominantly of silver on the composite side, and that on the substrate side they are "pads" of transfer film. Correspondingly, the size of the contact spots is more or less equal to the size of the transfer film pads, and similarly it is at least extremely likely that many wear flakes which may be collected are such pads, unless broken while being detached and/or on their way out between the gap. Thus the size and structure of unbroken wear chips are considered to reflect the size and structure of the pads. Hence the otherwise inaccessible interface during sliding can be revealed through the careful examination of the wear chips, wherein always the largest and seemingly least "mangled" will be determining.

An additional tool for the study of the tribological behavior of those composites is the determination of the local temperature at the contact spots, i.e. the flash temperatures. No experimental means are available for doing so. However, the flash temperature in excess of the ambient temperature (ΔT_f) can be computed with some degree of confidence, using an adaptation of the Blok-Jaeger theory of ΔT_f (12) as applied and defined for typical wear cases (13,14).

A requisite input parameter for these computations is the normally unknown number of contact spots (N). Deducing the average radius, $\underline{a}$, of the contact spots from the average wear chip size, and calculating the total contact spot area (A), from $A = P/H$ with P the normal force between the two sides and H the impression hardness of the softer side (in this case the silver-graphite composite), permits to assess N as $N \simeq A/\pi a^2$. This has been done in a recent investigation (15), with the result that the earlier estimate of typically $N \simeq 10$ contact spots for silver-graphite sliding on copper has been vindicated. Albeit, it is well possible that the number is as low as 5 or as high as 20 or even 40.(14,15)

The number of contact spots is reduced through thermal mounding (compare refs. 16 and 17, for example) whereby statistically large contact spots bear a correspondingly larger share of the load and similarly conduct a larger share of the current than smaller ones. Therefore, the heating rate of them is larger and they bulge out more strongly through thermal expansion, thus tending to grow still further in size and to crowd out smaller contact spots. In the extreme case this can lead to just one or a

very few contact spots, but for the present case of silver-graphite sliding on copper at speeds below 40 m/sec, the natural surface roughness maintains the contact spot number at a somewhat higher level.

Two sets of correlated experiments have been made recently (14,15) in which the same silver-graphite composites have been slid against the same copper substrate under conditions meant to deliberately impose a range of different flash temperatures but in a manner either to stimulate or to suppress thermal mounding. This was done through "oven experiments" in which 0.5 cm^2 samples were slid at v = 0.36 m/sec. under P = 9.7 N normal force without current flow at controlled "ambient" (oven) temperatures up to 225°C, and in "current change" experiments at v = 7.2 m/sec. P = 4.9 N and currents I up to 220 A in the open atmosphere.

Some aspects of these experiments have already been published (15). They have greatly strengthened confidence in the computations of ΔT_f. In particular, a minimum of wear chip size was found in the oven experiments at about 160°C to 180°C which is the range of transfer film temperatures that had previously been found for the transition between mode I and mode II (5-7), and this in turn agreed well with the correlated flash temperature computations (15). Moreover, the simultaneously calculated contact spot sizes and electrical contact resistances also harmonized with the measurements in ref. 15, as well as with the early determinations by Dillich (5-7).

From the experimental work by Dillich (5-7) and from additional tests ranging up to extremely high current densities (8,9) it had been concluded that the interfacial transfer film in mode I consists of stacked thin layers of graphite and silver oriented parallel to the interface, and that the transfer film in mode II consists of silver, perhaps containing graphite inclusions but no continuous graphite layers on which sliding could take place. This model explains why in mode I the coefficient of friction of $0.15 \leq \mu \leq 0.2$ is much as expected for ordinary graphite lubrication, while the electrical resistance is found several times higher than would be expected for pure silver films or pads. For mode II by contrast, $\mu \simeq 0.35$ is indeed much as would be expected for sliding in pure silver (18), and the electrical film resistance is very small. In fact, it probably is undiscoverable, and the remaining film resistivity of about $\sigma_f = 10^{-12}$ Ωm^2 may be due to an interposed monomolecular layer of adsorbed gas between the film/pads and the copper and/or the silver-graphite composites. The adsorbed gas may be oxygen or water vapor.

TYPES OF WEAR PARTICLES - Recent studies on the wear particles have been performed by means of scanning electron microscopy (SEM). The results obtained are consistent with the above model of the two types of transfer films. It now seems highly reasonable to believe that at least many of the pads are formed through the "wedge" mechanism previously studied by Cox (19,20) and Antler (21). In this mechanism a lamellar wear particle is partly formed and slides up and over the surface of the softer side, but before it is completely detached, a new wear lamella has started to form, and on to the next and next, until finally one particle is completely detached and the whole stack adheres to the (locally) harder side. Figure 1 models the mechanism of the wedge formation wherein the locally harder side is at the top. From Fig. 1a to 1d the harder side is moving progressively to the right while the softer side at the bottom is considered to be stationary. This is indicated by the movement of the point P, stationary relative to the upper side, and the fixed position of the point Q on the lower side.

All of the plastic deformation is taking place on the lower side, principally by slip on the first glide system, the direction of the slip plane being indicated by the long arrow. The shearing is supplemented, here and there, by slip also on the secondary system, the shorter arrow indicating its glide direction. Positions in which plastic deformation is presumed to be particularly strong are indicated by the corresponding hatching and the letter S.

Note then in Fig. 1a at point P, where the asperity on the upper side impinges on the softer side at point Q, that the softer side flattens against it over a small area. Through the resulting frictional force, this flattened piece is formed into a lamella while being pushed to the right. The requisite plastic deformation is mediated principally by translation on the first

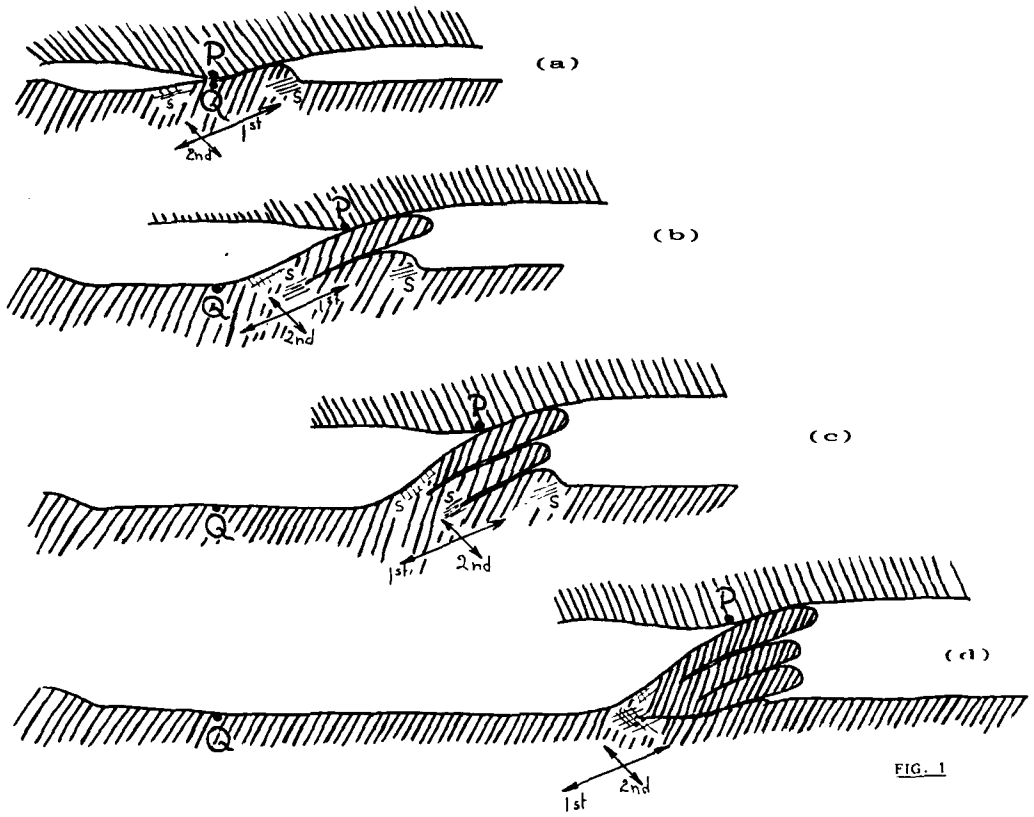


FIG. 1

Fig.1 - Model for the generation of "pads" commonly found on the harder substrate, shown on top, by the wedge mechanism according to Cocks (19, 20) and Antler (21). Stacks of lamellae of softer material, at bottom. are formed through the action of an asperity on the narder side. The two arrows indicate the glide plane orientations of the first and second slip system. Regions in which intense shearing takes place shown by hatching.

slip system in the zone marked S to the right of Q, and by double slip (which is necessary to stretch out the material at the trailing edge) again marked with S on the left side of Q. The resulting tongue or lamella of material, is indicated in Fig. 1b. As this lamella pushes on further to the right it rides up on the lower side and exerts increasing frictional force on it. This causes a new bulge to form on the soft side as indicated in Fig. 1b and the process outlined in Fig. 1a is now repeated on that new bulge. As a result in Fig. 1c an additional lamella has formed and by frictional force due to it, a third bulge arises which is seen to be completed in Fig. 1d.

In the drawings of Fig. 1 it is somewhat arbitrarily assumed that the leading edges of the lamella line up such that a vertical wall is formed by their envelope. This is not at all necessary, though. It is well possible that the leading edges of successive lamellae are increasingly falling behind the front edge of the first lamella, or that conversely the bulges form further and further ahead of the leading edge of the top lamella.

In a recent investigation (22) on copper sliding on copper, cases have been observed which exhibit two lamellae, i.e. corresponding to Fig. 1c, in which, however, the second lamella was formed well ahead of the first, i.e. in our figure well to the right of the top lamella. That same advanced generation of new lamellae was also the case in the examples shown by Cox (19,20), where very many lamellae were formed. It does not seem that in the present case of silver-graphite sliding on copper, there is ever a large number of successive lamellae. The process ceases when, as indicated in Fig. 1 d, one of the lamallae finally shears off completely due to the tensile stress

exerted on the trailing edge, indicated by the cross hatching. Also, by geometrical undulations in the two surfaces the two sides can simply part and the process not come to completion in one continuous motion, which is indeed the most probable case. At any rate, if the wear particle, once detached from the softer side, does not fall free immediately, it will commonly remain attached to the harder side, in our case the upper side, until it is dislodged by some subsequent encounter.

Due to temperature fluctuations as well as local fluctuations in composition, it is not a foregone conclusion which of the two sides is the harder. In our investigations commonly copper will serve the function of the harder side, and correspondingly it will be worn more slowly than the silver-graphite composite. Yet, a certain amount of wear by the wedge mechanism may be expected also there, and corresponding wear particles are indeed occasionally observed.

The appearance of some of the best preserved wear particles in both modes is compatible with the wedge mechanism of Fig.1. Figure 2 shows an example from an oven experiment at 175°C,i.e. mode II. As may be seen from a comparison between Figs. 2 and 3, the latter a copper particle formed in a current



Fig.2 - Scanning electron micrograph (SEM) of a wear particle of 95w/o Ag-C from an oven experiment at 175°C, presumed to be formed by the wedge mechanism, in mode II.



Fig.3 - SEM of a particle presumed to be formed by the wedge mechanism in mode I. (Current-change experiment with I = 40Amp, 70w/o Ag-C). Interestingly, this is a copper particle, but it is indistinguishable from silver wedge-particles.



Fig.4 - Particle of consolidated silver fragments from a 95w/o Ag-C sample in a 175°C oven experiment.



Fig.5 - Wear debris from a 70w/o Ag-C sample from a 225°C oven experiment. Note the two largest fragments are believed to have been cut from from the copper surface.

change experiment with I=40 Amp, the particles are not obviously morphologically, different between mode I and mode II, and whether they are of silver or copper. Even so, details on how the interleaving of silver and graphite may occur in mode I are still obscure. We shall return to these below, as well as to the problem of why such interleaving does not take place in mode II, or at the least is so much reduced, such that the stacks in mode II are substantially pure silver.

Two additional types of wear particle have been observed in both stages, namely lumps of consolidated silver. (Fig. 4) and particles which seem to have resulted from cutting wear as in Fig. 5. The occurence of consolidated particles is not surprising. Evidently fragments of silver, down to the smallest sizes are broken off from bigger particles in large numbers, as may be seen from Fig. 6 showing a sampling of many particles formed in mode II. These will tend to weld together as they collide with each other in the interface before making their way out of the gap between the two sides.

More problematical is the occurence of wear chips indicating a cutting mechanism, as in Fig. 5, especially since one may find these both of silver and of copper. It is, of course, possible that, depending on local variations of hardness, either of the two metals may on occasion cut the opposite side. However at this point it appears much more likely that graphite particles with their basal planes oriented steeply against the interfaces are the agents which cut. Such cutting action of tilted graphite does not appear to depend on the presence or absence of moisture. This is to be expected since glide on any but the basal plane is virtually impossible in graphite, i.e. tilted graphite flakes must abrade the surfaces. Thus, one may tentatively conclude that graphite particles which are wedged into some depressions on either side, with their basal plane at a steep angle to the interface, exert cutting action and are responsible for the generation of this type of chips.

DISTRIBUTION OF GRAPHITE IN THE WEAR DEBRIS - in ordinary (i.e. secondary electron emission, or SEI) scanning electron microscopy, the contrast of metal and graphite particles is much the same so that they can hardly be distinguished. Further, as has already been noted by Schreurs, Johnson and McNab (3), the wear particles have an extraordinarily high metal content, much above the relative volume fraction of graphite in the original silver-graphite composite (wherein it is not yet clear where the missing graphite went, except that some may oxidize). Moreover, the atomic number of carbon falls below the capability of the EDX system wherewith chemical analysis is otherwise routine in scanning electron microscopy. It therefore became necessary to employ also the BEI, or back-scattered electron mode, in which carbon yields a very low intensity, to identify graphite in the wear debris.

Similarly, it is very desirable, in fact probably necessary for the reliable interpretation of micrographs, to obtain a three dimensional imaging. For this reason, taking matched pairs of stereo micrographs, one in the SEI mode the other in the BEI mode, was adopted as standard procedure. With graphite and metal virtually indistinguishable in the SEI mode, and with graphite dark or disappearing against the background of the typical graphite stub in the BEI mode, the spatial distribution of graphite can thus be easily recognized.

Even so, the investigation of wear debris samples in the manner outlined, beginning with their collection in the oven and current change experiments, to their transport, to preparing the SEM carbon stubs, and to searching for "representative" wear chips, is fraught with difficulties. At each stage there is a great possibility, indeed probability, of sampling errors. These by themselves could well account for the relative paucity of graphite. Certainly the lightest particles have the greatest possibility of being wafted away in air currents or of adhering to the surfaces of scoops and bags so that they may never make it to the SEM stubs. Also, the identification of "typical" wear chips is a highly idiosynchratic process wherein expectation must doubtless play a role.

The principle adopted in order to reduce the arbitrariness of the last step somewhat, was to assume that always the largest particles, showing the least fractures, are the most pertinent. This is so because the pads, which, in regard to the role of graphite lubrication, are the focus of our attention, are relatively large, namely on the order of tens of microns, and they quite routinely will fracture on the way out from between the two sides,

as already pointed out. Further fracture takes place during bagging, and again during removal of samples from bags onto the stubs. Indeed, unbroken, undamaged wear chips were never seen, while incipient fractures were most plentiful, as also were evident edges at which fractures have taken place. Such will be readily recognized in all micrographs shown.

In light of the above, features which could not possibly be due to random damage, and which thus must have formed at the contact spots, are highly pertinent. This is true in particular of very thin slivers of metal and graphite, whether bonded together or single. Therefore their appearance and relative frequency was taken to be an indicator of the "typical" condition of the interface during wear. Even so, remember that there must of necessity be a very wide range of conditions among the contact spots within any one experiment. The "average" contact spot, after all, is a mathematically definable but practically very elusive entity, with one half of the contact spots larger and hotter than the "average" and one half of the contact spots smaller and cooler. Thus, within some transition range of currents as well as oven experiments one must expect to see typical mode II pad remnants also in mode I conditions and vice-verse. In fact interesting instabilities exist, leading to cycling between mode I and mode II, that have been previously described (5,7).

As to the evidence, very thin slivers of metal,- mostly silver but also of copper-, are found in both modes, except that in mode II these appear on average to be smoother and thinner than in mode I . Next, thin slivers of graphite are relatively frequent in mode I but practically absent in mode II. They are difficult to see due to low contrast and their intimate association with silver. This is demonstrated by Fig. 7 showing a part of what may be a badly damaged wedge particle of mode I. From it projects to the left a very thin piece of graphite which in fact appears to consist of layers. In mode II, by contrast, we see chunks of separate graphite but almost never in mode I. Very thin slivers of metal, mostly silver but also of copper, are found in both modes, except that in mode II these appear on average to be smoother and thinner than in mode I.

DISCUSSION

MODEL FOR CUTTING WEAR - Figure 9a is a somewhat idealized cross section through a piece of the silver graphite composite before sliding, beginning with an undistorted polished surface. Once asperities of the copper slide along the surface of the composite, sideways plastic deformation can take place on the silver surface, and as a result silver will be smeared out somewhat over the adjoining graphite particles, as indicated in Fig. 9b. Only rarely and coincidentally, however, will the graphite be oriented with its basal plane closely parallel to the interface, so that it can translate sideways in response to the passage of copper asperities. Instead, almost universally graphite pieces will break out because the basal plane is not oriented suitably.

The graphite chunks which are visible in Figs. 6 and 8 are believed to have been broken out in the manner indicated in Fig. 9b. Their future fate will be discussed in the next section. Occasionally there will be fragments such as the middle one under the letter C, which although broken loose remain wedged in the surface. Such particles will be very hard relative to sideways deformation since their only possible glide plane remains almost unstressed. If stubby enough, such particles will thus cut out pieces of copper as it slides past, and this is the mechanism believed to be responsible for the type of wear debris shown in Fig. 5.

Occasionally, we must expect that little pieces of graphite with their basal planes similarly inclined against the interface will become embedded, also, in the copper, resulting in the corresponding cutting action on the silver. The left cutting-type particle in Fig. 5 in fact is preponderantly of silver, while the right one is of copper. Yet that silver-rich particle is probably not due to cutting by a graphite piece embedded in the copper surface. Rather, as first shown by Schreurs, Johnson and McNab (3), the pads which form on the copper through the wedge mechanism can be quite firmly bonded, either through cold welding or perhaps diffusionally. The mixed silver-graphite composition of the discussed particle therefore suggests that it originated on the copper where a pad had just become dislodged. In fact, it appears that the majority of the cut-



Fig.6a - An assembly of wear particles of 70w/o Ag-C from an oven experiment at 225°C, i.e. mode II, in SEI illumination.

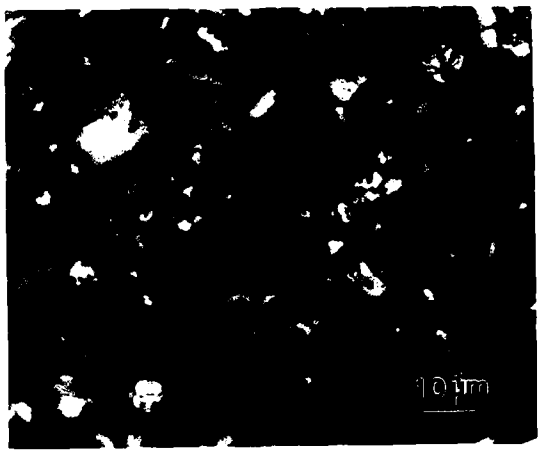


Fig.6b - As Fig.6a but in BEI illumination in which graphite is (almost) invisible. Comparison with Fig.6a will reveal graphite chunks.

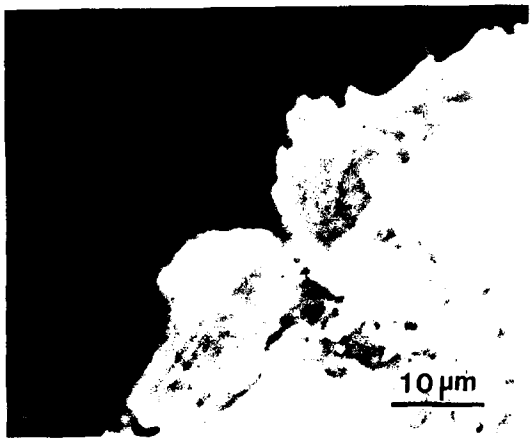


Fig.7a - Part of a mode I particle showing a very thin film projecting at the top left, as seen in SEI.

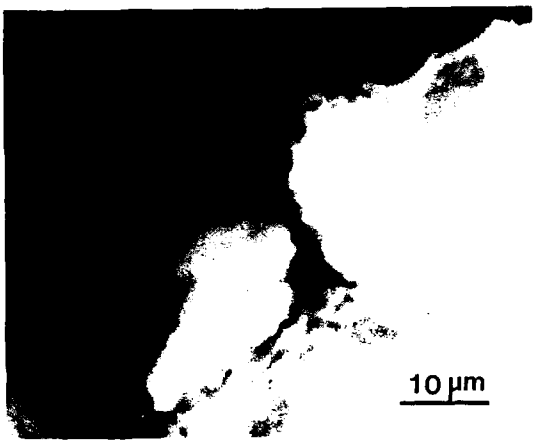


Fig.7b - As Fig.7a, but in BEI. The lamellar projection at top right is now invisible, i.e. it is graphite.

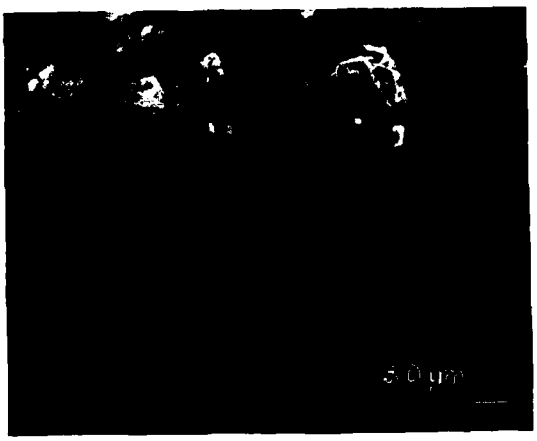


Fig.8a - Mode II wear debris from a 70w/o Ag-C sample after a 225°C oven experiment in SEI.



Fig.8b - As Fig.8a but in BEI. Comparison reveals that the large particle at center field is a chunk of graphite with almost no adhesion to silver.

ting type debris is of copper and that therefore wedging of graphite fragments as indicated in Fig. 9b gives rise to the considerable majority of cutting incidences, accounting for the bulk of wear on the copper but making little contribution to the wear of the silver-graphite composite.

The sequence shown in Fig. 9a - c explains why in the worn silver-graphite composite surface, graphite is found to be recessed and why the silver fraction is larger than in the virgin material. However, as will be discussed presently, especially in the presence of water vapor the majority of the broken out graphite particles will not become wedged but will be redeposited on the surface of the composite and there smear out into thin flakes which cover the silver as indicated in Fig. 9c. Such thin graphite layers will be difficult to observe, but through subsequent wear, these flakes will be incorporated among the wear debris.

THE EFFECT OF ADSORBED WATER ON STRENGTH AND ADHESION - In mode I, thin lamellae or "slivers", of metal and graphite joined together are relatively prevalent. This means, firstly, that there must be adhesive forces between the metal and graphite. Secondly, it means that extensive shear deformation has taken place. Namely, in silver as well as in copper the close-packed (111) planes are the by far preferred glide planes, and in graphite the close-packed basal plane is the only glide plane, as has already been discussed. Now, extensive single glide transforms initially more or less equiaxed fragments into lamellae parallel to the glide plane. Hence, with high probability the great majority of any lamellae in the wear debris must have been generated through extensive plastic shearing, such shearing must have taken place at the contact spots, and the lamellae must expose the close-packed planes.

As already discussed, in mode II there are graphite chunks but no lamellae, indicating that graphite remains undeformable in mode II, whereas silver lamellae are found in both modes and apparently thinner and smoother in mode II than in mode II, as would be in line with the increasing deformability of silver with rising temperature. This state of affairs is doubly surprising because the overall geometry of the sliding, of the wear pads, and of the cutting, is so similar in both modes.

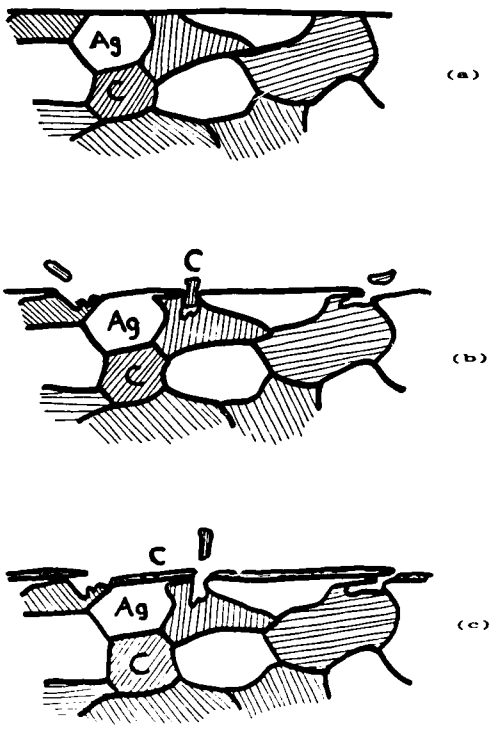


Fig.9 - Model of the major changes at the metal-graphite composite surface away from a contact spot. (a) shows the initial condition. In (b) some chunks of graphite have broken off and metal is smeared over the graphite. One piece at C remained wedged in the surface and will cut the opposite side. In (c) graphite pieces have smeared out over the surface and the last piece has become free.

The normal stresses between graphite and silver at the contact spots must have been of similar magnitude in mode II as in mode I. Even so, they evidently caused extensive graphite shear deformation in mode I but not in mode II.

The picture which thus emerges is of graphite accommodating the bulk of the translation between the two sides in mode I, silver taking over completely in mode II. We may rationalize this state of affairs on the basis of specific surface energy: Since, as already indicated, extensive shear deformation generates large amounts of new surface area parallel to the operating slip plane, the ease of sliding must depend on the specific surface energy of the crystallographic plane of sliding. Therefore, if the adsorption

of water on the basal plane of graphite greatly lowers its specific surface energy, then the critical resolved shear stress for basal glide will be correspondingly lowered, - evidently below that for either of the two metals, while without adsorbed water it is significantly higher.

The general appearance of wear debris in mode II is as if there are only very small adhesive forces acting i.e. colloquially the metal and graphite debris pieces in mode II appear to ignore each other (compare Fig. 8, for example). The thereby demonstrated origin of the adhesive forces between metal and graphite, and more specifically between the basal plane of graphite and the metals, as due to an adsorbed water film, is also easily understood if it is assumed that the adsorbed water layer is electrically dipolar. In that case image forces of the charged outer surface of the adsorbed moisture layer would cause a corresponding bonding to any metal. Thus the adsorbed water layer would form a kind of glue between the basal plane of graphite and metals.

MODEL FOR WEDGE FORMATION WITH GRAPHITE - Figure 10 depicts a possible model of the modification of the wedge mechanism of Fig. 1 through graphite. In Fig. 10a a graphite fragment lodges between two lamellae. In the case of mode II, Fig. 10b would apply, i.e. the graphite chunk would not deform and thus simply be incorporated in the pad without otherwise influencing the process to any great extent. In mode I, by contrast, the strong adsorptive forces between the basal plane of the graphite and the metal, together with its now lower hardness than that of silver, would cause the graphite to shear on the basal plane, flatten out, and thus provide a slippery layer which inhibits the beginning of a new lamella. As the graphite shears, the lamella ruptures at the substrate, and further translation occurs through sliding in the graphite layer as indicated in Fig. 10c. With continuing translation, the graphite layer will become thinner and thinner until finally it is no longer able to serve as a lubricant. Now a new lamella may start and the process be repeated.

DEPENDENCE OF WEAR RATE ON GRAPHITE CONCENTRATION AND TEMPERATURE - As long as graphite is present to lubricate in the manner indicated in Fig. 10c, no further wear of metal will take place. This, then, accounts for the greatly reduced wear rate in mode I as compared to mode II or, correspondingly by comparison with Fig.1, the greatly reduced wear rate in a silver graphite composite as compared to pure silver.

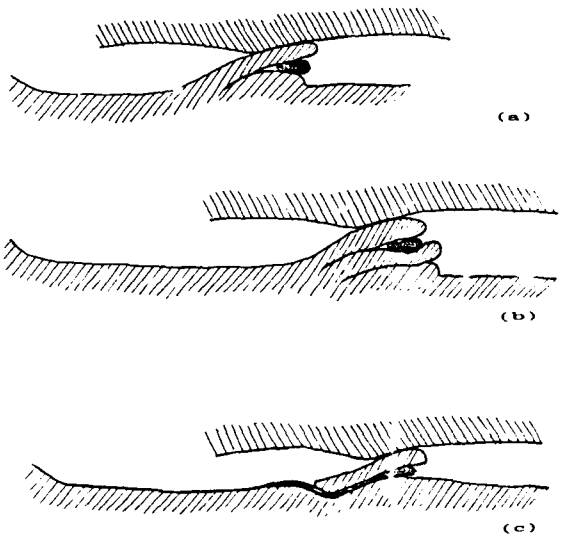


Fig.10 - Model of the modification which graphite causes in the wedge mechanism of Fig.1. In (a) a chunk of graphite has lodged between a lamealla and the softer surface. In mode II (b) that chunk will not deform and be incorporated in the pad. In mode I (c) the critical resolved shear strength of graphite is less than that of the metal so that it will deform and thus serve as a lubricant.

The incidences of graphite particles lodging between lamellae will necessarily depend on the relative concentration of graphite to silver. Thus at high graphite concentration there may on average be one or more graphite particles between any two silver lamellae. As a result, the pads will contain on average a very few and perhaps only one or two silver lamellae. At low graphite concentration, by contrast, graphite may not be present among all adjacent silver lamellae and the pads will grow thicker. Thus the steeply rising wear rate with decreasing graphite content is easily explained.

An additional contribution to wear reduction through moisture will be made by the thin layer of graphite presumed to overlay silver in mode I in accordance with Fig. 9c. In fact, much of the relative sliding probably is accommodated by such layers, and wedge formation is a statistically comparatively rare process which occurs when the glide plane in the metal is slightly tilted against the interface in the manner indicated in Fig. 1.

Finally, wear in mode II will be further increased relative to mode I because of the described cutting action of chunks of graphite wedged in the surface as in Fig. 9b, since in the presence of adsorbed water the chunks will have a strong tendency to lie flat on the interface.

FLASH TEMPERATURE CALCULATIONS - Computed flash temperatures are consonant with the model and the previously deduced values of film resistivity and contact spot numbers. Figure 11 shows

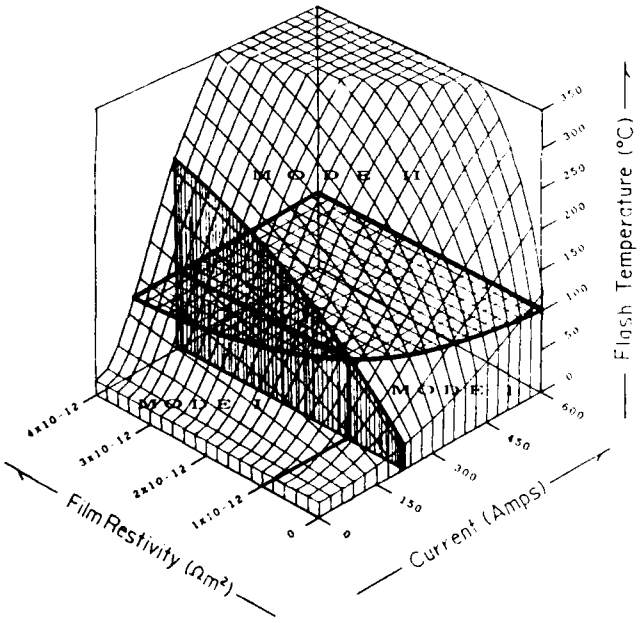


Fig.11 - Flash temperature calculation for 70w/o Ag-C sliding on copper in accordance with ref.14, assuming N = 10 contact spots and the conditions of the current-change experiments. Given that mode II begins at 160°C and the rotor has a temperature of 60°C, the reigmes of mode I and II would be as indicated. At a current of 220A, which was the highest used, and with $\sigma_f = 10^{-11} \Omega m^2$, this would just be on the borderline, as it appears to be.

the expected regimes of modes I and II assuming N=10 contact spots and, as repeatedly indicated, that the local temperature of water vapor desorption is about 160-180°C. A range of film resistivities is considered. In the current change experiments, the test at I=220A indicated that the transition between mode I and II was not quite attained. The computation of Fig. 11 thus suggests that the film resistivity was $\sigma_F \simeq 1 \times 10^{-11}$ ΩM², which is a reasonable value (3-7). As flash temperatures scale more or less like $1/\sqrt{N}$, one would find $\sigma_F \simeq 1.5 \times 10^{-11}$ ΩM² for N=20, - near the average of previously estimated σ_F values in mode II.

RELATING THE MODEL TO THE PREVIOUS LITERATURE - The proposed model for cutting wear and of the role of water vapor in the friction and wear behavior of metal-graphite composites is closely related to prior literature. In fact, according to Savage (10) already Holm (23) proposed that water layers adsorbed on the graphite basal plane may be "acting as a glue", and also that graphite fragments with their basal plane tilted against the interface cause cutting wear. This cutting wear, he thus concluded, was inhibited by adsorbed moisture films in which the fragments would lie flat against the interface, - just as suggested above.

Previously unobserved and unsuspected appears to be the mechanism of Fig. 10c, or indeed the formation of very thin graphite lamellae on account of extensive basal glide in the presence of adsorbed water.

The proposed gluing action through adsorbed water films depends on these being rather thicker than one molecular layer so that the electrostatic image forces from top and bottom do not largely cancel. The existence of such a "thick" adsorbed water film on metals is indicated by recent studies using atomic force microscopy (AFM) (24) and scanning tunneling microscopy (STM) (25,26). In one particular study (26), tunneling current measurements were taken of a tungsten tip approaching and contacting a cleaved basal plane of graphite. In laboratory air these measurements show a tip-surface interaction distance of approximately 11nm, but in a high vacuum (1×10^{-10} mm Hg) this distance is reduced to about 5nm. Baking out the graphite at 1000° C for 1 hour further reduces it to approximately 0.5 nm, with a final reduction to about 0.1 nm being achieved by field

emission cleaning of the tungsten tip in the high vacuum. The pertinent conclusion is that in laboratory air, in mode I, there is a film of adsorbed water on graphite which is several or even many molecular layers thick.

Some indirect support for the contention that the adsorbed water layers are ordered so as to exhibit electrostatic dipolarity may be derived from a study by Buckley and Johnson (27). They proposed that the adhesion of graphite to metals in air is caused by a metal-oxygen-carbon linkage. This agrees with the earlier chemical analysis of graphite rubbed on copper films by van Brunt (28), as reported by Savage (10), in which microchemical methods were used to determine that the surface of copper sliding on graphite consists of copper, oxygen and carbon, with the carbon forming the outer exposed surface of the thin layer. When compared to a more recent Auger investigation of the adsorbed layers formed on copper (3), this closely resembles the surface configuration of oxygen and hydrogen on a copper substrate proposed by Schreurs, Johnson and McNab (3) but with the addition of an outer layer of carbon.

As to the breakdown of the lubricating properties of graphite in air with increasing temperature (and similarly with reduced atmospheric pressure, as in high-flying air craft) this has been known for a long time. New, however, appears to be the concept that adhesion between graphite and metal, mediated by adsorbed water films, is essential for graphite lubrication.

CONCLUSIONS - In silver-graphite composites sliding on copper (and by implication in other similar metal graphite composites sliding on a harder substrate) the primary wear events are (i) cutting by graphite particles whose basal plane is steeply inclined against the interface and (ii) successive wear lamella formation by the wedge mechanism.

Depending on whether or not water is adsorbed on the graphite, two wear modes arise, called mode I and mode II. Below about 160° to 180° C, in mode I, there exists a relatively thick ordered water layer on the graphite which has two effects. Firstly, it permits extensive plastic shear on the basal plane of graphite so as to transform initially more or less equiaxed particles into thin lamellae exposing the basal plane. Presumably this occurs because the adsorbed moisture layer drastically lowers the free surface energy of the basal plane. Secondly, the layer has the effect of "gluing" together graphite and metal, especially the close-packed planes exposed on graphite and metal lamellae that are formed through extended glide. That gluing action is presumed to arise through electrostatic image forces due to the surface charge on the outer surface of the adsorbed water film.

As a result of these two effects, in the presence of adsorbed water wear rates are reduced by two mechanisms. Firstly, many of the graphite pieces which otherwise would cause abrasive (cutting) wear lie flat. Secondly, sliding in the wedge mechanism is predominantly accommodated in graphite instead of the metal.

In mode II the temperature is, at least locally at the contact spots, so high that the water film is desorbed. This causes the critical resolved shear stress of graphite to rise above that of the metals. Consequently no shear takes place in the graphite, and the wedge mechanism operates only through the plastic shearing of the softer metal which thus wears at a much faster rate. Also cutting wear is increased.

In both mode I and mode II the wedge mechanism causes "pads" on the harder side. These incorporate graphite layers parallel to the interface in mode I, but consist of parallel silver lamellae probably with occasional graphite inclusions in mode II. Correspondingly in mode I the coefficient of friction is essentially that of graphite, namely between 0.15 and 0.2, but it equals that of silver in mode II, namely about 0.35. At the same time the film resistivity is much higher in mode I than in mode II.

ACKNOWLEDGEMENTS

The financial support of this research through the Materials Division (Tribology) of the Office of Naval Research, Arlington, VA as well as through the Defense Advanced Research Projects Agency, TTO, (Contract P-7911 (1308) - 1102), is gratefully acknowledged.

REFERENCES

1. Stöckel, D., "New Developments and Applications in Composites", eds. D. Kuhlmann-Wilsdorf and W.C. Harrigan, TMS/AIME, Warrendale, PA (1979) p. 139 -165.

2. Schreurs, J., J.L. Johnson, and I.R. McNab, "Electrical Contacts - 1979", Ill. Inst. Techn., Chicago, IL, p. 145-151 (1979); also IEEE Trans. CHMT-3(1), 83 (1980).

3. Schreurs, J., J.L. Johnson, and I.R. McNab, "Electrical Contacts - 1980", Ill. Inst. Techn., Chicago, IL, p. 59-65 (1980); also IEEE Trans., CHMT-4, (1), p. 30-35 (1981).

4. Johnson, J.L. and J. Schreurs, Wear, 78, 219-232 (1982).

5. Dillich, S., "Electrical Contact Behavior of Silver-Graphite (75% Ag) Brushes", Ph.D. Dissertation, Dept. of Materials Science, University of Virginia, Charlottesville, VA (1981).

6. Dillich, S. and D. Kuhlmann-Wilsdorf, "Electrical Contacts - 1979", Ill. Inst. Techn., Chicago, IL, p. 185-190 (1979); also IEEE Trans., CHMT-3 (1), 37-41 (1980).

7. Kuhlmann-Wilsdorf, D. and S. Dillich, "Electrical Contacts - 1982", Ill. Inst. Techn., Chicago, IL, p. 201-212 (1982).

8. Dillich, S. and D. Kuhlmann-Wilsdorf, Mater. Sci. and Eng., 57, L13-L16, (1983).

9. Johnson, L.B. Jr., and D. Kuhlmann-Wilsdorf, Mater. Sci. and Engr., 58, L1-L4 (1983).

10. Savage, R.H., J. Appl. Phys. 19, 1-10 (1948).

11. Holm, R., "Electric Contacts", Springer, Berlin/Heidelberg/New York, 4th Ed., (1967).

12. Kuhlmann-Wilsdorf, D., Mat. Sci. Eng., 93, 107-118; 119-133 (1987).

13. Kuhlmann-Wilsdorf, D., ASME, J. of Tribology, 109, 321-329 (1987).

14. Kuhlmann-Wilsdorf, D., D.D. Makel and N.A. Sondergaard, "Proc. Engineered Materials for Advanced Friction and Wear Applicat ons", Gaithersburg, MD; Eds. F. Smidt and P.J. Blau, ASM, Metals Park, OH (1988) in press.

15. Kuhlmann-Wilsdorf, D., D.D. Makel, N.A. Sondergaard and D.W. Maribo, 14th International Conference on Electrical Contacts, Paris, IEEE, New York, (1988) in press.

16. Burton, R.A. ed., "Thermal Deformation in Frictionally Heated Systems", Elsevier Sequoia, Lausanne/ New York (1980).

17. Kennedy, F.E. ed., "Thermomechanical Effects in Sliding Systems", Elsevier Sequoia, Lausanne/New York (1985).

18. Kuhlmann-Wilsdorf, D., "Fundamentals of Friction and Wear of Materials", Ed. D.A. Rigney, TMS/AIME, Metals Park, Ohio (1980) p. 119-186.

19. Cocks, M., J. Appl. Phys., 29, 1609-1670 (1958).

20. Cocks, M., J. Appl. Phys., 35, 1807-1814 (1964).

21. Antler, M.A., "Electrical Contacts - 1980", Ill. Inst. Techn., Chicago, IL, p. 3-24 (1980).

22. Chang, Y.J. and D. Kuhlmann-Wilsdorf, "Wear of Materials - 1987", Ed. K.C. Ludema, Am. Soc. Mech. Eng., New York, p. 163-174.

23. Holm, R., "Electrical Contacts", Hugo, Gerber, Forlons, Stockholm, (1946) p. 193.

24. Mate, C.M., G.M. McClelland, R. Erlandsson and S. Chiang, Phys. Rev. Lett., 59, 1942-1945 (1987).

25. McClelland, G.M., "Proc. Engineered Materials for Advanced Friction and Wear Applications" Gaithersburg, MD 1988, eds. F. Smidt and P.J. Blau; ASM, Metals Park, OH (1988) in the press.

26. Mamin, H.J., E. Ganz, D.W. Abraham, R.E. Thomson and J. Clarke, Phys. Rev., B34, 9015-9018 (1986).

27. Buckley, D.H. and R.L. Johnson, ASLE Trans., 7, 91-100 (1964).

28. van Brunt, C., Gen. Elec. Rev., 47, 28 (1944).

INFLUENCE OF REINFORCEMENT ON THE TRIBOLOGICAL BEHAVIOUR OF AN ALUMINUM ALLOY

A. P. Monteiro Baptista, A. Barbedo de Magalhães, Rui Neto, José Duarte
Dep. Mec. Ing., Fac. of Ing. Universidade do Porto
Porto, Portugal

ABSTRACT

Using a reciprocating tribometer, the authors have tested an Al Si 12 Cu Ni Mg alloy with and without reinforcement. The reinforcement was Al_2O_3 short fibers and the antagonist used has been a liner type phosphorous grey cast iron.

Under loads up to 100 N it was found that the reinforced aluminum alloy had a lower weight loss. But for loads over 100 N (up to 250 N) the wear of the aluminum MMC was greater than that of the non reinforced one.

The authors explain this behaviour taking into account the existence of three body abrasive wear, the abrasive particles pulled out from the MMC being responsables for this fact.

This work is the first part of a research project involving the Faculty of Engineering of the University of Porto (FEUP) - Portugal and other foreign partners.

REINFORCEMENT OF METALS by the inclusion of hard fibers is a general approach to improve some of their physical properties. Reduction in thermal expansion coefficient, increasing high temperature resistance and wear resistance, is expected to be obtained by this mean.

To optimise material formulation and technological parameters concerning the production process it's necessary to characterize relevant properties of the materials being produced. In the first place, a comparison between the performances of the reinforced material and those of the non reinforced material is adequate.

Traditional applications of aluminum alloys, like motor pistons, require high temperature stability and resistance and wear resistance. Squeeze casting of aluminum alloys to infiltrate ceramic preforms,provides a wide variety of new materials. In fact, the type (nature and morphology) of the ceramic fibers, the chemical composition of the alloy and the volumic proportions of both, can be largely modified.Very litle information is avalaible,as far as the authors know, about the tribological behaviour of this kind of materials.

In a long therm study we wish to know how the different options affect material performances For the present we start to compare the tribological properties of a particular MMC with those of a similar, but non reinforced material, in order to get the basis for further developments.

EQUIPMENT, MATERIALS AND EXPERIMENTAL PROCEDURE

Flat on flat geometry in dry reciprocating rectilinear sliding, in air, were the general chosen conditions for the tribological tests.

EQUIPMENT - A four station tribometer already described elsewhere (1,2), has been used in this study. A general view of this machine is presented in the fig. 1.

MATERIALS AND SPECIMENS GEOMETRY - The test pieces of the materials under study, AS12 UNG type aluminum alloys with and without reinforcement, were obtained by two different ways:

1. From a specialy squeeze cast disc, in an ICI alumina preform, giving a 0,2 volume fiber fraction MMC.

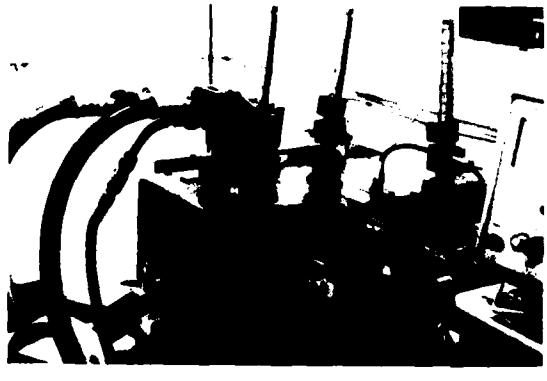


Fig. 1 - General view of the reciprocating tribometer

2. From the head of a commercialy available die casted motor piston.

In first case, as the fibers are concentrated near one of the base planes, the specimens were cut following the scheme presented in the fig. 2, to guarantee that the wear surface is a really reinforced one. The dimensions* of these smaller blocks are 3x6,5x11, and its wear surfaces (3x11,5) were ground to Ra=0,4 µm. Scanning electron microscope (SEM) views of a partially unworn surface of this kind are shown later (fig. 4).

As counterpart (and primary surface) a cylider type phosphorus grey cast iron, (c.i) cut from a ϕ120 real motor liner has been used, in all the tests. This moving block (6x22x40) runs parallel to its greater dimension during the test. The wear surface (22x40) is ground to Ra=0,4 µm in such a way that the machining traces form 45° angle with the direction of motion. Care has been taken in order that the wear surface stay as near as possible to the honed cylindrical inner surface of the liner.

EXPERIMENTAL CONDITIONS AND PROCEDURES - All tests have been performed in dry conditions in air. A fixed frequency of 7Hz and a fixed extension of 5000 double strokes (2x30mm) have been chosen, corresponding to a total sliding lenght of 300 meter.

Each test have been run under a constant load, applied by suspended weights, and wear mesure was determined by weight loss.

Prior to the test, both specimens were ultrasonically cleaned in trichloroethane and then in ether, weighed and mounted in the tribometer. After calibration of the load cell and all other setting up operations, just before starting, the wear surfaces of both specimens were cleaned again with the same solvents, to eliminate eventual traces resulting from manipulation.

TRIBOLOGICAL BEHAVIOUR

WEAR OF THE ALUMINUM ALLOYS - The mean wear rate of the reinforced and non reinforced aluminum test pieces is represented in the fig. 3.

* All non specified dimensions are in mm

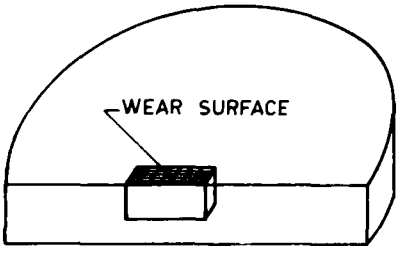


Fig. 2 - Position of the test pieces in the squeeze cast disc. Scheme

Under loads up to 100N, the reinforced aluminum alloy have a lower weight loss. For higher loads a reverse behaviour is observed. The grey c.i. counterpart presents a similar trend.

In the case of tests under low loads, for the reinforced specimens, the effective contact area is only a fraction (1/5 to 4/5) of the apparent one, as we can see in fig. 4. This fact results from an initial mismatch between the test pices, which is not corrected by material removal. The intensity of the wear processes isn't enough to allow full contact within test extension.

For loads over 25N for the MMC and over 15N for the non reinforced aluminum alloy (NRAA) all machining traces have been removed from the wear surfaces.

The main differences which have been observed in the behaviour of both materials are as follows:

a) Iron transfer to the aluminum test pieces occurs under lower load in the case of the MMC.
b) The quantity of transferred iron, which seems to increase with load, is more important in the case of MMC.
c) The wear rate of the MMC is greater then that of the NRAA, for loads higher then 100N.
d) The dimensions pf the wear scratches are longer for the MMC.
e) The plastic deformation of the surface layers, increases with load and is less marked in the case of the MMC.

Iron transfer - The quantity of iron visible in the surface shown in fig. 5 (tested under 95N) is much greater than that in the fig. 4B (25N) in both cases the distribution is relatively heterougeneous. Note that the abrasion scracthes lenght in fig. 5 equals the dimension of the test piece.

As in the case of the MMC, for low loads, the non reinforced aluminum alloy does not presente full contact in the test piece surface, fig. 6. Some of the abrasion scracthes are shorte and doesn't cross the wear surface. Increasing the load, the intensity of the wear process and the plastic deformation of the surface layer also increases, as we can see in the fig. 7. The quantity of transferred iron to this material is significantly less than for the MMC, even in the case of the higher load, fig. 8.

For the MMC, iron is always transferred, as we can see in the fig. 9 and 10. Note that the applied load in the first case is only 3N. Comparatively the transfer of iron is irrelevant for the non reinforced material, fig. 11.

Plastic deformation - The plastic deformation on the aluminum test pieces is much more evident in the case of the non reinforced material. The SEM picture in the fig. 12 shows clear evidence of plastic deformation of the surface material which is smeared and partially covers the abrasive grooves.

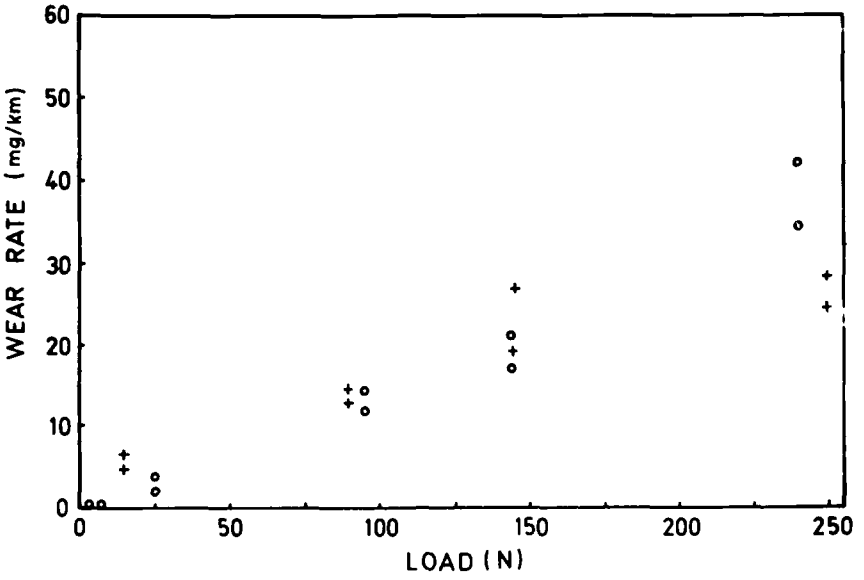


Fig. 3 - Mean wear rate of the reinforced (o) and non reinforced (+) aluminum blocks. Reciprocating dry sliding against grey c.i. in the air.

On the contrary, the picture on the fig. 13 shows two very large (> 100 μm) scoring grooves, but the MMC material doesn't seem to be much deformed.

However, detailed SEM inspection on the MMC wear surfaces, trying to detect alumina fibers, was not successful. This might suggest that the metallic matrix deforms over the fibers. Alternative explanation for this fact are:

a) the oxidation of the surface, producing a material Al_2O_3 which is chemicaly identical to the one being studied and so providing "camouflage of the fibers";

b) the wear of the counterpart and the transferred iron, which covers great extensions of the MMC surfaces and so preventing fiber detection.

Measuring the increase in the test piece length (in the direction of motion) it's possible a evaluate the percentual increase in the apparent contact area, which results from the plastic deformation. Experimental results presented in fig. 14, allow the following conclusions to be drawn:

- The plastic deformation increases with load.
- The plastic deformation is much more important for the non reinforced aluminum alloy.

WEAR OF THE CAST IRON COUNTERPART - Under low and intermediate loads there is not much difference between the wear rate of the cast



A B

Fig. 4 - SEM views of MMC wear surface after 300m dry sliding under 25N. Vertical machine traces are visible in A. White areas in B correspond to the presence of iron . A - Secondary electrons (SE); B - Backscattered electrons (BE).



Fig. 5 - BE, SEM view of MMC wear surface after 300m dry sliding under 95N. Much more iron is visible than in fig. 4B.

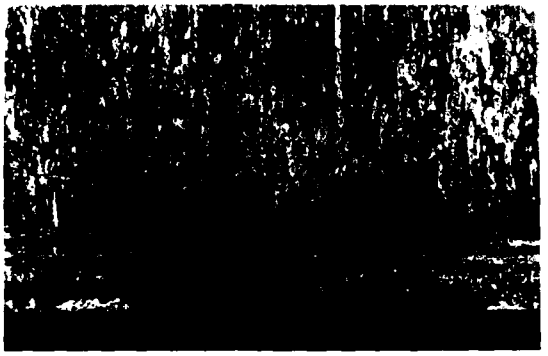


Fig. 6 - BE, SEM view of a NRAA wear surface after 300m dry sliding under 15N. Just a few machining(horizontal) traces and abrasion scratches.

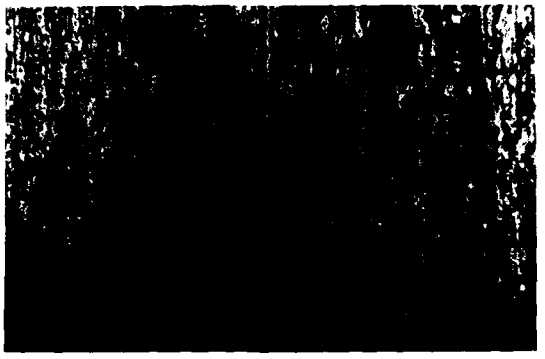


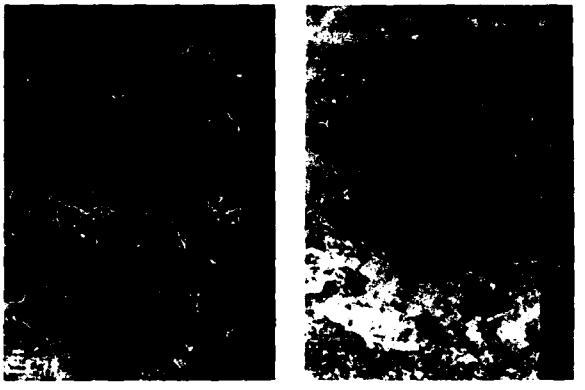
Fig. 7 - BE, SEM view of a NRAA wear surface after 300m dry sliding under 90N. Abrasion traces - Plastic deformation.



Fig. 8 - BE, SEM view of a NRAA wear surface after 300m dry sliding under 245N. Small amount of transferred iron.

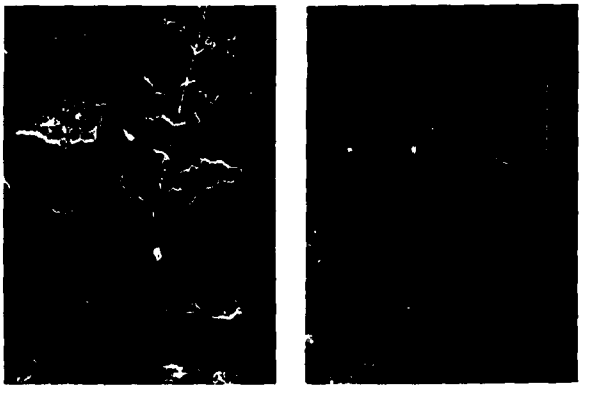


Fig. 9 - BE, SEM view of the MMC wear surface 300m dry sliding under 3N. Located area wiht high quantity transferred iron.



A-(SE) B-(BE)

Fig. 10 - SEM view of the MMC wear surface. 300m dry sliding under 25N. Transferred iron on the surface and compacted wear particles in abrasive grooves.



A-(SE) B-(BE)

Fig. 11 - SEM view of a NRAA wear surface. 300m dry sliding under 15N. Fine scratching, plastic deformation and not significant iron transfer.

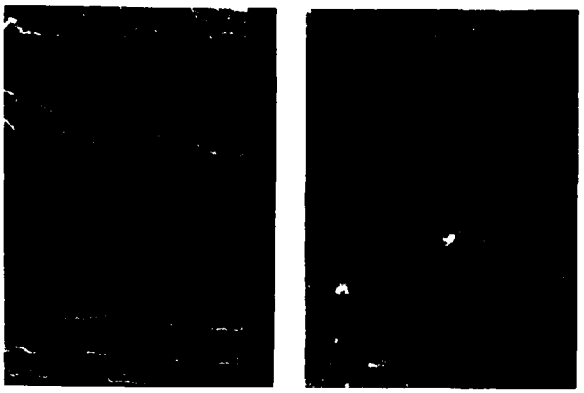


Fig. 12 - SEM views of a NRAA wear surface. 300m dry sliding under 245N. A - SE intensive plastic deformation over abrasion grooves. B - BE not significant iron transfer (white).



Fig. 13 - SE, SEM views of the MMC. 300m dry sliding under 144N. Two large scorring grooves (> 100 μm)

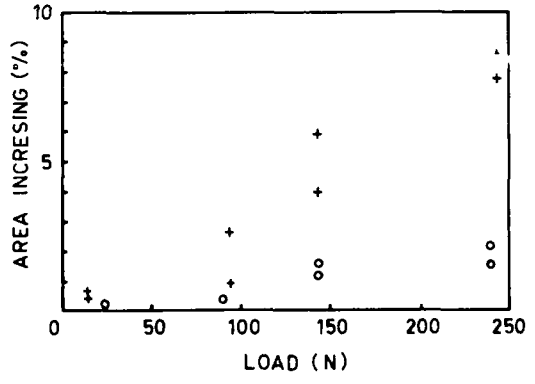


Fig. 14 - Increase in the apparent contact area (percentage) in function of the applied load (o)-MMC; (+)-NRAA.

iron test pieces - 3 to 15mg/Km of sliding distance. For loads over 100N the increase is more important for c.i. specimens tested against the MMC; wear rate can attain 57mg/Km under 240N. For those tested against the NRAA a maximum wear rate of 22mg/Km was observed under 245N.

In both cases, not surprisingly, there is some aluminum transfer for the cast iron surfaces, but the specimens worn against the MMC present a clear abrasive pattern as we can see in the fig. 15 and 16. The first of these figures shows the inclined machining traces which were not removed during this mild wear process. Minor abrasive scratches are clearly visible, although the applied load was only 7N.

Under high load the cast iron worn surface is severely damaged. The wear mechanism is mainly cutting abrasion as can bee seen in fig. 16.



Fig. 15 - SE, SEM view of the cast iron wear surface, after 300m dry sliding under 7N against the MMC. Inclined machining traces and fine abrasive scratches.

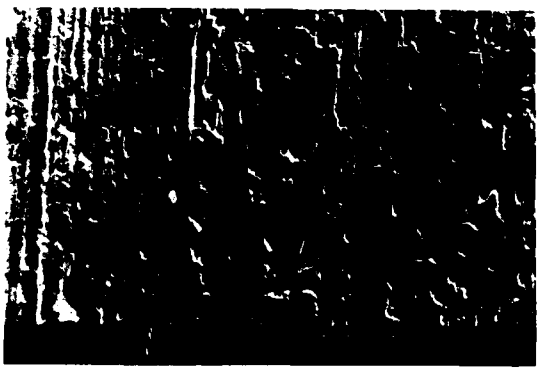


Fig. 16 - SE, SEM view of the cast iron wear surface after 300m dry sliding under 240N against the MMC. Severe scoring.

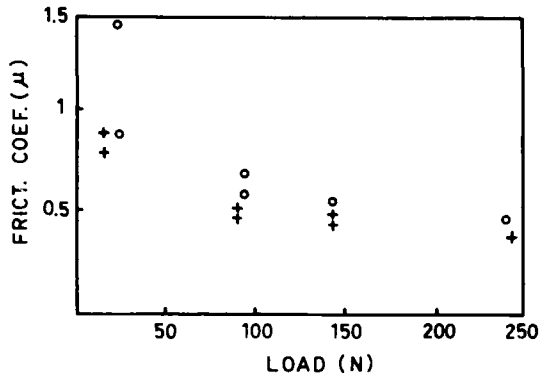


Fig. 17 - Maximum friction coefficient values against applied load. Reciprocating dry sliding of phosphorus flake graphite grey cast iron against: (o)-MMC; (+)-NRAA.

FRICTION - The friction force has been continuously measured during all tests. The maximum friction coefficient values are plotted against the applied load in the fig. 17. In both cases a decrease with increasing load is observed. This behaviour has been observed in many material couples.

The friction coefficient, under similar loads, is allways less for the non reinforced aluminum alloy. The difference exceeds 0.1, which represents more than 20%. Hardening the softer material of a tribological couple, reduces the real contact area, so reducing the adhesive component of friction. In this case an opposite effect seems to be achieved. The inclusion of alumina fibers, though increasing compression resistance, doesn't really increase the matrix hardness. On the other hand, the hard alumina fibers cut the cast iron counterpart, thus increasing the cutting component of friction.

CONCLUSIONS

The study reported in this paper is to be continued during the next three years. So, the following statements must be seen as preliminary conclusions:

1. An AS 12 UNG non reinforced aluminium alloy sliding in reciprocating dry conditions against cast iron give a mainly adhesive type of wear. Abrasion is less intensive in this case than if the aluminum alloy is reinforced with alumina fibers.
2. Under low loads the wear rate is less for the MMC than for the NRAA. For loads over 100N the reverse behaviour is observed.
3. The same trend has been observed for the cast iron counterpart.
4. The increase of the wear rates of the MMC and its c.i. counterpart for high loads, is attributed to the presence of hard alumina particles in the third body.
5. Under equivalent loads, the dry friction coefficient is 20% higher for the MMC than for the NRAA, when using the same c.i. counterpart.

REFERENCES

1. A.P.MONTEIRO BAPTISTA: Comportement Tribologique en glissement sec de fontes à chemises de moteurs thermiques. Thèse Doc. Ing. - ISMCM - St. OUEN, France - 1986.
2. A. CAVALHEIRO, M.T.VIEIRA et A.P.MONTEIRO BAPTISTA; Étude de l'influence des revêtements de PTFE, obtenus par pulvérisation cathodique, sur les proprietés des matériaux métalliques. - 5Th Int. Congr. on Heat Treat.of Materials - Budapest, Hungary - Oct. 20-24, 1986.

TRIBOLOGICAL BEHAVIOR OF Al ALLOY-GRAPHITE AND Al ALLOY-MICROCRYSTALLINE CARBON PARTICLE COMPOSITES

P. K. Rohatgi, N. B. Dahotre, Y. Liu, M. Yin, T. L. Barr
Materials Science Department
University of Wisconsin-Milwaukee
Milwaukee, Wisconsin 53201 USA

ABSTRACT

Wear and friction behavior of Al alloy-graphite composites, Al alloy-microcrystalline carbon composites, matrix alloys and pure graphite have been investigated. The Al alloy-graphite composite, in comparison to its matrix alloy, shows excellent wear resistance and a lower coefficient of friction, whereas Al alloy-microcrystalline carbon composites exhibit higher weight-loss than that of the matrix alloy and both have almost equal values for coefficients of friction. ESCA analysis reveals that the Al alloy-microcrystalline carbon composite surfaces undergo extensive oxidation during tribo-deformation. It also points out the transfer of Fe from the wear wheel to the worn surface.

INTRODUCTION

IN THE LAST FEW YEARS, high temperature lubrication has been attracting considerable attention in connection with advanced heat engines. In certain designs, for example pistons, liners and bearings, the localized or overall temperatures experienced are of the order of 500°C (1), while similar or even greater temperatures exist within advanced gas turbines. For these and many other applications, some form of solid lubrication becomes essential. When components are lubricated by thin, solid films deposited prior to assembly, the wear lives of such films are inevitably limited by the length of time the coating lasts. A continuous supply of solid lubricant through transfer process offers the possibility of greatly increased component life. In light of these requirements, a "built in" supply of lubricant to a load carrying component seems to be a most appropriate solution. Thus the metal matrix composites containing self lubricating elements serve as "2-body transfer lubrication systems" (2). Cast Al-matrix particulate composites are the most widely considered materials as self lubricating elements. It has been found that dispersion of over two volume percentage graphite particles markedly improved the wear resistance of aluminum alloys and allowed aluminum alloys to run under conditions of boundary lubrication without seizing (3). It has also been demonstrated that after operating under conditions of boundary lubrication and tribological deformation of mating surfaces and the subsurface regions, a large fraction of surface is covered by a graphite film. Rohatgi and coworkers (4) have demonstrated that the use of aluminum alloy-graphite particle composite pistons and/or liners in diesel and petrol engines resulted in reduced frictional horse power and reduced wear of piston, liner and rings. The advantages of aluminum-graphite liners have been confirmed in high performance engines by Associated Engineering Company of Italy (5). It has been shown by Japanese (6) workers that the wear properties of cast copper graphite current collectors were better than the alloys of the same composition produced by powder metallurgy. Soviet (7) researchers have reported successful use of aluminum graphite bearing in tractor and marine engines. However, in order to extend the use of this concept of metal matrix solid lubricant composite to other systems, it has become extremely essential to understand the basic mechanism of formation of graphite film, as well as formation of any new species and their role in lubrication. The present paper provides an insight into the wear and friction behavior of selected Al alloy matrix composites containing microcrystalline or crystalline graphite and relates them to tribo-chemical changes at the mating surface studied by ESCA techniques.

EXPERIMENTAL PROCEDURE

The materials selected for this study are shown in Table 1. The composites were prepared by conventional foundry techniques described in previous publications (8-9). The matrix alloys

were melted in an induction furnace in a controlled atmosphere. Crystalline graphite or microcrystalline carbon (10 wt.%) were added to the melt prior to casting.

Table 1. List of Materials

Matrix	Type of Dispersoid	wt. % of Dispersion	Condition of Alloy
Flake Graphite		0	Pressed
Granule Microcrystalline Carbon	Pure Al	10	Hot Pressed
Al-319	None	0	As-Cast Commercial Stock
Al-2014	None	0	As-Rolled Commercial Stock
Al-319 (6.3% Si, 3.6% Cu)	Flake Graphite	10	As Cast
Al-2014 (0.8% Si, 4.4% Cu, 0.8% Mn, 0.4% Mg)	Granule Microcrystalline Carbon	10	As Cast

In order to study the response of pure graphite during tribo-deformation, graphite blocks were made by pressing graphite powder using 6000 psi pressure. It was not possible to make similar blocks from microcrystalline carbon powder, therefore, the microcrystalline carbon (10 wt.%) - pure Al composite blocks were made by pressing a mixture of aluminum and microcrystalline carbon powder using 6000 psi pressure at 400° F.

Wear tests were carried out under dry sliding conditions against a rotating steel disk using a block-on-disk apparatus. Small rectangular samples with 10 x 10 x 20 mm^3 dimensions were used for this study. The counterface rotating steel samples were weighed accurately before and after tribo-deformation. The coefficient of friction was calculated using measurements of change in voltage and current in the electrical circuit of the motor driving the block-on-disk apparatus before and after loading. Based on the principle of energy conservation, the frictional energy is equal to the difference of electrical work before and after loading or,

$$W_A - W_B = W_F \qquad (1)$$

where W_F is the frictional energy, W_A is the work after loading and W_B is the work before loading. From friction theory, we know that

$$W_F = \mu NV \qquad (2)$$

where μ is the coefficient of friction, N is the normal load and V is the linear speed of disk. The calculated values of the coefficient of friction in the present study are in good agreement with earlier studies (10, 11).

In the present experiments, tribo-deformation was carried out at a fixed load (780 gm), with a constant surface speed of the disk equal to 200 mm/sec. The time of wear deformation was varied from 75 seconds to 1200 seconds. In order to detect the type of carbon and other chemical species on the surface after wear deformation, ESCA analysis of tribo-deformed surface was carried out. ESCA analysis was performed in an ESCA system with spectrometer MGK (1253.6 eV) as a x-ray source. All ESCA results reported earlier (12) were acheived with a PHI in the Analytical Laboratories of the Physical Electronics Co. This system features an x-ray monochromator as well as small (~200 μm) spot capacity. The use of an additional electron flood gun plays key role in the reported results.

RESULTS AND DISCUSSION

WEAR AND FRICTION BEHAVIOR - The plot of measured weight-loss as a function of sliding time for the specimens is shown in Figure 1. The weight-loss in both Al-319 and Al-2014 increases with time of sliding, however, Al-319 alloys show higher weight-loss compared to weight-loss in Al-2014 alloy. The compact block made from graphite powder shows increasing weight-loss but its weight loss is lower than alloy Al-319. The Al-319-10 wt. % graphite particle composite exhibits excellent wear resistance compared with Al-319 matrix alloy. In Al-319-10 wt. % graphite alloy,

there is very little additional weight loss after the initial period and after 1200 seconds wearing time weight loss is nearly three times lower than the matrix alloy (Al-319). By contrast, the weight-loss in Al-2014-microcrystalline carbon composite remains higher than matrix alloy (Al-2014) throughout the wear cycle. This may be due to the fact that microcrystalline carbon powder does not reduce wear rate like crystalline graphite does.

The coefficient of sliding friction as a function of sliding time for matrix alloys, graphite and composites is shown in Figure 2. Al-2014 alloy shows slightly higher value of coefficient of friction than Al-319 alloy. Under dry friction conditions the graphite compact block exhibits the lowest friction coefficient (close to 0.1) which remains constant with time. The coefficient of friction of graphite is about one third lower than other materials. The coefficient of friction of Al-319-graphite composites is lower than Al-319 alloy and also coefficient of friction decreases with time. The coefficient of friction of Al-319-graphite composite is in between the coefficient of friction for graphite and Al-319 alloy. The coefficient of friction for Al-2014-10 wt. % microcrystalline carbon is not very different from the values for matrix alloy indicating that microcrystalline carbon does not decrease the coefficient of friction.

THE MECHANISM OF FORMATION AND FAILURE OF LUBRICANT FILMS - Al-319 and Al-2014 are both hypoeutectic alloys. Their microstructure consists of primary Al phase and a eutectic. In Al-319 the amount of eutectic in the structure increases as the Si content in the alloy increases. The finer eutectic Si platelets act as fracture initiation sites during sliding wear and cause discontinuous chip formation allowing the displaced lip of material to be more easily removed. This should be the reason for higher weight-loss in Al-319 alloy compared to Al-2014 alloy during sliding wear.

During sliding wear of Al-alloy graphite composites the transfer of graphite particles to counterface and to the surface of the composite sample itself depends on such factors as strength of the particle-matrix interface, surface finish of the counterface and sample, sliding velocity, operating temperature, atmosphere and graphite particle size. Initially, during sliding graphite crystallites with suitable orientation are embedded into the counterface and the surface of the composite through an abrasion mechanism. This results in a higher weight-loss [Figure 1] and higher values for the coefficient of friction [Figure 2]. As sliding wear continues, the effectiveness of the abrading asperities is reduced by their getting buried under graphite crystallites. An increasing fraction of the load is taken by this debris which becomes compacted and presumably develops a basal orientation approximately parallel to the surface. The initial rate of formation of these compacted areas is very large but after specific sliding time (about 150 seconds for Al-319-graphite composite and 600 seconds for graphite) is required before an equilibrium wear rate [Figure 1] and stable coefficient of friction is established [Figure 2].

Microcrystalline carbon has a short range order structure compared to crystalline graphite. Microcrystalline carbon particles are removed from the matrix without formation of a thin film on the tribo-deformed surface unlike the situation with graphite. Presumably the absence of formation of a thin film results in higher weight-loss [Figure 1] and a higher value of the coefficient of friction [Figure 2] during sliding wear of Al-2014-microcrystalline carbon composite as compared to Al-319-graphite composite.

ESCA ANALYSIS - As with the previous study (12) the ESCA technique was used to investigate the surface and subsurface chemistry of the samples before and after tribo-deformation. The following preliminary observations were conducted on the basis of the present ESCA studies.

Figures 3(a), (b) and (c) show the C(1s), O(1s) and Al(2p) spectra respectively for Al-319-graphite composite samples subjected to tribo-deformation for different durations. Two kinds of carbon were detected on the surface: graphitic carbon released from the matrix of the composite during sliding wear and adventitious (12) carbon. As there is no difference between their (1s) spectra, it becomes difficult to distinguish them from each other. However, the adsorbed carbon content on the surface suffers the charging shift [Figure 3(a)] because of the insulating support (oxide layer) whereas the graphitic carbon released from the matrix renders the surface conductive. The magnitude of the charging shift thus, depends on the surface condition i.e., roughness, completeness of coverage and the amount of conductive carbon on the surface. The Figure 3(a) also exhibits a C(1s) shoulder at about 290 eV. That shoulder corresponds to the presence of carbon oxides (C-OH, -C=C-C=O etc.). The shoulder grows larger with sliding wear duration indicating more and more oxidation of carbon is formed during tribo-deformation.

The above observations are also supported by the studies of the O(1s) spectra [Figure 3(b)] obtained for the same samples, as a result of the presence of surface absorbed oxygen. The position of this O(1s) peak, corresponds to the type of C-O bonding. The decrease in the charging shift (from 533.6 eV for a nondeformed to 532.4 eV for a 1200 seconds tribo-deformed sample) suggests that the more and more (conductive) carbon is released from the matrix and it covers the surface. This is in confirmation with optical and scanning studies reported earlier (12) on increasing coverage of tribosurface by carbon layer during tribo-deformation of aluminum graphite composite.

In Figure 3(c), the Al (2p) spectra show alumina peaks at about 75 eV and an Al° peak at about 72.8 eV. The [Al_2O_3/Al] peak ratio increases as the wearing time increases, suggesting that the worn surface gets increasingly contaminated by oxide formation even in the case of a graphite containing composite.

Figures 4(a), (b) and (c) show the C(1s), Al(2p) and O(1s) spectra respectively for Al-2014-microcrystalline carbon composite samples subjected to tribo-deformation for different durations. As seen in Figure 4(a), the C(1s) shoulder at about 290 eV becomes smaller as the sample is subjected to increasing sliding wear. This suggests that microcrystalline carbon is chemically more stable and does not react easily with oxygen to form oxides. According to Figure 4(b), the [Al_2O_3/Al] ratio increases as the wearing time increases. Further it suggests that the magnitude of the increase in the [Al_2O_3/Al] ratio is much larger for the Al-2014-microcrystalline samples than the comparatively treated Al-319-graphite samples.

Correspondingly it should be noted that the Al(sp) [Figure 4(b)] and O(1s) [Figure 4(c)] spectra of that nondeformed Al-2014-microcrystalline carbon sample exhibit larger charging shift than the tribo-deformed samples (about 1 eV higher), however, these charging shifts remain at about the same value regardless of how long the sliding wear is carried on. This suggests that the microcrystalline carbon released from the matrix does not seem to form a thin film on the oxidized surface of the sample in a manner similar to the tribo-deformed Al-319-crystalline graphite sample. This may be the reason that microcrystalline carbon does not perform as well as a good lubricant as graphite.

It was previously noted (12) through ESCA studies, that Fe particles were transferred from the counterface to the Al-2014-microcrystalline carbon samples. This was confirmed through the visibility of ESCA Fe signals from samples (0% for nondeformed, 0.4% for 75 seconds tribo-deformed and 0.52% for 1200 seconds tribo-deformed sample). These observations further confirm our suppositions regarding the different tribological behaviors of crystalline graphite and microcrystalline carbon in Al-319 and Al-2014 respectively.

CONCLUSIONS

1) Al-319 alloy shows higher weight-loss and lower coefficient of friction than Al-2014 alloy.
2) The wear rate of Al-319-10% graphite is much lower than either the matrix alloy or graphite block. The friction coefficient of Al-319-10% graphite composite lies between those of the matrix alloy and 100% graphite. The weight-loss of Al-319-10% graphite composite becomes constant after the initial loss suggesting the formation of graphite film.
3) The wear rate of Al-2014-10% microcrystalline carbon composite is higher than the base alloy while their friction coefficients are similar to the base alloy.
4) ESCA studies show aluminum and its oxide on the tribo-deformed surface and transfer of iron from the mating surface to Al-2014-10% microcrystalline carbon composite sample.
5) The large charging shift in ESCA studies suggests that increasingly continuous layer of carbon forms during tribo-deformation of Al-319-crystalline graphite samples. The formation of carbon-oxygen compounds on the tribo-deformed surfaces is much greater in the case of Al-319-graphite composite as compared to Al-2014-microcrystalline carbon composite.

ACKNOWLEDGMENT

The authors wish to acknowledge the Office of Naval Research for their support of this work under Grant N00014-87-K-0399.

REFERENCES

(1) Toyama, K., et al., Heat Insulated Turbo-Compound Engine, SAE Paper 831345 (1983).
(2) Lancaster, J. K. J. of Tribology, 107, 437 (1985).
(3) Gibson, P. R., A. J. Clegg and A. A. Das, Wear 95, 193-198 (1984).
(4) Rohatgi, P. K., R. Asthana, and S. Das, International Metals Review 31, 115 (1986).
(5) Holt, J. W. and A. E. Engine Components, Inc., Copia Ricevuta, 207 (Sept. 29, 1987).
(6) Hitachi Graphite Dispersed Cast Alloy--Gradia, Ibaraki, Japan, Hitachi Chemical Co. (1981).
(7) Gorbunov, V. G., V. D. Parshine and V V. Panin, Litenove Proizod, (USSR), 8, 20 (1974).
(8) Surappa M. K. and P. K. Rohatgi, J. Mater. Sci., 16, 983 (1981).
(9) Rohatgi, P. K. Modern Casting, 4, 47 (1988).
(10) Fusaro, R. L. ASLE Proceedings, 3rd International Conference on Solid Lubrication, 1984, 1-10, Denver, Colorado, August 7-10, (1984).
(11) Lancaster, J. K. Tribology in the 80's, Proceedings of an International Conference held at NASA Lewis Research Center, Cleveland, OH, 333-355, April 18-21, (1983).
(12) Rohatgi, P. K., N. B. Dahotre, Y. Liu and T. Barr, Engineered Materials for Advanced Friction and Wear Application, editors: F. A. Smidt and P. J. Blau, ASM International, Warrendale, PA. (1988).

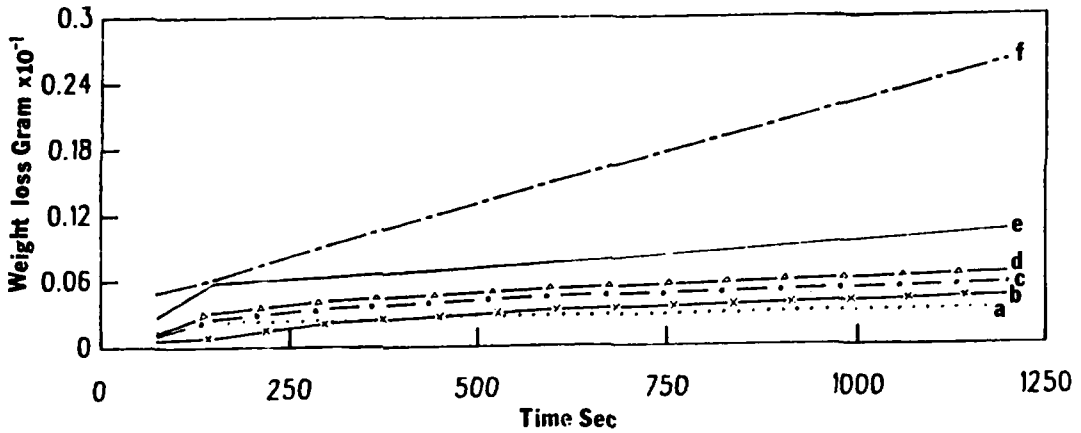


Fig. 1. The average weight-loss plotted against the sliding time (sliding velocity = 200 mm/sec., load = 0.78 kg) for (a) Al-319-10% crystalline graphite composite, (b) pure graphite, (c) Al-2014 alloy (d) Al-2014-10% microcrystalline carbon composite, (e) Al-319 alloy, and (f) 10% microcrystalline carbon-pure Al composite.

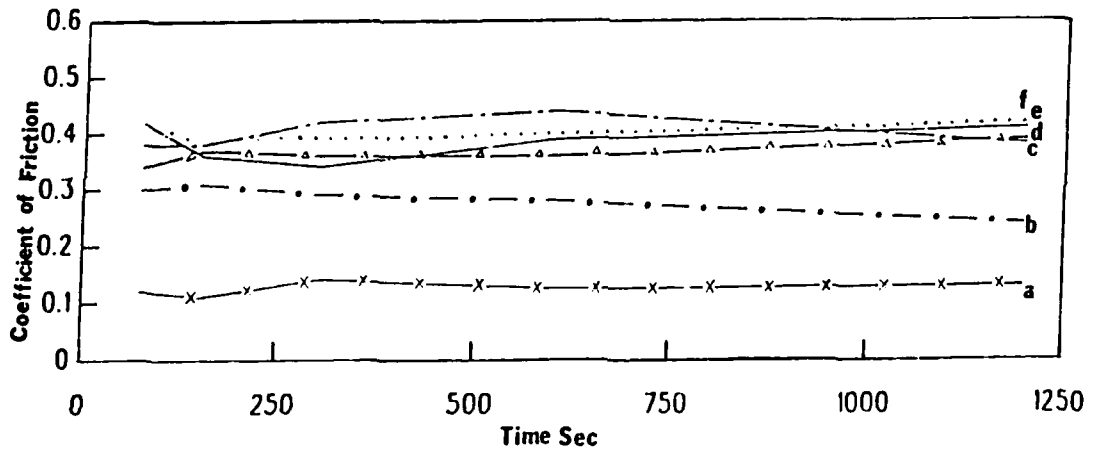


Fig. 2. The coefficient of friction plotted against sliding time (sliding velocity = 200 mm/sec, load = 0.78 kg) for (a) pure graphite, b) Al-319-10% crystalline graphite composite, (c) 10% microcrystalline carbon-pure Al, (d) Al-319 alloy, (e) Al-2014-10% microcrystalline carbon composite, and (f) Al-2014 alloy.

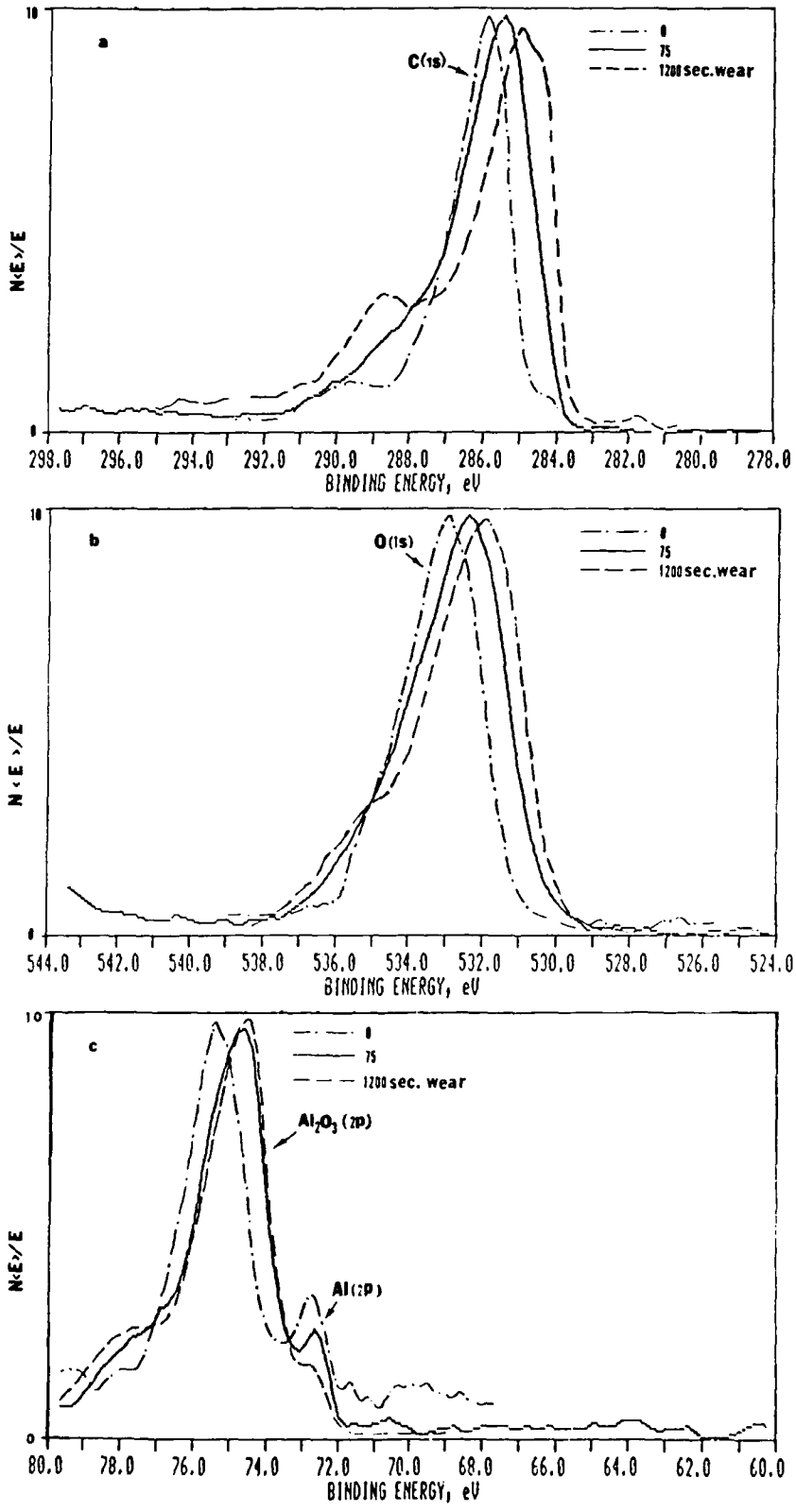


Fig. 3. XPS spectra for Al-319-10% crystalline graphite composite samples subjected to tribo-deformation for different durations, (a) C(1s), (b) O(1s), and (c) Al(2p).

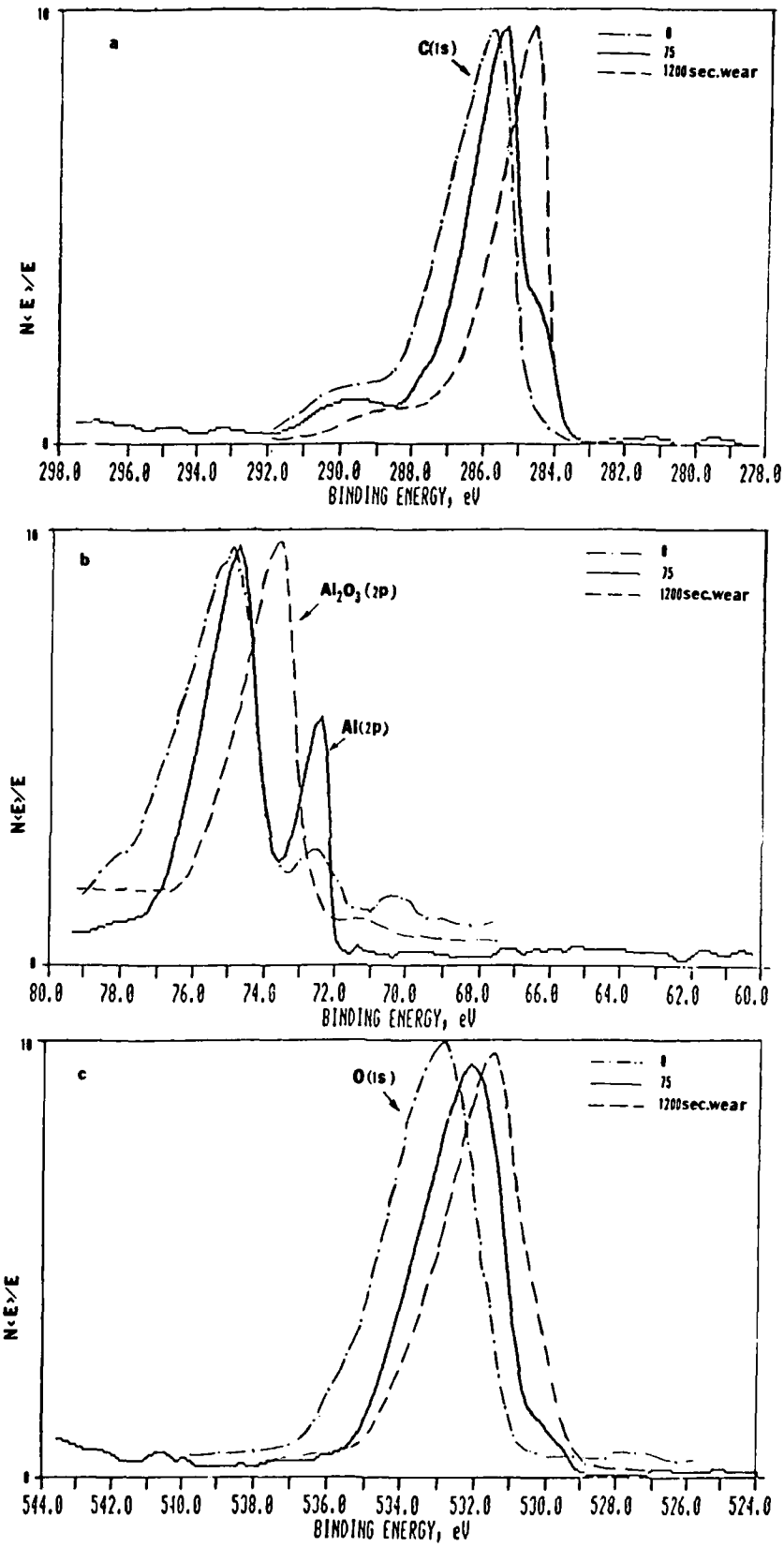


Fig. 4. XPS spectra for Al-2014-10% microcrystalline carbon composite samples subjected to tribo-deformation for different durations, (a) C(1s), (b) Al(2p), and (c) O(1s).

DAMPING CAPACITY OF ALUMINUM ALLOY MATRIX COMPOSITES

P. K. Rohatgi, R. Asthana, Ashok Kumar
Materials Department, University of Wisconsin-Milwaukee, Milwaukee, Wisconsin 53201 USA

D. Nath
Department of Metallurgical Engineering
Banaras Hindu University, Varansi, India

S. Schroeffer
Control Data Corporation
Minneapolis, Minnesota, USA

ABSTRACT

The specific damping capacity (SDC) to density ratio of cast Al alloy-ceramic particle composites containing dispersed particles of flake graphite (400 μm; 4.1%) and flake mica (40 μm; 2.55%) were measured at constant strain amplitude using a torsion pendulum. The SDC to density ratio of these composites increased linearly with increasing concentration of particles in the matrix, and exceeded the SDC to density ratio of cast iron. Optical microscopy and SEM analysis of these composite materials has been made to determine the possible damping mechanisms. These results will be discussed in view of other measurements reported in the literature on particulate and fiber reinforced metal matrix composites to plot normalized damping curves as a function of volume percentage of particles or fibers.

INTRODUCTION

IN VIEW OF THEIR ADVANCED structural applications in aerospace, metal matrix composites are required to have good vibration damping properties. Several recent studies have indicated improved damping capacity of matrix alloy as a result of reinforcement with fibers or particles. In the two phase materials such as metal matrix composites and cast irons (1) damping of vibrational energy could stem from several sources, most notably the nature of reinforcement (shear strength), interfacial bond quality, dislocation substructure at the particle-matrix interface and the matrix void content.

This paper primarily discusses damping of particle filled metal matrix composites produced by solidification processing. Due to their lower cost at a little expense of strength, particle filled composites could be potentially more useful than fiber composites for damping application in consumer and automotive industry. This paper highlights damping experiments on cast Al-graphite, Al-mica and Cu-graphite particle composites and compares the normalized damping properties of particle and fiber composites synthesized by different processing techniques.

CAST PARTICULATE COMPOSITES

(i) AL/GR AND CU-GR COMPOSITES - Experiments on the following Al casting alloys containing dispersion of graphite particles were conducted (2) to characterize their damping properties

(i) Al-0.89 Cu-0.42 Si-0.92 Graphite (size ~ 302 μm)
(ii) Al-2.20 Cu-0.42 Si-1.216 Graphite (~ 302 μm)
(iii) Al-2.08 Cu-0.42 Si-2.05 Graphite (~ 546 μm)
(iv) Al-3.48 Cu-0.42 Si-3.42 Graphite (~ 546 μm)
(v) Cast Iron (4.5% Graphite, size: 150 μm)

These metal-matrix composites were synthesized by a liquid metallurgy technique which consisted of dispersion of copper coated graphite powder into a vigorously agitated base alloy melt. The resulting Al alloy-graphite suspension were gravity cast into rods and bars of required dimension. Samples for damping capacity tests were machined from cast rods and are shown in Fig. 1. The damping capacity tests were also conducted on cast iron for comparison with graphite-aluminum alloys. A typical microstructure of cast graphite aluminum alloy used in this study is shown in Fig. 2.

The damping capacity measurements were made using a torsion pendulum instrumented as shown in Fig. 3. The torsional deflection is varied by adjusting the air gap between the electromagnets and the inertia bar. All measurements of damping capacity were made at an angle of twist of less than 10° for Al alloys and 5° for cast iron; these correspond to strain levels of 0.12 radians and 0.006 radians respectively. The damping capacity of the material under test

was evaluated from the mean logarithmic decrements of successive amplitude of vibrations. The mean logarithmic decrements was calculated as

$$\ln\left(\frac{An}{An+1}\right)$$

where A is the amplitude of any cycles n and n+1. In addition, the specific damping capacity was calculated from:

$$SDC = \left(\frac{An^2 - An^2+1}{An^2}\right) * 100$$

The SDC and SDC to density ratios of various materials tested are listed in Table I. Broadly, these results are in agreement with those of other workers (3,4). Cast irons show vastly superior vibration damping properties compared with mild steel as well as graphite-free base alloys. The damping capacity of Al alloys is improved by the dispersion of flake graphite particles. The test results also show that as the volume fraction of dispersed graphite increases, the damping capacity increases, and it is likely to approach that of cast iron when sufficient volume fraction of dispersed graphite is incorporated into Al-alloy matrices. Since iron is heavier than graphite, the same weight percentage of graphite implies a much larger volume percent of graphite in cast iron then in Al alloys and apparently the volume percentage determines the damping capacity of composite materials. Figure 4 shows a plot of SDC vs. vol.% graphite for these alloys.

In other studies on damping capacity of graphite dispersed Al and Cu casting alloys, Onuki et al. (5) used higher (20 vol.%) percentage of coarse (177-900 μm) graphite particles in various composites prepared by a liquid metallurgy technique. They used natural graphite powder in three different size ranges: 177-250 μm, 250-500 μm, 500-700 μm and 700-900 μm, respectively. These powders were coated with copper and nickel by non-electrolytic method for dispersing in Cu and Al casting alloys respectively. Matrix alloys used were (5):

Cu-5 Sn-5 Zn-4 Pb-0.8 Ti, Al-12 Si-3 Cu-0.03 Mg; Cu-27.5 Mn; Cu-5 Sn-5 Zn-0.8 Ti, Al-12 Si and Al.

The surface nickel coating on graphite dissolved in metal during particle dispersion and became part of the alloy. Thus with dispersion of 20 vol.% graphite, the nickel content in the alloy was found to increase to 4.7%.

These Al and Cu casting alloys containing up to 20 vol.% graphite were pressure cast using a pressure of 61.7 MPa to form 30 x 50 x 150 mm^3 pieces of the composites. For damping tests, specimens of 5 x 2 x 120 mm^3 were cut out, and in order to eliminate any cutting stresses, the specimens were stress-relieved at 300-400° C for 1 hour followed by normal cooling. Damping test results of the above Al and Cu alloys containing graphite particles were compared and contrasted

Table I
DAMPING PROPERTIES OF METAL-MATRIX COMPOSITES
(Experimental Data from the Literature)

Material	Volume Fraction	Frequency Hz	Strain Amplitude	Specific Damping Capacity (SDC) %
Mg 8% Al 0.4% Zn 0.1% Mn	--	30	$3.3 * 10^{-4}$	1.5 - 4.4
P100Gr/AZ91C		50-140	--	1.0 - 1.2
Ti foil	0.45	180-250	--	1.4 - 2.0
Al_2O_3/Al-2Li	0.52	2100	$\leq 10^{-6}$	0.13
SiC/B/6061 Al (AVCO)	--	2100	$\leq 10^{-6}$	0.275
B/Al (1100)	0.50	2000	$\leq 10^{-6}$	0.415
B/Al (6061)(TRW)	0.51	2000	$\leq 10^{-6}$	0.375
SiC/Ti-6Al-4V	--	2100	$\leq 10^{-6}$	0.16
SiC/Ti	--	1200	$\leq 10^{-6}$	0.11
P55Gr/6061Al	0.3847	35.4	60	5.02(90°)** 2.51(0°)**
P55Gr/6061Al	0.3847	35.4	600	16.33(90°) 8.79(0°)
55MSI Gr/6061Al	0.34	0.4	$150 * 10^{-6}$	$19.5 * 10^3$(0°)
		1.4	$150 * 10^{-6}$	$16.8 * 10^3$(0°)
		0.4	$325 * 10^{-6}$	$38.7 * 10^3$(0°)
		1.0	$325 * 10^{-6}$	$33.5 * 10^3$(0°)
		0.4	$150 * 10^{-6}$	$12.4 * 10^3$(90°)
		2.0	$150 * 10^{-6}$	$11.25 * 10^3$(90°)
		0.4	$566 * 10^{-6}$	$10.75 * 10^3$(90°)
		2.0	$566 * 10^{-6}$	$7.95 * 10^3$(90°)
Al-4Cu-Mica	1.5*	--	--	0.37
Al-4Cu-1.5Mg-Mica	0.75*	--	--	1.83
Al-4Cu-1.5Mg-Mica	1.0*	--	--	2.14
Al-4Cu-1.5Mg-Mica	2.0*	--	--	3.12
Al-4Cu-1.5Mg-Mica	2.25*	--	--	4.24
6061 T-6	--	15	--	3.64
P100/AZ91C/AZ31B	0.265	8.6	--	11.84
P100/6061	--	38	--	15.32
Al-0.89Cu-0.42% Si graphite flake	1.082	--	0.12 rad/in	2.981
Al-2.2%Cu-0.42% Si graphite	1.45	--	0.12 rad/in	2.935
Al-2.08%Cu-0.42% Si graphite	2.43	--	0.12 rad/in	4.101
Al-3.18%Cu-0.42% Si graphite	0.049	--	0.12 rad/in	6.332
Al-3%Cu-0.7% Si without graphite	--	--	0.12 rad/in	0.02
Al-4%Cu-6% Si without graphite	--	--	--	1.375
P100/6061	0.34	1.00	--	17.33
P100/AZ91C/AZ31B	0.265	1.00	--	16.08
6061-0	--	24	550	8.16

*weight percent
** 0°: parallel to fiber direction
90°: perpendicular to fiber direction

with similar tests carried out on 65% Mn-35% Cu alloy and flaky graphite cast iron FC-10 and FC-25.

The vibrator set up used for damping measurements consisted of a self oscillatory circuit, operating at the resonance frequency of the sample, while the sample drive and pick-up were operated electrostatically (5). The test sample was heated to 150° C at a rate of 1° C/minute to eliminate any non-uniformity in temperature in the entire sample. The measuring set up was evacuated to 10^{-3} mm of Hg and the deflection was of the order of 10^{-6}.

When only small quantities of nickel plated graphite (500-700 μm) particles were added to Al, Al-12 Si and Al-12 Si-3 Cu-0.3 Mg alloys, nickel content of the alloy does not change appreciably. Under this condition, Ni additions were separately made. However, when graphite volume percent is more than 20, it did not disperse uniformly in casting while Ni dissolved in Al alloy. The overall Ni content remains practically constant.

The damping capacity (Q^{-1}) of these alloys before any graphite additions is very low i.e., of the order of $4 * 10^{-4}$. As a result of graphite addition, damping capacity increased almost linearly and beyond 20 vol.% graphite the damping capacity values were greater than $5 * 10^{-3}$. Also at a constant volume percent of graphite damping capacity was independent of the base alloy composition.

In the case of copper alloys containing Pb (Cu-5 Sn-5 Zn-4 Pb-0.8 Ti). The damping capacity was higher than other alloys (Cu-27.5 Mn; Cu-5 Sn-5 Zn-0.8 Ti) since Pb itself has a very high value of damping capacity. However, in all these alloys damping capacity increases linearly with graphite content and is practically uninfluenced by alloy composition. The damping capacity of Cu alloys containing 16 vol.% graphite is almost $4 * 10^{-3}$. Figure 8 plots these data (as normalized SDC defined as ratio of SDC of composite to that of the matrix alloy) as a function of vol.% particles. For a given volume percentage of graphite, the damping capacity is same for both Al and Cu alloys, indicating that damping capacity of these composites material is mainly due to the presence of graphite particles, and is not affected by matrix alloy composition.

(ii) EFFECT OF PARTICLE SIZE AND SHAPE - It is well known that in the case of flake graphite cast iron, the damping capacity increases with graphite quantity as well as with graphite size. Similar results are obtained on Al or Cu-graphite particle composites (5). The influence of graphite particles size on damping capacity of composites has been studied by Suwa et al. (5) for Al-4.7 Ni-12 Si-3 Cu-0.3 Mg-20 vol.% graphite; and in Cu-5 Sn-5 Zn-4 Pb-0.8 Ti-16 vol.% graphite composites. The value of damping was found to increase with graphite particle size in both these composites in a manner similar to the increase in wear resistance with graphite size reported for these composites material (6). The damping capacity (measured as Q^{-1}) for copper casting alloy containing 16 vol.% graphite is 3.1×10^{-3} at 200 μm graphite size, and it increases almost linearly to 5.4×10^{-3} at 700 μm size. Similarly Q^{-1} for Al casting alloy containing 20 vol.% graphite is 3.5×10^{-3} at 177 μm graphite size, whereas at 500 μm graphite size, the Q^{-1} value increases to $4.8 * 10^{-3}$. The damping mechanism in these composites appears to be the frictional losses at the interphase boundaries, and the absorption of vibrational energy during the microplastic deformation of the particle itself.

In addition to the volume fraction and size effects of dispersed particles, the damping capacity is also affected by the shape of the particles. Thus in cast irons of about the same composition the damping capacity becomes progressively lower as the shape of graphite is changed from flake to round. This may be possibly due to the larger interphase boundary area in the former where the greater frictional losses at the interfaces could account for higher damping capacity of flake graphite cast irons.

(iii) AL/MICA COMPOSITES - Damping capacity measurements carried out on Al-4 Cu-1.5 Mg alloys containing progressively higher volume percentage of flaky mica particles show (7) a progressive increase in the damping capacity. Figure 5 shows the microstructure of Al alloy mica particle composites. Al mica levels more than 2 wt.% the ratio of specific damping capacity (SDC) and density of these composite materials is greater than that of flake graphite cast irons.

Rohatgi et al. (7) have measured the damping capacity of cast Al alloy-mica particle composites by using the torsion pendulum set up of Fig. 3. The damping tests were carried out at a shear stress level of 1.4×10^6 kg m^2 for Al alloys and $2.10 * 10^6$ kg/m^2 for cast irons (1,3,8).

A typical SEM fractograph of Al-4.5 Cu-1.5 Mg-1.7% mica particle composite produced by a liquid metallurgy technique is shown in Fig. 6. The poor particle matrix bonding evident in this fractograph could be the contributing factor to the high damping capacity of this composite. The (SDC) of mica composite increases linearly with mica percentage (x) according to (% SDC) = 1.5x + 0.42 where x is the weight percentage of dispersed mica (≈ volume percentage of mica since density of mica is close to that of matrix alloy). Figure 7 shows a plot of % SDC vs wt.% for Al/mica composite. The SDC-to-density ratio of some mica composites exceeds that of gray cast iron (having quasi-flake graphite particles) above 2% mica levels. The tensile fracture surface of the composite (Fig. 6) shows some voids around the particles, suggesting a relatively weak particle-matrix band. It is therefore expected that in Al alloy-mica particle composites, there is a greater likelihood of energy dissipation at particle-matrix inter-

face due to void formation or microplastic deformation than within the mica itself. The percent increase in damping capacity with a given volume percentage of 40 μm size flake mica powders is lower than the increase in damping capacity with equal amounts of 350-550 μm spheroidal graphite dispersions. Although the interfacial area is much greater in the former (due to flaky shape of mica), graphite could be more effective for improving damping capacity since its shear strength is twenty times lower (9) than mica and can dissipate lots of energy in microplastic deformation of mica itself

FIBER REINFORCED METAL MATRIX COMPOSITES

Recent studies on several fiber-reinforced MMC's including continuous graphite fiber/Al alloy composites (10-14) produced by diffusion bonding have shown that these composites possess excellent damping properties compared to several conventional structural alloys. Fiber-reinforced MMC's are candidate structural materials for aerospace applications (12) because of their high specific modulus, low coefficient of thermal expansion, high electrical and thermal conductivities, and excellent environmental resistance. For MMC's, damping behavior results from a combined influence of interfaces, and the constituents fiber and matrix materials. Generally, imperfectly bonded MMC's exhibit higher damping capacity than well bonded MMC's. Even at low stress levels, the interfacial disbonds and microcracks provide sites for vibrational energy dissipation, and thereby contribute to improved damping properties of MMC's. Damping at the fiber matrix interface could also occur since dislocations, which are associated with residual stresses generated due to thermal expansion mismatch during fabrication, tend to become mobile. The existence of such dislocation substructures has been actually confirmed by TEM examinations of interfaces in MMC's (10,11).

Several other studies on fiber-reinforced MMC's have confirmed the above correlations between interface character and the dynamic mechanical properties. For example, in one such study (15), room temperature tests of logarithmic decrement on twenty Gr/Al wires were carried out for torsional (Freq. = 0.5 Hz) as well as flexural (Freq. 10-5000 Hz) modes, and the test results correlated well with X-ray diffraction studies of composites. Poor impregnation of Al in graphite fibers resulted in the formation of voids in composite wires which imparted better damping to MMC.

EVALUATION OF DAMPING CAPACITY OF CAST PARTICLE AND FIBER REINFORCED COMPOSITES

A plot of normalized specific damping capacity vs. volume percent second phase is shown in Fig. 8 for several particle filled as well as fiber reinforced metal matrix composites. This plot confirms that for all composite systems shown the normalized SDC increases with volume % second phase.

The room temperature damping capacity data plotted in Fig. 8 show clearly that reinforcement with fibers and particles enhance the damping capacity of the matrix alloy. The damping data from various studies are summarized in Table 1. It can be seen from this table, for example, that as low as 4.4 wt.% graphite powder in Al alloy can give SDC of 6.33%. The SDC of graphite dispersed Al alloys correlates with wt.% graphite by the following linear equation (Fig. 4):

$$\% \text{ SDC} = 0.94 \text{ (wt.\% graphite)} + 2.1115$$

Computation using the above equation suggest that 26 vol.% graphite particle dispersions in Al-Cu alloys give SDC of 21%. This value is much larger compared to the measured SDC (16%) of fiber reinforced composite P100 Gr/Az 91C/Az 313 at equivalent volume percentage of graphite fibers. The above value for particle composites is also larger than SDC of P100 Gr/6061 Al composites containing as high as 34 vol.% fibers. This is also evident from the data on fiber composite shown in Fig. 8. Thus cheaper and more abundant graphite powder can be used instead of costly fibers to achieve higher damping capacity.

From Fig. 8 it is seen that at equal vol. fraction of graphite particles, damping is higher for composites made by Rohatgi et al. (curve 2) than the ones made by Suwa (curve 3). This difference might have been caused by better matrix-particle interfacial bonding in Suwa's system who used Cu and Ni coated particles which would give relatively lower damping compared to Rohatgi et al. data. Furthermore, the coarser (177-900 μm) graphite size used by Suwa et al. in their study as compared to Rohatgi et al. who used relatively finer (150-546 μm) size could have contributed to higher interfacial area at constant volume fraction and higher damping in the latter case as seen in Fig. 8. Another important difference between the two studies is the difference in processing method. While Rohatgi et al. used gravity casting in permanent molds, Suwa employed squeeze casting to synthesize composites. This difference would further change the bonding, void content and the matrix microstructure in the two studies.

One difficulty with quantitative comparisons of SDC of different composite material is the considerable variability in the test condition (frequency, strain amplitude, temperature), the test procedures (flexure, torsion, fatigue etc.), sample size and geometry and processing technique. While damping data available in the literature on composite materials have not been used to generate damping mechanism maps based on normalized test variables to eliminate the above variability in test condition, generalized trends in the damping properties can still be discerned although quantification is difficult. This remains a potentially fruitful

area of research. This paper represents a first attempt to compare the normalized damping properties of different composites produced by different processing methods.

CONCLUSIONS

A comparison of normalized damping capacity of metal matrix composites shows that reinforcement of metal matrices with fibers or particulate can considerably enhance the vibration damping properties of metals. Both particle filled and fiber reinforced alloys show progressive increase in the damping capacity with increasing volume percentage of the filler. However the damping capacity is a strong function of size, shape bonding of the dispersoid and also of the technique of processing of composites. The cast particle composite of Al alloys containing particulate fillers like graphite and mica can have much higher damping capacity compared to several diffusion bonded fiber reinforced composites under conditions used in this study. These cast particulate composites could be potential candidates for vibration insulating applications in consumer industries whereas the costly fiber reinforced composite are economically useful only for application in advanced aerospace structure.

REFERENCES

(1) Adams, R. D. and M. A. O. Fox, J. Iron Steel Inst., 211, 37 (1973).
(2) Rohatgi, P. K., N. Murali, H. R. Shetty and R. Chandrashekhar, Mater. Sci. Engg., 26, 115 (1976).
(3) Fox, M. A. O. and R. D. Adams, J. Mech. Engg. Sci., 15, 81 (1973).
(4) Adams, R. D., J. Sound Vib., 23, 199 (1972).
(5) Onuki, J., K. Soeno and M. Suwa, J. Jpn. Inst. Met., 43, 8 (1979).
(6) Suwa, M., K. Komuro and K. Soeno, J. Jpn. Inst. Met., 42, 1034 (1978).
(7) Nath, D., R. Narayan and R. K. Rohatgi, J. Mater. Sci., 16, 3025 (1981).
(8) Kaufman, J. G., Mater. Des. Engg., 104 (1962).
(9) E. P. Bowden and D. Tabor, "Friction and Lubrication of Solids," Clarendon Press, Oxford, 199 (1974).
(10) S. P. Rawal and M. S. Misra, "Interfaces and Damping in Continuous Gr/Al Composites," Tech. Rep., Martin Marietta Aerospace, Denver, CO (1986).
(11) M. S. Misra and P. D. LeGreco, "Damping Behavior of MMC's," Vibration Damping - 1984, (Workshop Proc.) AFWAL-TR-84-3064, V-1, Nov. 1984.
(12) E. G. Crawley, G. L. Sarver and D. G. Mohr, "Experimental Measurement of Passive Materials and Structural Damping for Flexible Space Structure," in Vibration Damping - 1984, (Workshop Proc.), AFWAL-TR-84-3064, A-23.
(13) M. S. Misra, "Metallurgical Characterization of Interfaces and the Damping Mechanism in MMC's," Martin Marietta Aerospace Co., AS-Al 69186/R/WS, Apr. 1986.
(14) "High strength, high abrasion resistant vibration damping Mg alloy composites," Nissan Motor Co. Ltd., Jpn Patent No. 8247843 (Chem. Abstr. No. 97-7720g).
(15) G. F. Lee and C. W. Anderson, "Vibration Damping Workshop Proceedings," Naval Surface Weapons Center, Long Beach, California, Feb. 1984, AD-P004, 703/5/WMS, Nov. 1984.



Fig. 1. Damping test specimen used for graphite and mica particles dispersed Al alloys.

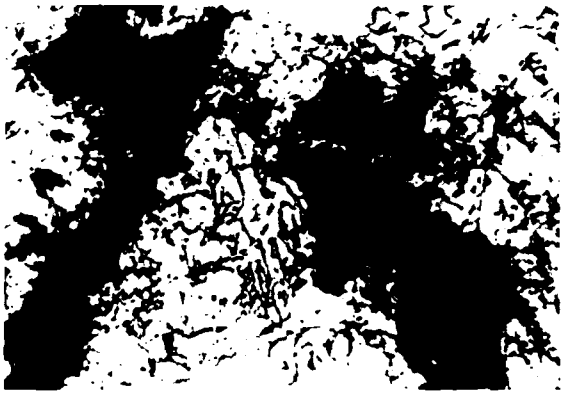


Fig. 2. Microstructure of cast Al-2.08 Cu-0.42 Si-2.05 graphite alloys (x 200).

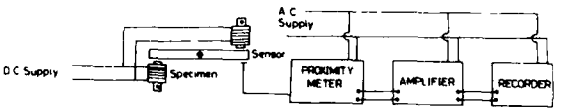


Fig. 3. Schematic of damping test device used for particulate composites.

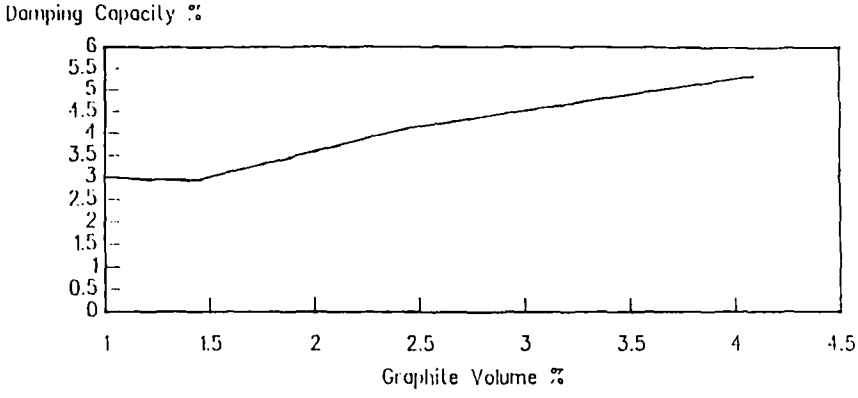


Fig. 4. % SDC vs. vol.% graphite for cast Al-alloy-graphite particle composites.



Fig. 5. Microstructure of cast Al alloy-mica particle composite (Arrows indicate mica particles) (x 210).

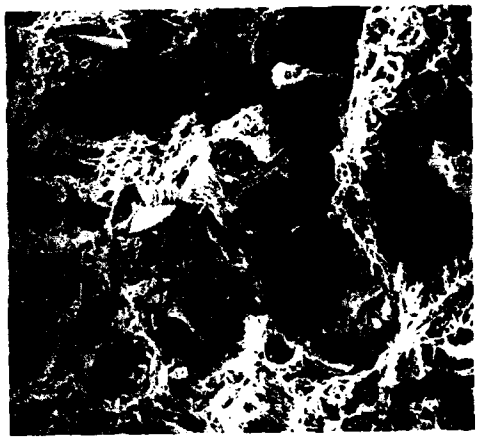


Fig. 6. Tensile fracture surface of Al-alloy-mica particle composite (X 80).

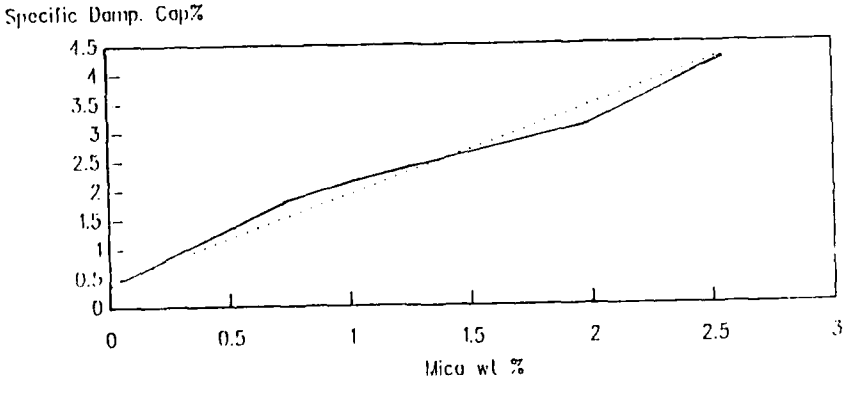


Fig. 7. % SDC vs. wt.% mica for Al alloy-mica particle composite (--- Expt, ... Theory).

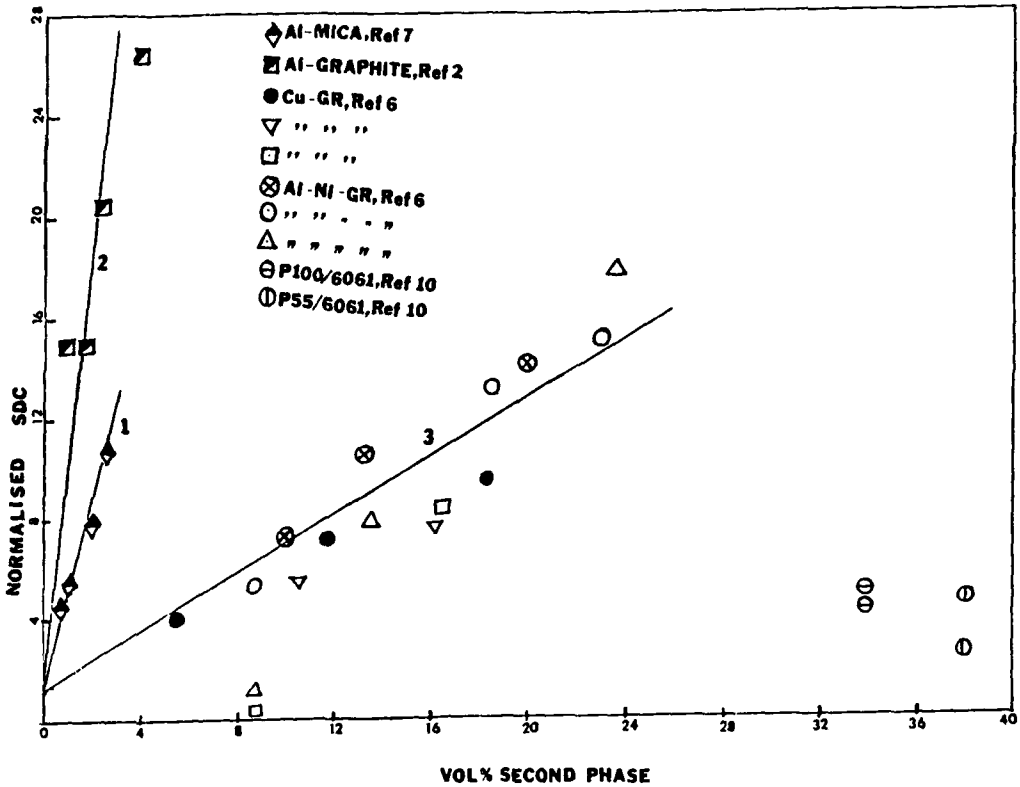
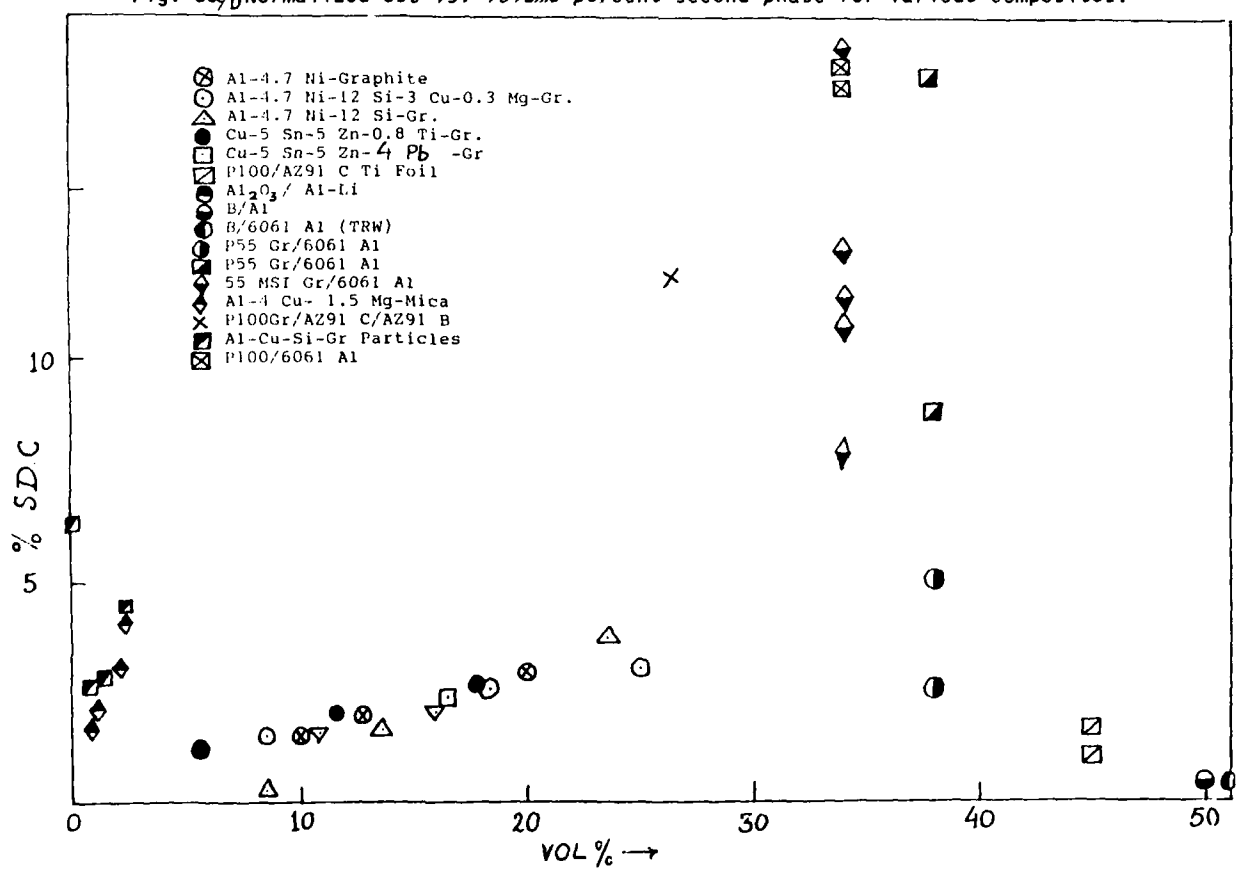


Fig. 8a/b Normalized SDC vs. volume percent second phase for various composites.



CORROSION OF METAL MATRIX COMPOSITES

T. Otani
Komatsu Ltd., Japan

B. McEnaney, V. D. Scott
School of Materials Science,
University of Bath, Bath, BA2 7AY UK

INTRODUCTION

Although published studies concerning the corrosion behaviour of metal matrix composites (MMCs) are few, all have stated that MMCs suffer more severe attack than the respective non-reinforced metals. Several reasons have been given for the degradation including galvanic corrosion between fibre and matrix (1,2), galvanic corrosion between any intermetallic compounds and matrix (3), preferential attack on carbon diffused from fibre into matrix (4), and an increase in the number of anodic sites at interfaces (5). Clearly, the variety of explanations stem from the different fibre/matrix combinations investigated and their different fabrication methods. In this paper, results obtained using a double cyclic polarisation (DCP) technique, an accelerated test, to study the corrosion behaviour of MMCs are compared with those given by a simple, long-term immersion (LTI) test. The electrochemical data are complemented by microstructural analysis and the combined information used to compare the corrosion behaviour of several fibre-reinforced aluminium alloys immersed in a 3.5% NaCl solution.

EXPERIMENTAL METHODS

MATERIALS - Two matrix metals have been studied: commercially pure aluminium and an Al-Si-Mg alloy referred to here as 357. The effect of two types of reinforcement have been investigated: firstly alumina, a short fibre of 100μm length and 3μm diameter (Saffil); secondly continuous silicon carbide fibres of 15μm diameter (Nicalon). The fibres were made into preforms and incorporated in the metal matrix using a liquid metal infiltration technique. All specimens were studied in the as-fabricated condition. The chemical composition of metal matrices are given in Table 1 together with the fibre volume fraction. Note the high impurity level of some of the MMCs.

POLARISATION TEST - Polarisation measurements were carried out in an all-glass cell, electrode potentials being measured with a saturated calomel electrode (SCE) using a Luggin capillary technique. The test solution, 3.5% NaCl, was made from reagent-grade NaCl and distilled water. It was kept constant at 25±0.5°C and oxygen-free nitrogen gas was bubbled through the solution prior to and during the test. Specimens were first mounted in an epoxy resin and polished using 6μm diamond paste; electrical contact was made with a copper wire insulated by PTFE. They were held in the test solution 10 minutes before applying the potential in order to establish stable corrosion conditions. A double cyclic polarisation (DCP) method was adopted with the potential sweep controlled by a computer. A sweep rate of 20mV/min was used, each test being repeated at least three times.

IMMERSION TEST - The experimental conditions (specimen and solution) were the same as for the polarisation test. The open circuit potential was recorded as a function of time over a period of three weeks. Weight loss measurements were carried out on unmounted specimens immersed for the full three week period, the corrosion products being removed by scrubbing the specimens with a bristle brush and dipping them into 10% nitric acid for 10 minutes.

MICROSTRUCTURAL ANALYSIS - Specimens were examined before and after corrosion by scanning electron microscopy (SEM). The corroded areas of samples were measured quantitatively using an image analyser. Electron-probe microanalysis (EPMA), with an energy-dispersive spectrometer fitted to the SEM, was used to identify the different constituents present in specimens, including the composition of corrosion products. The EPMA technique was adopted also to measure the thickness of oxide film. This involved recording the oxide x-ray emission intensity from the specimen and comparing it with that from a standard pure alumina. The intensity ratio was then converted into oxide film thickness using the correction procedure developed by Love and Scott (6).

RESULTS

NON-REINFORCED METALS - The aluminium samples possessed a typical cast structure with a large grain size. 357 alloy (Fig.1) contained a large amount of eutectic consisting of almost pure silicon and pure aluminium, together with needles identified by EPMA as $FeSiAl_5$, the magnesium in this alloy was found to be located mainly near the needles although its concentration was very low.

A typical polarisation curve obtained on 357 alloy is shown in Fig.2. The corrosion potential, the pitting potential (pits initiate above this potential) and the protection potential (pits do not initiate but existing pits propagate above this potential) are indicated in the diagram; the hysteresis area is shaded. Polarisation data from aluminium and 357 alloy are given in Table 2 and plotted in Fig.3. It may be seen that the corrosion potential of 357 alloy is more positive than that of aluminium but that the pitting potentials are nearly the same. The hysteresis area (HA) and the difference potential (DP), Epit-Eprot, of 357 alloy are greater than those of aluminium, both parameters corresponding to the speed of corrosion propagation. The observation that the corroded area of 357 alloy is about twice as large as that of aluminium (Table 2) is in accord with this. Corrosive attack on aluminium and 357 alloy during the DCP test was highly localised, showing crystallographic pits on the former (Fig.4) and preferential attack on the aluminium regions of the eutectic in the alloy (Fig.5). The latter results from the difference in corrosion potential between aluminium (-0.85V) and silicon (-0.26V) (7). in that aluminium acts as anode and silicon acts as cathode. The thickness of oxide film on aluminium and 357 alloy was estimated to be 3nm using the EPMA technique, compared with 2.6nm of residual oxide measured on the polished surfaces before the corrosion experiment.

The change in potential of specimens during the LTI tests (Fig.6) shows that pits are initiated in aluminium and 357 alloy upon immersion. After a period of one day, the potential decreases suddenly to give the bare metal potential (-1.2V) (8) as a consequence of the destruction of cathodic sites. The weight loss of 357 alloy was 5.6g/m2 compared with the 3.0g/m2 on aluminium, as expected form the polarisation data. The characteristics of the LTI test were similar to those of the DCP test except that much thicker oxide films were produced on the former (120nm thick as measured by the EPMA technique) together with large corrosion particles, Fig.7 and 8. These thick oxide films have a high ionic conductivity and are less protective because they may be considered as hydrated oxides containing up to 30% water.

ALUMINA REINFORCED METALS - The microstructure of Saffil-reinforced aluminium is illustrated in Fig.9. It may be seen that the eutectic phase, which was found to consist of a mixture of FeAl6 and aluminium, segregated around fibres, Similar segregation effects have been found in cast aluminium alloys reinforced with Borsic fibres (9). It was deduced that during the MMC solidification process the primary aluminium dendrites were nucleated between fibres and, as they grew, solute was rejected ahead of the solidification front until the solute levels were such that second phases were formed in the region of the fibre/matrix interface. In 357/Sfl, it was found that the eutectic phase, a mixture of aluminium and silicon was segregated around the fibres (Fig.10). The effect of the fibre on the microstructure of 357/Sfl is to reduce the scale of silicon segregation compared with 357 alloy. This may be attributed to disturbance of the eutectic growth by the fibre. The white needles in Fig.10 were found to be rich in iron and were identified as FeSiAl5; much more of this phase was found in the reinforced 357 alloy, Table 1.

Measured potentials are given in Table 2 and HA and DP are plotted in Fig.3. The greater anodic pitting potential of Al/Sfl indicates that it is more difficult to initiate pits in this material but, once they do, the growth is greater as shown in the larger values of HA and DP. The corroded surface of Al/Sfl, Fig.11, shows the attack is concentrated on the eutectic phase; in some regions it is very deep and reveals crystallographic features. Such localised attack may be attributed to the difference of corrosion potential between aluminium (-0.85V) and FeAl6 which is close to the value of -0.56V published for FeAl3 (7). Corrosive attack of 357/Sfl is highly localised at Al-Si eutectic regions (Fig.12), exposing the fibres. Fibres which are remote from the eutectic are, however, not attacked. As seen in Table 2, the corroded area of 357/Sfl produced by the DCP test is similar to that of 357 alloy although the size of pits on 357/Sfl is much smaller. Thus pit size is closely related to the size scale of silicon segregation as expected. The interesting point which emerges from a comparison of Fig.11 and 12 is that the FeAl6 phase (in Al/Sfl) is strongly attacked while the FeSiAl5 phase (in 357/Sfl) is not.

Potential changes measured in LTI tests (Fig.13) show that both curves differed from those obtained from non-reinforced metals, cf Fig.6 Al/Sfl exhibits a more marked potential change after approximately one day's immersion which is followed by some peaks, possibly associated with detachment of corrosion products. The abrupt potential change of 357/Sfl occurred much sooner, after just one hour's immersion. The corroded surface of Al/Sfl is seen to be covered with very thick oxide film, Fig.14, greater than 250nm which is the upper limit of EPMA technique. Over much of the surface, the oxide film is broken away to show substrate material with evidence of enhanced attack in the eutectic regions. A similar oxide film was formed on 357/Sfl, with deep pits. Attempts to measure weight loss were made but with little reproducibility. Some samples showed, in fact, weight grains despite the use of 10% nitric acid found successful for removing corrosion products on non-reinforced metals. It appeared that much of the corrosion product remained attached to the materials and that this was helped by the presence of fibres.

With regard to 357/Smx, its microstructure was similar to that of 357/Sfl except for the smaller amount of FeSiAl5 reflected in the different level of iron. Pitting and protection potentials (Table 2) and the values of HA and DP (Fig.3) are also nearly the same as those of 357/Sfl. These observations support the above findings in which the iron impurity did not strongly effect the corrosion behaviour of composite materials based upon 357 alloy.

SiC REINFORCED METALS - The microstructures of the SiC reinforced metals are shown in Figs.15 and 16. Al/SiC contains the eutectic mixtures of FeAl6 and aluminium which tend to be located around fibres like the eutectic of Al/Sfl. In (357/SiC)a, however, the silicon does not appear as the Al-Si eutectic but as almost pure silicon rods which are hardly visible in the SEM micrograph. The white needles in Fig.16 consist of FeSiAl5 as found in 357/Sfl.

DCP test data, Table 2 and Fig.3, show that the HA and DP values of Al/SiC are very similar to those of Al/Sfl, whilst the HA and the DP of (357/SiC)a tend to be larger than those of 357/Sfl. The major sites of attack in Al/SiC took place at the eutectic phase (Fig.17) as noted previously in Al/Sfl. These observations suggest that the presence of the FeAl6 phase dominates the corrosion behaviour of Al-based composite material and that the affect of the fibre is much less significant. Moreover, the corrosion mode of (357/Sic)a may be divided into two types: deep pits in the matrix

close to clusters of fibres (Fig.18) and shallow pits in the matrix between fibres (Fig.19). Both types of corrosion are, however, affected by silicon segregation and the FeSiAl5 needles not only resist attack but also act as a physical barrier to pit propagation. The fibres themselves also appear to act as physical barriers.

Potential changes measured in the LTI tests show high stability throughout the three week period (Fig.20). The corroded surface of Al/SiC (Fig.21) is covered with a severely cracked oxide film with a duplex structure (67nm and 225nm thick respectively).

The relation between (357/SiC)a and (357/SiC)b appears the same as that of 357/Sfl and 357/Smx.

DISCUSSION

ASSESSMENT OF CORROSION TEST METHOD - With regard to the corrosion of non-reinforced metals, there is good correlation between specimen weight losses incurred in the long-term immersion (LTI) tests and difference potentials (DP), Epit-Eprot, as measured in the double cyclic polarisation (DCP) experiments (Fig.22). Furthermore, the corrosion modes are the same in LTI and DCP tests. Thus, we conclude that the corrosion behaviour of the metal can be predicted from the DCP test data, in particular DP values as argued in an earlier paper (10). A second DCP parameter, hysteresis area (HA), also shows some correlation with weight loss, Fig.22 although at this stage of technique development it appears not to be as satisfactory for prediction purposes. The possibility of using the measurement of corroded area was also investigated since the prospects of applying a computer-controlled image analysis method were attractive. Certainly, the method seems to be promising when applied to samples where the corrosion mode was the same.

As far as MMCs are concerned, the situation is not so clear. As mentioned before, errors produced in weight loss measurements were high due to entrapment of corrosion product on the material surface and a more suitable etchant is needed. This problem makes it difficult to assess the usefulness of DCP data obtained on MMCs.In our view, however, DP values may nevertheless provide a useful way of assessing corrosion susceptibility of complex structures such as MMCs: certainly, they would be adequate for placing different MMCs systems in ranking order. Possibly, HA data may also be useful, although further work is needed here. The prospects for developing a technique of image analysis of the corroded area are, however, not so good due to the fact that the depth of pits was found to be unpredictable in MMC systems and the area could not, therefore, be directly correlated weight loss.

CORROSION BEHAVIOUR OF MMCs - We have found no evidence to show that the corrosion of aluminium and its alloys is accelerated by the presence of either alumina or silicon carbide (SiC) fibres. This finding is not inconsistent with published data on SiC reinforced aluminium alloys (11). The fibre does, however, play a secondary role as far as MMC corrosion characteristics are concerned, either by acting as a relatively inert physical barrier to the development of a corrosion pit or by modifying the microstructure of the matrix metal.

The major influence on the corrosion behaviour of the MMCs studied here was the microstructure and composition of the metal matrix. This is exemplified in the silicon and iron-containing aluminium and its alloys. The presence of a large quantity of second phase such as FeAl6 with its much more positive corrosion potential produces a strong microgalvanic corrosion effect. Such segregation of second phase is, of course, a common feature of the casting process as adopted in the manufacture of the present MMCs and clearly, efforts should be directed towards some form of remedial action, such as improving the quality of the metal and/or the subsequent application of homogenizing treatments.

In connection with the marked effects on corrosion caused by the FeAl6, it was interesting to discover that iron did not have degrading effect on 357 alloy. In this material there was sufficient silicon present to form FeSiAl5 rather than FeAl6 and the ternary phase was not severely attacked. There was an indication also that 357 alloy (Al-Si-Mg) with its Al-Si eutectic segregation suffered greater attack than metal containing iron and silicon together.

Finally, it is suggested that when choosing MMC systems for use in corrosive environments a matrix alloy should be adopted which contains elements such as magnesium or zinc with a more negative corrosion potential in order to reduce localised attack on any second phases present.

ACKNOWLEDGEMENT

The authors gratefully acknowledge Mr RL Trumper for providing materials and helpful advice.

REFERENCES

(1) D.L. Dull, W.C. Harrington, Jr., and M.F. Amateau, Vol.1, pp399-, Air Force Materials Laboratory Report AMFL-TR-75-42, Dayton, OH (1975).
(2) M.G. Vassilaros, D.A. Davis, G.L. Steckel, and J.P. Gudas, Proc. Tri-Service Confereence on Corrosion, US Air Force Academy, Colorado, November 1980, Vol. II, pp335-.
(3) S.L. Pholman, Corrosion, 34, 156 (1978).
(4) D.M. Aylor and P.J. Moran, J. Electrochem. Soc.132, 1277 (1985).
(5) A.J. Sedriks, J.A.S. Green, and D.L. Novak, Metall. Trans., 2, 871 (1971).
(6) G. Love and V.D. Scott, private communication.
(7) "Metals handbook 9th edition", Vol.2, ASM.
(8) G.W. Akimov, Corrosion, 11, 515 (1955).
(9) M.E Saggese, V.D. Scott and R.L. Trumper, J. Mat. Sci. Technol., in press.
(10) B.E. Wilde and E. Williams, Electrochemical Acta, 16, (1971).
(11) P.P. Trzaskoma, E. McCafferty and C.R. Crowe, J. Electrochem. Soc., 130, 1804 (1983).

Table 1. Materials

Designation	Chemical composition of matrix metals	Vf %
Al	99.99 Al	0
357	7.22 Si, 0.38 Mg, 0.05 Ti, 0.13 Fe, rem.Al	0
Al/Sfl	0.55 Fe, 0.16 Cr, 0.14 Ni, rem.Al	18
357/Sfl	7.22 Si, 0.38 Mg, 0.05 Ti, 0.32 Fe, 0.16Cr, 0.14 Ni, rem.Al	18
357/Smx	Not yet available	20
Al/SiC	0.32 Fe, 0.16 Cr, 0.14 Ni, rem.Al	50
(375/SiC)a	7.22 Si, 0.38 Mg, 0.05 Ti, 0.32 Fe, 0.16 Cr, 0.14 Ni, rem.Al	50
(357/SiC)b	Not yet available	50

Sfl = Saffil; Smax = Safimax

TABLE 2. Corrosion data (DCP tests)

	Al	357	Al/Sfl	357/Sfl	357/Smx	Al/SiC	(357/SiC)a	(357/SiC)b
Ecor(mV)	-975	-889	-806	-844	-1037	-776	-825	-779
Epit(mV)	-732	-711	-676	-756	-761	-690	-730	-706
Eprot(mV)	-768	-776	-749	-722	-771	-758	-783	-759
CA(%)	3.4	7.2	5.1	8.1	-	3.1	7.9	-
MD(μm)	170	240	80	80	-	44	66	-

CA = Corroded area: MD = Mean diameter



Fig.1.

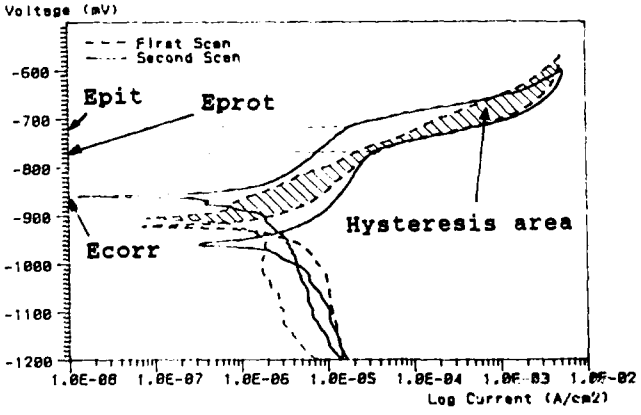


Fig.2.

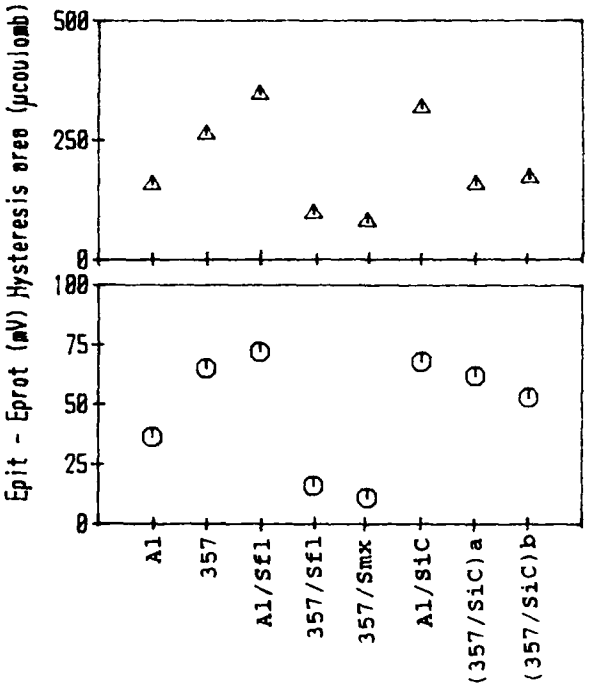


Fig.3.

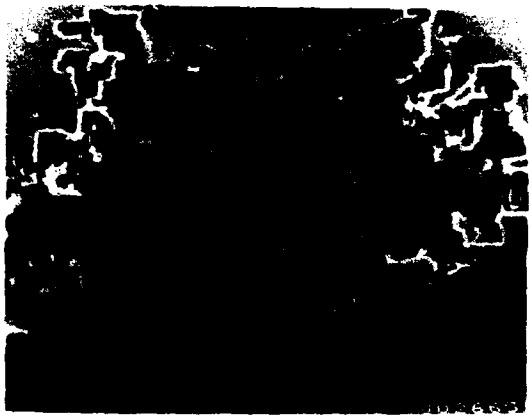


Fig.4.

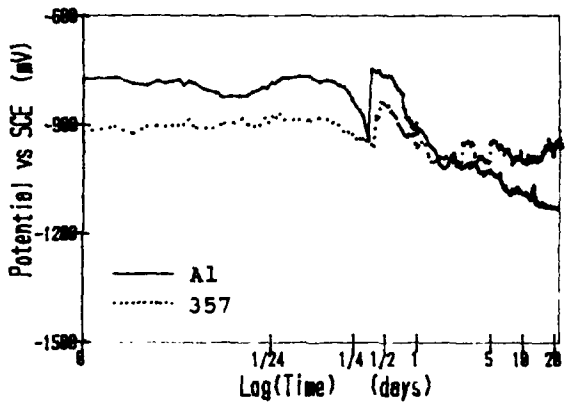


Fig.6.

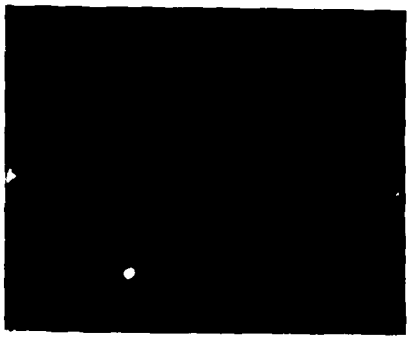


Fig.5.



Fig.7.



Fig.8.



Fig.9.

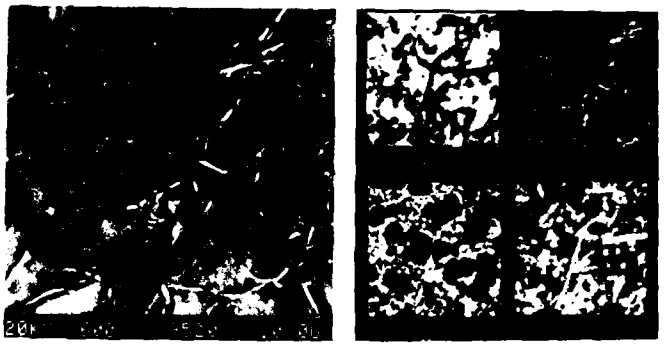


Fig.10.



Fig.11.

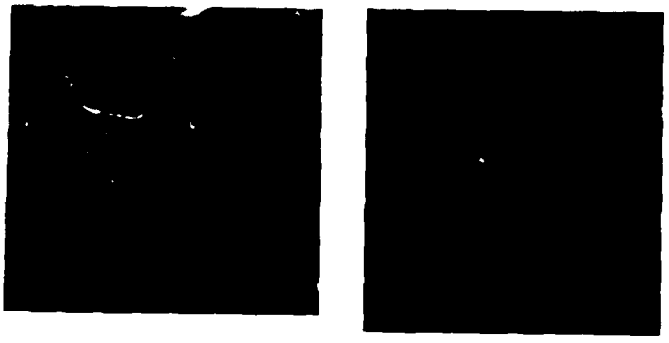


Fig.12.

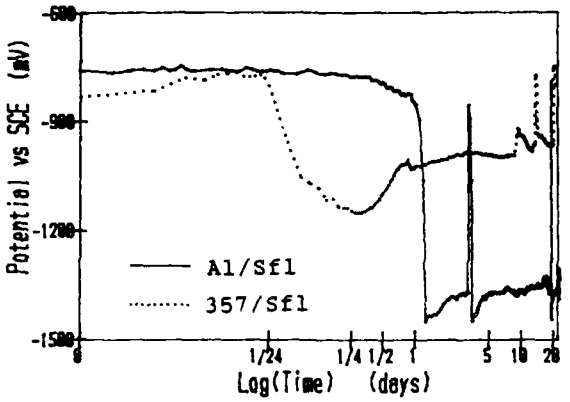


Fig.13.



Fig.14.

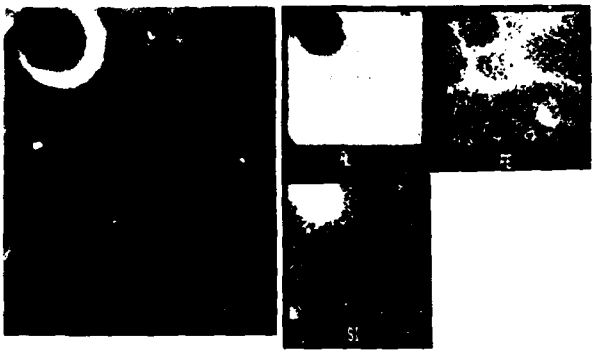


Fig.15.



Fig.16.



Fig.17.



Fig.18.



Fig.19.

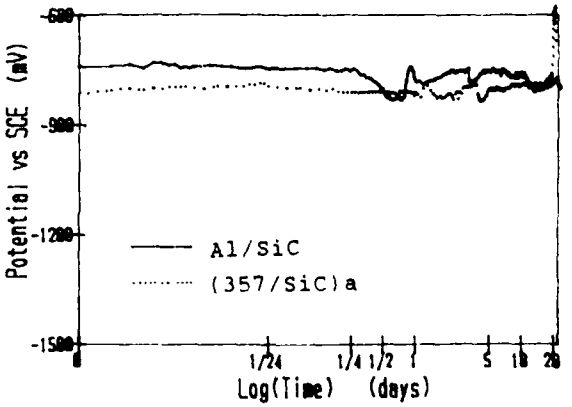


Fig.20.



Fig.21.

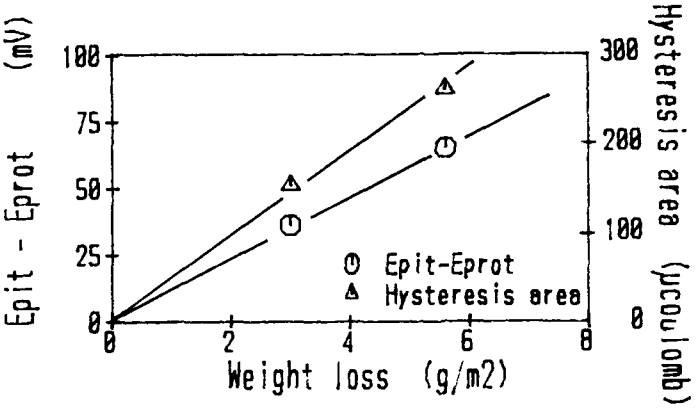

Epit - Eprot (mV)
100
75
50
25
0
0
2
4
6
8
Weight loss (g/m2)
300
200
100
0
Hysteresis area (μcoulomb)
Epit-Eprot
Hysteresis area

Fig.22.

MICROMECHANISM OF HIGH SPEED ABRASIVE WATERJET CUTTING OF CAST METAL MATRIX COMPOSITES

P. K. Rohatgi, N. B. Dahotre, S. C. Gopinathan, D. Alberts, K. F. Neusen
University of Wisconsin-Milwaukee, Milwaukee, Wisconsin 53201 USA

ABSTRACT

Micromechanisms of the abrasive waterjet cutting characteristics of cast metal matrix composites have been investigated in this paper. Specifically cutting characteristics of Al-2014-SiC particle composite and Dural Al-357-SiC particle composite by water-garnet streams have been examined. The composites were prepared using conventional casting techniques. The abrasive waterjet cut surfaces were examined under optical and scanning electron microscopes in order to study the nature of the surfaces generated, and to understand the mechanism of cutting and removal of composites. Several combinations of waterjet cutting conditions were used to cut each material. The waterjet traverse speed, which was controlled by a robotic positioner, was varied from approximately 12.7 to 254 mm/min (0.5 to 10 inch/min). The stand-off distance of 2.54 mm was maintained and 80 mesh size garnet particles were used as an abrasive material.

INTRODUCTION

INTEREST IN THE METAL MATRIX composites has grown in the past few years due to their high strength, high modulus and several other tailored properties not obtainable in monolithic materials. Silicon carbide reinforced cast aluminum alloy, for example, compared to the unreinforced base metal, exhibits higher strength, higher stiffness, reduced thermal expansion coefficient (1) and improved wear and abrasion resistance (2). The presence of hard silicon carbide particles in Al-alloy-SiC composite presents difficulties in machining by conventional methods such as milling and sawing. The presence of hard silicon carbide particles leads to very rapid tool wear. Consequently, even though the cast base metal is easily machined by conventional methods, machining the composites with these methods result in frequent and expensive tool changes, as well as excessive time required to complete the job.

Abrasive waterjet cutting seems to be a viable choice forming parts out of metal matrix composites. The abrasive particles entrained in the continuous high-velocity waterjet do the machining, and there is no need to halt to replace a dull tool. No heat affected zone (HAZ), unlike in laser cutting is produced when parts are cut by waterjet. This is specially important for composites where deleterious reactions can occur at the interfaces due to heat pulses. Airborne dust is virtually eliminated. The jet can pierce the stock and thereby enables cuts to be started away from the edges. A small diameter jet has inherent omnidirectional cutting potential and this makes it a logical candidate for integration with a robotic system.

Abrasive waterjet cutting as a technology with commercial application has a relatively short history. It is a complicated event involving several parameters together. Very limited studies have been reported on waterjet cutting of different materials, especially composites. M. Hashish (3,4) first reported the results on cutting of steel and concrete with abrasive waterjet which established the range of cutting parameters for these two materials. Similar results were reported by Saunders (5) for steel and rock. Hashish further extended the research on optimization criteria for selecting abrasive waterjet parameters for aluminum and titanium (6). A study of piercing performance of abrasive waterjets on aluminum, steel, super alloys and ceramics was conducted by Hunt et al. (7). The quality of cut surfaces produced by abrasive waterjets varies significantly with the choice of cutting parameters. A model for the production of surface finish was presented by Tan (8).

EXPERIMENTAL SETUP

High pressure water to produce the waterjet was provided by a dual intensifier pump at pressures up to 379 MPa (55,000 psi). For this series of experiments, the high pressure water

was admitted to a 0.33 mm (0.013 inch) sapphire nozzle to create the waterjet. This jet was directed into an induction chamber where abrasive particles were entrained and then to a 1.19 mm (0.067 inch) tungsten carbide nozzle/ mixing tube.

Water velocities up to 750 mps (2500 fps) are produced at the sapphire nozzle exit. Abrasive particles are accelerated to an estimated 450 mps (1500 fps) in the tungsten carbide nozzle. The rate of abrasive flow is controlled by a calibrated restriction attached to a hopper. All of the present experiments were carried out using # 80 mesh garnet as the abrasive. A five axis, 6 kg robot was used to control the abrasive waterjet positioning. The robot's point to point velocity control also provided the required range of constant traverse speeds. In this study, the stand off distance was 2.54 mm and the materials used in this study are shown in Table 1.

Table 1. List of Materials

Matrix	Reinforcing Material and wt.%
Al-2014 (0.8% Si, 4.4% Cu, 0.8% Mn, 0.4% Mg)	None
Al-2014	SiC Particles, 20%
Al-357 (7% Si, 0.5% Mg)	None
Dural (Al-357 + SiC)	SiC Particles, 15%

Prior to using the garnet for cutting, chemical analysis data and scanning microphotographs were obtained for this mineral. The chemical compositions are given in Table 2.

Table 2. Nominal Composition of Garnet (percent of elements)

Location	Al	Si	Ca	Mn	Fe
Surface (from SEM)	13.8	43.2	4.0	3.6	35.4
Bulk (from Supplier)	19.3	19.9	0.0	3.0	57.8

The difference in the surface and bulk analysis could be due to surface segregation and absorption of species. Figure 1 shows the scanning microphotograph of garnet particles indicating the angular nature of the abrasive. The iron and silicon images confirm the presence of these elements in garnet.

The silicon carbide used to produce the composites was also examined separately. Figure 2 shows the scanning microphotograph and the silicon image of the SiC particles that were dispersed in the Aluminum 2014 alloys. Since both garnet and SiC contain silicon, the presence of iron makes it possible to distinguish between the two types of particles.

SURFACE ROUGHNESS

The measurement of the surface roughness is done using a moving stylus profilometer. In the present measurements, the arithmetic mean values of the roughness were obtained at several locations on each cut surface. Figure 3 shows a typical cut surface generated by the abrasive waterjet. It is clear from this photograph that the cut surface generates two distinct regions of different roughness. The upper region has relatively smoother surface compared to the lower region. The ratio of the height of upper region (h_1) to the height of lower region (h_2) decreases as the traverse speed increases (Figures 4 and 5) for both the matrix alloys as well as both the composites studied. The nature of cut surface and its division into two distinct regions of roughness are indicative of mechanism involved in abrasive waterjet cutting. As explained by Hashish (9) the top portion of the cut surface is subjected to particle erosion at shallow angle due to a coherent waterjet. As the jet travels further down it looses coherency and bottom portion of the surface undergoes erosive wear at large angles of attack. When the kinetic energy in the particles drops below the level after which they are not able to penetrate the material, they get deflected upward. After deflection, the particles are in contact with top portion which undergoes erosive wear at somewhat larger angle of attack. Predominately this repeated wear and principally shallower angle of erosion of top portion results in smoother surface compared to bottom portion. As the traverse speed of waterjet increases, its time of interaction with material decreases and this leads to decrease in the ratio (h_1/h_2). Tables 3 and 4 give the arithmetic mean values of the roughness in top and bottom region of waterjet cut samples of Al-2014, Al-2014-SiC composite and Al-357, Dural composite respectively.

DEPTH OF CUT

When the abrasive waterjet was applied to very thick pieces of stock, for a given traverse speed a maximum depth of cut is achieved. Figure 6 is a photograph of a sample showing the extent of the depth of cut produced for different traverse speeds. The relationship between depth of cut and traverse speed for Al-2014, Al-2014-SiC composite and Al-357, Dural composites is shown in Figures 7 and 8 respectively. In all cases the depth of cut increases as the

Table 3. Surface Roughness Data for Waterjet Cut Al-357 and Dural Composite

Sample	Cutting Speed (mm/sec)	Surface Roughness (microns) Top	Bottom
	5	4.45	5.08
Al-357	4	5.08	5.00
	3	4.83	6.22
	5	4.82	5.59
Dural	4	4.06	4.83
	0.5	3.81	3.81

Table 4. Surface Roughness Data for Waterjet Cut Al-2014 Composite and Al-2014-SiC

Sample	Cutting Speed (mm/sec)	Surface Roughness (microns) Top	Bottom
	1	4.72	4.94
Al-2014	2	4.96	5.10
	3	5.93	6.86
	1	4.72	5.25
Al-2014 + SiC	2	4.90	7.22
	3	6.44	7.98

traverse speed decreases. This may be again due to the longer duration of interaction of waterjet with the material being cut. At lower traverse speed, the erosion of material by abrasive particles is carried out repeatedly for relatively longer time and this results in having deeper cuts. Figures 7 and 8 also illustrate that for a given traverse speed, base alloys (Al-2014 and Al-357) produce deeper cuts than the respective composites of the same alloys containing silicon carbide particles. The incorporation of SiC particles into Al-alloy matrices make them difficult to cut. The abrasive particles have to loose most of their kinetic energy in producing shallow cuts in these composites. The depth of cut in Al-alloy-SiC particle composites also depends on such factor as strength of the particle-matrix interface. If this interface is not strong enough, the reinforced particles may come loose easily and they will participate in the erosion process along with abrading particles. This probably will lead to the cut as deep as in base alloy or even higher. In the present study, the reduction in maximum depth of cut in SiC containing samples is an indirect reflection of good bonding at the particle matrix interface.

SCANNING ELECTRON AND OPTICAL MICROSCOPY

Scanning micrographs of abrasive waterjet cut surface of Al-357 and Dural composite are shown in Figures 9 and 10 respectively. These micrographs show that individual garnet particles lodged at the end of the final wear tracks. The garnet particles are lodged at the end of the track, apparently after their kinetic energy drops below the level needed to permit further movement of the particles. In certain cases, the morphology of the lodged particles appears to be different from the morphology of the starting garnet particles. This could be due to fragmentation and wear of garnet particles in the process of waterjet mixing and cutting. The geometry of some wear tracks preceding the lodged garnet particle correspond to the contour of the particles lodged at the end of the track. This is indicative of the fact that, that particular particle in the field of view was responsible in at least some portion of the wear track in the particular field of view. The elemental analysis done by scanning electron microscope on Al-357 and Dural composite cut surfaces (Figures 9 and 10) delineates the presence of iron in them. This suggests the presence of garnet on the cut surface.

The waterjet cut edge of Al-357 and Dural composite were observed under an optical microscope (Figures 11 and 12 respectively). They indicate that on microscopic scale the profile is rough for both. The width of cut seems to be larger in Al-357 compared to the Dural composite. The material seems to be opened via microcracks in interdendritic region produced due to the impact of abrasive particles. In case of composite sample, SiC particles seem to have been retained, eroded or dislodged.

SUMMARY

1. The abrasive waterjet cut surface produces two distinct zones of roughness on the cut surface in the matrix as well as in the composite material. Top region is considerably smoother compared to bottom region which is much rougher. The ratio of height of smooth region to rough region decreases as the traverse speed increases for both the matrix and composite materials.
2. The depth of cut increases with decreasing traverse speed in both the matrix alloys

as well as the composite. For a given traverse speed, the depth of cut is greater in base alloy than in the composites studied.

3. The existence of iron on the waterjet cut surfaces, as reflected by SEM is due to the presence of garnet particles which were lodged onto the abrasive waterjet cut surface at the end of wear tracks.

ACKNOWLEDGEMENTS

We gratefully acknowledge the support of the General Motors Corporation, BOC Division and Office of Naval Research for partial support of this research work. We thank Mr. C. Vaidyanathan for conducting some part of this experimental work. We also extent our gratitude to Norton Company for the SiC, Dural for aluminum-silicon carbide composite, Flow Systems Inc., for the Abrasive Waterjet Cutting Machine.

REFERENCES

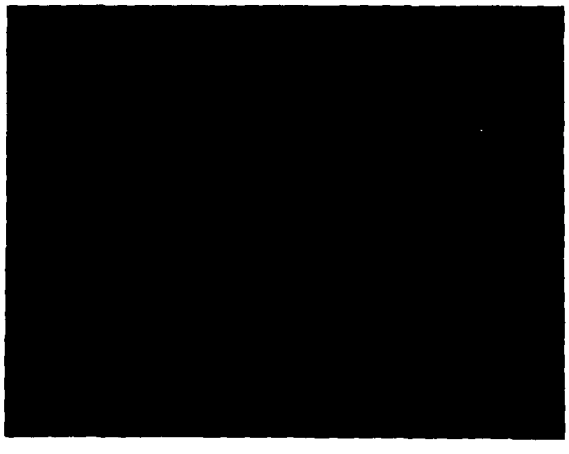
1. Dural Aluminum Composites Corporation; Technical Marketing Department, San Diego, CA 92121 (1987).
2. Hosking, F. M., F. Folgew Portillo, R. Wunderlin and R. Mehrabian, J. Materials Sc., 17, 477-498 (1982).
3. Hashish, M., Proceedings of 6th International Symposium on Jet Cutting Technology, BHRA Fluids Engineering, Cranfield, Bedford, England, 465-87 (1982).
4. Hashish, M., Proceedings of 6th International Symposium on Jet Cutting Technology, BHRA Fluids Engineering, Cranfield, Bedford, England, 447-63 (1982).
5. Saunders, D. H., Proceedings of 6th International Symposium on Jet Cutting Technology, BHRA Fluids Engineering, Cranfield, Bedford, England, 503-518 (1982).
6. Hashish, M., Proceedings of 8th International Symposium on Jet Cutting Technology, BHRA Fluids Engineering, Cranfield, Bedford, England, 297-308 (1986).
7. Hunt, D. C., T. J. Kim, and J. G. Sylvia, Proceedings of 8th International Symposium on Jet Cutting Technology, BHRA Fluids Engineering, Cranfield, Bedford, England, 287-296 (1986).
8. Tan, D. K. M., Proceedings of 8th International Symposium on Jet Cutting Technology, BHRA Fluids Engineering, Cranfield, Bedford, England, 309-313 (1986).
9. Hashish, M., Proceedings of 7th International Symposium on Jet Cutting Technology, BHRA The Fluids Engineering Center, Cranfield, Bedford, England, 249-265 (1984).



Fig. 1. SEM of #80 mesh garnet, 100x.



(a) Scanning microphotograph, 1000x.



(b) Silicon image, 1000x

Fig. 2. SEM of #400 mesh silicon carbide.



Fig. 3. Typical waterjet cut surface showing the smooth and rough regions.

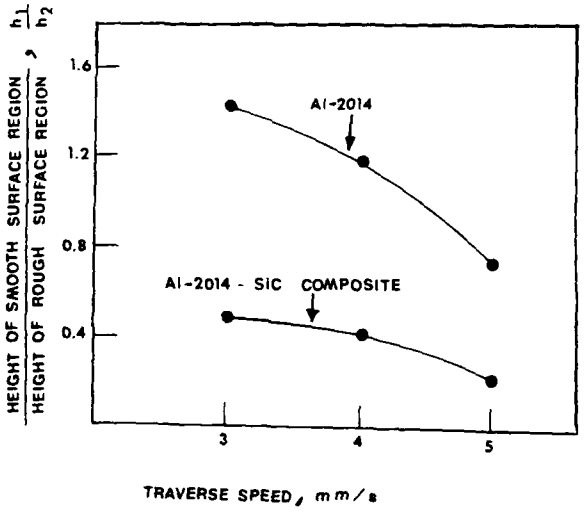


Fig. 4. Traverse speed versus h_1/h_2 ratio for Al-2014 and Al-2014-SiC composite.

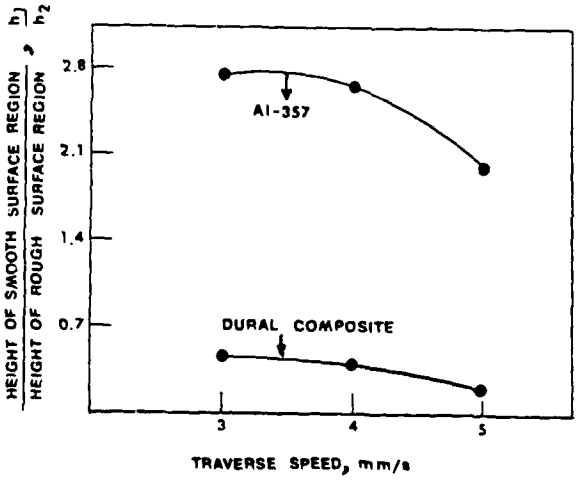


Fig. 5. Traverse speed versus h_1/h_2 ratio for Al-357 and Dural composite.

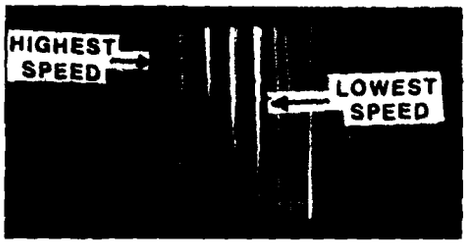


Fig. 6. Sample showing depth of cut for different traverse speeds.

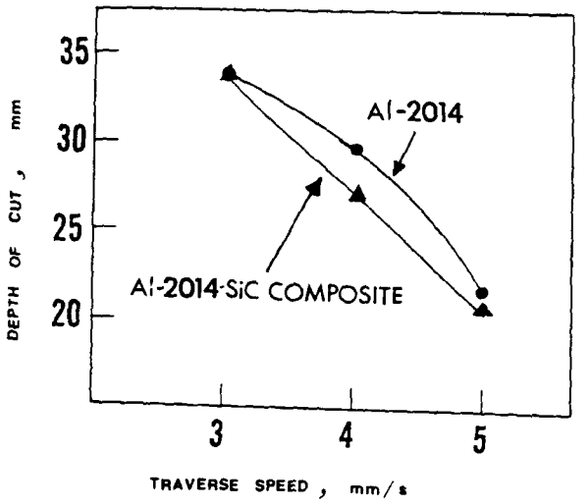


Fig. 7. Traverse speed versus depth of cut for Al-2014 and Al-2014-SiC composite.

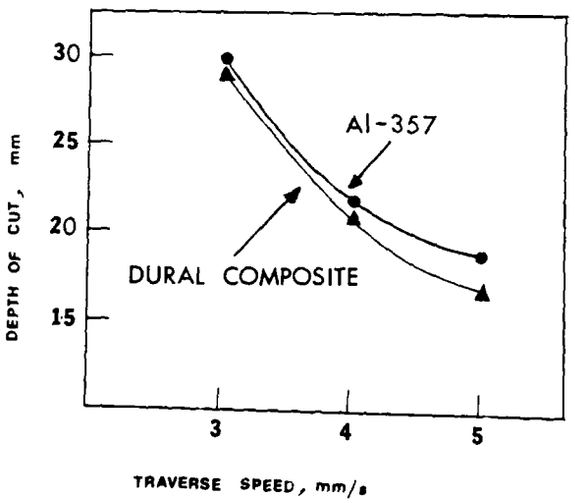
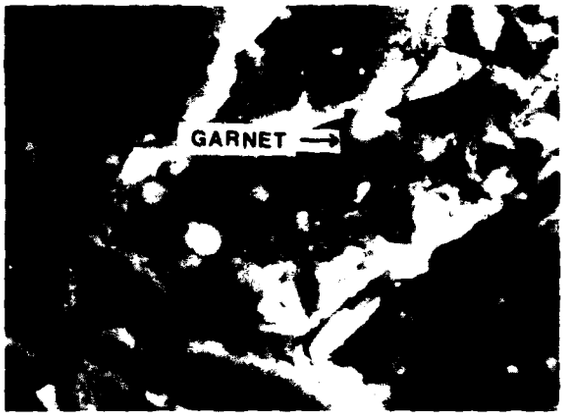


Fig. 8. Traverse speed versus depth of cut for Al-357 and Dural composite.



(a) SEM of Al-357, 1000x



(b) Iron image, 1000x

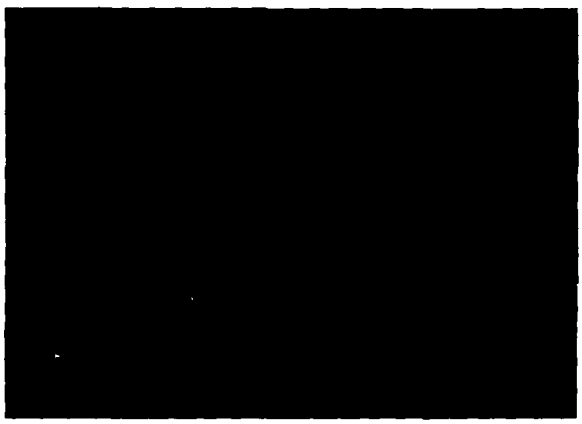


(c) Silicon image, 1000x

Fig. 9. SEM of surface of waterjet cut Al-357 specimen showing the embedded garnet particle and the track made by it.



(a) SEM of Dural composite, 1000x



(b) Iron image, 1000x



(c) Silicon image, 1000x

Fig. 10. SEM of surface of waterjet cut Dural composite showing the embedde. garnet particle and its track.

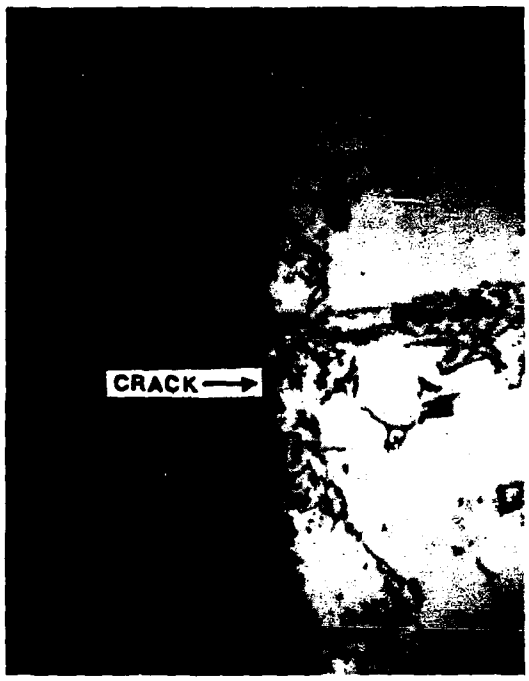


Fig. 11. Photomicrograph of edge of waterjet cut Al-357 surface, 400x.

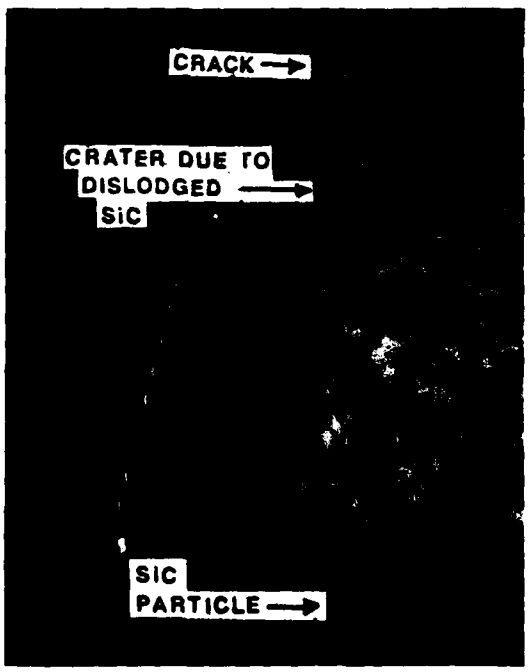


Fig. 12. Photomicrograph of edge of waterjet cut Dural composite surface, 400x.

LOGARITHMIC DECREMENT MEASUREMENTS ON MECHANICALLY ALLOYED ALUMINUM AND SiC PARTICULATE REINFORCED ALUMINUM MATRIX COMPOSITES

Ram B. Bhagat, Maurice F. Amateau, Edward C. Smith
Applied Research Laboratory
The Pennsylvania State University
P.O. Box 30
State College, Pennsylvania 16804 USA

ABSTRACT

Damping capacity of 6061 Al, mechanically alloyed Al-Mg alloy, and SiC particulate reinforced Al-Cu alloy matrix composites has been investigated. The experimental work includes measurement of the logarithmic decrement of freely decaying resonance oscillations of clamped-free cantilever beam specimens over a wide range of resonant frequencies (300 Hz - 12,000 Hz). The damping results are obtained in the first three modes of flexure under ambient conditions; and the maximum peak stress at the root of the beams is maintained under 1.4 MPa. These results are presented in terms of loss factor which is a more commonly used measure of the damping capacity of materials.

Our results indicate that the damping capacity of mechanically alloyed Al-Mg alloy is comparable to that of 6061 Al over the entire range of resonant frequency (300 Hz - 12,000 Hz). However, the SiC particulate reinforced Al-Cu alloy matrix composite exhibits a peak in its damping values plotted against the resonant frequencies. The peak consistently occurs at about 1318 Hz and it is 2.43 times and 2.82 times the damping of the mechanically alloyed Al-Mg alloy and 6061 Al, respectively, at the same resonant frequency.

DAMPING CAPACITY of a material plays an important role in alleviating commonly encountered vibration-induced operational problems, such as fatigue degradation, excessive acoustical radiation, and undesired aeroelastic phenomena of flutter and divergence. Mechanically alloyed materials [1-11] and particulate reinforced metal matrix composites [12-14] are often used in applications requiring the minimization of such effects. However, there has been only limited work to evaluate the damping response of these advanced materials [15-19]. The concept behind the damping behavior of the conventional materials are well documented [20-24]. There are several experimental methods which are used to measure the damping capacity of a material [18,25-27]. The damping results are reported in terms of one or other measures of damping capacity, such as (a) specific damping capacity (ψ), (b) loss factor (η), (c) loss tangent ($\tan\phi$ or ϕ), (d) logarithmic decrement (δ), and (e) quality factor (Q^{-1}). For metals and alloys, which are inherently low damping materials, the various damping measures are related by the following equation:

$$\frac{\psi}{2\pi} = \eta = \phi = \frac{\delta}{\pi} = \frac{1}{Q} \qquad (1)$$

and the details can be found in standard texts [20,21]. Basically, the specific damping capacity (ψ) is the ratio of the energy dissipated in one cycle to the maximum strain energy during a cycle. In metals and alloys, the capability of these materials to absorb or dissipate vibrational energy is closely related to the micromechanisms involving crystal defects; as such the damping of a metal or alloy is also known as internal friction [20-24]. It is likely that the new engineered materials, such as mechanically alloyed metals and composites may provide additional sources of energy dissipation resulting in improved damping.

In view of the foregoing, the objective of the present investigation was to carry out experimental work for measuring and evaluating the damping response of a typical mechanically alloyed metal and a typical particulate composite.

EXPERIMENTAL WORK

Mechanically alloyed Al-Mg alloy and SiC particulate reinforced Al-Cu alloy matrix composite were obtained from INCO in the form of slabs (approximately 100 mm × 90 mm × 25 mm). The chemical composition and mechanical properties of these materials are presented in

Table 1. Nominal Composition and Properties of Materials

Materials	Normal Composition	Properties	Source
6061-T6 Al	0.6 % Si 0.28% Cu 1.0 % Mg 0.2 % Cr balance Al	YS = 275 MPa (40 ksi) UTS = 310 MPa (45 ksi) elong. = 12% E = 69 GPa (10 Msi)	28
Mechanically Alloyed Al-Mg Alloy	4.0% Mg 1.2% C 0.8% O balance Al	YS = 379 MPa (55 ksi) UTS = 448 MPa (65 ksi) E = 75 GPa (11 Msi) ρ = 2.67 g/cm^3 (0.096 lb/in^3)	4,7
SiC_p/Al-Cu Composite (V_f = 0.15) Mechanically Alloyed, Hot Pressed and Extruded	4.0% Cu 1.5% Mg 1.2% C 0.8% O balance Al	(In T6 Condition) YS = 531 MPa (77 ksi) UTS = 586 MPa (85 ksi) elong. = 2.2% E = 103 GPa (15 Msi) ρ = 2.81 g/cm^3 (0.101 lb/in^3)	4,7

Table 1. Table 1 also includes data on 6061 Al which was used as a reference material for damping measurement.

The experimental setup was designed to measure logarithmic decrement of freely decaying resonance oscillations of clamped-free cantilever beam specimens. A summary of the specific characteristics of the experiment design is presented in Table 2. The beam specimens were precision-machined with carbide and diamond tooling. A typical beam (~ 100 mm × 5 mm × 1.8 mm) can be seen clamped at one end in Fig. 1. The beam is vibrated electromagnetically by the use of a samarium-cobalt magnet attached to the free end. A photoaccumulator device is used to measure the deflection near the free end. The experimental setup is adapted from the setup used by Eckstein [29] for plate specimens. At a resonant frequency, the signal to the coil is cut-off and the free decay oscillations are recorded and stored in a storage oscilloscope. A photograph of the recorded oscillations is shown in Fig. 2. Loss factor is calculated by the following relationship:

$$\eta = \frac{1}{\pi n} \ln \frac{x_0}{x_n} \qquad (2)$$

where x_0 is initial vibration amplitude and x_n is amplitude after n cycles. Specimens were vibrated up to first three flexure modes and the resonant frequencies and the corresponding loss factor values were obtained for the three materials mentioned earlier.

Table 2. Summary of Damping Measurement System Characteristics

Measurement System Type:	Free Decay Resonance Method
Damping Term Measured:	Loss Factor (η)
Specimen Shape:	Cantilever Beam
Deflection Mode:	Flexure
Oscillation Modes:	I, II, III
Frequency Range:	300 Hz - 12,000 Hz
Driving Force:	Non-Contact Electromagnetic
Maximum Stress Level:	1.4 MPa
Measurement Device:	Photoaccumulator Sensor
Maximum Tip Deflections:	0.051 mm
Temperature Conditions:	Room Temperature
Atmosphere Conditions:	Air

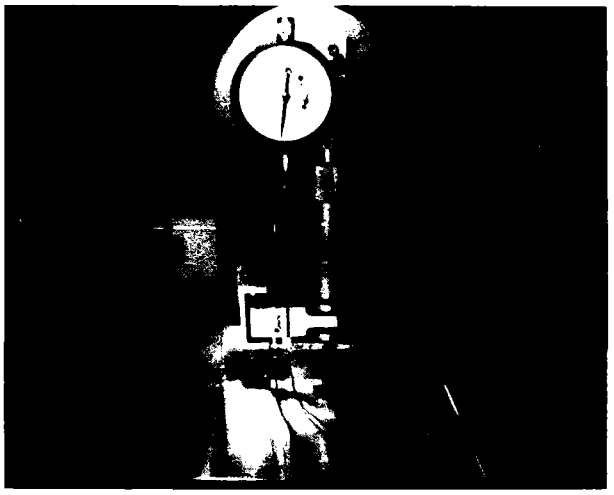


Fig. 1. Experimental set-up for vibrating a beam specimen electromagnetically. One end of the beam is clamped, the other end is between a coil and the photo- accumulator sensor probe. A samarium-cobalt magnet is attached to the beam and the magnet faces the coil. A thin aluminum foil is attached to the beam and the foil faces the sensor probe.

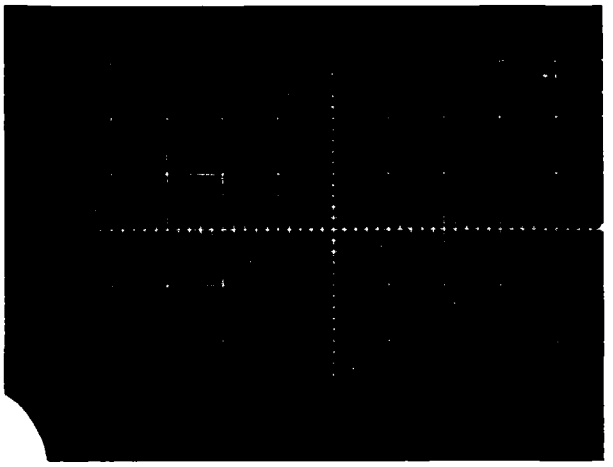


Fig. 2. Picture as recorded and stored in storage oscilloscope; it shows freely decaying resonance oscillations of a clamped-free cantilever beam of SiC particulate reinforced Al-Cu alloy matrix composite (V_f = 0.15). The beam was vibrated at a resonant frequency of 1481 Hz and the calculated loss factor equals 0.00366.

RESULTS AND DISCUSSION

Loss factor of 6061 Al has been plotted against resonant frequency in the first three flexure modes (Fig. 3). Large number of resonant frequencies in each mode were obtained by changing the dimensions of the beam specimens. It is clearly evident from

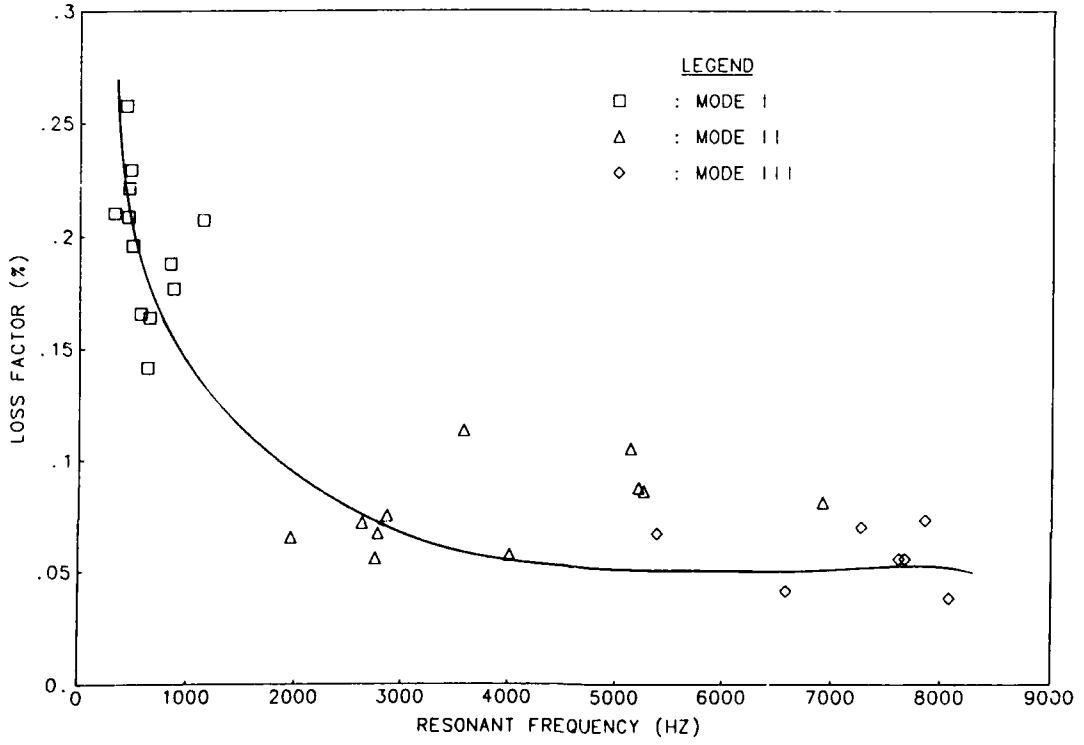


Fig. 3. Experimental damping data of 6061 Al cantilevered beam specimens vibrated in the first three flexure modes. The curve shows the general trend for the dependence of the loss factor on the resonant frequency.

Fig. 3 that the loss factor of 6061 Al is dependent on oscillation mode and resonant frequency. This is consistent with the findings of other researcners [29-31]. The modal averages of the loss factor of 6061 Al are 0.00197, 0.00079, and 0.00057 for Mode I, Mode II and Mode III, respectively. These results are comparable with those obtained on free-free-free-free 6061 Al plate vibrated in different modes by Eckstein [29]. Thus, the damping measurement setup and the procedures followed in the present investigation provide a greater confidence in producing accurate results for loss factor for the selected materials.

Figure 4 shows the resonant frequency vs loss factor plot for mechanically alloyed Al-Mg alloy. The general trend for the dependence of the loss factor of this alloy on the resonant frequency is similar to that of 6061 Al. The modal averages of the loss factor are 0.00182, 0.00080, and 0.00049 for Mode I, Mode II, and Mode III, respectively. These values are comparable with those of 6061 Al. Thus, it is important to note that the mechanical alloying which enhances strength and stiffness of aluminum alloys, as reported elsewhere [4,7], does not reduce damping capacity of these alloys within the range of resonant frequency investigated in the present work.

Figure 5 shows a unique behavior of the loss factor of silicon carbide particulate reinforced Al-Cu alloy matrix composite with respect to the resonant frequency. In Mode I, the loss factor consistently increases within the range of resonant frequency, i.e., 542 Hz to 1481 Hz investigated. The loss factor reaches a peak and then rapidly drops to relatively lower values in Mode II and Mode III. The existence of a peak damping is unique to the particulate composite and the peak corresponds to a loss factor value of 0.00352 occurring at a resonant frequency of about 1318 Hz. The modal averages of loss factor in Mode II and Mode III of the composite are 0.00074 and 0.00067, respectively. These two values are comparable to those in Mode II and Mode III of 6061 Al and mechanically alloyed Al-Mg alloy. However, the peak damping of the composite is much higher than that of 6061 Al and mechanically alloyed Al-Mg alloy. Figure 6 presents a comparison of the loss factor of the three materials investigated. For 6061 Al and Al-Mg alloy, the loss factor values represent the modal averages in the three modes of oscillation. Mode I loss factor value of the composite in Fig. 6 represents the peak value (as seen in Fig. 5) and the other values are modal averages. The modal averages of the loss factor (see Fig. 6) are valid for a relatively large range of resonant frequency in each mode; and that

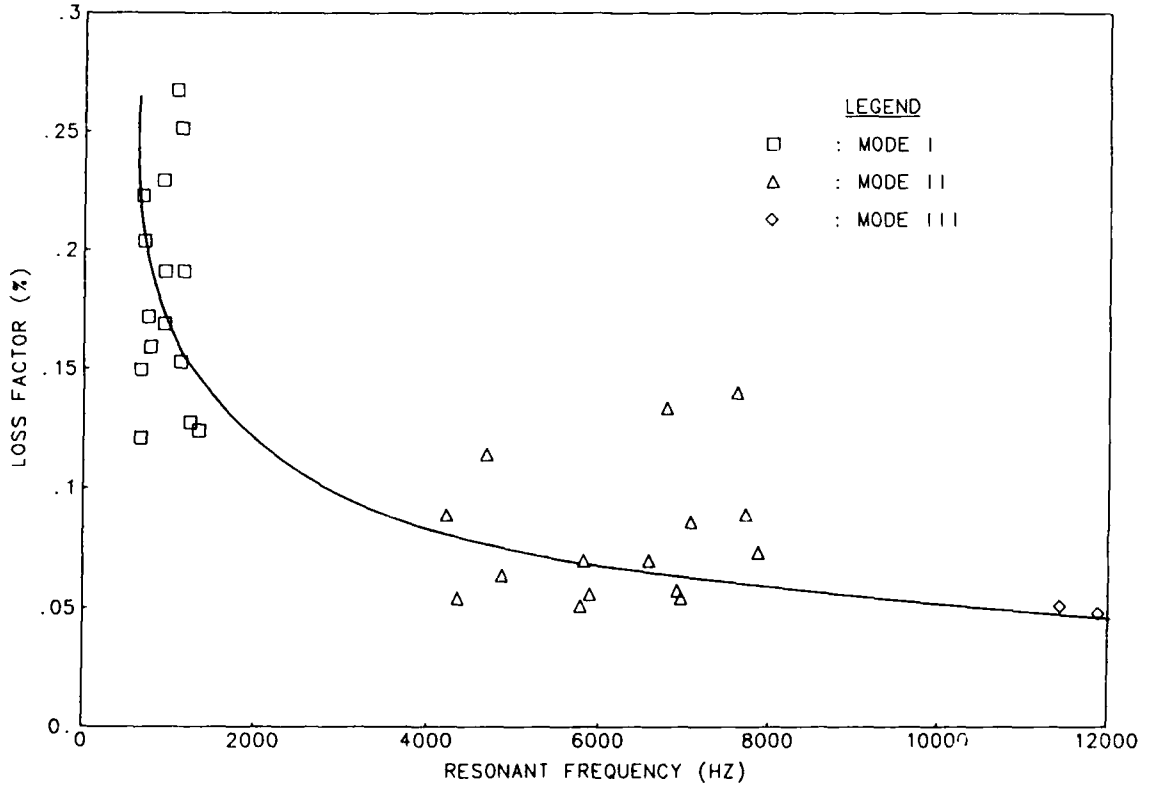


Fig. 4. Experimental damping data of the mechanically alloyed Al-Mg alloy beam specimens. The curve shows the general frequency-dependence of the loss factor.

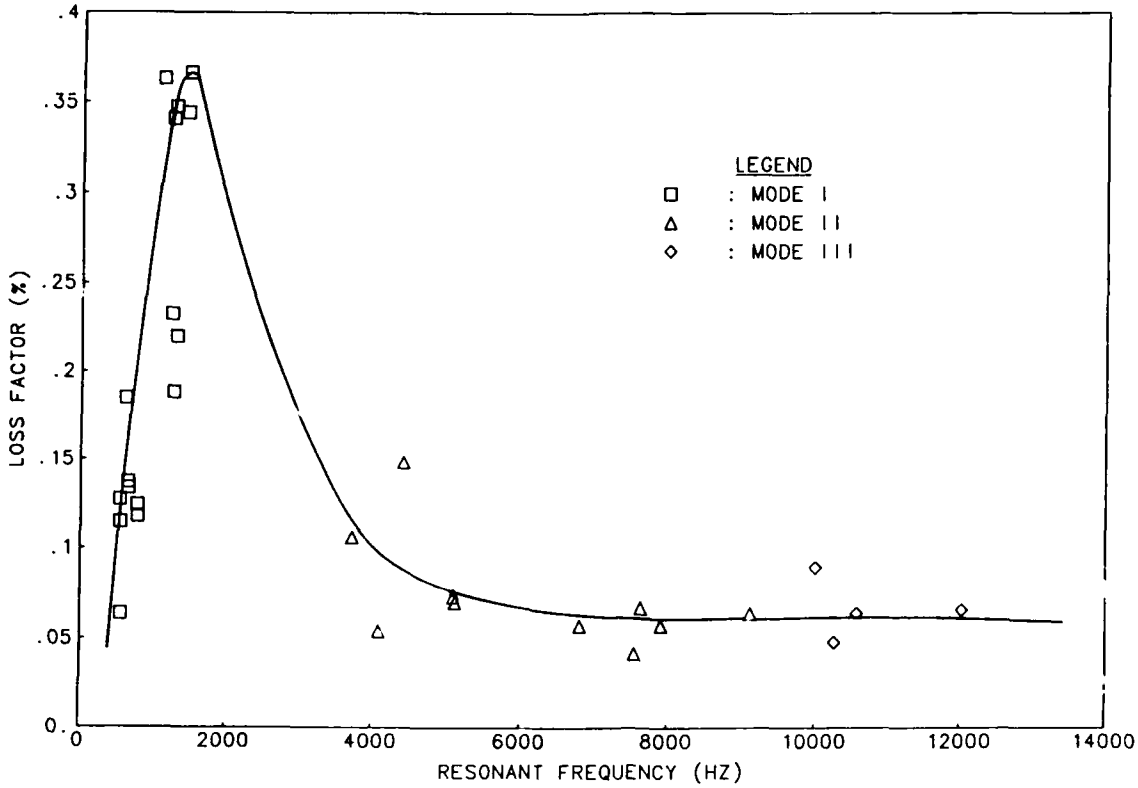


Fig. 5. Experimental damping data of SiC particulate reinforced Al-Cu alloy matrix composite (V_f = 0.15) beam specimens. The plot shows a unique peak damping at about a frequency of 1318 Hz.

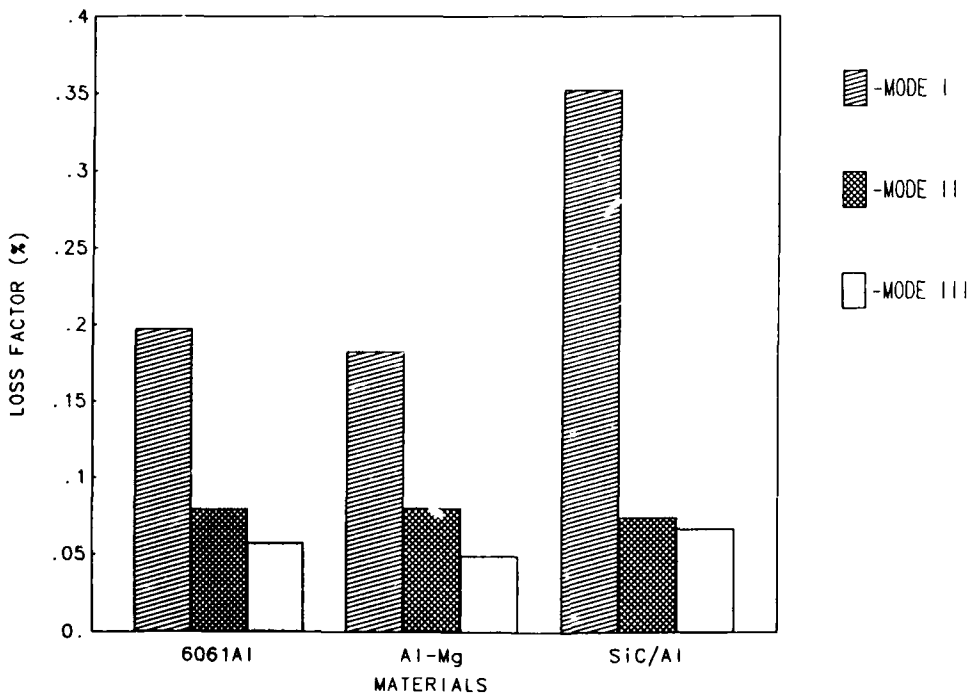


Fig. 6. Comparative damping results on 6061 Al, Al-Mg alloy and SiC_p/Al composite. The loss factor values are modal averages for all the three materials with the exception of that of SiC_p/Al in Mode I which is an average value representing the peak as observed in Fig. 5.

range too is different for different materials (see Figs. 3, 4 and 5). Thus, a better comparison of the peak damping of the composite can be made by comparing the loss factor values of other materials at the specific resonant frequency of the peak, i.e., 1318 Hz. Such a comparison is made in Fig. 7. which shows similar loss factors for 6061 Al and mechanically alloyed Al-Mg alloy. However, the composite exhibits a significantly improved damping. The loss factor of 0.00352 for the composite is 2.43 times and 2.82 times that of Al-Mg alloy and 6061 Al, respectively.

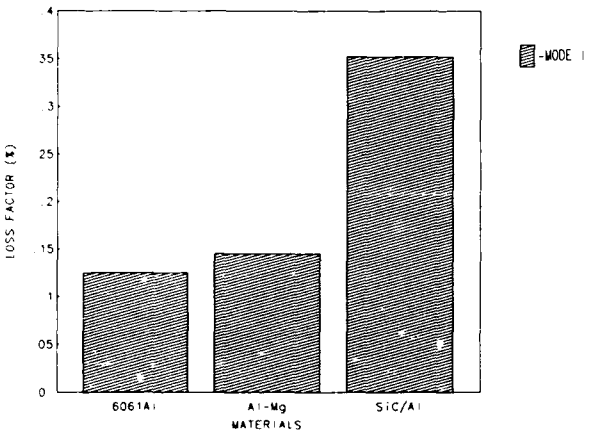


Fig. 7. Comparison of the peak damping of the SiC_p/Al composite with the damping of 6061 Al and Al-Mg alloy at a resonant frequency of 1318 Hz. The peak is observed at 1318 Hz (see Fig. 5).

Further investigation is underway to establish a suitable damping mechanism responsible for the observed peak damping in the particulate composite.

CONCLUSIONS

Logarithmic decrement method has been used to determine the loss factor of 6061 Al, mechanically alloyed Al-Mg alloy, and SiC particulate reinforced Al-Cu alloy matrix composite over resonant frequencies ranging from 300 Hz to 12,000 Hz which include the first three modes of oscillation. It has been established that the composite exhibits a peak loss factor of 0.00352 at about 1318 Hz. Such a peak is not observed in the other two materials. Comparison of their loss factor at 1318 Hz reveals that the damping of the composite is 2.43 times and 2.82 times that of Al-Mg alloy and 6061 Al, respectively. Over the range of frequency investigated, 6061 Al and the mechanically alloyed Al-Mg alloy do not show any marked difference in their damping values exhibiting identical frequency-dependent trend.

ACKNOWLEDGMENTS

The authors thank Robert D. Schelleng of INCO alloys International, Huntington, WV, for providing mechanically alloyed Al-Mg alloy and SiC particulate reinforced Al-Cu alloy matrix composite materials.

LIST OF REFERENCES

(1) Benjamin, J. S. and T. S. Volin, Metall. Trans. 5:1929 (1974).
(2) Benjamin, J. S. and M. J. Bomford, Metall. Trans. 8A:1301 (1977).
(3) Singer, R. F., W. C. Oliver and W. D. Nix, Metall. Trans. 11A:1895 (1980).
(4) Benjamin, J. S. and R. D. Schelleng, Metall. Trans. 12A:1827 (1981).
(5) Kim, Y. W. and L. R. Bidwell, Scripta Metall. 16:799 (1982).
(6) Erich, D. L. and S. J. Donachie, Metal Prog. 121:22 (1982).
(7) Schelleng, R. D. and S. J. Donachie, Metal Powder Report 38:10 (1983).
(8) Renard, A., A. S. Cheng, R. de la Veaux and C. Laird, Mater. Sci. Eng. 60:113 (1983).
(9) Chen, R. T. and E. A. Starke, Jr., Mater. Sci. Eng. 67:229 (1984).
(10) Nieh, T. G., P. S. Gilman and J. Wadsworth, Scripta Metall. 19:1375 (1985).
(11) Sundaresan, R. and F. H. Froes, J. Metals, pp. 22-27 (August 1987).
(12) Divecha, A. P., S. G. Fishman and S. D. Karmarkar, J. Metals 33:12 (September 1981).
(13) Schuster, D. M., M. Skibo and F. Yep, J. Metals, p. 60 (1987).
(14) Mohn, W. R., Research & Development, pp. 54-58 (July 1987).
(15) Arsenault, R. J. and R. M. Fisher, Scripta Met. 17:67-71 (1983).
(16) Bert, C. W., Proc. ASME Winter Meeting, pp. 98-111 (1980).
(17) Timmerman, N. S., AMML TR 82-19, pp. 1-25 (1982).
(18) Ledbetter, H. M. and S. K. Datta, Proc. Vibration Damping Workshop, AFWAB, Wright-Patterson Air Force Base, OH, pp. 78-84 (1984).
(19) Crawley, E. F. and M. C. van Schoor, J. Composite Materials 21:553-568 (1987).
(20) Zener, C., "Elasticity and Aeroelasticity of Metals", University of Chicago Press, Chicago (1952).
(21) Lazan, B. J., "Damping of Materials and Members in Structural Mechanics", Pergammon Press, New York (1968).
(22) De Batist, R., "Internal Friction of Structural Defects in Crystalline Solids", North Holland (1972).
(23) Norwick, A. S. and B. S. Berry, "An Elastic Relaxation in Crystalline Solids", Academic Press (1972).
(24) Beshers, D. N., "Techniques of Metals

Research, Vol. VII, Part 2, John Wiley, New York, pp. 529-707 (1976).
(25) Saurez, S. A., R. F. Gibson and L. R. Deobald, Proc. SESA Fall Meeting, pp. 255-261 (1983).
(26) Baker, W. E., W. E. Woolham and D. Young, International J. of Mechanical Scientists 9:743-752 (1967).
(27) Guild, F. J. and R. D. Adams, J. Phys. E. Sci. Instrum. 14:355-363 (1981).
(28) Properties and Selection: Non-Ferrous Alloys and Pure Metals, Metals Handbook, Ninth Edition, Vol. 2, ASM International, Metals Park, OH (1979).
(29) Eckstein, F. D., On the Specially Orthotropic Free-Free-Free-Free Square Plate in Resonance. Master's Thesis, Department of Engineering Science and Mechanics, The Pennsylvania State University (1986).
(30) Gibson, R. F. and R. Plunkett, Experimental Mechanics, pp. 297-302 (August 1977).
(31) Granick, N. and J. E. Stern, NASA Technical Note D-2893, NASA Goddard Space Flight Center, Greenbelt, MD, pp. 1-21.

DAMPING BEHAVIOR OF SQUEEZE CAST PLANAR RANDOM CARBON FIBER REINFORCED 6061 Al MATRIX COMPOSITES

Ram B. Bhagat, Maurice F. Amateau, Edward C. Smith
Applied Research Laboratory
The Pennsylvania State University
P.O. Box 30
State College, Pennsylvania 16804 USA

ABSTRACT

This paper describes the damping behavior of carbon fiber reinforced aluminum matrix composites. The composites were fabricated by high pressure squeeze casting technique using planar random carbon fiber mats as the reinforcement and 6061 Al as the matrix. The damping measurements were carried out on clamped-free cantilever beam specimens vibrated at resonant frequencies in the first three modes of flexure vibration. The damping capacity of the matrix aluminum and the composites ($0.10 \leq V_f \leq 0.36$) are reported in terms of loss factor (η) up to a resonant frequency of 12 kHz.

Two damping peaks were found in the frequency range between ~ 850 Hz and ~ 4700 Hz for composites with fiber fractions from .1 to .36. The modal peak damping and the off-peak damping of the composites are dependent on their fiber volume fraction. The frequency of the damping peaks were not particularly sensitive to fiber fraction. In conclusion, the squeeze cast carbon/aluminum composites offer improved damping capacity which is over an order of magnitude greater than those of the aluminum matrix and up to six times that of the carbon fiber.

AN INCREASING INTEREST in metal matrix composites in lightweight load bearing structures to be used at intermediate and high temperatures has recently attracted several investigators to evaluate the damping behavior of the composites [1-8]. Gibson and Plunkett [7] and Bert [8] have provided good overviews of the damping response of composites. In addition to the classical damping mechanisms, such as thermoelastic, hysteretic, coulombic, magnetoelastic, dislocation unpinning and grain boundary relaxation of the metals and alloys [9-14], metal matrix composites can also undergo energy dissipation at the fiber/matrix interface. For metal composites, vibration energy can be dissipated by interfacial slip, microplasticity of the matrix, dislocation breakaway and microcracking at or near the fiber/matrix interface.

Baker [15] subjected aluminum matrix composites to sufficiently high loads to cause the matrix to deform plastically and studied their damping response. He developed a relationship between the specific damping capacity as a function of the strain. In terms of the loss factor (η), this relationship is represented by:

$$\eta = \frac{0.318\ \sigma_{my}(1 - V_f)\Delta\varepsilon_{mp}}{(E_f V_f/2)(\Delta\varepsilon_{mp} + \varepsilon_{my})^2 + 2(1 - V_f)\varepsilon_{my}\sigma_{my}} \quad (1)$$

where E_f is the Young's modulus of fiber and V_f is the fiber volume fraction. $\Delta\varepsilon_{mp}$ is the plastic strain range endured by the matrix, σ_{my} and ε_{my} are the matrix yield strength and yield strain, respectively. It can be seen from Eq. (1) that for a constant fiber volume fraction, η depends only on the plastic strain range. According to Baker [15], $\eta \rightarrow \eta_{max}$ when the buildup of elastic energy equals the loss of energy due to plastic deformation of the matrix. Varschavsky [16] and Weiss [17] also reported improved damping of boron/aluminum and stainless steel/aluminum composites, respectively, because of the plastic deformation of the matrix during fatigue tests. Weiss [17] established an expression for optimum fiber volume fraction for maximum damping capacity of the composites:

$$(V_f)_{opt} = [1 + (E_f/E_m)(\varepsilon_{fy}/\varepsilon_{my} - 2)]^{1/2} \quad (2)$$

where ε_{fy} and ε_{my} are the yield strains of fiber and matrix, respectively, and E_m is the Young's modulus of the matrix.

Recently, Timmerman [5] measured damping

capacity of a series of metal matrix composites. The carbon composites showed the highest loss factor (0.11% - 0.39%), followed by FP alumina composites and SiC composites. Sample-to-sample variations in damping ranged from 10% to 30%. Timmerman [5] has not reported experimental data on the damping capacity of matrix materials or any other standard materials with well established loss factor. Thus, it is difficult to reconcile her results with those of other investigators [6,18,19]. For Gr(pitch)/6061 Al composites, Misra [6] found loss factors ranging from 0.95% to 1.38% on beam specimens having fibers in the longitudinal direction. In the transverse direction, the loss factors ranged from 1.88% to 2.76%. Misra [6] also measured the loss factor of 6061-T6 Al equal to 0.58%. Thus, he demonstrated improved damping capacity of the composites relative to the matrix aluminum. It should also be noted that the damping in the transverse direction is about twice as much as that in the longitudinal direction. Similar studies have been done by Ledbetter [1] on boron/aluminum composites at high frequencies (50 kHz to 80 kHz). He found the loss factors in the longitudinal direction and the transverse direction equal to 0.056% and 0.17%, respectively; transverse damping being about three times the longitudinal damping.

From the foregoing, it is clear that the specific effects of interfacial properties have not been specifically addressed and therefore an important mechanism for composite damping remains poorly understood. The objectives of the present investigation, therefore, were to fabricate fiber reinforced aluminum matrix composites with relatively weak fiber/matrix interface and to evaluate their damping capacity over a wide range of resonant frequency in order to develop an understanding of the interface-controlled mechanisms of damping.

EXPERIMENTAL WORK

Planar random carbon fiber reinforced 6061 Al matrix composites were fabricated by high pressure squeeze casting techniques. The details of the experimental procedures to fabricate the composites are presented elsewhere [20]. Each of the fabricated composite disks (114 mm diameter, approximately 3 mm thick) were slit and machined into a dog-bone tensile test specimen and several thin beam specimens using diamond cutting tools. Dog-bone specimens were tested for stiffness and tensile strength using an Instron machine. The thin beam specimens were used as cantilevered beams for the measurement of loss factor at resonant frequencies.

A schematic of the experimental setup to measure loss factor (η) is shown in Fig. 1. This setup is adapted from the setup used by Eckstein [21] on plate specimens. The free end of the clamped-free beams is electro-magnetically vibrated and its flexure deflection is measured by a photoaccumulator device. At a resonant frequency, the signal to the coil is cut-off and the free decay is recorded and stored in a storage oscilloscope. Such a free decay is schematically shown in Fig. 2. Damping capacity of the composites and the matrix aluminum alloy (6061 Al) are reported in terms of loss factor (η) which is given by the following relationship:

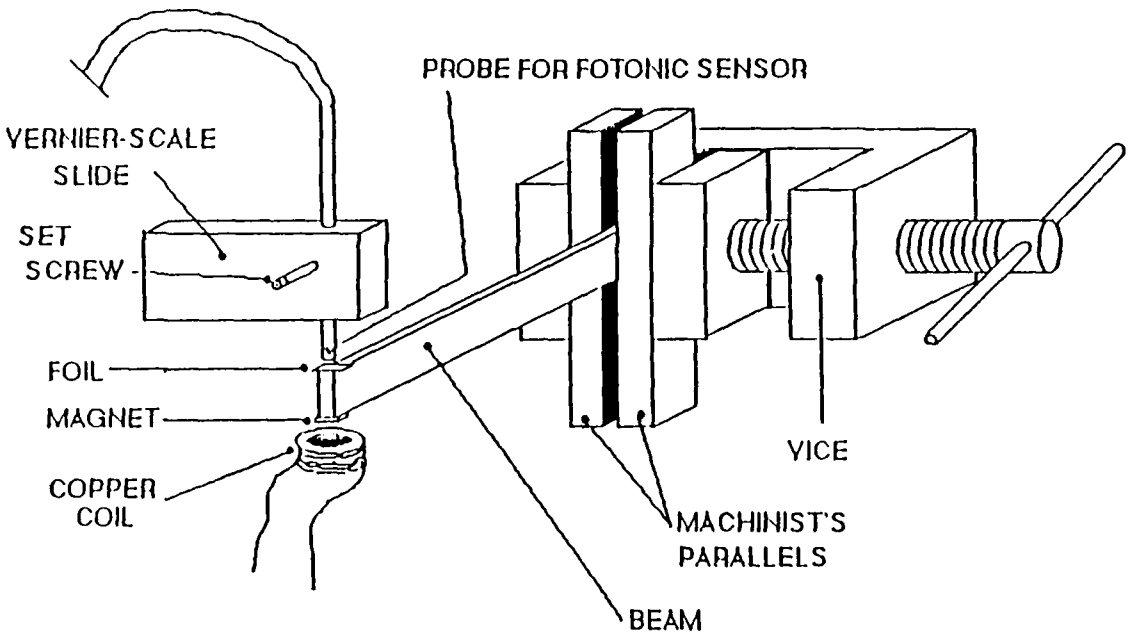


Fig. 1. Schematic diagram showing a cantilever beam clamped at one end. The free end is vibrated by an electromagnetic driving force.

$$\eta = \frac{1}{\pi n} \ln \frac{x_0}{x_n} \qquad (3)$$

where x_0 is initial vibration amplitude and x_n is amplitude after n cycles. Further details on the damping measurement are reported elsewhere [22] in this volume.

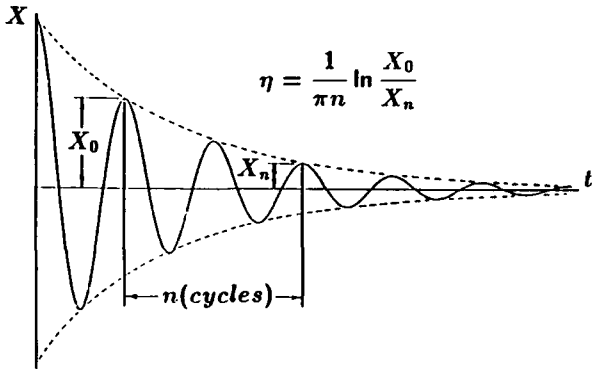


Fig. 2. Schematic of vibration decay for determining the loss factor.

RESULTS AND DISCUSSION

Table I includes experimentally determined stiffness and tensile strength of planar random carbon fiber reinforced 6061 Al matrix composites. Stiffness increases with the increase in fiber volume fraction. However, the tensile strength of the composites first increases and then decreases with further increase in fiber volume fraction. This type of dependence of the strength on fiber volume fraction is expected for planar random fiber reinforced composites. Only moderate increase in stiffness and tensile strength of the composites (refer to Table I) is indicative of relatively poor fiber-to-matrix bonding. Microscopic studies have revealed that the fiber-to-matrix bonding in the squeeze cast composites is primarily of adhesion type. It is expected then that some vibration energy may dissipate at the relatively weak interface and the composites should exhibit relatively high damping. Figure 3 shows plots of loss factor vs resonant frequency at four different volume fractions. Also included in Fig. 3 are the loss factors of carbon fiber as reported by Pulgrano and Miner [23,24] and the loss factor of the matrix aluminum as experimentally measured in the present investigation. For the sake of clarity, only a curve (dotted in Fig. 3), representing the loss factor values of aluminum, is plotted without showing the actual experimental data. Several observations can be made from the plots in Fig. 3:

(a) The damping of composites far exceeds the damping of the matrix aluminum and the carbon fiber.
(b) Irrespective of the fiber volume fractions, the composites show damping peaks both in Mode I and Mode II of the flexure vibration. Similar trend is not obvious in Mode III of the flexure vibration because of limited experimental data.
(c) In the vibration Modes I and II, the peaks occur around a narrow range of resonant frequency.

We hypothesize that certain mechanisms are activated in the squeeze cast composites at almost a fixed resonant frequency in each of the first two modes. In view of the fact that the peak damping values are much higher than those of the constituents (fiber and matrix) of the composites, we suggest that certain unique characteristics of the fiber/matrix interface are primarily responsible for activating certain mechanisms leading to high damping. Similar peak damping has been predicted for composites with discontinuous fibers by Pompe and Schultrich [25] as reported by Bert [8]. In their model, Pompe and Schultrich [25] incorporated matrix-fiber interfacial slip and claimed to have correlated the location of the damping peaks with the shear strength of the fiber-matrix bond. It is expected that the composites fabricated in this investigation will have some residual stress because of the large mismatch of coefficients of thermal expansion between the fiber and the matrix. This is most likely to be present as a complex stress state in the fabricated composites. Such a residual stress may cause microplasticity of the matrix at the fiber/matrix interface at

Table I. Experimental Data on Stiffness and Tensile Strength of Squeeze Cast C/Al Composites

Materials	V_f (%)	E (GPa)	UTS (MPa)
6061 Al	---	69	179
	10	75	225
	19	81	251
C/Al	24	---	319
	31	87	276
	36	---	239
C	---	227*	2758*

*Courtesy of International Paper Co., New York.

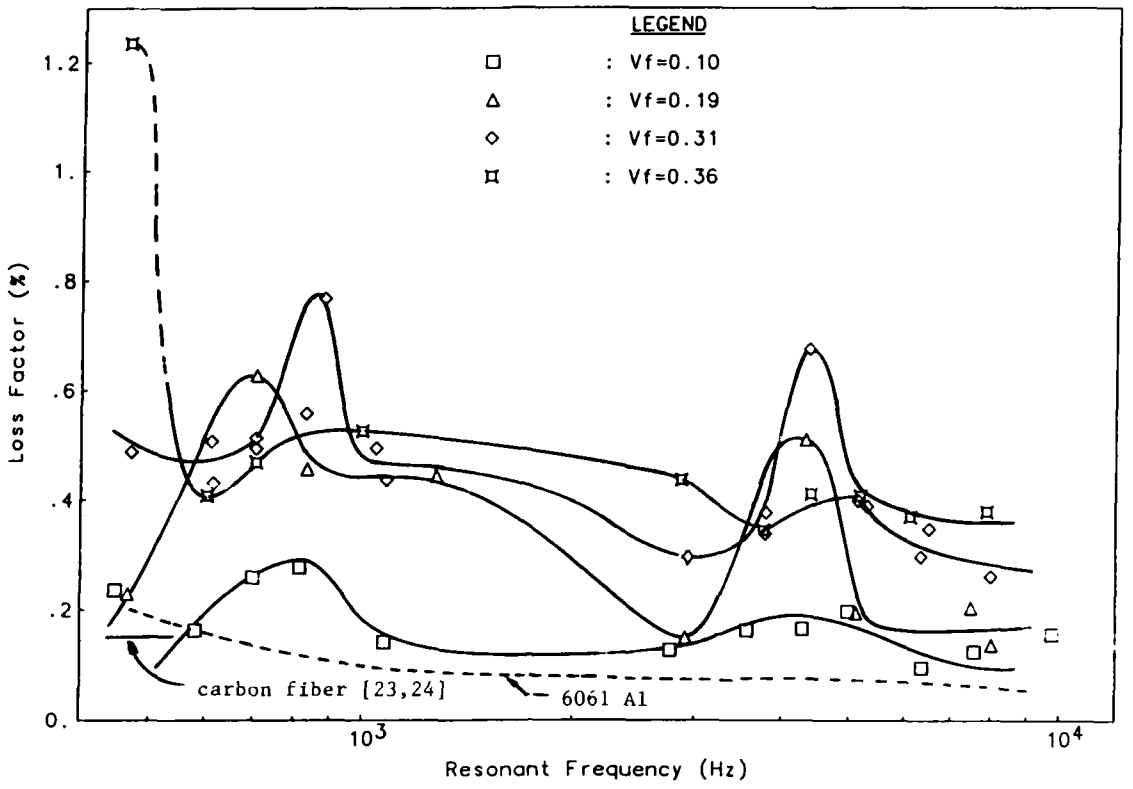


Fig. 3. Plots for the damping of C/Al composites as dependent on resonant frequency. Irrespective of the fiber volume fractions, damping peaks at certain frequencies for all the composites.

certain resonant frequencies even under the relatively low bending stresses (< 1.4 MPa) on the composite beams.

Also, it is well documented that because of the large mismatch between the coefficients of thermal expansion of carbon and aluminum, there are dislocation tangles with dislocation density ≈ $4 \times 10^{14}/m^2$ [26]. These dislocations may breakaway at certain resonant frequencies under the influence of a complex stress state of the residual stress thereby resulting in damping peaks. Similar mechanism of strain-dependent dislocations breakaway has been established for the peak damping in SiC particulate reinforced aluminum matrix composites [19].

Figure 4 shows the dependence of the peak damping (as observed in Fig. 3) of the composites on their fiber volume fraction. Interestingly, curves for both Modes I and II are identical and exhibit maxima at around a fiber volume fraction of about 30%. These maxima are about 300% higher than the damping of the composites having a fiber volume fraction of 10%. The presence of these maxima can also be explained in terms of the residual stress and the dislocation tangles at the interface. In addition to the earlier discussion, the stress state at the interface in the fabricated composites may get further complicated with increasing fiber volume fraction. It is possible, therefore, that at higher fiber volume fractions large interfacial surface area in conjunction with complex stress state may lead to enhanced microplasticity and more unpinning of dislocation tangles. As a consequence, damping will increase with increasing fiber volume fraction. However, consistent with Eq. (2), we expect that there will be an optimum fiber volume fraction when the buildup of elastic energy will equal the cumulative loss of energy due to the matrix microplasticity and dislocation breakaway at the interface. Such an optimum fiber volume fraction is found to be about 30% for the fabricated composites, exhibiting the maxima of the peak damping [see Fig. 4].

Aside from the peaks in Fig. 3, comparison has been made for the off-peak damping values of the composites. Such a comparison is included in Fig. 5. It is seen in Fig. 5 that, in general, the damping of the composites increases with increase in fiber volume fraction without exhibiting any maximum which is in contrast to those in Fig. 4. The rate of increase of the off-peak damping with respect to the fiber volume fraction increases with the increase in the fiber volume fraction as it can be seen in Fig. 5. Just the opposite observation was found for the peak damping of the

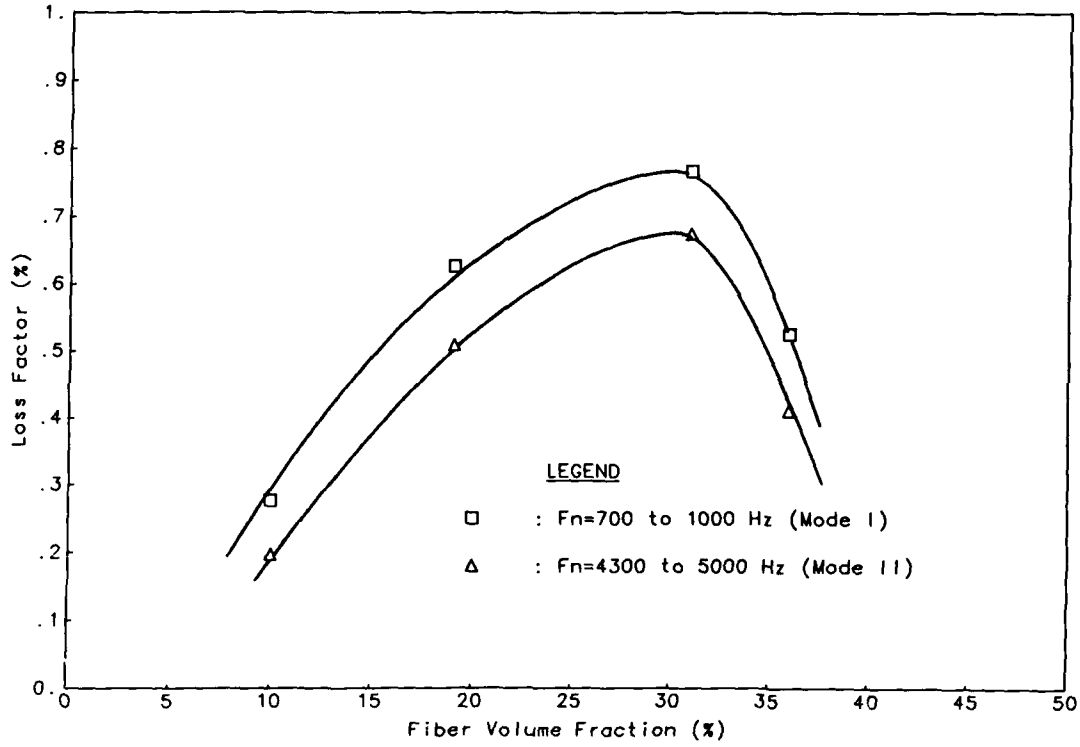


Fig. 4. Plots showing the dependence of the modal peak damping (as observed in Fig. 3) on the fiber volume fraction of the C/Al composites; each plot exhibiting a maximum value of the peak damping.

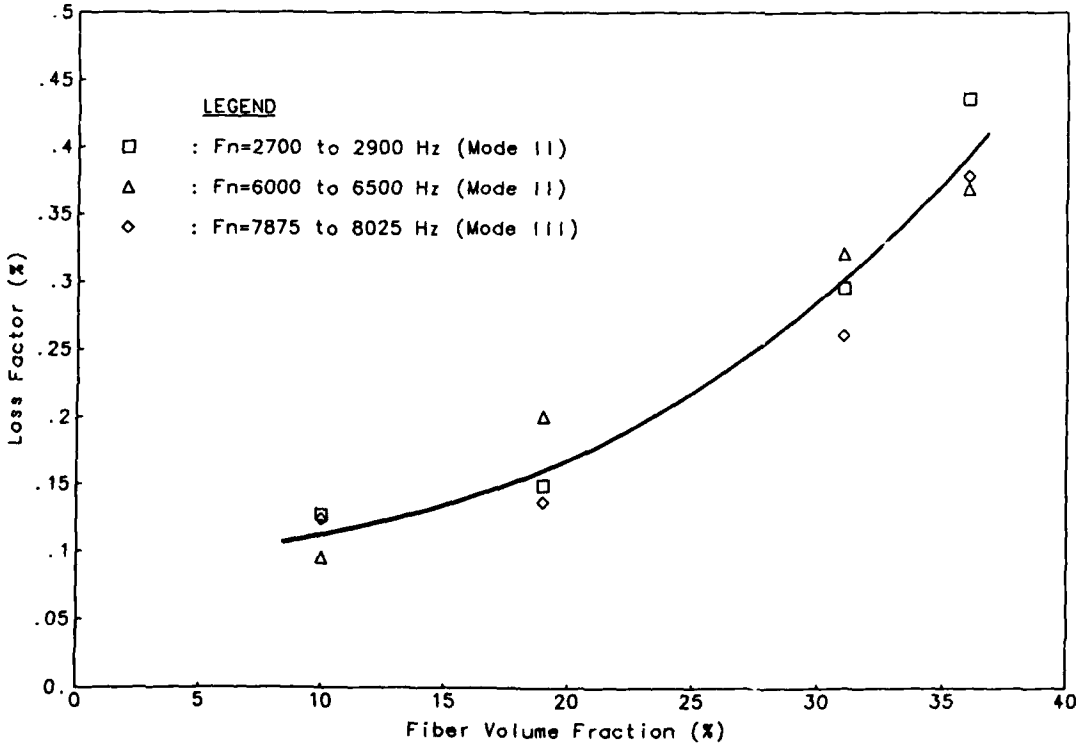


Fig. 5. Dependence of the off-peak damping (see Fig. 3) on the fiber volume fraction of the C/Al composites.

composites [see Fig. 4] suggesting that the dominating mechanisms of the peak damping are different from those of the off-peak damping.

CONCLUSIONS

Squeeze cast planar random carbon fiber reinforced 6061 Al matrix composites have been evaluated for their damping capacity by logarithmic decrement method using clamped-free cantilever beams. These composites ($0.10 \leq V_f \leq 0.36$) possess damping capacity which is over an order of magnitude higher than that of the aluminum matrix and up to six times that of the carbon fiber. The composites exhibit peak damping at certain resonant frequencies in Modes I and II of the flexure vibration. The modal peak damping first increases with increasing fiber volume fraction and then decreases with further increase in fiber volume fraction. The enhanced damping of the composites is attributed to (a) microplasticity of the aluminum matrix and (b) dislocations breakaway at the fiber/matrix interface. Further investigation is suggested for establishing these mechanisms of energy dissipation at the interface.

ACKNOWLEDGMENT

Support from the George F. Wislicenus Program at The Applied Research Laboratory of The Pennsylvania State University is greatly appreciated.

LIST OF REFERENCES

(1) Ledbetter, H. M., "Elastic Constants and Internal Friction of Fiber-Reinforced Composites," Composite Materials: Mechanics, Mechanical Properties and Fabrication, Proc. Japan-U.S. Conf., K. Kawata and T. Akasaka (Eds.), Japan Society for Composite Materials, Tokyo, pp. 441-448 (1981).

(2) DiCarlo, J. A. and J. E. Maisel, "Measurement of the Time Temperature Dependent Dynamic Mechanical Properties of Boron/Aluminum Composites," ASTM STP 674, pp. 201-227 (1979).

(3) DiCarlo, J. A. and J. E. Maisel, "High Temperature Dynamic Modulus and Damping of Aluminum and Titanium Matrix Composites," NASA TM-79080 (1979).

(4) Yamane, T., Y. Umakoshi, M. Tomishima and N. Kazuyoshi, "A Study of Internal Friction in Fiber-Reinforcement Copper Composites (Tungsten Wire)," Mech. Behavior Matl. V:220-226, Society of Material Science, Kyoto, Japan (1972).

(5) Timmerman, H. S., "Damping Characteristics of Metal Matrix Composites," AMMRC TR 82-19, Army Materials and Mechanics Research Center, Watertown, MA, pp. 1-25 (1982).

(6) Misra, M. S., "Metallurgical Characterization of the Interfaces and the Damping Mechanisms in Metal Matrix Composites," Progress Report No. 1, Martin Marietta, Denver, CO, pp. 1-11 (1985).

(7) Gibson, R. F. and R. Plunkett, "Dynamic Stiffness and Damping of Fiber-Reinforced Composite Materials," Shock and Vibration Digest 9(2):9-18 (1977).

(8) Bert, C. W., "Composite Materials: A Survey of the Damping Capacity of Fiber Reinforced Composites," Proc. ASME Winter Annual Meeting, Chicago, IL, pp. 53-63 (16-21 November 1980).

(9) Zener, C., "Elasticity and Aeroelasticity of Metals", University of Chicago Press, Chicago (1952).

(10) Lazan, B. J., "Damping of Materials and Members in Structural Mechanics", Pergammon Press, New York (1968).

(11) De Batist, R., "Internal Friction of Structural Defects in Crystalline Solids", North Holland (1972).

(12) Norwick, A. S. and B. S. Berry, "An Elastic Relaxation in Crystalline Solids", Academic Press (1972).

(13) Beshers, D. N., "Techniques of Metals Research", Vol. VII, Part 2, R. F. Bunshan (Ed.), John Wiley & Sons, New York, pp. 529-707 (1976).

(14) Parker, B. A., "High Damping Structural Materials," Proc. Noise, Shock and Vibration Conference, Monash University, Melbourne, pp. 266-271 (1974).

(15) Baker, A. A., "The Fatigue of Fiber Reinforced Aluminum," J. Mat. Sci. 3(4):412-423 (1968).

(16) Varshavsky, A., "The Matrix Fatigue Behavior of Fiber Composite Subjected to Repeated Tensile Loads," J. Mat. Sci. 7(2):159-167 (1972).

(17) Weiss, H. J., "The Effect of Axial Residual Stresses on the Mechanical Behavior of Composites," J. Mat. Sci. 12(4):797-809 (1977).

(18) Ledbetter, H. M. and S. K. Datta, "Damping in Metal-Matrix Composites: Measurement and Modeling," Proc. Vibration Damping Workshop, Wright-Patterson Air Force Base, pp. 78-84 (1984).

(19) Hartman, J. T., Jr., K. H. Keene, R. J. Armstrong and A. Wolfenden, "Dislocation Density Determinations in Composites," Journal of Metals, pp. 33-35 (April 1986).

(20) Sample, R. J., R. B. Bhagat and M. F. Amateau, "High Pressure Squeeze Casting of Unidirectional Graphite Fiber Reinforced Aluminum Matrix Composites," Proc. International Symposium on Cast Metal Composites, 1988 World Materials Congress, Chicago, IL (in press).

(21) Eckstein, F. D., On the Specially Orthotropic Free-Free-Free-Free Square Plate in Resonance, Master's Thesis, Department of Engineering Science and Mechanics, The Pennsylvania State University (1986).
(22) Bhagat, R. B., M. F. Amateau and E. C. Smith, "Logarithmic Decrement Measurements on Mechanically Alloyed Aluminum and SiC Particulate Reinforced Aluminum Matrix Composites," Proc. International Symposium on Cast Metal Composites, 1988 World Materials Congress, Chicago, IL (in press).
(23) Pulgrano, L. J. and L. H. Miner, "Effect of Fiber and Resin on the Vibration Damping of Composites Reinforced with Fiberglass, Graphite and Aramid," Proc. 28th National SAMPE Symposium, pp. 56-64 (12-14 April 1983).
(24) Pulgrano, L. J. and L. H. Miner, "Vibration and Damping of Composites," Proc. 25th National SAMPE Symposium and Exhibition, pp. 557-575 (6-8 May 1980).
(25) Pompe, W. and B. Schultrich, "Zur Grenzschichtdampfung von Verbundwerkstoffen mit Kurzfasrigen Einlagerungen," Annalen der Physik 31(2):101-119 (1974).
(26) Raval, S. P., L. F. Allard and M. S. Misra, "Characterization of Interface Structure in Gr/Al and Gr/Mg Composites," ICCM-VI & ECCM 2, Vol. 2, Elsevier, New York, pp. 2.169-2.182 (1987).